

# DTIC FILE COPY

(2)

SECURITY CLASSIFICATION OF THIS PAGE

## REPORT DOCUMENTATION PAGE

1a REPORT SECURITY CLASSIFICATION Unclassified		1b RESTRICTIVE MARKINGS	
2a SECURITY CLASSIFICATION DEC 26 1990		3 DISTRIBUTION / AVAILABILITY OF REPORT See Distribution List	
2b DECLASSIFICATION / DOWNGRADING SCHEDULE		4 PERFORMING ORGANIZATION REPORT NUMBER(S) <b>AD-A230 024</b>	
5. MONITORING ORGANIZATION REPORT NUMBER(S) AFOSR-TR- 1168		6a NAME OF MONITORING ORGANIZATION AFOSR/NE	
6b OFFICE SYMBOL (If applicable)		7a ADDRESS (City, State, and ZIP Code) Bldg 410 Bolling AFB DC 20332-6448	
6c ADDRESS (City, State, and ZIP Code) Dept. of Metallurgical & Materials Science Carnegie Mellon University Pittsburgh, PA 15213		7b OFFICE SYMBOL (If applicable) NE	
9a NAME OF FUNDING / SPONSORING ORGANIZATION Air Force Ofs. of Sci. Res.		9b OFFICE SYMBOL (If applicable) NE	
9c ADDRESS (City, State, and ZIP Code) Bldg 410 Bolling AFB DC 20332-6448		10 SOURCE OF FUNDING NUMBERS	
PROGRAM ELEMENT NO. 61102F		PROJECT NO. 3484	
TASK NO. A3		WORK UNIT ACCESSION NO.	
11 TITLE (Include Security Classification) High-temperature Metal Matrix Composites			
12 PERSONAL AUTHOR(S) A.W. Thompson and those listed in table of contents			
13a TYPE OF REPORT Final Report		13b TIME COVERED FROM 10/1/86 TO 9/30/89	
14 DATE OF REPORT (Year, Month, Day) 1990 June 1		15 PAGE COUNT 370	
16 SUPPLEMENTARY NOTATION			

17 COSATI CODES			18 SUBJECT TERMS (Continue on reverse if necessary and identify by block number)
FIELD	GROUP	SUB-GROUP	

19 ABSTRACT (Continue on reverse if necessary and identify by block number)

The Final Report, incorporating Year 3 of the University Research Initiative grant at Carnegie Mellon University on High-temperature Metal Matrix Structural Composites contains sections on processing, characterization, and mechanical properties. These are further divided into reports from individual tasks on powder blending and consolidation, composite performance, structure and composition of composite interfaces, fatigue crack growth, creep, and fracture behavior. Detailed findings, together with listings of technical presentations and publications, are presented in the individual reports from the six tasks conducted under this Grant.

20 DISTRIBUTION / AVAILABILITY OF ABSTRACT <input checked="" type="checkbox"/> UNCLASSIFIED/UNLIMITED <input type="checkbox"/> SAME AS RPT <input type="checkbox"/> DTIC USERS		21 ABSTRACT SECURITY CLASSIFICATION Unclassified	
22a NAME OF RESPONSIBLE INDIVIDUAL A.W. Thompson-Rosenstein		22b TELEPHONE (Include Area Code) (202) 761-4933	
		22c OFFICE SYMBOL NE	

# **HIGH-TEMPERATURE METAL MATRIX COMPOSITES**

## **FINAL REPORT**

(incorporates Year 3)

**AIR FORCE OFFICE OF SCIENTIFIC RESEARCH  
Contract No. F49620-87-C-0017**

**October 1, 1986 - September 30, 1989**

**CARNEGIE MELLON UNIVERSITY  
Pittsburgh, PA 15213**

**Principal Investigator, A.W. Thompson**

**with**

**University of California, Berkeley  
Clemson University**

**June 1, 1990**

# TABLE OF CONTENTS

	Page
<b>SUMMARY</b>	<b>1</b>
<b>TECHNICAL PROGRESS REPORT</b>	
<b>PART 1, Processing</b>	<b>3</b>
<b>Task 1: "Blending of P/M Metal Matrix Composite Systems",</b> <b>J.O.G. Parent, J. Iyengar, J.H. Bytnar and H. Henein</b>	<b>7</b>
<b>"Deformation Processing of Composites", H.R. Piehler,</b> <b>D.M. Watkins, M. Kuhni and J. Richter</b>	<b>5 3</b>
<b>Task 2: "High Temperature Structural Materials", H.J. Rack</b>	<b>6 3</b>
<b>PART 2, Characterization</b>	<b>1 8 7</b>
<b>Task 3: "Interfacial Structure and Stability in Metal</b> <b>and Intermetallic Matrix Composites", J.M. Howe</b>	<b>1 8 9</b>
<b>PART 3, Properties and Performance</b>	<b>2 1 9</b>
<b>Task 4: "Toughness and Fatigue of Metal Matrix</b> <b>Composites", R.O. Ritchie and J.-K. Shang</b>	<b>2 2 3</b>
<b>Task 5: "Creep of High Temperature Composite</b> <b>Matrices", A.W. Thompson</b>	<b>2 8 1</b>
<b>Task 6: "Fracture and History Effects in Composites",</b> <b>D. Symons and W.M. Garrison</b>	<b>3 2 5</b>

[illegible]

## SUMMARY

This Final Report, incorporating the third Annual Report, for the University Research Initiative program at Carnegie Mellon University, including subcontracted research efforts at Clemson University and at the University of California (UC), Berkeley, contains technical summaries for each of six task areas. These are listed below by Task title and Task Investigator(s). The individual sections in the body of the report follow in this same order, and are grouped into three major parts, Processing (Tasks 1 and 2), Characterization (Task 3), and Properties and Performance (Tasks 4, 5 and 6). Task 2 was conducted at Clemson and Task 4 at UC Berkeley.

- Task 1. Processing of Composites. H. Henein, H.R. Piehler
- Task 2. High Temperature Behavior of Structural Composites. H.J. Rack
- Task 3. Structure and Composition of Interfaces in Composites. J.M. Howe
- Task 4. Toughness and Fatigue of Metal Matrix Composites. R.O. Ritchie
- Task 5. Creep of High Temperature Composite Matrices. A.W. Thompson
- Task 6. Fracture and History Effects in Composites. W.M. Garrison

The Processing part of the report comprises three reports. The first of these, by Henein and his co-investigators, addresses several issues in powder blending as a processing step for metal matrix composites. Emphasis in Henein's project was placed on fundamental understanding of the mechanisms of blending, with account being taken of powder characteristics and operating and design variables, toward a goal of using physical models to identify scale-up criteria in blending. Results were concentrated on spherical particle experiments, with successful definition and measurement of a segregation behavior diagram for binary mixtures. The second report, completing the summary for Task 1, is by Piehler and co-authors, on the subject of consolidation processing, as a natural complement to the first part of Task 1. The primary accomplishment has been achieving operational status for and preliminary results from the hot triaxial compaction apparatus, which can apply shear in addition to hydrostatic stresses. This equipment has impressive capabilities and has been described as unique in the United States. Among the early efforts was to test Ashby's hot isostatic pressing diagrams, and to extend them to the conditions of superimposed shear. Completing the Processing part is the Task 2 report, from H.J. Rack, addressing several topics related to consolidation and performance of metal matrix composites. A sub-task on interfacial modification for fiber reinforcements in metal matrix composites has yielded several important results, particularly for carbon fibers. Two other sub-tasks have addressed composite performance, one in titanium aluminides and the other in model systems, Inconel 718 reinforced with TiC particulates as well as Mg-6 Zn reinforced with SiC particles.

The Characterization part of the report, from J.M. Howe, had two objectives. The first was a study of residual strains in a model composite system, a SiC-whisker reinforced aluminum alloy. This work has been finished, and submitted for publication. The second objective was to continue work on the structure and the deformation behavior of interfaces in alloys based on TiAl and Ti<sub>3</sub>Al. Both the structure and the deformation response of  $\alpha_2/\gamma$  interfaces have been studied, and interesting results have been obtained for both ordered and disordered hcp/bcc interfaces. Of particular interest was the study of artifacts introduced as a function of crystal and beam tilt in simulated high-resolution TEM images, since avoidance of such artifacts is essential for reliable understanding of HRTEM images.



The Properties and Performance part of the report contains reports from three tasks. The first, from R.O. Ritchie, addresses micromechanisms of critical and sub-critical crack advance in composites. Work was been carried out in model composite systems with particulate reinforcement. At low fatigue crack growth rates, it was found that crack hindrance or trapping and roughness-induced crack closure occurred, resulting in lower growth rates than in unreinforced materials. At intermediate growth rates, the composite also showed improved crack growth resistance, now due to crack tip bridging, a behavior which was successfully modeled. The second report in this part, directed by A.W. Thompson, has the topic of creep and deformation of aluminide materials. Fairly complete reports on creep in the two  $\text{Ti}_3\text{Al}$ -based alloys, Ti-24 Al-11 Nb and Ti-25 Al-10 Nb-3 V-1 Mo, are included. It was found that microstructure of both alloys strongly influenced creep behavior, and that mechanistic evidence indicated dislocation-controlled creep, with an activation energy consistent with literature values. Both alloys, particularly Ti-25-10-3-1, were more creep resistant than near-alpha titanium alloys recently developed for creep performance. The third report in this part, by Garrison and Symons, discusses work on fracture and history effects. The work on history effects was on titanium aluminide ternary alloys including Ti-24 Al-11Nb. Mechanical properties and thermal stability of the microstructures obtainable in these alloys have been studied to provide guidance for additional work. A second study was conducted on a model system with SiC particulate reinforcement of an aluminum alloy matrix, examining details of the ductile fracture behavior of this material.

**PART 1**

**PROCESSING**

BLANK

## PROCESSING

The processing portion of the URI program on High-temperature Metal Matrix Composites has been accomplished in the form of two tasks. The first task was conducted at Carnegie Mellon University and had two parts, each with its own Investigator. The first part, under H. Henein, addressed powder blending, particularly as it affects consolidation issues. The second part was directed by H.R. Piehler and was concerned with deformation processing of composites, both for fiber and particulate reinforcements. The second task in the processing portion of the program was being carried out at Clemson University under the direction of H.J. Rack. Under a general task title of "Modeling of Consolidation and Deformation Processing of Composites", this task addressed several interrelated topics, as described on p. 63. These include modification of the interface of composite reinforcements for improved performance; a study of a series of Ti-Al-Nb-V and Ti-Al-V aluminide alloys for high-temperature properties; and the first part of a study of creep in a model composite, Inconel 718 reinforced with particulate TiC.

	<u>Page</u>
<b>Task 1: "Blending of P/M Metal Matrix Composite Systems",</b> J.O.G. Parent, J. Iyengar, J.H. Bytnar and H. Henein	7
 "Deformation Processing of Composites", H.R. Piehler, D.M. Watkins, M. Kuhn and J. Richter	53
<b>Task 2: "High Temperature Structural Materials",</b> H.J. Rack, H.G. Spencer, P. Chaudhury, J.P. Clement, M. Long, E. Wachtel, K.T. Wu and J. Wung	63

BLANK

# **TASK 1**

**Blending of P/M Metal-Matrix Composite Systems**

**Final Report**

## **Part I**

This report is composed of three parts. The first outlines the structure of the report and provides information on personnel and productivity during the course of the URI-AFOSR contract. Part II provides an in-depth review of the current state of the blending science as it applies to metal-matrix composites systems. The modelling studies undertaken in this task are described in Part III, along with the experimental facilities developed.

### **Personnel:**

J. Bytnar: Graduate Student, M. Eng. Candidate, February 1989 - September 1989.

J. Iyengar: Research Engineer (100%), January 1988 - January 1989.

M. Khuni: Research Engineer (25%), October 1986 - September 1989.

J.O.G. Parent: Graduate Student, PhD Candidate Oct 1986 - August 1989.

H. Henein: Principal Investigator of Blending Task.

### **Productivity:**

#### **Papers -**

J.O.G. Parent, J. Iyengar and H. Henein: "Powder Blending in Metal Matrix Composites Systems," Advances in Powder Metallurgy, T.G. Gasbarre and W.F. Jandeska, Eds., MPIF/APMI, New Jersey, 1989, v. 1, pp 25-37.

J.O.G. Parent, J. Iyengar and H. Henein: "A Review of Powder Blending in Metal Matrix Composites Systems," manuscript in preparation.

J. Bytnar, J.O.G. Parent, J. Iyengar and H. Henein: "Mapping Macro-Segregation Patterns for the Blending of Metal Matrix Composites," manuscript in preparation.

#### **Presentations -**

J.O.G. Parent, J. Iyengar and H. Henein: "Powder Blending in Metal Matrix Composites Systems," APMI Annual Meeting, San Diego, June 1989.

J.O.G. Parent, J. Iyengar and H. Henein: "Powder Blending in Metal-Matrix Composite Systems," TMS Annual Meeting, Las Vegas, February 1989.

H. Henein: "URI: Metal-Matrix Composites Program at C-MU", SOHIO Advanced Materials, Niagara Falls, NY, October 1986.

## **Part II**

### **A Review of the State-of-the-Art in Powder Blending for Metal-Matrix Composite Systems**

**J.O.G. Parent, J. Iyengar and H. Henein**

#### **Abstract**

In the manufacture of metal-matrix composites (MMC) via the P/M route, blending of matrix and reinforcement materials is a critical operation which has received little attention in P/M processing. Past investigations have generally focussed on studies of mixing in large-scale and uniform sized systems (particles with diameters in millimeter size range) and inferred segregation behavior of powders. Several workers, however, have investigated the segregation tendency of particles with different characteristics. It has been found that particle size ratio is the most important material variable. Scale-up parameters for segregation include size ratio, and Froude number (the ratio of inertial to gravitational forces). Another important conclusion is that in order to obtain a homogeneous mixture, the powder mass must be assessed for both macro- and micro-mixed states. Some preliminary experimental results have also shown that the type and pressure of gas in the blender can have a significant effect on the blending characteristics of a powder mixture.

#### **Introduction**

The need to achieve reproducible structure and properties in the processing of composite materials has prompted considerable interest in the materials research community. Several methods are available to produce such materials: liquid metal infiltration, powder metallurgy (P/M) processing, formation of composites from the melt and spray deposition techniques are but a few. Those techniques which use the liquid metal as a starting point seem to provide an inexpensive means of processing metal matrix composites (MMC's). In many cases, however, concerns about possible contamination of the matrix material while in the liquid form, as well as prohibitively high melting points make liquid metal techniques inappropriate. In such cases, the powder metallurgy route provides a better controlled means of forming the product. An overview of the P/M processing route is shown in Figure 1.

This approach has its inherent problems. The requirement of a uniform distribution of the reinforcement material is not always readily achieved. In P/M, the procedure generally entails a mixing stage (to achieve a preliminary blend of the matrix and reinforcement material), followed by a consolidation process involving prolonged exposure at high temperatures and possibly high pressures. While some redistribution of the constituent powders may occur during the consolidation step, it is in the mixing stage that the character of the composite will be determined, and it is this step which is the most critical.<sup>1</sup> As in the case of metal-matrix composite systems, mixtures that have two or more constituents possessing significantly different physical properties very often do not mix well, resulting in the formation of regions which have a higher proportion of one or the other constituent powder. In order to properly assess the effectiveness of a mixing operation, it is necessary to identify those operating and design variables which will give the best mixture as well as the means to scale-up the laboratory results. Although some work has been



done in large-scale systems to address this problem, little has been done to determine if the observed relationships will apply to powder systems, and especially to those systems of interest in metal-matrix applications.

There are a variety of mixer systems available for blending MMC powder. These range from V-blenders and ribbon blenders, where the mixing action is complicated and therefore not easily characterized, to the more simple geometry of the horizontal (and sometimes inclined) rotary blenders. Horizontal cylinders are most often used in basic research since the bed action is relatively uncomplicated and is easily controllable. Hence, fundamental mixing and segregation mechanisms can be controlled. As a result, this review will deal with this type of blender exclusively.

While there are hundreds of papers in the literature dealing with the mixing and segregation of particulates and powders, only a small fraction present results relevant to mixing MMC powders. Thus, this paper will focus on an analysis of the pertinent literature to MMC powder processing by blending. In particular the issues to be addressed are a definition of the various types of bed behavior encountered in horizontal rotary cylinders, an understanding of the mechanisms associated with the blending of MMC powder, the effect of powder characteristics, operating and design variables on the formation of a disperse-homogeneous MMC powder mixture, the development of the scale-up criteria for MMC powder blending, using physical modelling principles, and the effect of gas pressure on the blending operation.

### Bed Behavior

The shape of the bed, the type of bed motion occurring in a horizontal rotary cylinder and the attendant particulate flow patterns for cohesionless solids have been studied experimentally in some detail,<sup>2,3,4</sup> and have been mathematically modelled.<sup>5</sup> The bed motion has been found to be a function of the rotational speed of the cylinder being used, the amount of material present within the drum, the size of the cylinder being used, the static and dynamic angles of repose of the material as well as the particle size. Six specific types of bed motion have been identified, these being slipping, slumping, rolling, cascading, cataracting and centrifuging (see Figure 2).

At low rotational speeds or low Froude numbers (dimensionless ratio of inertial and gravitational forces,  $Fr = (w^2 R)/g = 1$ ), the bed may undergo slipping motion. This has been discussed to be composed of three different motions, depending on the specific value of the bed depth or per cent fill, the rotational speed within this regime and the bed wall friction angle.<sup>5</sup> First, the bed may move as a whole along with the cylinder as it rotates. At the point where the frictional forces along the wall are exceeded (the maximum angle of repose), the entire bed slides down the wall and comes to rest at an angle less than the static angle, from which point the process is repeated. Second, the bed may move with the wall but at a lower rotational speed, with the solids rolling slowly along the free surface of the bed. Finally, the bed may adopt a particular position along the cylinder wall where it is observed to slide continuously. Since slipping results in little relative motion between the particulates, this type of bed motion is undesirable as it results in little mixing.

For higher bed/wall friction and low rpms, motion of the bed would be a slumping mode. This is characterized by the bed moving up with the wall to the static angle of repose, at which point a wedge of solids separates from the bulk of the bed and rolls down the bed surface, resulting in a reduced angle of repose. The process then repeats itself in a regular manner, the slumping frequency being dependent upon the rotational speed of the cylinder, the physical properties of the material and the cylinder diameter.<sup>3</sup>

Further increases in speed results in a transition to the rolling mode. The bed in this phase of motion is characterized by the continuous motion of the solids over the bed surface. At low rotational speeds, the bed has a flat surface and adopts a constant angle of inclination, known as the dynamic angle of repose. At higher speeds the solids in the upper corner of the bed ride farther up the cylinder wall before detaching, resulting in a kidney-shaped bed cross-section. At this point the bed is said to be in a cascading mode. It is this mode which is generally associated with the best mixing, as the particulates are subjected to the maximum shearing action within the bed.<sup>6</sup>

Increasing the speed past the cascading regime results in cataracting. In this mode the solids detach themselves completely from the wall at the top of the travel. They are then flung through the freeboard of the cylinder, landing on the surface of the bed at some point near the bottom of the bed. Finally, at the point where the inertial forces imparted by the rotation balance the gravitational forces experienced by the bed (the critical speed, with the Froude number,  $Fr = 1$ ) centrifuging begins. As in the case of the slipping mode, very little mixing occurs due to the fact that there is no relative particle motion in this mode.

It has been clearly shown that the scale-up parameters for bed motion are the Froude number (ie. the ratio of inertial to gravitational forces), the percent fill of the cylinder, the static and dynamic angles of repose and the particle size.<sup>6</sup> If the same uniformly sized material is placed in cylinders having different diameters and rotated at different RPMs, the same bed motion will be observed at the same Froude number and percent fill.

For the bulk of mixing operations, the useful range of motion exists between the rolling and cascading modes. As will be discussed later, segregation can occur in rolling and cataracting beds where differences exist in the physical properties of the materials. Furthermore, it is important to note that the extent of the regions of the various bed motions changes with the composition of the bed.<sup>7</sup> At a given RPM, the presence of segregation can therefore change both the motion of the bed as well as the degree and effectiveness of the mixing operation. In order to determine optimum mixing conditions, it is not sufficient to observe bed motion with particles of uniform properties or characteristics (ie. size, shape and density). In order to understand the effect of the bed motion on the segregative behavior of a mixture, the range of motion in the system must be analyzed for the bed compositions which will be used in segregation studies. However, it would be expected that the scale-up parameters of bed motion for a bed with uniform material properties will also play a role in the bed motion of solids with a range of properties (ie. size, shape and density).

It should be mentioned here that in all cases (except perhaps the centrifuging mode) the flow patterns in the bed may be divided into three separate regions.<sup>2,8,9,10</sup> This is shown pictorially in Figure 3. In the passive region, very little particle motion is observed, and material is transported through this region without changing its position in the bed. The active region of the bed (the "active layer" or "shear layer") comprises a small portion of the bed, usually only a few particle dimensions in thickness. It is in this region that the bulk of the mixing and segregation action occurs, especially at lower rpm's. As will be seen later, the interaction in this layer between particles, voids and even the mixer account for the redistribution of material observed. In some cases (for beds with greater than 50% fill<sup>10</sup>), a "dead-" or "zero-velocity" zone can occur in the bed. Particles which find their way into this area remain trapped here and are removed from further interaction with the remainder of the bed. This zone is of special importance in systems showing segregative behavior, but can also occur in "ideal" systems for certain combinations of the operating parameters.

## Mixing

Early work focussed on a determination of the fundamental mechanisms responsible for the mixing action observed in all types of mixers. Lacey was perhaps the first to directly state the mechanisms involved in mixing.<sup>8</sup> These are:

1. **Diffusive** - This involves the redistribution of particles due to their random motion.
2. **Convection** - Motion of groups of particles from one location in the solids mass to another.
3. **Shear** - This mechanism occurs when shear planes are formed or occur within the particulate bodies.

In particular, Lacey asserted that in the case of mixing of mono-sized particles in a drum mixer, diffusion was the dominant mechanism in mixing. Diffusive mixing was accomplished by the random scattering of particles over the surface of the bed, and thus the mixing planes were restricted to the surface layers of the bed. It should be noted that this diffusive mixing mechanism was applied to the axial mixing of similar particles. The presence of diffusion as a mixing mechanism has been supported by additional workers,<sup>9,11,12,13</sup> but the contribution of additional mechanisms are worth examining in more detail.

Donald and Roseman<sup>12</sup> studied both the axial and radial mixing characteristics of drum mixers. They found that mixing in the radial direction occurred as a result of changes in the path of circulation of particles in the bed. This can be understood in terms of the regions identified in Figure 3. They postulated that the particles travelling through the active layers in the bed will fall into voids of the next layer down. When the particle is carried into the passive layer, it should not change its position relative to the mass, and any change in the radial direction should then occur only if the particle travels a different path in the active layers and thus gets trapped at a different position in the passive layer than it occupied originally. The opening of voids and subsequent trapping of the particles in the passive layers was explained to be a result of differences in the velocity between the two bed regions. It was found that mixing was optimized for intermediate values of the operating speed, and that the mixing time was decreased for increased percent fill, showing no variation with the particle size (for beds composed of mono-sized particles). For axial mixing, they separate the bed into two regions. Away from the end walls of the cylinder, mixing was found to proceed slowly and thus thought to be a result of diffusive processes only. Near the end walls, however, axial mixing was accelerated due to the presence of steep velocity gradients.

Later work by Rutgers<sup>4,14</sup> also considered both axial and radial mixing. The best radial mixing for beds composed of a single particle size was found to occur at speeds ranging between the rolling and cataracting modes. For longitudinal mixing, he again supported the concept that it is the result of random deflections at the surface, with the rate of axial mixing increasing with decreases in the particle size.

Later Cahn and co-workers,<sup>9</sup> again using systems in which the beds were composed of particles with similar physical properties, confirmed the presence of the diffusive mechanism as the mixing mechanism predominating for axial mixing. Again the action was limited to the active layers in the bed (and more specifically the surface of the bed), with diffusion resulting from an axial component to the motion of the particles across the surface coupled with trapping of the particles in voids in the underlying active layers. Subsequent work<sup>11</sup> led to the inclusion of particle-mixer collisions as a contribution to the diffusive mechanism, and efforts to develop a probabilistic model of the particle motion led to reasonable estimates of the 'diffusion' coefficient. Diffusion was found to depend on both the load in the cylinder and the speed of operation.

Work by Hogg et al.<sup>13</sup> and Hogg and Fuerstenau<sup>15</sup> continued to examine the role of diffusion in mixing in rotary cylinders. Hogg et al.<sup>13</sup> refined the diffusion model for axial mixing to include the effect of the presence of the cylinder ends for long mixing times. The modification comes in as a different solution to the diffusion equation for long and short times. For short times the mixing goes as  $N^{1/2}$  (where  $N$  is the number of revolutions), whereas as at long times the mixing proceeds as  $\exp(N)$ . As in the case of the works of Cahn and Lacey, the mixing proceeds as the movement of a planar diffusional front along the axial direction. Radial mixing was considered in the later work.<sup>15</sup> Hogg and Fuerstenau proposed that the shear mechanism of Lacey is actually a combination of the convective and diffusive mechanisms. In this case, the mixing of material in the radial direction occurs as a result of the interchange of particles between different circulation paths in the bed, and as this exchange is random, it must then be "diffusive". The convective component to the mixing process comes in as a means of reducing the distance over which the diffusion occurs. This results in a striated structure to the bed across the cross-section, with the thickness of the striations decreasing with increasing number of rotations. The convective component was thought to arise from differences in the residence time of particles at different radial positions in the bed. The limitation to this work, however, is that it applies only to the limited "ideal" systems which have been studied. A significant point raised by Hogg in this work, however, is the importance of the considering both macro- and micromixing, i.e., the difference between the combining of separate components into an apparently well-mixed bed (macromixing) and the short range mixing required between regions rich in one component to regions rich in another. As will be seen in the next section, this has important consequences in P/M MMC applications where the microscopic distribution determines the properties of the final consolidated product.

More recent developments have begun to cast some doubt on the validity of the diffusion mechanism as a means of explaining the observed mixing phenomena. Bridgwater<sup>15</sup> contends that the diffusive process may actually be a purely convective process which, due to the probabilistic nature of the mixing process appears to be diffusive. Also, Bridgwater indicated that some redistribution of the particles may occur at a particle to particle (or 'micro-') level in the passive region of the bed, and that this redistribution is likely not a result of any diffusive process. Later work by Scott and Bridgwater<sup>16</sup> proposed a different mechanism for mixing to occur to account for this micro-distribution. They envisage the bed as a series of "convective blocks" surrounded by failure zones. These convective blocks account for macroscopic movement of the particulate materials, whereas mixing at the microscopic level would occur as a result of interparticle percolation. They predict that this mechanism would become important for particle sizes greater than 30mm, and be commonplace for mixtures with particle sizes greater than 100 mm. Their work indicated that the application of strain to the shear zones, resulting in expansion of the bulk is sufficient to allow particles to pass through voids between other particles, thus allowing percolation to proceed. The rate of mixing due to this mechanism depended on the amount of strain imposed on the material and the relative volumes of the constituent particles (the density having been found to be unimportant).

It is important to realize the previously mentioned studies represent only a small portion of the available literature on mixing, much work having been done to evaluate the efficiency of industrial systems and alternative mixers. It is also notable that in all of the cases, the bulk of the work was performed on systems in which the particles showed no significant differences in physical properties (size, shape, density, etc.) and thus are limited in their usefulness to the understanding of real systems where such ideality in the particle properties rarely exists. The discussions above have focussed on some of the more important studies looking at the fundamentals of the mixing process, especially that applied to rotating cylinder mixers. These studies clearly outline the mechanisms by which particles flow in mixers. In systems with tendencies for segregation, the mixing mechanisms described above will still be present. The extent to which they will contribute

to the final state of the mixture will depend on the segregative tendencies of the mixture. It is thus important to study the literature dealing specifically with non-ideal systems. This is done in the following section.

## Segregation

### Effect of Variables

Detailed investigations into the mixing properties of beds containing particles of non-uniform physical properties originated in the sixties with the work of Donald and Roseman<sup>12,17</sup> and Campbell and Bauer<sup>2</sup>. Donald and Roseman reported the formation of segregated regions in the bed of a rotating cylinder for cases where significant differences in the physical properties of the constituent particles existed. In their case, they considered only differences in either the size or density of the materials used. They found that segregation could occur in both the axial and the radial directions, and that the final shape of the segregated regions depended on the static angle of repose of the materials being used. For the case where the segregating material (the smaller or denser material) has the lower angle of repose, and considering a situation where there are negligible end effects, a segregation core forms along the length of the cylinder at some point below the active layer of the bed (see Figure 4(a)). When end effects become important, such as in the case of increased speed and/or rough walls, the core at the ends of the cylinder become unstable and small regions of banding perpendicular to the cylinder axis may form at the ends, as shown in Figure 4(b). Finally, for the case where the segregating material has the higher static angle of repose, the bed will form only bands along the length of the cylinder (Figure 4(c)). Their explanation for these effects lies with the fact that changes in the angle of repose will affect the velocity which the material sees as it travels down the surface. For low angles of repose, the material will have a low velocity along the surface, and thus the chances that it can drop through the active layers without being scattered axially increases, and thus the radial segregation core may be formed.

Donald and Roseman also investigated the role of material and process variables on the segregation phenomenon. They found that for density and size ratios greater than 1.2, segregation occurred rapidly and the final form of the mixed bed was one of the configurations explained above. Contrary to some of the ideas of Rose,<sup>18</sup> Donald and Roseman also found that the formation of the segregated regions did not depend on the initial position of the components. Also, they determined that the rate at which segregation occurs decreases with increasing percent fines (for particles differing in size) and would be slowest for equal volumes of coarse and fine particles. This was due to a decrease in the number of free voids available for the smaller particles to fall into. Finally, they observed that the shape of the material had apparently little effect on the segregative behavior when compared to size and density differences. It isn't clear what actual size of materials was used in this study, however, it will be seen later that shape effects can be important for fine materials (i.e. powders).

Campbell and Bauer<sup>2</sup> extended some of these concepts to examine the effect of changes in the particle shape on the segregative behavior. They confirmed the ideas of Donald and Roseman that the degree of segregation encountered depends on the size ratio of the particles being mixed. They expressed their observations, though, as the volume ratio of the particles being mixed. In considering the effect of changes from spherical particles to needle-like particles, they used the weight of individual particles to determine an equivalent spherical volume for the acicular materials. They then found that for mixtures of acicular and spherical particles, segregation was minimized for those cases where the equivalent spherical volume was equal to the volume of the spherical particles. Thus the volume of the particles was found to be the determining factor in, segregation, rather than the shape.

Also, Campbell and Bauer determined that the density differences were minor when compared to differences in the volume of the materials being mixed. This was, however, for a density ratio of only 1.26, which is very near the limit stated by Donald and Roseman for the density to have an effect on the segregation.

Later work by Ullrich<sup>19</sup> considered that two segregative tendencies would dominate, that due to size differences and that due to density differences. Using steel and glass balls, he determined that a segregated core formed along the cylinder axis, composed of the finer (or denser) material. The experiments were restricted to consider the effect of changes in the size ratio and operating speed (expressed as  $w^2R/g$ ) only (although no effect of changes in the drum speed were reported). He was able to show that to some extent the tendency to form a segregated core can be minimized by making the denser particle larger than the finer. For a size ratio of denser:finer of 1.4:1, segregation was minimized. He also pointed out, however, that at the point of minimum segregation, the mixture could not be considered to be stochastically well-mixed. This implies that elimination of segregation is likely to be very difficult, and that macroscopically well-mixed beds may still show significant segregation at the microscopic level.

Rogers and Clements<sup>20</sup> looked at the effect of the rotational speed in more detail, for mixtures of coarse granular materials (500-600 mm). For low rpms and short operating times, a segregated core was observed along the length of the mixer. As the operation time was increased, the fines were seen to move towards the ends of the mixer, resulting in large cores at the ends of the mixer, and a fines-depleted region in the center. Increases in the rpm led to more band formation, with the number of bands increasing for increasing rpm. The percent fines was observed to affect the size of the bands formed, but only at higher rpm. Rogers and Clements also noted that even for systems with similar physical properties between the particles, segregation can still occur, despite the fact that the bed may appear to be visually homogeneous. This again implies that segregation on a microscopic scale is important.

This last point was borne out by the work of Sauer.<sup>21,22</sup> Using iron and copper powders in size ranges typical to powder metallurgy applications (~60 - 200 mm), Sauer was able to look at the effect of particle properties on mixing at both the macroscopic and microscopic level. Sauer deduced that macroscopic segregation in these systems occurred for both differences in density as well as differences in size, primarily due to changes in the kinetic behavior of the particles resulting from differences in the mass of the individual particles. Sauer also credits part of the segregation resulting from size differences to the fact that the smaller particles may fall into voids in the charge. Again segregation was seen to increase with increases in the size ratio, and size variations accounted for more of the observed segregation than did the variations in density. Sauer also showed, however, that the shape of the particles affected the mixing and segregation processes in these materials. Increased surface interference between irregular particles was found to reduce the rate at which segregation occurred, and this effect increased with decreases in the overall particle size due to the attendant increase in the surface area. At the microscopic level, it was found that the size ratio had qualitatively the same effect as in the macroscopic case. In this case, however, the absolute size and shape of the particles determined more critically the distribution observed. Sauer found that as the particle size decreased, the distribution became worse, but that this could be minimized somewhat by the addition of an appropriate mixing additive. Also, it was shown that if even one of the components of the bed had an irregular shape, good mixing at the microscopic level was not achieved. This obviously has important consequences for MMC applications, where the reinforcement phase is not likely to be spherical with a smooth surface.

## Segregation Mechanisms

To this point little has been said as to the mechanisms governing the segregation process. Most of the above work relied on traditional interpretations of the phenomena governing the motion of the particles (i.e. the motion being governed by convective and diffusive mechanisms). Williams asserts, however, that in segregative processes, different mechanisms govern the motion of the particles<sup>23</sup>. He states more formally that segregation can result from four factors, these being:

- differences in particle size
- differences in particle density
- differences in particle shape
- variations in particle resilience

In these cases the motion of the particles will be governed by the following mechanisms:

**1. Trajectory or flow segregation** - in which segregation occurs due to differences in the distance over which the particles travel on the surface of the bed.

**2. Percolation** - as described in the section on mixing, this involves the motion of particles through voids in the bed. This mechanism has been alluded to in the previous work on segregation, though never formally addressed as a mechanism for the segregation.

**3. Vibration** - in which motion of particles through the bed occurs due to variations in the bed voidage resulting from externally imposed vibrations. This mechanism is of little importance in rotary cylinders.

The role of the first two mechanisms has been addressed in very few studies. The most notable involve the work of Henein et al.<sup>7</sup> and Nityanand et al.<sup>6</sup> In examining the segregation behavior of a model rotary kiln system, Henein et al. found that segregation occurred both axially and radially, and in particular, for bed motions in the slumping and rolling regimes. The segregated core was found to have the same general shape as the bed, and lay at some point below the active layer, though usually in the top half of the bed. Based upon their observations of the formation of the core, they postulated that it could not have formed as a result of any convective or diffusive process, and proposed that the percolation mechanism was primarily responsible for the segregation process. They also allowed for some contribution of the trajectory mechanism, though considered it to be of minor importance. This experimental work was conducted on irregular shaped solids.

In the work of Nityanand et al.<sup>6</sup> the goal was to determine the rate at which segregation proceeded, and to see if percolation was indeed responsible for the formation of the segregated core. Using spherical plastic beads, the observations of Henein et al. as to the shape and location of the bed were confirmed for a more general case. Segregation was again found to occur for slumping and rolling beds, and for rolling beds the segregated core was located just below the active layer. Direct measurement of the formation of the core indicated that formation of the core followed zero order kinetics, with the kinetics a linear function of the rotational speed, and independent of the percent fill and bed depth. This is not consistent with either a diffusive or convective mechanism, and direct observation of the bed confirmed that the fines reported to the core by means of percolation. The presence of flow segregation could not be discounted, however, since the number of coarse particles present in the core was less than was expected by maximum packing of the mixture. Since percolation cannot account for the removal of coarse particles from the core, flow segregation must still be operative. The rate of segregation increased with increasing size ratio, and also increased with increases in the size of the cylinder. This led to the development of

the size ratio and the dimensionless speed  $w^2R/g$  as scale-up criteria for segregation phenomena. This should allow comparison of results of macromixing investigations of powder systems to these larger systems to determine whether percolation dominates for the smaller systems, and also to determine the relative importance of additional effects such as the shape differences and increased surface area.

### Effect of Gas Atmosphere

Recent work has indicated that a complete analysis of powder operations requires an understanding of the interaction between the gas atmosphere in the apparatus of interest and the powders. This interaction depends not only on the properties and state of the gas (i.e., gas viscosity  $\mu$  and pressure), but also on the properties of the powders involved (powder density and particle size) and the typical operating speed of the apparatus itself. In essence, the effect of the gas atmosphere is to change the state of fluidization of the powder bed, thus altering the flow characteristics and properties of the powder bed.

In determining the extent to which the gas has an effect of the flow properties of the bed, Rietema<sup>24</sup> considered the hydrodynamic interactions between the gas and the powder mass. He reasoned that in cases where the typical velocity of the powder-handling apparatus exceeded the rate at which the entrapped gas could escape the bed, the powder would remain fluidized and in an expanded state. The removal of the gas from the bed can be followed as the movement of a "continuity shock wave", above which the porosity of the bed is that of the expanded state, and below which the porosity is that of the settled bed,  $\epsilon_0$ . The velocity of the shock wave is given by the expression

$$V_{CS} = \frac{\rho_d d_p^2 g}{150 \mu} \frac{\epsilon^3}{(\epsilon - \epsilon_0)} \quad \dots(1)$$

In this expression,  $\rho_d$  = the powder density,  $d_p$  = the powder particle size,  $g$  = gravitational acceleration,  $\mu$  = the gas viscosity and  $\epsilon$  = the porosity in the fluidized portion of the bed. For a typical powder handling speed  $V_a$ , the bed can be expected to remain fluidized for conditions where  $V_a \gg V_{CS}$ . Rietema then uses this condition to arrive at an expression for predicting the influence of a gas atmosphere, the so-called Gas Interaction Number,  $N_I$ . The expression for this number is:

$$N_I = \frac{\rho_d d_p g}{\mu V_a} \ll 100 \quad \dots(2)$$

The physical significance of  $N_I$  is as follows: for values of the gas interaction number less than 100, the gas atmosphere will remain trapped in the powder mass. This effect increases for decreasing values of the gas interaction number, i.e., the lower the value of  $N_I$ , the greater the influence of the gas. From the form of the equation, it can be seen that low values of  $N_I$  can be achieved for large values of both the gas viscosity and the powder-handling apparatus speed. The effect of the speed of the apparatus can be readily understood, as it arises from the derivation of the expression. If the speed of the apparatus is low, the  $V_a$  will be less than  $V_{CS}$  and the gas will be able to leave the powder mass. The porosity of the powder bed will remain close to  $\epsilon_0$  and there will appear to be no gas effect. As  $V_a$  increases and becomes larger than  $V_{CS}$  the gas will remain



trapped in the bed. The pressure exerted by this entrapped gas will then cause the powder bed to expand, and the bed will thus flow more readily.

The influence of the viscosity of the gas can be explained in the following manner. For increases in the gas viscosity, the momentum exchange between the gas molecules is large. This results in increased force on the powder particles, and thus the observed increase in the interaction between the gas atmosphere and the powder mass. As the viscosity decreases the mean free path,  $\lambda$ , increases and the number of gas molecule collisions decreases. This results in a lower rate of momentum transfer, and thus a decreased interaction between the gas and the powder. For low values of  $m$  and  $V_a$ , then, the bed will be collapsed and relatively static, as compared to its free flowing behavior for large values of these two variables. The effect of changes in both the viscosity and the speed can be seen graphically in Figure 5. The values of the variables used are shown in Table 1N1Vadat, and correspond to quantities which might be encountered in metal-matrix composite applications. It can be seen that the value of  $N_I$  remains well below 100 even for relatively high speeds and low viscosities. The effect of variations in the particle size can be seen in Figure 6. The increasing viscosity here corresponds to the same range as the previous figure (see Table 2 for the values used). It can be seen clearly in this case that changes in the rotational speed have a significant effect on the gas interaction behavior. It is apparent that at low rpms, the bed will be fluidized for small particles only. As the rotational speed is increased, the fluidizing effect of the atmosphere is extended to include the larger particles. For a rotational speed of 100 rpm (which is a reasonable number for the cascading regime in these blenders) it can be seen that, for a system with all particles less than 100  $\mu\text{m}$  the entire bed will be fluidized. Thus it is expected that the kinetics of mixing in this regime will be enhanced for all the particles in the system. At the lower speeds, where segregation is usually a problem, it appears that the smaller reinforcement particles could be fluidized, but that the larger matrix particles would not. This could have some as-yet unknown and interesting effects on the nature and extent of segregation observed.

It is reasonable to assume that the pressure of the gas will also have some effect on the behavior of the powder bed. It is not apparent from the previous expressions, however, how the changes in the pressure should affect the bed behavior. If one were to assume that the viscosity in Rietema's expression is the absolute viscosity, then its value would change very little with pressure, and the gas interaction number could not be used to predict the influence of the atmosphere for changes in the pressure. In a later paper, however, Cottaar and Rietema<sup>25</sup> did consider the effect of a change in the pressure. They looked at two cases: first, the case where  $l$  is much smaller than some critical dimension  $R$  (for powder masses, this would correspond to the size of the interparticle voids); and secondly, the case where  $\lambda > R$ . They develop their arguments based on considerations of the force  $F$  exerted by a flowing gas at speed  $U$  on a tube of length  $L$  and radius  $R$ .

The first case corresponds to the case of viscous flow in the tube. In this case the result can be readily obtained from fluid mechanics with the result that

$$\frac{F}{L} = 8 \pi \mu_1 U \quad \dots(3)$$

Here  $\mu_1$  corresponds to the viscosity of the gas at high pressure. As mentioned, this is for the case of  $\lambda \ll R$ , and thus an expression for the gas viscosity can be obtained from the kinetic gas law, based on the assumption that the viscous forces will arise predominantly from momentum exchange between the gas molecules and not from interactions between the gas and the tube walls. In this case the expression for the viscosity is

$$\mu_1 = \frac{1}{2} \rho \lambda v_t \quad \dots(4)$$

where  $\rho$  is the gas density and  $v_t$  is the thermal velocity of the gas molecules (i.e., the actual velocity of the gas molecules for the temperature at which the gas is held). The quantity  $\rho\lambda$  is independent of pressure and thus the viscosity at high pressures remains at a relatively constant value.

For the case of gases at low pressure (and thus large  $\lambda$ ), Cottaar and Rietema consider the situation as one representing free molecular flow. The momentum exchange of one molecule is thus considered. For molecules of mass  $M$ , and assuming that the wall and molecules are in thermal equilibrium so that the momentum exchange due to thermal velocity is on average zero, the net momentum exchange for the molecule will be  $MU$ , where  $U$  is again the gas flow velocity. Since the gas molecule will on average travel over a maximum distance of  $R$  between collisions, the total number of effective collisions becomes  $L/R$  and the total force per unit length becomes

$$\frac{F}{L} = \pi \rho U^2 R \quad \dots(5)$$

From this a new expression for an apparent viscosity  $\mu_2$  was obtained, given as

$$\mu_2 = \frac{1}{8} \rho R U \quad \dots(6)$$

Thus the effect of gas pressure can be seen as a modification of the value of the viscosity. This effect is two-fold. First, the distance that a molecule travels changes from the value of  $\lambda$  for the particular conditions experienced by the gas, to the size of the opening through which the gas is forced to pass. Secondly, the velocity at which the gas moves decreases from the value of the thermal velocity to the value of  $U$ , which is typically several orders of magnitude smaller than the thermal velocity<sup>25</sup>. Thus, as the pressure of the gas is decreased, the apparent viscosity of the gas is reduced. In terms of its effect on the gas interaction number, then, as the pressure of the gas decreases, the value of  $N_I$  will increase. This indicates that the effect of pressure is similar to that of viscosity: for beds that show fluidized behavior, the extent of fluidization and thus the ease of flow of the powder mass decreases with decreasing pressure (and decreasing apparent viscosity). An additional point is that since the value of the apparent viscosity is a function of  $R$ , and  $R$  is of the order of the interparticle spacing, the particle size has a role in determining the value of the interaction number directly (due to its presence in the expression for  $N_I$  and indirectly, inasmuch as it changes the value of the apparent viscosity).

Experiments have been performed to determine how changes in the gas atmosphere affect the performance of ball milling<sup>25,26,27,28</sup> and mixing<sup>29</sup> operations. The behavior predicted by the gas interaction number was found to be observed in all cases, i.e., for high values of either the gas pressure or the gas viscosity, and thus low values of  $N_I$  the beds were observed to be very fluid, with good intermixing of the powders in the bed. For the studies on milling operations, it was found that the rate of breakage of the product increased with increases in pressure and  $\mu$ . The

uniformity of the end product increased, with less fines being produced, and the number of agglomerates formed during the milling operation decreased. Thus for the case of milling, improvements in both the quality and efficiency of the operation can be achieved with the use of either highly viscous gases or high gas pressures.

In the mixing studies, systems of similar particles (differing only in color) and systems showing segregative behavior were considered. In the first case, using variance as a measure of the progress of the mixing operation, it was found that an increase in the powder mobility (again, due to increases in either the pressure or the viscosity) resulted in increases in the diffusion coefficient (i.e., the rate at which random movement of the particles occurs) of the process, as well as decreases in the variance in the sample. Since the mixture of similar particles is a random process, this improvement in the mixing process is a reasonable one. In the case where the samples showed a tendency to segregate during mixing, it has found that the opposite conditions were beneficial, i.e., low gas pressures and low viscosities resulted in a decrease in the mobility of the powders and thus reduced the tendency towards segregative behavior. Again the improvements were demonstrated by a decrease in the variance of the measured samples of the mixtures considered. In terms of the gas interaction number, then, high values of  $N_I$  will be beneficial in reducing the extent of segregation observed in those systems predisposed to its occurrence, whereas low values of  $N_I$  will benefit those operations which rely on increases in the rate of occurrence of random particle movements (pure mixing).

### Summary

It is obvious from the discussion above that a complete assessment of the success of a blending operation is a difficult task. Identification of the dominant mode of particle movement can be expected to be obscured by overlying observations of segregation when materials of differing physical properties are involved. The situation is further complicated by the role of the circumambient gas in the drum, which can markedly alter the kinematics of the bed motion, and thus the degree of mixing and segregation which occurs. Also, the conditions which can lead to apparently good macromixing will not necessarily lead to a proper microdistribution of the components, which is of great importance in creating a suitable final product for composite applications. The benefits of the previous work on large scale materials, however, is in providing a framework from which to begin an analysis of mixing using fine powder materials. The concept of similarity may also allow an identification of the contribution from additional small particle forces (van der Waals, electrostatic, etc.) in the event that the dynamics and mechanisms of mixing and segregation are found to be comparable in the case of small versus large particles.

### References

1. T.C. Willis: "Spray Deposition Process for Metal Matrix Composites Manufacture", *Metals and Materials*, August 1988, pp 485-488.
2. Campbell H., and Bauer W.C.: "Cause and Cure of Demixing in Solid-Solid Mixers," *Chemical Engineering*, Vol. 73(19), 1966, pp 179-185.
3. Henein H., Brimacombe J.K., and Watkinson A.P.: "Experimental Study of Transverse Bed Motion in Rotary Kilns," *Metallurgical Transactions B*, Vol 14B, 1983, pp 191-205.
4. Rutgers R.: "Longitudinal Mixing of Granular Material Flowing Through a Rotating Cylinder: Part 1. Descriptive and Theoretical," *Chemical Engineering Science*, Vol 20, 1965, pp 1079-1087.
5. Henein H., Brimacombe J.K., and Watkinson A.P.: "The Modeling of Transverse Motion in Rotary Kilns," *Metallurgical Transactions B*, Vol 14B", 1983, pp 207-220.
6. Nityanand N., Manley B., and Henein H.: "An Analysis of Radial Segregation for Different Sized Spherical Solids in Rotary Cylinders," *Metallurgical Transactions B*, Vol 17B, 1986, pp 247-257.
7. Henein H., Brimacombe J.K., and Watkinson A.P.: "An Experimental Study of Segregation in Rotary Kilns," *Metallurgical Transactions B*, Vol 16B, 1985, pp 763-774.
8. Lacey P.M.C.: "Developments in the Theory of Particle Mixing," *Journal of Applied Chemistry*, Vol 4, 1954, pp 257-268.
9. Cahn D.S., Fuerstenau D.W., Healy T.W., Hogg R., and Rose H.E.: "Diffusional Mechanism of Solid-Solid Mixing," *Nature*, Vol 209, 1966, pp 494-496.
10. Hogg R., and Fuerstenau D.W.: "Transverse Mixing in Rotary Cylinders," *Powder Technology*, Vol 6, 1972, pp 139-148.
11. Cahn D.S., and Fuerstenau D.W.: "A Probabilistic Model of the Diffusional Mixing of Particulate Solids," *Powder Technology*, Vol 2, 1968, pp 215-222.
12. Donald M.B., and Roseman B.: "Mixing and De-Mixing of Solid Particles: Part 1. Mechanisms of Mixing in a Horizontal Drum Mixer," *British Chemical Engineering*, Vol 7(10), 1962, pp 749-753.
13. Hogg R., Cahn D.S., Healy T.W., and Fuerstenau D.W.: "Diffusional Mixing in an Ideal System," *Chemical Engineering Science*, Vol 21, 1966, pp 1025-1038.
14. Rutgers R.: "Longitudinal Mixing of Granular Material Flowing Through a Rotating Cylinder: Part 2. Experimental," *Chemical Engineering Science*, Vol 20, 1965, pp 1089-1100.

15. Bridgwater J.: "Fundamental Powder Mixing Mechanisms," Powder Technology, Vol 15, 1976, pp 215-236.
16. Scott A.M., and Bridgwater J.: "Interparticle Percolation: A Fundamental Solids Mixing Mechanism," Industrial and Engineering Chemistry - Fundamentals, Vol 14(1), 1975, pp 22-27.
17. Roseman B., and Donald M.B.: "Mixing and De-Mixing of Solid Particles: Part 2. Effects of Varying the Operating Conditions of a Horizontal Drum Mixer," British Chemical Engineering, Vol 7(11), 1962, pp 823-827.
18. Rose H.E.: "A Suggested Equation Relating to the Mixing of Powders and its Application to the Study of the Performance of Certain Types of Machines," Transactions of the Institution of Chemical Engineers, Vol 37, 1959, pp 47-64.
19. Ullrich M.: "Entmischungserscheinungen in Kugelschuttungen (translation on hand)," Chemie-Ingenieur Technik, Vol 41(16), 1969, pp 903-907.
20. Rogers A.R., and Clements J.A.: "The Examination of Segregation of Granular Materials in a Tumbling Mixer," Powder Technology, Vol 5, 1971, pp 167-178.
21. Sauer C. von.: "Mischungs- und Entmischungsprobleme bei Metallpulvern. Teil 1: Verhalten von Metallpulvern beim Mischprozeß - Makroverteilung der Komponenten (translation on hand)," Neue Hutte, Vol 17(6), 1972, pp 358-362.
22. Sauer C. von.: "Mischungs- und Entmischungsprobleme bei Metallpulvern Teil 2: Verhalten von Metallpulvern beim Mischprozeß - Mikroverteilung der Komponenten (translation on hand)," Neue Hutte, Vol 18(10), 1973, pp 231-234.
23. Williams J.C.: "The Segregation of Particulate Materials. A Review," Powder Technology, Vol 15, 1975, pp 245-251.
24. Rietema K.: "Powders, What Are They?," Powder Technology, Vol 37, 1984, pp 5-23.
25. Cottaar W., and Rietema K.: "The Effect of Interstitial Gas on Milling," Powder Technology, Vol 38, 1984, pp 183-194.
26. Cottaar W., Rietema K., and Stermerding S.: "The Effect of Interstitial Gas on Milling. Part 2," Powder Technology, Vol 43, 1985, pp 189-198.
27. Cottaar W., and Rietema K.: "The Effect of Interstitial Gas on Milling. Part 3. Correlation Between Ball and Powder Behavior and the Milling Characteristics," Powder Technology, Vol 46, 1986, pp 89-98.
28. Rietema K., and Cottaar W.: "The Effect on Interstitial and Circumambient Gas in Fine Powders on the Scaling Up of Powder-Handling Apparatus as Illustrated by the Ball Milling Operation," Powder Technology, Vol 50, 1987, pp 147-154.
29. Cottaar W., and Rietema K.: "Effect of Interstitial Gas on the Mixing of Fine Powders," Powder Technology, Vol 46, 1986, pp 219-225.

Table 1: Data for Calculation of  $N_I$  as a Function of the Apparatus Speed

$d_p$	$1 \times 10^{-4}$	m
$r$	4500	$\text{kg m}^{-3}$
$g$	9.81	$\text{m s}^{-2}$
m	$2.217 \times 10^{-5}$	$\text{kg m}^{-1} \text{s}^{-1}$ for Ar at 20°C and 1 atm
	$1.781 \times 10^{-5}$	$\text{kg m}^{-1} \text{s}^{-1}$ for N <sub>2</sub> at 27.4°C and 1 atm
	$8.76 \times 10^{-6}$	$\text{kg m}^{-1} \text{s}^{-1}$ for H <sub>2</sub> at 20.7°C and 1 atm

Table 2: Data for Calculation of  $N_I$  as a Function of the Particle Size

$d_p$	$2 \times 10^{-5} \text{ m to } 1.8 \times 10^{-4} \text{ m}$	
$r$	4500	$\text{kg m}^{-3}$
$g$	9.81	$\text{m s}^{-2}$
m	$2.217 \times 10^{-5}$	$\text{kg m}^{-1} \text{s}^{-1}$ for Ar at 20°C and 1 atm
	$1.781 \times 10^{-5}$	$\text{kg m}^{-1} \text{s}^{-1}$ for N <sub>2</sub> at 27.4°C and 1 atm
	$8.76 \times 10^{-6}$	$\text{kg m}^{-1} \text{s}^{-1}$ for H <sub>2</sub> at 20.7°C and 1 atm
$V_a$	20.0	rpm
	100.0	rpm

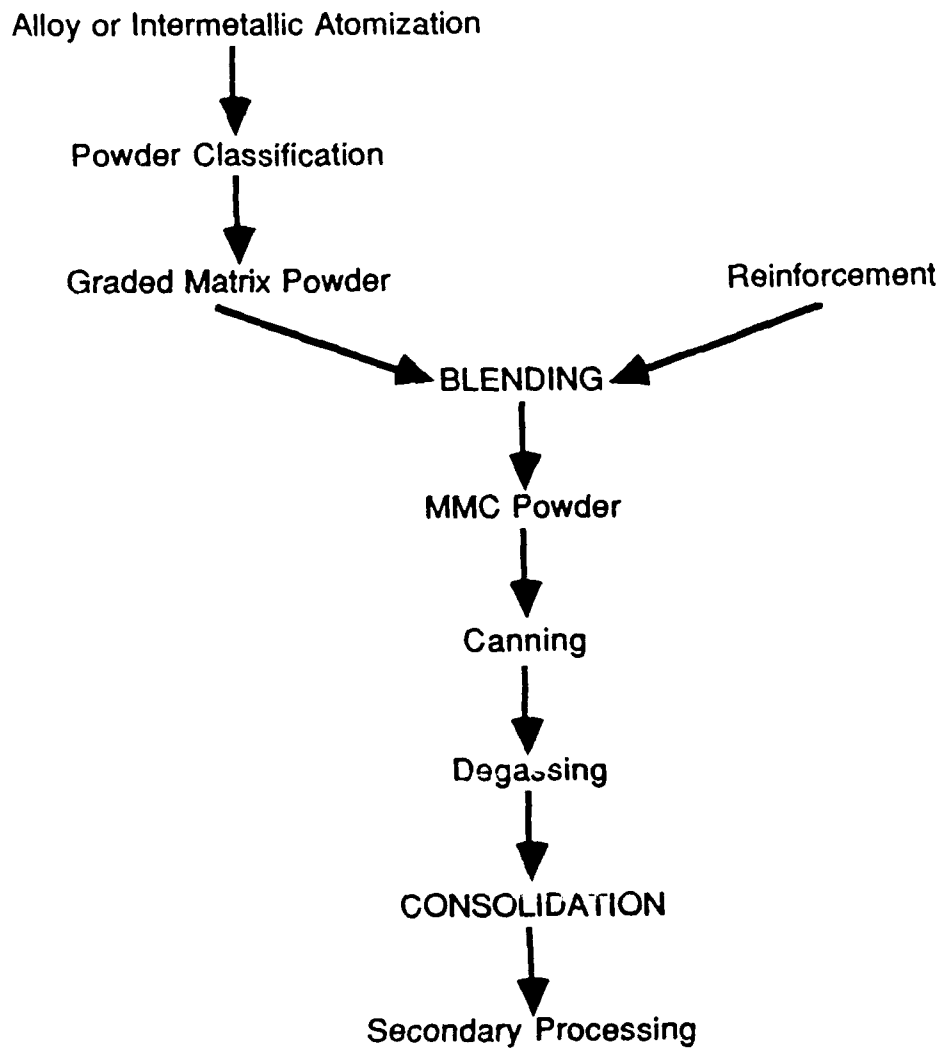
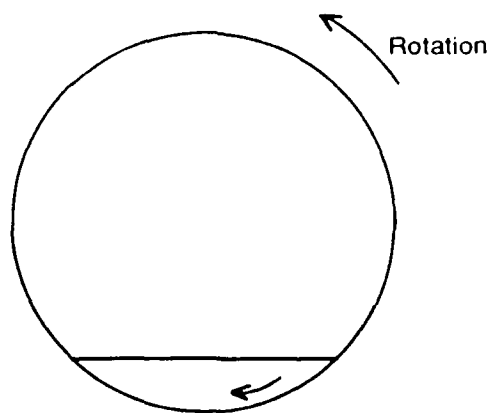
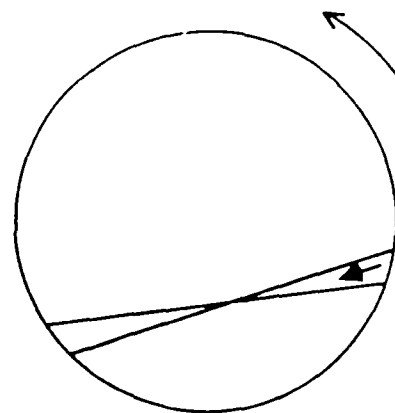


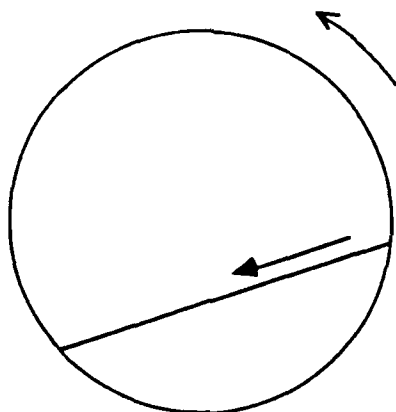
Figure 1: Powder metallurgy processing route (adapted from Willis<sup>1</sup>).



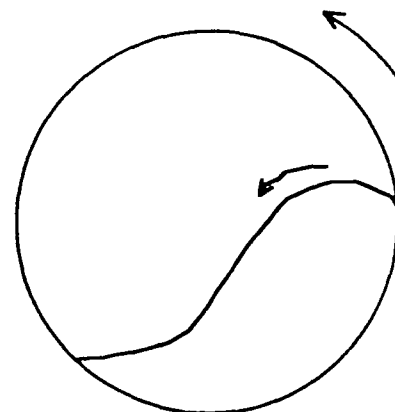
Slipping



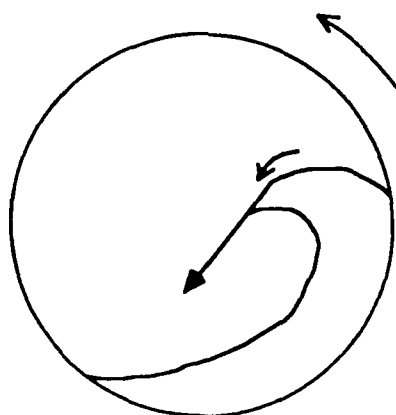
Slumping



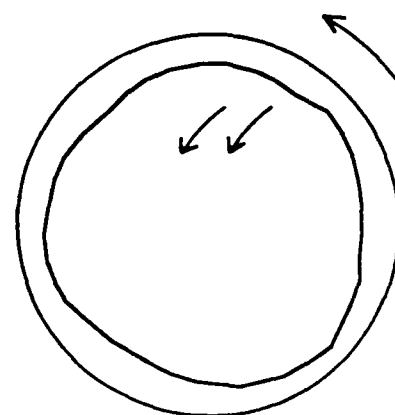
Rolling



Cascading



Cataracting



Centrifuging

Figure 2: Modes of Transverse Bed Motion (adapted from Henein et al.<sup>3</sup>).



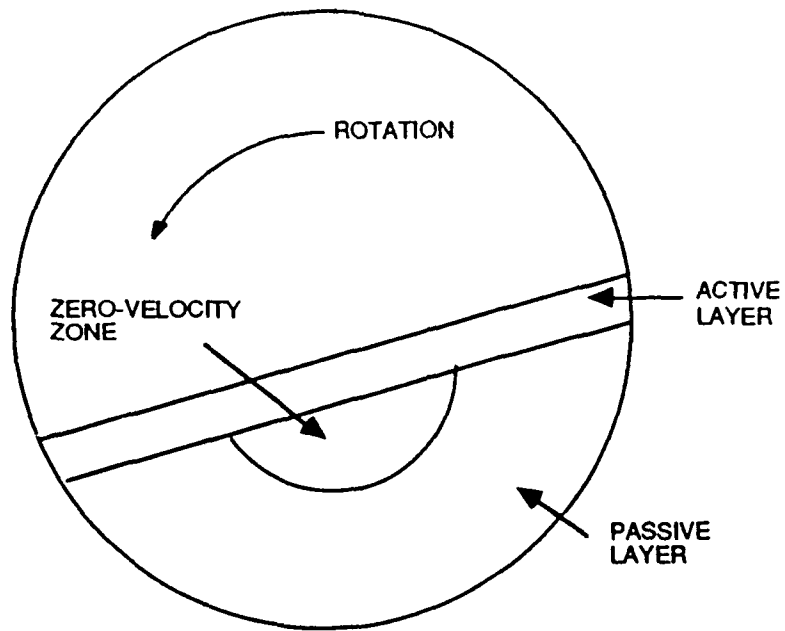
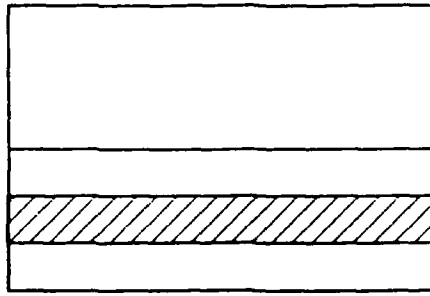
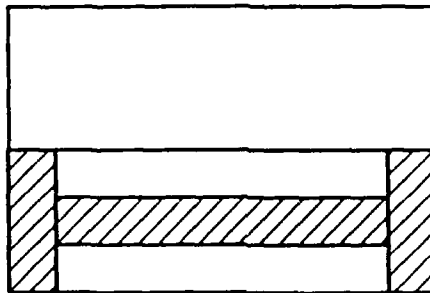


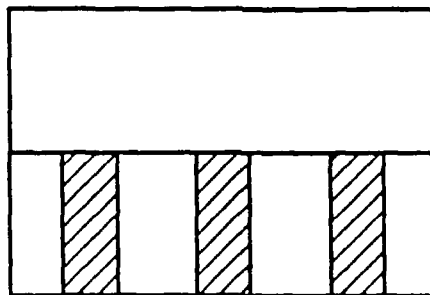
Figure 3: Regions of Mixing in the Bed of a Rotary System



(a).



(b).



(c).

Figure 4: Segregated region formation (adapted from Donald and Roseman<sup>12</sup>).]

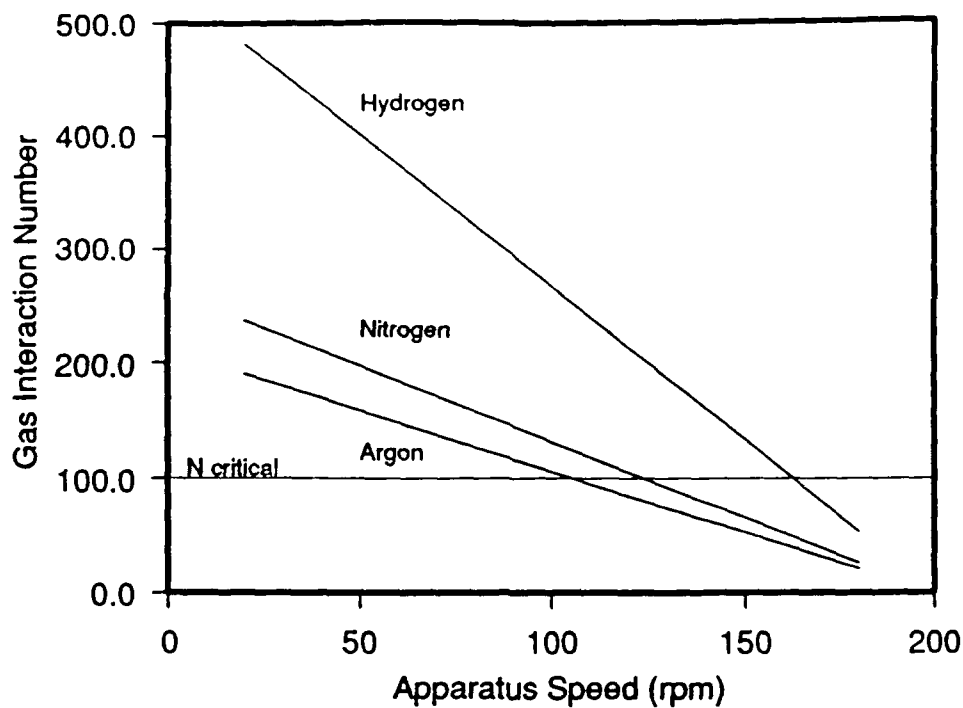


Figure 5: Effect of Apparatus Speed ( $V_a$ ) and Viscosity ( $m$ ) on the Gas Interaction Number

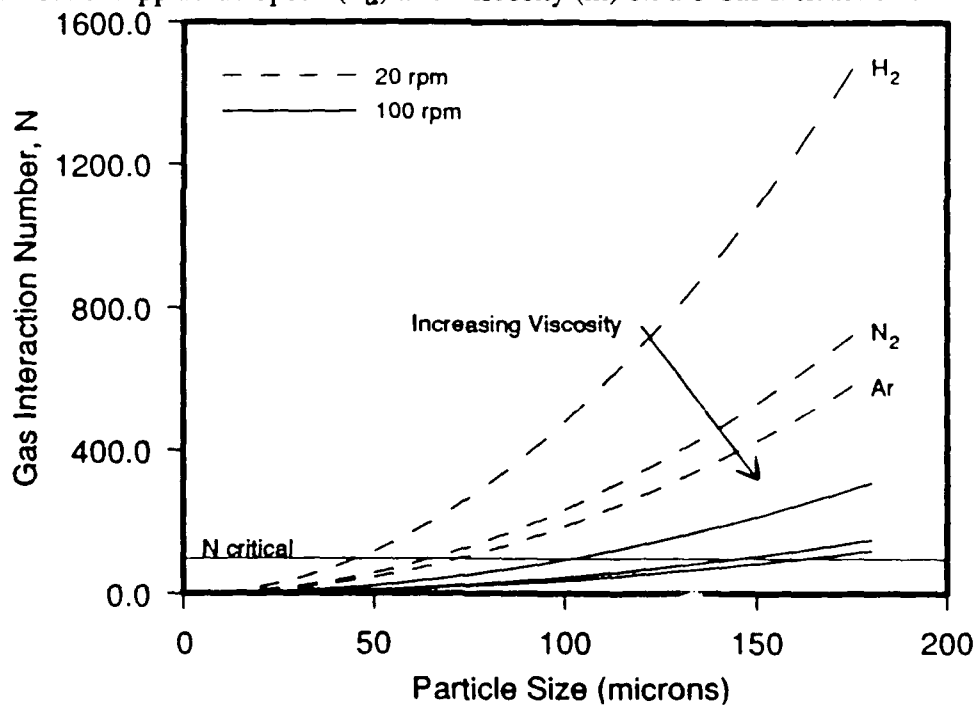


Figure 6: Effect of Particle Size ( $d_p$ ), Viscosity ( $m$ ) and Apparatus Speed ( $V_a$ ) on the Gas Interaction Number.

## BLENDING OF PARTICULATE MATERIALS

J.O.G. Parent, J.H. Bytnar, H. Henein and J. Iyengar  
Carnegie Mellon University, Pittsburgh, PA 15213

### ABSTRACT

#### 1 Introduction

In Part I of the series, a brief review of the work done to date in the area of the blending of particulate materials was presented. From this review a list of the most important material and operating variables that affect a blending operation can be made. These are:

1. The relative size of the particles in the system.
2. The relative amounts of the particles in the system (% fines).
3. The amount of material present in the blending apparatus (% fill).
4. The relative density of the particles in the system.
5. The type of gas atmosphere present in the blending apparatus.
6. The type and geometry of the blending apparatus itself.
7. The speed at which the blending apparatus is operated.
8. The shape of the particulate materials.

Consideration of these and other minor variables led to a refined set of experiments in this work, the primary goal of which was to examine the effect of these traditional variables on the blending and segregation characteristics of both model materials (large scale blending) and powder materials typical to powder metallurgy applications (small scale blending).

#### 2 Experimental Apparatus and Program

The research program was divided into two main areas: investigations performed on model materials to examine the relationship between the operating parameters and segregation behavior in rotation cylinders; and parallel experiments done on powder materials. In this way it was hoped that the effect of variables peculiar to powder systems (such as surface roughness and shape) could be separated from the more traditional variables such as those mentioned in the introduction. In both cases, macromixing behavior (mixing degree visible to the eye) was the main focus.

##### 2.1 Model Materials

### 2.1.1 Experimental Setup

The schematic of the experimental setup is shown in Figure 1. An aluminum cylinder of internal diameter and length 20 cm. was mounted on two rollers, one of which was driven by a variable speed motor. With this arrangement the cylinder speed could range from 0 to 140 rpm. A rough fabric was used to line the inside surface of the cylinder to eliminate slippage between the particulates and the cylinder wall. Observations of the bed behaviour were made from one end of the cylinder which had a transparent glass plate attached to it. The model materials used were monosized spherical particles of four different sizes and two different densities. The size ratios of the model materials were chosen between 1.3 and 3.04 (see also Table 2), which was within the range of that available for the powder materials. The model materials were also chosen such that the density ratio (1.8) was within the range of that available for the powder materials. The physical properties of the two materials are summarized in Table 1.

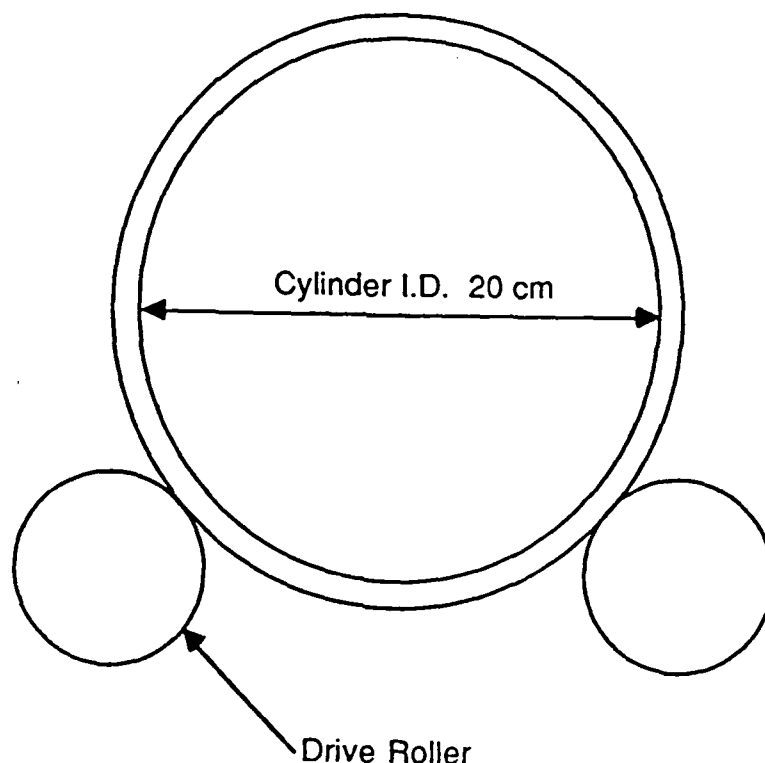


Figure 1: Schematic of drum arrangement for model material experiments.

### 2.1.2 Experimental Variables and Procedures

The following operating variables were tested using the model materials:

1. Size ratio -  $d_{coarser}/d_{finer}$
2. Percent fill -  $(V_{mixture}/V_{cylinder}) \times 100$
3. Percent fines -  $(V_{fines}/V_{mixture}) \times 100$
4. Density Ratio -  $\rho_{coarser}/\rho_{finer}$

Table 1: Model Material Characteristics

Material	Size (mm)	Density (g/cm <sup>3</sup> )	Shape
Acrylic	9.5	1.3	Spherical
	6.4		
	4.0		
	3.1		
Alumina	3.1	0.72	Spherical

### 5. Cylinder Speed (RPM)

Table 2 provides a list of the operating variables that were tested. The following portion of this section outlines the important parameters and the basic procedure used in the different set of experiments.

1. First Set - Binary mixtures of acrylic spheres with a density ratio of 1.0, a percent fill of 35% and percent fines of 14% were used in this set. With these parameters fixed, six binary mixtures ranging in size ratio from 1.3 to 3.04 were tested. In each case, the cylinder speed was increased from 0 rpm to 140 rpm, and the bed behavior and macro-segregation or mixing were observed and photographically recorded.
2. Second Set - In this set of experiments, all of the conditions were kept the same as in the first case, except that the speed was decreased from 140 rpm to 0 rpm, to examine the effect of decreasing speed on the bed behavior.
3. Third Set - This set was conducted to examine the effect of changes in the percent fines. Thus the percent fines was set to 20%, and the percent fill changed to 37%, all other variables being held fixed.
4. Fourth Set - In this case the bed was composed of a mixture of acrylic and alumina spheres. This changed the density ratio to 1.8. The percent fill and percent fines were set to 35% and 14% respectively, and only three size ratios were investigated: 1.3, 2.1 and 3.04.

In each case, the cylinder was loaded with a measured quantity of the binary mixture and was well shaken to form a randomly mixed bed. The cylinder was then placed on the drive rollers and the speed either increased or decreased, as required by the experiments. The flow of the fines was observed in each case.

## 2.2 Powder Materials

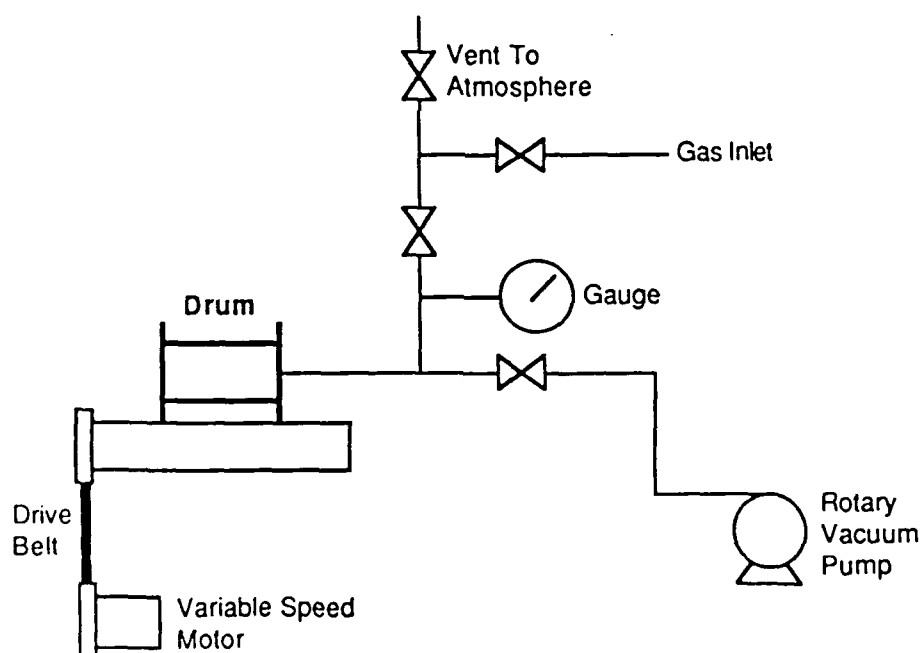
### 2.2.1 Apparatus and Materials

The rotary blenders for the powder material experiments were constructed of steel pipe with titanium liners, which were grooved to reduce the possibility of slip at the cylinder wall. Drums of nominally 5 and 10 cm i.d. with  $L/D = 1$  were used, capable of withstanding either pressures of up to 3 atm of a selected gas or a vacuum of better than  $10^{-2}$  atm. Glass end plates were used for the front end of the drum to allow visual observation of the macroscopic blending process. Gas exchange is accomplished through the use of a rotating gas seal, allowing for atmosphere control during the course of an entire

**Table 2: Experimental Variables**

Materials	Size Ratio	Density Ratio	Percent Fill	Percent Fines
Acrylic/Acrylic	3.04	1.0	35	14
	2.4		37	20
	2.1			
	1.6			
	1.5			
	1.3			
Acrylic/Alumina	3.04	1.8	35	14
	2.1			
	1.3			

experiment. Figure 2 shows a schematic view of the gas delivery system as well as the experimental setup. The speed of the drum is controlled in the same manner as with the model material experiments, i.e., through the use of belt driven rollers connected to a variable speed motor.

**Figure 2:** Schematic of gas delivery system for powder material experiments.

All of the materials used in the experiments were commercially available products, the choice having been made based on the availability of materials as well as an analysis of the size distribution, shape and density. Table 3 lists the materials that were used, as well as their most salient characteristics. The materials were chosen such that the size and density ratios fell within the range used in the model

material experiments, though it was not considered critical that the size and density ratios matched exactly between the two cases.

Table 3: Materials for Blending Experiments

Material ( )-supplier	Size	Density (g/cm <sup>3</sup> )	Shape
PREP Ti-6Al-4V (Nuclear Metals)	-100 +120 mesh	4.51	Spherical
cp Ti (Atlantic Equipment Engineers)	-100 +120 mesh	4.5	Irregular
Silicon Carbide (Norton Company)	-170 +200 mesh -200 +230 mesh -230 +270 mesh -270 +325 mesh	3.20	Irregular Sharp

### 2.2.2 Experimental Variables and Procedures

In the case of the powder materials, the list of important variables for the experiments was changed somewhat from that of the model materials. The percent fill and percent fines were not considered to be important in determining the type of mixing behavior observed and so were not used as variables in this series of experiments. This resulted in a smaller number of variables and so a reduced number of experiments to be run. The variables of interest in the powder materials case were:

1. Size ratio.
2. Rotating speed of the drum (rpm).
3. Gas atmosphere.
4. Particle shape (both matrix and reinforcement).

The experiments were run in the same manner as for the model materials, i.e., one variable was changed, keeping all others fixed, and the effect of that variable on the mixing properties of the bed was examined as a function of the rpm. In other words, the rpm was used as the independent variable for all of the experiments. The analysis of the mixing behavior was performed visually and photographically through the glass end plate of the drum.

The initial placement of the powder materials was a concern early on in the experimental program. It was thought that reproducibility could be improved if the coarser and finer materials were loaded in a repeatable manner for each set of experiments. To this end, a procedure was developed that resulted in an initial configuration that consisted of the coarser material being evenly distributed in the drum, and the finer material lying on top of the coarse material, along the drum axis. It was observed, however, that the finer material was completely incorporated into the coarse material within the coarse material after just a few revolutions. After further experiments, it was decided that the initial placement was not



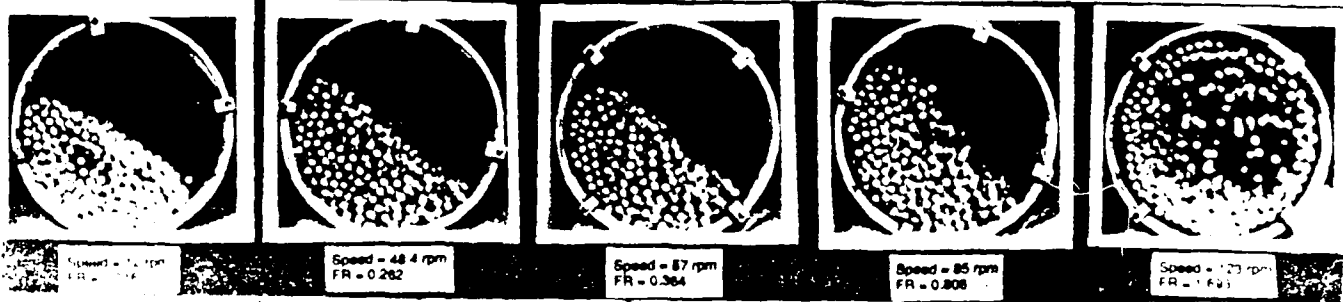
as important as had been previously supposed, and the more practical initial placement, that of a well mixed bed, was chosen as the starting point for the experiments. As a result, the coarse and fine were merely loaded together into the drum, and the drum was then rotated for several revolutions with the bed in early cataracting mode to ensure the creation of a well-mixed bed. Using this starting point also facilitated the determination of the percent fill of the bed, as this was calculated from measurements of the bed depth for each set of experiments.

### 3 Results and Discussion

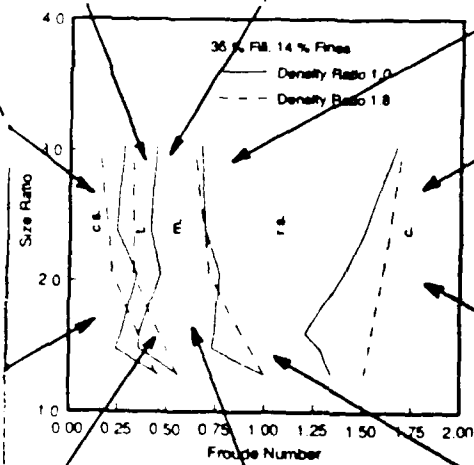
#### 3.1 Model Materials

Figure 3 shows the typical behavior that was observed at progressively increasing speeds. At low speeds a central segregated core made up of fines was observed, by rotating the cylinder at a constant speed for a few seconds. The behavior was observed for each case tested (see Figure 3 a,f,k). On further increasing the cylinder speed, the fines began to disperse gradually to the other parts of the bed (see Figure 3 b,g,l). This dispersion of the fines promoted mixing of the fines in the bed. However, even distribution of the fines in the bed did not occur at any particular speed but over a range of speeds. This range of speeds, over which the fines were evenly distributed throughout the bed, is defined as the transition zone from core segregation to mixing. The lowest speed at which the fines dispersed from the center and began to mix with the other parts of the bed marked the beginning of the transition zone. Starting at this speed the motion of the cylinder was arrested at various speeds to observe the distribution of the fines in the bed. The end of the transition zone or the beginning of the mixing zone was determined by this procedure. Once this was determined, the cylinder speed was further increased and mixing continued (see Figure 3 c,h,m) until the larger particles began to move towards the center of the cylinder. This determined the beginning of reverse segregation. As the speed was further increased, reverse segregation continued (see Figure 3 d,i,n) until the fines began to form a monolayer against the inner wall of the cylinder. This speed marked the beginning of centrifuging (see Figure 3 e,j,o) and the cylinder remained centrifuged with any further increases in the rotational speed. The boundaries of the various zones (core segregation, transition, mixing, reverse segregation and centrifuging) were thus determined in each case. This procedure was repeated seven times for each size ratio in each set, and the speeds which determined the boundaries of the various zones were typically within two standard deviations ( $2\sigma$ , where  $\sigma$  varied between 0.5 and 3.1 rpm) of the mean speed calculated in each case, indicating that the experimental error is within acceptable limits. The photographs shown in Figure 3 provide a good representation of the bed behavior that was observed visually. This figure shows that the bed behavior at low, high and intermediate speeds were similar in each case, except that the boundary speeds varied with size ratio. These observations provided information on that mixing patterns when the speed of the mixer is increased, starting with a segregated bed. The results discussed so far were similar for the first, third and fourth set, showing that the variation in percent fill, percent fines and density ratio did not make any qualitative difference in the mixing patterns for binary mixtures. The second set of experiments were performed to study the effects of decreasing the speed, starting with a centrifuging bed. In this case the bed behavior changed from centrifuging to reverse segregation, then mixing, transition and core segregation. The overall results, though, were similar to the other cases and are discussed later in this section.

Size Ratio = 3.04, Density Ratio = 1.0



(a) (b) (c) (d) (e)



FR - Froude Number ( $\omega \cdot R \cdot g$ )

c.s. - Core Segregation

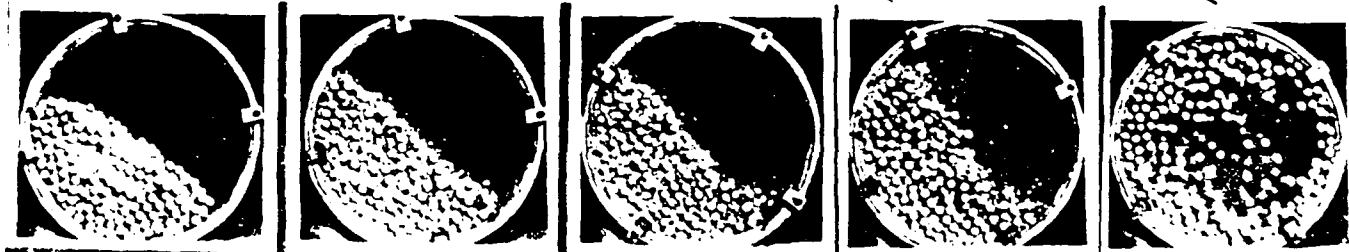
t. - Transition

m. - Mixing

r.s. - Reverse Segregation

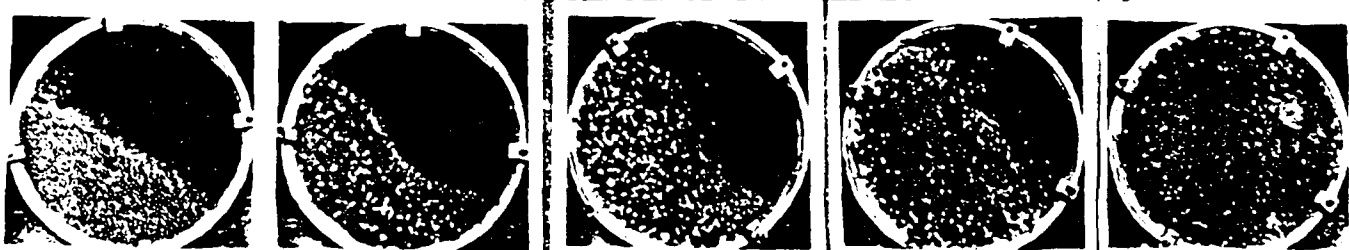
c. - Centrifuging

Size Ratio = 3.04, Density Ratio = 1.8



(f) (g) (h) (i) (j)

Size Ratio = 1.3, Density Ratio = 1.8



(k) (l) (m) (n) (o)

Figure 3 : Experimental results for model materials, for increasing speed

In the review it was seen that the non-dimensionalized number  $\omega^2 R/g$  provides a useful means of expressing the important parameters. Therefore the results for each set of experiments are expressed in terms of plots of  $\omega^2 R/g$  versus size ratio. The results of the experiments with acrylic/acrylic mixtures are shown in Figures 4 and 5. The zones on either side of the mixing region can be classified as the segregated regions. The figures show that at very low and very high speeds the bed is segregated, and at intermediate speeds thorough mixing occurs. The figures indicate that at a size ratio of 1.3 (mixture of 4.0 mm and 3.125 mm spheres), not only is the mixing zone shifted to the right, indicating that the mixing begins at higher speeds, but the mixing zone is larger as well. At size ratios above 1.5, there is a very slight variation in the transition boundary (from 43 to 46 rpm between the size ratios of 1.5 and 3.04). Previous work by Roseman and Donald<sup>1</sup> indicates that up to a diameter ratio of 1.2, the smaller particles cannot slip through the voids of the larger particles, which results in very little segregation. A similar result is seen in this work, which shows a larger mixing region for a mixture of diameter ratio 1.3. The results also indicate that the width of the mixing zone decreases with increasing size ratio. It is also seen that centrifuging occurs at values of  $\omega^2 R/g$  greater than 1.0. This could be due to some slippage between the cylinder's inner wall and the spheres. It can also be seen that in general, the speed at which centrifuging occurs increases with increases in the size ratio. From Figure 4 it is seen that the mixing region obtained by increasing the speed from an initially segregated bed is smaller than that obtained by decreasing the speed from an initially centrifuging bed. Figure 5 shows that there is negligible effect on the mixing patterns for varying percent fines.

Figure 6 compares the results of the acrylic/acrylic case with the acrylic/alumina case, showing that the same trend is observed in both instances. The only difference is that that data for the acrylic/alumina mixtures are shifted slightly to the left, indicating that the transition from core segregation to mixing and mixing to reverse segregation occurs at lower speeds for higher size ratios.

### 3.2 Powder Materials

Much the same behavior was observed in the blending of the powder materials as was seen in the case of the model materials. At low rpm (thus low values of  $\omega^2 R/g$ ) the fines were seen to form a segregated core lying below an active layer which was only several coarse particle (in this case Ti-6Al-4V) diameters in thickness. The core was, however, a proportionally smaller percentage of the cross-sectional area of the bed than was observed in the case of the model materials. In addition, a second form of low-rpm segregation was observed in many of the cases examined for the powder materials. This consisted of radial bands originating at the core and extending to the cylinder wall. From the experiments conducted with the irregular titanium (sponge) powder as the coarse material, it appears that the bands are formed as a result of a shearing of the core at the active/passive layer boundary. The sheared material is then entrained and distributed along the boundary, and as the material passes into the passive layer it forms a radial band with some associated curvature. It should be noted that this mechanism was only observed in the case of the sponge experiments, where the kinetics of formation of these bands was slow enough to permit direct observation. In the case of the spherical Ti powders, the formation of the bands was not directly observed, and there is some indication that the bands may also be the result of starting with an improperly mixed bed.

As the rpm was increased, the core was observed to shrink in size and to begin to migrate towards the

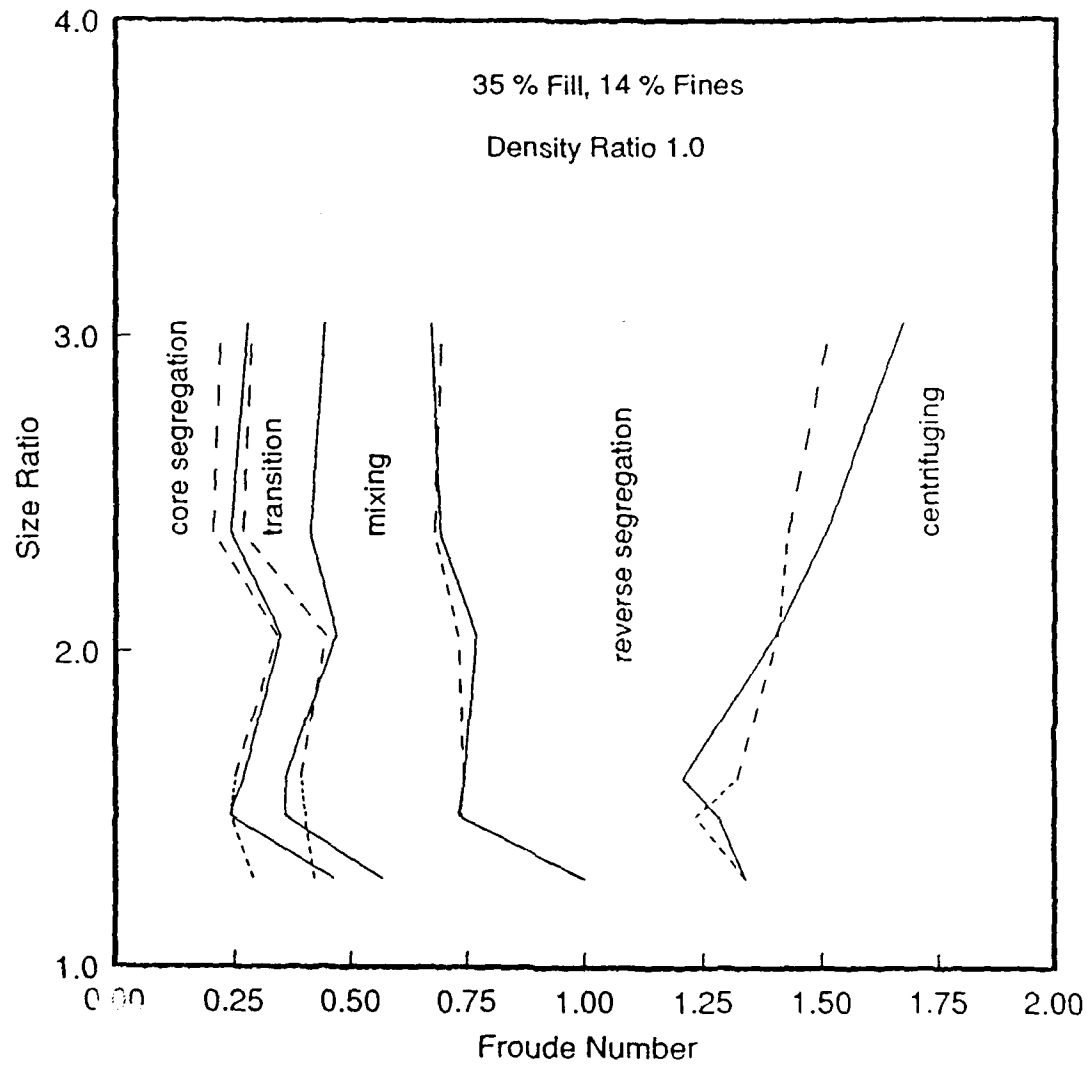


Figure 4: Model material segregation behavior for varying size ratios and drum speeds, for increasing speed (solid lines) and decreasing speed (dashed lines).

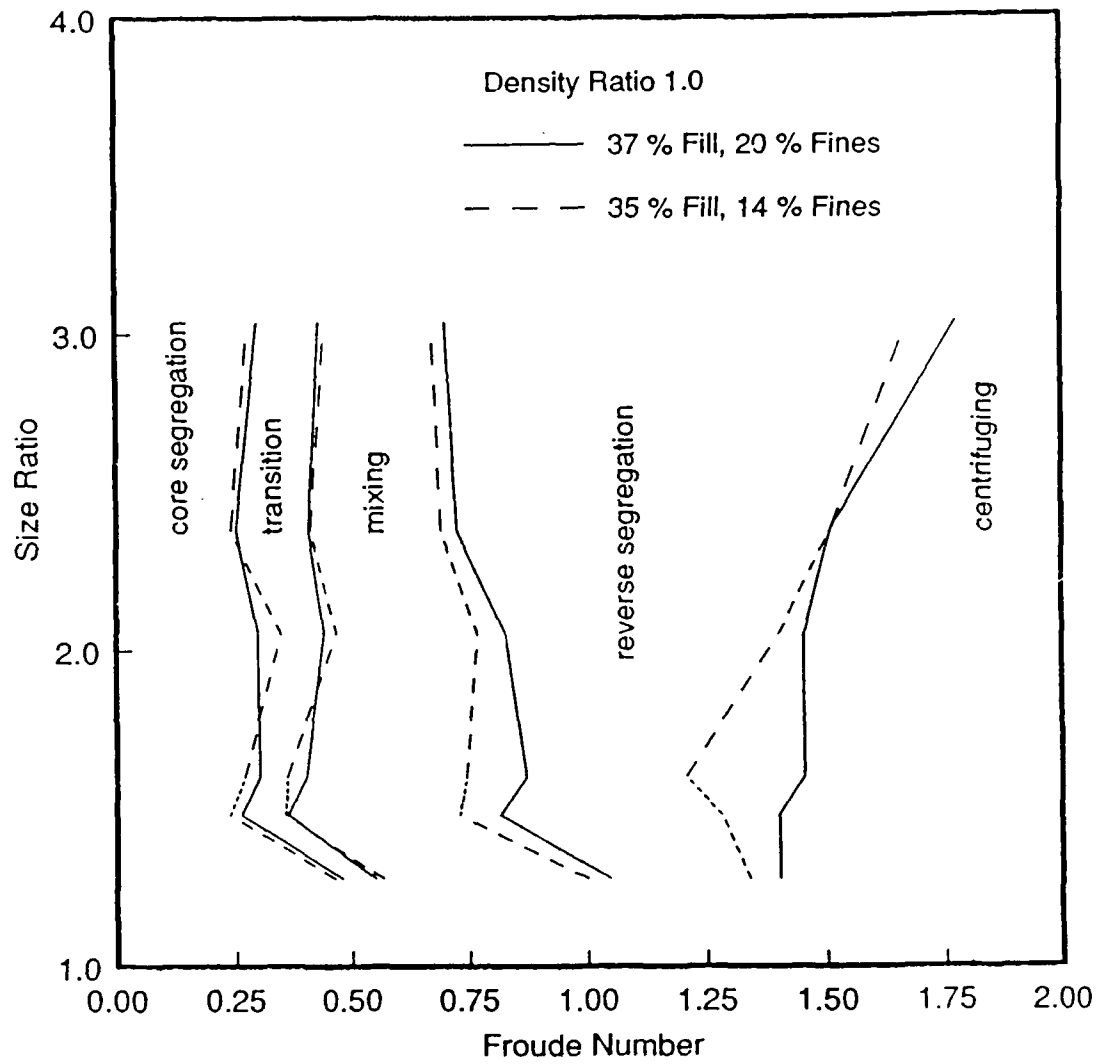


Figure 5: Model material segregation behavior for varying percent fines and percent fill.

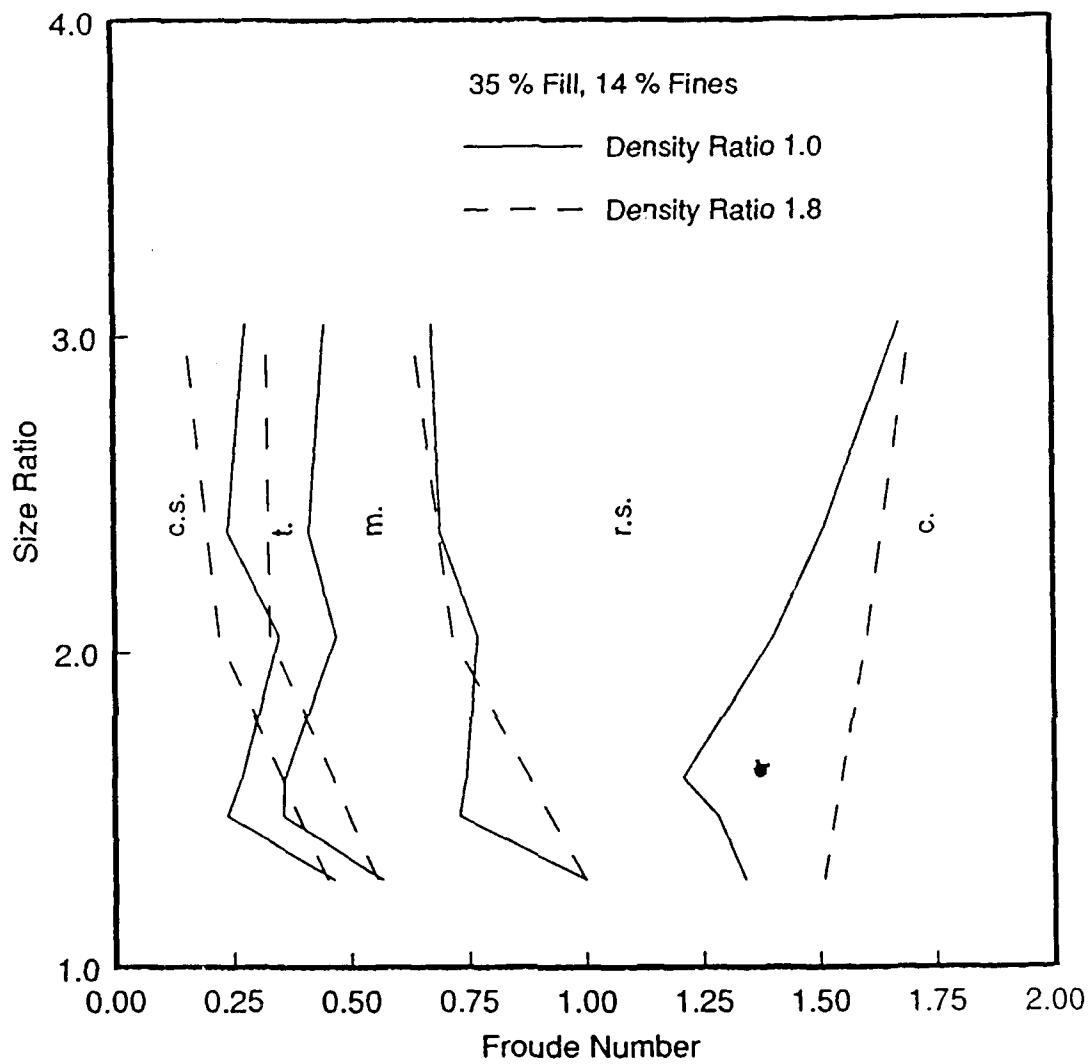


Figure 6: Model material segregation behavior for varying density ratio.

top end of the bed. This occurrence marked the beginning of the transition region, and was observed in all cases. The end of the transition region was determined to be that point where the core was last observed. In most cases, this coincided with the onset of cataracting, rather than cascading, as was observed in other work(\*\*references here\*\*). In fact, the cascading region was not observed to produce good mixing in any of the experiments conducted. Once cataracting initiated, the core was broken up and the bulk of the bed evidenced good mixing, i.e., there was no observable segregation pattern in the bed. The end of the mixing regime was determined to be that point at which permanent banding in the circumferential direction was observed. The upper transition region extended to the point where this banding moved to the outer wall of the cylinder, resulting in an inner region of material devoid of fines - the onset of reverse segregation. As will be seen in more detail later, the onset of reverse segregation occurred for very high values of  $\omega^2 R/g$ , near to or exceeding a value of 1.0, the theoretical point at which centrifuging occurs. It is interesting to note that in none of the cases observed was centrifuging achieved. This would indicate that the goal of a slip-free surface at the drum wall was not achieved, or perhaps that the influence of the gas atmosphere is sufficient to cause increased particle/particle slippage, thus retarding the onset of centrifuging and resulting in the high values of  $\omega^2 R/g$  observed.

Figure 7 is the segregation behavior diagram obtained for the experiments conducted with Ti-6Al-4V (spherical) and SiC (particulate) with a gas atmosphere at ambient conditions (1 atm and 20°C). This represents a fairly typical example of the segregation behavior of the mixtures, and shows the expected behavior of the mixing regime, i.e., that the broadest range of mixing occurs at the lowest value of the size ratio. It can be seen here that the transition regions are fairly large, especially in the case of the transition from mixing to reverse segregation.

Figure 8 shows the results obtained for the same materials but with the experiments conducted in the 10 cm i.d. drum. These experiments were conducted to test the idea of scale-up for the mixing of the powders. According to previous work<sup>2</sup>, the scale-up criteria for radial segregation are the size ratio and the Froude number ( $\omega^2 R/g$ ). Thus for equivalent operating conditions, the segregation behavior diagrams for the 5 and 10 cm drum cases should be relatively the same. As can be seen from the figure, there are significant differences between the two cases. In the case of the 10 cm drum, the region of segregation at low rpm is smaller, extending for less than half of the range of Froude numbers than in the 5 cm case. Also, the lower transition region shows a decrease in extent with increasing size ratio, whereas in the 5 cm case the size of this region remained relatively constant. The mixing region also shows more variability for the larger drum, and is smaller in extent than in the case of the smaller drum. The upper transition region occupies approximately the same fraction of the operating speed range, but begins at a much lower rpm and progressively decreases with increasing size ratio. Reverse segregation also begins much sooner in the 10 cm drum, and appears to be more uniform in starting point than in the case of the smaller drum. It should be noted that the percent fill is significantly different between the two cases, and this may have had some effect on the results obtained. It may be that the volume of the material used in the larger drum introduced some error into the determination of the boundary points, but it is unlikely that this error was large enough to cause such a significant deviation between the two cases. This suggests that the percent fill may be a factor in determining the scale-up between the smaller and larger cases, at least in determining the extent to which the different regions of behavior are observed.

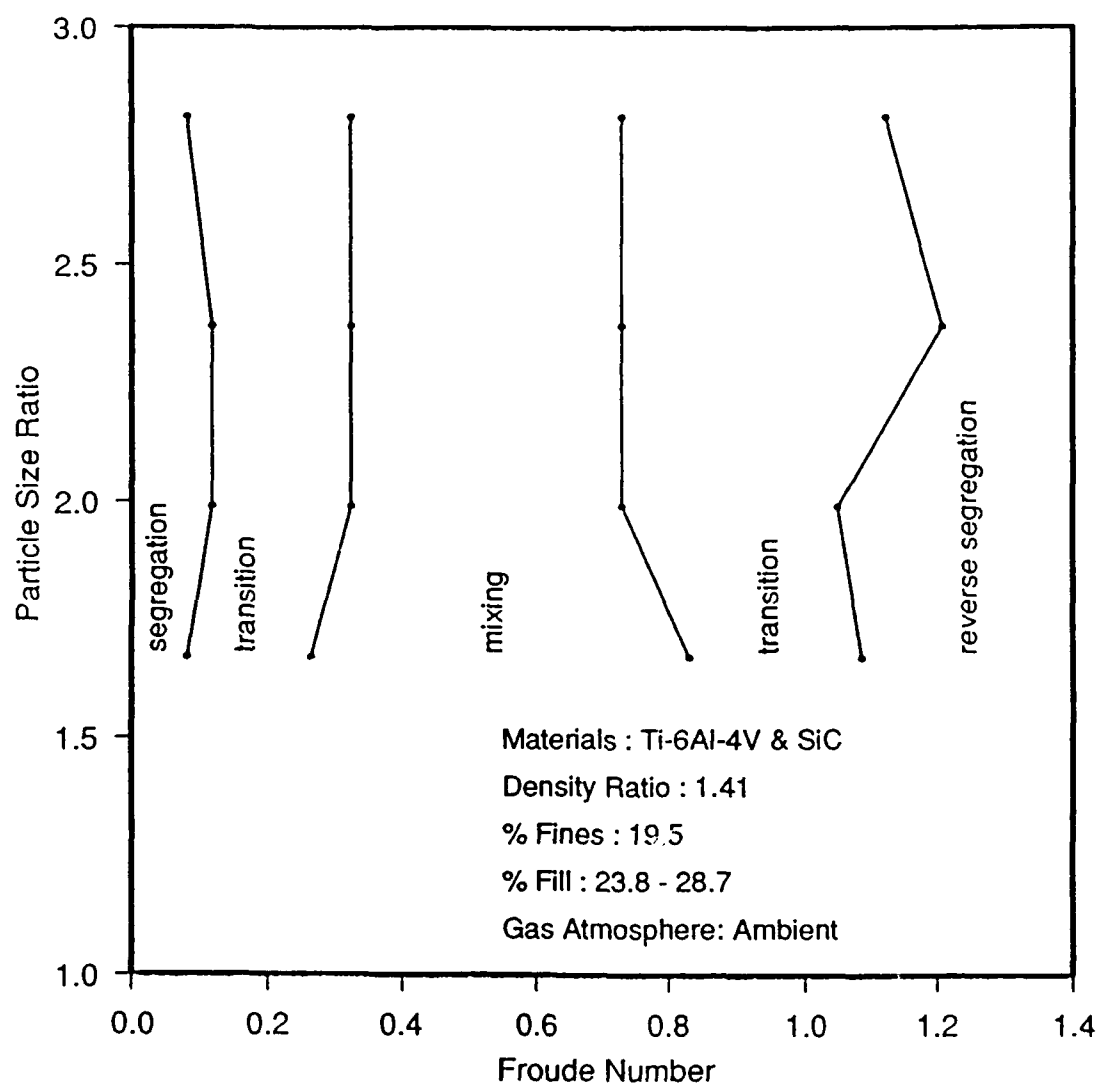


Figure 7: Segregation Behavior Diagram for ambient atmospheric conditions.



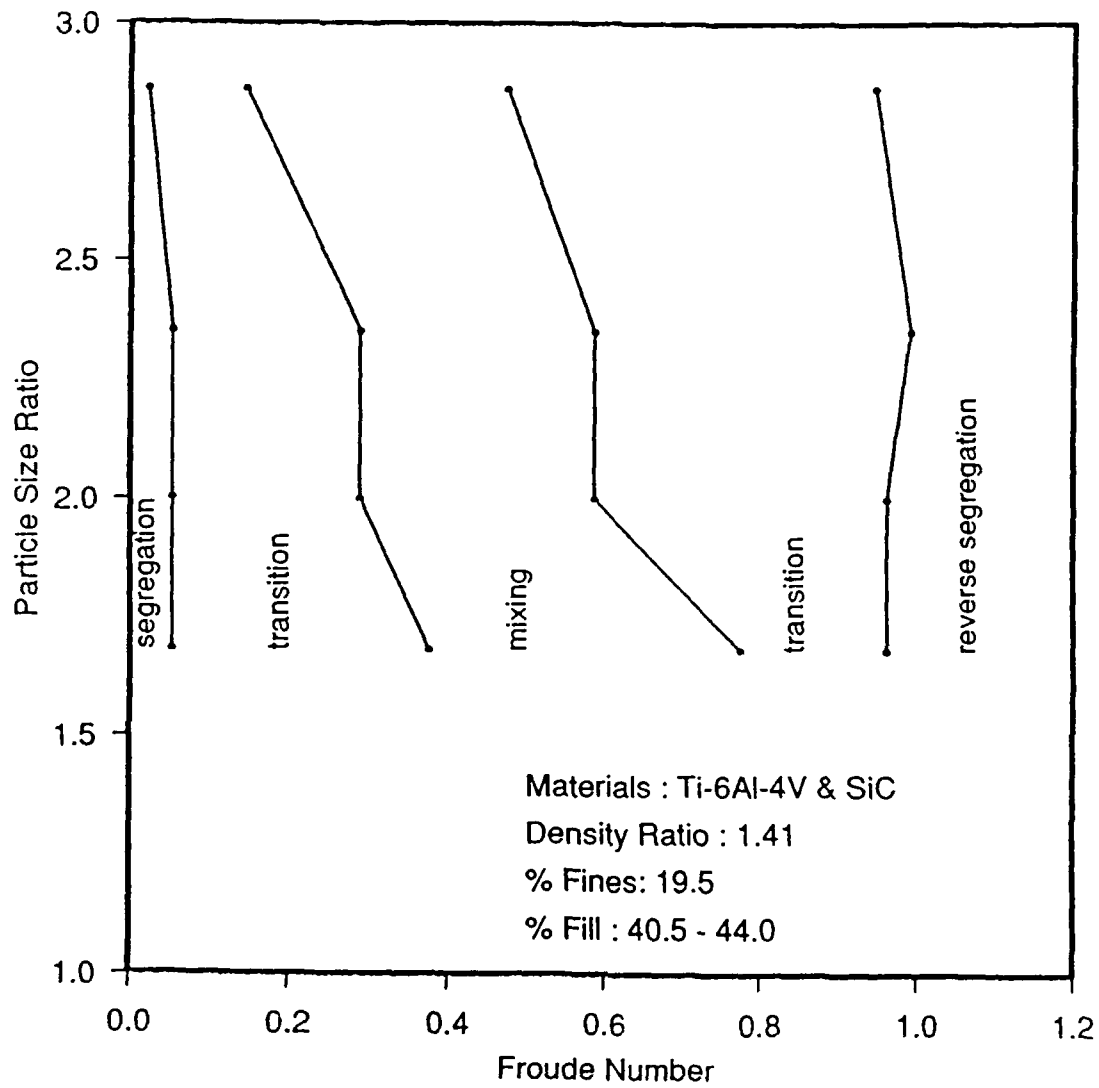


Figure 8: Segregation Behavior Diagram for 10 cm drum experiments.

The effect of changing the coarse particle geometry was investigated in the case of the sponge material as the coarse particulate. The results of this set of experiments are shown in Figure 9. It should first be noted that the percent fines used in this set of runs is very much higher than that used in all the other experiments. This resulted from difficulties encountered while trying to observe the experiments visually. Due to the shape of the sponge, the bed was very porous, and as a result allowed the finer material to be driven away from the end walls of the cylinder, as a result of the velocity gradient present there. For 19.5% fines, this resulted in the end wall area of the bed being devoid of fines, thus making observation of the segregation process impossible. When the middle of the bed was disturbed, the core of segregated material was found to lie exactly in the position expected, i.e., a few coarse particle diameters below the surface of the bed, but away from the end walls of the drum. As a result, it was decided to saturate the bed with just enough fines to permit observation of the segregation process. This resulted in the decidedly unusual results of Figure 9. The experiments would seem to suggest that the sponge material, in combination with the silicon carbide, would result in better mixing properties than with the spherical coarse powder, as evidenced by the small segregation and transition zones at the low end of the diagram, and the much larger mixing regime than was observed in the original case. What is likely happening is that the voids in the bed are being completely filled by the finer material, resulting in an apparently well-mixed bed at small values of the Froude number. This problem would be greater at the higher values of the size ratio, as this corresponds to smaller fines material which would move through the bed at a faster rate. This is evidenced by the decrease in the boundary values of the Froude number as the size ratio increases. Thus it is unlikely that good mixing can be achieved in any realistic sense with the irregular sponge material as the coarse particle.

In order to properly assess the effect that changes in the gas atmosphere have on the segregation behavior of these materials, it is first necessary to determine the likelihood that the gas has an effect on the particles comprising the bed. To this end, the gas interaction number was determined for the two atmospheres being used (air and nitrogen) for both the coarse and fine materials. Figure 10 shows the variation of gas interaction number with rotating speed of the drum (expressed as the Froude number) for air and nitrogen. It can be seen from these figures that for most of the speeds over which the blending operations are taking place the gas atmosphere would have little effect on the behavior of the Ti powders used. In other words, it is unlikely that for these two gases that the Ti powder mass would be fluidized in any way, and thus the mixing and flow characteristics for the Ti powder should remain relatively unaffected by the gas atmosphere. In the case of the finer material (SiC), the effect of the gas atmosphere would be expected to be significant, as indicated by Figure 11. Here the value of the gas interaction number drops below 100 (the critical value) for very low rpm's, and thus for most of the range of speeds that the experiments use, it would be expected that the SiC would be fluidized to some extent. This would result in improved flowability for the SiC powder, which might be reasonably be expected to result in more significant segregation problems. It should be noted that the diagrams presented are for 1 atm of nitrogen and air. In the experiments conducted the pressure of the nitrogen was varied from 0.3 atm to 3 atm. For the pressures below one atmosphere, the effective viscosity of the gas would be reduced, which would have the effect of shifting the curves towards higher values of the gas interaction number, resulting in less fluidization of the components of the bed. For the pressures above 1 atm, little effect on the curves would be observed as the viscosity of the gas changes little with increases in pressure above 1 atm.

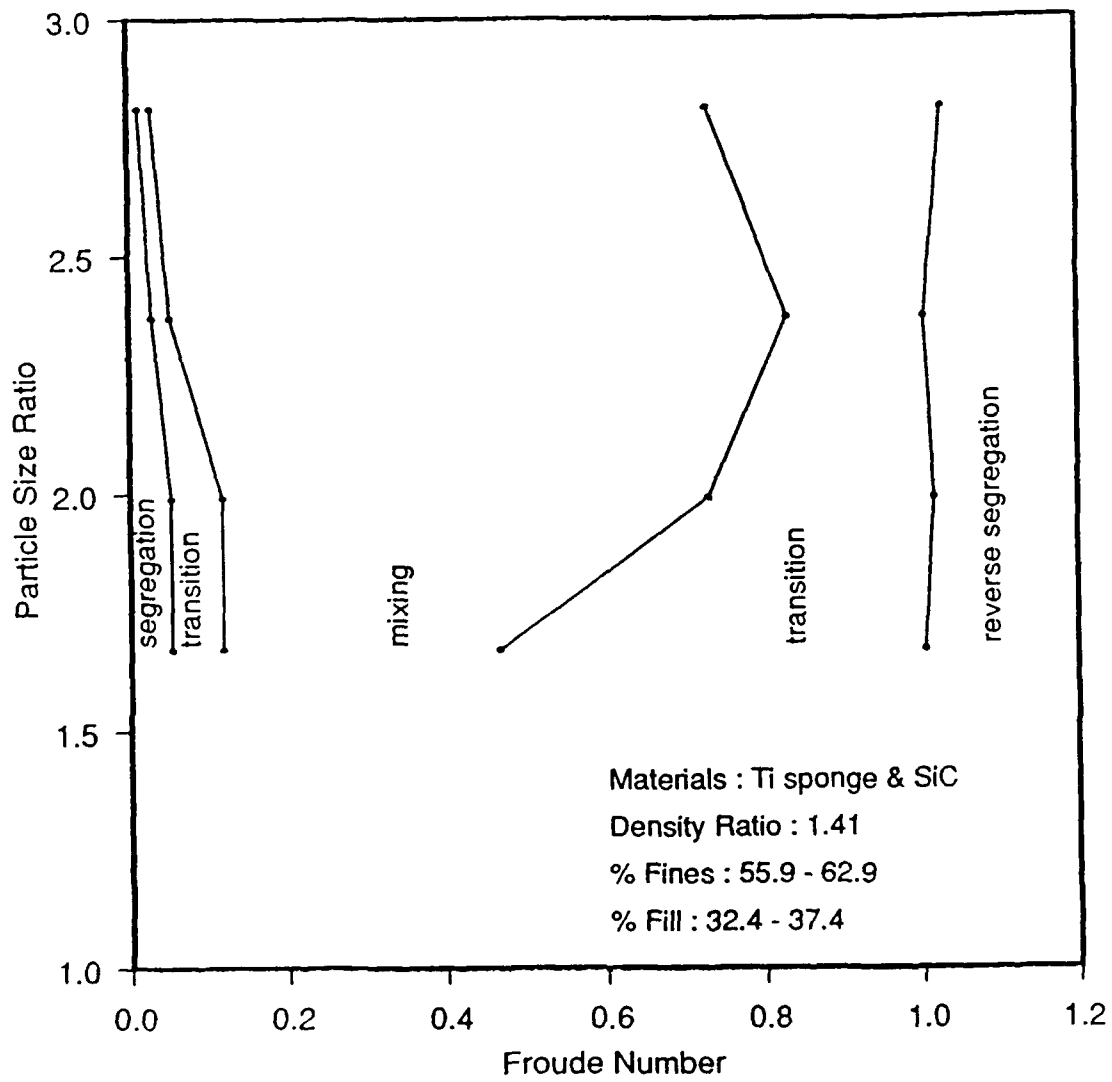


Figure 9: Segregation Behavior Diagram for sponge material.

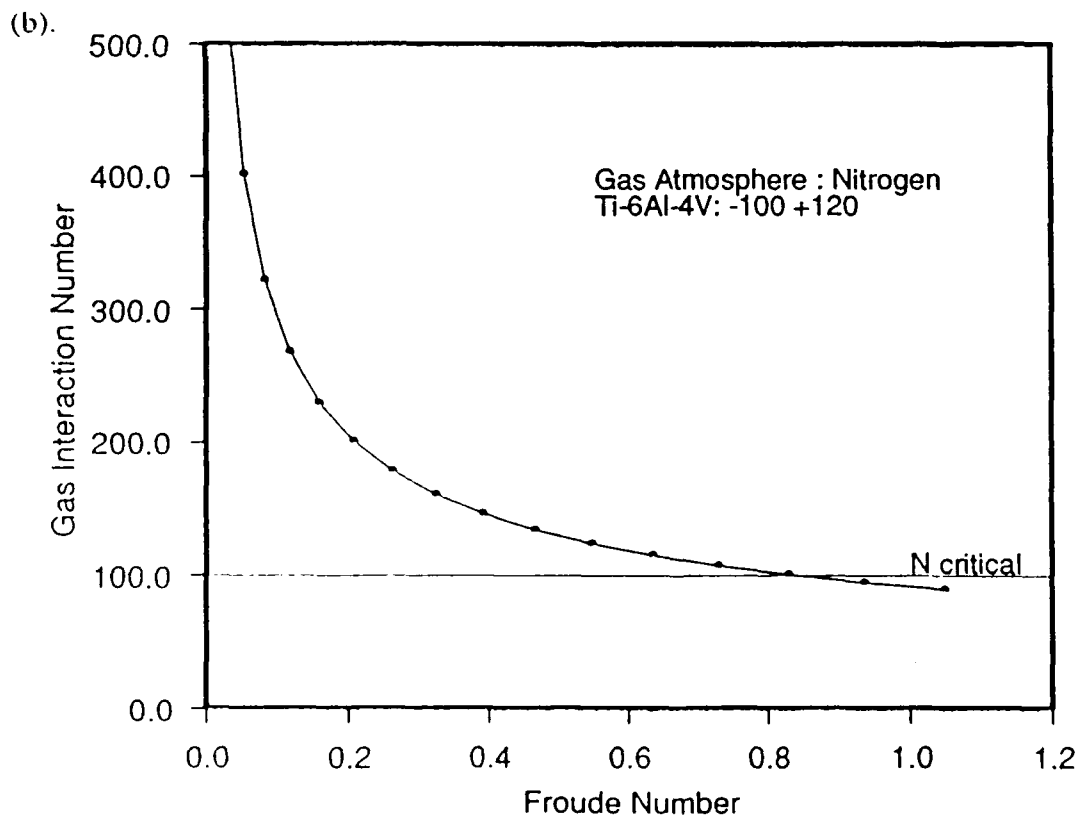
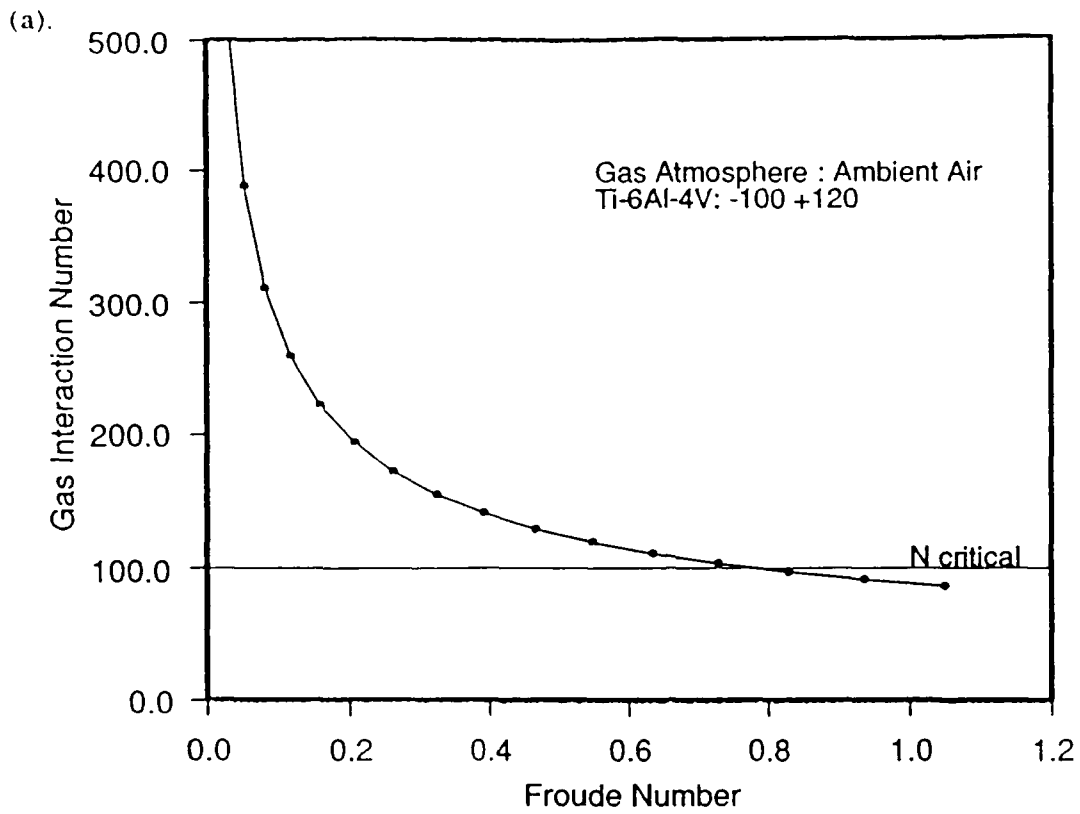


Figure 10: Gas Interaction Number vs.  $\omega^2 R/g$  for Ti powder for (a) ambient air and (b) nitrogen.

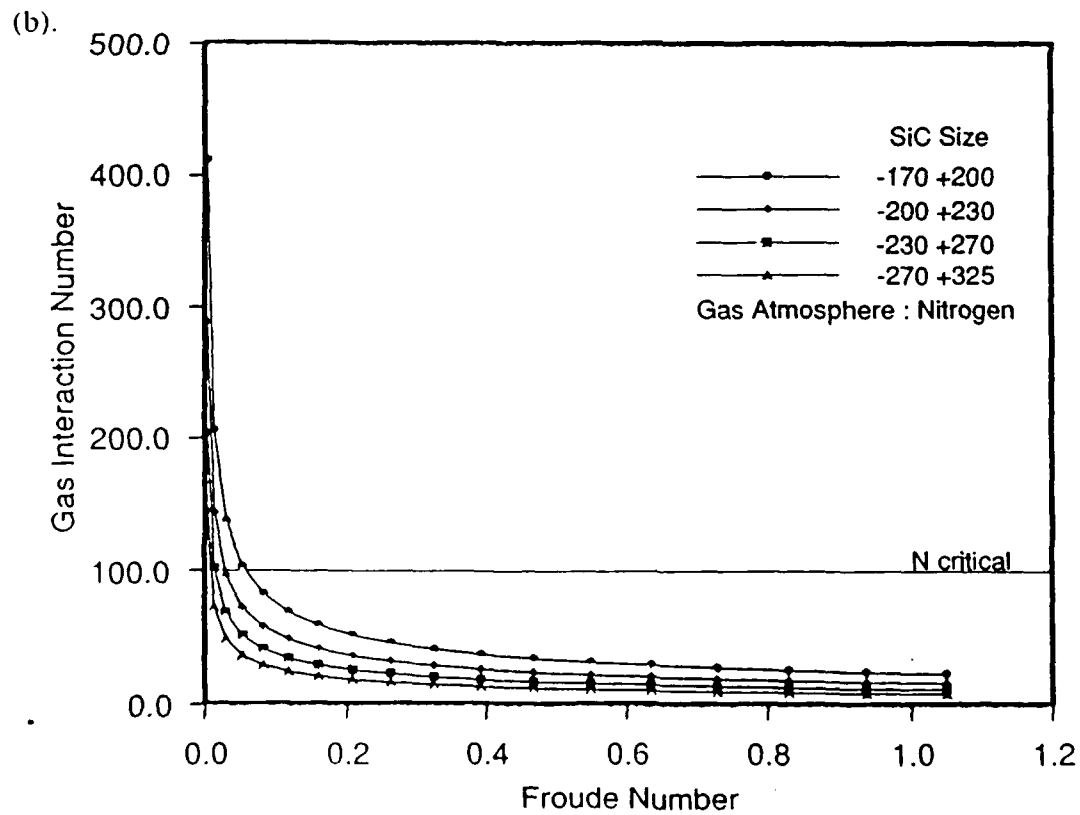
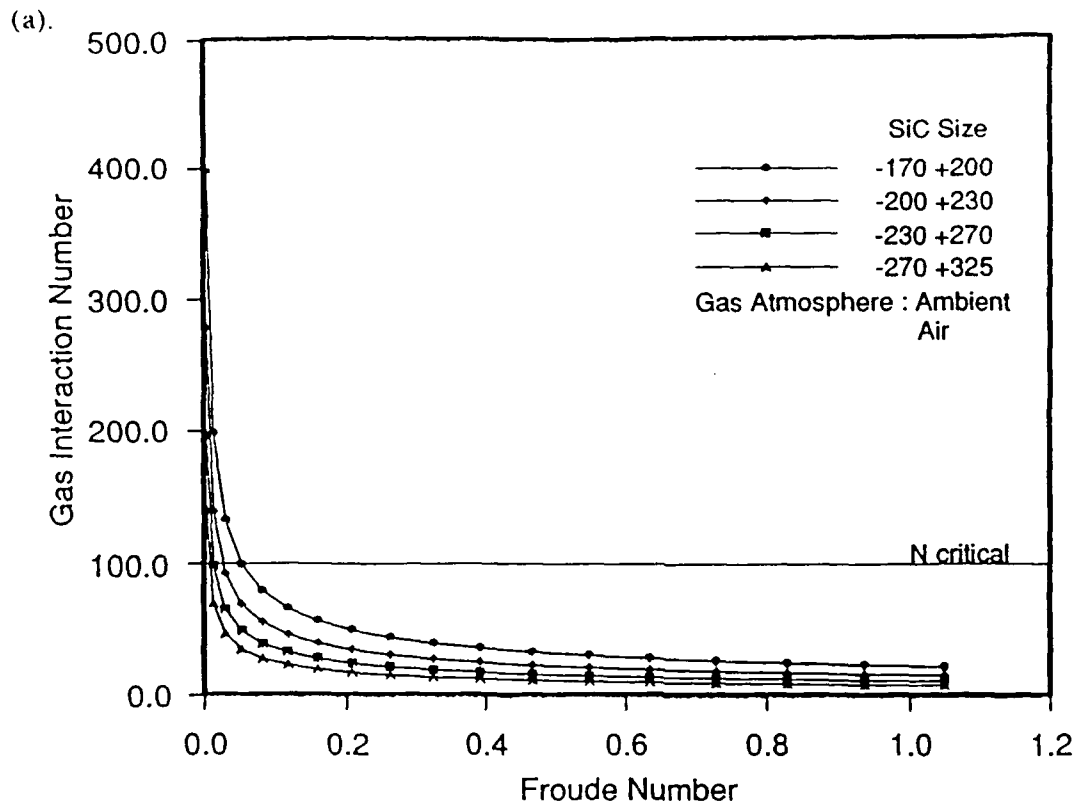


Figure 11: Gas Interaction Number vs.  $\omega^2 R/g$  for SiC powder for (a) ambient air and (b) nitrogen.

The results of the experiments with the nitrogen gas atmosphere are shown in Figures 12 to 15, corresponding to changes in atmosphere from 0.3 atm of  $N_2$  to 3.0 atm of  $N_2$ . Qualitatively, there appears to be little difference in the range of speeds over which the transitions between the various regimes of behavior, especially in the case of the transition from the segregation to the transition region. Here it would be expected that the fluidizing influence of the atmosphere might result in aggravated segregation at the higher pressures, but it can be seen that there is little variation in the boundary speeds from the lowest to the highest pressure. More variation is seen in the boundary between the mixing regime and the upper transition, but it does not appear to be related in any consistent manner with the changes in the gas atmosphere. There does appear to be some trend, however, in the location of the boundary between the upper transition and reverse segregation, with a slight shift to the right occurring for increases in the gas pressure. It would thus appear that there is some retardation of the onset of reverse segregation for higher gas pressures. This may be due to the fact that the SiC powders experience improved flowability, especially at high rpm, and thus can remain in the center of the bed for longer periods of time.

Comparing the gas results with the tests done at ambient atmospheric conditions, it can be seen that there is again very little difference in the values for the boundaries between the various regions. The only major differences lie in the slightly broader upper transition regions in the 0.3, 0.6 and 3.0 atm cases for the nitrogen, and the fact that the occurrence of reverse segregation begins at generally higher values of  $\omega^2 R/g$  for the ambient atmosphere case. From the plots of gas interaction number, it is not surprising that the two cases are so similar. The values for the viscosity of air and nitrogen are quite close, and thus any effect of gas on the mixing of the powders should be similar for the two instances.

### 3.3 Comparison of Model and Powder Material Behavior

In general, the two sets of results (model material and powder material) exhibit the same behavior, though a few small differences can be observed in the position of the region boundaries. First, it appears that the model material experiences core segregation of a wider range of speeds than the powder materials, with the model materials showing core segregation up to values of  $\omega^2 R/g$  greater than 0.25, whereas the powder materials very rarely reached 0.2. The lower transition region, while a little broader in the powder materials, generally appears to end at about the same value of Froude number, approximately 0.4. The range of the mixing region also appears to be fairly uniform between the two cases, with the widest range of the mixing region occurring in most cases for the lowest values of the size ratio in both types of materials. It is difficult to compare the high  $\omega^2 R/g$  behavior due to some differences in the observations, but it would appear that the model materials segregate at lower values of the rpm. This may be due to the fact that the model materials were all spherical in shape, and the fines in the powder material case were irregular. This irregular shape may have impeded motion of the fine powders through the bed and thus retarded the onset of reverse segregation in the powder materials.

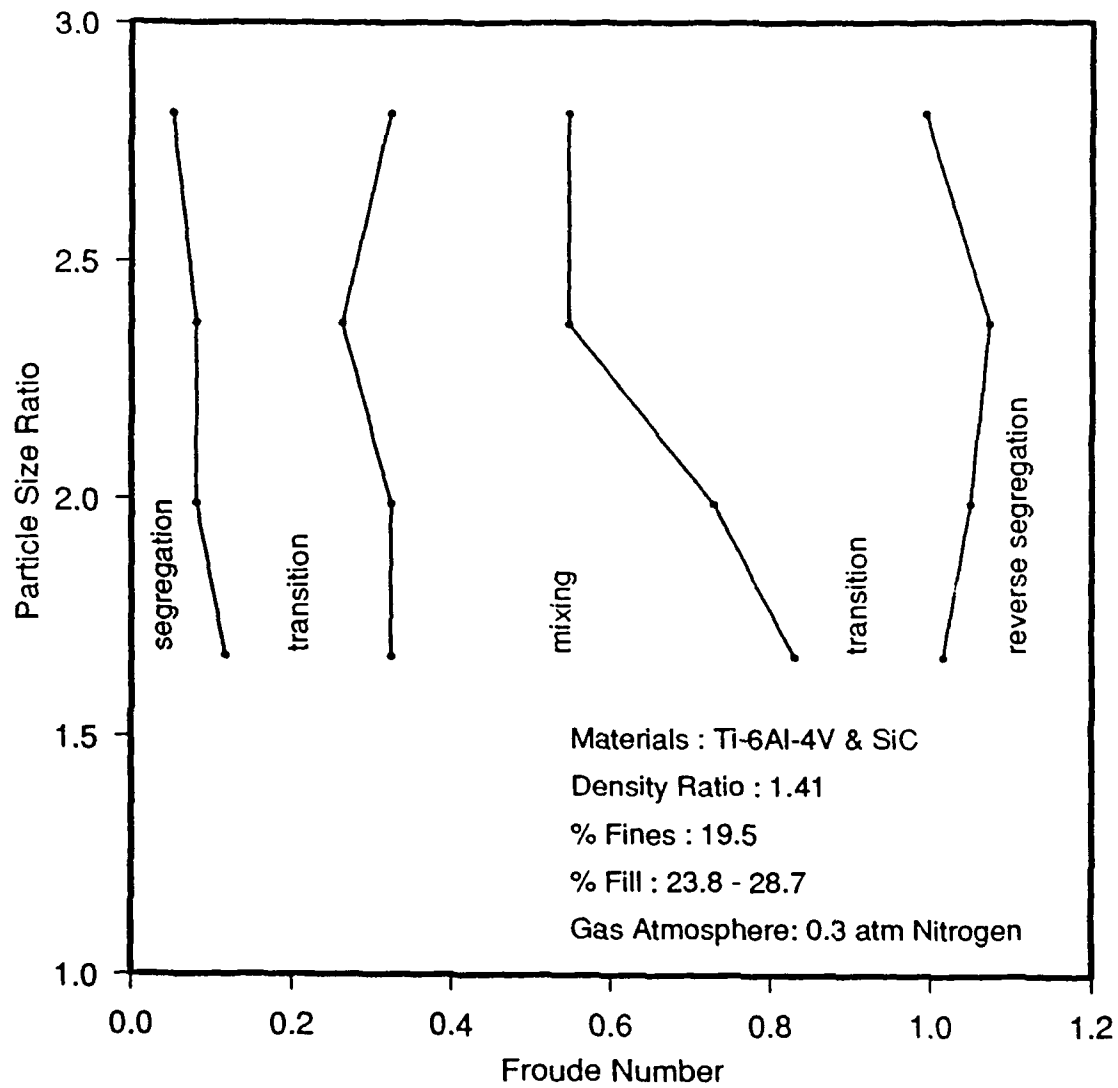


Figure 12: Segregation Behavior Diagram for 0.3 atm Nitrogen.

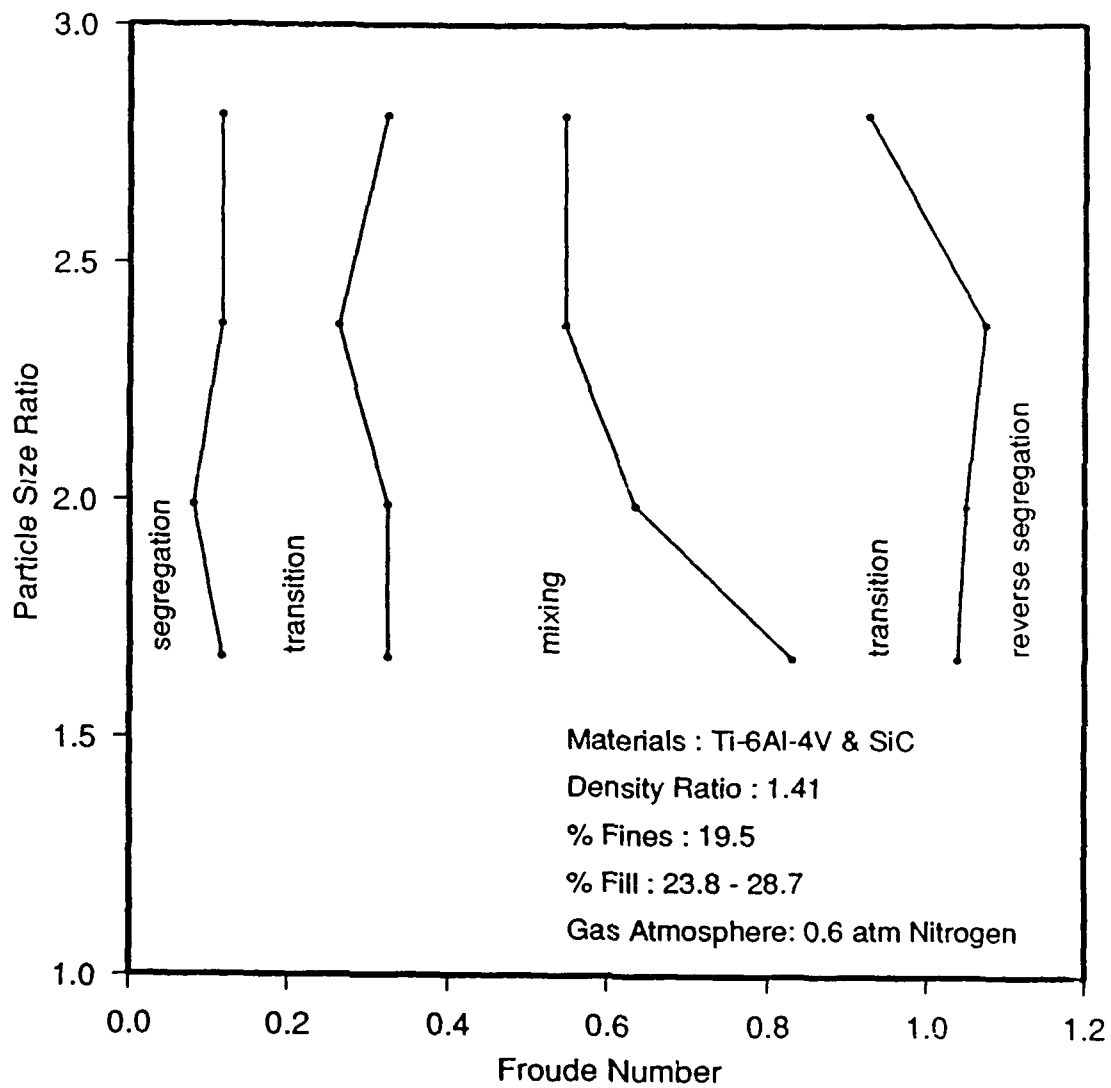


Figure 13: Segregation Behavior Diagram for 0.6 atm Nitrogen.



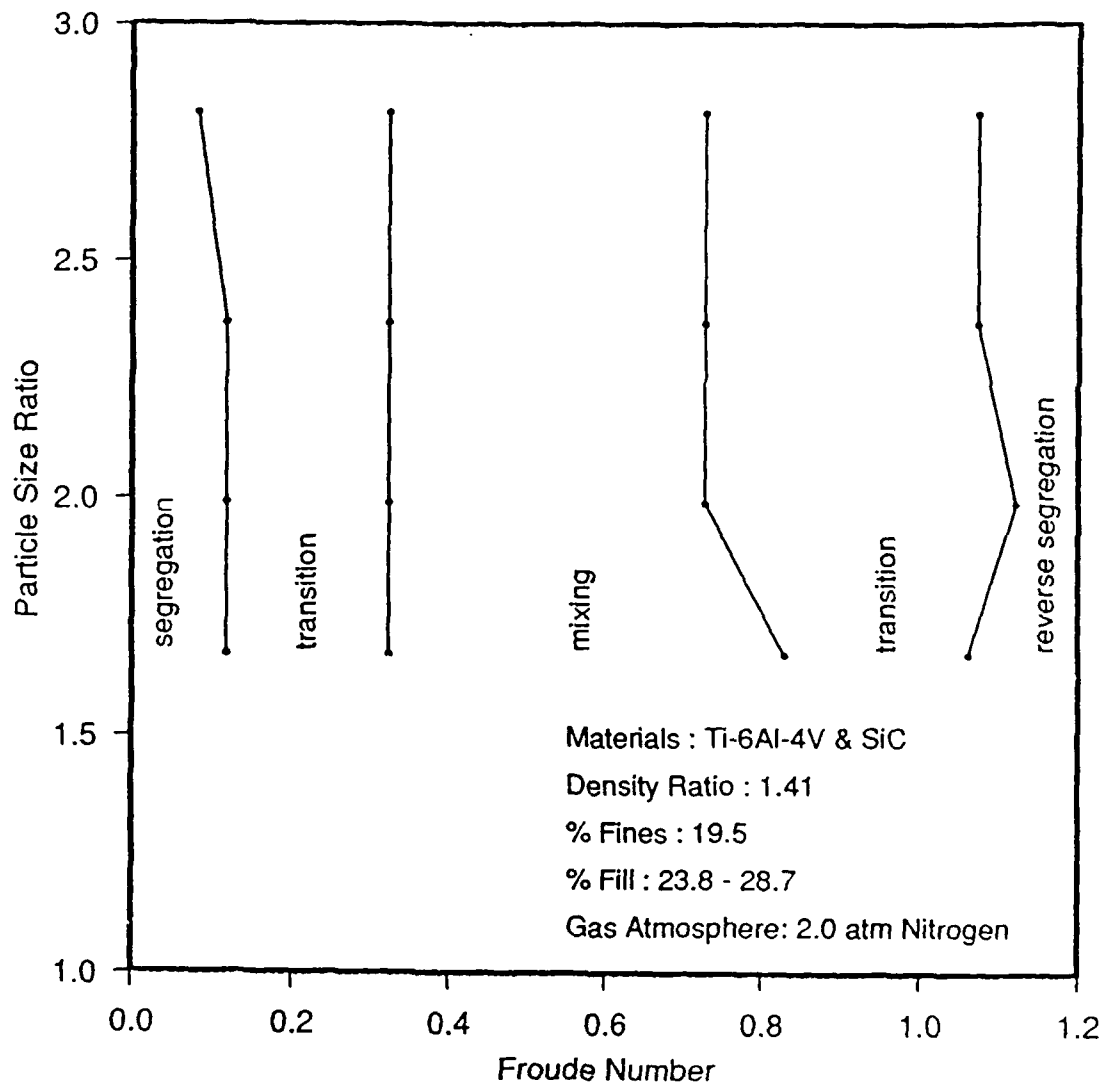


Figure 14: Segregation Behavior Diagram for 2.0 atm Nitrogen.

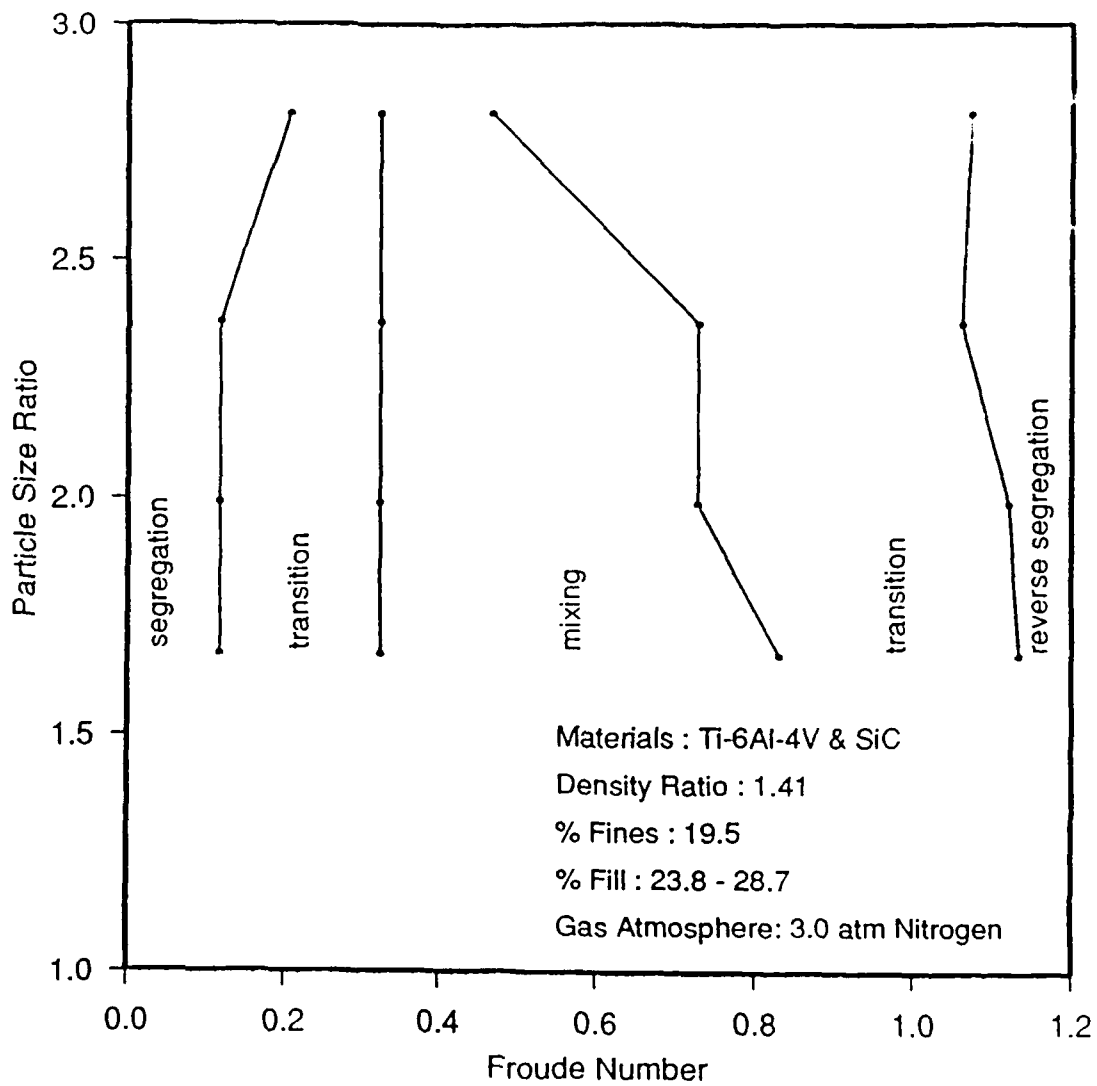


Figure 15: Segregation Behavior Diagram for 3.0 atm Nitrogen.

## References

1. Roseman B., and Donald M.B., "Mixing and De-Mixing of Solid Particles: Part 2. Effects of Varying the Operating Conditions of a Horizontal Drum Mixer", *British Chemical Engineering*, Vol. 7(11), 1962, p. 823-827.
2. Nityanand N., Manley B., and Henein H., "An Analysis of Radial Segregation for Different Sized Spherical Solids in Rotary Cylinders", *Metallurgical Transactions B*, Vol. 17B, 1986, p. 247-257.

## **TASK 1**

**Third-Year Progress Report for the Project**

# **Deformation Processing of Composites**

**Henry R. Piehler  
Daniel M. Watkins  
Michael Kuhni  
John Richter**

**Deformation Processing Laboratory  
Department of Metallurgical Engineering & Materials Science  
Carnegie Mellon University  
Pittsburgh, Pennsylvania 152213-3890**

## *Project Summary*

The objective of this project was to develop a fundamental understanding of the deformation processing of short-fiber, powder-based metal matrix composites for high temperature applications. The knowledge gained from this composite deformation processing study was designed to aid in the selection, fabrication, and performance of these materials and link with the blending research at Carnegie Mellon described in the previous section. The approach used here was to select model composite geometries and materials and design advanced deformation processing equipment in order to be able to physically and analytically model existing and novel composite processing conditions.

We have previously reported on and published our work on HIPing of 7-filament arrays. We have also previously reported on our initial work on hot triaxial compaction (HTC). The rationale for compacting monolithic powders and powder-based metal matrix composites using hot triaxial compaction is that adding a shear component of stress should both enhance compaction and improve the properties of the final compact. We have reported on the design of our unique hot triaxial compaction apparatus and our initial experimental results as well <sup>1</sup>. A copy of this presentation and forthcoming paper is appended. Our unique hot triaxial compaction facility is widely regarded as the most versatile and sophisticated laboratory hot consolidation apparatus in the world.

We have recently successfully blended a composite of SiC whiskers and Ti-6Al-4V REP powders using a wet blending technique that controls the pH to overlap the isoelectric points of both components. We also explored the use of low pressure plasma spraying as a canning technique prior to HTCing, but time and resources prevented our completing this task. These SiC/Ti-6Al-4V compacts will be sinterforged in the near future.

We are in the process of patenting our HTC apparatus and envision a steady stream of process patents using this apparatus in the near future. Work on hot triaxial compaction is continuing under NSF and Alcoa sponsorship. The current focus is on the effects of shear on the mechanisms of hot consolidation of aluminum and alumina powder compacts. A study of HTCing of mechanically alloyed Ti-Al-Nb intermetallics will also be initiated in the near future, again with Alcoa funding.

This year the following degrees have been conferred on students whose theses were performed under this project:

James Bytnar, M.S. in Materials Science and Engineering

Elizabeth Patts, B.S. in Materials Science and Engineering

Daniel Watkins, M.E. in Materials Science and Engineering

Dan is currently involved in the HTCing of aluminum and alumina study described above and is scheduled to complete his Ph.D. in May of 1991.

1. Piehler, H.R. and D.M. Watkins, "Hot Triaxial Compaction: Equipment Description and Initial Experimental Results," *Proc. 2nd International Conf. on Hot Isostatic Pressing*, ASM International, Materials Park, Ohio, in press.

# HOT TRIAXIAL COMPACTION: EQUIPMENT DESCRIPTION AND INITIAL EXPERIMENTAL RESULTS

Henry R. Piehler and Daniel M. Watkins  
Deformation Processing Laboratory  
Department of Metallurgical Engineering and Materials Science  
Carnegie Mellon University  
Pittsburgh, Pennsylvania 15213-3890

Presented at Second International Conference on Hot Isostatic Pressing  
Gaithersburg, Maryland, June 9, 1989

## ABSTRACT

Experiments have been performed in which well controlled shear and hydrostatic stresses are applied to a powder compact during consolidation at elevated temperature. This process, hot triaxial compaction (HTC), involves the addition of an axial stress to the powder compact during hot isostatic pressing (HIPing). The resulting shear stress can have three primary effects in monolithic materials: (1) it can increase the density by increasing both the instantaneous (plastic) volumetric strain and the subsequent (viscous) volumetric strain rate, (2) it can impart strain energy leading to interfacial and/or microstructural changes in the product, and (3) it can disrupt heterogeneities. The superposition of a shear stress during consolidation can also influence the fracture behavior of reinforcing constituents in composites. Initial experimental observations comparing HIPed versus HTCed Ti-6Al-4V spherical powders and a Ti-6Al-4V/SiC particulate composite are presented. A theoretical rationale for the volumetric strain and strain rate effect resulting from the application of shear is also discussed.

The expected benefits from increasing volumetric strain and strain rate via a shear stress in powder metallurgy (P/M) processes include reducing the extent of reaction zones by allowing for consolidation at lower temperature; in essence, trading shear stresses for temperature to obtain the same density. Likewise, this reduction in thermal exposure can be used to limit decomposition of unstable microstructures in rapidly solidified materials and reduce grain growth in metals and ceramics.

## 1. INTRODUCTION

Interest in the effect of shear on powder compaction is motivated by the need for ceramics, composites, rapidly solidified metals, intermetallics and other advanced materials where P/M is an attractive, or possibly the only, processing route. In the most common consolidation techniques shear is absent (sintering, HIPing) or is difficult to characterize or control (hot pressing, powder extrusion). Some existing processes (Ceracon process [1], combined die forging [2], rapid omnidirectional compaction [3]) can impart shear stresses during compaction, but characterization and control of these stresses is also limited. By imposing a well controlled stress state, HTC can be used to understand the role of shear in these processes and, perhaps, to suggest new processes. A first attempt has been made to describe the micromechanisms through which the strain rate and achievable volumetric strain are increased. These micromechanisms include [4] plasticity, power law creep, diffusional creep, diffusion, and interparticle sliding.

**Hot Triaxial Compaction (HTC)** - In HTC the powder compact is loaded by both the gas pressure (as in HIP) and by a ram which exerts an axial force on the specimen. In order to differentiate between the mean stress (i.e., one third of the trace of the stress tensor) and the gas pressure, the latter will always be referred to as the gas pressure or the confining pressure.

When a powder compact is subjected to the most general homogeneous, triaxial stress state, the hydrostatic and deviatoric components of macroscopic stress are

$$\sigma_m = \frac{1}{3} \sigma_{ii} \quad (1)$$

$$\sigma'_{ij} = \sigma_{ij} - \delta_{ij} \sigma_m \quad (2)$$

respectively. Since all experiments and processes to date (including this research) involve an axisymmetric stress state, the notation shown in figure (1) is adopted.

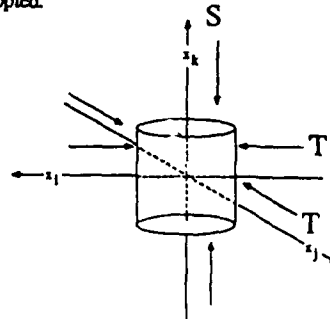


Fig. 1 General axisymmetric triaxial stress state. S and T are the applied normal stresses. The confining pressure is equal to T and the additional axial force equal to S-T.

Thus equations (1,2) become

$$\sigma_m = \frac{2T+S}{3} \quad (3)$$

and

$$\sigma'_{11} = -2\sigma'_{22} = -2\sigma'_{33} = \frac{2}{3}(S - T) \quad (4)$$

and the effective stress, defined as

$$\bar{\sigma} = \sqrt{\frac{3}{2}(\sigma'_{11}{}^2 + \sigma'_{22}{}^2 + \sigma'_{33}{}^2)} \quad (5)$$

becomes

$$\bar{\sigma} = (S - T) \quad (6)$$

This stress,  $\bar{\sigma}$ , is the stress which, absent in HIP, enhances densification in HTC.

**Background** - The evidence that shear stresses enhance the consolidation of metallic and ceramic compacts is found in several key works and a large collection of "indications" from studies focused in other directions. For instance, geological and geotechnical materials are often porous and a wealth of literature exists for hot triaxial testing of these materials under conditions of a compressive volumetric strain. However, it appears that the dilatant rather than the compressive behavior has been of primary interest in these geological studies. The work on void growth in creep is also relevant to this study.

Enhanced consolidation in the plastic regime has been well documented. Koerner [5] triaxially compacted iron powders using an axisymmetric stress state at room temperature. Figure (2) shows Koerner's results replotted in deviatoric stress - hydrostatic stress space. These results are typical for powder metal consolidation. Schock, et al., [6] performed hydrostatic and triaxial compaction experiments on aluminum preforms containing 23.6% initial porosity. These experiments show that shear enhanced compaction is most evident at higher confining pressures (>0.5 GPa) and higher density. In fact, in the hydrostatic case, the volume strain appears to reach an asymptotically limiting value with increasing pressure, indicating that, in addition to the increase in densification rate, the absolute density attainable may be increased by shear.

Because of experimental difficulty, a much smaller body of research exists for elevated temperature compaction. Hot pressing studies are common but the inhomogeneous stress state induced by wall friction and the difficulty in determining the lateral force without having a developed flow model, *a priori*, makes analysis extremely difficult. Another experimental technique, sinterforging, involves uniaxial pressing (S only) on a sintering compact. In experiments on sinterforging of alumina [7] and superalloy powders [8], higher densities were achieved more rapidly with the addition of S. Sinterforging provides for the application of known hydrostatic and shear stresses, unlike hot pressing where T is unknown and may tend toward S as relative density, D, approaches one,  $D \rightarrow 1$ . For sinterforging  $T=0$ , so the stress state is described by:

$$\sigma_m = \frac{S}{3} \quad (7)$$

$$\bar{\sigma} = S \quad (8)$$

Thus, in sinterforging the shear and hydrostatic stress components are coupled and not independently variable. If plotted in  $\sigma_m - \bar{\sigma}$  space, the sinterforging data all fall on the single line:  $3\sigma_m = \bar{\sigma}$ .

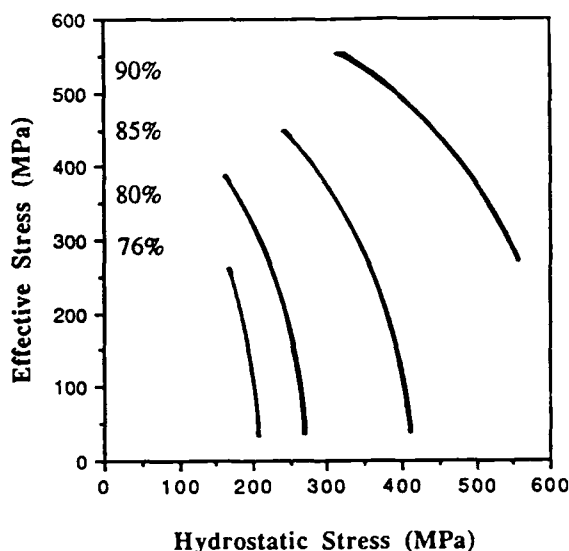


Fig. 2 Yield surfaces in  $\sigma_m - \bar{\sigma}$  space showing the effect of shear stress on room temperature powder compaction. From Koerner [5].

In the only previous hot triaxial processing of powders of which the authors are aware, Buschow, et al., [9] consolidated  $\text{SmCo}_5$  powder in a hot triaxial compaction unit capable of processing permanent magnet powders at 2.0 GPa confining pressure and temperatures up to  $300^\circ\text{C}$ . At  $\sigma_m = 3.2\text{ GPa}$  and  $\bar{\sigma} = 3.6\text{ GPa}$ , the compact density reached 97% of theoretical density (at which time fracture occurs in the constant strain rate test) whereas in a purely hydrostatic test,  $\sigma_m = 4.0\text{ GPa}$ , the maximum density achieved is only 86%. These results further illustrate the dramatic density enhancement achieved when a shear stress is added to the usual hydrostatic component.

## 2. EXPERIMENTAL PROCEDURES

Equipment for room temperature triaxial consolidation of P/M materials is described by Koerner [5] and in detail by Meerman and Knaapen [10]. Extension to high temperature studies involves considerable modification because of space limitations, electrical feed-throughs, and thermocouple feed-throughs. The furnace design for cold wall vessels is also critical in that conductive and convective heat flow must be limited yet force must be transmitted to the specimen by load bearing members [11,12]. Considerable expertise does exist for designing the smaller furnaces used in creep testing of rocks (specimen size < 10mm diameter). Some ideas for the CMU HTC unit are borrowed from this technology. The basic design philosophy for pressure vessels and furnaces used in geological testing is described in the excellent review by Patterson [12].

The HTC apparatus used for these experiments is a modified HIP unit. A schematic of the unit is shown in figure (3). A redesigned lower closure in the 300 MPa, 11.4 cm. (4.5 in.) diameter bore, tie rod pressure vessel allows a ram to move into the hot zone and apply the additional axial stress to the specimen. Bridgman type unsupported area pressure seals are utilized. The ram is motivated by a 600 kN force hydraulic cylinder. Force is measured via a spindle shaped column set into the adaptor between the hydraulic cylinder and the ram. This type of external load cell has the disadvantage of incorporating an unknown seal friction into the load measurement. In these present experiments,

the axial load is applied after the final pressure is achieved and the differential force is taken to be the applied axial load, thus minimizing the effect of the unknown frictional force. Pressure is measured via bourdon tube dial gages and an electronic transducer.

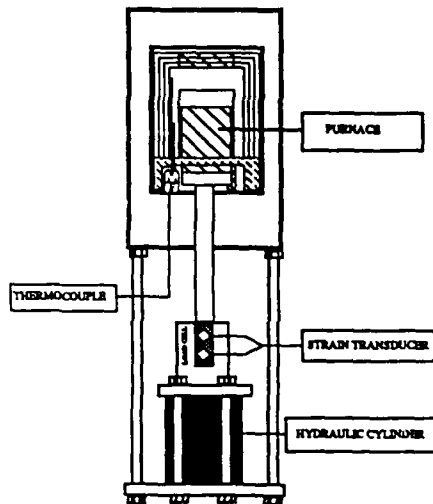


Fig. 3 Schematic of HTC unit. Load cell is mounted externally.

The heating elements are molybdenum wire resistance heaters. In order to accommodate the force transmission and limit thermal conductivity, low conductivity zirconia ceramic discs are inserted between the ram and the specimen.

### 3. EXPERIMENTAL RESULTS AND DISCUSSION

Ti-6Al-4V spherical PREP powders, 100-150  $\mu\text{m}$  in diameter, supplied by RMI (Niles, Ohio), were encapsulated in carbon steel (1020) tubes whose ends were both subsequently pinched while under vacuum. No hot degassing was used in these initial experiments. The apparatus is then ramped to the predetermined temperature and pressure. All ramp times, pressures, and temperatures were imposed as identically as possible to allow for comparability among samples. The processing schedules for all specimens are contained in Table 1.

After compaction, the steel cans are chemically removed and the specimens sectioned near the center. All micrographs on all specimens are taken on the longitudinal plane near the center of the compact. Typical sections are presented in all of the following figures. Relative density was determined by a simple point count method with an estimated accuracy of  $\pm 0.05\%$ . Although specimen 1B appears fully dense, any feature which could be very small scale porosity was counted as such, giving us the most conservative (lower bound) estimate of the density possible.

Figures (4) (HIPed) and (5) (HTCed) show the effect of the absence or presence of shear on densification for the same hydrostatic stress, temperature, and hold time. Though the hydrostatic component of stress is maintained equal for both specimens, the specimen with additional shear or deviatoric stress (the HTCed specimen) is nearly fully dense. The HIPed specimen shows noticeably higher porosity (99.5% dense). The ramp up pressure profile for each sample was chosen to be as close to the final gas pressure as possible when the final temperature was achieved. This gas pressure for the HTCed sample is less than that for the HIPed sample, since a part of the final hydrostatic stress on the HTCed sample is imposed only when the axial load is applied. Thus one would expect that the HIPed sample was more dense than the HTCed specimen at the beginning of the 30 minute hold. Even so, a dramatic increase in density is seen for the HTC process; virtually no pores are visible in the HTCed sample.

The composites were processed to achieve full density in order to observe any alignment of or damage to the reinforcing phase (SiC). Figure (6), a scanning electron micrograph of the HIPed composite sample shows no preferential alignment of the SiC particles, while the HTCed sample in Figure (7) shows a marked vertical alignment of the SiC (the direction of the axial force is horizontal). Figures (8) (HIPed) and (9) (HTCed) show that particulate fracture is actually enhanced by HTCing for the particular processing parameters used here. Figure (10) is a higher magnification scanning electron micrograph of a fractured SiC particle after HIPing, showing displacement and rotation of the SiC fragments after fracture.

### 4. IMPLICATIONS FOR MODELING OF DENSIFICATION PROCESSES

Following Coble [13] we shall define stage one as the range of densification up to the transition to isolated porosity, at which point stage 2 begins. Helle, et al., [4] define this transition at approximately  $D = 0.9$ . Since the experiments here included significant ramp time prior to the application of the axial force, the porosity is assumed to be isolated during the triaxial part of the test. Thus only the final stage of densification is of relevance here.

The micromechanisms operating in HIPing are identified by Wilkinson [14] as power law creep, plasticity, and diffusion. Helle, et al., [4] extend the analysis to include Nabarro-Herring-Coble creep and grain growth effects. The addition of shear is expected to modify these mechanisms and possibly their interactions. As a first estimate, the possible shear-caused densification enhancement mechanisms operating in the final stage include:

1. Enhanced viscous collapse of pores, causing power law or diffusional creep to be the dominant mechanism to higher densities.
2. Enhanced diffusional densification.
3. Activation barrier for creep is achieved even at high density.
4. Increased time independent plastic flow.

Specimen	Composition	Time (hr)	Temp ( $^{\circ}\text{C}$ )	T(MPa)	S(MPa)	$\sigma_m$ (MPa)	$\bar{\sigma}$ (MPa)	$D_{final}(\%)$
1A	Ti-6Al-4V	.5	850	117	0.0	117	0	99.59
1B	Ti-6Al-4V	.5	850	89.7	169	116	79.3	99.84
2A	Ti-6Al-4V + ~20% SiC	.5	850	135	0.0	135	0	100
2B	Ti-6Al-4V + ~20% SiC	.5	850	101	180	128	79.3	100

TABLE 1. Experimental conditions, stress states, and densities for HIPed (1A,2A) and HTCed (1B,2B) compacts.



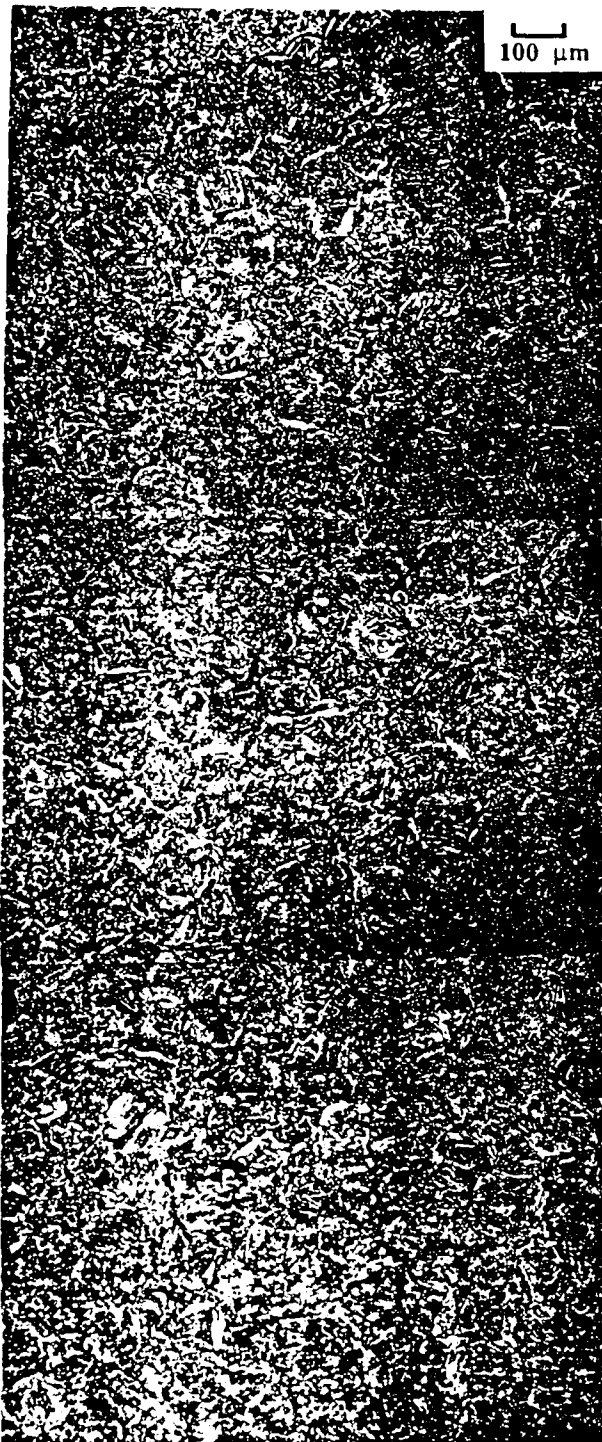


Fig. 4. Specimen 1A (HIP'd) showing significant residual porosity. Steel container is at the top of the figure.

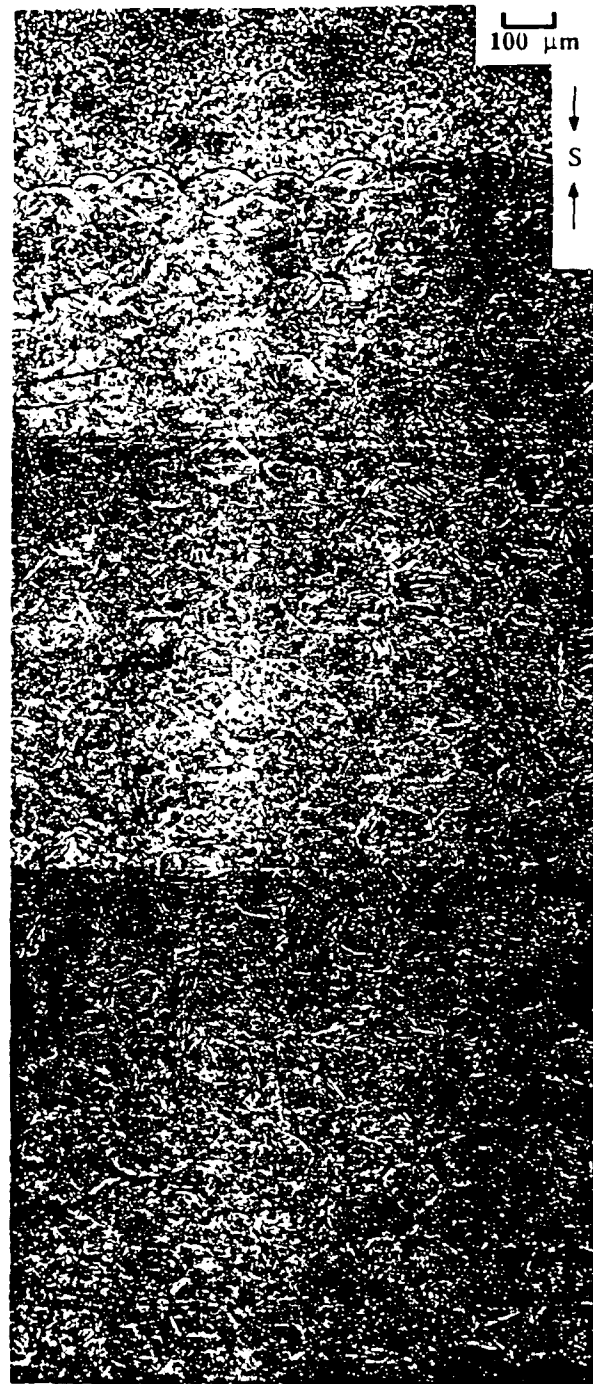


Fig. 5. Specimen 1B (HIP'd) appears nearly fully dense. Processed at the same hydrostatic stress as specimen 1A plus an additional deviatoric stress. The direction of stress is shown.

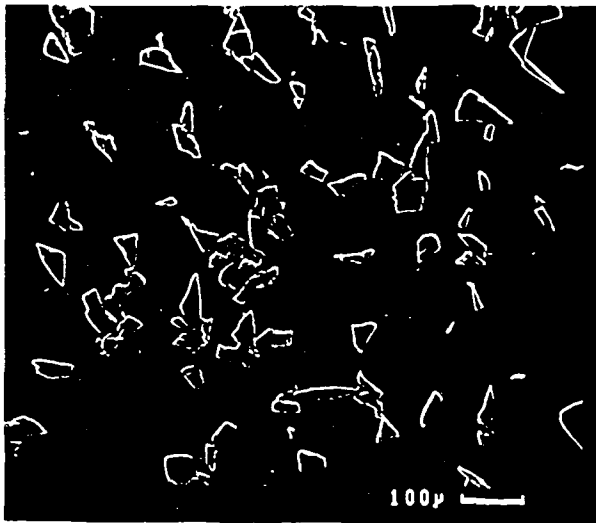


Fig. 6 Specimen 2A (HIPed) shows no alignment of the SiC particulates.

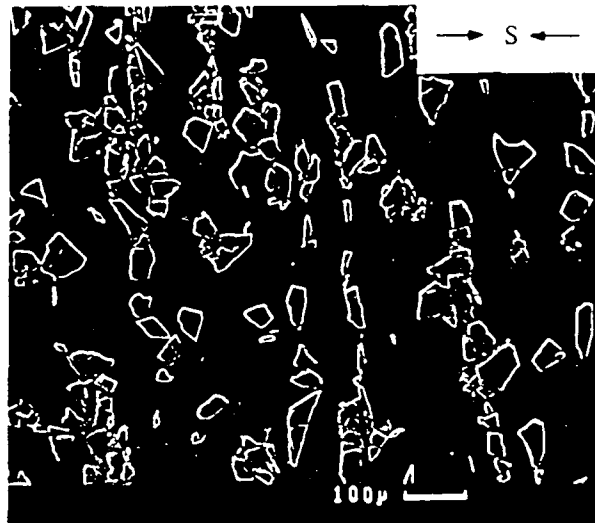


Fig. 7 Specimen 2B (HTCed) shows alignment perpendicular to the applied axial force.

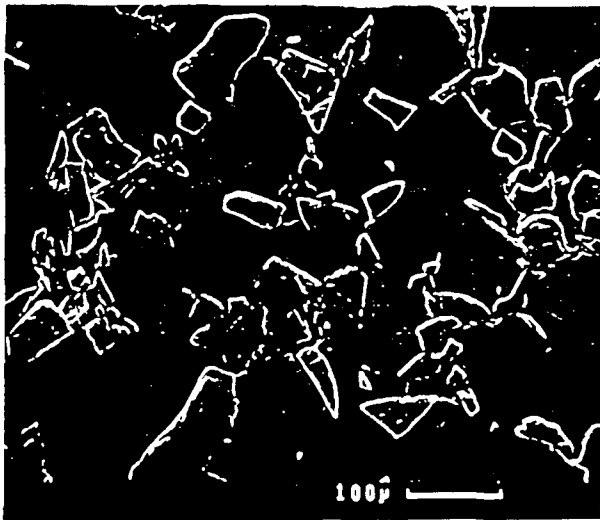


Fig. 8 Specimen 2A (HIPed) shows large, unfractured particulate. Notice large particles at upper and lower left of micrograph.

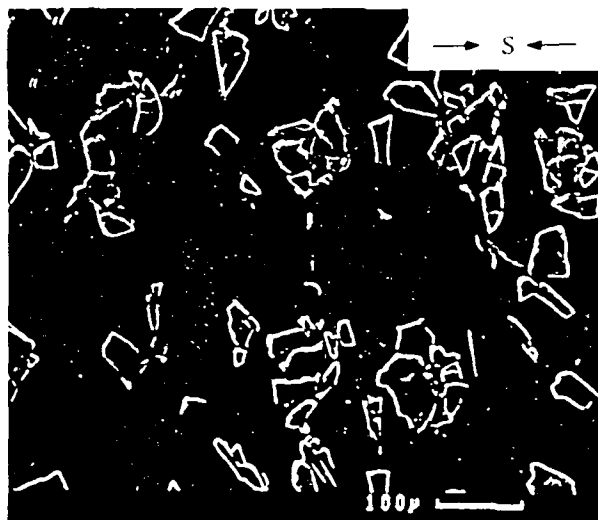


Fig. 9 Specimen 2B (HTCed) shows few large unfractured particles. Magnification is the same as fig. 8.

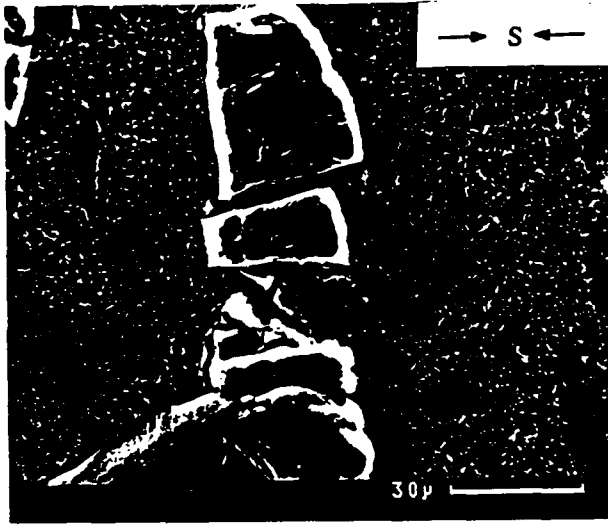


Fig. 10 Displacement and rotation of SiC particle fractured during processing in specimen 2B (HTCed).

The following is a short discussion on each possible effect and appropriate equations to illustrate the potential for volumetric strain and strain rate enhancement resulting from deviatoric stress:

**Viscous collapse of pores** - Pores can collapse (or grow) by power law (PLC) or diffusional creep of the surrounding material. In the simplest case, a spherical pore (physically realistic in the case of rapid surface diffusion) is seen to be compressed at a higher rate when the hydrostatic stress state is imbalanced by a shear. In the hydrostatic case, the local deviatoric strains caused by the porosity become smaller as the theoretical density approaches 1 and the amount of material to move (per the boundary condition for pore spacing) increases relative to the pore size. Thus, at some point as  $D \rightarrow 1$ , it is expected that the contribution of creep to compaction approaches zero and may actually be zero. Under HTC conditions, since the hydrostatic stress state is imbalanced, the entire compact should continually exhibit some creep, even at  $D=1$ . Dislocations would move more easily in the geometrically constrained regions around the pore. Further, the climb processes in the bulk during creep may contribute to the flux of atoms to the pore through vacancy elimination. The equation of Norton's Law for multiaxial creep

$$\dot{\epsilon}_{ij} = \frac{3}{2} \dot{\epsilon}_0 (\bar{\sigma}/\sigma_0)^{n-1} \sigma'_{ij} / \sigma_0 \quad (9)$$

illustrates the role of the effective stress at a microscopic level. If an increase in effective stress is realized through the addition of a macroscopic, far field, stress, then the densification rate is expected to increase.

Several models exist through which the effect of a far field stress on a pore can be analyzed. Wilkinson [14] presents a simple model for the spherical pore, hydrostatic pressure case, Hellan [15] presents a model for sphere growth in non-hydrostatic creep, Budiansky, et al., [16] and Banks-Sills and Budiansky [17] present a model for any axisymmetric strain state. The complexity of the Budiansky model makes a first analysis easier if we assume that the pore remains roughly spherical, the rate of collapse is given by [16]:

$$\frac{\dot{V}}{V} = - \frac{3\dot{\epsilon}_0}{2\sigma_0^n} \left( \frac{3\sigma_m}{2n} + \frac{(n-1)(n+0.4031)}{n^2} |\bar{\sigma}| \right)^n \quad (10)$$

Using the relationship

$$\dot{D} = D(1-D) \frac{\dot{V}}{V} \quad (11)$$

results in

$$\dot{D} = D(1-D) \frac{3\dot{\epsilon}_0}{2\sigma_0^n} \left( \frac{3\sigma_m}{2n} + \frac{(n-1)(n+0.4031)}{n^2} |\bar{\sigma}| \right)^n \quad (12)$$

This equation predicts no contribution to densification from shear stress when the material is linearly viscous and spherical porosity is maintained. But when, for example,  $n=4$  and the stress state is taken to be that for our specimens 1A and 1B the ratio of densification rates can be estimated, using equation (12), as:

$$\frac{\dot{D}_{1B(HTC)}}{\dot{D}_{1A(HIP)}} = 42.5 \quad (13)$$

So the closure rate for the porosity in the final stage is 1-2 orders of magnitude higher for the HTCed compact. Constraining the pore to remain spherical in the HTCed sample is thought to give a lower bound estimate for this ratio.

**Enhanced diffusional densification** - In present models for both stress assisted diffusional sintering [4,13] and for diffusional void growth in a creeping matrix [18] the predicted volumetric strain rate is linear with normal stress on prior particle boundaries. Thus, these models predict that constant hydrostatic stress should define a unique volumetric strain rate regardless of deviatoric stress. But, when the material is simultaneously creeping, coupled mechanism effects may arise.

The most obvious effect is the predicted pore collapse to a penny shaped crack [16,17] during creep in a non-hydrostatic macroscopic stress field. The curvature of the pore will be changed and thus the driving force for diffusional flow [13]

$$\frac{\gamma}{r} + \frac{P}{\kappa} \quad (14)$$

will be increased in the plane of maximum  $P$ , where  $\gamma$  is the surface energy of the pore,  $r$  is the radius of curvature,  $P$  is the applied normal stress and is equal to  $S$  in the plane of minimum  $r$ . The contribution is small though (10% at  $r=0.6\mu\text{m}$  when  $\gamma=2\text{ J/m}^2$  and  $S=100\text{MPa}$ ) and depends on the competition between surface diffusion (spheroidizing the

pore) and creep (closing the pore to a penny shaped crack). It is also unknown what the integrated effect is around the entire pore; curvature is increased in some directions and decreased in others. No high aspect ratio pores were observed in the HTCed compact (1B).

The second possible effect is that of creep on the stress distribution to modify the diffusion potential gradient. An analysis has yet to be made on this coupled effect.

**Activation Energy Barrier to Creep Achieved** - It is well known that, under some circumstances, creep requires a minimum effective stress to operate. In some materials this barrier could be a constraint to final stage densification in the HIP process as the material far from pores becomes subject to a more hydrostatic state of stress. The macroscopic effective stress introduced by HTC would circumvent this barrier.

**Increased Time Independent Plastic Flow** - Yield functions for porous materials are generally of the form [19]

$$A\bar{\sigma}^3 + B\sigma_m^2 = \delta Y_0^2 \quad (15)$$

where A, B, and  $\delta$  are functions of density and  $Y_0$  is the yield stress of the fully dense material. The plot of the yield function in figure (11) shows that yielding by  $\sigma_m$  alone is increasingly difficult. If yield surface normality is considered, the plastic strain vector for a combined hydrostatic and deviatoric loading has a component along  $\sigma_m$ . Thus densification is stimulated at a lower  $\sigma_m$  than for  $\bar{\sigma}=0$ . This is especially important where D is close to unity since, as  $D \rightarrow 1$ ,  $\sigma_m(\text{yield}) \rightarrow \infty$ .

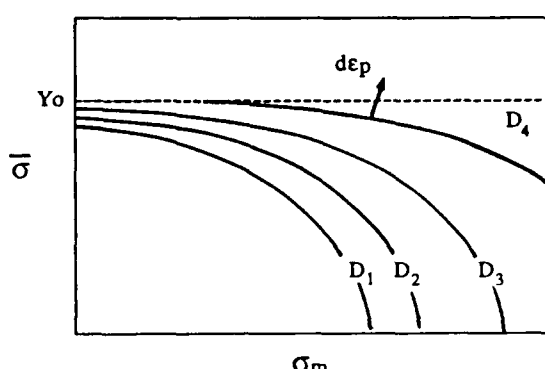


Fig. 11 Yield surface for a porous material.  $Y_0$  is the yield stress of a 100% dense specimen. The plastic strain vector,  $dep$ , is shown normal to the yield surface. With the addition of shear stresses, plastic strain in the volumetric direction is stimulated at a lower hydrostatic stress than required in the absence of shear. Note:  $D_4 > D_3 > D_2 > D_1$ .

## 5. CONCLUSIONS

1. A Hot Triaxial Compaction apparatus has been built to study consolidation under triaxial stress states at elevated temperatures.
2. Enhanced second stage densification was observed in HTCed Ti-6Al-4V spherical powder compacts compared to comparable HIP compacts.

3. Hot triaxial compacted particulate composites were observed to exhibit greater particle alignment and increased particle fracture than comparable HIP processed composites.

4. Densification is enhanced through creep and plastic flow mechanisms by the addition of a macroscopic deviatoric stress component to the usual HIP process. The effect of shear on diffusional densification is not clear.

## ACKNOWLEDGMENTS

We appreciate support of this work by the U.S. Air Force Office of Scientific Research, contract F49620-87-C-0017, as part of the University Research Initiative program on High Temperature Metal Matrix Composites at Carnegie Mellon University, by Alcoa, and by the National Science Foundation under contract MSM 8714377.

The assistance of Michael Kuhn and John Richter is gratefully acknowledged.

## REFERENCES

1. C.G. Levi, R. Mehrabian, B. Oslin, R. L. Anderson, and S. M. L. Sastry, *J. Mater. Shaping Technol.* vol. 6, no. 2, 125-132 (1988)
2. W. Smarsly, W. Bunk, R. Kopp, in *Proc. 5th Int. Conf. on Titanium*, Munich (1984)
3. J. R. Lizenby, W. J. Rozmus, J. L. Barnard, and C. Kelto, A., in *Metal Powder Report Conference*, Zurich (1980)
4. A.S. Helle, K.E. Easterling, and M.F. Ashby, *Acta Metall.* vol. 33, 2163-2174 (1985)
5. R. M. Koerner, in *Powder Metallurgy Processing: New Techniques and Applications* (edited by H. A. Kuhn and A. Lawley), Academic Press, NY (1978)
6. R. N. Schock, A.B. Abey, and A. Duba, *J. Appl. Phys.* vol. 47, 53-63 (1976)
7. K. R. Venkatachari and R. Raj, *J. Am. Ceram. Soc.* vol. 69 no. 6, 499-506 (1986)
8. P. C. Panda, J. LaGraff, and R. Raj, *Cornell University Materials Science Report*, June 15 1987.
9. K. H. J. Buschow, P.A. Naastepad, and F. F. Westendorp, *J. Applied Phys.* vol. 40 no. 10, 4029-4032 (1969)
10. W. C.P.M. Meerman and A.C. Knaapen, *Powder Technology*, vol. 32, 271-278 (1979)
11. P. Malbunot, P.A. Meunier, and D. Vidal, *Chem. Eng. World* vol. 7, 53-58 (1972)
12. M. S. Patterson, *Int. J. Rock. Mech.* vol. 7, 517-526 (1970)
13. R. L. Coble, *J. Applied Phys.* vol. 41 no. 12, 4798-4807 (1970)
14. D.S. Wilkinson, Ph.D Thesis, University of Cambridge, UK (1978)
15. K. Hellan, *Int. J. Mech. Sci.* vol. 17, pp. 369-374 (1975)
16. B. Budiansky, J. W. Hutchinson, and S. Slutsky, in *Mechanics of Solids: The Rodney Hill 60th Anniversary Volume* (edited by H. G. Hopkins et al.), 13-45 (1982)
17. L. Banks-Sills and B. Budiansky, *Mechanics of Materials* vol. 1, 209-218 (1982)
18. R. Raj, H. M. Shih, and H. H. Johnson, *Scripta Metall.* vol. 11, 839-842 (1977)
19. S. M. Doraivelu, H. L. Gegel, J. S. Gunasekera, J. C. Malas, J. T. Morgan, and J. F. Thomas, *J. Mech. Sci.* vol. 26 no. 9/10, 527-535 (1984)

BLANK

## TASK 2

### High Temperature Structural Materials

H.J. Rack, Investigator

Task 2 of the URI on High-Temperature Metal Matrix Composites, the task title of which is "Modeling of Consolidation and Deformation Processing of Composites", was conducted at Clemson University in the form of three sub-tasks. The Annual Report for this Task consists of separate summaries for each of the three sub-task projects. They are listed below, with the titles of the summaries reflecting the topics of the individual projects. The first sub-task was an investigation of titanium aluminide alloys, including those of Ti-Al-V composition as well as the more widely studied Ti-Al-Nb-V alloys, with the intent to apply this knowledge to development of aluminide-matrix composites. The second addressed the need to understand and improve interfacial behavior and control of bonding between reinforcements and matrix in metal matrix composites, with emphasis on development of coating selection and application methods. The third sub-task was a study of two model composites, TiC-reinforced Inconel 718 and SiC-reinforced Mg-6 Zn, with a view to understanding their stability against coarsening. In both cases, the matrix alloy is a well-studied material, particularly the 718, which is a widely-used nickel-base superalloy of intermediate temperature capability. The particulate reinforcements of TiC and SiC, which are relatively stable in the respective alloys, were studied to understand changes, if any, in precipitation sequences and coarsening in the composites, relative to normal alloy matrices.

	<u>Page</u>
<b>SUB-TASK 1</b>	
"Elevated Temperature Flow Behavior of Titanium Intermetallic Alloys"	
H.J. Rack, M. Long, E. Wachtel, and J. Wung	67
<b>SUB-TASK 2</b>	
"Fiber-Matrix Interactions"	
H.J. Rack, H.G. Spencer, J.P. Clement and K.T. Wu	102
<b>SUB-TASK 3</b>	
"Matrix Precipitation and Coarsening"	
H.J. Rack, P. Chaudhury, E. Wachtel and J. Wung	133

BLANK

HIGH TEMPERATURE METAL MATRIX COMPOSITES

FINAL REPORT

H. J. Rack, H. G. Spencer, P. Chaudhury,  
J. P. Clement, M. Long, E. Wachtel, K. T. Wu and J. Wung

Materials Engineering Activity  
Department of Mechanical Engineering  
Clemson University  
Clemson, South Carolina 29634-0921

November 30, 1989



OBJECTIVE

This task's objective was to achieve a fundamental understanding of the elevated temperature flow and fracture behavior of metal matrix composites. High temperature flow behavior is being approached through a detailed examination of the temperature-strain rate behavior of selected titanium intermetallic matrices and composites. Parallel studies included reinforcement-matrix interactions, and matrix stability, precipitation and coarsening.

This report covers the period 1 January 1987 through 30 September 1990.

## SUB-TASK 1

### ELEVATED TEMPERATURE FLOW BEHAVIOR OF TITANIUM INTERMETALLIC ALLOYS

H. J. Rack, M. Long, E. Wachtel and J. Wung

This sub-task was designed to examine the high temperature flow and fracture behavior of titanium aluminide alloys intended for use as either monolithic materials or as matrices for advanced metal matrix composites. The thermodynamic stability of selected titanium aluminide alloys has been examined, with high temperature plasticity studies continuing under ONR/DARPA sponsorship.

#### INTRODUCTION

Titanium intermetallic compounds,  $TiAl$ , and  $Ti_3Al$ , offer great potential for elevated temperature application either as monolithic alloys or as matrix materials for fiber reinforced metal matrix composites. To date their application has, however, been limited by their low room temperature ductility and fracture toughness.

Various authors have suggested that the deformation behavior of these compounds can be enhanced through both alloying and appropriate thermomechanical treatment(1,2). Alloying involves introduction of ternary and quaternary elements which may enhance ductility and fracture toughness through either a change in the bond strength, for example, in  $\gamma$  alloys by a decrease in the c/a ratio or the cell volume, or through the introduction of a second phase, e.g.,  $\beta$  in  $\alpha_2$  and  $\alpha_2$ ,  $\beta$  in  $\gamma$  alloys.

Alternatively, it is envisioned that thermomechanical procedures can be utilized to control the metallurgical structure, e.g., the grain size, dispersion of  $\beta$  in  $\alpha_2$ , lamellar/ $\gamma$  plate thickness in  $\gamma$  alloys, etc., all

factors which appear to contribute to the ductility and fracture toughness behavior of  $\alpha_2$  and  $\gamma$ .

$\alpha_2$  Ti<sub>3</sub>Al and  $\gamma$  TiAl have ordered hexagonal DO<sub>19</sub> and face centered tetragonal L1<sub>0</sub> crystal structures, respectively, and exhibit a wide range of homogeneity, Figure 1. While the phase diagram shown in Figure 1 is still the subject of continuing investigation(3-8), it does indicate that on heating both  $\alpha_2$  and  $\gamma$  undergo a series of transformations, e.g.,  $\alpha_2 \rightarrow \alpha_2 \beta \rightarrow \beta$ . Clearly, if optimal use of thermomechanical processing procedures is to occur it is therefore important that processing be coupled with a knowledge of phase stability at elevated temperature.

The current investigation was designed to consider both effects in a series of  $\alpha_2$  and  $\gamma$  titanium aluminide alloys, with primary emphasis being placed on establishing a fundamental basis for describing the elevated temperature flow behavior of these systems under strain, strain rate and temperature conditions typical of those expected during thermomechanical processing. It was intended that these results form the framework for design of appropriate thermo-mechanical processing treatments aimed at optimizing the mechanical performance of  $\alpha_2$  and  $\gamma$  titanium aluminide alloys. Both commercial  $\alpha_2$ , Ti-24Al-11Nb/Ti-25Al-10Nb-3V-1Mo, and model  $\alpha_2$  and  $\gamma$  alloys have been included in this study.

## EXPERIMENTAL PROCEDURES

### Materials

Ti<sub>3</sub>Al,  $\alpha_2$ , and TiAl,  $\gamma$ , alloys are being examined in this investigation. The  $\alpha_2$  alloys included compositions representative of both the Ti-Al-Nb and the Ti-Al-V systems. The latter, together with appropriate  $\gamma$  alloys were selected following examination of available isothermal sections of the Ti-Al-

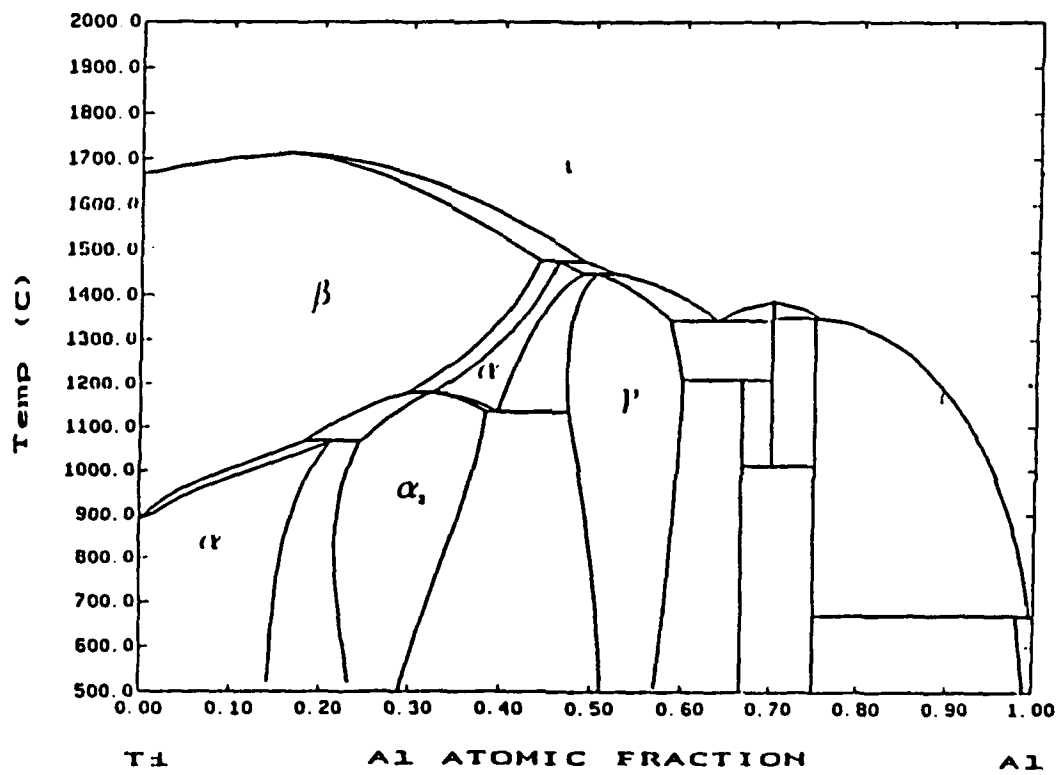


Figure 1: Ti-Al Binary Phase Diagram(3).

V ternary system, Figure 2, with the desire to examine the elevated temperature plastic flow behavior of relevant multi-phase alloys, e.g.,  $\alpha_2$ ,  $\alpha_2 + \alpha$ ,  $\alpha_2 + \beta$ ,  $\alpha_2 + \gamma$ ,  $\alpha_2 + \gamma + \beta$ ,  $\gamma + \beta$ . Chemical compositions of the alloys are tabulated on Table 1.

The  $\alpha_2$  Ti-Al-Nb intermetallic alloys, furnished by TIMET, Inc., Henderson, Nv., were received as 6 in. thick slabs having been hammer forged at 1260°C from 7500 lb. triple vacuum melted production heats; the  $\alpha_2$  and  $\gamma$  Ti-Al-V alloys were prepared by TIMET as 30 lb. triple vacuum melted ingots.

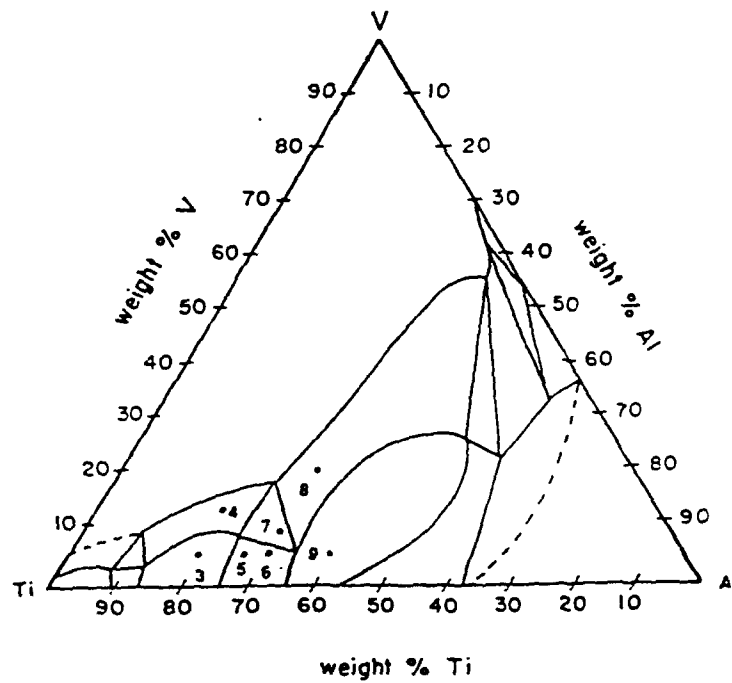
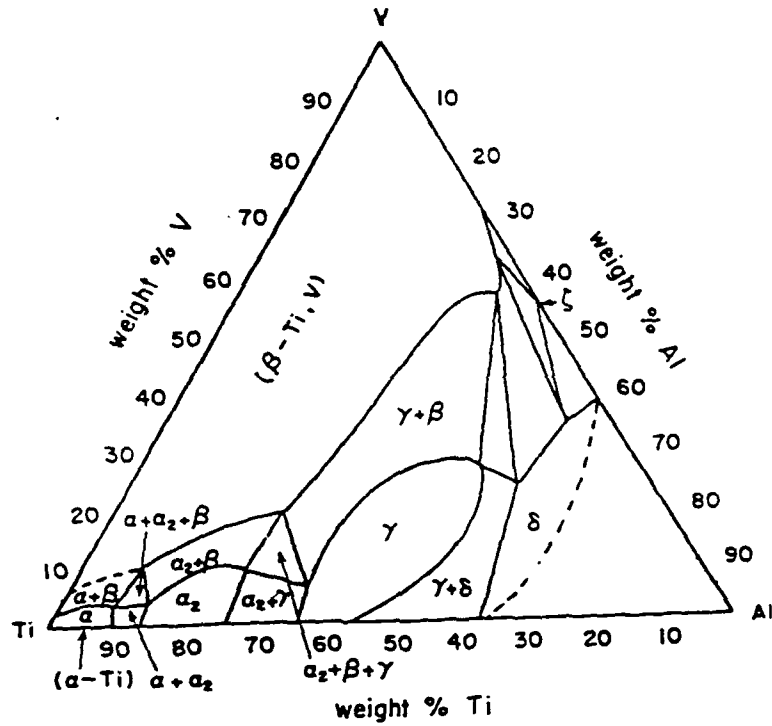
#### Microstructural Characterization

Microstructural characterization of the as-received titanium intermetallic alloys involved optical, scanning and analytical transmission electron microscopy, thermal analysis (DSC and DTA), and X-ray diffraction.

Preparation of optical microscopy samples involved standard metallographic procedures with final etching in Kroll's reagent. Scanning electron microscope samples were prepared in a similar manner, however they were examined without etching utilizing a JEOL 848 operated in the backscattered mode. Spot mode energy dispersive X-ray spectroscopy and NBS traceable standards for pure Ti, Al and V, facilitated determination of the chemical compositions of the various phases present in the Ti-Al-V system.

An Omnitherm High Temperature Thermal Analysis system was utilized for thermal analysis. The chemical reactivity of the titanium alloys required that these experiments be performed in a Ti gettered UHP Ar atmosphere, maintaining the  $O_2$  concentration below 1 ppb. Heating rates of 20°C per minutes over the temperature range 100 to 1400°C were employed.

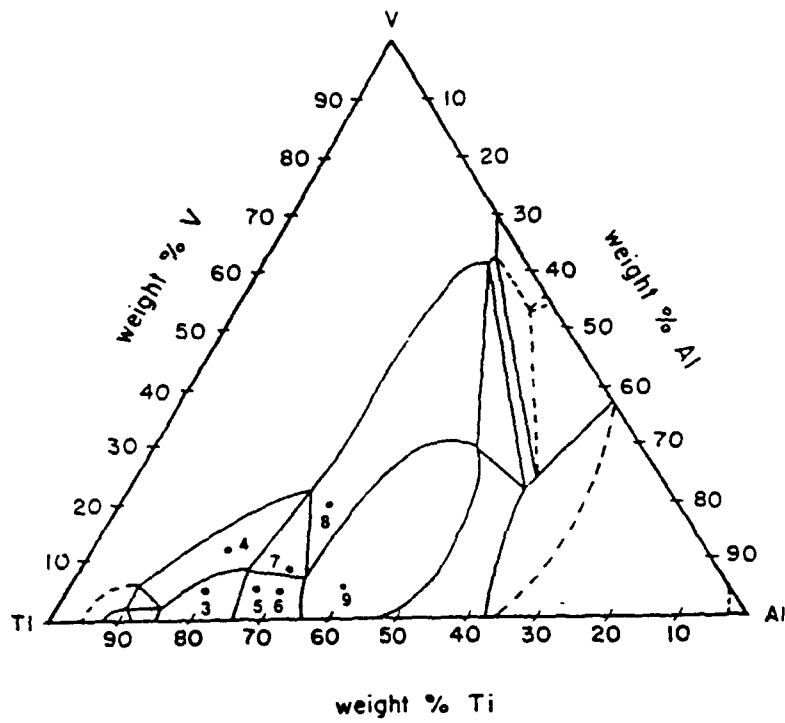
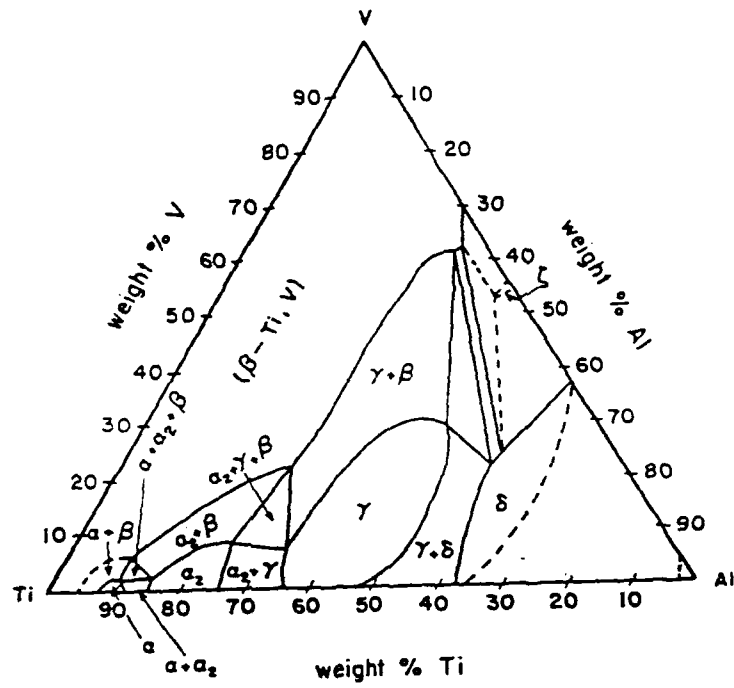
Finally, phase identification is continuing at the High Temperature Materials Laboratory, Oak Ridge National Laboratory, utilizing  $CuK\alpha$  radiation and either a room temperature Scintag PAD-5 diffractometer or an elevated temperature Scintag PAD-10 diffractometer.



(a) 800°C

Figure 2: Isothermal Sections of Ternary Ti-Al-V Phase

Diagram(9). (a) 800°C and (b) 1000°C.



(b) 1000°C

TABLE 1  
Chemical Composition

	Element (wt. pct)							
	Al	Nb	V	Mo	Fe	O	N	C
Ti-Al-Nb								
24Al-11Nb	14.25	21.3	-	-	0.05	0.09	0.012	-
25Al-10Nb-3V-1Mo	14.6	20.0	3.3	2.1	0.08	0.08	-	0.027
Ti-Al-V								
30Al-4V	20.25	-	4.97	-	0.075	0.170	0.007	-
30Al-10V	20.4	-	11.6	-	0.135	0.063	0.008	-
40Al-4V	27.95	-	5.11	-	0.093	0.085	0.004	-
43Al-4V	30.5	-	5.03	-	0.091	0.076	0.004	-
43Al-7V	30.55	-	8.92	-	0.095	0.067	0.006	-
43Al-15V	30.45	-	19.8	-	0.12	0.056	0.012	-
53Al-4V	40.05	-	4.83	-	0.084	0.123	0.003	-



### Elevated Temperature Mechanical Characterization

Figure 3 shows the elevated temperature mechanical characterization system that has been assembled to support this activity. It consists of the following principal components, an MTS 110 kip servo-hydraulic system with associated MTS 458 electronics, a Nicolet digital storage oscilloscope - suitable for high speed data acquisition, a Centorr 2000°C, inert atm.-hydrogen-vacuum furnace and an Ametek mass spectrograph. This system has been integrated with a 286/14 MHZ, personal computer which maintains system control while allowing constant true strain rate testing at elevated temperature. Development of this apparatus has also necessitated design of both high temperature compression platens, which consist of MoHfC rods with SiC/MoSi<sub>2</sub> inserts, and extensometry. Temperature measurement utilizes either type C thermocouples or optical pyrometry, with control provided through a programmable Honeywell UDC 5000 controller.

Finally, a high temperature air environment system has been assembled. This system again employs a computer controlled MTS 880 system equipped with a large bore, rapid response 1500°C ATS furnace.

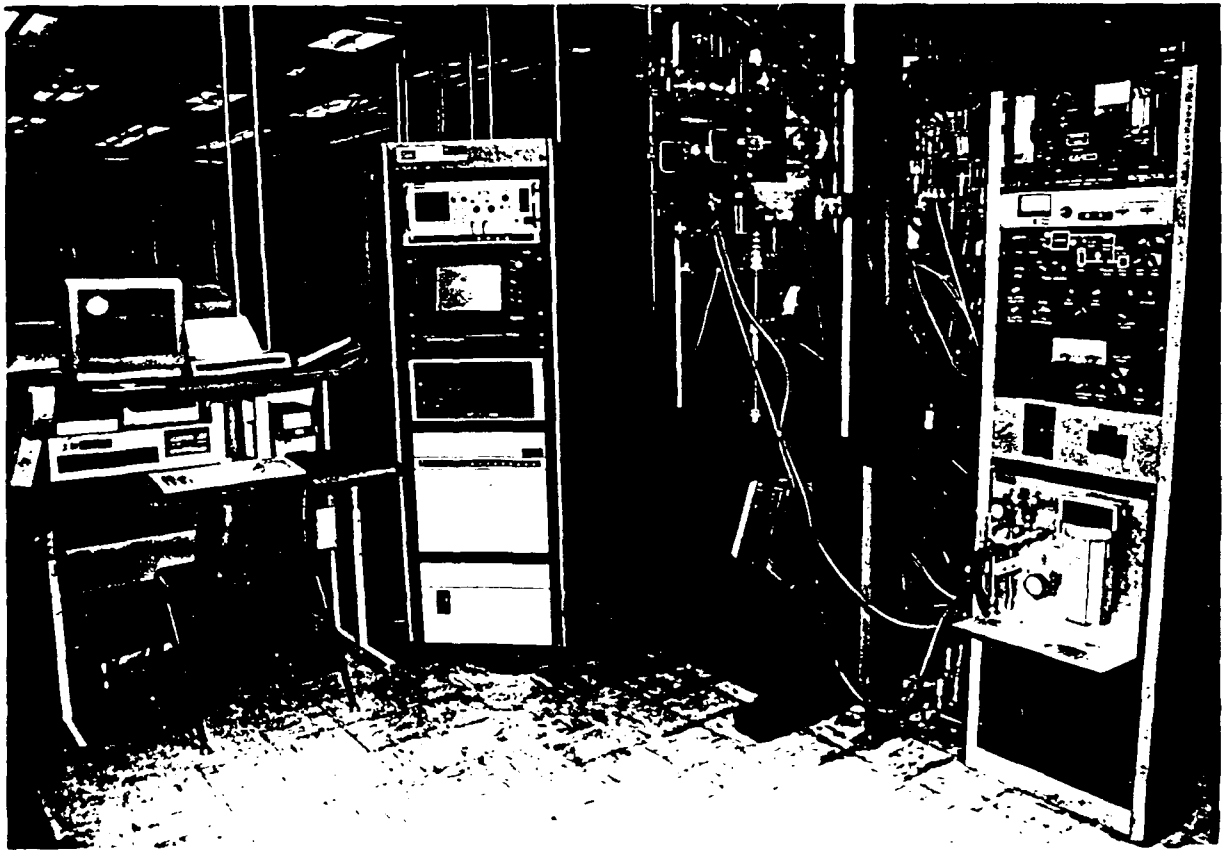


Figure 3: Elevated Temperature Environmental Mechanical  
Behavior System.

## RESULTS and DISCUSSION

### Optical Microscopy

Figures 4 and 5 illustrate the as-received microstructure of the Ti-Al-Nb alloys. Ti-24Al-11Nb, consisted of uniform blocky  $\alpha_2$  in a transformed  $\beta$  matrix. In contrast, Ti-25Al-10Nb-3V-1Mo had a finer, although non-uniform microstructure consisting of acicular and blocky  $\alpha_2$  in the matrix, with  $\alpha_2$  of varying thickness' lying along grain boundaries.

Optical micrographs of the Ti-43Al-4V, Ti-43Al-7V, and Ti-43Al-15V are shown in Figures 6 thru 8, respectively. These illustrate the coarse grained structure of the as-cast alloys which transforms to a fine microstructure upon cooling. In addition they show that increasing V content, from 5 to 20 wt. pct. (4 to 15 at. pct), results in the gradual coarsening of this fine platelet microstructure. In addition, Figure 8, suggests that this alloy contains three phases, which, after etching in Kroll's reagent, appear as a dark, internally structured phase, a light matrix and a precipitate phase within this matrix.

### Scanning Electron Microscopy

The principal focus of the scanning electron microscopy studies was to establish the chemical composition limits of the primary phases identified previously by optical microscopy. Typical results from Ti-43Al-15V are summarized in Table 2. These observations confirm that this alloy is three phase under the conditions examined. The darker etching phase seen in Figure 8, presumably  $\gamma$ , is enriched in Al and depleted in V, while the light etching matrix, presumably  $\beta$ , is enriched in V and depleted in Al. The third phase which appears as islands within the  $\beta$  matrix, illustrates the substantial solubility of V in what is presumably  $\alpha_2$ , in agreement with earlier reports in Ti-Al-Nb(10). Other alloys are currently being examined utilizing this technique, as well as analytical transmission electron microscopy.



Figure 4: Optical micrographs of Ti-24Al-11Nb.



Figure 4: Continued.

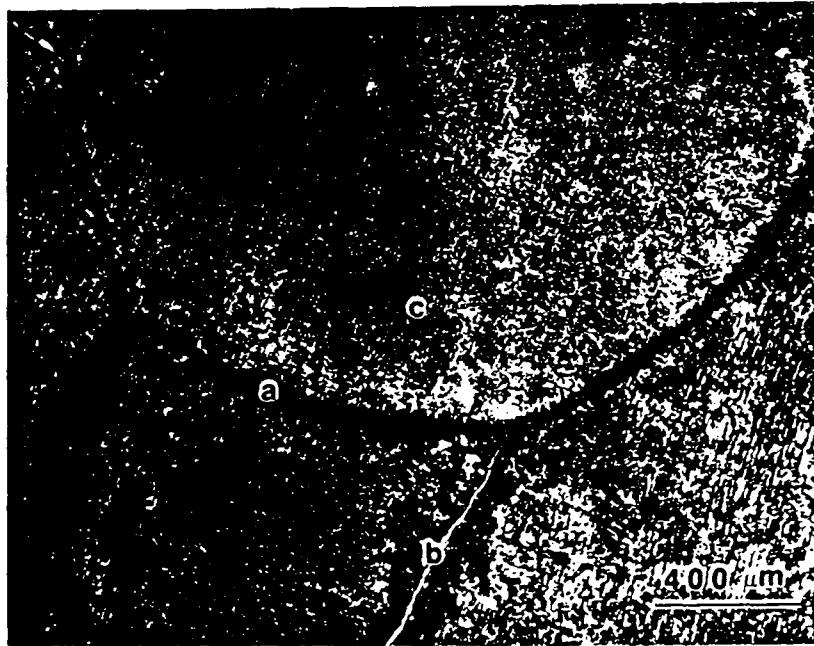


Figure 5: Optical micrographs of Ti-25Al-10Nb-3V-1Mo.

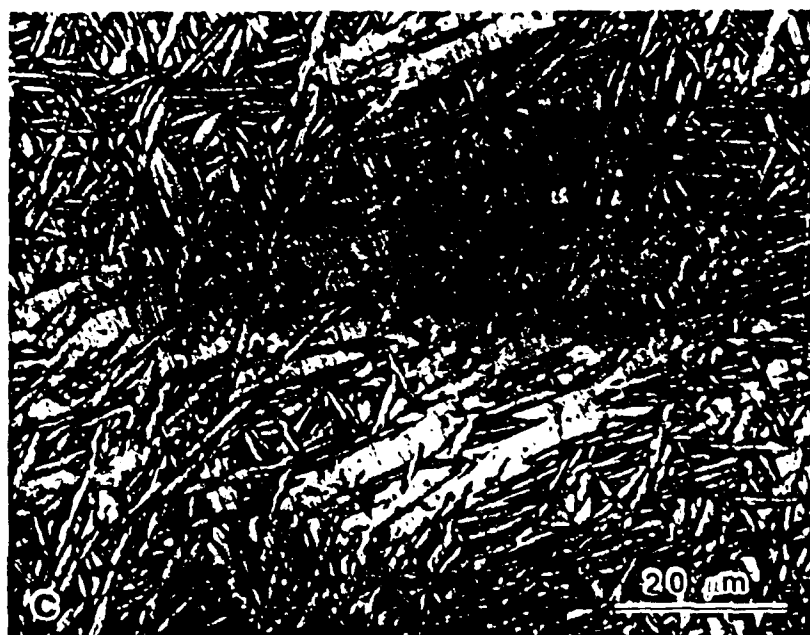
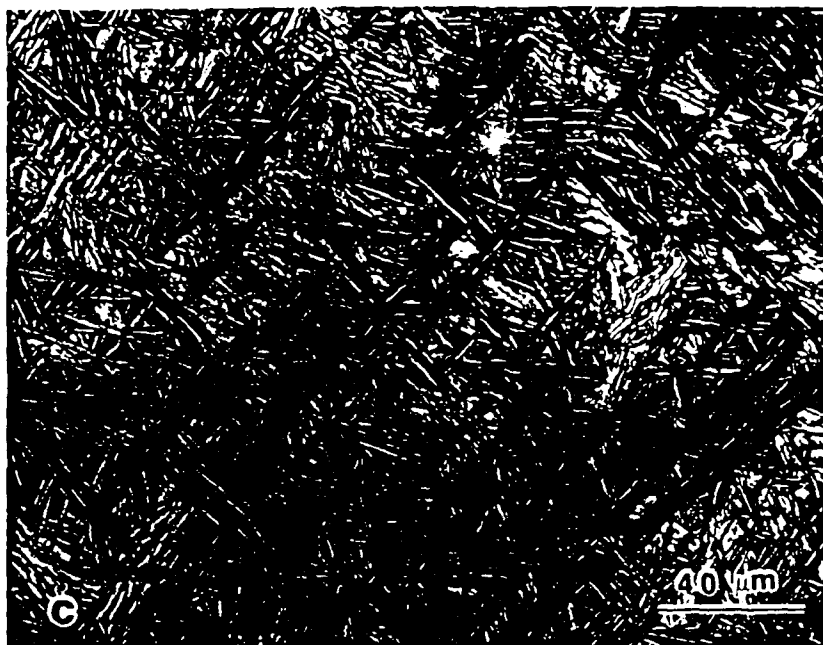


Figure 5: Continued.

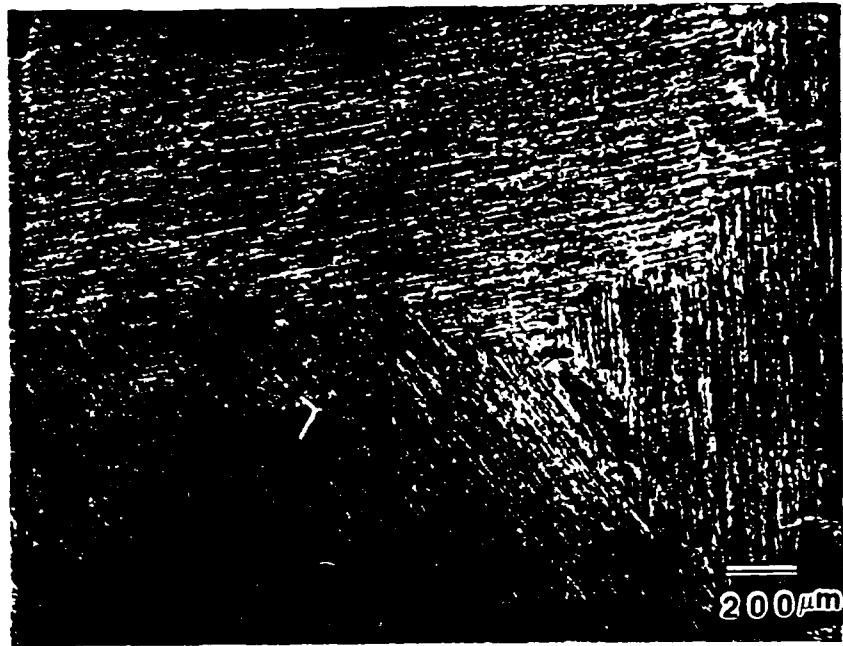


Figure 10. Micrograph of the surface of Ti-49Al-40.



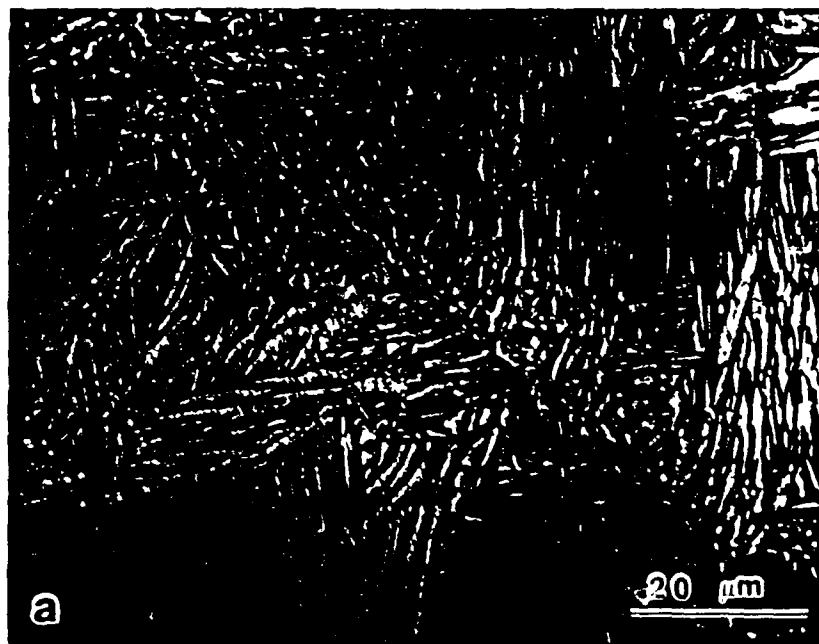
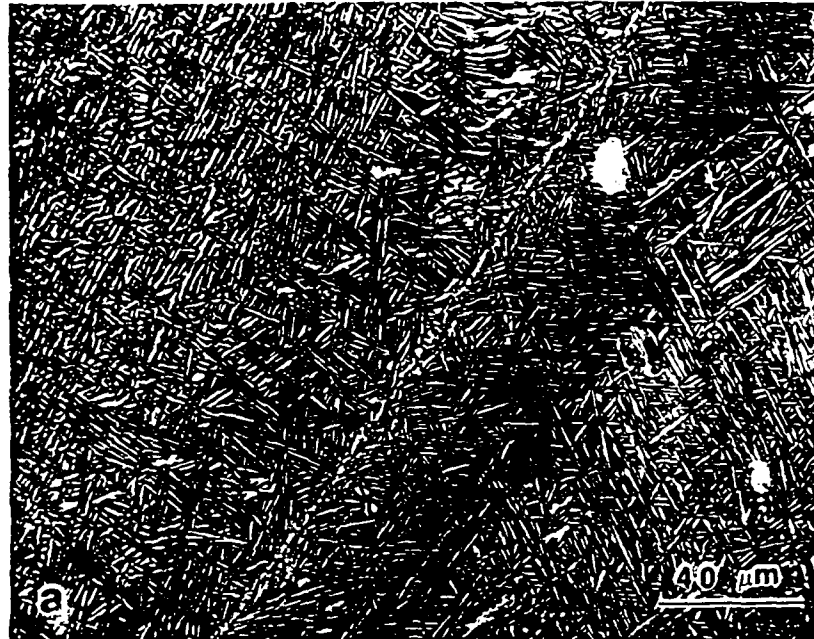


Figure 5: Continued.

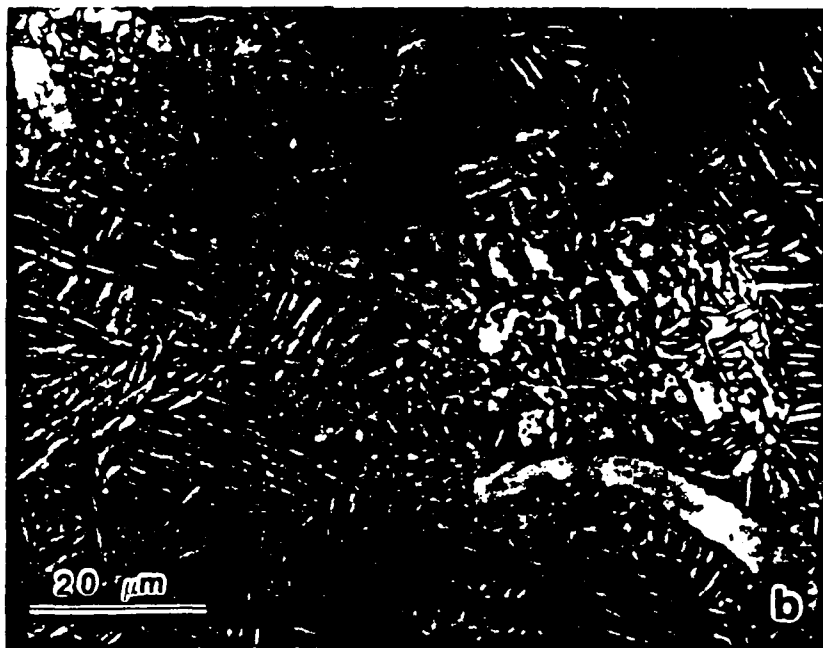


Figure 5: Continued.

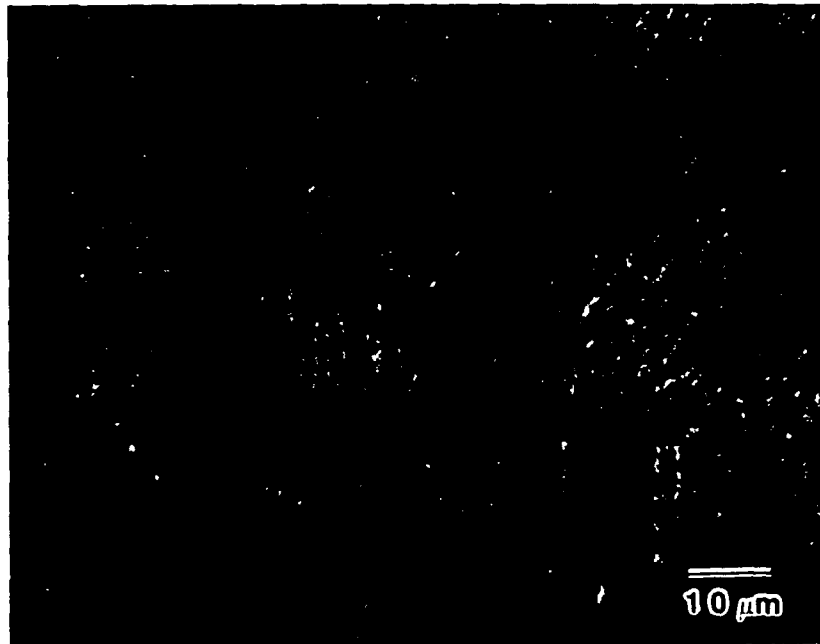
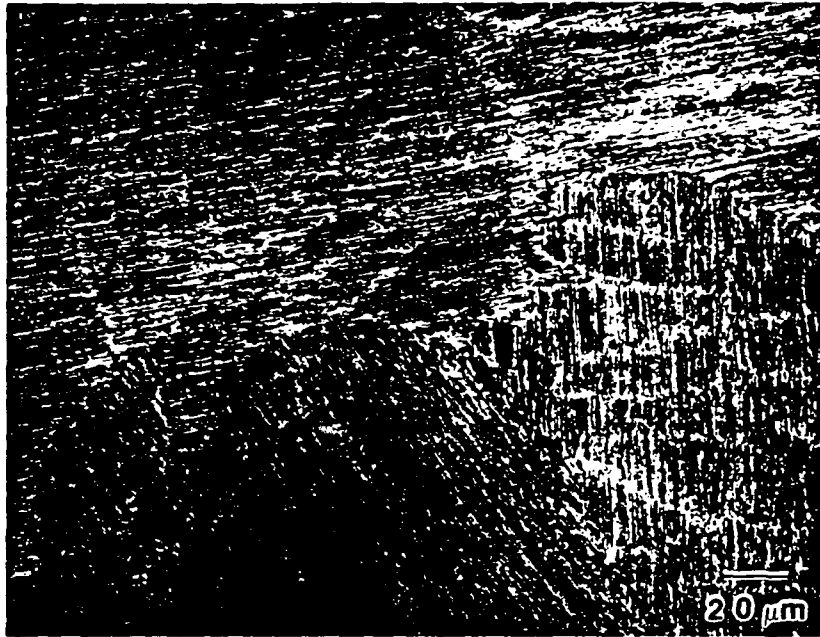


Figure 6: Continued.

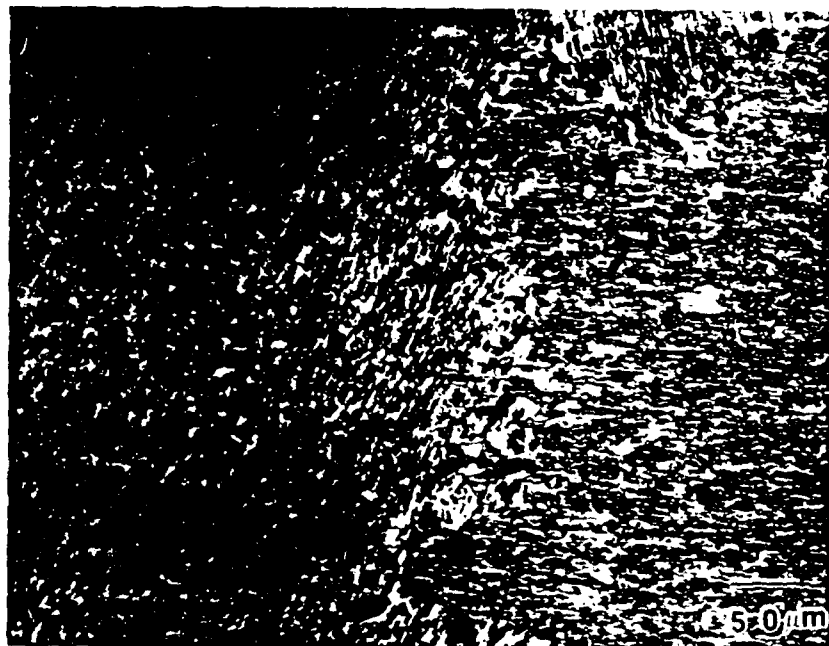


Figure 1. Optical micrographs of the surface.

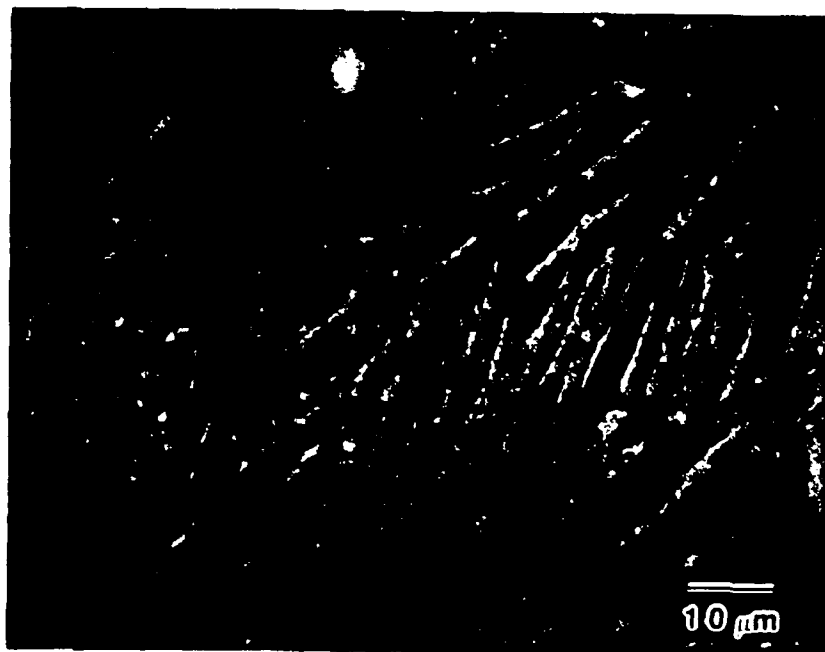
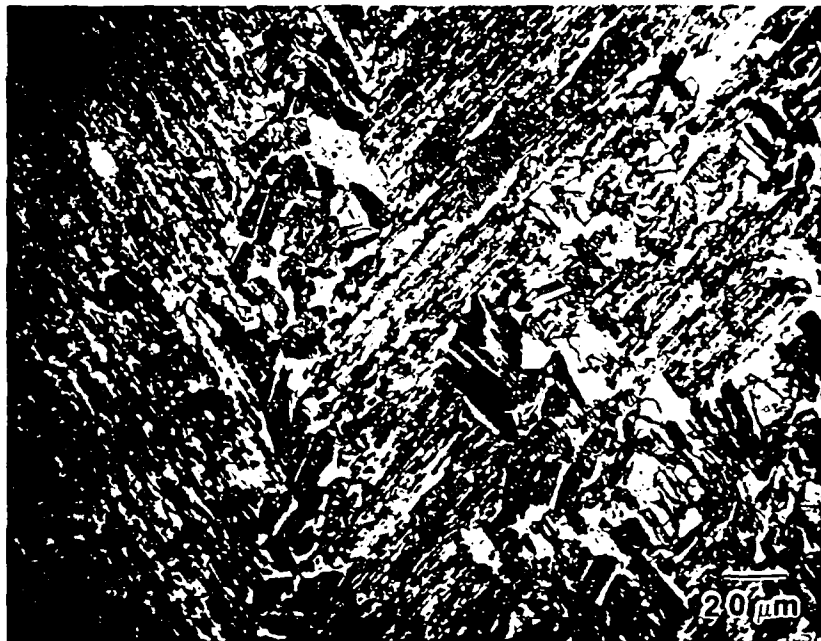


Figure 1. (continued)

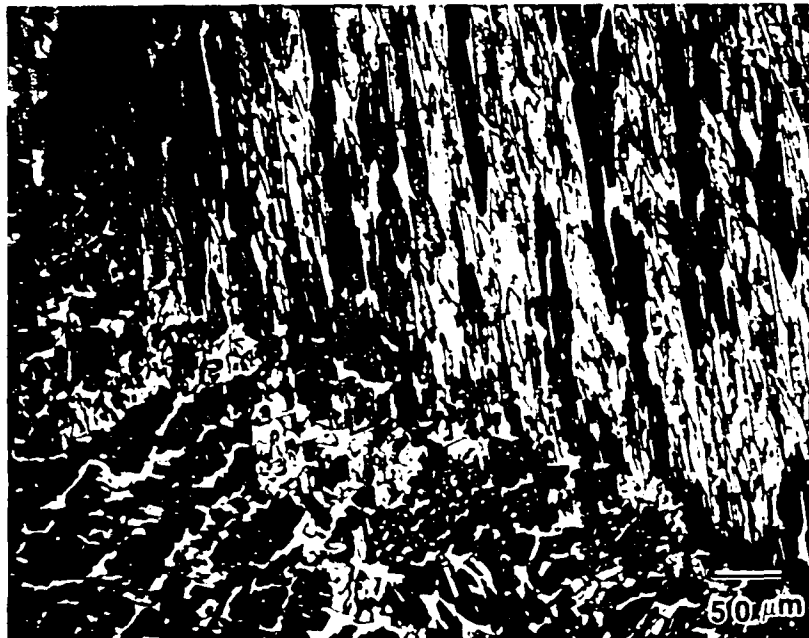
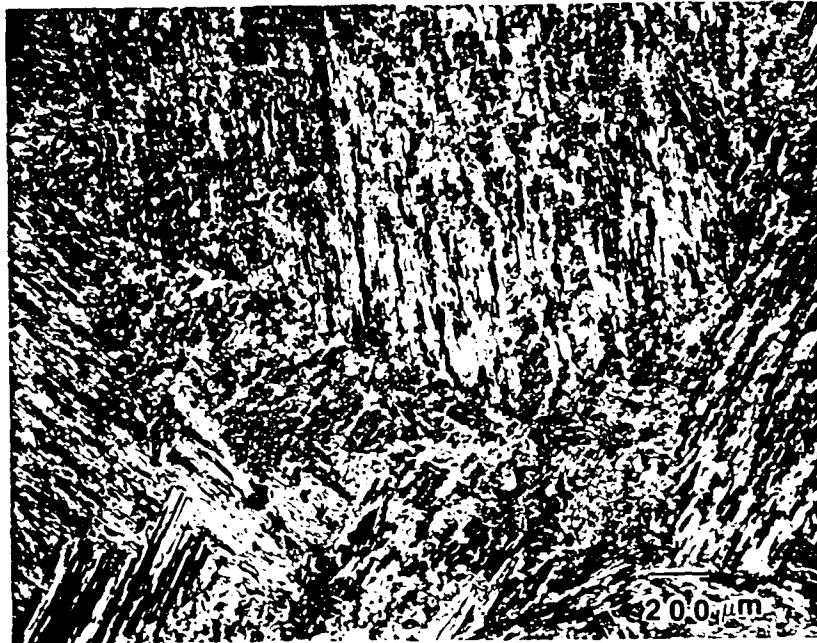


Figure 1. Textured surface of the T-4000-100.



TABLE 2

Chemical Composition of Phases in Ti-43Al-15V

	Element wt.pct (at. pct)		
	Ti	Al	V
Dark ( $\gamma$ )	54 (44)	33 (46)	13 (10)
Matrix ( $\beta$ )	40 (36)	20 (30)	40 (34)
Islands ( $\alpha_2$ )	54 (47)	23 (34)	23 (19)



### X-Ray Diffraction

Figure 9 shows a typical X-ray diffraction trace obtained from Ti-25Al-10Nb-3V-1Mo. This data as well as similar observations from Ti-24Al-11Nb, Ti-43Al-(4-15)V are summarized in Tables 3 and 4. The results for Ti-24Al-11Nb clearly indicate that this alloy contains, at a minimum, three (3) phases,  $\alpha_2$ ,  $\beta$ /B2, and an orthorombic phase. Similar results have been reported by Kestner-Weykamp et al.(11) who showed that, at room temperature, this alloy may contain  $\alpha_2$ ,  $\beta$ , B2 (an ordered CsCl structure) and an orthorombic phase depending on prior thermomechanical history. The X-ray data obtained from Ti-25Al-10Nb-3V-1Mo suggest that while there may be a small quantity of the orthorombic phase present, note the satellite peaks observed at 2Theta values of 75.6, 77.5 and 78.8, it is essentially two phase,  $\alpha_2 + \beta$ . Finally, Table 4 indicates that the Ti-43Al-(4-15)V alloys contain  $\alpha_2 + \gamma$ ,  $\alpha_2 + \gamma + \beta$ , and  $\gamma + \beta$ , respectively, in agreement with earlier phase equilibria studies.

### Thermal Analysis

The  $\alpha_2 + \beta \rightarrow \beta$  transformation temperatures suggested by Strychor et al(12) are in excellent agreement with those observed by differential scanning calorimetry in Ti-24Al-11Nb and Ti-25Al-10Nb-3V-1Mo, with increasing  $\beta$  solute content decreasing the  $\alpha_2 + \beta \rightarrow \beta$  transformation temperature, Figure 10. Further study indicates that a series of other transitions are observed in these alloys, e.g., between 500 and 800°C, at approximately 850°C in Ti-24Al-11Nb and at approximately 1300°C. Detailed analysis of these reactions are continuing.

Differential scanning calorimetry of the Ti-43Al-(4-15)V alloys, Figure 11, appears far simpler, with three principal transition observed. A low temperature reaction appears centered about 650°C, another starting at

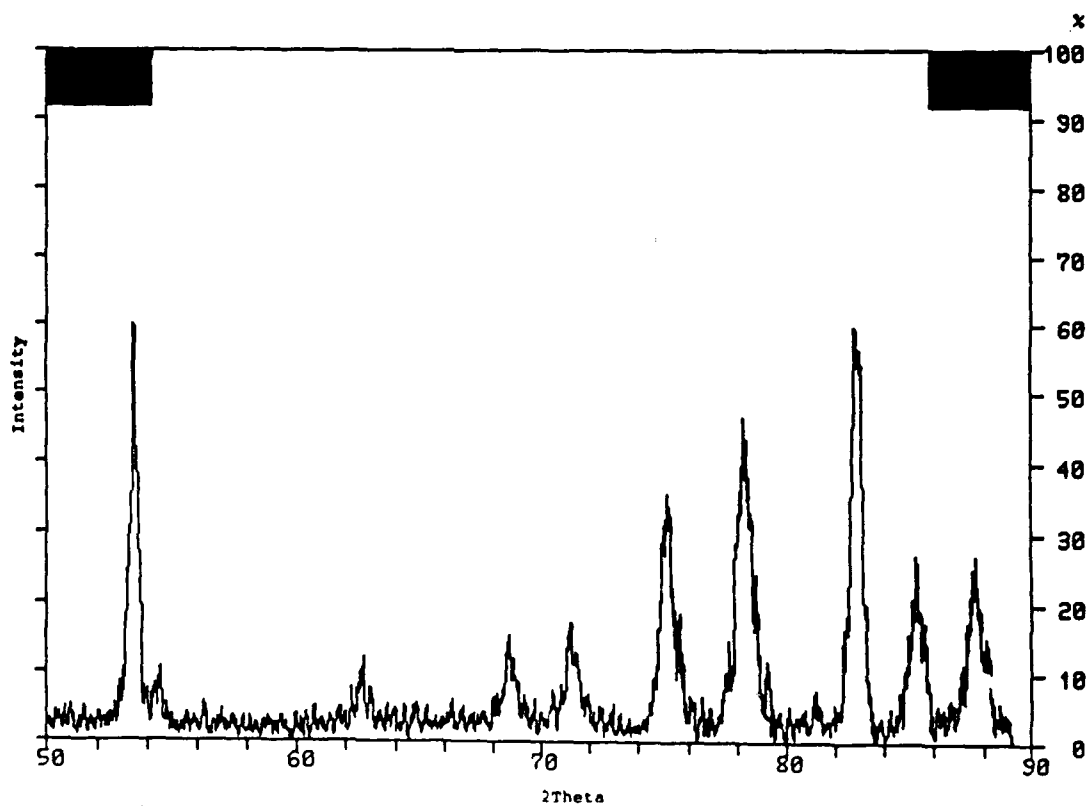
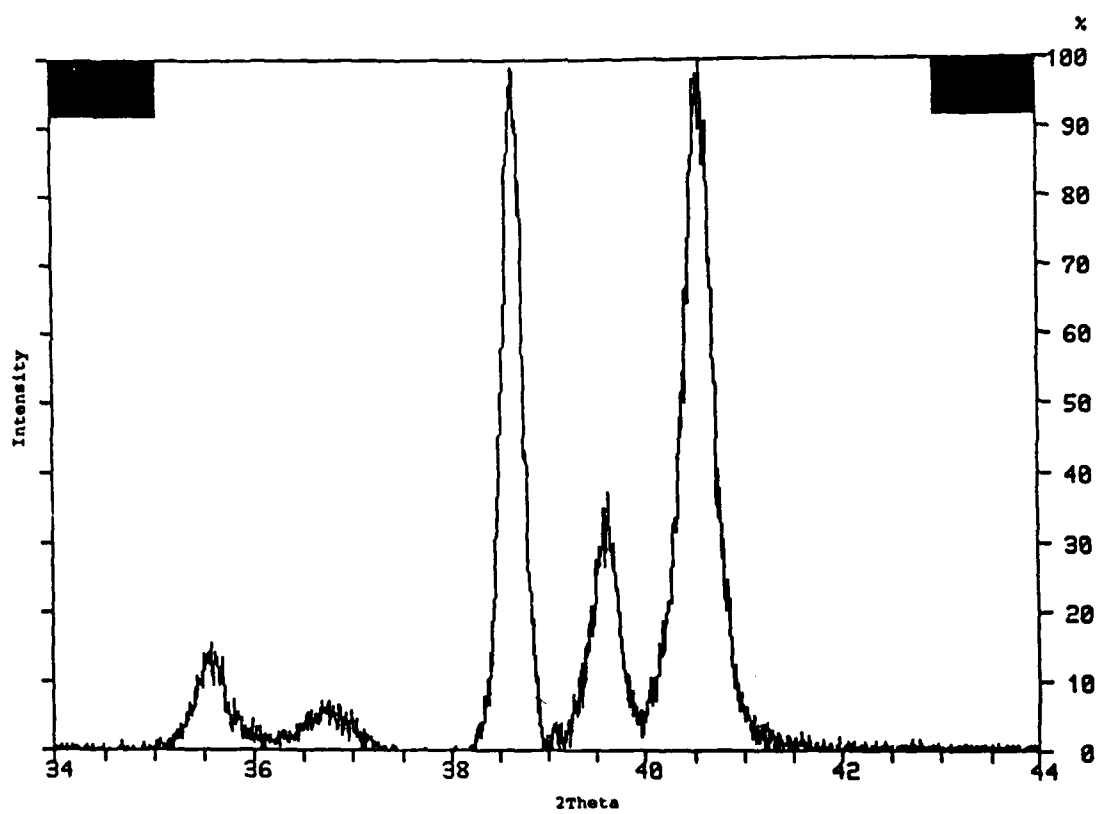


Figure 9: X-Ray Trace for Ti-25Al-10Nb-3V-1Mo

Table 3  
X-Ray Diffraction Results Ti-Al-Nb Alloys

Ti-25Al-10Nb-3V-1Mo

$2\theta_{\text{obs}}$	$d_{\text{obs}}$	$d_{\text{cal}}$	phase	hkl	$I/I_M$
35.54	2.524	2.529	$\alpha_2$	020	14
		2.531	orth	220	
36.71	2.446	2.474	$\alpha_2$	111	6
		2.442	orth	131	
38.65	2.328	2.330	$\alpha_2$	002	100
		2.325	orth	002	
39.62	2.273	2.277	$\beta/B_2$	011	34
40.56	2.223	2.223	$\alpha_2$	021	99
		2.223	orth	221	
53.50	1.712	1.714	$\alpha_2$	022	5
		1.721	orth	222	
54.40	1.685	1.686	$\alpha_2$	030	
		1.687	orth	330	
62.50	1.485	1.485	$\alpha_2$	013	
		1.483	orth	312	
63.00	1.474	1.478	$\alpha_2$	122	
		1.475	orth	400	
68.40	1.370	1.371	$\alpha_2$	113	
		1.372	orth	203	
71.00	1.326	1.324	$\alpha_2$	023	
		1.322	orth	223	
71.40	1.320	1.315	$\beta/B_2$	112	
74.80	1.268	1.264	$\alpha_2$	040	
75.60	1.257	1.265	orth	440	
77.50	1.231	1.236	orth	412	
78.30	1.220	1.220	$\alpha_2$	041	
		1.221	orth	441	
78.80	1.214	1.217	orth	303	
79.20	1.208	1.206	$\alpha_2$	123	
		1.208	orth	313	
82.79	1.165	1.165	$\alpha_2$	004	5
		1.165	orth	432	
85.30	1.137	1.135	$\alpha_2$	014	
85.60	1.134	1.138	$\beta/B_2$	022	
		1.138	orth	024	
87.2	1.117	1.125	$\alpha_2$	231	
87.50	1.114	1.111	$\alpha_2$	042	
		1.111	orth	124	
88.00	1.109	1.111	$\alpha_2$	042	
		1.111	orth	442	

Table 3 (Cont.)

Ti-24Al-11Nb

$2\theta_{\text{obs}}$	$d_{\text{obs}}$	$d_{\text{cal}}$	phase	hkl	$I/I_M$
35.775	2.508	2.507	$\alpha 2$	020	70
		2.491	orth	201	
38.597	2.331	2.330	$\alpha 2$	002	27
38.800	2.319	2.325	orth	002	19
39.941	2.255	2.284	$\beta/B2$	011	
		2.263	orth	012	
40.782	2.211	2.207	$\alpha 2$	021	100
		2.223	orth	221	
41.256	2.187	2.176	orth	041	13
42.800	2.111	2.113	$\alpha 2$	012	
		2.113	orth	112	
48.000	1.894	1.895	$\alpha 2$	120	
		1.865	$\beta/B2$	111	
		1.890	orth	240	
50.000	1.823	1.815	$\alpha 2$	112	
		1.826	orth	202	
		1.826	orth	320	
52.000	1.757	1.756	$\alpha 2$	121	
		1.751	orth	241	
53.635	1.707	1.707	$\alpha 2$	022	21
		1.712	orth	222	
		1.700	orth	321	
63.790	1.458	1.459	orth	410	13
		1.459	orth	341	
64.343	1.447	1.447	$\alpha 2$	220	25
64.688	1.440	1.444	B2	012	8
		1.436	orth	322	
70.334	1.337	1.345	orth	430	13
70.451	1.336	1.333	$\alpha 2$	131	14
71.308	1.322	1.320	$\alpha 2$	023	42
		1.319	$\beta/B2$	112	
		1.322	orth	223	
73.700	1.284	1.282	orth	342	
75.751	1.255	1.254	$\alpha 2$	040	8
77.345	1.233	1.236	orth	412	17
77.519	1.230	1.230	$\alpha 2$	222	21
78.447	1.218	1.217	orth	303	9
78.925	1.212	1.211	$\alpha 2$	041	13

Table 4

## X-Ray Diffraction Results: Ti-Al-V Alloys

## Ti-43Al-4V

$2\theta_{\text{obs}}$	$d_{\text{obs}}$	$d_{\text{calc}}$	Structure	Plane
31.437	2.8430	2.81	L1 <sub>0</sub>	1 1 0
36.225	2.4759	2.498	D0 <sub>19</sub>	2 0 0
38.877	2.3147	2.31	L1 <sub>0</sub>	1 1 1
39.149	2.2990	2.307	D0 <sub>19</sub>	0 0 2
41.228	2.1879	2.191	D0 <sub>19</sub>	2 0 1
45.045	2.0110	2.04	L1 <sub>0</sub>	0 0 2
45.256	2.0021	1.99	L1 <sub>0</sub>	2 0 0
54.207	1.6907	1.699	D0 <sub>19</sub>	2 0 2
55.897	1.6435	1.65	L1 <sub>0</sub>	1 1 2
65.172	1.4303	1.424	L1 <sub>0</sub>	2 0 2
65.793	1.4183	1.407	L1 <sub>0</sub>	2 2 0
77.517	1.2304	1.225	D0 <sub>19</sub>	2 2 2
78.965	1.2114	1.204	D0 <sub>19</sub>	4 0 1
		1.203	L1 <sub>0</sub>	3 1 1
83.034	1.1621	1.159	L1 <sub>0</sub>	2 2 2
		1.156	D0 <sub>19</sub>	0 0 4

## Ti-43Al-7V

$2\theta_{\text{obs}}$	$d_{\text{obs}}$	$d_{\text{calc}}$	Structure	Plane
38.844	2.3145	2.31	L1 <sub>0</sub>	1 1 1
39.163	2.2987	2.306	D0 <sub>19</sub>	0 0 2
40.150	2.2445	2.227	BCC	0 1 1
44.877	2.0181	2.04	L1 <sub>0</sub>	0 0 2
45.276	2.0037	1.99	L1 <sub>0</sub>	2 0 0
65.621	1.4187	1.424	L1 <sub>0</sub>	2 0 2
66.057	1.4132	1.407	L1 <sub>0</sub>	2 2 0
72.402	1.3041	1.310	D0 <sub>19</sub>	2 0 3
72.908	1.2963	1.286	BCC	1 1 2
79.276	1.2079	1.203	L1 <sub>0</sub>	3 1 1
		1.204	D0 <sub>19</sub>	4 0 1
83.448	1.1576	1.159	L1 <sub>0</sub>	2 2 2
		1.156	D0 <sub>19</sub>	0 0 4
86.612	1.1231	1.114	BCC	0 2 2

Table 4 (cont.)  
Ti-43Al-15V

$2\theta_{\text{obs}}$	$d_{\text{obs}}$	$d_{\text{calc}}$	Structure	Plane
31.905	2.8025	2.81	L1 <sub>O</sub>	1 1 0
38.991	2.3081	2.31	L1 <sub>O</sub>	1 1 1
40.594	2.2205	2.227	BCC	0 1 1
44.730	2.0244	2.04	L1 <sub>O</sub>	0 0 2
45.606	1.9875	1.99	L1 <sub>O</sub>	2 0 0
55.907	1.6435	1.65	L1 <sub>O</sub>	1 1 2
65.741	1.4192	1.424	L1 <sub>O</sub>	2 0 2
66.415	1.4064	1.407	L1 <sub>O</sub>	2 2 0
78.507	1.2173	1.224	L1 <sub>O</sub>	1 1 3
79.736	1.2016	1.203	L1 <sub>O</sub>	3 1 1
83.448	1.1574	1.159	L1 <sub>O</sub>	2 2 2

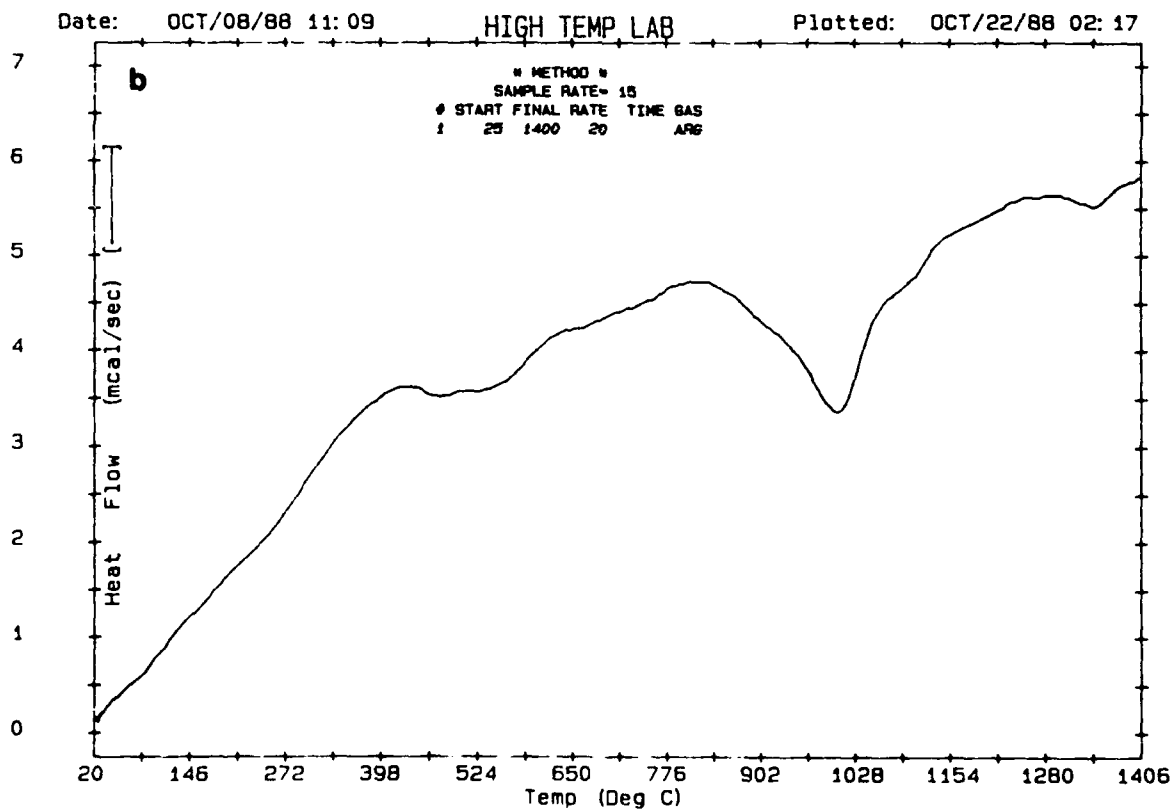
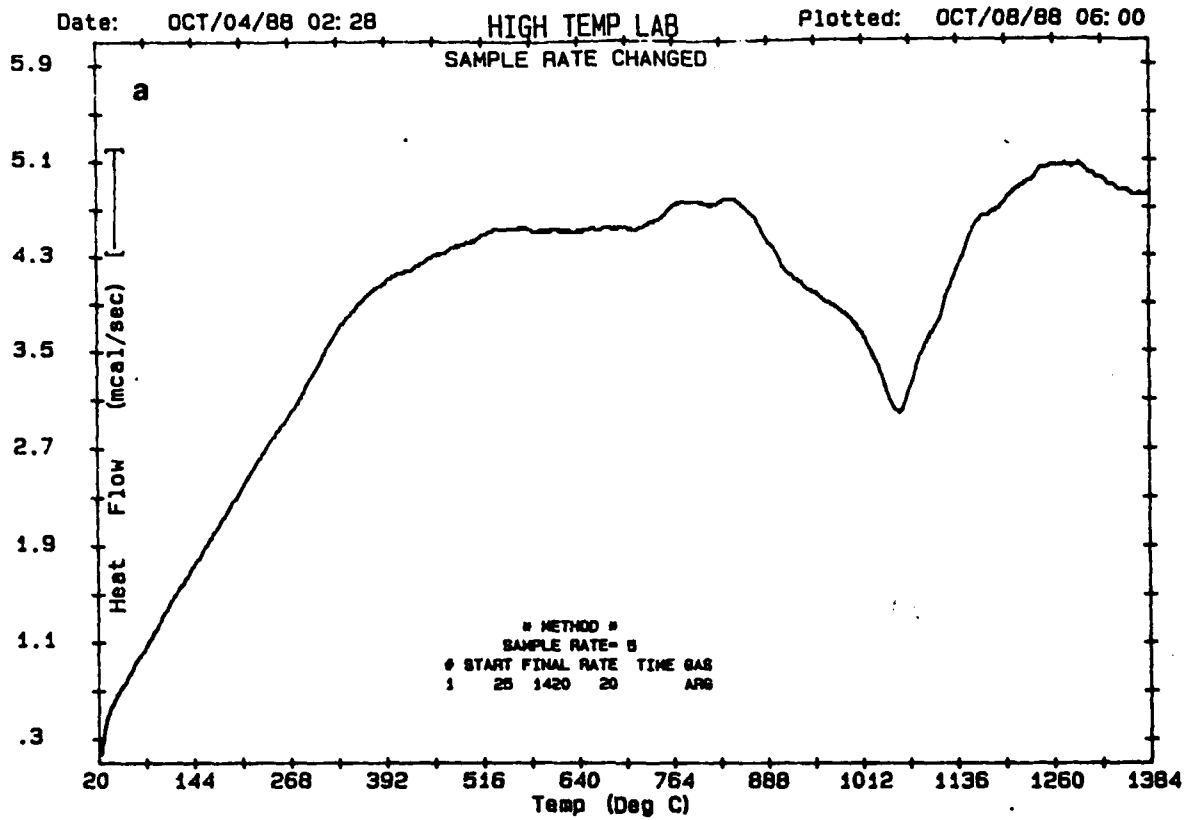


Figure 10: Differential Scanning Calorimetry (a) Ti-24Al-11Nb,

(b) Ti-25Al-10Nb-3V-1Mo.

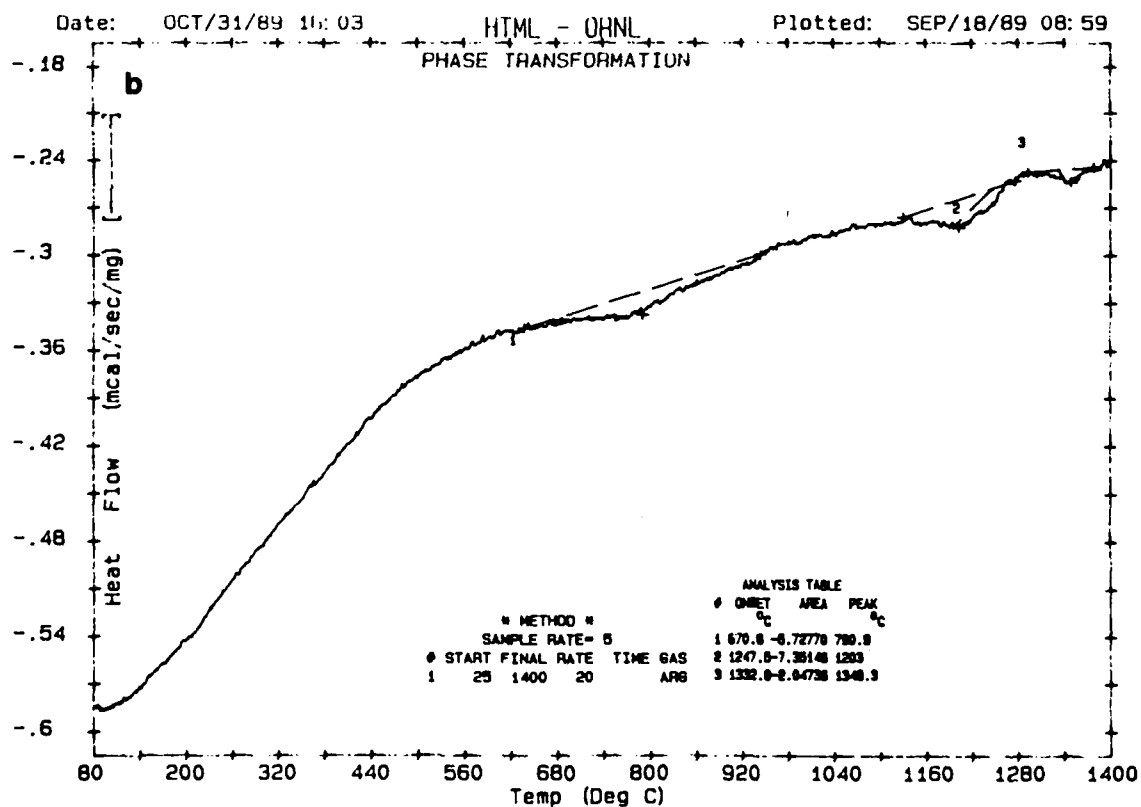
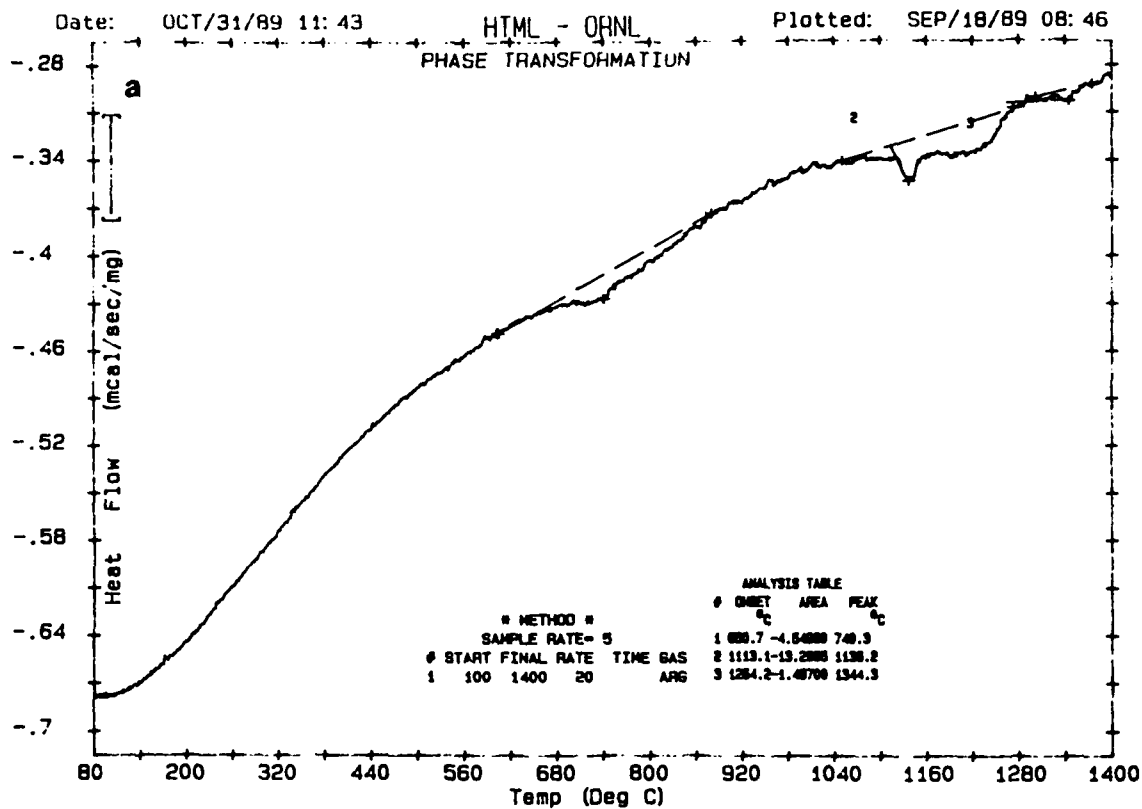


Figure 11: Differential Scanning Calorimetry (a) Ti-43Al-4V,

(b) Ti-43Al-7V, and (c) Ti-43Al-15V.



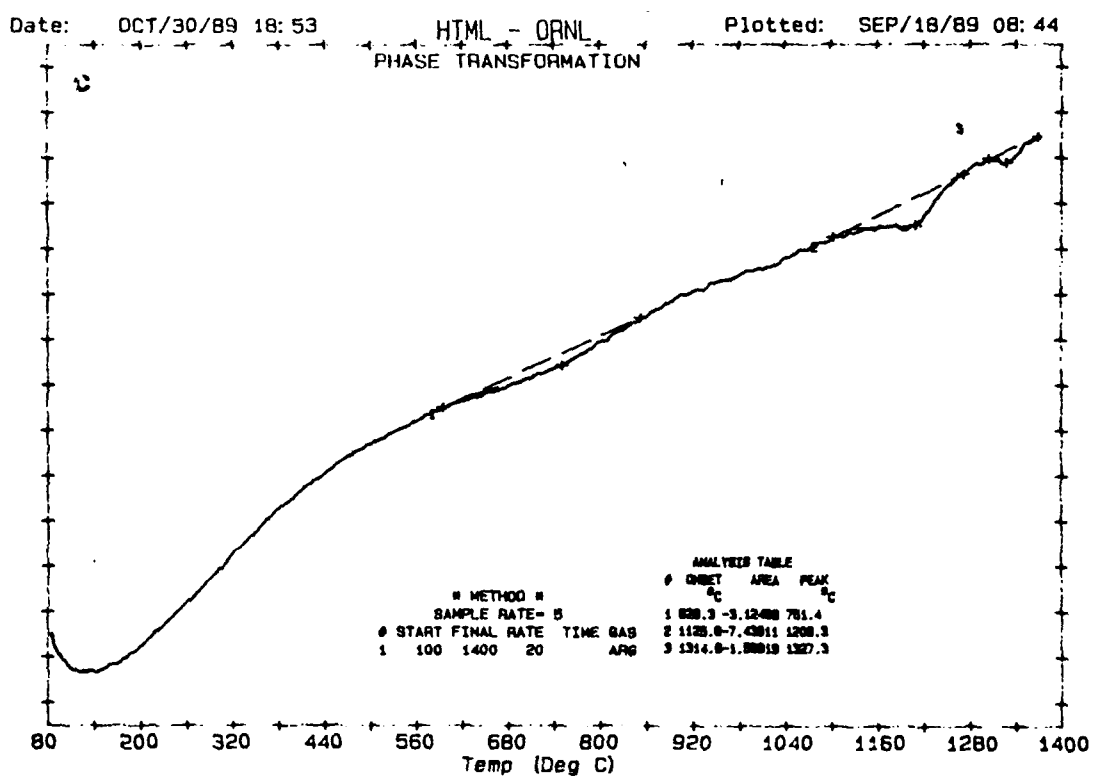


Figure 11: Continued

1125°C and a final transition at 1310°C. The latter appears to be related to the  $\gamma$  to  $\alpha$  transition reported by McCullough et al.(7), while the reaction at 1125°C appears to be associated with the  $\beta$  to  $\alpha$  transformation. Finally, the origin of the low temperature reaction is still questionable, however it should be noted that a similar reaction has been observed in all alloys.

#### ACKNOWLEDGMENT

The cooperation and assistance of Mr. Ed Mild and Dr. Paul Bania, TIMET, Inc., Henderson, Nv., who prepared the titanium aluminide alloys, Dr. C. Hubbard, High Temperature Materials Laboratory, Oak Ridge National Laboratory, who assisted with the DSC and X-ray studies and J. Hudson are gratefully acknowledged.

# REFERENCES

1. H. A. Lipsett, "Titanium Aluminides-An Overview", High Temperature Ordered Intermetallic Alloys, C. C. Koch, C. T. Liu, and N. S. Stoloff, eds., Materials Research Society, Pittsburgh, PA, 1984, pp. 351-364.
2. Y.-W. Kim, "Intermetallic Alloys Based on Gamma Titanium Aluminide", Jn. Metals 41, #7 (1989) 24-30.
3. J. C. Mishurda, J. C. Lin, Y. A. Chang and J. H. Perepezko, "Titanium-Aluminide Alloys Between the Compositions  $Ti_3Al$  and  $TiAl$ ", High Temperature Ordered Intermetallic Alloys III, C. T. Liu, A. I. Taub, N. S. Stoloff and C. C. Koch, eds., Materials Research Society, Pittsburgh, PA, 1989, pp.57-62.
4. C. McCullough, J. J. Valencia, H. Mateos, C. G. Levi, R. Mehrabian and K. A. Rhyne, "The High Temperature  $\alpha$  Field in the Titanium-Aluminum Phase Diagram", Scripta Metallurgica, 22 (1988) 1131-1136.
5. J. L. Murray, "Calculation of the Titanium-Aluminum Phase Diagram", Metall. Trans., 19A (1988) 243-247.
6. J. P. Gros, B. Sundman and I. Ansara, "Thermodynamic Modeling of the Ti-Rich Phases in the Ti-Al System", Scripta Metallurgica, 22 (1988) 1587-1591.
7. C. McCullough, J. J. Valencia, C. G. Levi and R. Mehrabian, "Phase Equilibria and Solidification in Ti-Al Alloys", Acta Metall., 37 (1989) 1321-1336.
8. J. J. Valencia, C. McCullough, C. G. Levi and R. Mehrabian, "Solidification Microstructure of Supercooled Ti-Al Alloys Containing Intermetallic Phases", Acta Metall., 37 (1989) 2517-2530.
9. K. Hashimoto, H. Doi and T. Tsujimoto, "Reexamination of the Ti-Al-V Ternary Phase Diagram", Trans. Japan Inst. Metals, 27 (1986) 741-749.

10. T. J. Jewett, J. C. Lin, N. R. Bonda, L. E. Seitzman, K. C. Hsieh, Y. A. Chang and J. H. Perepezko, "Experimental Determination of the Ti-Nb-Al Phase Diagram at 1200 °C", High Temperature Ordered Intermetallic Alloys III, C. T. Liu, A. I. Taub, N. S. Stoloff and C. C. Koch, eds., Materials Research Society, Pittsburgh, PA, 1989, pp. 69-74.
11. H. T. Kestner-Weykamp, C. H. Ward, T. F. Broderick and M. J. Kaufman, "Microstructures and Phase Relationships in the  $Ti_3Al+Nb$  System", Scripta Metallurgica, 23 (1989) 1697-1702.
12. R. Strychor, J. C. Williams and W. A. Soffa, "Phase Transformations and Modulated Microstructures in Ti-Al-Nb Alloys", Metall. Trans, 19A (1988) 225-234.

## SUB-TASK 2

### FIBER-MATRIX INTERACTIONS

H. J. Rack, H. G. Spencer, J. P. Clement and K. T. Wu

This sub-task examined the potential for modifying and controlling the chemical and mechanical performance of the fiber-matrix region thru the use of sol-gel coatings. A generalized methodology was developed for selecting and applying the appropriate coating. The procedure results in a uniform, homogeneous, nanocrystalline oxide coating which can be tailored to the particular application and which can be applied to continuous reinforcements, either in the form of tows or individual fibers, or to discontinuous reinforcements, e.g., SiC whiskers. Furthermore, it has been shown that this coating procedure is not limited to composite reinforcements but can be applied to any surface to control wettability, wear resistance, etc.

Based on this effort the following appended manuscripts have either been submitted, accepted or published:

Submitted:

K. T. Wu, H. G. Spencer and H. J. Rack, "Surface Modification of SiC Whiskers", Scripta Metallurgica, submitted October, 1989.

Accepted:

J. P. Clement, H. J. Rack, K. T. Wu and H. G. Spencer, "Interfacial Modification in Metal Matrix Composites by the Sol-Gel Process", Materials and Manufacturing Processes, 1989, in press.

Published:

J. P. Clement and H. J. Rack, "Interfacial Modification G/Al Metal Matrix Composites", Proc. Sym. on High Temperature Composites, Am. Soc. Comp., Dayton, Ohio, June 13-15, 1989.

Published:

P. Chaudhury and H. J. Rack, "Age Hardening of SiC Reinforced Mg-6Zn",  
Light-Weight Alloys for Aerospace Applications, E. W. Lee, E. H. Chia and N.  
J. Kim, eds.,  
The Minerals, Metals and Materials Society, Warrendale, PA., 1989, pp. 345-  
357.

The cooperation and assistance of DWA Associates, Chatsworth, Cal., who  
supplied the TiC reinforced In 718, and the Dow Chemical Corporation, Lake  
Jackson, Texas, who supplied the SiC particulate reinforced Mg-6 Zn is  
greatfully acknowledged. Finally, this effort is continuing under the  
sponsorship of the Wyman-Gordon Corporation as part of the high temperature  
plasticity study.

## FIBER-MATRIX INTERACTIONS

H. J. Rack, H. G. Spencer, J. P. Clement and K. T. Wu

This sub-task examined the potential for modifying and controlling the chemical and mechanical performance of the fiber-matrix region thru the use of sol-gel coatings. A generalized methodology was developed for selecting and applying the appropriate coating. The procedure results in a uniform, homogeneous, nanocrystalline oxide coating which can be tailored to the particular application and which can be applied to continuous reinforcements, either in the form of tows or individual fibers, or to discontinuous reinforcements, e.g., SiC whiskers. Furthermore, it has been shown that this coating procedure is not limited to composite reinforcements but can be applied to any surface to control wettability, wear resistance, etc.

Based on this effort the following appended manuscripts have either been submitted, accepted or published:

Submitted:

K. T. Wu, H. G. Spencer and H. J. Rack, "Surface Modification of SiC Whiskers", Scripta Metallurgica, submitted October, 1989.

Accepted:

J. P. Clement, H. J. Rack, K. T. Wu and H. G. Spencer, "Interfacial Modification in Metal Matrix Composites by the Sol-Gel Process", Materials and Manufacturing Processes, 1989, in press.

Published:

J. P. Clement and H. J. Rack, "Interfacial Modification G/Al Metal Matrix Composites", Proc. Sym. on High Temperature Composites, Am. Soc. Comp., Dayton, Ohio, June 13-15, 1989.

The cooperation and assistance of AMOCO Corporation, Greenville, South Carolina, who provided the C fibers, American Matrix, Inc., who provided the SiC whiskers, Aerospatial Inc., Paris, France, who provided a graduate fellowship(JPC) and the Clemson Center for Advanced Manufacturing, who provided partical financial support(HGS), is gratefully acknowledged. Further the detailed transmission electron microscructural studies of coated interfaces could not have been possible without the continued assistance Prof. J. Howe, Carnegie-Mellon University.

Finally, based on this research the following degree has been awarded:

J. P. Clement, Master of Science, Mechanical Engineering.



## INTERFACIAL MODIFICATION G/Al METAL MATRIX COMPOSITES

by

J. P. Clement and H. J. Rack

### ABSTRACT

Successful development of metal matrix composites has been limited by two recurrent problems: reinforcements are difficult to wet by molten metals, and chemical reactions take place at the fiber-matrix interface.

Detailed examination of thermodynamic and kinetic data suggest that it should be possible to develop either a matrix composition or interfacial barrier coating which promotes wetting, while simultaneously reducing interfacial interaction.

The current study has developed a procedure to coat carbon reinforcements with a thin, crack-free, protective oxide layer using a sol-gel technique, emphasis in this investigation being placed on  $\text{TiO}_2$  coating for inclusion in an aluminum metal matrix.

The effect of the solution composition and coating procedure on the coating uniformity, structure, and thickness were investigated. Fiber coating were performed utilizing high strength PAN base carbon fibers, with the coated fiber preforms being infiltrated by pure liquid aluminum. Subsequent examination included energy dispersive x-ray analysis, optical and transmission electron microscopy of the fiber-matrix interface.

### INTRODUCTION

Continuous carbon fiber-aluminum alloys, if properly integrated, form a class of metal matrix composite materials whose properties may be tailored to satisfy many demanding structural requirements. These lightweight composite materials exhibit high strength and stiffness, high thermal and electrical conductivities, and do not outgas in a vacuum. Unfortunately, carbon is difficult to wet with liquid aluminum at moderate temperatures, that is at less than  $500^\circ\text{C}$ , while at higher temperatures  $\text{Al}_4\text{C}_3$  formation occurs at the fiber-matrix interface [1]. Formation of the latter causes the strength of the composite to decrease [1].

$\text{TiB}_2$  coating applied by Chemical Vapor Deposition (CVD) is the approach currently used to prepare continuous C-Al composites [1,2]. Although CVD processing has been successful it is difficult to obtain a uniform coating around the circumference of each fiber using this process [1]. The fibers

---

J.P. Clement, formerly Graduate Student, now Materials Research Engineer, Aerospatiale TX, 78130 Les Mureaux, France, and H.J. Rack, Professor of Mechanical Engineering and Metallurgy, Clemson University, Clemson, SC 29634-0921.

must be well separated in order to avoid the problem of shadowing—when one fiber overlaps another and prevents it from being coated properly. In addition, this coating process is carried out at high temperature, and usually degrades the carbon fibers.

Another serious problem with a  $TiB_2$  coating is that it is not air stable. The coated fibers cannot be exposed to air before immersion in the molten aluminum, otherwise wetting will not take place [1,2].

Katzman [2] has recently suggested an alternative approach for the preparation of C-Al composites, one utilizing  $SiO_2$  sol-gel fiber coatings. This investigation has extended this effort focussing on  $TiO_2$  sol coatings.  $TiO_2$  was selected based upon its thermodynamic stability with respect to  $TiC$  formation, the known ability of Ti to enhance the wettability between metals and ceramics, and its ready availability in the form of a metal alkoxide precursor, titanium isopropoxide (TIP) [3,4].

The objectives of this research were to establish parameters for producing thin uniform  $TiO_2$  sol coatings on carbon fibers, to demonstrate the ability of aluminum to wet the  $TiO_2$  surface, to evaluate the effectiveness of the coating as a diffusion barrier to prevent  $Al_4C_3$  formation, and finally, to examine any interfacial reaction products.

## EXPERIMENTAL PROCEDURE

Sol preparation involved combining selected amounts of water and hydrochloric acid in a beaker containing 2-propanol and thoroughly mixing for 5 min to obtain the desired concentration. The required amount of titanium (IV) isopropoxide (TIP) was then added to the solution, and the solution was stirred in a covered beaker for at least 1 hr.

Glass microscope slides, carbon coated slides, and sapphire crystals were utilized to establish the initial sol-gel coating procedure. The slides and/or unsized PAN 650/42 carbon fiber tows were dipped into the coating solution for 1 min and withdrawn vertically at a constant speed. They were then dried at  $60^\circ C$  and fired in air at temperatures varying from  $300^\circ C$  through  $700^\circ C$ . Some carbon fiber samples were also fired in a carbon monoxide (CO) atmosphere at  $700^\circ C$ .

Potential C-Al interactions were examined utilizing squeeze cast pure aluminum composites containing 12 v/o carbon fibers with the temperature of the preform being selected to minimize the infiltration pressure [5]. The cooling rate of the infiltrated samples was approximately  $7^\circ C/min$ , pressures as low as 50 psi being used to infiltrate the fiber preforms.

Optical metallography was performed on samples after infiltration in order to establish the fiber dispersion and to qualitatively define the amount of reaction at the fiber-matrix interface. Composite thin foils were then prepared by mechanical thinning and ion milling, and observed utilizing a TEM JEOL 100C, and a Philips 420 equipped with a PGT EDX analysis system.

## RESULTS AND DISCUSSION

### Coating Evaluation

#### Thermal Effect

Once a substrate is coated, the heat treatment—drying and firing—is most critical. The DSC results shown in Fig. 1. revealed that drying—evaporation of the solvents—occurred between room temperature and  $200^\circ C$ , with maximum desorption of solvents at  $125^\circ C$ . Above  $200^\circ C$ , the desorption of the solvents was complete, the weak exothermic peak found at approxi-

mately 300°C being probably due to carbonization of the remaining OR groups [6]. A second weak exothermic peak due to the amorphous-anatase phase transformation, was also observed at approximately 420°C. The accompanying TGA observations, confirm that the maximum weight loss, 25%, occurs during drying, with the weight loss between 200°C and 400°C being smaller—approximately 5%. Above 400°C the weight loss is negligible.

#### Coating Thickness

Coating thicknesses, as determined initially on glass slides, depend upon the TIP concentration of the solution, the speed of withdrawal of the samples from the sol, the number of dips of the samples in the solution, and the firing temperature, Fig. 2. For example, as the speed of withdrawal,  $s$ , increased—at least within the range of withdrawal speed examined in this investigation—the thickness,  $t$ , of the coating increased, i.e.,  $t$  is proportional to  $s^n$  where  $n$  varied from 0.5 to 0.6. It was also observed that, at constant  $H_2O$  and  $HCl$  molarities,  $n$  increased as the TIP concentration increased, increasing from approximately 0.50 when the TIP concentration was 0.1 mol/l, to 0.61 when the TIP concentration was 0.5 mol/l. Finally, increasing the number of dips or the TIP concentration lead to a linear increase in the coating thickness.

Fig. 2. further suggests that the original surface energy and chemistry has an effect—albeit a seemingly secondary one—on the coating thickness. The initial dip resulted in a surface coating thickness of 25 nm, while each subsequent dip resulted in an increased thickness of 45 nm. The same phenomenon was also observed on carbon coated slides, where under identical conditions, fired sol coatings were thinner than those on clean glass slide.

Successful experiments were conducted on glass slides which produced, in a single dip, crack free  $TiO_2$  layer as thick as 200 nm. Above 200 nm, the coating cracked during the firing step at 300°C. Above 270 nm, layers even cracked during drying. Sherer [7] suggested that during drying, stresses arise from differential strains. These stresses result from the fact that, due to differences in permeability, the exterior and the interior surfaces do not shrink at the same rate. The stresses can be quite large for organometallic gels, exceeding the coating strength. However, thin films do not crack during drying; presumably because the stresses associated with differential shrinkage are relieved by strain relaxation [7].

#### Coating Structure

Experiments conducted on scratched glass slides revealed that polymerization was disturbed by substrate topography. Surface roughness caused imperfections in the coating uniformity, with enhanced hydroxide particle nucleation being associated with surface imperfections.

The effects of firing for 15 min on the coating crystal structure were determined for temperatures up to 700°C. Coatings—150 nm—were prepared on sapphire substrates utilizing the procedure described earlier. Coatings were amorphous as formed, and continued to be so up to 400°C, Fig. 3. At and above 400°C, crystallinity developed, anatase being the first ordered phase observed. Mukherjee [8] suggested that the anatase phase nucleates first because it is structurally closer to the reactant, and that the rutile phase forms later. The data do not indicate the anatase-rutile phase transformation, though there appears to be some evidence of the (110) rutile peak in the 700°C data.

### Carbon Fiber Coating

Carbon fibers were coated utilizing the dipping procedures previously described. The fibers were dipped as tows, 12000 filaments.

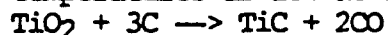
A multiple dip procedure at a lower TIP concentration was found to be much more efficient than a single dip procedure for obtaining a thin, uniform coating on the rough fiber surface. The first dip tended to smooth surface imperfections, and change surface chemistry allowing the second dip to deposit a more uniform layer. Multiple dipping also had the advantage of permitting gradual solvents evaporation during drying and firing, thereby resulting in lower residual stresses coating [7].

Because the inclusion of carbon fibers in aluminum was anticipated, the final firing temperature selected for coated fibers was 700°C. If coatings were directly heated in air to 700°C they cracked without regard to their thicknesses. When thin coatings were first fired at 400°C, and then at 700°C in air the appearance of the surface improved. This was thought due to structure homogenization throughout the coating thickness [7]. When fired directly at 700°C, at a rapid heating rate, the coating surface was presumably crystalline and the interior of the coating was still amorphous, and not as dense. Consequently, a high stress gradient was created throughout the coating thickness causing coating fracture. When fired first at 400°C, the coating structure homogenized under a smaller stress gradient, and was then better able to withstand the second firing at 700°C.

Selective firing between dips also improved the coating uniformity. Optimally the intermediate firing temperature should be kept as low as possible, i.e., 400°C, to minimize the exposure time of the coated fibers to high oxidizing temperatures. Coatings can still be fired if necessary at 700°C after the final dip.

Coatings on PAN fibers were uniform and crack free when fired in air for 15 min at temperatures below 650°C. At higher temperatures, however, coatings fractured, Fig. 4. In contrast, when fired at 700°C in a CO atmosphere the coatings did not crack. Summarizing, the best coating results were obtained using a multiple dip procedure with 400°C as the intermediate firing temperature, and 700°C in CO being the firing treatment after the final dip, Fig. 4.

The importance of firing atmosphere can be considered on a thermodynamic basis. Thermodynamic calculations show that in air the following reaction can take place at temperatures as low as 650°C [9].



In contrast, in a CO atmosphere  $\text{TiO}_2$  is stable with respect to TiC formation at temperatures higher than 1200°C.

Stronger gels may also be formed when fired in a CO atmosphere because, in the presence of oxygen, residual terminal bonds are not forced to share oxygen and, will therefore, create a looser oxide network [10]. Thus under a CO atmosphere, the following reaction takes place, and stronger coatings were produced.



These coatings are then able to better withstand the thermal stresses and the structure transformation occurring during firing.

Finally, the surface of all crack free coatings produced on fibers appeared very smooth. The coating grains were not visible under SEM, in contrast to coatings applied by sol-gel on  $\text{Al}_2\text{O}_3$ -Saffil fibers by An and Luhman [11].

### Examination of the Interface Fiber-Matrix

Transverse cross sections of cast composites revealed that  $\text{TiO}_2$  coatings enhanced the wettability of the fibers by molten aluminum, Fig. 5. In the case of non-coated fibers, the fibers were not dispersed in the matrix. When coated carbon fibers were used, however, the fibers were dispersed. The fiber distribution was however non-uniform due to the effect of the aluminum flow during infiltration.

Initial casting experiments were conducted with coated fibers directly fired at  $700^\circ\text{C}$  in air. The coating was already cracked in some places before infiltration, and a large  $\text{Al}_4\text{C}_3$  layer, 250 nm, was formed at the interface fiber-matrix. No Ti was found close to the interface; however, some was found in the matrix away from the fibers. The precracked coating was probably separated from the fiber during the infiltration process, the fibers were then unprotected and in contact with molten aluminium causing the formation of carbides.

Another set of casting experiments was conducted using fibers coated with a 330 nm crack free film fired in  $\text{CO}$ . This coating was made of three 110 nm layers. Each dip did not cover the whole fiber surface and in fact the actual average coating thickness was close to 220 nm. Analytical TEM work and TEM diffraction patterns confirmed that the coating was a very fine grain—15 nm average—polycrystalline anatase layer, Fig. 6. A small part of the coating reacted with aluminum to form a 70 nm  $\text{Al}_2\text{O}_3$ -Ti layer, allowing chemical wetting between the coated fibers and the matrix. Notice that even a thinner coating—110 nm—prevented the carbide formation as well.

Thermodynamically the coating should have been completely reduced by molten aluminum [9].



However, kinetic and diffusional effects take precedence and only a small amount of the coating was reduced, the 70 nm reaction layer preventing more species from diffusing. These findings are in agreement with work done by Katzman [2] and Chin and Nunes [12] on  $\text{SiO}_2$  sol-gel coated carbon fibers and magnesium.

### CONCLUSIONS

1. A technique to coat PAN fibers with a crack free, air stable, protective  $\text{TiO}_2$  layer by the sol-gel process has been developed.
2. Coating thickness can be controlled by the TIP concentration and the water content of the sol, the speed of substrate withdrawal, and the number of dips. Coating thickness is also influenced by the substrate geometry, chemistry, and structure.
3. Heat treatments reduce the coating thickness and change the coating structure. After heat treatment at  $400^\circ\text{C}$  for 15 min coatings reach their quasi-final thickness and are still amorphous. At temperatures between  $400^\circ\text{C}$  and  $700^\circ\text{C}$  the coating is transformed into a fine grain polycrystalline anatase layer.
4. 100 nm thick  $\text{TiO}_2$  coatings enhance the wettability of PAN carbon fibers by pure molten aluminum and prevent carbide formation at the interface fiber-matrix even after 9 min in contact with pure molten aluminum.
5. Part of the  $\text{TiO}_2$  coating reacts with aluminum to form an  $\text{Al}_2\text{O}_3$ -Ti layer allowing chemical wetting and acting as a diffusion barrier.

## ACKNOWLEDGEMENT

The support of this work by Aerospatiale (JPC) and the U.S. Air Force Office of Scientific Research, contract F49620-87-C-0017, as part of the University Research Initiative program on High Temperature Metal Matrix Composites at Carnegie Mellon University (HJR), is gratefully acknowledged.

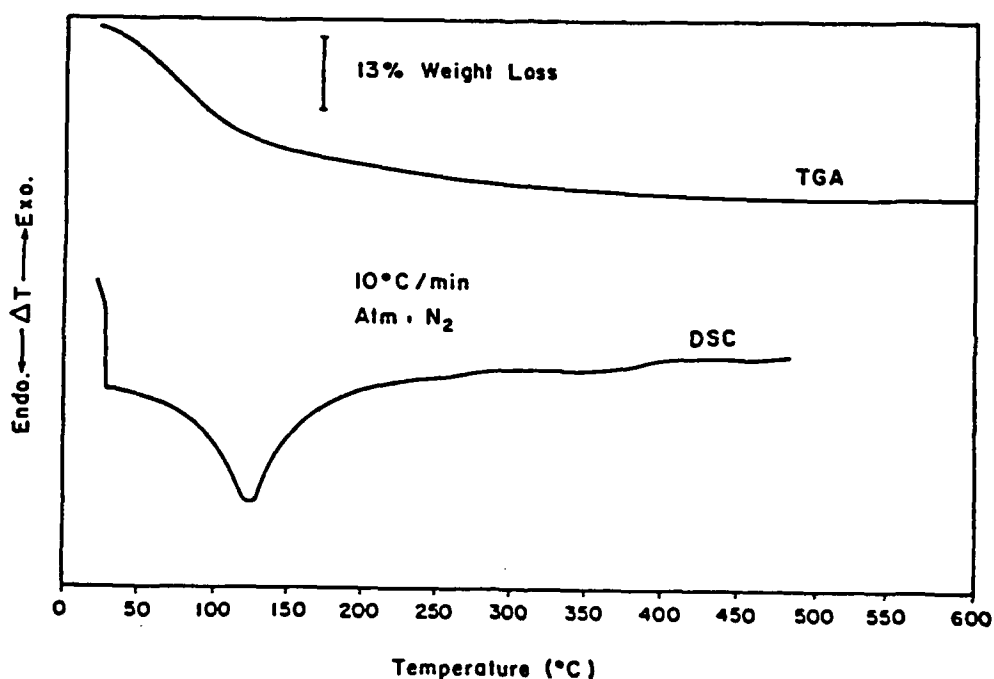


Fig. 1. Thermal analysis of  $\text{TiO}_2$  gel dried in air at room temperature.

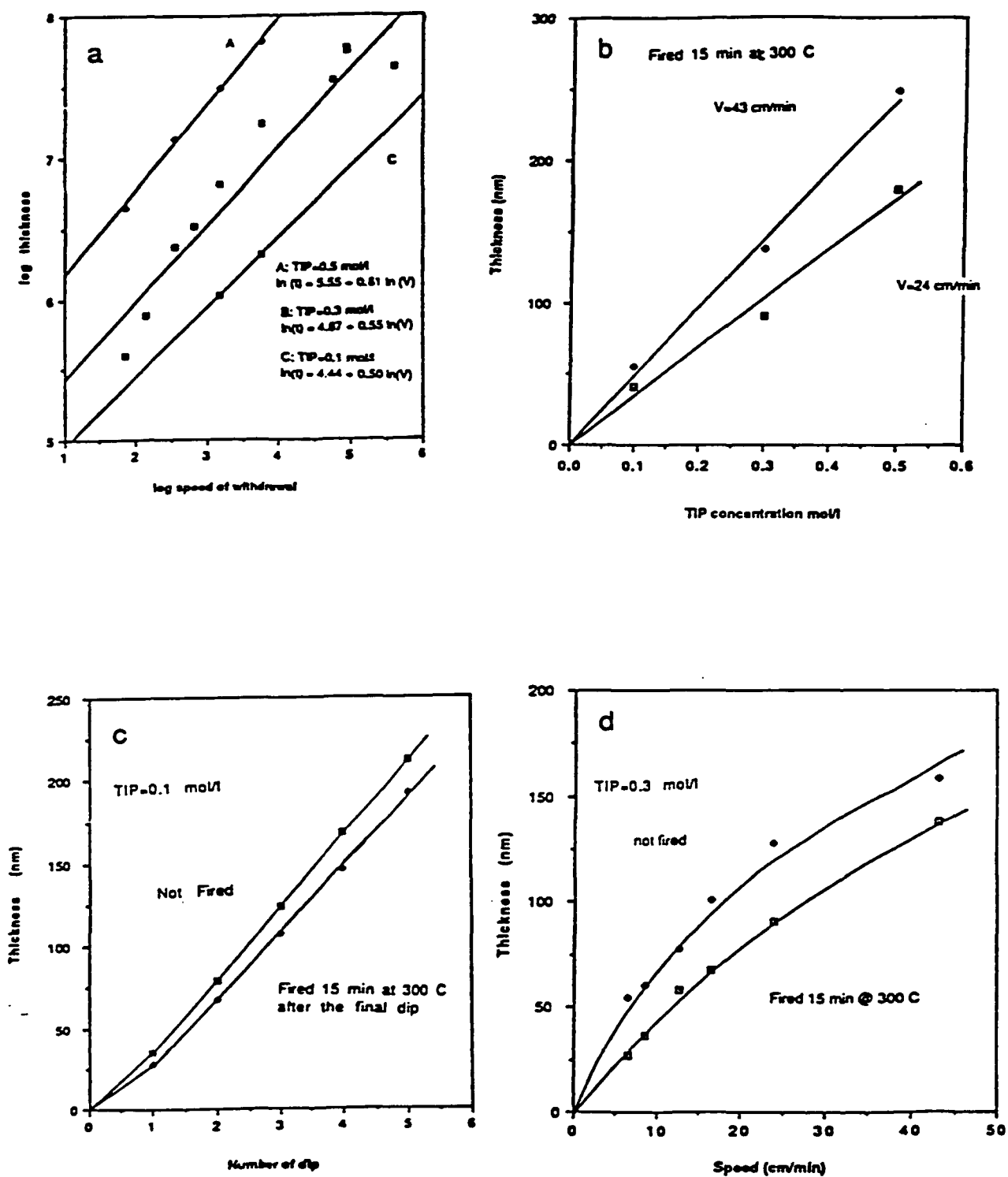


Fig. 2. Influence of (a) substrate withdrawal speed, (b) TIP molarity, (c) number of dips, and (d) firing on coating thickness.

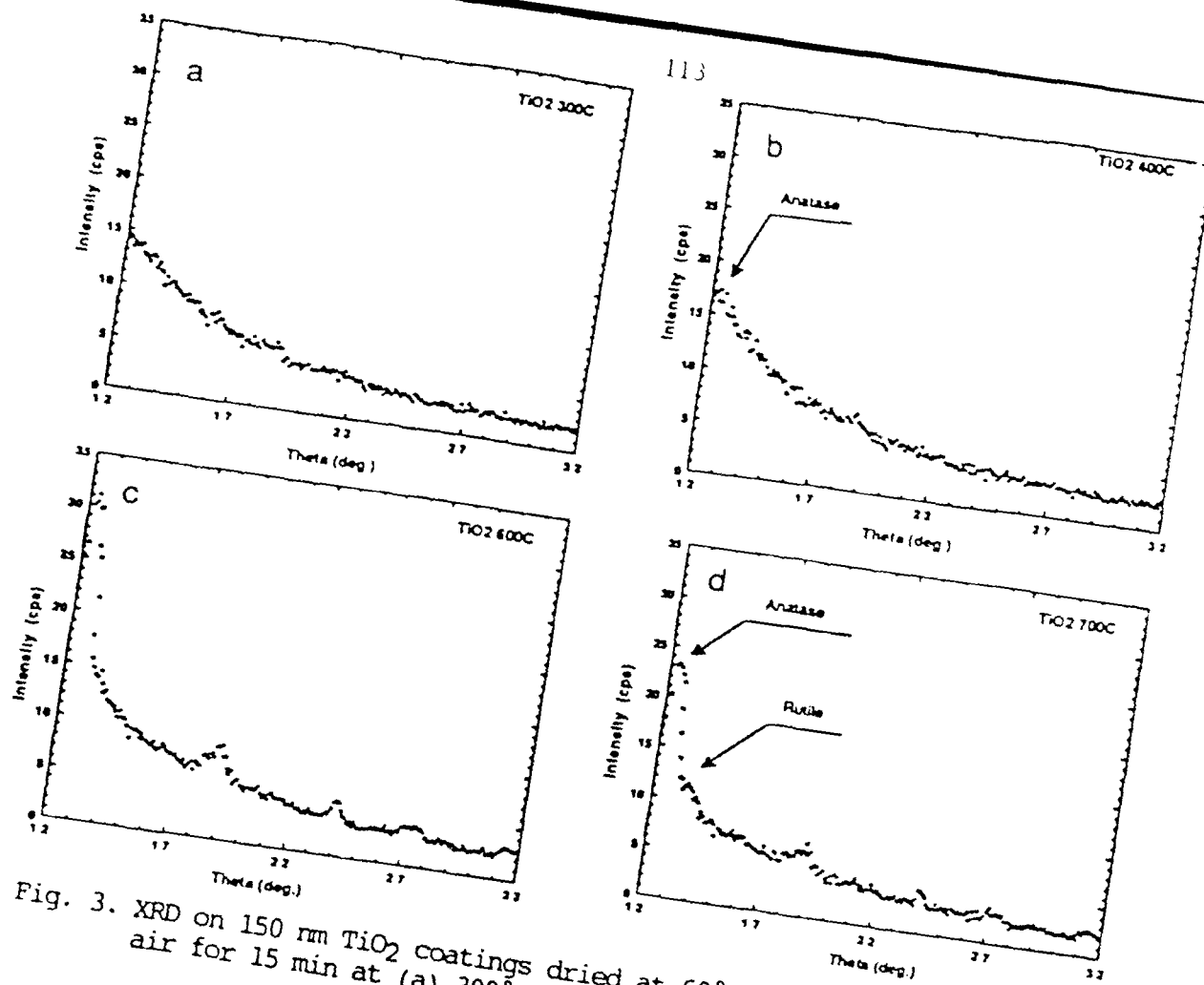


Fig. 3. XRD on 150 nm TiO<sub>2</sub> coatings dried at 60°C for 10 min and fired in air for 15 min at (a) 300°C, (b) 400°C, (c) 600°C, and (d) 700°C.

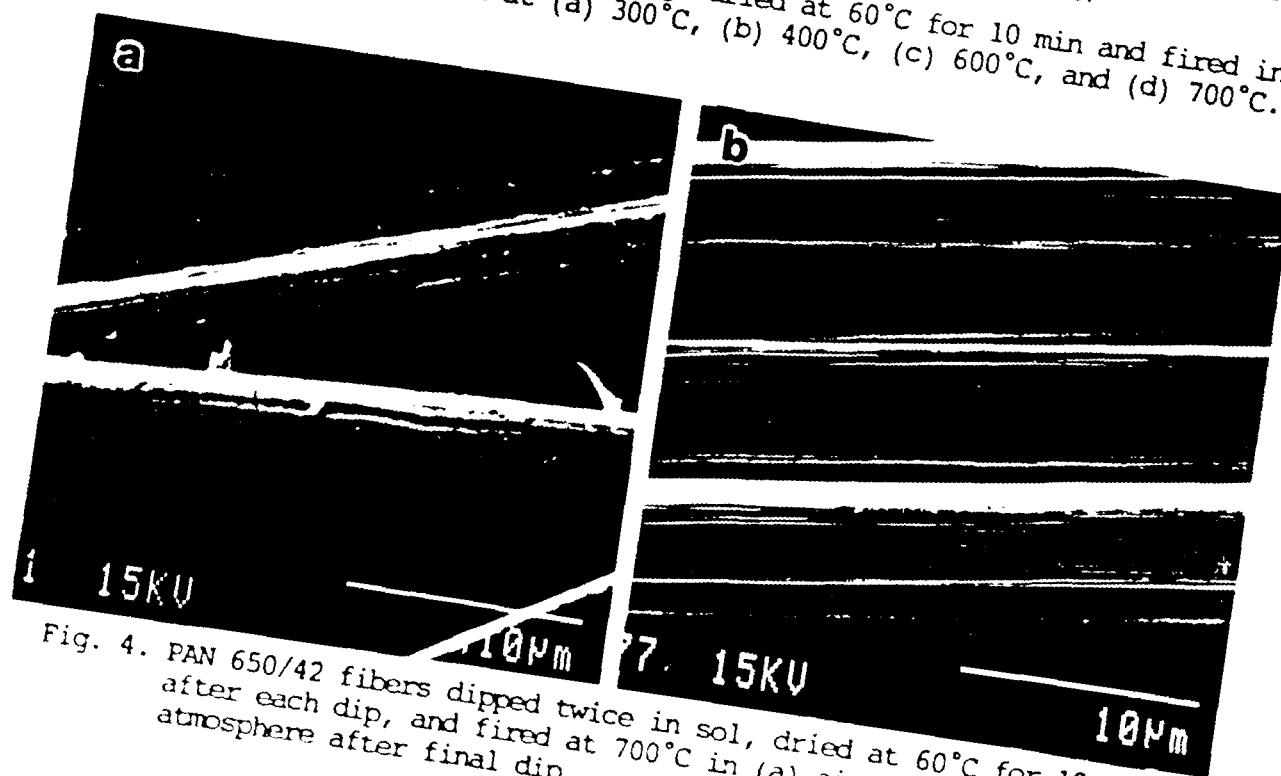


Fig. 4. PAN 650/42 fibers dipped twice in sol, dried at 60°C for 10 min after each dip, and fired at 700°C in (a) air, or (b) a CO atmosphere after final dip.



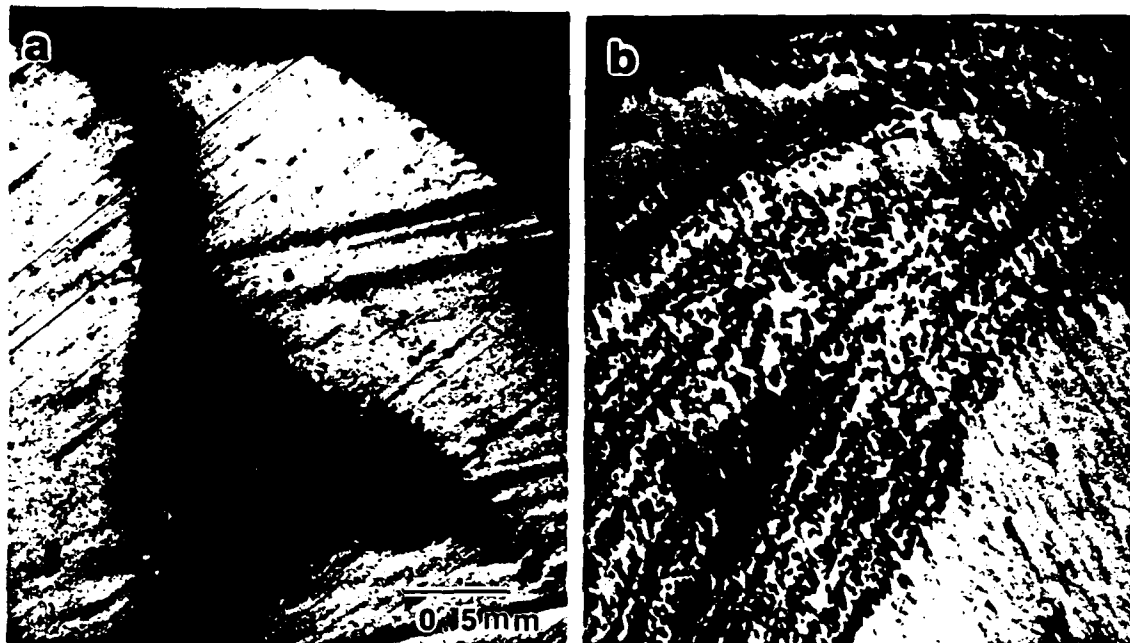


Fig. 5. Optical micrographs of pressure-infiltrated samples with (a) uncoated and (b) coated carbon fibers.

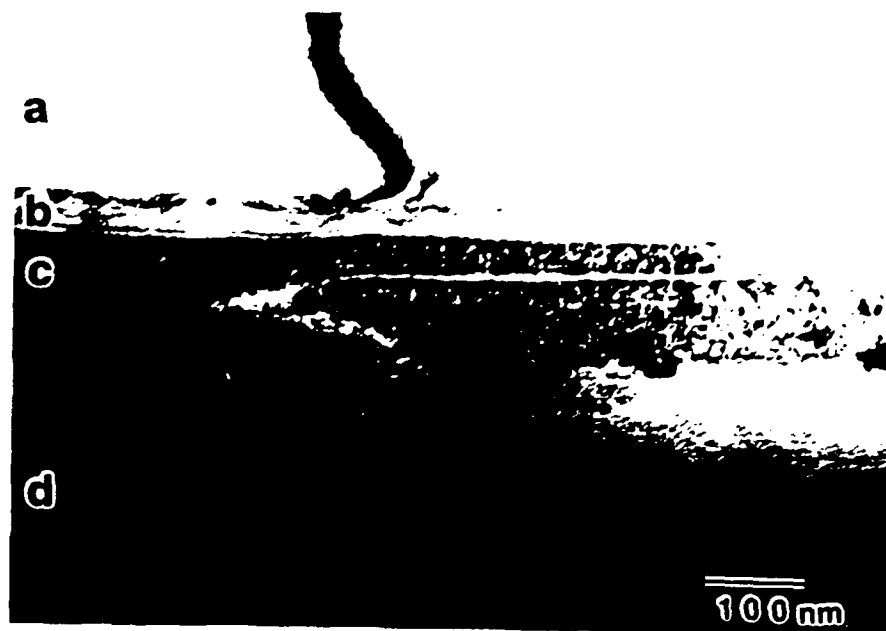


Fig. 6. TEM micrograph of the fiber-matrix interface; (a) aluminum, (b) reaction layer, (c)  $\text{TiO}_2$  coating, and (d) carbon fiber.

## REFERENCES

1. Amateau, M. F., "Progress in the Development of Graphite Aluminum Composites Using Liquid Infiltration Technology," Jn. of Composite Materials, Vol. 10, Oct. 1976, pp. 279-296.
2. Katzman, H. A., "Fibre Coatings for Fabrication of Graphite-Reinforced Magnesium Composites", Jn.Mat.Sci., Vol.22, 1987, pp. 144-148.
3. Bennett, M. J., "Application and Evaluation of Ceramic Coatings Produced by Sol-Gel Technology and Vapor Deposition Procedures," Coating for High Temperature Application, E. Lang, ed., Applied Science Publishers, New York, 1983, pp. 169-192.
4. Levitt, A., Di Cesare, E., and Wolf, S., Fabrication and Properties of Graphite Fiber Reinforced Magnesium, Army Materials and Mechanics Research Center; AMMRC TR 71-44; AD 735-313; Nov.1971.
5. Cornie, J. A., Mortensen, A., and Fleming, M. C., "Wetting, Fluidity and Solidification in Metal Matrix Composite Castings: a Research Summary", Sixth International Conference on Composite Materials, F. L. Matthews, N. C. Buskell, J. M. Hodgkinson, and J. Morton, eds., Elsevier Applied Science, London, 1987, Vol.2, pp. 2.297-2.319.
6. Cheng, J., and Wang, D., "Structural Transformation of the  $TiO_2-SiO_2$  System Gel During Heat-Treatment", Jn. of Non-Crystalline Solid, Vol. 100, North-Holland, Amsterdam, 1988, pp. 288-291.
7. Sherer, S., "Drying Gels II", Jn. of Non-Crystalline Solid, Vol. 89, North-Holland, Amsterdam, 1987, pp. 217-227.
8. Mukherjee, S. P., "Inorganic Oxide Gels and Gel-Monoliths: their Crystallization Behavior", Emergent Process Methods for High-Technology Ceramics, R. F. Davis, H. Palmour, and R. L. Porter, eds., Plenum Press, NY, 1984, pp.95-109.
9. Stull, D. R., and Prophet, H., JANAF Thermochemical Tables, second edition, National Standard Reference Data System, National Bureau of Standard publ., June 1972.
10. Yoldas, B. E., "Deposition and Properties of Optical Oxide Coating from Polymerized Solutions", Applied Optic, Vol. 21, N°16, August 82, pp. 2960-2964.
11. An, H. H., and Luhman, T. S., "Sol-Gel Coating Concepts for Very High Temperature Aluminium Matrix", Dispersion Strengthened Aluminium Alloys, Y. W. Kim, and W. M. Griffith, eds., The Mineral, Metals, and Materials Society, 1988, pp. 709-718.
12. Chin, E. C., and Nunes, J., Alloying Effects in Graphite-Magnesium Composites, Presented at the TMS Annual Meeting in Phoenix, Arizona January 26, 1988, Unpublished.

## INTERFACIAL MODIFICATION IN METAL MATRIX COMPOSITES

## BY THE SOL-GEL PROCESS

J. P. Clement\*, H. J. Rack, K. T. Wu, and H. G. Spencer

Departments of Mechanical Engineering and Chemistry  
Clemson University  
Clemson, SC 29634-0921

## Abstract

Detailed examination of thermodynamic and kinetic data suggest that it should be possible to develop an interfacial barrier coating which promotes wetting of metal matrix composite reinforcements, while simultaneously reducing deleterious interfacial chemical interactions.

The current study has examined the feasibility of developing a procedure to coat graphite reinforcements with a thin, crack-free, protective oxide layer. Emphasis in this investigation being placed on sol-gel,  $\text{TiO}_2$ , coated PAN 650/42 graphite for inclusion in an aluminum metal matrix.

Initially, the effect of the sol-gel composition and coating procedure on the coating uniformity, structure, and thickness were investigated. These procedures were then utilized for graphite fiber coating, with the coated fiber preforms being subsequently infiltrated by pure liquid aluminum. Energy dispersive x-ray analysis, optical and transmission electron microscopy confirmed that no reaction occurred at the  $\text{TiO}_2$ -C interface, while chemical wetting and formation of a mixed (Al, Ti) $\text{O}_2$  oxide occurred at the  $\text{TiO}_2$ -Al interface.

\* Now with Aerospatiale TX, 78130 Les Mureaux, France

## Introduction

Graphite fiber-aluminum alloys form a class of metal matrix composites whose properties may be tailored to satisfy many demanding structural applications. These light-weight composite materials exhibit high strength and stiffness, high thermal and electrical conductivities, and do not out gas in a vacuum. However, graphite is difficult to wet with liquid aluminum at moderate temperatures, less than 500°C, while at higher temperatures  $\text{Al}_4\text{C}_3$  formation occurs at the fiber-matrix interface (1). Formation of the latter causes the strength of the composite to decrease (1).

Normally, graphite fibers must therefore be coated prior to inclusion in a metal matrix composite. For example,  $\text{TiB}_2$  coatings, as applied by Chemical Vapor Deposition (CVD), have been extensively used to prepare continuous C-Al composites (1,2). Although CVD processing has been successful, the fibers must be well separated in order to avoid shadowing -- when one fiber overlaps another and prevents it from being coated properly. In addition, this coating process is carried out at high temperature, and therefore may degrade the carbon fibers.

Furthermore,  $\text{TiB}_2$  coatings are not air stable, that is, coated fibers cannot be exposed to air prior to their incorporation in aluminum.

Katzman (2) has recently suggested an alternative approach for the preparation of C-Al composites, one utilizing  $\text{SiO}_2$  sol-gel fiber coatings. Few details are provided by this author and it is not clear how applicable this technique may be to other sol-gel systems. The current investigation was therefore undertaken to examine the general applicability of the sol-gel coating process to the synthesis of interfacial barrier coatings for fiber reinforced composites.

$\text{TiO}_2$  sols were selected for this program. This selection was based upon the thermodynamic stability of  $\text{TiO}_2$  with respect to  $\text{TiC}$  formation, the known ability of Ti to enhance the wettability between metals and ceramics, and the ready availability of a Ti metal alkoxide precursor, titanium isopropoxide (TIP) (3,4).

The objectives of this research were to establish parameters for producing thin uniform  $\text{TiO}_2$  sol coatings on carbon fibers, to demonstrate the ability of aluminum to wet the  $\text{TiO}_2$  surface, to evaluate the effectiveness of the coating as a diffusion barrier to prevent  $\text{Al}_4\text{C}_3$  formation, and finally, to examine any interfacial reaction products.

## Experimental Procedure

Sol preparation involved combining selected amounts of water and hydrochloric acid in a beaker containing 2-propanol and thoroughly mixing for 5 min to obtain the desired concentration. The required amount of titanium (IV) isopropoxide (TIP) was then added to the solution, and the solution was stirred in a covered beaker for at least 1 hr.

Glass microscope slides, carbon coated slides, and sapphire crystals were utilized to establish the initial sol-gel coating procedure. The slides and/or unsized PAN 650/42 carbon fiber tows were dipped into the coating solution for 1 min and withdrawn vertically at a constant speed. They were then dried at 60°C and fired in air at temperatures varying from 300°C through 700°C. Some carbon fiber samples were also fired in a carbon monoxide ( $\text{CO}$ ) atmosphere at 700°C.

Potential C-Al interactions were examined utilizing squeeze cast pure aluminum composites containing 12 v/o carbon fibers with the temperature of the preform being selected to minimize the infiltration pressure (5). The cooling rate of the infiltrated samples was approximately 7°C/min, pressures as low as 0.35 MPa being used to infiltrate the fiber preforms.

Optical metallography was performed on samples after infiltration in order to establish the fiber dispersion and to qualitatively define the amount of reaction at the fiber-matrix interface. Composite thin foils were then prepared by mechanical thinning and ion milling, and observed utilizing a TEM JEOL 100C, and a Philips 420 equipped with a PGT EDX analysis system.

## Results and Discussion

### Coating Evaluation

**Thermal Effect.** Once a substrate is coated, the heat treatment, drying and firing, is most critical. The DSC results shown in Figure 1 revealed that drying, evaporation of the solvents, occurred between room temperature and 200°C, with maximum desorption of solvents at 125°C. Above 200°C, the desorption of the solvents was complete, the weak exothermic peak found at approximately 300°C being due to a chemical reaction, probably carbonization of the remaining OR groups (6). A second weak exothermic peak due to the amorphous-anatase phase transformation, was also observed at approximately 420°C. The accompanying TGA observations confirm that the maximum weight loss, 25%, occurs during drying with the weight loss between 200°C and 400°C being smaller, approximately 5%. Above 400°C the weight loss is negligible.

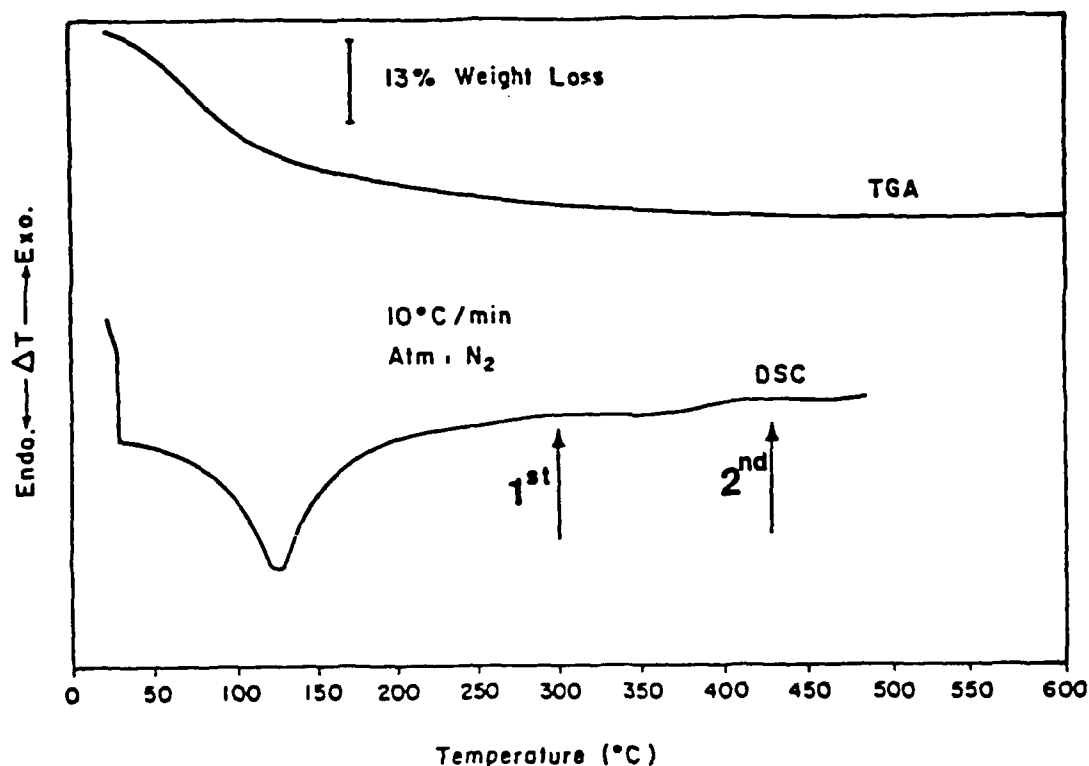


Figure 1. Thermal Analysis of TiO<sub>2</sub> Gel Dried Air at Room Temperature

**Coating Thickness.** Coating thicknesses, as determined initially on glass slides, depend upon the TIP concentration of the solution, the speed of withdrawal of the samples from the sol, the number of dips of the samples in the solution, and the firing temperature, Figure 2 and 3. For example, as the speed of withdrawal,  $s$ , increased -- at least within the range of withdrawal speed examined in this investigation -- the thickness,  $t$ , of the coating increased, i.e.,  $t$  is proportional to  $s^n$  where  $n$  varied from 0.5 to 0.6. It was also observed that, at constant H<sub>2</sub>O and HCl molarities,  $n$  increased as the TIP concentration increased, increasing from approximately 0.50 when the TIP concentration was 0.1 mol/l, to 0.61

when the TIP concentration was 0.5 mol/l. Measurements indicated that an approximate 30% reduction in thickness should be expected when a dried coating is fired, Figure 3. The use of higher firing temperatures  $F$  (e.g., 500°C versus 300°C) only slightly altered the final coating thickness. Finally, increasing the number of dips or the TIP concentration lead to a linear increase in the coating thickness.

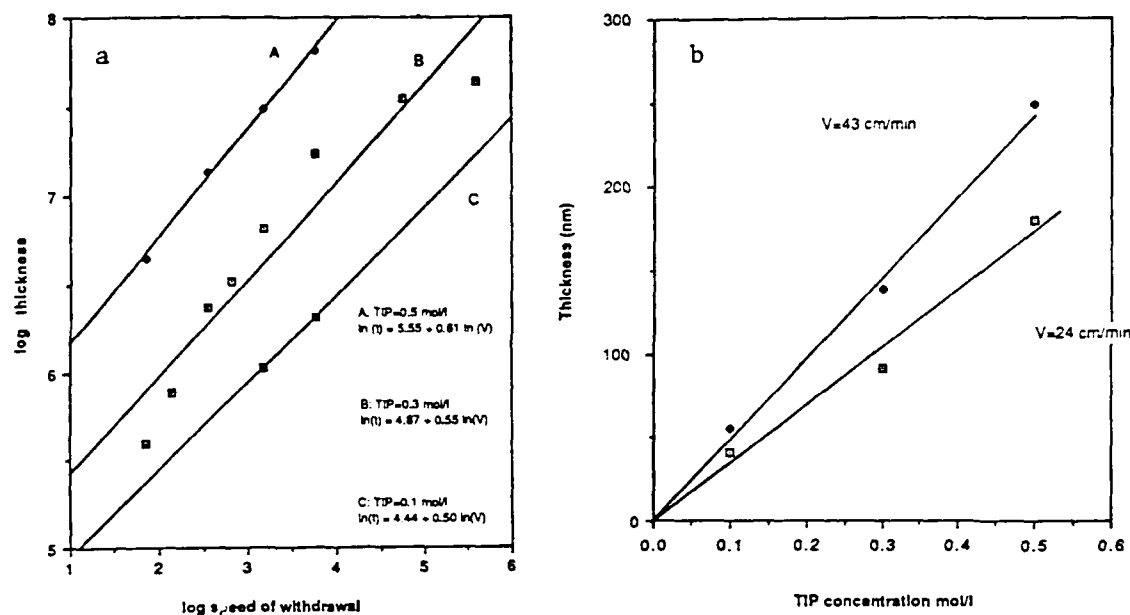


Figure 2. Influence of (a) Substrate Withdrawal Speed, and (b) TIP Molarity on Coating Thickness.

Figure 3 further suggests that the original surface energy and chemistry has an effect, albeit a seemingly secondary one, on the coating thickness. The initial dip resulted in a surface coating thickness of 25 nm, while each subsequent dip resulted in an increased thickness of 45 nm. The same phenomenon was also observed on carbon coated slides, where under identical conditions, fired sol coatings were thinner than those on clean glass slide.

Successful experiments were conducted on glass slides which produced, in a single dip, crack free  $TiO_2$  layer as thick as 200 nm. Above 200 nm, the coating cracked during the firing step at 300°C. Above 270 nm, layers even cracked during drying. Sherer (7) suggested that during drying, stresses arise from differential strains. These stresses result from the fact that, due to differences in permeability, the exterior and the interior surfaces do not shrink at the same rate. The stresses can be quite large for organometallic gels, exceeding the coating strength. However, thinner films do not crack during drying; presumably because the stresses associated with differential shrinkage are relieved by strain relaxation (7).

**Coating Structure.** Experiments conducted on scratched glass slides revealed that polymerization was disturbed by substrate topography. Surface roughness caused imperfections in the coating uniformity, with enhanced hydroxide particle nucleation being associated with surface imperfections.

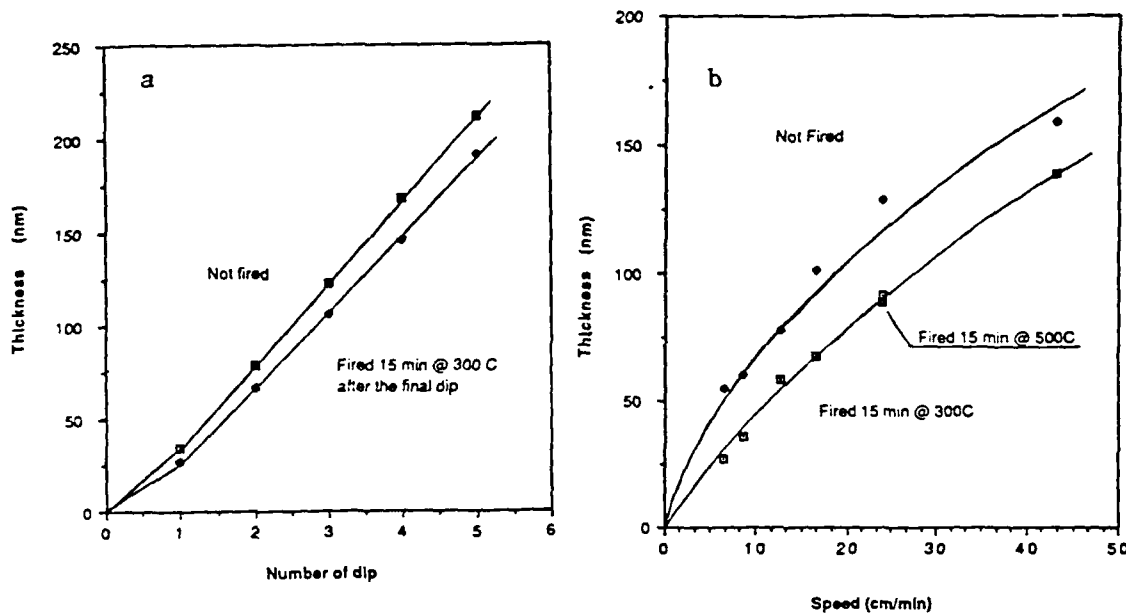


Figure 3. Influence of (a) Number of Dips, and (b) Firing on Coating Thickness.

The effects of firing for 15 min on the coating crystal structure were determined for temperatures up to 700°C. Coatings, 150 nm thick, were prepared on sapphire substrates utilizing the procedure described earlier. Coatings were amorphous as formed, and continued to be so up to 400°C, Figure 4. At and above 400°C, crystallinity developed, anatase being the first ordered phase observed. Mukherjee (8) suggested that the anatase phase nucleates first because it is structurally closer to the reactant, and that the rutile phase forms later. The data do not clearly indicate the anatase-rutile phase transformation, though there appears to be some evidence of the (110) rutile peak in the 700°C data, Figure 4.

### Carbon Fiber Coating

Pan 650/42 graphite fibers were coated utilizing the dipping procedures previously described. The fibers were dipped as tows, 12000 filaments.

A multiple dip procedure was found to be much more efficient than a single dip procedure for obtaining a thin, uniform coating on the rough fiber surface. The first dip tended to smooth surface imperfections, and change surface chemistry allowing the second dip to deposit a more uniform layer. Multiple dipping also had the advantage of permitting gradual solvents evaporation during drying and firing, thereby resulting in lower residual stresses coating (7).

Selective firing between dips improved the coating uniformity. Optimally the intermediate firing temperature should be kept as low as possible, i.e., 400°C, to minimize the exposure time of the coated fibers to high oxidizing temperatures.

Because the inclusion of carbon fibers in aluminum was anticipated, the final firing temperature selected for coated fibers was 700°C. Coatings on PAN fibers were uniform and crack free when fired in air for 15 min at temperature below 650°C. At higher temperatures, however, coatings fractured, Figure 5.

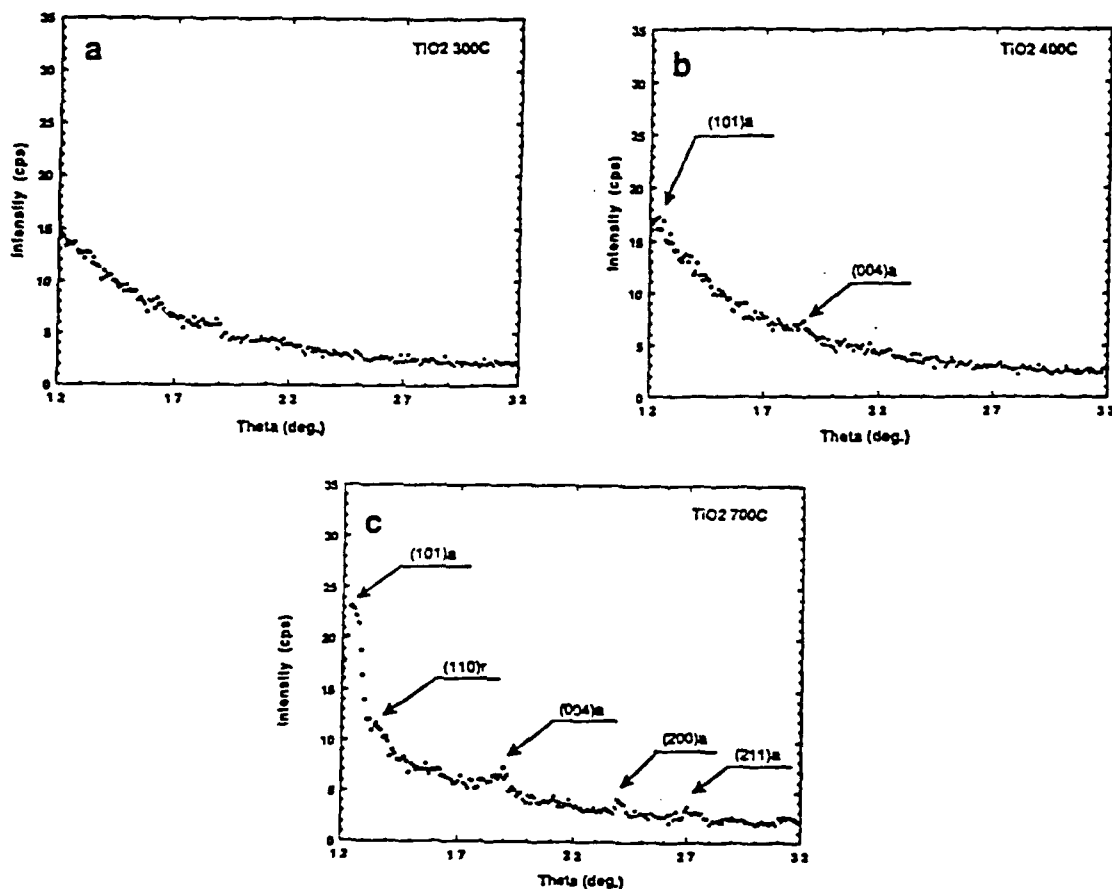
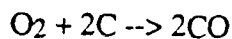
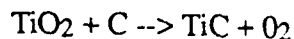


Figure 4. XRD on 150 nm TiO<sub>2</sub> Coatings Dried at 60°C for 10 min and Fired in Air for 15 min at (a) 300°C, (b) 400°C, and (c) 700°C

Several different factors may have contributed to the cracking observed in TiO<sub>2</sub> coated PAN fibers fired at high temperatures in air. Paramount among these is the firing environment. Indeed, cracking propensity increased as the exposure time increased, Figure 6. The fiber diameter also appeared to have been reduced as the exposure time exceeded one hour. This hypothesis is supported by the following consideration of the effect of firing environment on the thermodynamic stability of TiO<sub>2</sub>-C couples. TiO<sub>2</sub> can react with carbon fiber forming TiC and oxidizing the fibers, i.e.,



or



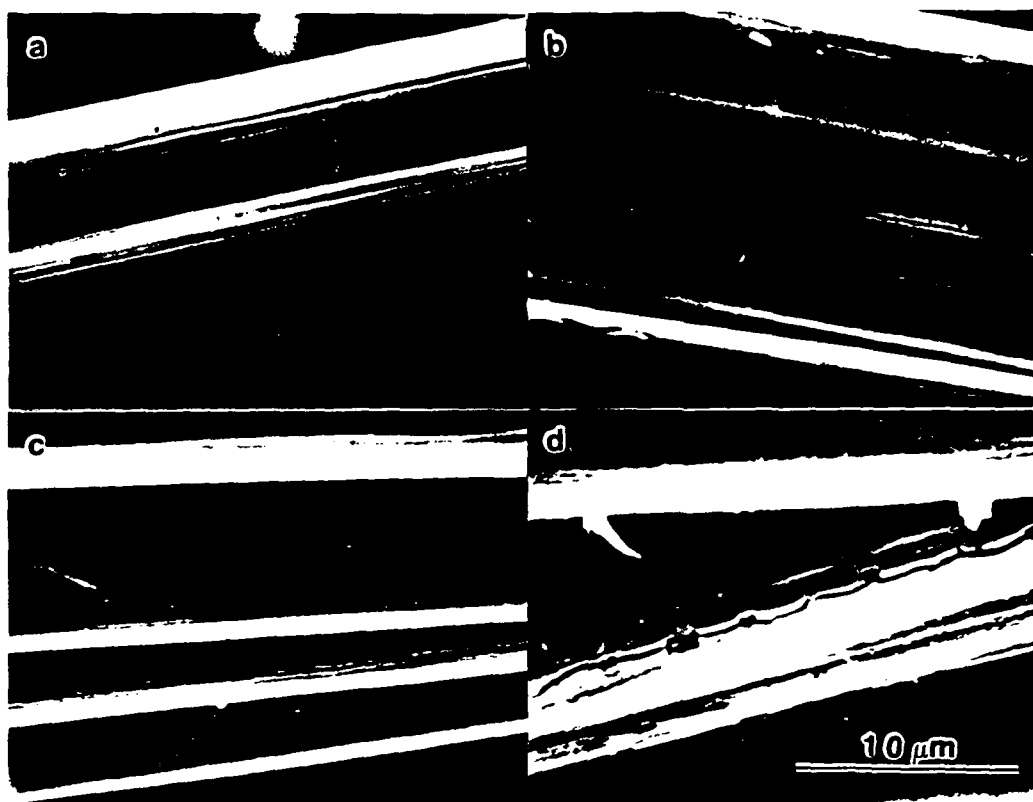
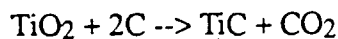
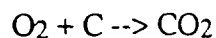
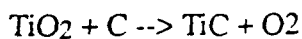


Figure 5. PAN 650/42 Fibers Dipped Twice in Sol, Dried at 60°C in Humidity Controlled Atmosphere for 10 min after Each Dip and Fired in Air at (a) 550°C, (b) 600°C, (c) 650°C, or (d) 700°C After Final Dip

Thermodynamic equilibrium and the reaction rates depend on  $P_{\text{CO}}$  and  $P_{\text{CO}_2}$ , i.e.,

$$\Delta G_1 = \Delta G_{01} + RT \ln(P_{\text{CO}})^2 \text{ and}$$

$$\Delta G_2 = \Delta G_{02} + RT \ln(P_{\text{CO}_2})$$

where  $\Delta G_1$  and  $\Delta G_2$  are the Gibbs free energy of the reactions,  $\Delta G_{01}$  and  $\Delta G_{02}$  are reference Gibbs free energy of the reactions,  $R$  is the ideal gas constant, and  $T$  is the absolute temperature. These reactions can take place when  $\Delta G_i(T)$  is negative, that is when  $\Delta G_{0i}(T)$  is smaller than  $RT \ln(P_{iX})$ . Figure 7 shows that, for samples fired in air, i.e.,  $P_{\text{CO}}=10^{-7}$  and  $P_{\text{CO}_2}=3.2 \times 10^{-4}$ ,  $\text{TiO}_2$  and  $\text{C}$  will react at temperatures above 650°C.

Further consideration of these reactions indicates that as  $P_{\text{CO}}$  approaches one, that is if firing is carried out in a  $\text{CO}$  atmosphere,  $\text{TiO}_2$  is stable at 700°C in  $\text{CO}$ .

Finally, the surface of all crack free coatings produced on fibers appeared very smooth. The coating grains were not visible under SEM, in contrast to coatings applied by sol-gel on  $\text{Al}_2\text{O}_3$ -Saffil fibers by An and Luhman (13).

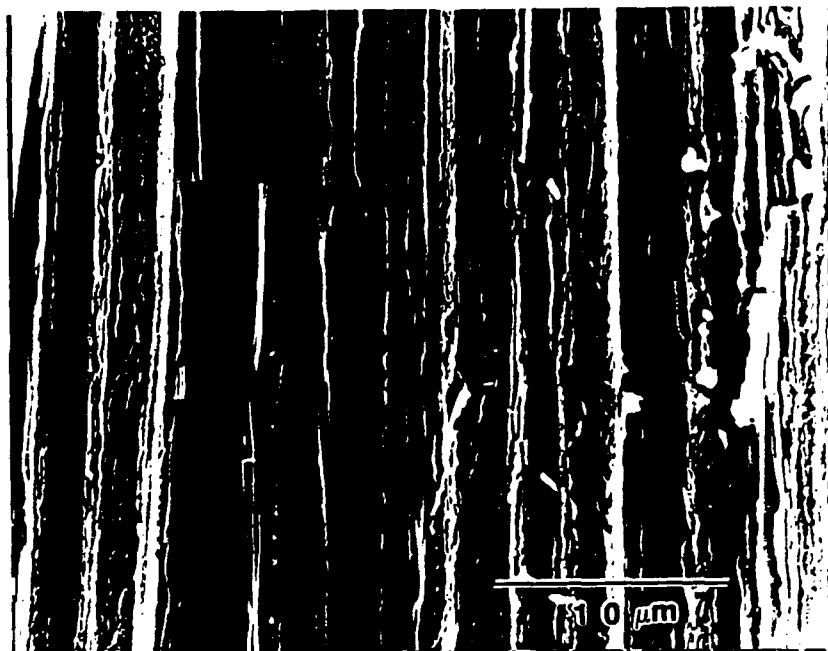


Figure 6. PAN 650/42 Fibers Dipped Four Times in Sol, Dried at 60°C in Humidity Controlled Atmosphere for 10 min and Fired at 700°C in Air for 15 min after Each Dip

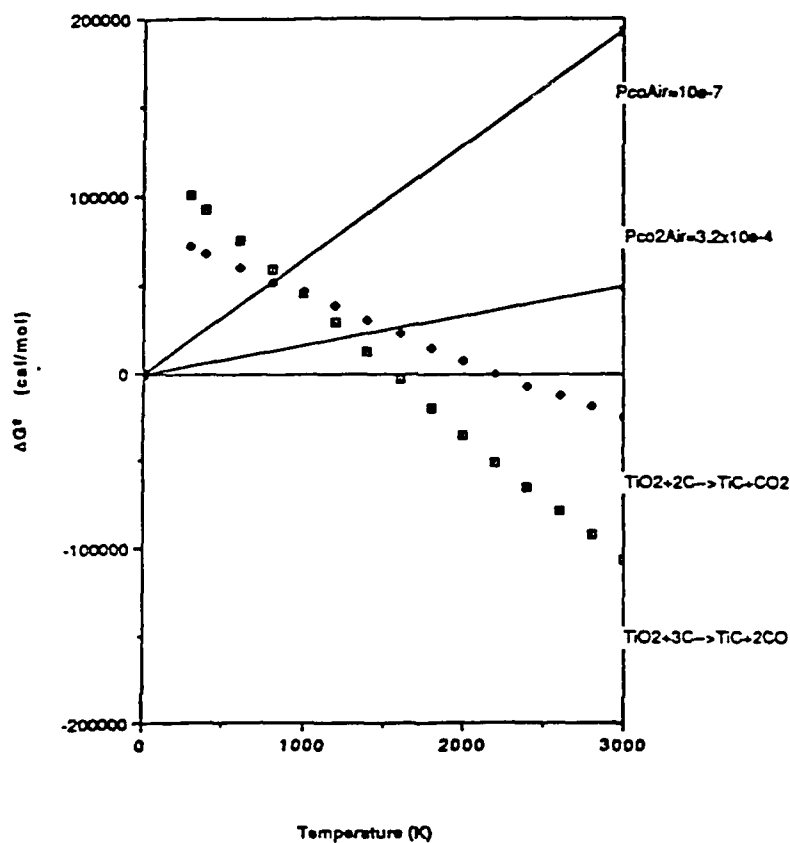


Figure 7. Stability of  $\text{TiO}_2$  in Air with Respect to  $\text{TiC}$  Formation (9)

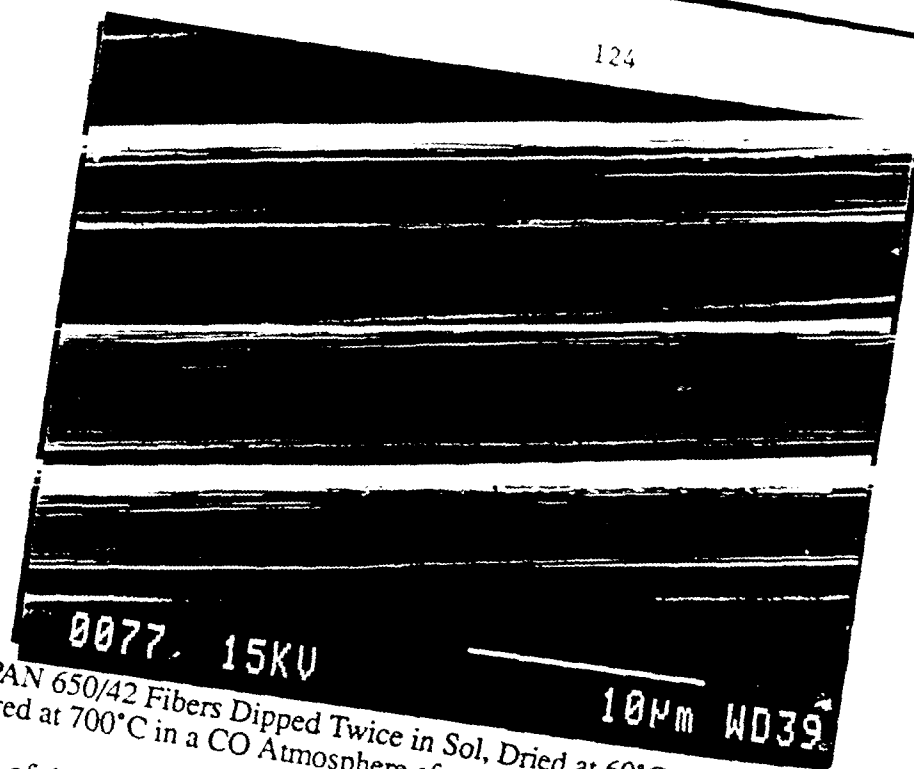


Figure 8. PAN 650/42 Fibers Dipped Twice in Sol, Dried at 60°C for 10 min after Each Dip, and Fired at 700°C in a CO Atmosphere after Final Dip

Examination of the Interface Fiber-Matrix

Transverse cross sections of cast composites revealed that TiO<sub>2</sub> coatings enhanced the wettability of the fibers by molten aluminum, Figure 9. In the case of non-coated fibers, the fibers were not dispersed in the matrix. When coated carbon fibers were used however, the fibers were dispersed. The fiber distribution was however nonuniform, due to the effect of the aluminum flow during infiltration.

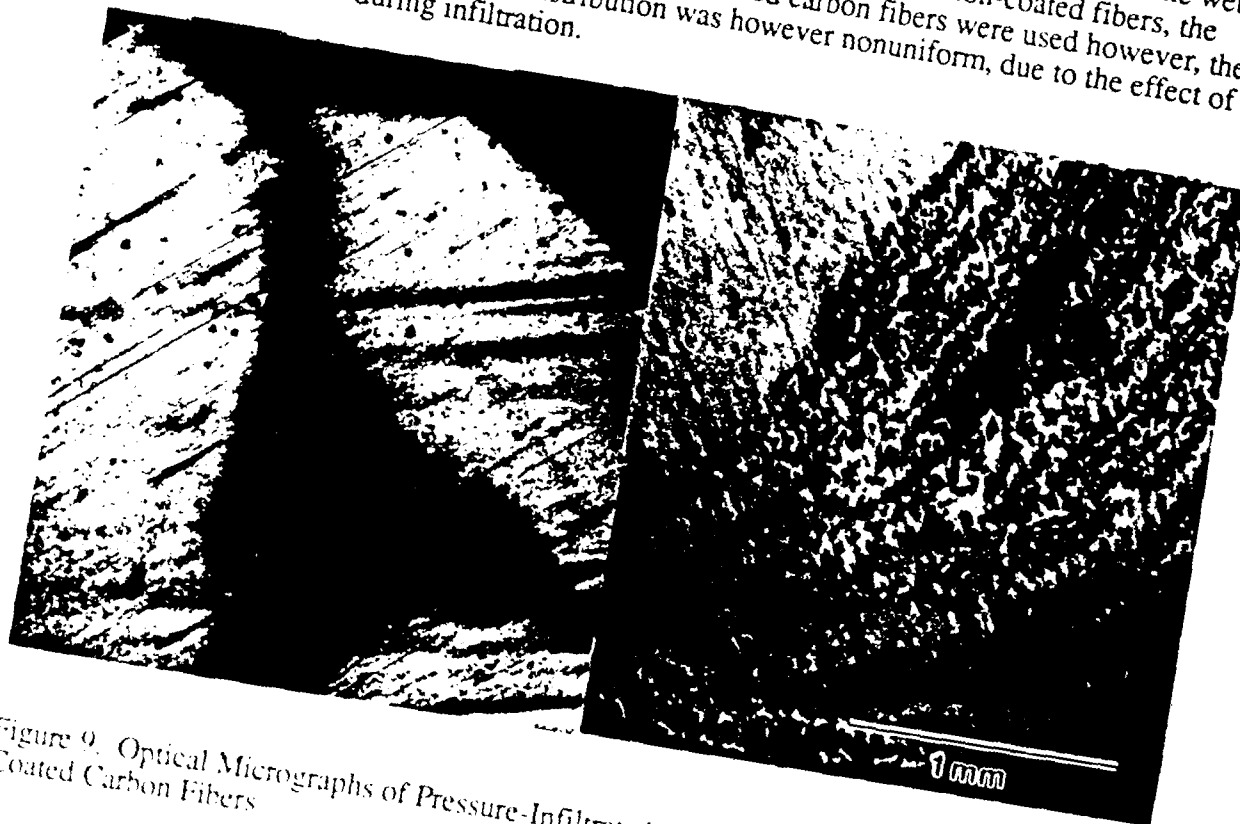


Figure 9. Optical Micrographs of Pressure-Infiltrated Samples with (a) Uncoated and (b) Coated Carbon Fibers

Initial casting experiments were conducted with coated fibers directly fired at 700°C in air. The coating was already cracked in some places before infiltration, and a large  $\text{Al}_4\text{C}_3$  layer, 250 nm, was formed at the interface fiber-matrix, Figure 10. No Ti was found close to the interface; however, some was found in the matrix away from the fibers. The precracked coating was probably separated from the fiber during the infiltration process, the fibers were then unprotected and in contact with molten aluminum causing the formation of carbides.

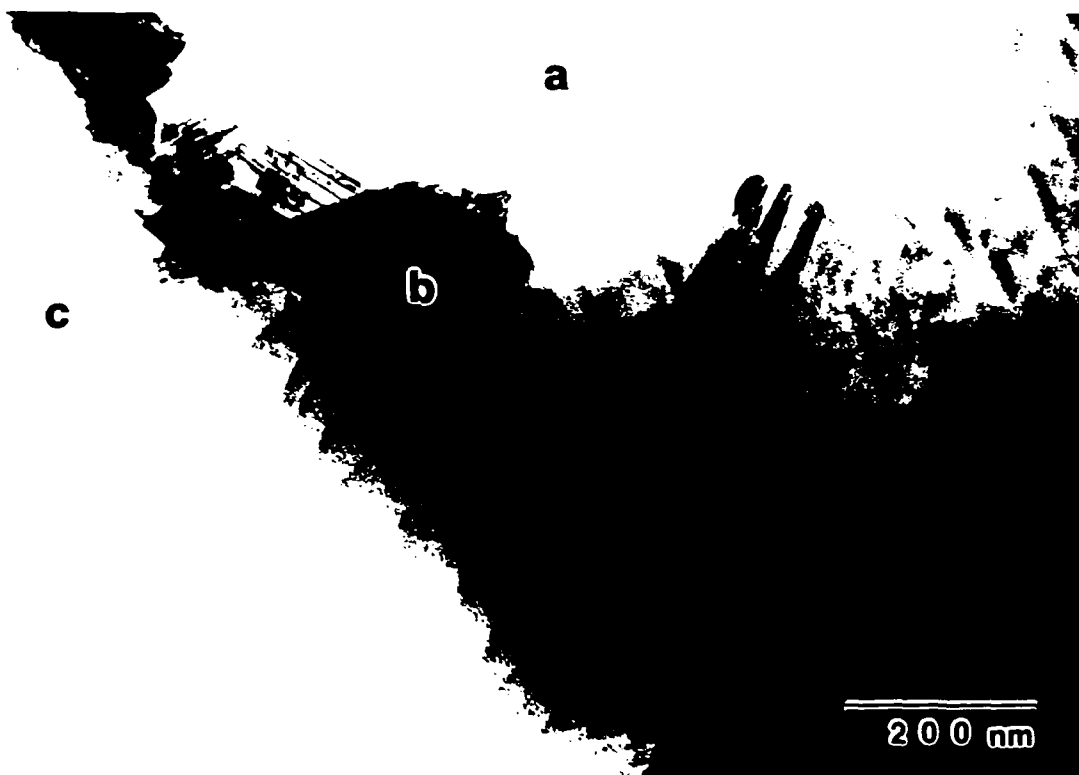
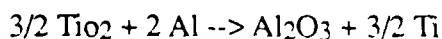


Figure 10. TEM Micrographs of the Fiber-Matrix Interface of a Cast Sample; Fibers Fired at 700°C in Air after Final Dip; (a) Fiber, (b)  $\text{Al}_4\text{C}_3$ , (c) Aluminum

Another set of casting experiments was conducted using fibers coated with a 330 nm crack free film fired in CO. This coating was made of three 110 nm layers. Each dip did not cover the whole fiber surface and in fact the actual average coating thickness was close to 220 nm, Figure 11. Analytical TEM work and TEM diffraction patterns confirmed that the coating was a very fine grain, 15 nm average, polycrystalline anatase layer, Figure 12. A small part of the coating reacted with aluminum to form a 70 nm  $\text{Al}_2\text{O}_3$ -Ti layer, allowing chemical wetting between the coated fibers and the matrix, Figure 13. Notice that even a thinner coating, 110 nm, prevented the carbide formation as well.

Thermodynamically the coating should have been completely reduce by molten aluminum (9).



However, kinetic and diffusional effects take precedence and only a small amount of the coating was reduce, the 70 nm reaction layer preventing more species from diffusing. These findings are in agreement with work done by Katzman (2) and Chin and Nunes (14) on  $\text{SiO}_2$  sol-gel coated carbon fibers and magnesium.

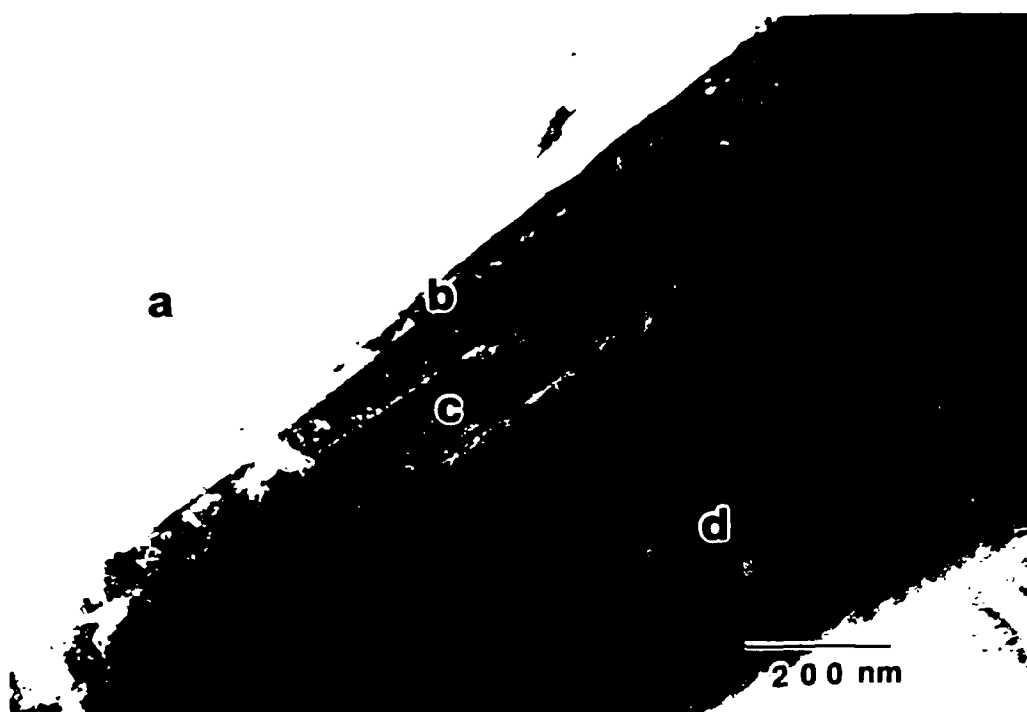


Figure 11. TEM Micrograph of the Fiber-Matrix Interface of a Cast Sample; Fibers Fired at 700°C in a CO Atmosphere after Final Dip; (a) Aluminum, (b) Reaction Layer, (c) Coating, and (d) Carbon Fiber



Figure 12. Diffraction Pattern of (a) PAN 650/42 Carbon Fibers, (b) Coating, (c) Aluminum Matrix in the (211) Zone Axes; Fibers Fired at 700°C in CO after Final Dip

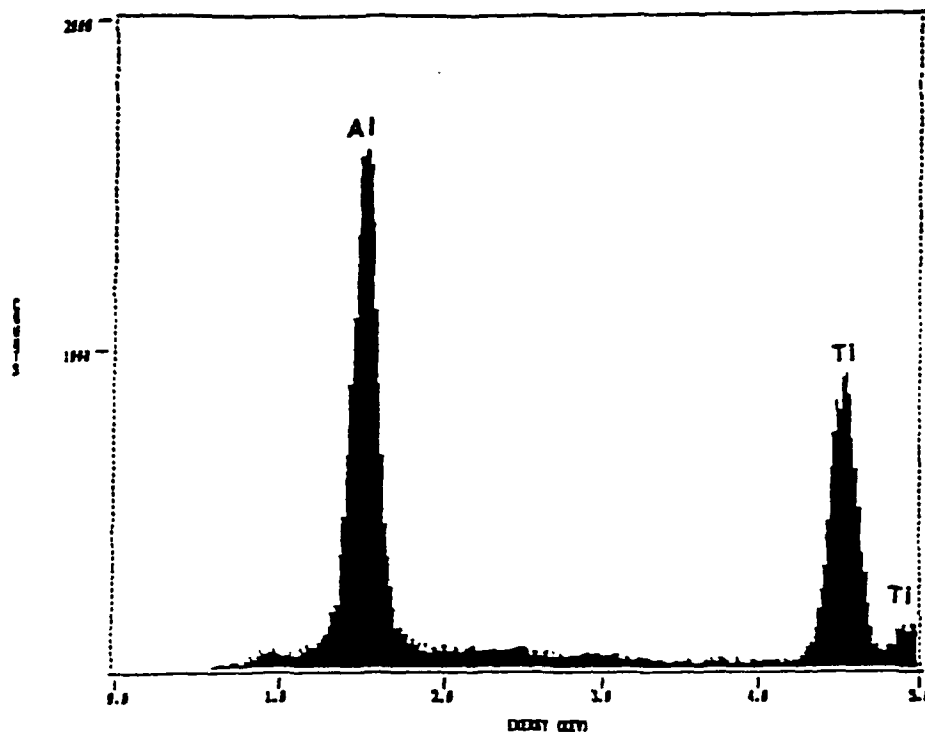


Figure 13. EDX Analysis of the Reaction Layer between Matrix and Coating; Fibers Dipped Three Times in Sol, Using 60°C and 400°C as Intermediate Drying and Firing Temperatures, and Fired at 700°C in CO after Final Dip

#### Conclusions

1. A technique to coat PAN fibers with a crack free, air stable, protective  $\text{TiO}_2$  layer by the sol-gel process has been developed.
2. Coating thickness can be controlled by the TIP concentration and the water content of the sol, the speed of substrate withdrawal, and the number of dips. Coating thickness is also influenced by the substrate geometry, chemistry, and structure.
3. Heat treatments reduce the coating thickness and change the coating structure. After heat treatment at 400°C for 15 min coatings reach their quasi-final thickness and are still amorphous. At temperatures between 400°C and 700°C the coating is transformed into a fine grain polycrystalline anatase layer.
4. 100 nm thick  $\text{TiO}_2$  coatings enhance the wettability of PAN carbon fibers by pure molten aluminum and prevent carbide formation at the interface fiber-matrix even after 9 min in contact with pure molten aluminum.
5. Part of the  $\text{TiO}_2$  coating reacts with aluminum to form an  $\text{Al}_2\text{O}_3$ -Ti layer allowing chemical wetting and acting as a diffusion barrier.

#### Acknowledgment

The support of this work by Aerospatiale (JPC) and the U.S. Air Force Office of Scientific Research, contract F49620-87-C-0017, as part of the University Research Initiative pro-

gram on High Temperature Metal Matrix Composites at Carnegie Mellon University (HJR), is gratefully acknowledged.

### References

1. M. F. Amateau, "Progress in the Development of Graphite Aluminum Composites Using Liquid Infiltration Technology," In. of Composite Materials, 10 (1976), 279-296.
2. H. A. Katzman, "Fibre Coatings for the Fabrication of Graphite-Reinforced Magnesium Composites," In. of Mat. Sci., 22 (1987), 144-148.
3. M. J. Bennett, "Application and Evaluation of Ceramic Coatings Produced by Sol-Gel Technology and Vapor Deposition Procedures," Coating for High Temperature Application, ed. E. Lang (New York: Applied Science, 1983), 169.
4. A. Levitt, E. Di Cesare and S. Wolf, "Fabrication and Properties of Graphite Fiber Reinforced Magnesium," (Report AMMRC TR 71-44, Army Materials and Mechanics Research Center, 1971).
5. J. A. Cornie, A. Mortenson and M. C. Fleming, "Wetting, Fluidity and Solidification in Metal Matrix Composites: a Research Summary," Proc. 6th Int. Conf. Comp. Mat., ed. F. L. Matthews, N. C. Buskell, J. M. Hodgkinson and J. Morton (London: Elsevier Applied Science, 1987), 2.297.
6. J. Cheng and D. Wang, "Structural Transformation of the  $\text{TiO}_2\text{-SiO}_2$  System Gel During Heat Treatment," In. of Non-Cryst. Solids, 100 (1988), 288-291.
7. G. W. Sherer, "Drying Gels II - Film and Flat Plate," In. of Non-Cryst. Solids, 89 (1987), 217.
8. S. P. Mukherjee, "Inorganic Oxide Gels and Gel-Monoliths: Their Crystallization Behavior," Emergent Process Methods for High-Technology Ceramics, ed. R. F. Davis, H. Palmer and R. L. Porter (New York: Plenum Press, 1984), 95.
9. D. R. Stull and H. Prophet, JANAF Thermochemical Tables, 2nd. Ed. (Washington: Nat'l Bureau of Standards, 1972).
10. E. M. Levin, H. F. McMurdie and F. P. Hall, Phase Diagrams for Ceramists, The American Ceramic Society, 1956.
11. H. Schroeder, "Oxide Layers Deposited from Organic Solutions," Phys. of Thin Films, 5 (1969), 87.
12. B. E. Yoldas, "Deposition and Properties of Optical Oxide Coatings from Polymerized Solutions," Applied Optic, 21 (1982), 2960.
13. H. H. An and T. Luhman, "Sol-Gel Coating Concepts for High Temperature Aluminum Matrix," Dispersion Strengthened Aluminum Alloys, eds. Y. W. Kim and W. M. Griffith (Warrendale, PA: The Metallurgical Society, 1988), 709.
14. E. C. Chin and J. Nunes, "Alloying Effects in Graphite-Magnesium Composites" (Paper presented at 117th AIME Annual Meeting, Phoenix, AZ, 26 January, 1988).

## SURFACE MODIFICATION OF SiC WHISKERS

K. T. Wu, H. G. Spencer  
Department of Chemistry  
and  
H.J. Rack  
Department of Mechanical Engineering  
Clemson University  
Clemson, South Carolina 29634

Introduction

The development of high temperature, high performance discontinuously reinforced metal and ceramic matrix composites has often been limited by reinforcement-matrix interactions. For example, attempts to utilize SiC to enhance the elevated temperature properties of titanium alloys has met with limited success, principally because of thermochemical instability, that is SiC and Ti react to form the more stable compounds TiC and  $Ti_5Si_3$  [1-5].

Recently Clement et al. [6,7] have demonstrated that thin, continuous, nano-crystalline,  $TiO_2$  coatings can mitigate such reactions, at least for continuous graphite reinforced aluminum. This development raises the possibility of achieving control of the interfacial properties of discontinuously reinforced metal and ceramic matrix composites. The research reported in this study has examined this potential by utilizing the procedure outlined by the latter authors to modify the surface chemistry of SiC whiskers.

Experimental Procedure

Materials. The silicon carbide whiskers, SiC<sub>w</sub>, utilized in this investigation were supplied by American Matrix, Inc., Knoxville, Tenn. Figure 1 shows that they were generally irregularly shaped rods with most having diameters less 1  $\mu m$  and lengths of approximately 20  $\mu m$ . Titanium isopropoxide (TIP) was obtained from Aldrich and the isopropanol from Fisher; all contained less than 0.015%  $H_2O$  as determined by Karl Fisher titration [8]. Finally, the hydrochloric (HCl) acid was reagent grade containing 3.5 moles of  $H_2O$  per mole HCl.

Coating Procedure. Initially, the whiskers were alternately ultrasonically washed in  $H_2O$  and isopropanol. Following drying, the SiC whiskers were either (a) heated in air for 30 min. at 383 K, (b) heated in air for 30 min. at 523 K, (c) washed in concentrated  $HNO_3$  for 30 min. at 353 K, followed by drying for 30 min. at 523 K, or (d) heated in air for 2 hours at 873 K.

Two metal alkoxide solutions in isopropanol were examined. One contained 0.1 M TIP, 0.1 M  $H_2O$  and 0.008 M HCl, while the other contained 0.5 M TIP, 0.5 M  $H_2O$ , and 0.008 M HCl, that is the  $H_2O/TIP$  ratio was kept constant while the TIP concentration was increased. Coating was accomplished by placing a sample of the washed SiC whiskers in the sol, gently stirring, decanting and drying. This latter step was accomplished at 333 K in a saturated  $H_2O$  atmosphere for 1 hr. and was followed by firing at 673 K for 15 min. Finally, coating thickness control was achieved by simply repeating the above procedure, eliminating the pre-wash.

Monitoring. The development of the  $TiO_2$  coating was monitored by (a) measurements of the streaming potential [9] and (b) scanning electron microscopy. Streaming potential measurements, as illustrated schematically in Figure 2, involved potential measurement of a SiC<sub>w</sub> sample placed on a fritted glass filter sealed in a glass tube as a function of the flow velocity and pH of a 0.001 M KCl solution. Silver/silver chloride electrodes placed on both sides of the sample were utilized in concert with a high impedance voltmeter to determine the potential. The pH of the solution was adjusted through the addition of HCl or KOH, the ionic strength of the solution being maintained at 0.001 M. While the magnitude of the streaming potential was a function of the SiC<sub>w</sub> packing density, the isoelectric point, that is the pH at which the change in the streaming potential with velocity,  $\partial E/\partial V$ , is zero, was independent of this parameter and could be used as a measure of the extent of coating.

Results

Figure 3 shows representative data illustrating the dependence of the streaming potential on velocity at a constant pH. In general the streaming potential was a linear function of velocity. These data have, together with that obtained for



uncoated, but washed whiskers, been replotted in Figure 4 to determine the isoelectric point. Clearly, the isoelectric point has been shifted by exposure to the sol coating process.

The isoelectric point measurements have been summarized in Table 1. These results indicate that whisker pre-treatment has a small, but measurable effect on the uncoated whisker surface. Comparison of these isoelectric points with those previously reported for SiC and SiO<sub>2</sub> [10] suggest that this effect is related to the formation of a SiO<sub>2</sub> film on the whisker surface. Repeated exposure of the SiC whiskers to the coating procedure resulted in a gradual increase in the isoelectric point, until the isoelectric point of TiO<sub>2</sub>, 4.4, is reached\*\*. Although complete coverage is indicated for pretreatments C and D after three cycles, additional cycles of these whiskers produced a slightly lower isoelectric point which may indicate development of coating defects, perhaps by the mechanical or thermal treatments involved. The number of cycles required to achieve this isoelectric point depended upon the TIP concentration, compare D and D\*, increasing TIP concentration decreasing the number of required cycles. Unfortunately, the effect of whisker pre-treatment on the number of cycles required for coating is not as clear, although the data do suggest that the more severely oxidized pre-treatments decrease the number of cycles required.

TABLE 1

Isoelectric Points of Silicon Carbide Whiskers Coated with Acidified Solutions of Titanium Isopropoxide

Number of Cycles	A	B	Pretreatments C	D	D*
0	2.6	2.8	2.9	2.8	2.8
1	3.2	3.4	3.3	3.5	3.9
2	3.5	3.7	4.0	4.0	4.2
3	3.9	4.0	4.4	4.4	-
4	4.0	4.1	4.1	4.2	-
5	4.1	4.1	4.1	4.2	-

(A) Heated at 383K, coated with 0.1 M TIP.

(B) Heated at 523K, coated with 0.1 M TIP.

(C) Treated with concentrated HNO<sub>3</sub>, coated with 0.1 M TIP.

(D) Heated at 873K, coated with 0.1 M TIP.

(D\*) Heated at 873K, coated with 0.5 M TIP.

Figure 5 illustrates the morphological differences observed after whisker coating with 0.1 M and 0.5 M TIP. In both instances, energy dispersive analysis indicates the presence of a TiO<sub>2</sub> coating on the whisker surface. Detailed examination shows that the coating achieved with the lower concentration contains a smaller number of distinct TiO<sub>2</sub> particles.

#### Discussion

This study has demonstrated the feasibility of altering the surface chemistry of short fiber, SiC whisker reinforcements, through sol-gel coating. Further, it has also shown that the uniformity of the coating depends upon the prior sol chemistry, dilute solutions leading to more uniform, particle free coatings. These observations suggest that the coatings grain or crystallite size may be controllable through selection of the sol degree of polymerization, or more directly, the polymer chain length, prior to coating. Certainly the presence of large discrete particles can be avoided by using dilute, acid catalyzed sols.

Historically, dilute sol concentrations have been avoided, most investigators having emphasized the use of concentrated solutions where greater coating thickness' can be achieved with fewer steps. However, when coating uniformity

\*\*The isoelectric point of TiO<sub>2</sub> was established by measurements utilizing TiO<sub>2</sub> precipitated from the sol coating solution.

and the absence of "pinholes" are essential, as, for example, when long time high temperature compatibility is desired coating thickness increases appear to be best achieved by repeated application of thin layers, rather than application of single thick layer.

#### Acknowledgments

The authors wish to acknowledge the financial support of the Clemson University Center for Advanced Manufacturing and the U.S. Air Force Office of Scientific Research, contract F49620-87-0017, as part of the University Research Initiative program on High Temperature Metal Matrix Composites at Carnegie-Mellon University.

#### References

1. H. J. Dudek, R. Leucht and G. Ziegler, in *Titanium Science and Technology*, edited by G. Lutering, U. Zwick and W. Bunk (Deutsche Gesellschaft für Metallkunde, Munich, FRG, 1985) p. 1773.
2. T. E. Steelman, R. H. Lorenz, G. R. Martin and R. P. Robelotto, in *Silicon Carbide/Titanium Material and Process Fundamentals*, AFWAL-TR-82-4036, May, 1982.
3. C. G. Rhodes and R. A. Spurling, in *Recent Advances in Composites in the United States and Japan*, edited by R. Vinson and M. Taya, ASTM STP 864 (ASTM, Philadelphia, Pa., 1985) p. 585.
4. E. P. Zironi and H. Poppa, *J. of Mater. Sci.*, 16(1981)3115.
5. H. J. Dudek, L. A. Larsen and R. Browning, *Surface and Interface Analysis*, 6(1984)274.
6. J. P. Clement and H. J. Rack, in *Proceedings of the Symposium on High Temperature Composites*, Dayton, Ohio, June, 1989 (Am. Soc. of Comp. Mats, Dayton, Ohio) in press.
7. J. P. Clement, K. T. Wu, H. G. Spencer and H. J. Rack, *Materials and Manufacturing Processes*, in press.
8. J. Mitchell and D. M. Smith, in *Aquamestry*, 2nd, Ed., Interscience, New York, 1977.
9. P.C. Hiemenz, in *Principles of Colloid and Surface Chemistry*, Marcel Dekker, New York, 1986.
10. M.J. Crimp, R.E. Johnson, Jr., J.W. Halloran and D.L. Feke, in *Science of Ceramic Chemical Processing*, edited by L.L. Hench and D.R. Ulrich, Wiley, New York, 1986.

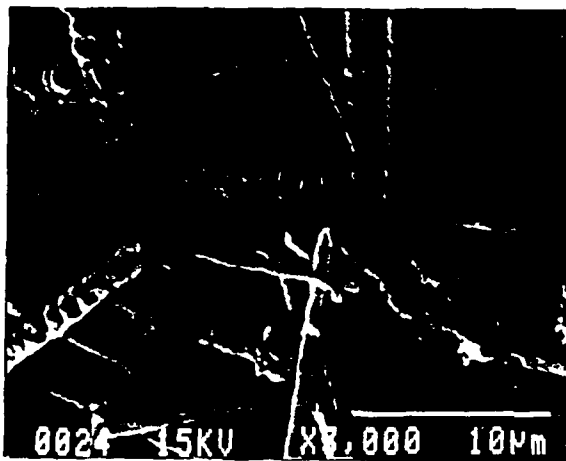


FIG. 1. Scanning electron micrograph of washed, uncoated SiC whiskers.

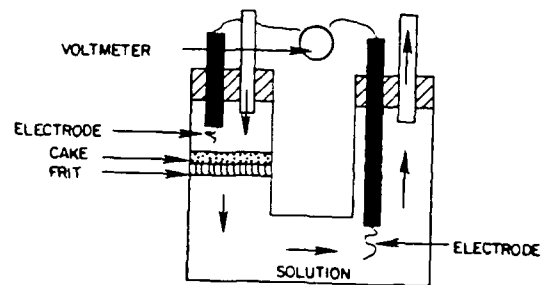


FIG. 2. Schematic diagram illustrating streaming potential methodology.

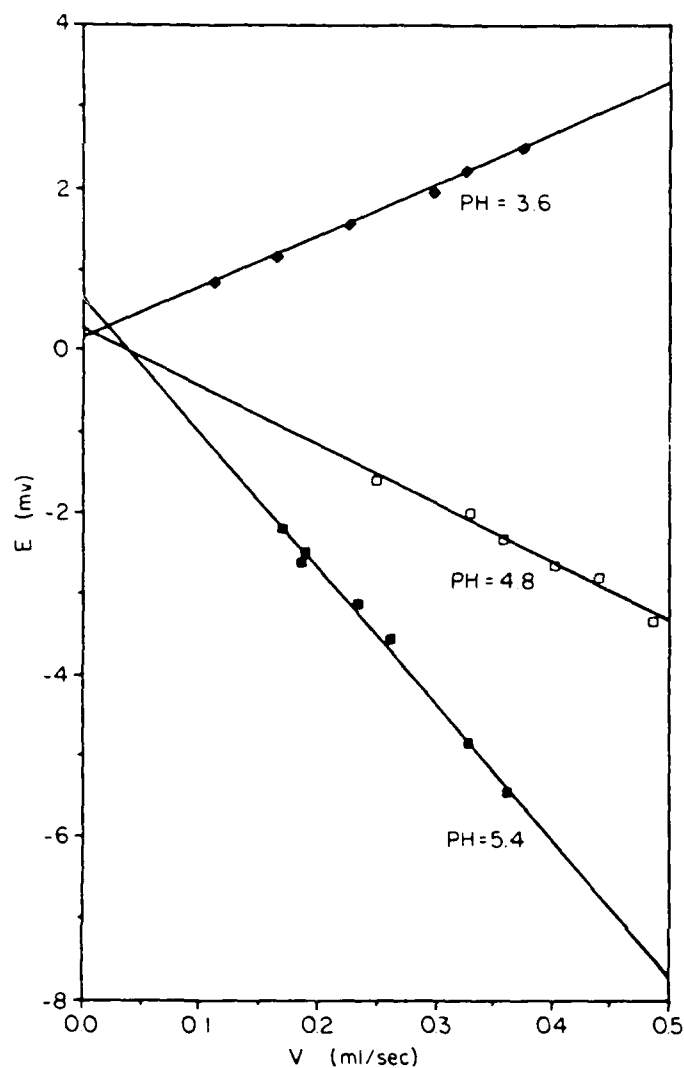


FIG. 3. Streaming potential as a function of velocity and pH for SiC whiskers heated at 873 K and coated utilizing 0.1 M TIP (4 cycles).

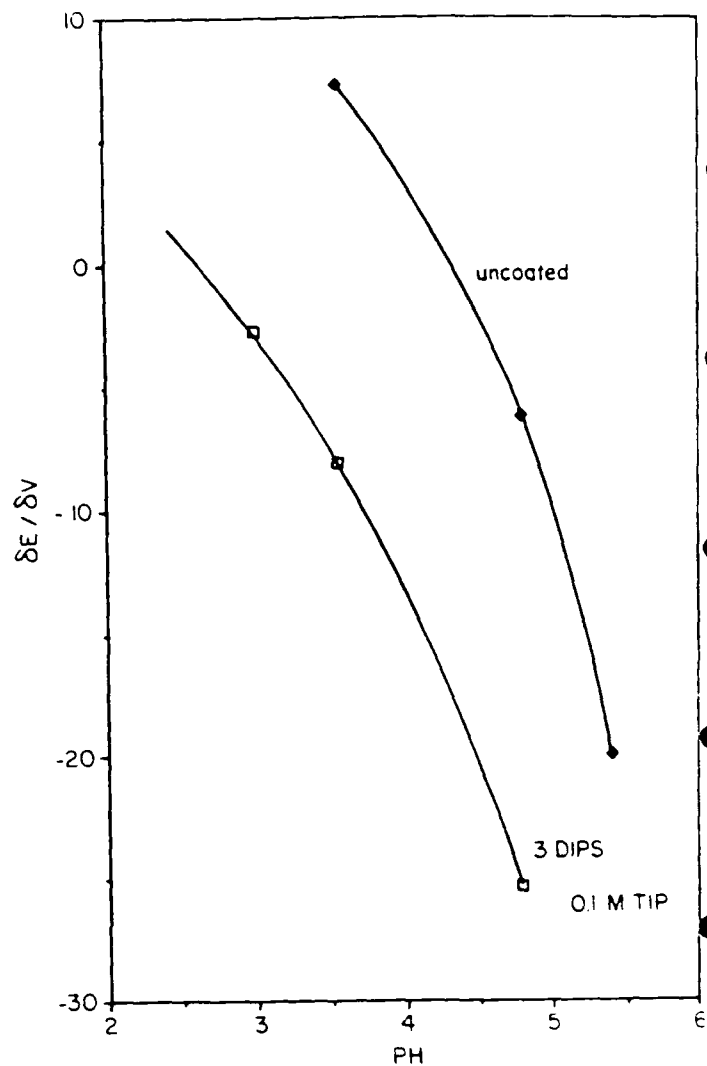


FIG. 4. Differential of streaming potential with velocity as a function of pH for uncoated and coated SiC whiskers.

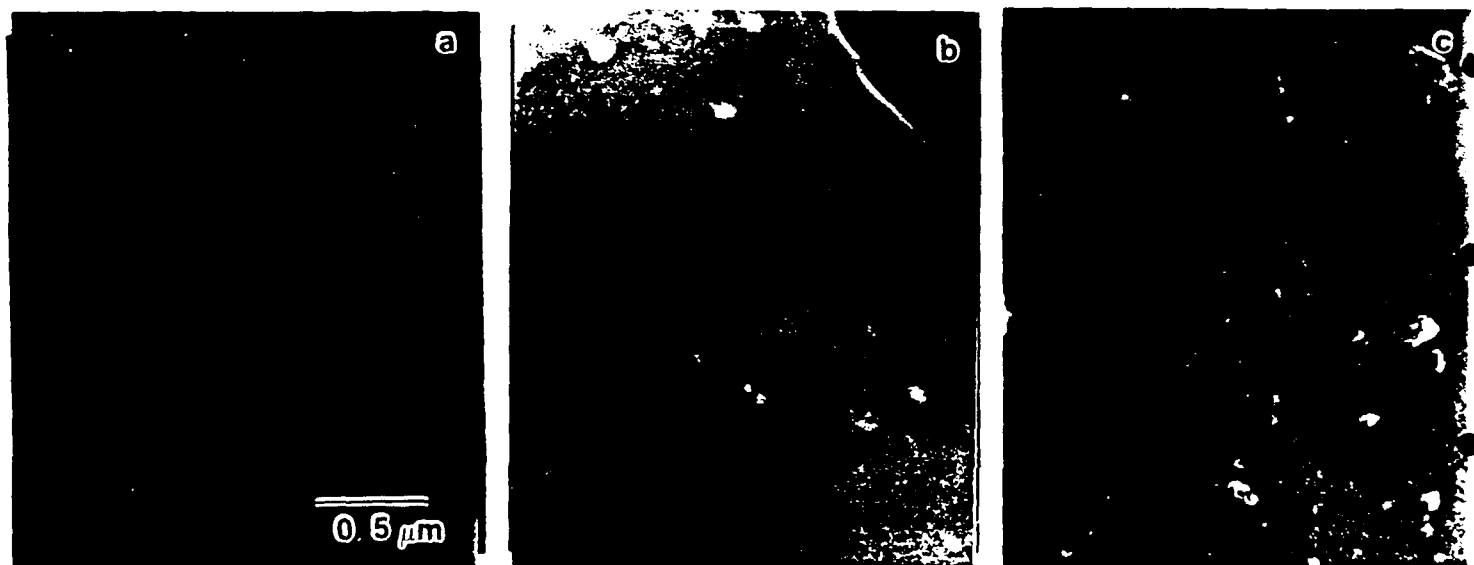


FIG. 5. Scanning electron micrographs of SiC whiskers (a) uncoated, (b) coated: 0.1 M TIP (3 cycles) and (c) coated: 0.5 M TIP (2 cycles).

### SUB-TASK 3

#### MATRIX PRECIPITATION AND COARSENING

H. J. Rack, P. Chaudhury, E. Wachtel and J. Wung

This sub-task examined the matrix precipitation and coarsening behavior of discontinuously reinforced metal matrix composites that are candidates for high temperature application. The study included TiC reinforced IN 718 and SiC particulate reinforced Mg-6 Zn.

Based on this effort the following appended manuscripts have either been submitted, accepted or published:

Submitted:

P. K. Chaudhury, H. J. Rack and B. A. Mikucki, "Effect of Double Aging on Mechanical Properties of Mg-6Zn Reinforced with SiC Particulates", Jn. of Materials Science, submitted September, 1989.

Accepted:

E. F. Wachtel and H. J. Rack, "Phase Stability and Aging Response of TiC Reinforced Alloy 718", Superalloy 718 - Metallurgy and Applications, The Minerals, Metals and Materials Society, Warrendale, PA., 1989, in press.

Published:

P. Chaudhury and H. J. Rack, "Age Hardening of SiC Reinforced Mg-6Zn", Light-Weight Alloys for Aerospace Applications, E. W. Lee, E. H. Chia and N. J. Kim, eds., The Minerals, Metals and Materials Society, Warrendale, PA., 1989, pp. 345-357.

The cooperation and assistance of DWA Associates, Chatsworth, Cal., who supplied the TiC reinforced In 718, and the Dow Chemical Corporation, Lake Jackson, Texas, who supplied the SiC particulate reinforced Mg-6 Zn is greatly acknowledged. Finally, this effort is continuing under the sponsorship of the Wyman-Gordon Corporation as part of the high temperature plasticity study.

## AGE HARDENING OF CAST SiC REINFORCED Mg-6Zn

H. J. Rack and P. K. Chaudhury

Materials Engineering Activity  
Department of Mechanical Engineering  
Clemson University  
Clemson, South Carolina 29634-0921

## ABSTRACT

This study has considered the age hardening behavior of cast and extruded Mg-6Zn reinforced with 20 volume percent 1000 grit SiC particulate. It has been shown that the age hardening sequence in this reinforced alloy is similar to that observed in unreinforced Mg-Zn alloys, with little influence of the reinforcement. This lack of sensitivity has been related to the absence of a SiC<sub>p</sub>/matrix associated dislocation substructure, in agreement with other studies and comparisons between cast and powder metallurgy based discontinuously reinforced metal matrix composites.

## Introduction

Several studies have recently examined the age hardening behavior of discontinuously reinforced aluminum metal matrix composites (1-10). Most results, obtained largely through examinations of powder processed composites, indicate that the aging response of aluminum metal matrix composites is normally accelerated when compared to the unreinforced matrix. While the aluminum matrix precipitation sequence does not appear to be altered by the reinforcement, the aging temperatures and times associated with the presence of any precipitate phase, for example, GP zones in 6061, may be drastically altered (3, 8).

Other investigations of ingot processed aluminum matrix composites indicate that, in these materials, there may be little, if any, enhancement in the aging response. Indeed, the results of Friend and Luxton (10) suggest that the addition of a discontinuous reinforcement to an ingot alloy may actually have a detrimental effect on the maximum achievable hardness and strength.

To date little information has been reported on the general applicability of these observations to other age hardenable discontinuously reinforced composite systems, for example Mg and Ni alloys. The current study has considered this question for one system, SiC particulate reinforced Mg-Zn alloys.

## Experimental Procedure

The study reported herein considers the age hardening response of ingot processed, 20 volume percent, SiC<sub>p</sub> reinforced Mg-Zn. Extruded bar, 2.5 inch diameter, having a composition, Mg-6Zn-0.3Ca, was provided by the Dow Chemical Corporation, Lake Jackson, Texas. This bar had been extruded from a 7 inch diameter by 25 inch length casting, the latter having been prepared by Dow utilizing 1000 grit SiC particulate, nominally 8-10  $\mu$ m diameter, containing approximately 1% free carbon (11,12).

The aging kinetics of the Mg-Zn composite were monitored through Rockwell B hardness and eddy current measurements, the latter utilizing a Verimet monitor. All samples were initially solution treated at 330°C for 1 hour in a protective atmosphere of flowing argon and water quenched. Following water quenching, the samples were immediately aged at temperatures between 75 and 200°C, for times up to 2500 hours. Individual samples were then air cooled and metallographically polished through 600 grit SiC abrasive prior to hardness and eddy current testing.

Finally, selected aged conditions were examined utilizing transmission electron microscopy. Foil preparation included diamond sectioning, hand grinding to approximately 0.1 mm., dimple grinding and ultimately argon ion milling at 5 kv, 0.3 ma and 15° impingement angle.

## Results

Figure 1 summarizes the results of the hardness and eddy current measurements. Aging of SiC<sub>p</sub> reinforced Mg-6 Zn clearly involves a number of discrete steps. At short times, and/or low aging temperatures, a number of small, but discernible and reproducible, hardness peaks were observed. For example, at 75°C these peaks occur at approximately 1, 8, and 128 hours. These hardness peaks were not accompanied by noticeable changes in electrical conductivity.

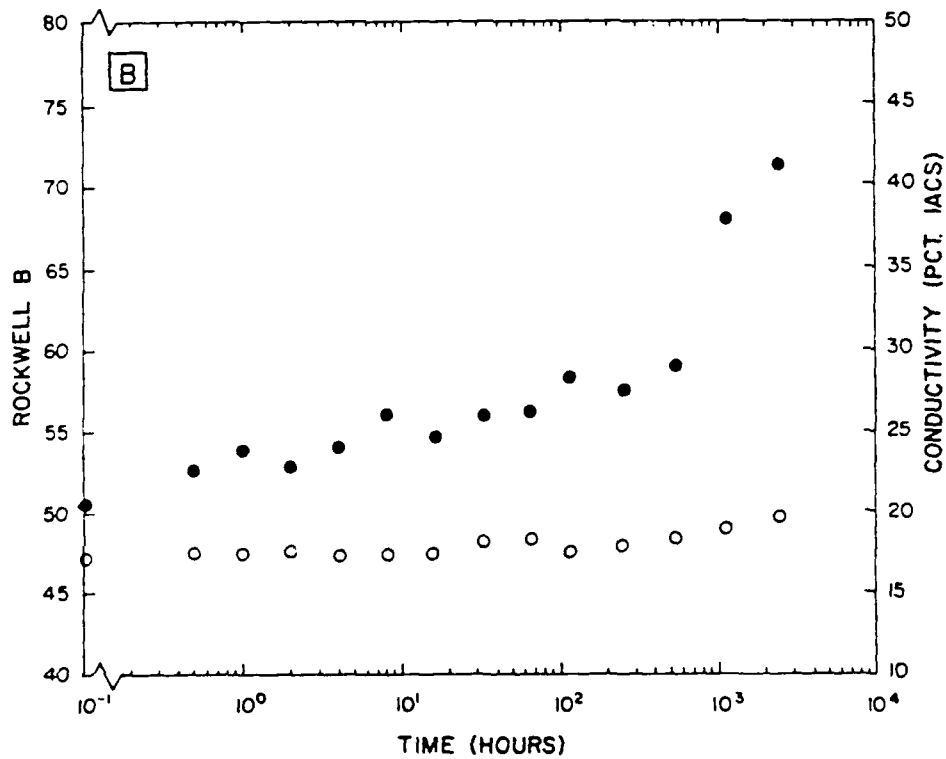
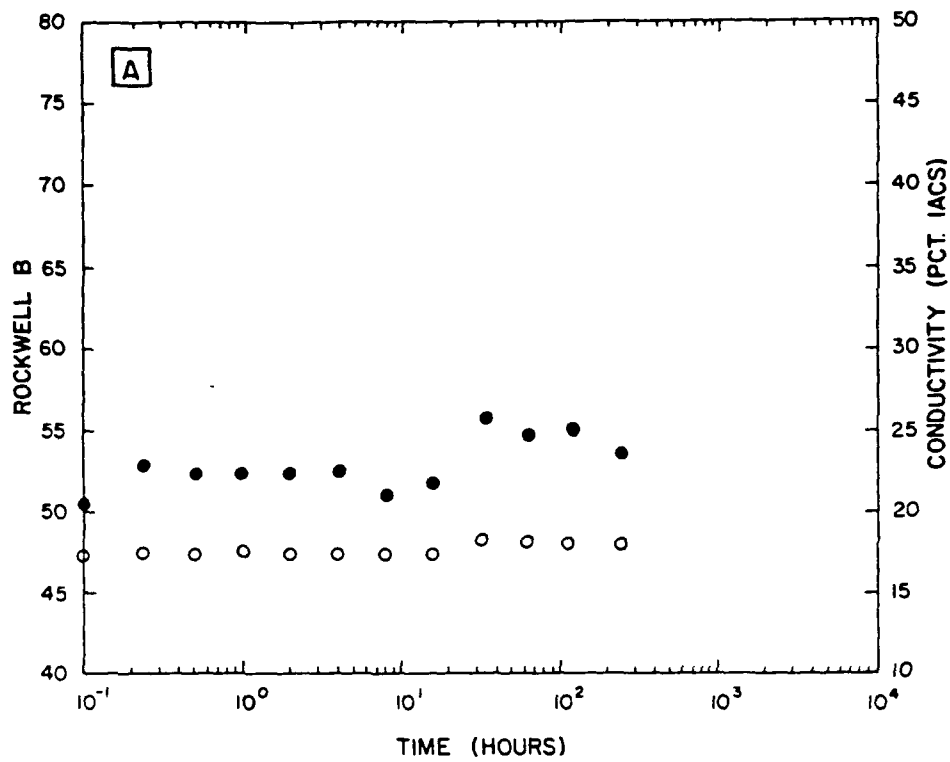


Figure 1: Isothermal aging kinetics of Mg-6Zn reinforced with 20 volume percent SiC<sub>p</sub>, solution treated at 330°C, 1 hour, water quenched and aged at (a) 25°C, (b) 75°C, (c) 100°C, (d) 125°C, (e) 150°C, (f) 175°C and (g) 200°C.

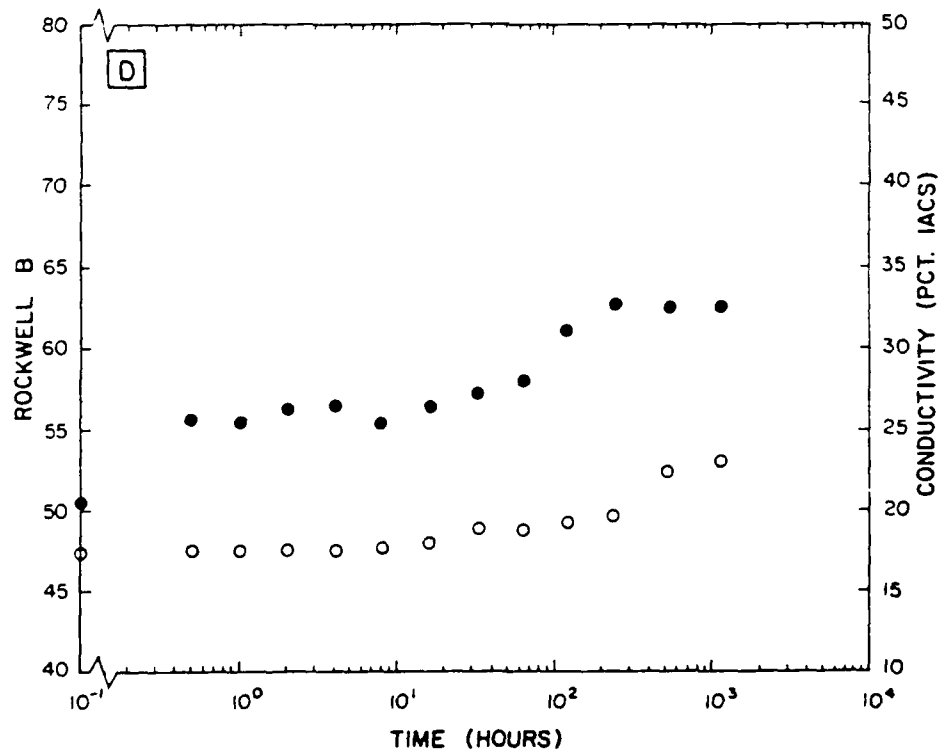
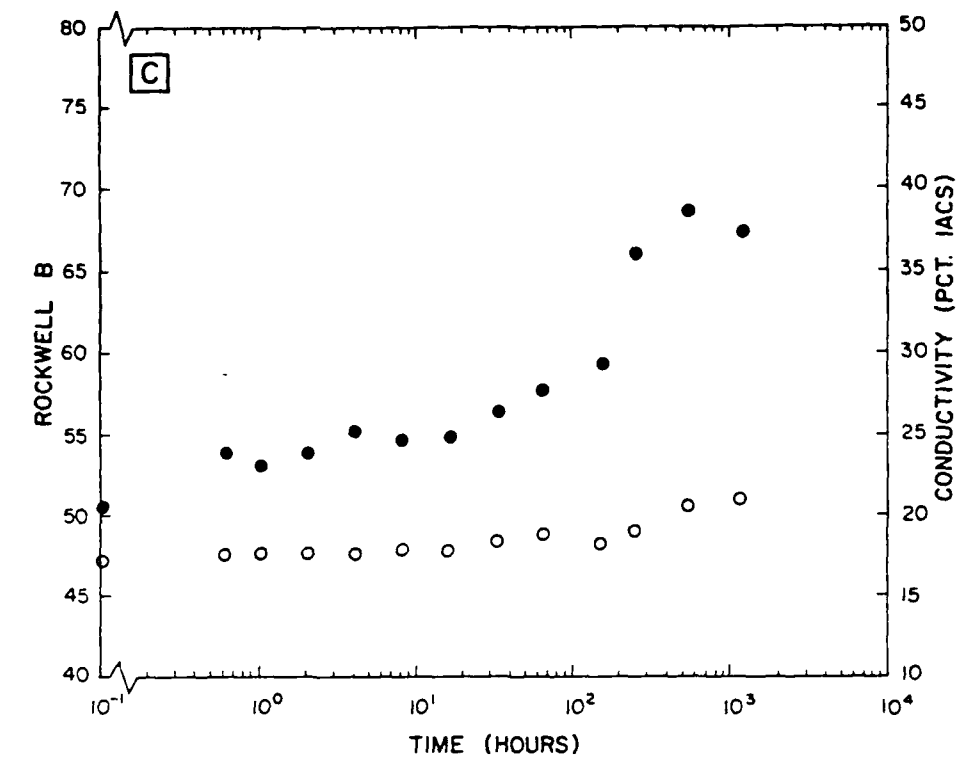


Figure 1: Continued.



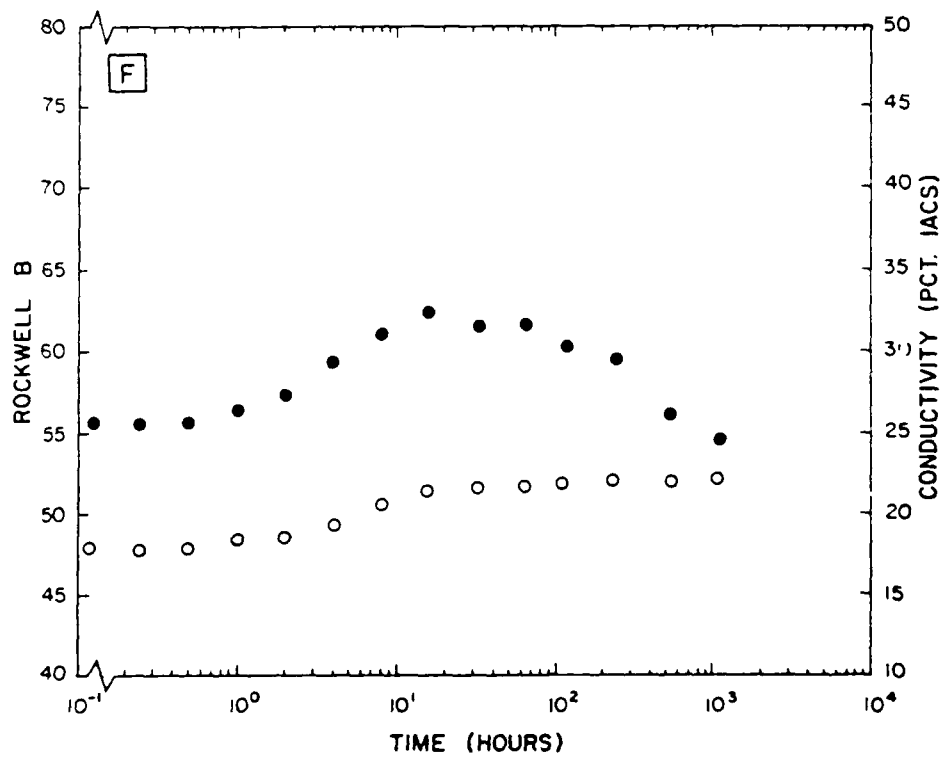
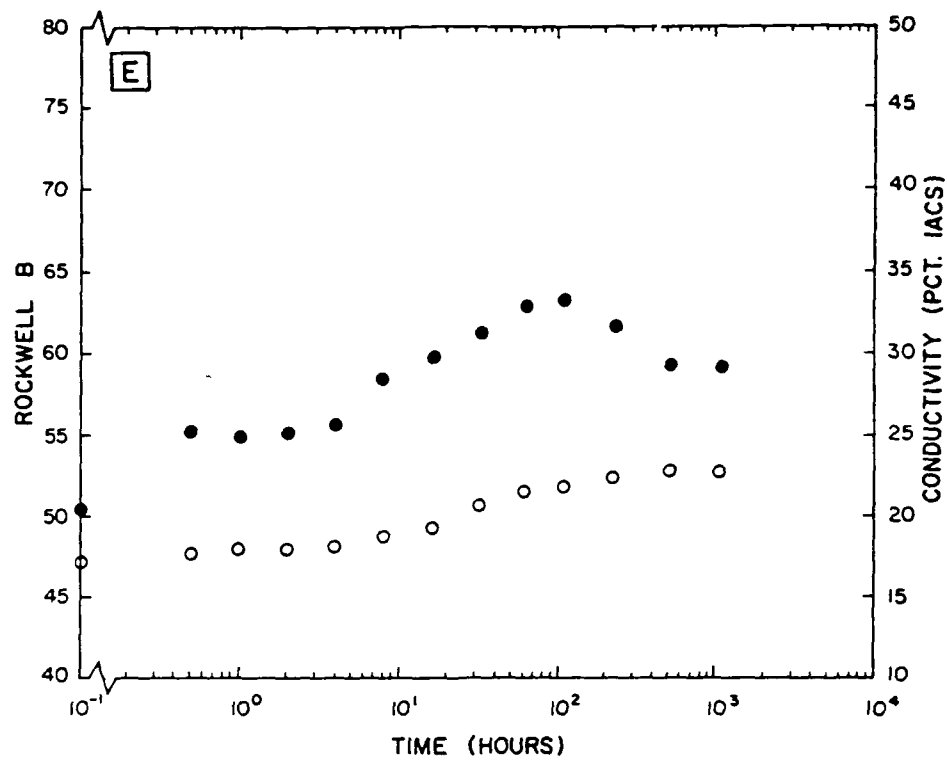


Figure 1: Continued.

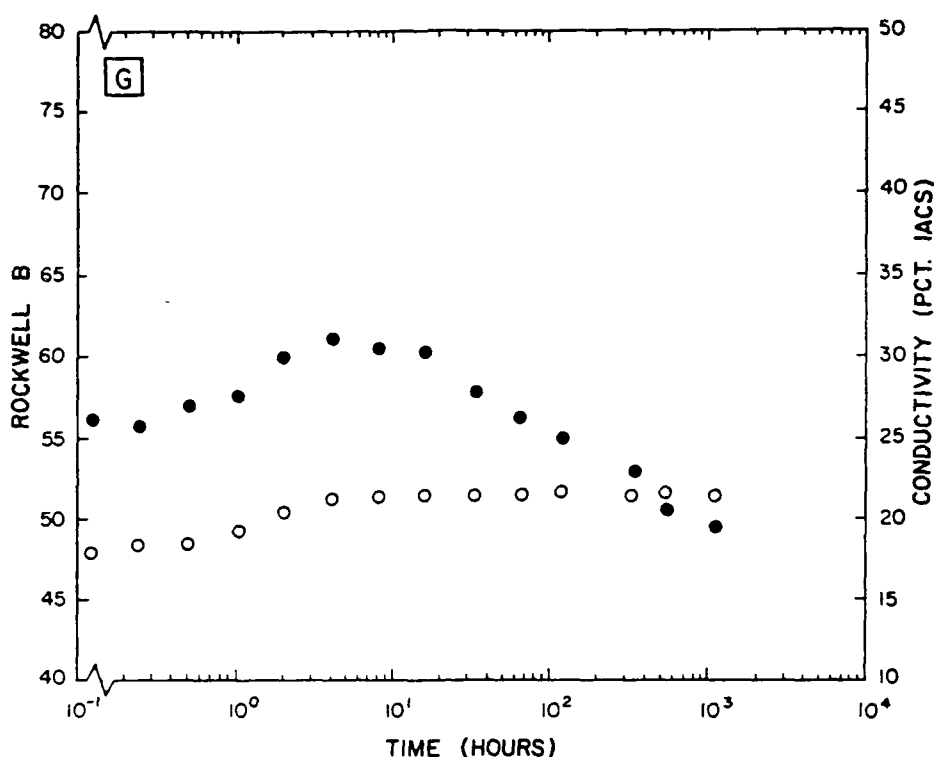


Figure 1: Continued.

At longer times, and/or higher temperatures, a marked increase in hardness was observed. This hardness increase appears to be typical of many age hardening systems where under, peak and overaging is observed. The time required to reach maximum hardness, and the maximum hardness observed, both decreased with increasing aging temperature in  $\text{SiC}_p$  reinforced Mg-6Zn. This hardness increase was, in addition, accompanied by an increase in the electrical conductivity, a constant electrical conductivity level being associated with overaging.

Transmission electron microscopy indicated that the primary precipitation hardening reaction in  $\text{SiC}_p$  reinforced Mg-6Zn involved the formation of rod shaped  $\beta'$  and  $\beta$  MgZn precipitates. Initial aging under conditions where both a hardness and electrical conductivity change was observed, Figure 2(a), resulted in the formation of fine, relatively short rods, which subsequently grew during continued exposure at temperature, Figure 2(b). Comparison of the latter with Figure 3, an electron micrograph of a sample aged 2500 hours at 75°C, showed that the higher peak hardness observed at the lower aging temperature was associated with a finer and more closely spaced precipitate structure. Little evidence for heterogeneous precipitation of  $\beta$  MgZn was observed in overaged conditions, overaging having resulted from growth of  $\beta'$  and formation of  $\beta$ . These observations are in excellent agreement with previous studies of unreinforced Mg-6 Zn (14).

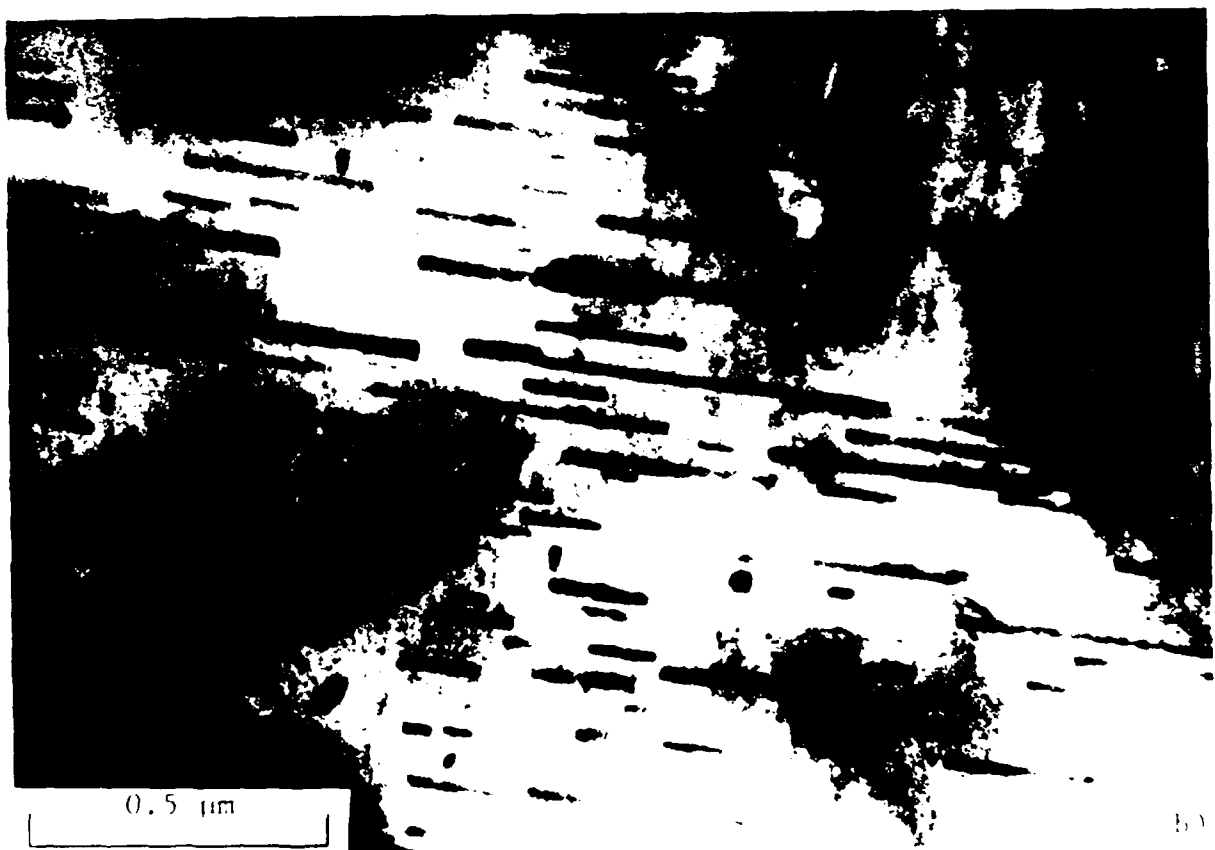
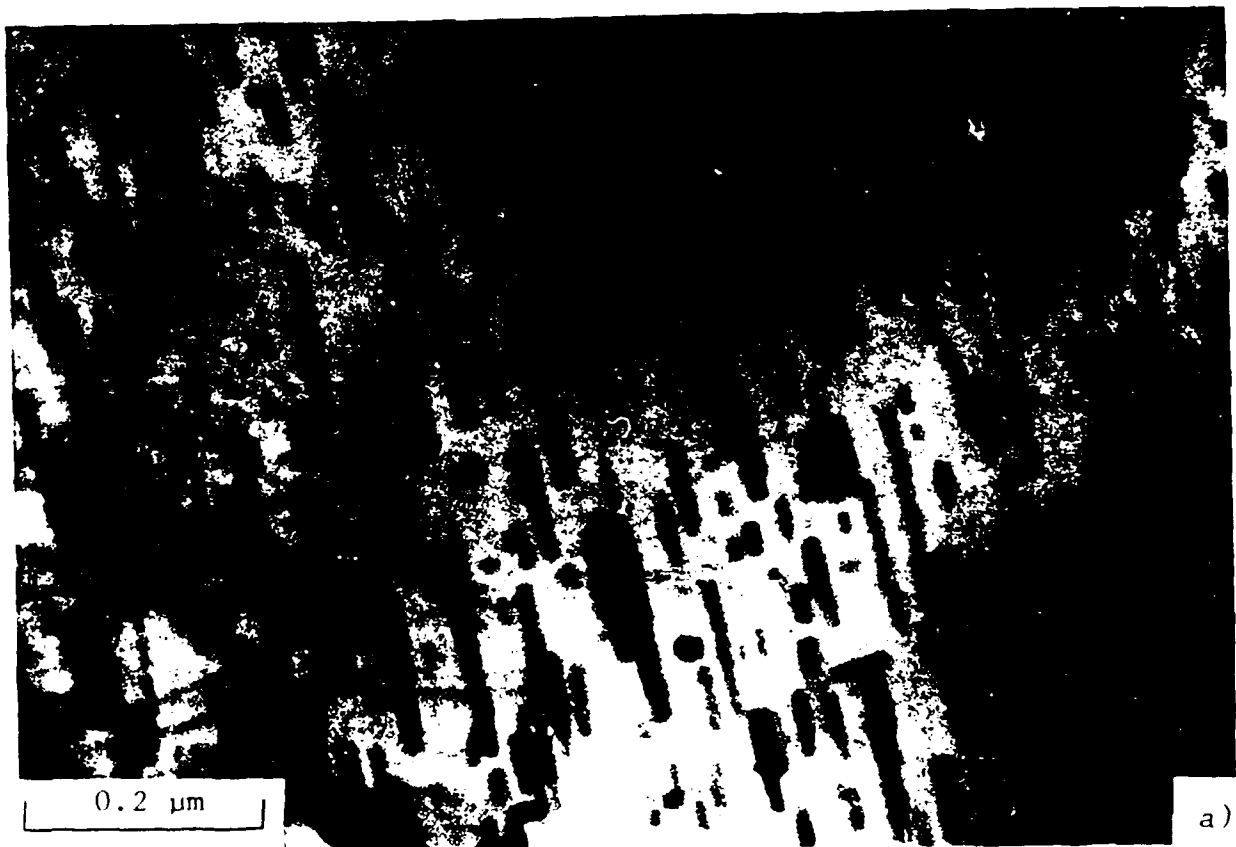


Figure 2: Transmission electron micrographs of Mg-cEn reinforced with 20 volume percent  $\text{SiO}_2$ . (a) before treatment at  $100^\circ\text{C}$ , 1 hour, water quen, and aged at  $170^\circ\text{C}$  for 1, 2, 4 hours, and (b) 128 hours.

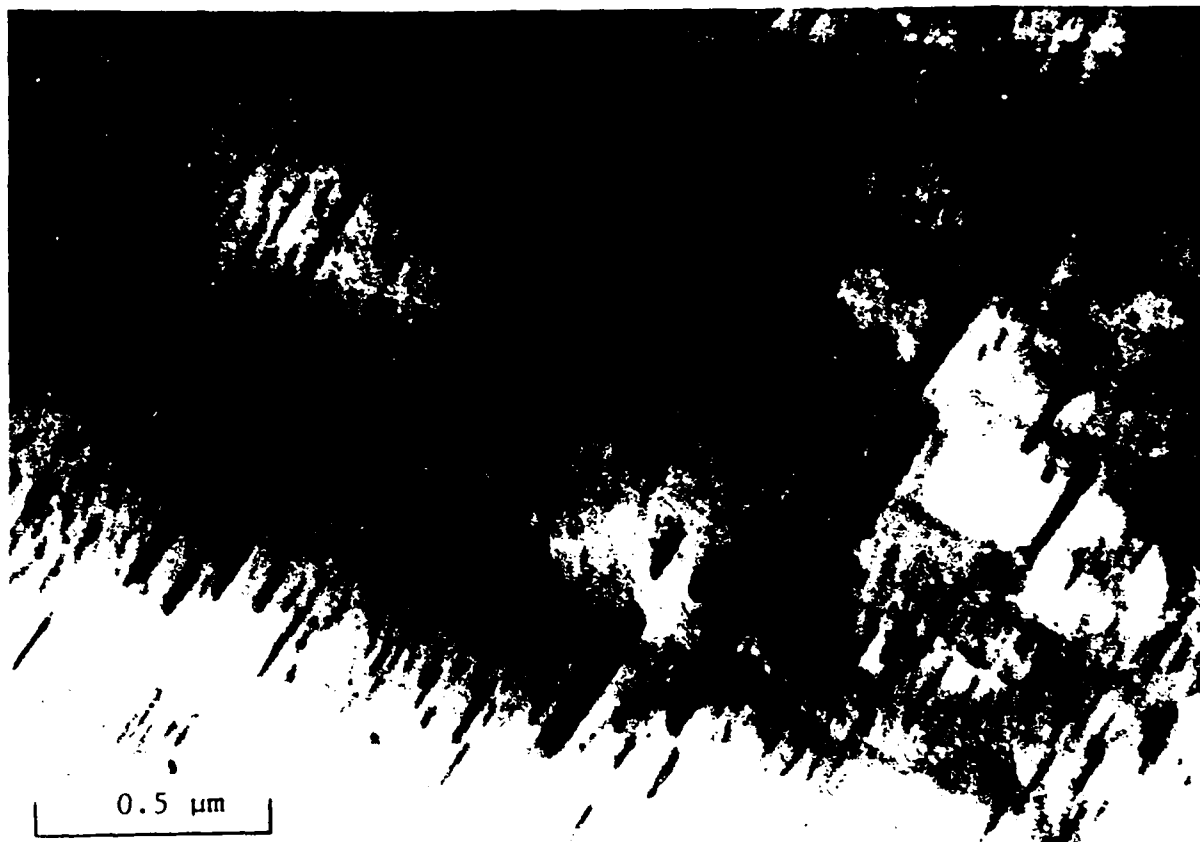


Figure 3: Transmission electron micrograph of Mg-6Zn reinforced with 20 volume percent  $\text{SiC}_p$ , solution treated at  $330^\circ\text{C}$ , 1 hour, water quenched and aged at  $75^\circ\text{C}$  for 2500 hours.

Detailed examination of  $\text{SiC}_p$  interfaces also indicated that they were relatively free of precipitates, and that there did not appear to be an extensive  $\text{SiC}_p$  associated dislocation network, as has previously been reported in P/M  $\text{SiC}$  aluminum composites, Figure 4. Finally, additional characterization showed that precipitate free zones (PFZ's) were present at many  $\text{SiC}/\text{matrix}$  and grain boundaries, Figure 5.

#### Discussion

While direct comparison with an unreinforced Mg-6Zn alloy processed in a manner identical to that of the reinforced composites considered in this study is not possible, comparison of the current results with previous examinations of the age hardening behavior of binary Mg-Zn alloys (13-21) suggests that the aging sequence in the reinforced alloy is similar to that observed in unreinforced compositions, i.e.,

supersaturated solid solution  $\rightarrow$  GP zones  $\rightarrow \beta' \rightarrow \beta$  (MgZn).

This conclusion is reinforced if it is assumed that precipitate formation and growth is a thermally activated process, i.e.,

$$\frac{\delta \ln t}{\delta (1/T)} = \frac{Q}{R}$$

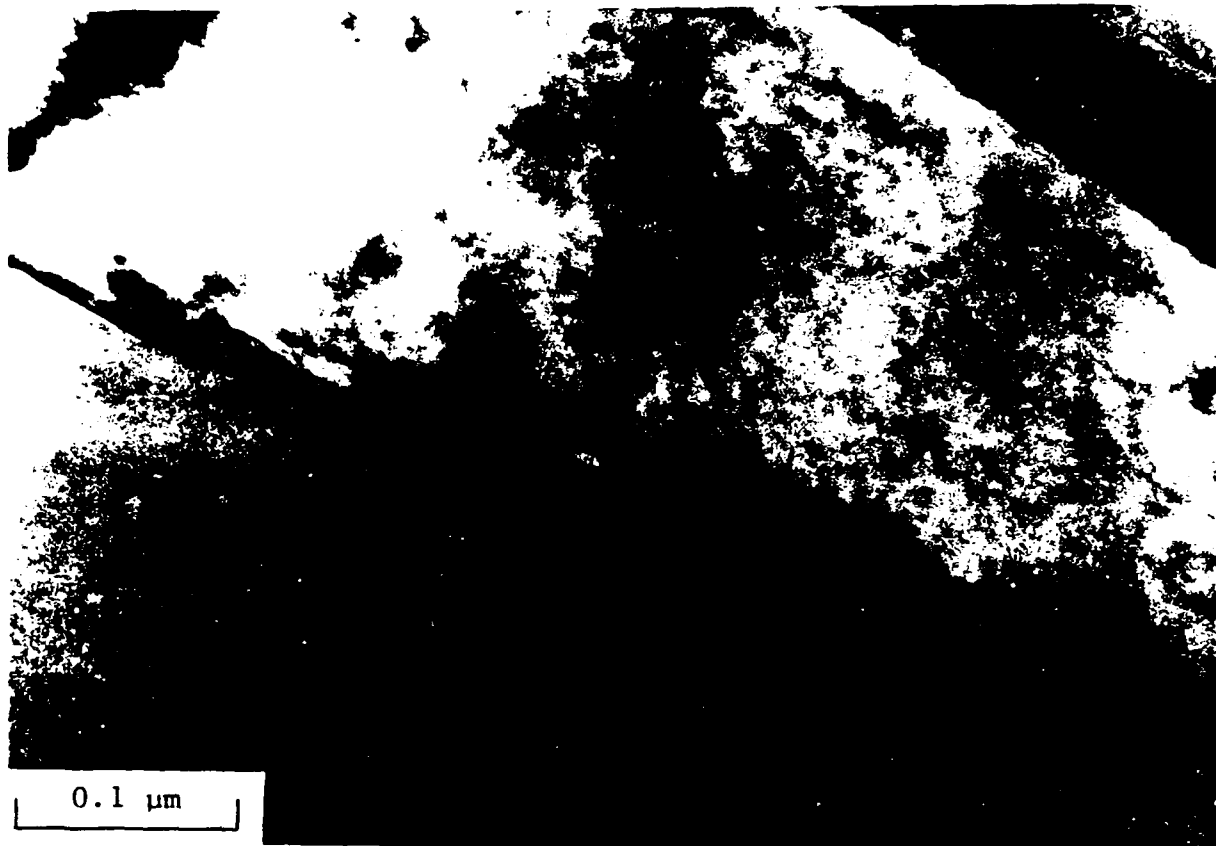


Figure 4: Transmission electron micrograph of  $\text{SiC}_p$ /matrix interface in Mg-6Zn reinforced with 20 volume percent  $\text{SiC}_p$ , solution treated at  $330^\circ\text{C}$ , 1 hour, water quenched and aged at  $150^\circ\text{C}$  for 128 hours.

where  $t$  is the aging time required for a fixed amount of precipitation,  $T$  is the artificial aging temperature in  $^\circ\text{K}$ , and  $Q$  is the activation energy for atomic migration. Figure 6 shows a plot of  $\log t$  versus  $1/T$ , where  $t$  represents either the time for the initial increase in the electrical conductivity or the time required to achieve maximum hardness. Precipitation in  $\text{SiC}_p$  reinforced Mg-6Zn, as in binary unreinforced alloys, cannot be described, over the entire range of artificial aging temperatures considered in this study, by a single activated process. Further, values of  $Q$  derived from Figure 6, and shown in Table 1, are in good agreement with those previously reported for binary Mg-Zn alloys (16, 18, 19).

Table 1: Activation Energies for  $\text{SiC}_p$  Mg-6Zn

Aging Temperature( $^\circ\text{C}$ )	Method	$Q(\text{kcal/mole})$
150 - 200	Hardness	33.1
100 - 150		8.6
100 - 200	Eddy Current	24.2
75 - 100		8.6

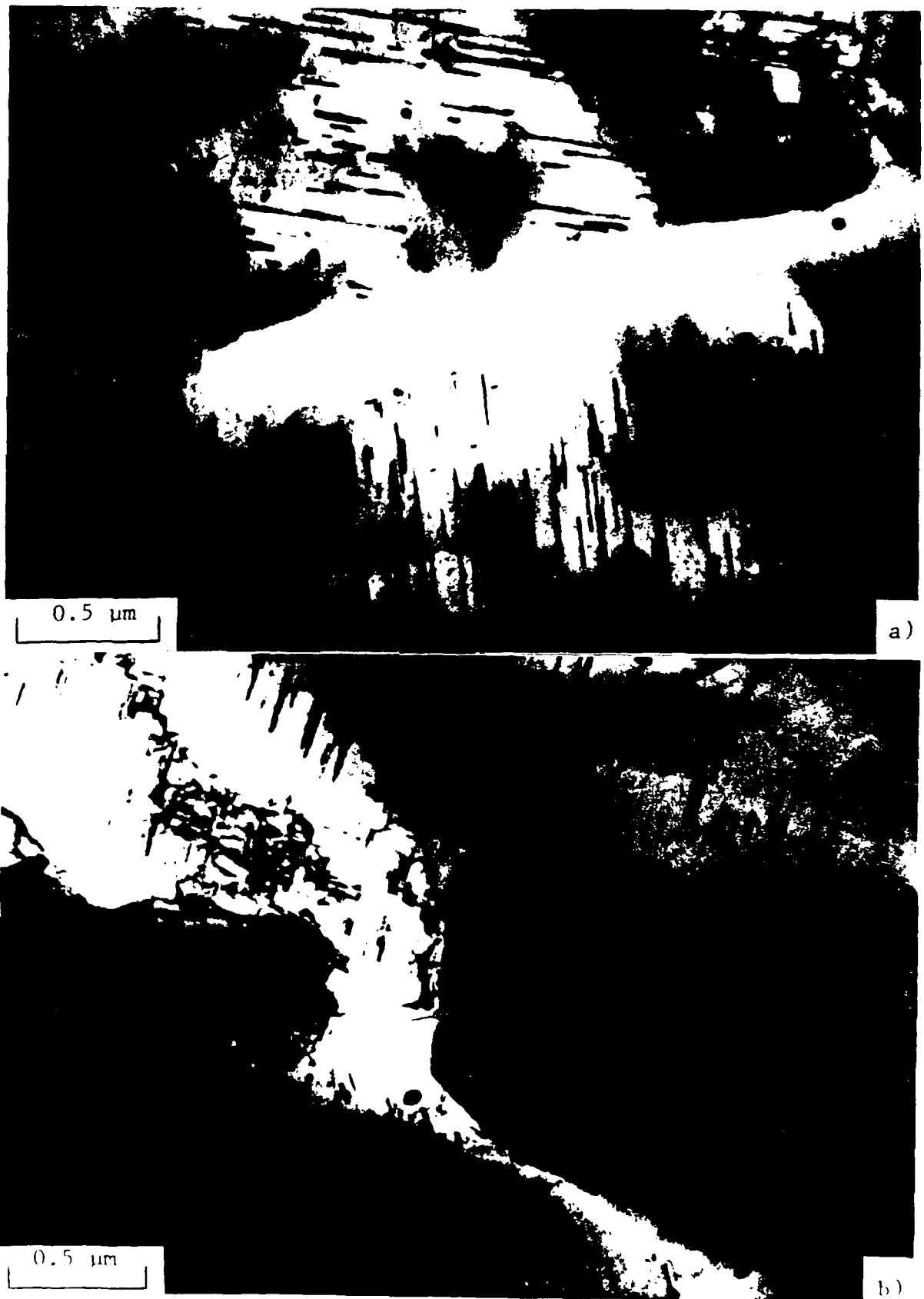


Figure 5: Transmission electron micrographs illustrating precipitate free regions in Mg-6Zn reinforced with 20 volume percent SiC<sub>p</sub>, solution treated at 330°C, 1 hour, water quenched and aged at 150°C for 128 hours. (a) Precipitate free zone at matrix grain boundary and (b) precipitate free region at SiC<sub>p</sub>/matrix interface and between SiC<sub>p</sub> particulates.

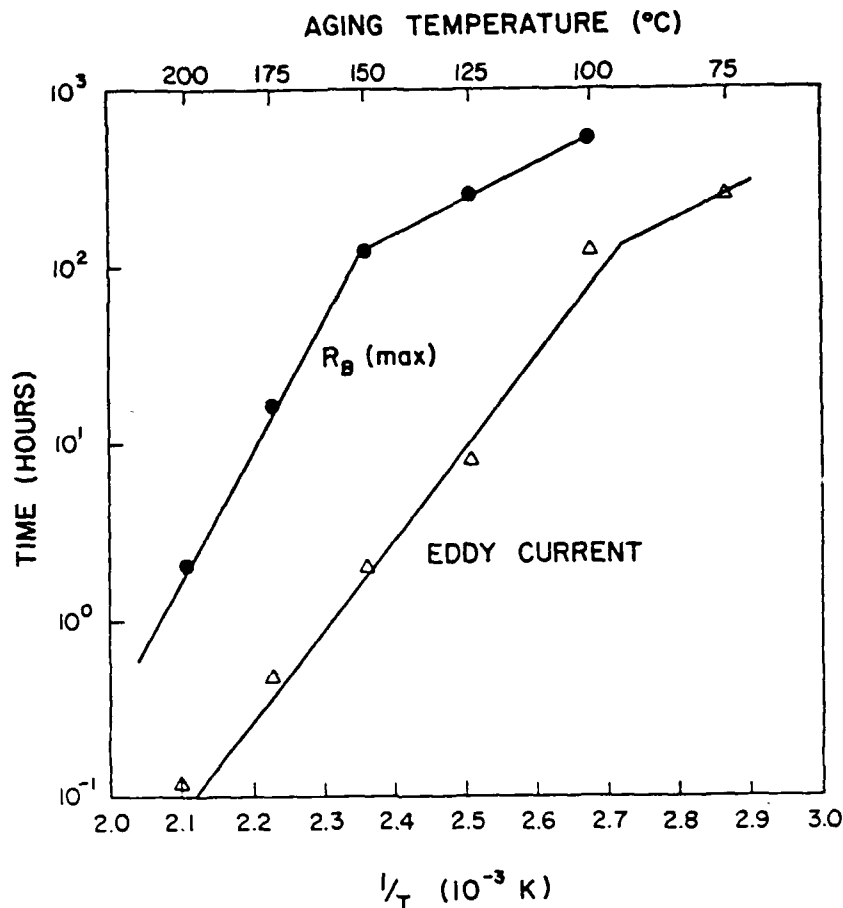


Figure 6: Activation analysis for aging process in Mg-6Zn reinforced with 20 volume percent  $\text{SiC}_p$ , solution treated at  $330^\circ\text{C}$ , 1 hour, and water quenched.

This study further supports the observations of Arsenault and Wu(7), who emphasize the importance of the reinforcement/matrix interface in establishing the aging kinetics of discontinuously reinforced metal matrix composites. This interface, if strongly bonded, as in powder metallurgy  $\text{SiC}$  whisker reinforced aluminum composites, can serve as a source of dislocations, principally due to relaxation of thermally induced strains. If, as is apparently the case in  $\delta \text{Al}_2\text{O}_3$  reinforced 6061 (10), and in the present investigation, the interface is weakly bonded, little dislocation formation will occur; indeed the interface may actually serve as a vacancy sink, thereby inhibiting GP zone formation and age hardening. The presence of precipitation free zones in  $\text{SiC}_p$  reinforced Mg-6Zn, Figure 5, without the formation of either an extensive dislocation network or heterogeneous  $\beta$  MgZn precipitation, suggests that, here again, the reinforcement/matrix interface is rather weak, and precipitation hardening will at best parallel that of an unreinforced alloy.

#### Summary and Conclusions

This study has considered the influence of a  $\text{SiC}_p$  reinforcement on the age hardening behavior of a Mg-6Zn alloy. It has been shown that the age hardening behavior of this composite is similar to that observed in the unreinforced alloy. This observation has been shown to be consistent with previous suggestions that the enhancement in aging observed in powder met-

allurgy aluminum alloys is due to the introduction of a thermally strain induced dislocation network, this network not being observed in SiC<sub>p</sub> reinforced Mg-6Zn.

#### Acknowledgements

This work was supported by the Air Force Office of Scientific Research under the University Research Initiative Contract No. F49620-87-C-0017 to Carnegie-Mellon University, Dr. A. H. Rosenstein acting as contract monitor. The authors wish to acknowledge B. A. Mikucki of Dow Chemical for supplying the Mg-Zn composite, M. Binder and J. Lanham for experimental assistance.

#### References

1. T. G. Nieh and R. F. Karlek, "Aging Characteristics of B<sub>4</sub> C-Reinforced 6061 Aluminum", Scripta Metallurgica, 18 (1984) 25-28.
2. S. Nutt and R. W. Carpenter, "Non-Equilibrium Phase Distribution in an Al-SiC Composite", Material Science and Engineering, 75 (1985) 169-177.
3. H. J. Rack, "Age Hardening Behavior of SiC Whisker Reinforced 6061 Aluminum", Proceedings ICCM-VI, Vol. 2, ed., F. L. Mathews, N. C. R. Buskell, J. M. Hodgkinson and J. M. Morton (London: Elsevier Applied Science, 1987) 382.
4. H. J. Rack, "P/M Aluminum Metal Matrix Composites", Dispersion Strengthened Aluminum Alloys, ed., Y-W Kim (Warrendale, PA: The Metallurgical Society, 1988) 649.
5. H. J. Rack, "Light-Weight, High-Performance Metal Matrix Composites", Powder Metallurgy Composites, ed., P. Kumar, K. Vedula and A. Ritter (Warrendale, PA: The Metallurgical Society, 1988) 155.
6. T. Christman and S. Suresh, "Microstructural Development in an Aluminum Alloy - SiC Whisker Composite", Acta Metallurgical, 36 (1988) 1691-1704.
7. R. J. Arsenault and S. B. Wu, "A Comparison of P/M vs. Melted SiC/Al Composites", Scripta Metallurgica, 22 (1988) 767-772.
8. J. M. Papazian, "Effects of SiC Whiskers and Particles on Precipitation in Aluminum Matrix Composites", Met. Trans., 19A (1988) 2945-2953.
9. H. J. Rack and P. Ratnaparkhi, "Powder Metal Composites", Encyclopedia of Composites, VCH Publishers, New York, 1989, in press.
10. C. M. Friend and S. D. Luxton, "The Effect of  $\delta$  Alumina Fibre Arrays on the Age Hardening Characteristics of an Al-Mg-Si Alloy", Jn. of Materials Science, 23 (1988) 3173-3180.
11. S. O. Shook and W. G. Green, "Improving Magnesium's Wear Resistance - A Composites Approach", (Paper presented at International Congress and Exposition, Detroit, Michigan, 25 February - 1 March 1985, SAE Tech. Paper 850421).



12. B. A. Mikucki, S. C. Shook, W. E. Mercer, II, and W. G. Green, "Magnesium Matrix Composites at Dow: Status Report", Light Metal Age, 44 (1986) 16-21.
13. L. Sturkey and J. B. Clark, "Mechanism of Age-Hardening in Magnesium-Zinc Alloys," Jn. Inst. of Metals, 88 (1959-60) 177-181.
14. J. B. Clark, "Transmission Electron Microscopy of Age Hardening in a Mg-5 wt.% Zn Alloy", Acta Met., 13 (1965) 1281-1289.
15. E. O. Hall, "The Age-Hardening Characteristics of Two Magnesium-Zinc Alloys", Jn. Inst. of Metals, 96 (1968) 21-27.
16. G. Mima and Y. Tanaka, "The Aging Characteristic of Mg-4 wt%Zn Alloy", Nippon Kinzoku Gakkaishi, 33 (1969) 796-800.
17. J. S. Chun, J. G. Byrne and A. Bornemann, "The Inhibition of Deformation Twinning by Precipitates in a Magnesium-Zinc Alloy", Phil. Mag., 20 (1969) 291-300.
18. G. Mima and Y. Tanaka, "The Effects of Silver on the Aging Characteristics of Mg-5.5 wt% Zn Alloys", Nippon Kinzoku Gakkaishi, 34 (1970) 209-214.
19. G. Mima and Y. Tanaka, "Mechanism of Precipitation Hardening of Magnesium-Zinc Alloys," Trans. JIM, 12 (1971) 323-328.
20. B. Lagowski, "Aging of Mg-9 Al-Zn Alloys", Trans. Am. Found. Soc., 79 (1971) 115-120.
21. G. Mima and Y. Tanaka, "Grain Size Dependence of Yield and Flow Stress in the Age-Hardened Mg-Zn Alloy", Nippon Kinzoku Gakkaishi, 35 (1971) 339-344.

## Phase Stability and Aging Response of TiC Reinforced Alloy 718

E. F. Wachtel and H. J. Rack

Materials Engineering Program  
Department of Mechanical Engineering  
Clemson University  
Clemson, South Carolina, 29634-0921

### Abstract

The aging kinetics and precipitation reactions of an alloy 718 matrix composite were analyzed and compared to ingot and P/M alloy 718 material. The techniques employed in this study included isothermal aging, hardness testing, differential scanning calorimetry, scanning and transmission electron microscopy and energy dispersive X-ray spectroscopy. It was found that the aging kinetics of the composite were generally faster and that the precipitation sequence is different than that of conventional alloy 718. These differences in kinetics and precipitation sequence are attributed to the reaction between the matrix and the reinforcing phase; the titanium carbide reacts with the matrix niobium forming a mixed MC carbide, resulting in a matrix depleted of niobium and enriched in titanium.

## INTRODUCTION

Metal matrix composites (MMC's) are being developed to improve specific stiffness ( $E/\rho$ ), specific strength ( $\sigma/\rho$ ), and high temperature performance. They are intended to combine the high toughness and ductility of a metal matrix with the high strength and stiffness of a ceramic reinforcing phase. While properties of discontinuously reinforced MMC's typically fall short of the values predicted by the Rule of Mixtures, substantial property improvements can still be made. While most previous efforts have involved an aluminum, titanium or magnesium matrix, recent advances in material processing technology have resulted in the development of an intermediate temperature MMC based on a matrix of alloy 718.

The precipitation reactions in alloy 718 have been studied extensively. The precipitation sequence is shown in Table 1 and the time-temperature-transformation curve (TTT) is depicted in Figure 1. The  $\gamma'$  phase is a disc or cuboidal shaped, coherent precipitate with an ordered FCC structure ( $L1_2$ ) having a stoichiometry based on the  $Ni_3Al$  composition, with Ti freely substituting for Al.  $\gamma''$  is a metastable, lens shaped, coherent precipitate with an ordered body centered tetragonal crystal structure ( $D0_{22}$ ) having a stoichiometry based on  $Ni_3Nb$ . Ti and possibly Al can substitute for the Nb.  $\delta$  is a stable, plate-like, incoherent precipitate with an orthorhombic structure ( $DO_a$ ), having a stoichiometry based on  $Ni_3Nb$ . Studies on material produced using a powder metallurgy (P/M) processing approach have shown that the precipitation reactions are similar to those of the conventional products (13,14).

Table I. Precipitation Reactions In Alloy 718

## PRECIPITATION REACTIONS IN ALLOY 718

$\gamma$	$\Rightarrow$	$\gamma'$	$\Rightarrow$	$\gamma''$	$\Rightarrow$	$\delta$
FCC		FCC		BCT		ORTHORHOMBIC
		$L1_2$		$D0_{22}$		$DO_a$ ( $Cu_3Ti$ )
		CUBOIDAL		LENS SHAPED		PLATELET
$a = 0.359nm$		$a = 0.362nm$		$a = 0.362nm$		$a = 0.514nm$
				$b = 0.741nm$		$b = 0.425nm$
						$c = 0.453nm$

Various carbides are present in the alloy 718 system including: an MC type (usually Ti or Nb carbide or carbo-nitride) with a blocky morphology and a  $B_1$  structure, an  $M_6C$  type, which is derived from the decomposition of MC and which typically has a blocky, grain boundary morphology, a  $Cr_7C_3$  type which has a blocky intergranular morphology and a  $M_{23}C_6$  type which forms from the decomposition of either MC or  $Cr_7C_3$  and has a grain boundary platelet morphology. In addition to  $\gamma'$  strengthening, investigators have suggested that Niobium Carbide (NbC) precipitation may also enhance the properties of alloy 718 (1,2,5,7,8,9,15). Carbide type,

distribution and morphology have been shown to affect properties, particularly ductility and stress rupture (15). Finally, it is reported that the solubility of carbon in alloy 718 increases substantially at temperatures above 980°C (15).

Previous experience with aluminum and magnesium matrix composites has shown that the aging kinetics and precipitation reactions may be altered by the presence of a reinforcing phase (16-19). This phenomenon is particularly pronounced in systems where the precipitation reactions exhibit heterogeneous nucleation. Heterogeneous nucleation is enhanced due to a minimization of the distortional free energy associated with a dislocation network. In addition, the growth of precipitates is enhanced by dislocation pipe diffusion. One possible cause of a dislocation network is thermal strain associated with the mismatch in coefficient of thermal expansion between the matrix and the reinforcement. Dislocation densities on the order of  $10^{13}/\text{cm}^2$  have been reported at the matrix reinforcement interface (20).

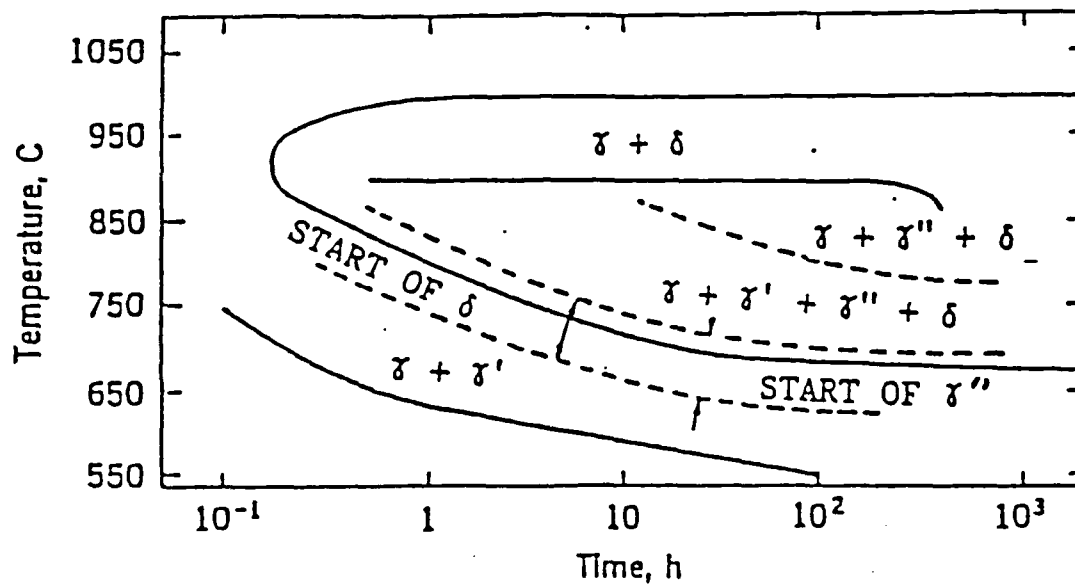


Figure 1. TTT diagram of alloy 718. Ref 10.

It is well established that the  $\gamma'$  phase nucleates heterogeneously in alloy 718, typically at extrinsic stacking faults or at intrinsic slip dislocations (4,21,22).  $\gamma'$  nucleation is reported to be intimately associated with existing  $\gamma'$  precipitates (7). In addition, NbC is reported to nucleate heterogeneously (1,2,7,23). Based on the above considerations, it would be anticipated that the aging kinetics of alloy 718 would be affected by the addition of a ceramic reinforcing phase.

The primary objective of this study is to determine the effect of a reinforcing phase addition on the precipitation reactions and aging kinetics of an alloy 718 matrix composite. The secondary objective is to study the stability of TiC as a reinforcing phase in nickel base superalloy MMC's.

### EXPERIMENTAL PROCEDURES

The materials used in this study were as follows: a P/M composite of alloy 718 with a 20 volume percent addition of TiC, P/M 718 and ingot 718. The composition of the ingot and the powder are shown in Table 2. It can be seen that the composition of the ingot and the powder are almost identical in every respect, thereby eliminating the effect of compositional variation on the

aging response. The composite and the P/M material were produced by DWA Composite Specialists. Gas atomized powder with a -200 mesh size was supplied by Carpenter Technology, INC, Figure 2(a). The reinforcing phase for the composite was TiC, Figure 2(b). The P/M materials were wet blended, dried, canned in mild steel and evacuated. Compaction of the material was achieved by hot isostatic pressing at 1150°C for three hours at a pressure of 15 KSI, with subsequent extrusion being carried out at 1040°C with an extrusion ratio of 19:1. In order to eliminate the effect of thermo-mechanical processing history on the aging response, the ingot material was subjected to the same processing sequence.

Table II. Chemical Composition of Ingot and Powder Material

Element	Ni	Fe	Cr	Mo	Ti	Al	Nb	Mn	Si
Powder	52.81	18.28	18.38	3.08	.99	.61	5.31	.12	.16
Ingot	52.52	18.67	18.29	3.07	.97	.59	5.37	.09	.10

The microstructure of the composite material was evaluated using a JEOL JSM IC848 scanning electron microscope in the backscatter mode. Backscatter SEM provides Z number contrast, which allows identification of phases with different composition. Semi-quantitative analysis of the various phases present in the backscatter micrographs was done using energy dispersive X-ray spectroscopy (EDS) in the spot mode (beam spot diameter of .02  $\mu$ m), the system being calibrated using a copper standard.

The aging kinetics of the three materials were examined through isothermal aging studies. The hardness of solution treated and quenched samples was measured as a function of isothermal aging time for a variety of aging temperatures. These studies were carried out utilizing temperatures varying from 650°C to 870°C with times ranging from 0.5 to 1000 hours. In addition, differential scanning calorimetry was used to compare the P/M material to the composite.

Thin foil transmission electron microscopy studies were conducted to determine the location and nature of the precipitate reactions and the type and extent of the matrix/reinforcing phase interfacial reaction. Precipitates and reaction products were analyzed using selected area electron diffraction (SAED) and energy dispersive spectroscopy (EDS).

## RESULTS AND DISCUSSION

Figure 3 shows typical SEM backscatter electron micrographs of the 1150°C solution treated composite. Three distinct phases are obvious in these micrographs. Using the EDS capability in the spot mode, the three phases have been identified. The spectrum for the black phase (TiC) is shown in Figure 4. In general, the TiC was evenly distributed throughout the matrix. The volume fraction of the reinforcing phase and the size of the particulate were much smaller than anticipated. The average volume fraction of particulate was on the order of five percent (5%) and the particulate size ranged from 5 to 10 microns. The spectrum for the gray phase is shown in Figure 5. This phase appears to be a mixed carbide of Ti and Nb, probably a mixed MC type carbide. This is reasonable since both carbides have the same structure B<sub>1</sub> and are completely soluble in one another with Ti and Nb occupying various sites on a carbon sublattice. In some cases, the TiC is surrounded by the mixed MC carbide. This is due to competition between Ti and Nb at the reinforcement interface, resulting in the formation of the mixed carbide, depletion of the matrix Nb and an increase in the matrix Ti content. Finally, the spectrum for the light phase is shown in Figure 6. This is the matrix, alloy 718.

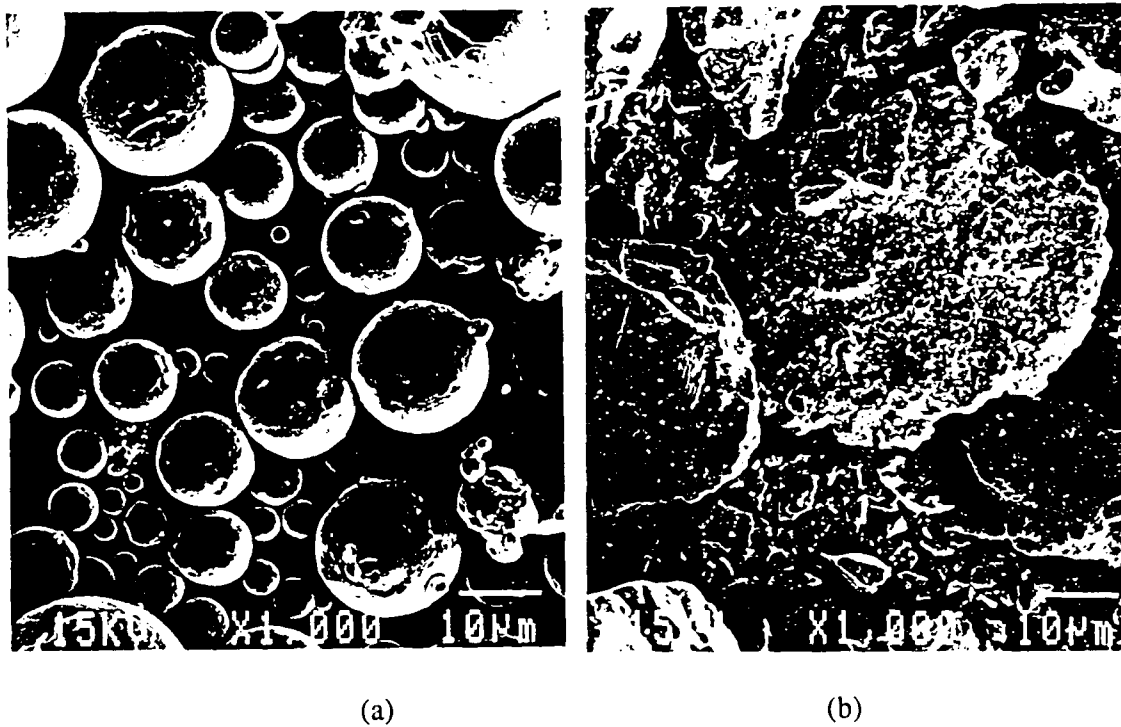


Figure 2. SEM micrograph of (a) 718 powder and (b) titanium carbide powder.



Figure 3. Backscatter SEM micrograph of as solution treated composite.

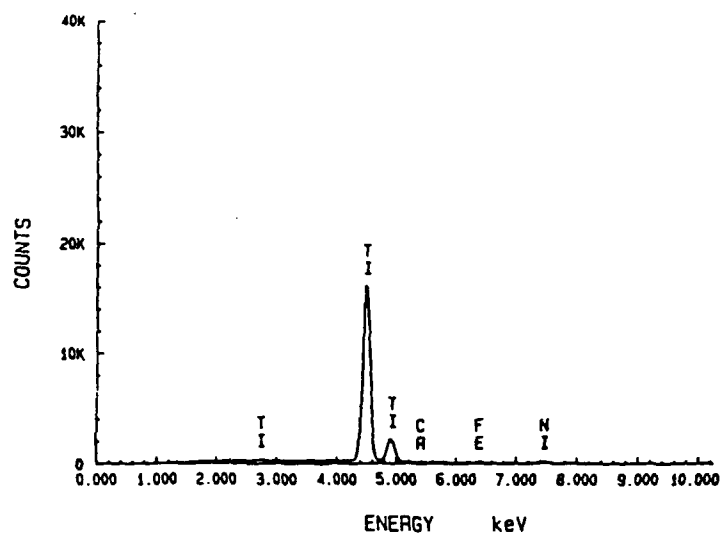


Figure 4. EDS spectrum of titanium carbide.

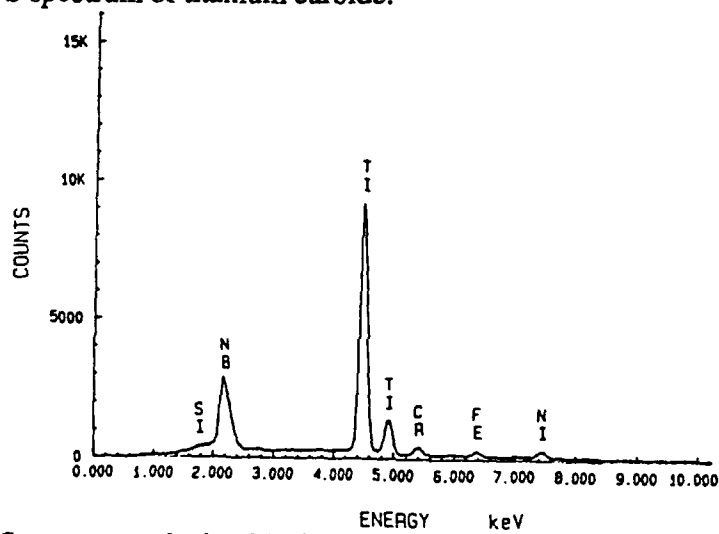


Figure 5. EDS spectrum of mixed MC carbide.

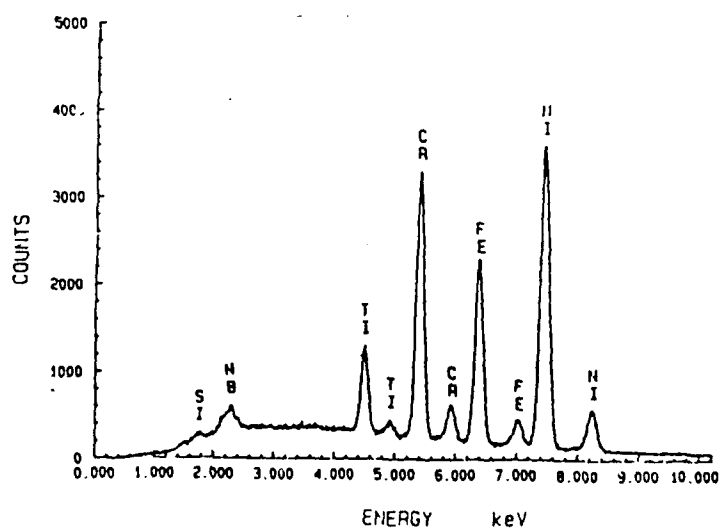
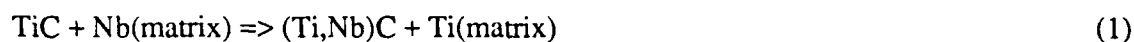


Figure 6. EDS spectrum of matrix, alloy 718.

Preliminary results of the DSC scans are shown in Figure 7. The DSC results indicate differences in the precipitation reactions between the two systems. The scan of the P/M material shows three main peaks; the sharp peak at 810°C is believed to be due to precipitation of the  $\delta$  phase, the broad peak from 550 - 650°C to a combination of gamma prime and gamma double prime precipitation while the diffuse peak from 300 - 400°C is most likely due to carbide precipitation. The scan of the composite material has four distinct peaks; the peak at 1000°C is believed to be due to dissolution and/or decomposition of the carbides, the peak at 690°C to the precipitation of the eta phase, while the peak at 550°C has been attributed to the gamma prime phase. Once again the broad peak from 300 - 400°C is thought to be due to carbide precipitation. The differential scanning calorimetry experiments are continuing, 100 hour isothermal scans are planned for temperatures ranging from 400°C to 1100°C to reevaluate the TTT diagram.

Results of the aging studies are shown in Figure 8. It is apparent from these that the aging kinetics of the composite vary considerably from the aging kinetics of the unreinforced material. At aging temperatures below 815°C, the aging kinetics of the composite are substantially faster than those of the unreinforced material. At temperatures of 815°C and above, the kinetics of both are similar, with overaging occurring in less than 0.5 hours.

It is hypothesized that the acceleration of the aging kinetics in the composite system is based on the reaction shown in equation 1.



During elevated temperature thermo-mechanical processes, some of the reinforcing phase goes into solution. On cooling, Nb tends to compete with Ti at the matrix/precipitate interface resulting in the formation of mixed MC carbides and a matrix which has been enriched in Ti and depleted of Nb.

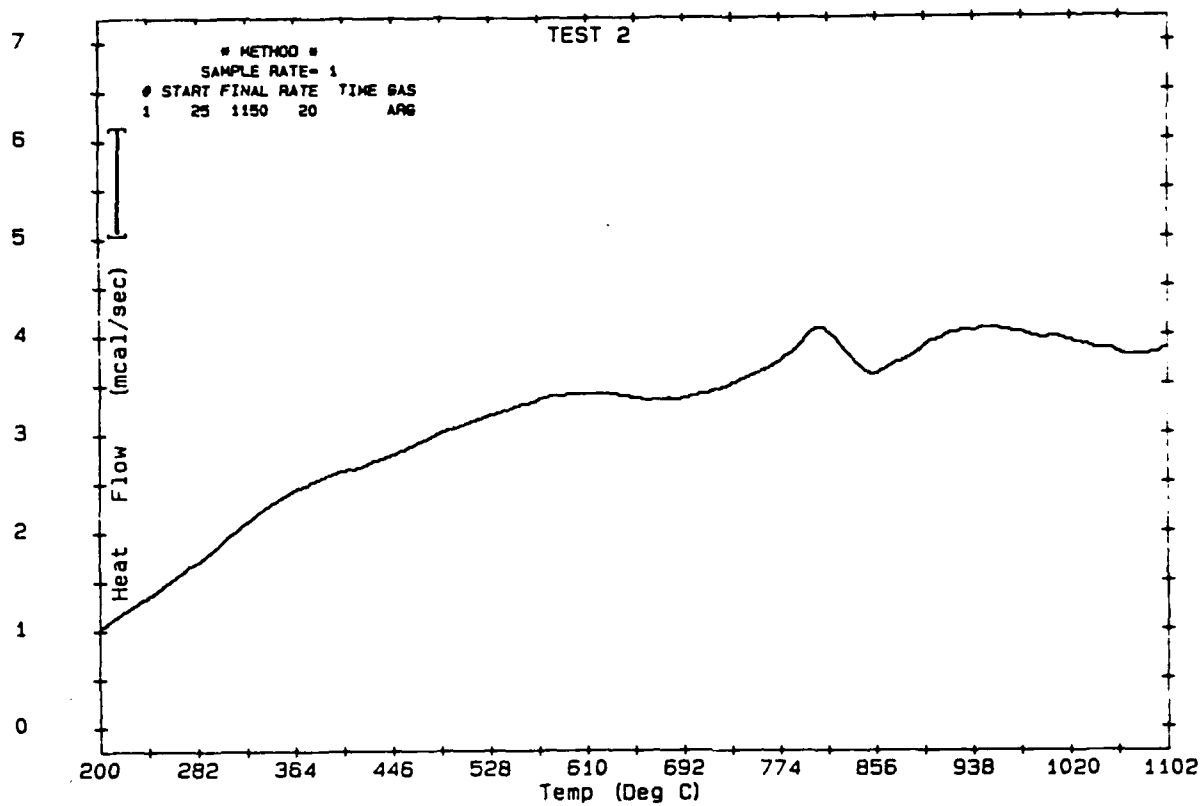
TEM studies have confirmed this hypothesis, precipitates of (Ti,Nb)C have been detected in the composite material at all temperatures, a typical TEM micrograph and EDS spectra are shown in Figure 9. These results confirm the earlier EDS work on the SEM but indicated that the actual Nb concentration of the precipitates is as high as 40%.

Increases in Ti content has been shown to accelerate the formation of  $\gamma'$  precipitates (10,23,28). In addition, increased matrix Ti content could promote the formation of the  $\eta$  phase ( $\text{Ni}_3\text{Ti}$ ) which is not normally observed in alloy 718, but which has been reported in nickel base superalloys having high Ti contents (10). Eta phase has been detected in the composite material at both the 815 and 870°C aging temperatures, as shown in Figure 10. Finally, the matrix Ti content was much higher in the composite material.

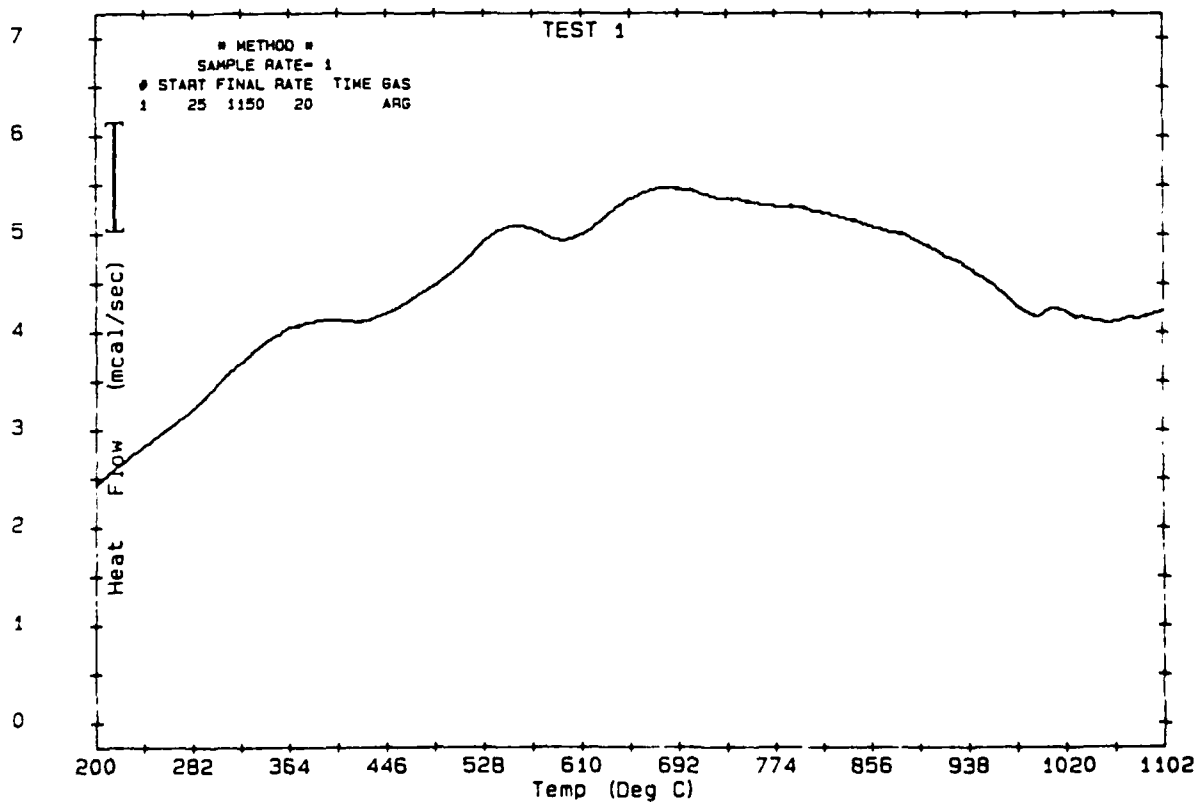
## CONCLUSIONS

1. The the aging kinetics (rate of reaction) of the composite material is substantially different than that of the unreinforced materials, while the ingot and the P/M material are similar at all temperatures.
2. The matrix and reinforcement react to form a mixed MC carbide (Ti/Nb)C. This reaction alters the matrix chemistry, depleting the Nb concentration and increasing the Ti concentration. As a result of the modification in matrix chemistry, the precipitation kinetics and reaction sequence is altered. The increased Ti concentration results in accelerated  $\gamma'$  coarsening and the precipitation of the eta phase.





(a)



(b)

Figure 7. Differential scanning calorimetry scans of a) alloy 718 and b) composite material.

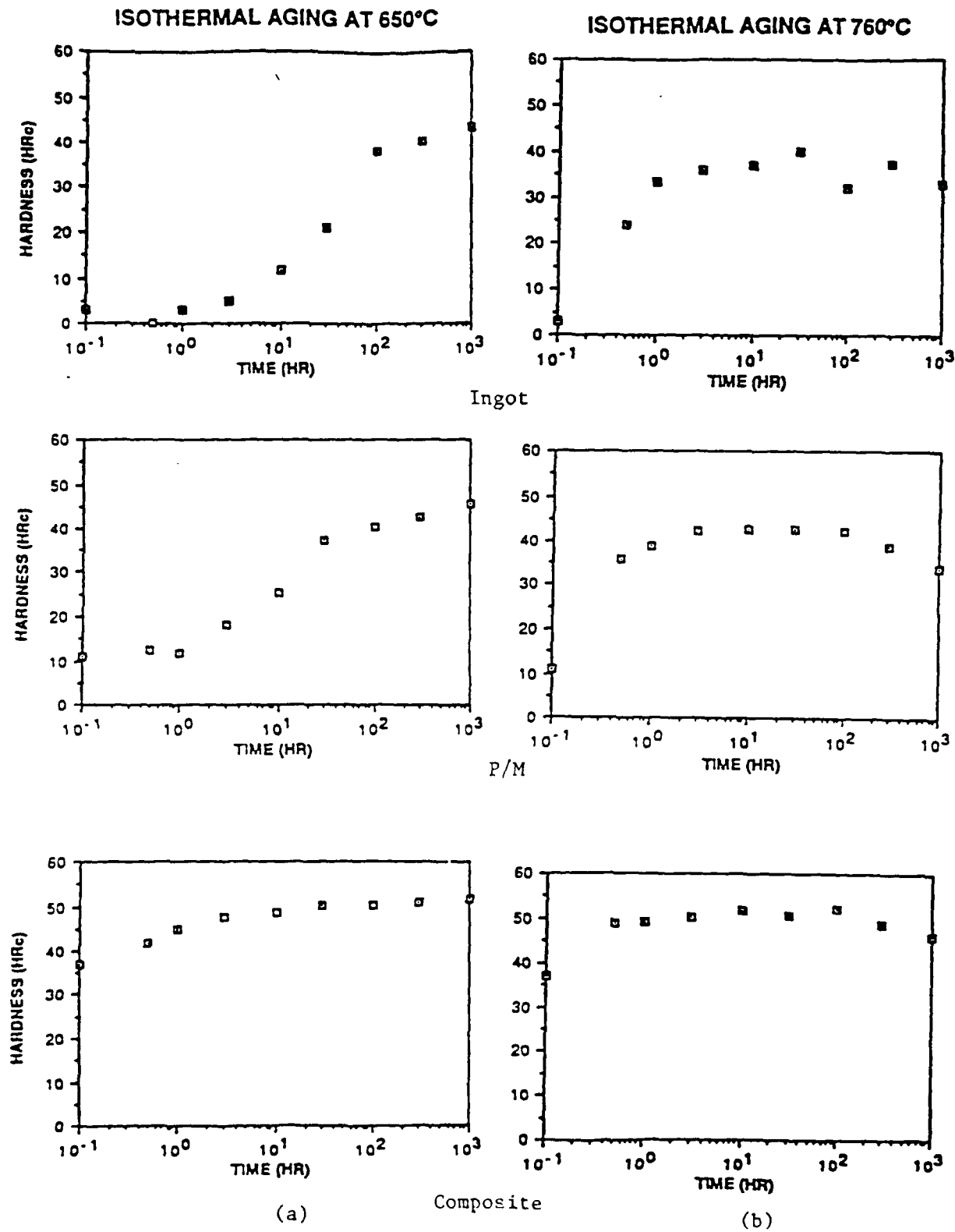
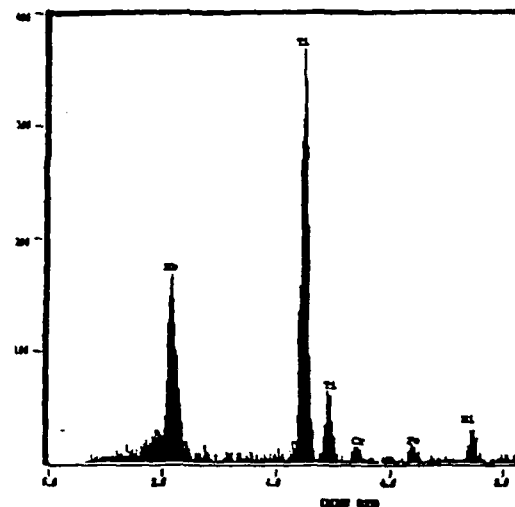


Figure 8. Isothermal aging response for ingot, P/M and composite material at a) 650 C and b) 760 C.



(a)

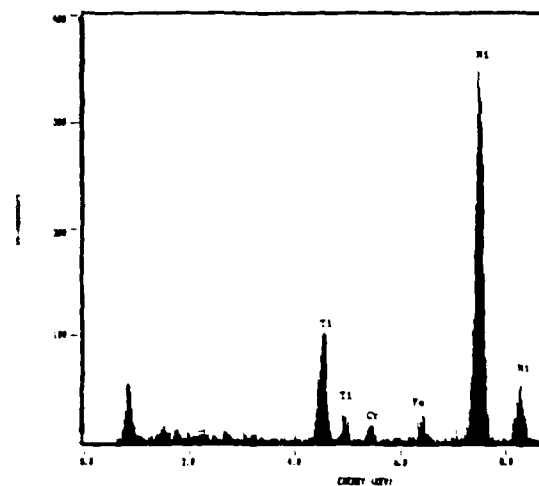


(b)

Figure 9. TEM micrograph of (a) solution treated composite and (b) EDS spectrum of carbide particle.



(a)



(b)

Figure 10. TEM micrograph of (a) composite material aged at 870°C for 300 hours, showing eta precipitate and (b) EDS spectrum of the eta precipitate.

### ACKNOWLEDGEMENT

The authors appreciate support of this work by the U.S. Air Force Office of Scientific Research, contract F49620-87-C-0017, as part of the University Research Initiative program on High Temperature Metal Matrix Composites at Carnegie-Mellon University.

### REFERENCES

1. H. L. Eiselstein, ASTM STP 369, Philadelphia, 1965, 62-79.
2. M. Kaufman and A. E. Palty, Trans. of the Met. Society of AIME 221, 1253-1261 (1961).
3. J. F. Barker, E. W. Ross, and J. F. Radavich, J. of Metals 22, 31-41, (1970).
4. R. S. Cremisio, J. F. Radavich, and H. M. Butler, Int. Symp. on Structural Stability in Superalloys, Seven Springs, PA, 1968, 597-618.
5. W. J. Boesch and H. B. Canada, Ibid.
6. D. F. Paulonis, J. M. Oblak, and D. S. Duvall, Trans. of the ASM 62, 611 - 622 (1969).
7. R. Cozar and A. Pineau, Met. Trans. 4, 47-59 (1973).
8. J. W. Brooks and P. J. Bridges, High Temperature Alloys for Gas Turbines and Other Applications 1986, ed. W. Betz, et al., D. Reidel Publishing Co., Dordrecht, Holland, 1968, 1431-1440.
9. J. F. Barker, D. D. Kruger, and D. R. Chang, Advanced High-Temperature Alloys: Processing and Properties, ed. S. Allen, R. M. Pelloux, and R. Witmer, ASM, Metals Park, OH, 1986, 125-137.
10. R. F. Decker, Steel Strengthening Mechanisms Symposium, Zurich, Switzerland, May 1969, 147-170.
11. E. A. Fell, Metallurgia 63, 157-166, (1961).
12. J. M. Oblak, W. A. Owczarski, and B. H. Kear, Acta Met., 19, 355-363, (1971).
13. H. F. Merrick, Met. Trans. 7A, 505-514 (1976).
14. K. Hajmrle, R. Angers, and G. Dufour, Met. Trans. 13A, 5-12.
15. E. L. Raymond, Trans. of the Met. Society of AIME 239, 1415-1422 (1967).
16. H. J. Rack and J. W. Mullins, High Strength Powder Metallurgy Aluminum Alloys II, ed. G. J. Hildeman and M. J. Koczak, AIME, 1986, 155-171.
17. H. J. Rack, Dispersion Strengthened Aluminum Alloys, ed. Y-W. Kim, The Met. Society, Warrendale, PA, 1988, in press.
18. H. J. Rack and R. W. Krenzer, Met. Trans. 8A, 335-346.
19. H. J. Rack, Mat. Sci. and Eng., 29, 179-188 (1977).

20. M. Vogelsang, R. J. Arsenault, and R. M. Fisher, *Met. Trans.*, 17A, 379-389, (1986).
21. A. A. Guimaraes and J. J. Jonas, *Met. Trans.* 12A, 1655- 1666.
22. D. D. Krueger, S. D. Antolovich, and R. H. Van Stone, *Met. Trans.* 18A, 1431-1449, (1987).
23. F. J. Rizzo and J. D. Buzzanell, *Int. Symp. on Structural Stability in Superalloys*, Seven Springs, PA, 1968, 501-543.
24. *ASM Metals Handbook*; 9th Edition, Volume 3, ASM, Metals Park, OH, 1980.
25. *Aerospace Structural Metals Handbook*, Metals and Ceramics Information Center, Battelle Columbus Division.
26. E. Supan, DWA Composite Specialists, Unpublished Data.
27. P. S. Korval, *Trans. Met. Society of AIME*, Vol. 242, 1764-5, (1968).
28. J. P. Collier, S. H. Wong, J. C. Phillips, and J. K. Tien, *Met. Trans.*, Vol. 19A, 1657-1666, (1988).
29. M. Sundararaman, P. Mukhopadhyay, and S. Banerjee, *Met. Trans.*, Vol. 19A, 453-465, (1988).
30. M. J. Donachie and O. H. Kriege, *J. of Materials*, JMLSA, Vol.7 (3), 269-278, (1972).

EFFECT OF DOUBLE AGING ON MECHANICAL PROPERTIES OF Mg-6Zn  
REINFORCED WITH SiC PARTICULATES

Prabir K. Chaudhury<sup>1</sup>, H. J. Rack<sup>1</sup>, and Barry A. Mikucki<sup>2</sup>

ABSTRACT

Double age hardening characteristics of a Mg-6%Zn alloy reinforced with 20 vol.% SiC particulates have been examined. Tensile tests were conducted using specimens with two different double aging treatments. Examination of the fracture surface using SEM and EDX, and study of precipitation process using TEM have been undertaken to supplement the mechanical test data. The results show pre-aging below the GP zone solvus strengthens the matrix through refinement of precipitates, and in turn leads to an increase in strength and decrease in composite ductility. In addition, as the yield and ultimate tensile strength of the composite increase, involvement of SiC<sub>p</sub> in the fracture process increases.

<sup>1</sup> Research Associate and Professor, respectively, Department of Mechanical Engineering, Clemson University, Clemson, SC 29634.

<sup>2</sup> The Dow Chemical Company, Lake Jackson Research Center, Freeport, Texas.

## 1. INTRODUCTION

Increasing demands for material with higher specific strengths and stiffness' have resulted in the development of light weight metal matrix composites. While most studies have been focused on aluminum metal matrix composites, magnesium, with suitable alloying and reinforcement, has shown increasing potential in many applications [1,2]. Magnesium alloys reinforced with SiC particulates possess the following attractive features.

- (i) SiC particles are relatively inexpensive and can be successfully introduced by low cost liquid metallurgy techniques [3],
- (ii) conventional fabrication/shaping can be used, and
- (iii) mechanical properties of the matrix can be dramatically improved via alloying and thermo-mechanical treatments, e.g. Mg-Zn alloys with 4 - 8% Zn are capable of age hardening [4-11].

While the age hardening behavior of discontinuously reinforced aluminum alloy matrix composites has been investigated extensively [12-19] such efforts using Mg alloy matrix composite are very limited [20]. The present investigation considers the potential for increasing the mechanical performance of a cast and extruded Mg-6Zn matrix reinforced with SiC particulates utilizing a double aging technique. Mechanical properties, e.g., modulus of

elasticity, yield strength, ultimate tensile strength and ductility are evaluated, and correlated with microstructural and fracture surface examinations.

## 2. EXPERIMENTAL PROCEDURE

The material used in this investigation, an ingot processed Mg-6Zn-.3Ca alloy reinforced with 20 vol.% SiC particulate, was prepared at Dow Chemical Corporation, Lake Jackson, Texas. The reinforcement was introduced by a proprietary liquid metallurgy technique developed at Dow utilizing 1000 grit, nominally 8-10  $\mu\text{m}$  diameter, SiC particulate containing approximately 1% free carbon [3]. The composite material was then cast into an ingot, 63.5 cm long and 17.8 cm diameter, and extruded to a 6.35 cm diameter bar.

Cylindrical tensile specimens with gage length and diameter of 2.54 cm and 0.635 cm, respectively, were machined from the bar. All specimens were solution treated at 673K for 4 hours in a protective atmosphere of argon gas and water quenched. Finally, the specimens were double aged according to the following schedule.

Heat treatment # 1: Artificial aging at 343K for 24 hours  
followed by 423K for 48 hours.

Heat treatment # 2: Artificial aging at 353K for 24 hours  
followed by 423K for 48 hours.



Room temperature tensile tests were conducted on double aged specimens on an Instron servo-hydraulic machine at a strain rate of 0.01 per minute. For each aging schedule 9 - 12 tests were conducted and elastic modulus, yield strength, ultimate tensile strength and ductility were recorded. Fracture surfaces of selected specimens were examined using a JEOL 848 scanning electron microscope equipped with a Tracor Northern X-ray analyzer.

Finally, differences in precipitate substructure resulting from the two aging schedules were studied by transmission electron microscopy. Thin foils were prepared for examination utilizing a JEOL 100C transmission electron microscope operated at 100 kV by diamond sectioning, hand grinding to a 75  $\mu\text{m}$  thick disc and argon ion milling at 6 kV, 0.4 mA and a 15° impingement angle.

### 3. RESULTS

Tensile test results are summarized in Table 1 where elastic modulus,  $E$ , yield strength,  $S_y$ , ultimate tensile strength,  $S_u$ , and fracture strain,  $e_f$ , both plastic and total, are tabulated for the two double aging conditions. Comparison of these results with those normally observed in commercial wrought alloys, e.g., ZE63A in the T6 temper,  $E = 45$  GPa,  $S_y = 190$  MPa,  $S_u = 300$  MPa and  $e_f = 10\%$  [21], show large improvements in elastic modulus and strength

properties; however these improvements are associated with a considerable decrease in ductility. Similar behavior has been observed in SiC reinforced aluminum matrix composites [22-24] where age hardening of the matrix is associated with an increase in composite strength and a decrease in ductility.

Further, the yield strength and ultimate tensile strength decreased significantly as the pre-aging temperature was increased from 343K (heat treatment #1) to 353K (heat treatment #2). Similar heat treatments for unreinforced binary Mg-6Zn (solution treatment, water quench + 96 hr. at 338K + 16 hr. at 443K) and ternary Mg-6Zn-1Au (solution treatment, water quench + 24 hr. at 363K + 16 hr. at 443K) alloys have shown the benefits of low temperature pre-aging [6].

The transmission electron microscopy results are presented in Figures 1 and 2. In specimens pre-aged at 343K two types of closely spaced and orthogonally oriented, rod-like precipitates predominated, Figure 1. In contrast, pre-aging at 353K resulted in the formation of a mixture of large globular, Figure 2(a), and very fine and unidirectional rod-like precipitates, Figure 2(b). Precipitates with similar morphologies have been observed in several studies and are characteristic of precipitation in unreinforced Mg-Zn (4-8%) alloys [4-10]. The globular

precipitates are the equilibrium MgZn phase, the long rod-like precipitates, which grow along the c axis of the matrix are transition  $\beta_1'$  phase, Figures 1 and 2(b), while the comparatively shorter rods perpendicular to the  $\beta_1'$  precipitates are another transition phase,  $\beta_2'$ , Figure 1.

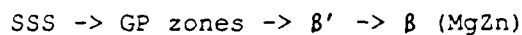
Results of the fracture surface examination are presented in Figures 3 through 6. SiC particle clumps, especially close to the tensile sample surface, serve as sites for fracture initiation. Figure 3 shows such an example where SEM photographs, at low, Figure 3(a), and high, Figure 3(b), magnifications, as well as EDS spectrum, Figure 3(c), for this area are presented. In addition, evidence exists that Ca containing inclusions, Figure 4, may also contribute to fracture initiation.

However, once initiated, the fracture mode for both aging conditions consists of a bimodal distribution of large dimples, typically associated with SiC particulates, and smaller dimples, Figure 5.

Further study indicates that the fracture path is dependent on aging practice. Quantitative analysis, utilizing Si mapping, indicates that the total amount of exposed SiC on the fracture surface was  $20.4 \pm 2$  vol.% and  $14.7 \pm 3$  vol.% in specimens pre-aged at 343K and 353K, respectively, Figure 6.

#### 4. DISCUSSION

A recent study of the age hardening response of Mg-6Zn reinforced with  $\text{SiC}_p$  showed [20] that the aging sequence in the composite is similar to that observed in the unreinforced alloy, i.e.,



While  $\beta$  is the equilibrium phase with a globular morphology,  $\beta'$  is a long and rod-like stable transition phase which is responsible for strengthening at peak-aged condition.  $\beta'$  has two morphological variables:  $\beta'_1$  and  $\beta'_2$ , both having a structure of Laves  $\text{MgZn}_2$  type [6,7]. The former variation has been observed to nucleate heterogeneously and grow parallel to the c axis of the matrix, while the latter has been observed to precipitate at longer times and/or higher temperatures with an orientation orthogonal to  $\beta'_1$  precipitates. The reported [6] lattice parameters and matrix-precipitate orientation relationships of  $\beta'_1$  and  $\beta'_2$  suggest that the delayed precipitation of  $\beta'_2$  is due to the difference in interfacial strain energy resulting from the anisotropic nature of the Mg matrix [25,26].

Double aging, as examined in this study, has been successfully applied to a wide range of age hardenable aluminum alloys [26,27]. In these alloys it normally consists of pre-aging at low temperature, typically below the GP zone solvus, followed by aging at higher temperatures.

The pre-aging treatment is designed to provide a uniformly distributed array of GP zones which can serve as subsequent sites for nucleation, and thereby facilitate homogeneous distribution of the hardening phase. It is well known that this treatment is particularly beneficial when the strain fields associated with the intermediate phases are large, in such cases precipitates of these intermediate phases are sensitive to lattice imperfections.

Present results, including tensile properties and TEM observations, have demonstrated that similar benefits may be achieved in age hardenable Mg-Zn composites. Overall response of the double aged  $\text{SiC}_p$  reinforced Mg-6Zn composite may be explained in terms of the existence of a metastable GP zone solvus at approximately 348K, as reported for binary Mg-6Zn [6]. Pre-aging below this temperature, i.e., at 343K, prior to aging at 423K results in a refined microstructure, and improved yield and ultimate tensile strengths. On the other hand, pre-aging at higher temperature, 353K, i.e., above the solvus, followed by aging at 423K leads to precipitation of coarser  $\beta$ .

Indeed, this double aging treatment when applied to  $\text{SiC}_p$  reinforced Mg-Zn composites can result in specific modulus and strength properties, which are comparable, and in some cases superior to, those achievable in either standard aluminum or reinforced aluminum alloys, Table 2.

Further, this study has shown that the tensile fracture initiation, of current  $\text{SiC}_p$  reinforced Mg-Zn composites is controlled by (a) the presence of tramp inclusions, and (b) the uniformity of  $\text{SiC}_p$  dispersion. Large Ca rich inclusions, together with non-uniformly distributed  $\text{SiC}_p$  clumps, serve as the initial site for failure initiation. Similar observations have been reported in early  $\text{SiC}_p$  reinforced aluminum alloys [29], subsequent processing modifications having largely eliminated this source of premature failure.

Finally, the ductility of  $\text{SiC}_p$  reinforced Mg-Zn alloys is limited by the ability of the matrix to redistribute stress concentration through plastic flow. For example, when these composites were pre-aged at 353K, quantitative analysis of the fracture surface indicated that the fracture path was matrix dominated, that is the volume percent  $\text{SiC}_p$  on the fracture surface, 14.7%, was less than that of the overall composite. However, when the aging treatment involved pre-aging at 343K, higher matrix flow properties were achieved, and the volume percent  $\text{SiC}_p$  present on the fracture surface increased to that of the overall composite. These observations are consistent with accumulating evidence in  $\text{SiC}_p$  reinforced aluminum alloys; tensile failure of lower strength 2124/ $\text{SiC}_p$  composites occurs randomly [30], while failure in higher strength 7xxx/ $\text{SiC}_p$  composites is dominated by the presence of the  $\text{SiC}_p$  [31].

## 5. CONCLUSIONS

1. Elastic modulus, yield strength and ultimate tensile strength of double aged Mg-Zn reinforced with 20 vol.% SiC particulates are higher than conventional age hardened Mg-Zn alloys. Specific strengths and modulus are comparable to high strength Al alloys and many SiC/Al composites.

2. Lower pre-aging temperatures result in higher yield and ultimate tensile strengths with some decrease in ductility.

3. Tensile failure is initiated at large SiC<sub>p</sub> rich or Ca rich areas.

4. The higher strengths are due to refinement of precipitates in the microstructure, while the loss of ductility is caused by the increased failure associated with SiC particulates.

## ACKNOWLEDGMENT

Two of the authors, PKC and HJR, wish to acknowledge financial support for this work provided by the U.S. Air Force Office of Scientific Research, contract F49620-C-0017, as part of the University Research Initiative program on High Temperature Metal Matrix Composites at Carnegie Mellon University.



## REFERENCES

1. Proc. 44th Annual World Magnesium Conference, Tokyo, Japan, May 17 - 20, 1987, International Magnesium Assoc., McLean, Virginia, USA.
2. S. J. Swindlehurst and I. W. Hall; in Proc. Int. Symp. on Advances in Cast Reinforced Metal Composites, S. G. Fishman and A. K. Dhingra, eds., ASM International, 1988, 281.
3. B. A. Mikucki, S. C. Shook, W. E. Mercer, II, and W. G. Green; Light Metal Age, **44** (1986), 16
4. L. Sturkey and J. B. Clark; J. Inst. Metals, **88** (1959-60), 177.
5. J. B. Clark; Acta Met., **13** (1965), 1281.
6. E. O. Hall; J. Inst. Metals, **96** (1968), 21.
7. M. Bernole, J. Gallot and R. Graf; J. Microscopie, **4** (1965), 787.
8. G. Mima and Y. Tanaka; Nippon Kinzoku Gakkaishi, **33** (1969), 796.
9. J. S. Chun, J. G. Byrne and A. Bornemann; Phil. Mag., **20** (1969), 291.
10. G. Mima and Y. Tanaka; Nippon Kinzoku Gakkaishi, **34** (1970), 209.
11. G. Mima and Y. Tanaka; Trans. JIM, **12** (1971), 323.
12. H. J. Rack; in "Powder Metallurgy Composites," P. Kumar, K. Vedula and A. Ritter eds., The Metallurgical Society, Warrendale, PA, 1988, 155.
13. H. J. Rack; in "Dispersion Strengthen Aluminum Alloys," Y-W Kim, ed., The Metallurgical Society, Warrendale, PA, 1988, 649.
14. T. Christman and S. Suresh; Acta Met., **36** (1988), 1691.
15. R. J. Arsenault and S. B. Wu; Scripta Met., **22** (1988), 767.
16. J. M. Papazian; Met. Trans. A, **19A** (1988), 2945.

17. H. J. Rack; in Proc. ICCM-VI, F. L. Mathews, N. C. R. Buskell, J. M. Hodgkinson and J. M. Morton, eds., Elsevier Applied Science, London, 2 (1987), 382.
18. S. Nutt and R. W. Carpenter; Mater. Sci. Eng., 75 (1985), 169.
19. T. G. Nieh and R. F. Karlak; Scripta Met., 18 (1984), 25.
20. H. J. Rack and P. K. Chaudhury; presented in TMS Fall Meeting, 20 - 25 February 1989, Las Vegas, Nevada.
21. Metals Handbook, Ninth edition, volume 2.
22. T. G. Nieh, R. A. Rainen and D. J. Chellman; in Proc. ICCM-V, W. C. Harrigan, Jr., J. Strife and A. K. Dhingra, eds., 1985, 825.
23. C. R. Crowe, R. A. Gray and D. F. Hasson; in Proc. ICCM-V, W. C. Harrigan, Jr., J. Strife and A. K. Dhingra, eds., 1985, 843.
24. D. McDanel; Met. Trans. A, 16A (1985), 1105.
25. J. K. Lee, D. M. Barnett and H. I. Aaronson; Met. Trans. A, 8A (1977), 963.
26. P. E. Marth, H. I. Aaronson, G. W. Lorimer, T. L. Bartel and K. C. Russell; Met Trans. A, 7A (1976), 1519.
27. H. Loftler, I. Kovacs and J. Lendvai; J. Mater. Sci., 18 (1983), 2215.
28. W. C. Harrigan, Jr.; in "Engineered Materials Handbook," ASM International, 1 (1987), 893.
29. J. W. Mullens and H. J. Rack; in "High Strength Powder Metallurgy Aluminum Alloys II," G. J. Hildeman and M. J. Koczak, eds., AIME, Warrendale, PA, 1986, 155.
30. C. P. You, A. W. Thompson and I. M. Bernstein; Scripta Met., 21 (1987), 181.
31. J. Shang and R. O. Ritchie; Mater. Sci. Eng., 102 (1988), 181.

TABLE 1: TENSILE PROPERTIES OF 20 vol.% SiC<sub>p</sub>/Mg-6Zn

Double aging condition	E	S <sub>y</sub>	S <sub>u</sub>	e <sub>f</sub> , %	
	GPa	MPa	MPa	total	plastic
1. 343K/24h + 423K/48h	75.9	411	467	2.9	2.3
2. 353K/24h + 423K/48h	77.2	348	425	4.9	4.3

TABLE 2: COMPARISON OF SPECIFIC MODULUS AND STRENGTH OF 20 vol.% SiCp/Mg-6Zn WITH OTHER MATERIALS.

Material	Condition	Sp. E kN-m/g	Sp. S <sub>y</sub> N-m/g	Sp. S <sub>u</sub> N-m/g
Double-aged				
20 vol.% SiCp/Mg-6Zn	#1	36.1	195.7	222.4
	#2	36.8	165.7	202.3
7050 Al Forging [20]	peak-aged at 373K	24.8	185.0	185.0
7475 Al T61 [20]	peak-aged at 373K	24.8	182.3	201.8
20% SiC <sub>p</sub> / 2124 Al [28]	peak-aged	36.2	140.0	193.1
20% SiC <sub>p</sub> / 6061 Al [28]	peak-aged	36.9	147.8	177.3
20% SiC <sub>p</sub> / 7090 Al [28]	peak-aged	35.9	225.8	249.6

FIGURE CAPTIONS

- Figure 1. Transmission electron micrograph of 20 vol.% SiC<sub>p</sub>/Mg-6Zn composite double-aged at 343K/24h + 423K/48h, showing precipitation of  $\beta_1$  and  $\beta_2$ .
- Figure 2. Transmission electron micrograph of 20 vol.% SiC<sub>p</sub>/Mg-6Zn composite double-aged at 353K/24h + 423K/48h, showing a) large  $\beta$  precipitates and b) fine  $\beta_1$  precipitates.
- Figure 3. Scanning electron micrograph and EDX spectrum of tensile fracture surface of double-aged 20 vol.% SiC<sub>p</sub>/Mg-6Zn composite, showing fracture initiation at SiC<sub>p</sub> rich area;  
 a) fracture surface at low magnification,  
 b) fracture initiation site as boxed in a) and  
 c) EDX spectrum of the boxed area in b), showing SiC<sub>p</sub> segregation at the fracture initiation site.
- Figure 4. Scanning electron micrograph, (a), and EDX spectrum, (b), of tensile fracture surface of double-aged 20 vol.% SiC<sub>p</sub>/Mg-6Zn composite, showing Ca rich inclusion.
- Figure 5. Scanning electron micrographs of tensile fracture surface of double-aged 20 vol.% SiC<sub>p</sub>/Mg-6Zn composites, showing bimodal distribution of large and small dimples under double-aging conditions,  
 a) 343K/24 hours + 423K/48 hours and  
 b) 353K/24 hours + 423K/48 hours.
- Figure 6. Si mapping on fracture surface showing amount of exposed SiC<sub>p</sub> on tensile fracture surface of 20 vol.% SiC<sub>p</sub>/Mg-6Zn composites under double-aging conditions of  
 a) 343K/24 hours + 423K/48 hours and  
 b) 353K/24 hours + 423K/48 hours.



Figure 1. Transmission electron micrograph of 20 vol.% SiC<sub>p</sub>/Mg-6Zn composite double-aged at 343K/24h + 423K/48h, showing precipitation of  $\beta'_1$  and  $\beta'_2$ .



Figure 2. Transmission electron micrograph of 20 vol.% SiC<sub>p</sub>/Mg-6Zn composite double-aged at 353K/24h + 423K/48h, showing a) large  $\beta$  precipitates and b) fine  $\beta_1$  precipitates.



Figure 2. Continued.



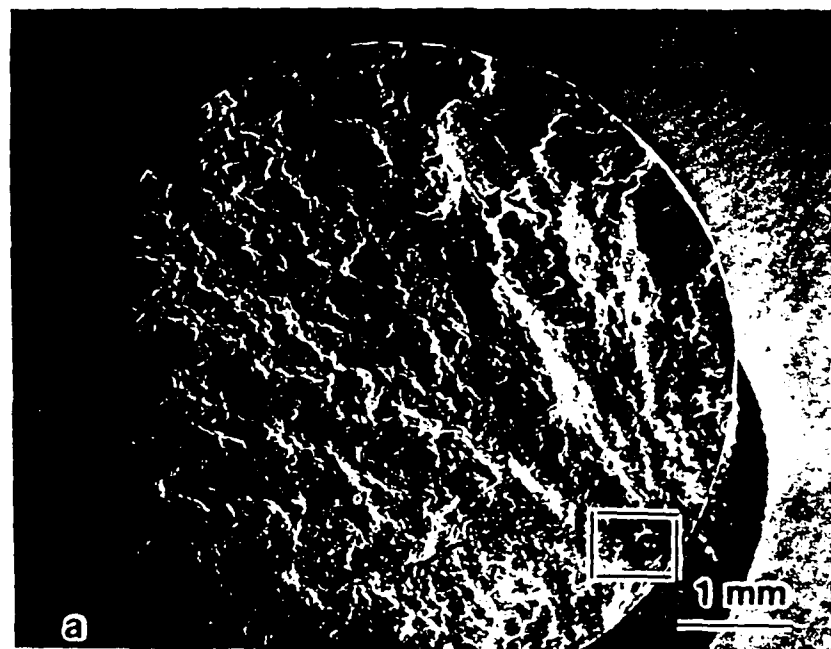


Figure 3. Scanning electron micrograph and EDX spectrum of tensile fracture surface of double-aged 20 vol.% SiCp/Mg-6Zn composite, showing fracture initiation at SiCp rich area;

- a) fracture surface at low magnification,
- b) fracture initiation site as boxed in a) and
- c) EDX spectrum of the boxed area in b), showing SiCp segregation at the fracture initiation site

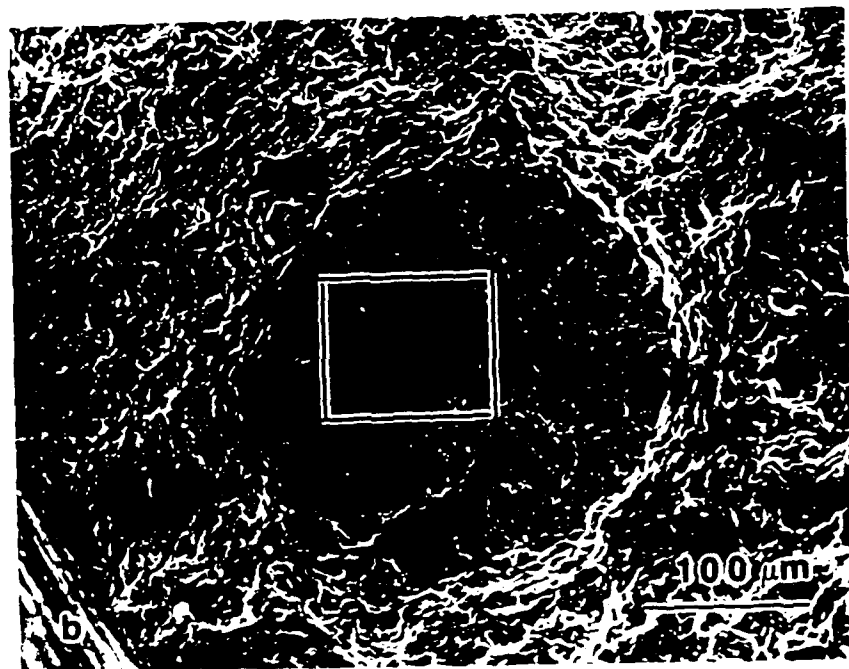


Figure 3. Continued.

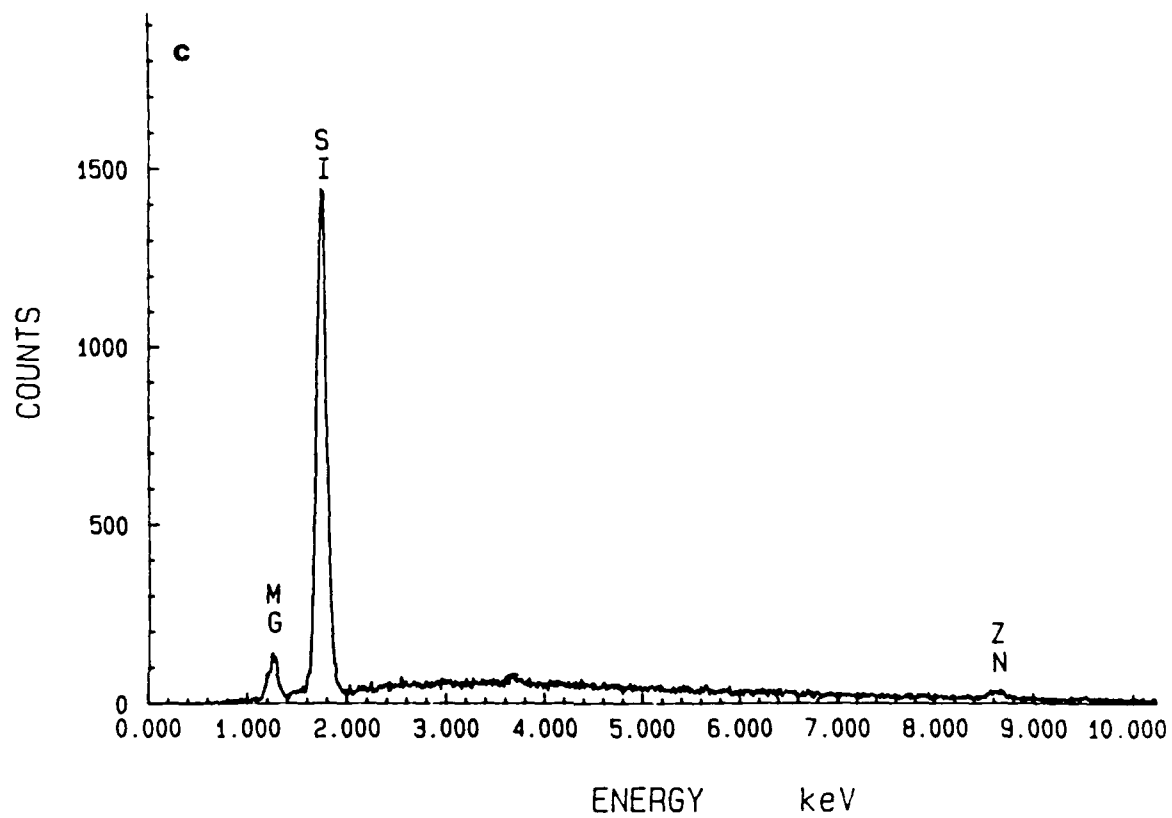


Figure 3. Continued.

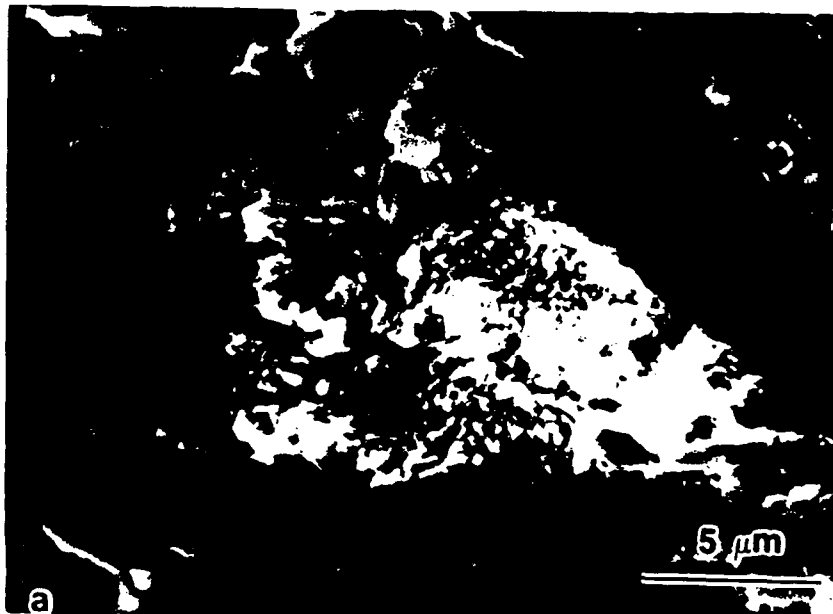


Figure 4. Scanning electron micrograph, (a), and EDX spectrum, (b), of tensile fracture surface of double-aged 20 vol.% SiC<sub>p</sub>/Mg-6Zn composite, showing Ca rich inclusion.

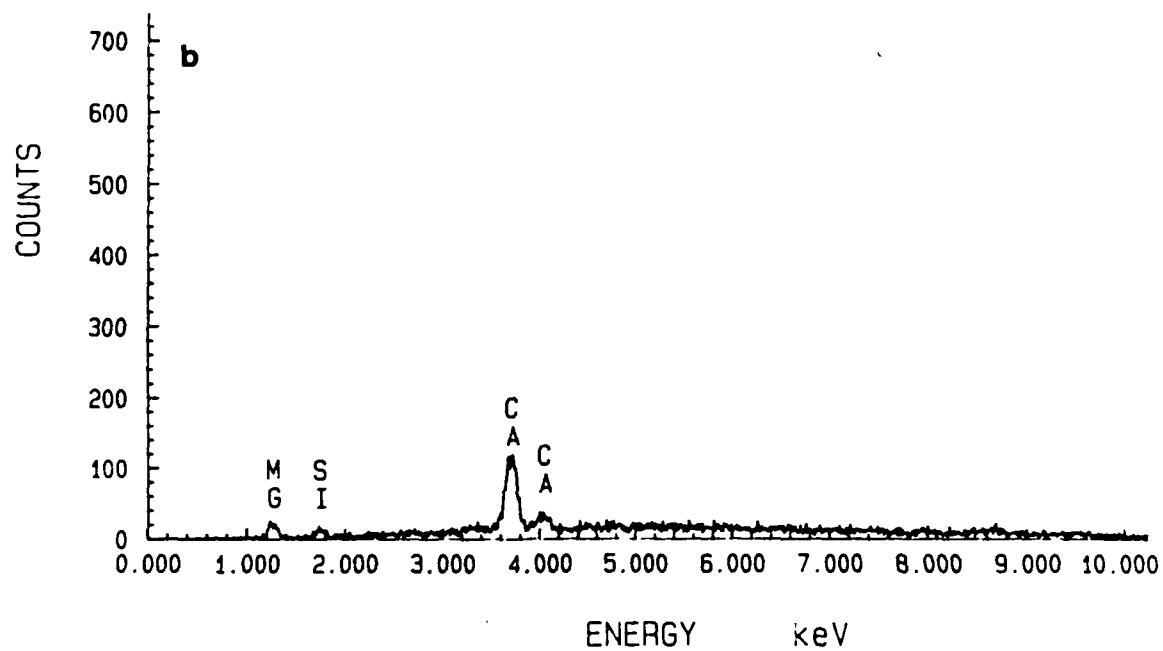


Figure 4. Continued.

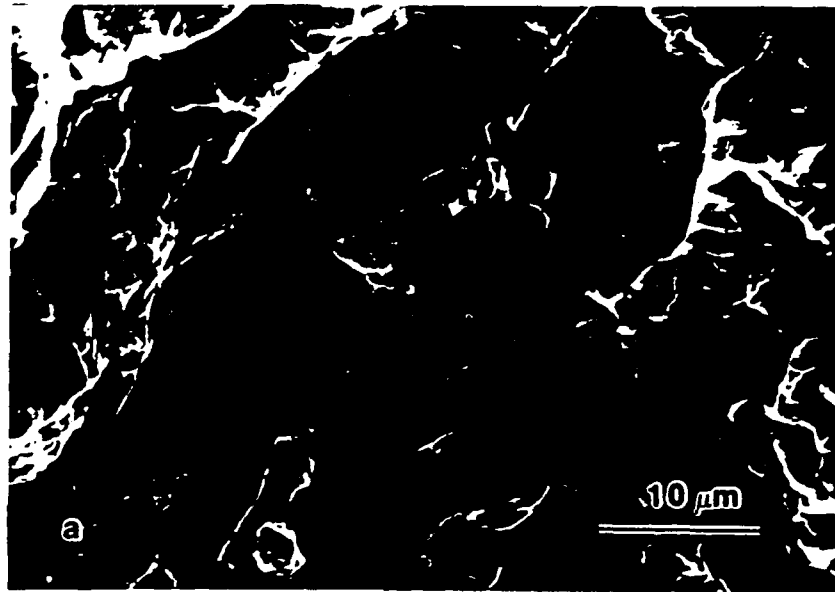


Figure 5. Scanning electron micrographs of tensile fracture surface of double-aged 20 vol.% SiC<sub>p</sub>/Mg-6Zn composites, showing bimodal distribution of large and small dimples under double-aging conditions, a) 343K/24 hours + 423K/48 hours and b) 353K/24 hours + 423K/48 hours.



Figure 5. Continued.

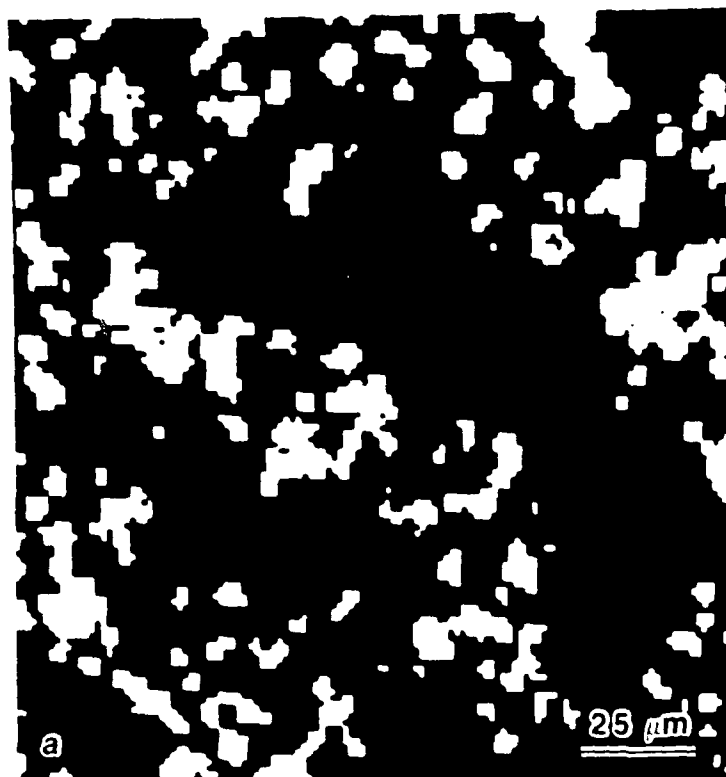


Figure 6. Si mapping on fracture surface showing amount of exposed  $\text{SiC}_p$  on tensile fracture surface of 20 vol.%  $\text{SiC}_p/\text{Mg-6Zn}$  composites under double-aging conditions of  
a) 343K/24 hours + 423K/48 hours and  
b) 353K/24 hours + 423K/48 hours.



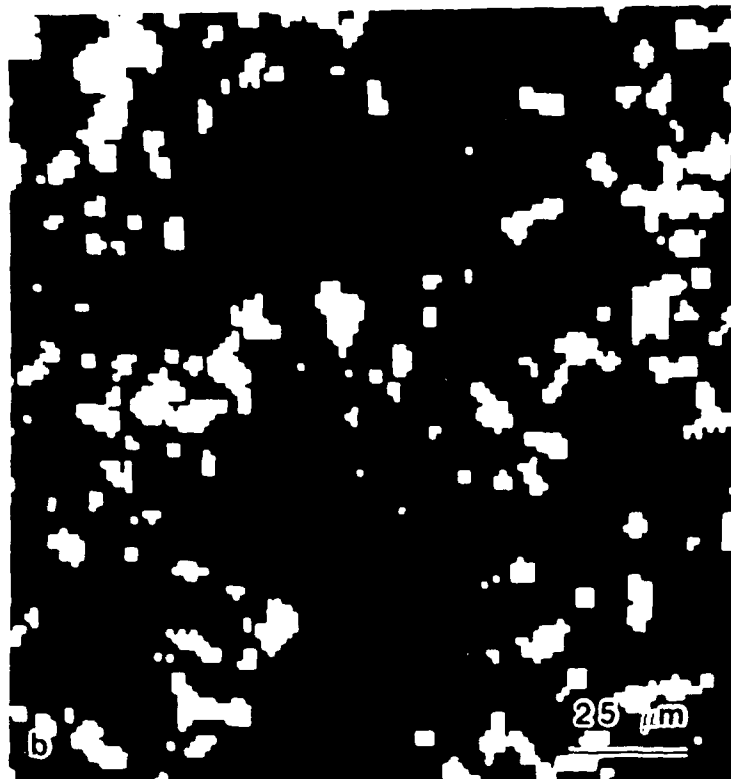


Figure 6. Continued.

**PART 2**

**CHARACTERIZATION**

BLANK

## TASK 3

### INTERFACIAL STRUCTURE AND STABILITY IN METAL AND INTERMETALLIC MATRIX COMPOSITES

James M. Howe (Principal Investigator)

#### Purpose

The purpose of this research was to investigate factors affecting the mechanical behavior of metal and intermetallic matrix composites, particularly the role of interfaces on mechanisms of deformation. This research concentrated on four main areas, which are listed below.

- i) Effect of whisker/matrix interface on the mechanical behavior of a 2124/SiC<sub>w</sub> composite,
- ii) Measurement of local residual stresses in an Al/SiC<sub>w</sub> composite by convergent-beam electron diffraction,
- iii) TEM investigation of interfaces and microstructural evolution in TiAl and Ti<sub>3</sub>Al base alloys, and
- iv) Mechanisms of deformation in two-phase TiAl and Ti<sub>3</sub>Al base alloys.

In addition, it was necessary to perform detailed investigations of the effects of specimen and microscope parameters on high-resolution TEM images of interfaces in Ti-Al alloys in order to be able to interpret experimental images. Thus, an extensive investigation of the effects of crystal and beam tilt on high-resolution TEM images of interfaces was also undertaken.

#### Publications

Publications which resulted from several of these studies were included as appendices to the 2nd Annual URI Report (1988). Publications which have resulted since then follow this summary. A complete list of publications produced under this grant is given below.

\*G. J. Mahon and J. M. Howe, "TEM Investigations of Interfaces in a Two-Phase TiAl Alloy," Metall. Trans. A, in press.

\*G. J. Mahon, J. M. Howe and A. K. Vasudevan, "Microstructural Development and the Effect of Interfacial Precipitation on the Tensile Properties of an Aluminum/Silicon Carbide Composite," *Acta Metall.*, in press.

\*G. J. Mahon and J. M. Howe, "Microstructural Development During Heat Treatment and Deformation of an Aluminum-Silicon Carbide Composite," *Proc. of the 46th Annual Meeting of the Electron Microscopy Society of America*, San Francisco Press, CA, p. 724 (1988).

\*J. M. Howe and G. J. Mahon, "High-Resolution TEM of Precipitate Plate Growth by Diffusional and Displacive Transformation Mechanisms," *Ultramicroscopy*, 30, 132 (1989).

\*J. M. Howe and G. J. Mahon, "High-Resolution TEM of Precipitate Plate Growth by Diffusional and Displacive Transformation Mechanisms," *Proc. of the 46th Annual Meeting of the Electron Microscopy Society of America*, San Francisco Press, CA, p. 760 (1988).

\*J. M. Howe and S. Rozeveld, "Effect of Beam and Crystal Tilt on High-Resolution TEM Images of Interfaces in Materials," *J. Electron Microscopy Technique*, submitted.

\*S. Rozeveld and J. M. Howe, "Techniques for Measurement of Small Strains by Convergent-Beam Electron Diffraction," *Philos. Mag. A*, in preparation.

\*S. Rozeveld and J. M. Howe, "Measurement of Residual Stress in an Al-SiC Metal Matrix Composite by Convergent-Beam Electron Diffraction," *Philos. Mag. A*, in preparation.

### Presentations

Presentations which resulted from this research are listed below. Portions of this research were also included in other review presentations.

\*J. M. Howe and G. J. Mahon, "TEM Investigation of Interfaces in a Two-Phase TiAl Alloy," *World Materials Congress*, Chicago, IL, October, 1988.

\*G. J. Mahon and J. M. Howe, "Microstructural Development During Heat Treatment and Deformation of an Aluminum-Silicon Carbide Composite," 46th Annual Meeting of the Electron Microscopy Society of America, Milwaukee, WI, August, 1988.

\*J. M. Howe and G. J. Mahon, "High-Resolution TEM of Precipitate Plate Growth by Diffusional and Displacive Transformation Mechanisms," (invited) 46th Annual Meeting of the Electron Microscopy Society of America, Milwaukee, WI, August, 1988.

\*J. M. Howe, G. J. Mahon and S. Rozeveld, "High-Resolution TEM of Interfaces in Ti Aluminides," (invited) Materials Laboratory, Wright-Patterson Airforce Base, Dayton, OH, June, 1989.

\*S. Rozeveld and J. M. Howe, "Structure and Deformation of the  $\beta/\alpha_2$  Interface in a Ti-Mo-Al Alloy," TMS-AIME Fall Meeting, Indianapolis, IN, October, 1989.

\*J. M. Howe and G. J. Mahon, "TEM Investigation of Interfaces in a Two-Phase TiAl Alloy," International Congress on Intergranular and Interphase Boundaries, Paris, France, September, 1989.

Research that was started under this URI and is still in progress includes TEM examination of the microstructure and deformation mechanisms in Ti-48Al-X and Ti-16Al-7Mo alloys. Publication of this research is planned for the MRS Fall Meeting, Boston, MA, 1990.

#### Personnel

Personnel supported under this grant other than the principal investigator were:

S. Rozeveld, graduate student research assistant, 1986-89,  
G. J. Mahon, post doctoral research associate, 1986-88, and  
S. R. Singh, post doctoral research associate, 1989.

## **Effect of Crystal and Beam Tilt on Simulated High-Resolution TEM Images of Interfaces**

J. M. Howe and S. Rozeveld

Department of Metallurgical Engineering  
and Materials Science  
Carnegie Mellon University  
Pittsburgh, PA 15213

### **Abstract**

The effects of crystal and beam tilt on HRTEM images of planar, coherent interfaces were investigated by multislice image simulations. It was found that a beam tilt of 0.5 Bragg angle ( $\theta_B$ ) was sufficient to introduce detrimental artifacts into most images of interfaces in crystals only  $1/8 \lambda_{000}$  thick, while crystal tilt had a much smaller effect even for crystals  $1 \lambda_{000}$  thick. Effects produced in HRTEM images of interfaces by crystal and beam tilt included the introduction of additional periodicities and loss of compositional detail across a boundary, translation of a boundary from its actual position and apparent mismatch of atomic planes across a perfectly coherent interface. These results indicate that alignment of the electron beam parallel to the optic axis is critical for reliable HRTEM imaging of interfaces in materials. Techniques for obtaining accurate alignment are also discussed.

## 1. Introduction

It is well known that only a few milliradians of crystal or beam tilt can produce image artifacts in high-resolution transmission electron microscope (HRTEM) images of crystals [1-3]. This presents a significant challenge to the experimentalist, since crystal and beam tilt are two of the most difficult alignments that must be performed during HRTEM imaging [3-5].

One important application of HRTEM is determining the atomic structures of interfaces in materials [6-8]. While it is intuitive that alignment of an interface parallel to the electron beam will be critical for obtaining accurate atomic-resolution images of the interface, a systematic study of the effects of crystal and beam tilt on HRTEM images of interfaces has not been performed. In fact, only a few studies have examined the effects of crystal or beam tilt on HRTEM images of crystal defects [4,9,10].

In this investigation, the effects of crystal and beam tilt on HRTEM images of planar, coherent interfaces were determined using multislice image simulations [11-13]. Interfaces in metallic materials ranging from simple f.c.c. and b.c.c. twin boundaries to relatively complex interphase boundaries between ordered h.c.p. ( $\text{D0}_{19}$ ) and b.c.c. phases in the Ti-Al system were examined and compared. Although this study was limited to coherent interfaces in metallic systems, similar effects are expected to occur in



comparable nonmetallic systems such as semiconductors and ceramics and for less coherent interfaces.

## 2. Experimental Procedures

The HRTEM image simulations were performed using the TEMPAS multislice program [14] and assuming typical operating conditions for a JEOL 4000EX microscope, namely, accelerating voltage = 400 kV, spherical aberration coefficient = 1.0 mm, objective lens defocus = -50.0 nm (Scherzer defocus), semi-angle of beam convergence = 0.5 mrad, half-width of Gaussian spread of focus = - 8.0 nm and radius of objective aperture = 6.5 nm<sup>-1</sup>. Since relatively small unit-cell crystals were examined, the phase-grating slice thickness was taken as the interplanar spacing parallel to the electron-beam direction, for example, 0.286 nm along <110> in Al. All beams out to at least 40.0 nm<sup>-1</sup> were included in the multislice calculations.

The coherent interfaces that were examined in this study are described in Table 1. The elements used in this study ranged from Al (atomic number = 13) to Au (atomic number = 79) and six different interfaces between f.c.c., h.c.p. and b.c.c. crystals with ordered and disordered structures were examined in one or more orientations. The crystals and electron beam were tilted one first-order diffraction vector  $\mathbf{g}$  (the equivalent of two Bragg-angles or  $2\theta_B$ ) either parallel, normal or in combination (parallel plus normal tilts) to the interface plane (about 4-10 mrad for the structures

examined), and images were calculated at thicknesses of  $1/8$ ,  $1/4$ ,  $1/2$ ,  $3/4$  and  $1 \xi_{000}$ . Much smaller increments of tilt were used in

Table 1. Crystallography of the interfaces examined in this study [15-17].

Crystal Structures	Lattice Param. (nm)	Interface Plane	Beam Direction	$1 \xi_{000}$ (nm)	$2 \theta_B$ (mrad)
Twin Boundaries					(h, k)*
i) Al, Au (f.c.c.)	0.404, 0.407	{111}	<110>	24.5	7.2, 10.0
ii) TiAl (L1 <sub>0</sub> )	a=0.398, c=0.408	(1 $\bar{1}$ 1)	[110]	12.8	7.2, 10.0
iii) Ti (b.c.c.)	0.328	{112}	<110>	24.4	6.1, 8.7
Interphase Boundaries					
i) Al/Ag <sub>2</sub> Al (f.c.c./h.c.p.)	a=0.286, c=0.467	{111}Al	<110>	12.8	7.1, 10.9
ii) TiAl/Ti <sub>3</sub> Al (L1 <sub>0</sub> /D0 <sub>19</sub> )	a=0.577, c=0.463	(1 $\bar{1}$ 1)TiAl	[110]	12.8	7.2, 10.0
iii) Ti/Ti <sub>3</sub> Al (b.c.c./D0 <sub>19</sub> )	a=0.577, c=0.463	{112}Ti	<111>	32.0	3.6, 3.6
		{112}Ti	<110>	23.0	3.6, 5.7

\* The h and k represent tilts normal and parallel to the interface, respectively.

one case to more closely study the effects of beam tilt on image contrast. In addition, intensity profiles were taken across several interfaces to quantify the change in image contrast due to crystal

and beam tilt. This method was particularly useful for twinned interfaces to show changes in image symmetry.

### 3. Results

The effects of crystal and beam tilt on HRTEM images were found to be similar for all of the interfaces studied, so that these effects can be illustrated by considering only a few representative examples. The interface between the ordered phases TiAl and Ti<sub>3</sub>Al (L1<sub>0</sub> and D0<sub>19</sub>) is a good example for analysis since the crystallography is relatively simple and the phases are ordered. Therefore, this interface will be considered in detail, followed by comparison with several other interfaces.

#### 3.1. Effects of Crystal and Beam Tilt on the TiAl/Ti<sub>3</sub>Al Interface

As shown in Fig. 1(a), TiAl has an L1<sub>0</sub> (f.c.c. derivative) structure, which consists of alternate (002) planes of Ti and Al with Ti atoms at the positions 0,0,0 and  $\frac{1}{2}, \frac{1}{2}, 0$  and Al atoms at the positions  $\frac{1}{2}, 0, \frac{1}{2}$  and  $0, \frac{1}{2}, \frac{1}{2}$ . The (1 $\bar{1}$ 1) close-packed plane is indicated in the unit cell, and it is apparent that columns of atoms along the [110] direction in the (1 $\bar{1}$ 1) plane are alternately composed of Ti and Al. The Ti<sub>3</sub>Al phase shown in Fig. 1(b) has a D0<sub>19</sub> (ordered h.c.p.) structure, in which each Al atom is surrounded by six Ti nearest neighbors in the basal plane. A planar interface is formed when the basal plane (0001) of the D0<sub>19</sub> structure abuts the close-

packed  $(1\bar{1}1)$  plane of the  $L1_0$  structure with the following orientation relationship between the phases  $(1\bar{1}1)\text{TiAl}||(\text{0001})\text{Ti}_3\text{Al}$  and  $[110]\text{TiAl}||\langle 11\bar{2}0 \rangle\text{Ti}_3\text{Al}$  [18]. When the interface is viewed edge-on along the  $[110]\text{TiAl}||\langle 11\bar{2}0 \rangle\text{Ti}_3\text{Al}$  direction, alternate columns of atoms in each basal plane have the composition Ti and Ti-50at.%Al (Fig. 1(c)).

### 3.1.1. Crystal Tilt

The effect of crystal tilt on HRTEM images of the  $\text{TiAl}/\text{Ti}_3\text{Al}$  interface is illustrated by the series of images shown in Fig. 2. The projected potential of the interface is shown in Fig. 2(a) with the interface plane indicated by a solid line, as in Fig. 1(c). The Ti-rich columns in  $\text{TiAl}$  and  $\text{Ti}_3\text{Al}$  can be distinguished by the brighter spots (larger charge density) in the projected potential. The remaining images in Fig. 2(a) illustrate the variation in image contrast without crystal tilt for sample thicknesses of  $1/4$ ,  $1/2$ ,  $3/4$  and  $1 \xi_{000}$ , where  $1 \xi_{000} = 12.8 \text{ nm}$ . Figure 2(b) shows images at the same thicknesses (including  $1/8 \xi_{000}$ ) with a crystal tilt of one first-order diffraction vector  $\mathbf{g}$  or two Bragg-angles ( $2\theta_B$ ) in the plane of the interface, where  $2\theta_B = 10.0 \text{ mrad}$ . A similar series of images for a crystal tilt of two Bragg-angles ( $2\theta_B = 7.2 \text{ mrad}$ ) normal to the interface plane is shown in the third row in Fig. 2(c), and Fig. 2(d) shows images taken for the combined tilts of  $2\theta_B$  parallel and normal to the interface plane. From these images it is evident that a crystal tilt of  $2\theta_B$  either parallel or normal to the interface does not produce a noticeable effect on the image contrast for a crystal

less than  $1/2 \xi_{000}$  thick. However, at a thickness of  $1/2 \xi_{000}$ , there are definite effects in the images, which becomes more pronounced as the thickness increases. The main effects produced are additional periodicities along the  $(1\bar{1}1)$  planes in TiAl as well as among the  $(0001)$  planes in  $\text{Ti}_3\text{Al}$ . These effects tend to mask but not eliminate the actual ordering of the  $(002)$  planes in TiAl and the  $(10\bar{1}0)$  planes in  $\text{Ti}_3\text{Al}$ . The image is more distorted when the crystal is tilted at an angle to the interface ( $2\theta_B$  both parallel and normal to the interface) in Fig. 2(d) than when it is tilted only parallel or normal by about the same angle in Figs. 2(b) or (c), respectively. In some cases, the combined tilt almost completely obscures the compositional order present in the TiAl and  $\text{Ti}_3\text{Al}$  phases. Such degradation does not occur for either parallel or normal tilts alone.

### 3.1.2. Beam Tilt

The effects of the same amount of beam tilt on the same interface are illustrated in Fig. 3. From this series of images it is evident that beam tilts of  $2\theta_B$  either parallel or normal to the interface (Figs. 3(b) and (c), respectively) produce large changes in image contrast even for a crystal thickness of only  $1/8 \xi_{000}$ , or 1.6 nm. In particular, the compositional order in  $\text{Ti}_3\text{Al}$  is *unrecognizable* at  $1/8 \xi_{000}$  thickness and the compositional order in TiAl, which usually produces strong contrast on alternate  $(002)$  planes, is completely absent for a thickness of  $1/4 \xi_{000}$  with normal and angular tilts. These effects increase with thickness such that the

image becomes almost unrecognizable for thicknesses greater than  $1/2 \xi_{000}$ . The effect of a combined tilt to the interface in Fig. 3(d) is also more severe than tilting either parallel or normal to it, similar to crystal tilt. This is apparent from the image at  $1/4 \xi_{000}$  in Fig. 3(d), in which there is no evidence of order within either phase and the interface is completely obscured. Therefore, comparison between Figs. 2 and 3 demonstrates that beam tilt has a more deleterious effect on image contrast of interfaces than crystal tilt, particularly for thin crystals. This is consistent with results obtained from analyses of the effects of crystal and beam tilt on images from single crystal materials [3].

Several other interesting effects occur in  $\text{Ti}_3\text{Al}$  and at the interface as the beam is tilted off the optic axis. Specifically, a bright/dark contrast develops among alternate (0002) planes in the  $\text{Ti}_3\text{Al}$  phase for beam tilts parallel to the interface plane for sample thicknesses greater than about  $1/8 \xi_{000}$ . Such contrast could be mistakenly interpreted as indication of additional long-range compositional order among alternate basal planes [3,19], i.e., bright and dark (0002) planes might indicate Al-rich and Ti-rich layers, respectively. However, this contrast is an imaging artifact that results from additional phase shifts which are produced in the diffracted beams when the incident beam is tilted off the optic axis, combined with multiple scattering that transfers intensity into the kinematically forbidden  $000\ell$ ,  $\ell=\text{odd}$  reflections [2]. These effects readily displace bright atom positions in an image from their actual sites in the crystal. Such contrast is considerably less

prominent for crystal tilt since the objective lens does not introduce additional phase shifts preferentially into certain diffracted beams in this case. It is also important to note that the position of the interface appears to translate from its actual position to that indicated by a solid line one or two planes down for a beam tilt of  $2\theta_B$  normal to the interface at  $1/4$  and  $1/8 \xi_{000}$  in Fig. 3(c). Therefore, a beam tilt of  $2\theta_B$  could cause the position of the interface to be incorrectly located in an image. It is also important to note that the interface remained completely coherent regardless of the crystal or beam tilts employed in this study.

A final set of images for the TiAl/Ti<sub>3</sub>Al interface is shown in Fig. 4. These images of the interface, at  $1/8 \xi_{000}$  thickness for beam-tilt increments of  $0.17\theta_B$  parallel (Fig. 4(a)) and normal (Fig. 4(b)) to the interface, demonstrate the effects of small beam tilts on the interface contrast. Examination of the images shows that a tilt of  $0.5\theta_B$  either normal or parallel to the interface ( $\sim 1.5$ - $2.5$  mrad, respectively) is sufficient to largely mask the image characteristics except for the fact that the atom positions remain dark on a bright background. Almost all of the contrast due to order in TiAl and Ti<sub>3</sub>Al is gone and additional contrast appears among alternate basal planes in Ti<sub>3</sub>Al, as discussed above. Further examination of the smallest tilts normal and parallel to the beam (which represent about  $0.6$ - $0.8$  mrad, respectively) show that the image contrast is slightly altered, although this amount of tilt would probably not complicate an analysis of the interface. Also note that beam tilts parallel to the interface produce bright/dark

contrast on alternate (0002) planes while those normal to it mask the (10 $\bar{1}$ 0) contrast in Ti<sub>3</sub>Al. Although it is not shown here, tilts normal to the interface generally produced more severe effects on image contrast than those parallel to it. A tilt of about  $1.5\theta_B$  was sufficient to cause the interface to move down into Ti<sub>3</sub>Al at  $1\frac{1}{2}\lambda_{000}$  thickness, similar to the effects in Fig. 3(c).

### 3.2. Effect of Crystal Tilt on b.c.c./D0<sub>19</sub> Interface

Figure 5 shows the Ti/Ti<sub>3</sub>Al interface viewed edge-on along a  $[111]_{\text{Ti}}||[11\bar{2}0]_{\text{Ti}_3\text{Al}}$  direction with an interface plane of  $[\bar{1}\bar{1}2]_{\text{Ti}}||(\bar{1}\bar{1}00)_{\text{Ti}_3\text{Al}}$ . An image without tilt is shown in Fig. 5(a), with the actual atom positions represented as bright spots. The image in Fig. 5(b) was included because a crystal tilt of  $2\theta_B$  parallel to the interface produced a displacement between the (110)<sub>Ti</sub>|(0002)<sub>Ti<sub>3</sub>Al</sub> planes which lie normal to the interface, for crystals greater than  $\frac{3}{8}\lambda_{000}$  thickness. This effect is illustrated in Fig. 5(b) by the mismatch of the straight lines superimposed on these planes. Such distortion of planes across the interface could be misinterpreted in an analysis of an experimental image as indicative of coherency strains or a rigid-body displacement, although it is entirely an artifact due to crystal tilt. It should be emphasized that even though such interface distortion has been observed in these studies, a loss of coherency was never observed for the range of tilts employed. The image in Fig. 5(c) illustrates the strong bright/dark contrast that was produced among alternate (0002)



planes in  $\text{Ti}_3\text{Al}$  for a beam tilt of  $0.4\theta_B$  normal to this interface at  $1/4 \xi_{000}$  thickness.

### 3.3. Effect of Crystal and Beam Tilt on a b.c.c. Twin Boundary

Since crystal and beam tilt produce similar changes in image contrast for twin boundaries and because the effects are also similar in magnitude with those for the  $\text{TiAl}/\text{Ti}_3\text{Al}$  interface discussed previously, only the effect of crystal tilt on the twin boundary in b.c.c. Ti is examined below.

Figure 6 shows four images of a  $\{111\}$  twin boundary in Ti, including corresponding intensity profiles across the atom positions near the center of the image (line in Fig. 6(a)), perpendicular to the twin boundary. The images are at  $1/2 \xi_{000}$  thickness, or 12.2 nm. At this thickness, crystal tilts of  $2\theta_B$  either parallel (Fig. 2(b)), normal (Fig. 2(c)) or in combination (Fig. 2(d)) to the interface produced characteristic effects in images of the twin. For example, crystal tilt parallel to the twin plane did not cause a loss of mirror symmetry across the twin in Fig. 6(b), although the image characteristics changed with this amount of tilt. The mirror symmetry is evident from the intensity profile in Fig. 6(b). On the other hand, similar tilts normal or at an angle to the twin plane caused a loss of mirror symmetry in the images. This effect was most pronounced for a combined tilt to the interface in Fig. 6(d), where the image and intensity profile were very different across the

interface. In addition, a translation of the twin boundary with crystal tilt normal to the interface is readily visible from the intensity profile in Fig. 6(c). Therefore, asymmetry in twin images and translation of the boundary from its actual position are possible artifacts that can be produced by a crystal tilt on the order of  $2\theta_B$ . As for the TiAl/Ti<sub>3</sub>Al interface above, these effects were even more apparent for small beam tilts about the interface.

#### 4. Discussion

The previous results demonstrate that crystal and beam tilt produce deleterious effects on HRTEM images of interfaces. In particular, alignment of the electron beam to within about 1.0 mrad or  $0.5\theta_B$  of the optic axis is necessary for reliable interpretation of the interface structure, particularly in ordered structures. Therefore, in addition to the stringent requirements imposed by specimen thickness, objective lens defocus and astigmatism correction, crystal and beam tilt can readily limit the resolution in HRTEM images of interfaces in materials. Although the effects of crystal and beam tilt can be included in image calculations for comparison with experimental images [20], it is more desirable to eliminate these effects prior to imaging of an interface. While a number of different techniques for crystal and beam alignment have been suggested in the literature [1,2], several are readily applied in practice, and these are discussed briefly below.

In the case of crystal tilt, it is often not sufficient to judge the crystal alignment from the intensities of spots in a selected-area diffraction pattern or convergent-beam electron diffraction (CBED) pattern. In theory, it is possible to use the symmetry information provided by broad intensity fringes in CBED disks to obtain precise crystal alignment. However, in practice, if the crystal displays such intensity fringes it is probably too thick for HRTEM imaging. One technique that can be useful for crystal alignment, particularly in metallic specimens which are prone to bending, is to center the zone axis produced by bend contours in the image mode directly on the area of interest. Even though it is sometimes difficult to manipulate the bend contours very near the foil edge, this technique often allows accurate crystal alignment to be obtained in the image mode and it can be applied to interfaces in practice.

Another useful technique that can be applied to interfaces, is to examine the symmetry of reflex images of the interface at high magnification as the objective lens is defocused [21]. When the crystal and beam are precisely aligned, the reflex images of the interface expand symmetrically about the bright-field image of the interface as the objective lens is defocused. While there is a dependence of the reflex images on astigmatism in addition to crystal and beam tilt, sufficiently accurate alignment of the specimen and microscope can be obtained by several successive iterations of crystal and beam alignment and astigmatism

correction. Asymmetric reflex images provide a definite indication that one or more of these parameters requires adjustment.

Due to the interplay among astigmatism, crystal and beam alignment in reflex images, it is desirable to have an independent method of aligning the beam. One of the most convenient techniques for obtaining the required accuracy in alignment is to apply equal and opposite tilts to the incident beam and compare the resulting images of an amorphous region at the foil edge [1,2]. The average beam tilts can be adjusted in the image mode at successively higher magnification until the same image appearance is produced at diametrically opposite tilts. This technique is applied after having corrected the voltage center by wobbling the high voltage and accuracies of a few tenths of a milliradian can be obtained in practice. Again, several successive iterations of this technique combined with astigmatism correction are usually required to obtain an accurate alignment.

One interesting artifact due to beam (and crystal) tilt was the loss of mirror symmetry across the interface. This was particularly evident for the case of twin boundaries with the beam tilted at an angle to the interface plane. The reason for this effect has been discussed in detail [2] and can be envisioned simply by comparing the effect of a crystal or beam tilt on the final symmetry of a CBED pattern with initial  $m\bar{m}$  symmetry [22]. This effect increased in severity with specimen thickness, amount of tilt and degree of order in the component crystals, and is analogous in most respects to

effects observed in single-crystal materials [2-5]. Therefore, it appears that HRTEM imaging of interfaces requires essentially the same accuracy of alignment as HRTEM imaging of single crystals. This imposes relatively stringent experimental requirements in terms of both crystal and beam tilt in order to obtain readily interpretable images.

## 5. Conclusions

A study of the effects of crystal and beam tilt on HRTEM images of planar, coherent interfaces was performed. The results of this study showed that:

- (1) A crystal tilt of  $2\theta_B$  parallel or normal to an interface does not produce a significant change in the interface contrast for samples less than  $1/2 \xi_{000}$  thick, although it will substantially alter the contrast for thicker samples.
- (2) A beam tilt of only  $0.5\theta_B$  parallel or normal to an interface will produce a major change in image contrast even for samples only  $1/8 \xi_{000}$  thick.
- (3) Beam tilt will introduce additional periodicities in ordered structures but this is not observed in disordered crystals.

- (4) Crystal or beam tilts with components both parallel and normal to the interface plane have the most detrimental effect on image contrast of an interface.
- (5) Effects of crystal and beam tilt on images of interfaces include the introduction of additional periodicities and loss of compositional detail across a boundary, translation of a boundary from its actual position and the creation of displacements across perfectly coherent interfaces.

### **Acknowledgements**

This research was supported by the Air Force Office of Scientific Research under Contract No. F49620-87-C-0017 and by the National Science Foundation under Grant Nos. DMR-8610439 and MSM-8714377.

### **References**

1. F. Zemlin, K. Weiss, P. Schiske, W. Kunath and K.-H. Herrmann, *Ultramicroscopy*, **3** (1978) 49.
2. D. J. Smith, W. O. Saxton, M. A. O'Keefe, G. J. Wood and W. M. Stobbs, *Ultramicroscopy*, **11** (1983) 263.
3. D. J. Smith, L. A. Bursill and G. J. Wood, *Ultramicroscopy*, **16** (1985) 19.

4. D. J. Smith, R. A. Camps, L. A. Freeman, M. A. O'Keefe, W. O. Saxton and G. J. Wood, *Ultramicroscopy*, **18** (1985) 63.
5. P. G. Self, R. W. Glaisher and A. E. C. Spargo, *Ultramicroscopy*, **18** (1985) 49.
6. J. M. Howe and G. J. Mahon, *Ultramicroscopy*, **30** (1989) 132.
7. J. M. Penisson and G. Regheere, *Mat. Sci. and Eng.*, **A107** (1989) 199.
8. A. Bourret, in *Mat. Res. Soc. Symp. Proc. Vol. 138*, B. C. Larson, M. Ruhle and D. N. Seidman, Eds., Materials Research Society, PA, p. 293 (1989).
9. A. Bourret, J. Desseaux and A. Renault, *Philos. Mag. A*, **45**(1) (1982) 1.
10. G. R. Anstis and D. J. H. Cockayne, *Acta Cryst.*, **A35** (1979) 511.
11. J. M. Cowley and A. F. Moodie, *Acta Cryst.*, **10** (1957) 609.
12. P. Goodman and A. F. Moodie, *Acta Cryst.*, **A30** (1974) 280.
13. M. A. O'Keefe and P. R. Buseck, *Trans. Amer. Cryst. Assoc.*, **15** (1979) 27.
14. R. Kilaas, in *Proc. 45th Annual Meeting Electron Micros. Soc. Amer.*, G. W. Bailey, Ed., San Francisco Press, CA, p. 66 (1987).
15. P. Duwez and J. L. Taylor, *J. Metals*, **Jan.** (1952) 70.
16. J. M. Howe, U. Dahmen and R. Gronsky, *Philos. Mag. A*, **56**(1) (1987) 31.

17. A. J. Goldak and J. Gordan Parr, *Trans. Met. Soc. AIME*, **221** (1961) 639.
18. D. Shechtman, M. J. Blackburn and H. A. Lipsitt, *Metall. Trans. A*, **5** (1974) 1373.
19. A. F. Moodie and H. J. Whitfield, *Ultramicroscopy*, **13** (1984) 265.
20. G. J. Mahon and J. M. Howe, *Metall. Trans. A*, in press.
21. K. Heinemann, *Optik*, **34** (1971) 113.
22. P. Goodman and H. J. Whitfield, *Acta Cryst.*, **A36** (1980) 219.



### Figure Captions

**Figure. 1.** The crystal structures of (a) TiAl, (b) Ti<sub>3</sub>Al and (c) the TiAl/Ti<sub>3</sub>Al interface [15,17,20].

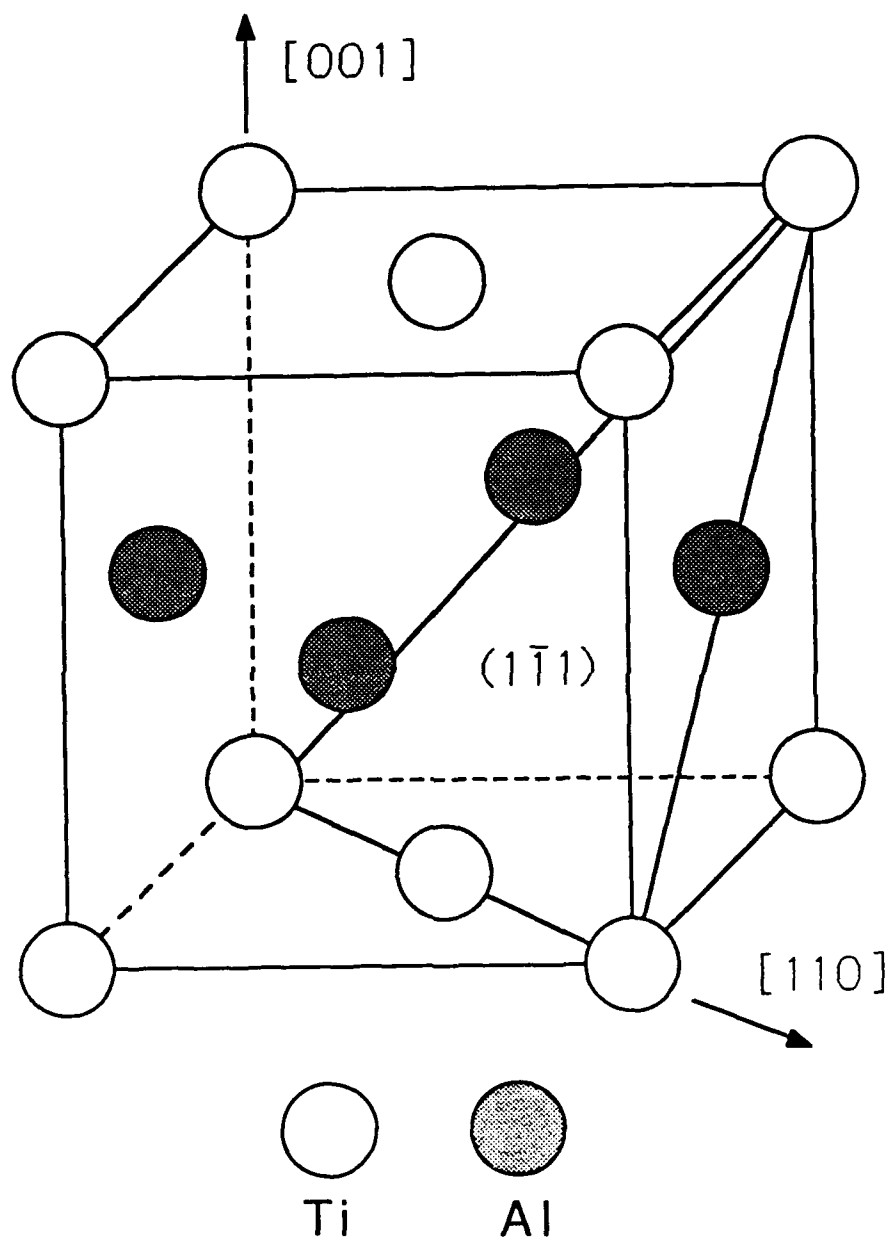
**Figure 2.** (a-d) Crystal tilt versus thickness for HRTEM images of the TiAl/Ti<sub>3</sub>Al interface, with  $1 \xi_{000} = 12.8 \text{ nm}$ .

**Figure 3.** (a-d) Beam tilt versus thickness for HRTEM images of the TiAl/Ti<sub>3</sub>Al interface, with  $1 \xi_{000} = 12.8 \text{ nm}$ .

**Figure 4.** Effect of small beam tilts (a) parallel and (b) normal to the interface plane on HRTEM images of the TiAl/Ti<sub>3</sub>Al interface for a crystal  $1/8 \xi_{000}$  thick.

**Figure 5.** High-resolution TEM images of a Ti/Ti<sub>3</sub>Al interface for a crystal (a)  $1/4 \xi_{000}$  thick without tilt, (b)  $1/2 \xi_{000}$  thick with crystal tilt, and (c)  $1/4 \xi_{000}$  thick with beam tilt.

**Figure 6.** (a-d) Effect of crystal tilt on HRTEM images of a twin boundary in Ti, with  $1 \xi_{000} = 12.2 \text{ nm}$ .

*Fig. 1(a)*

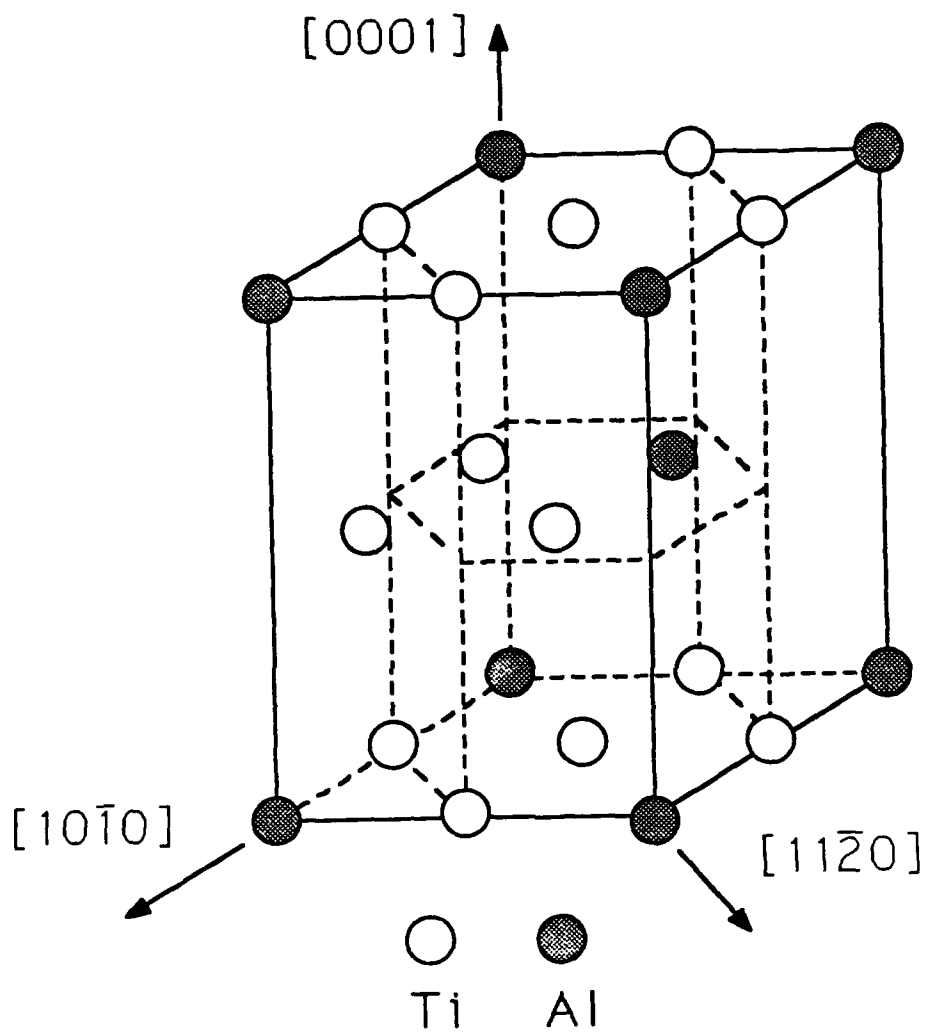


Fig. 1(b)

Crystal Tilt (2°)

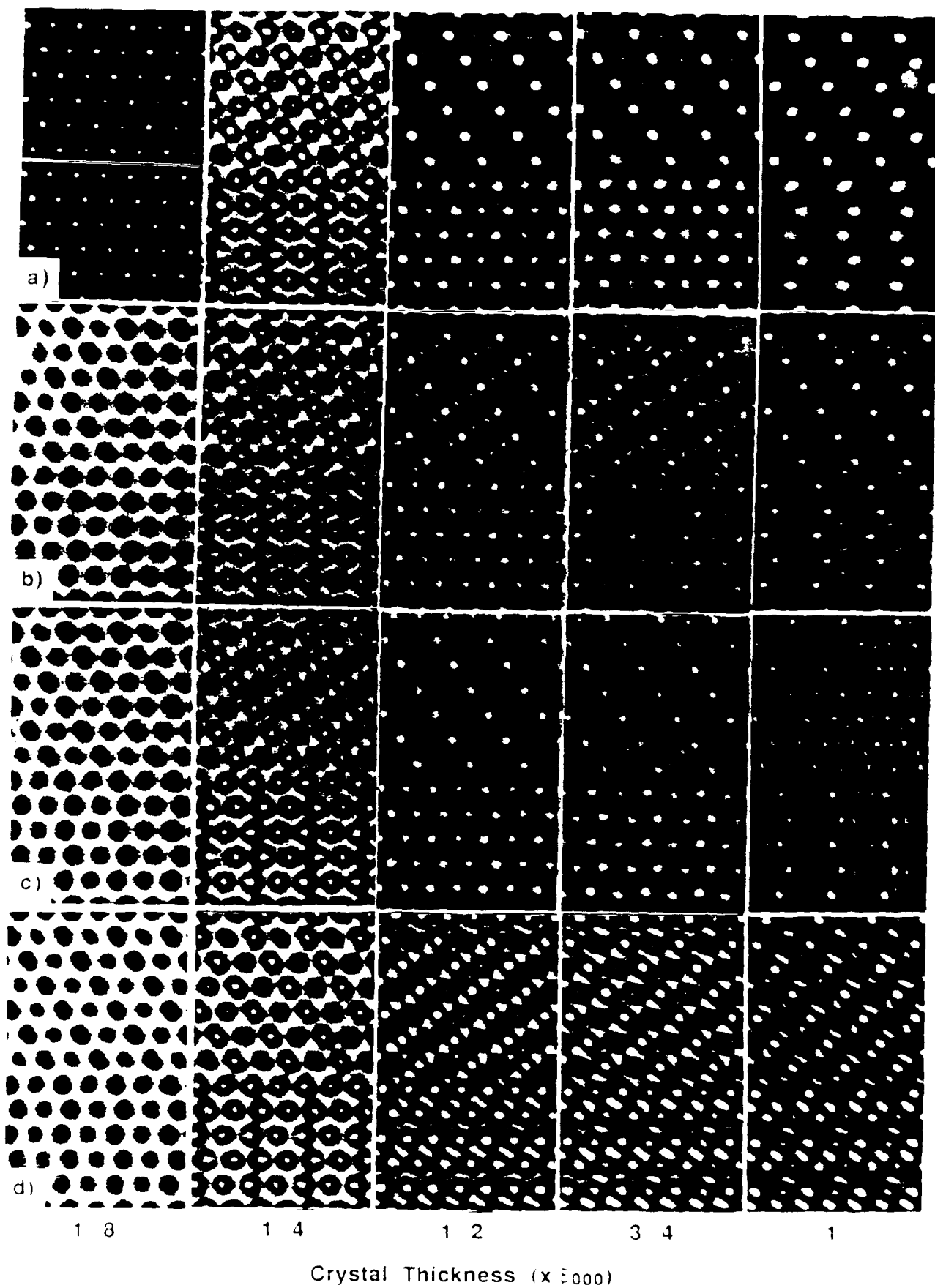


Fig-2

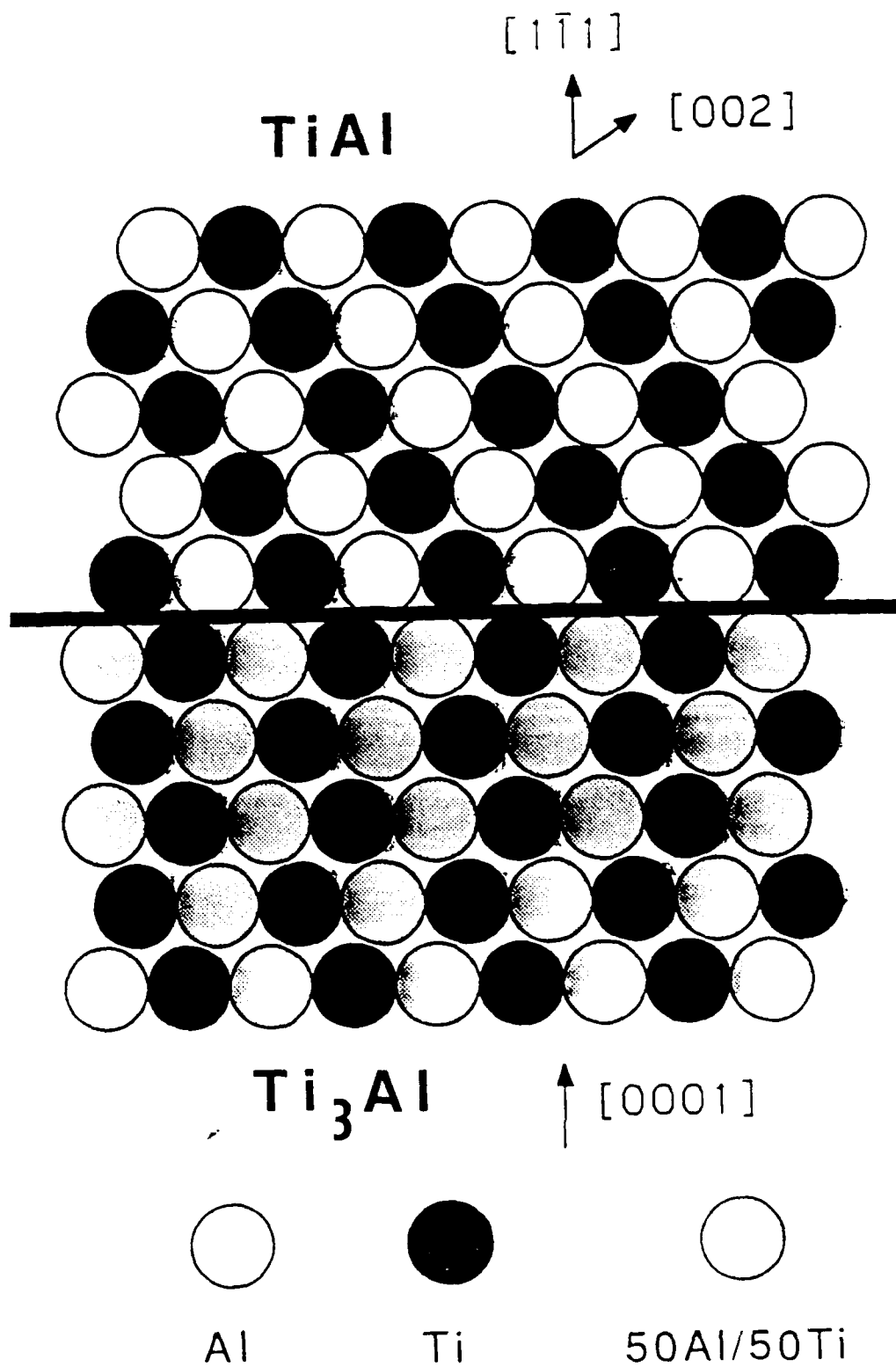


Fig. 1(c)

Beam Tilt ( $2\theta_B$ )

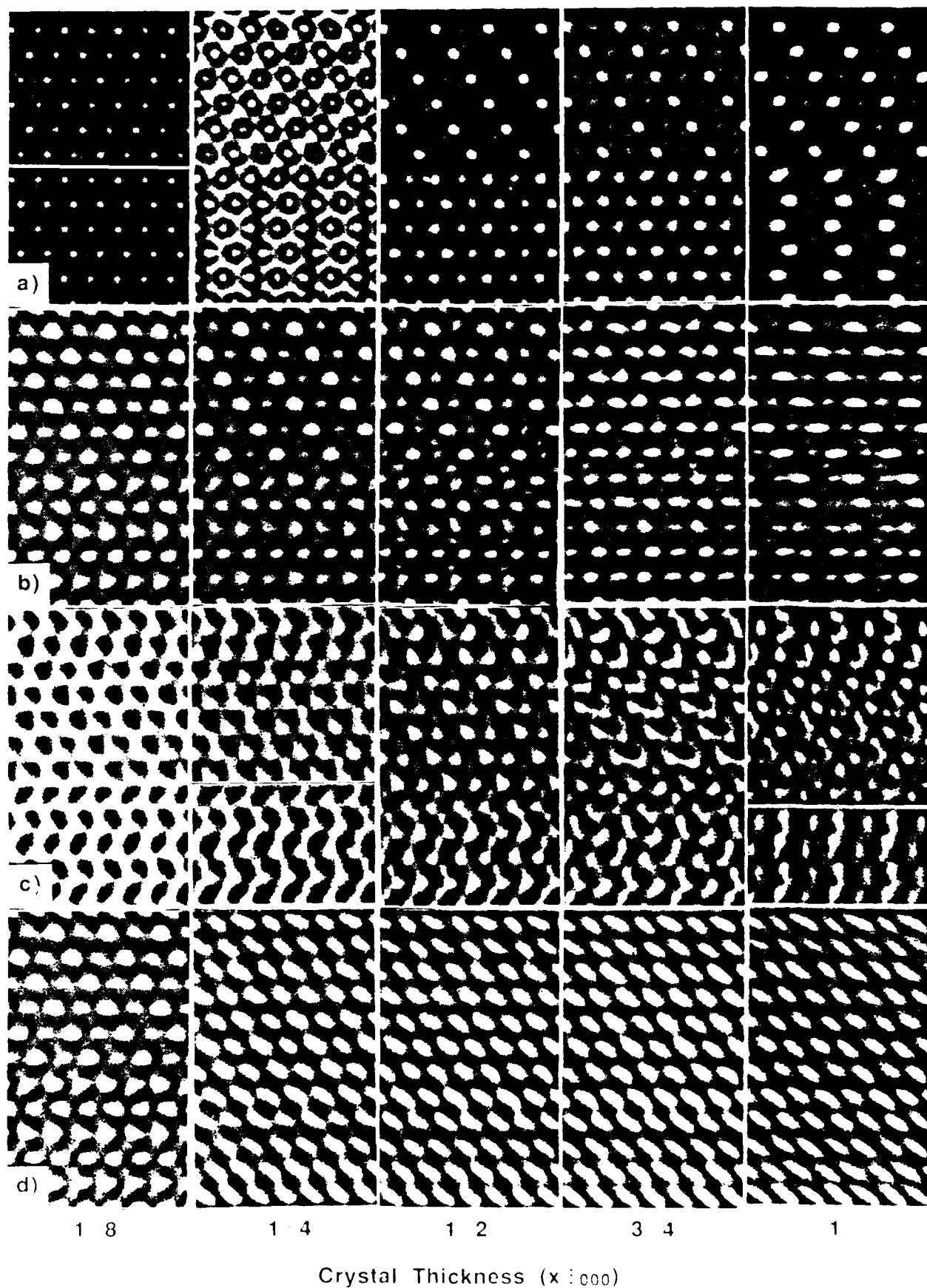
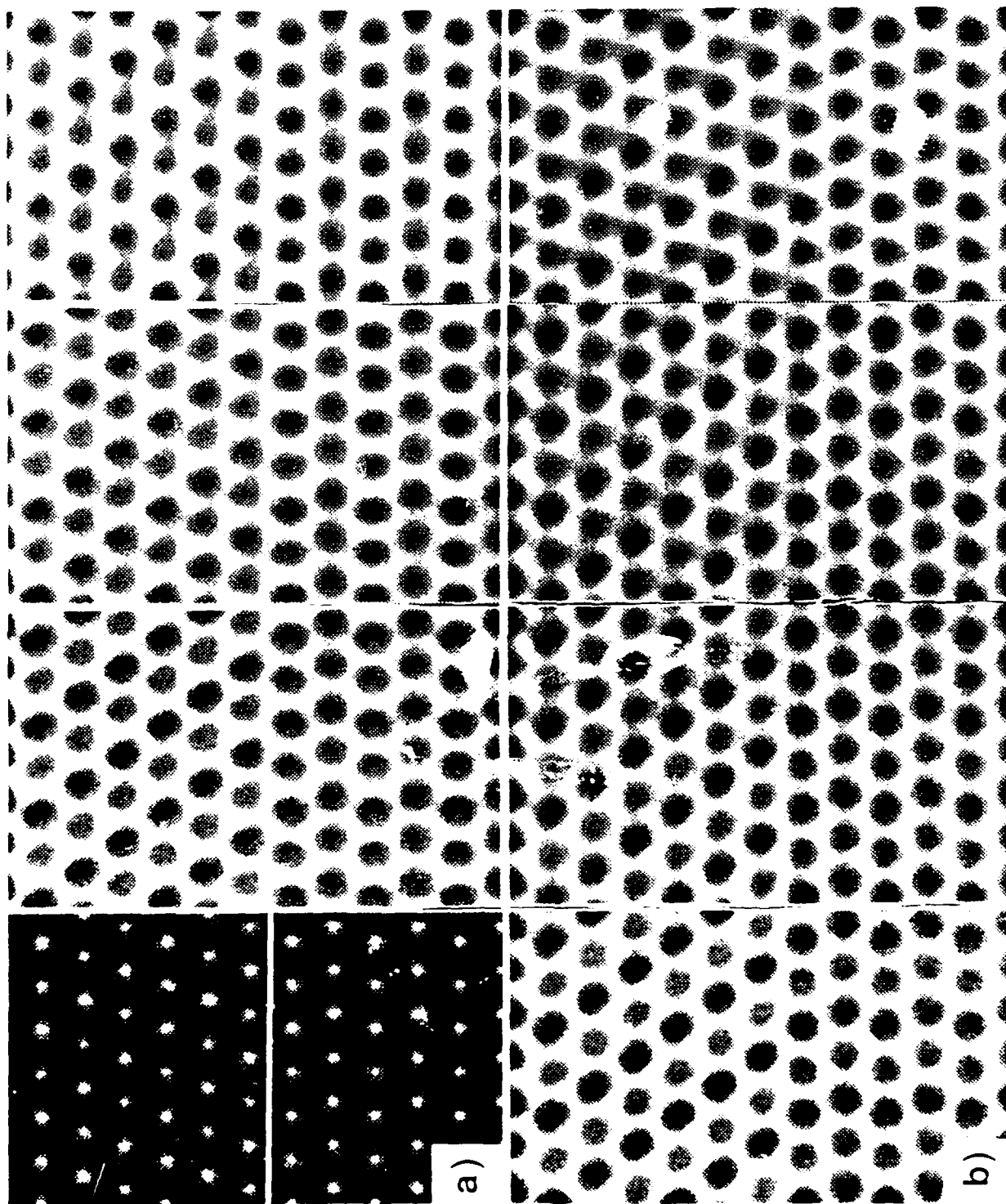


Fig. 3



4

3

2

1

Beam Tilt ( $\times 1/6 \theta_B$ )

Fig. 4

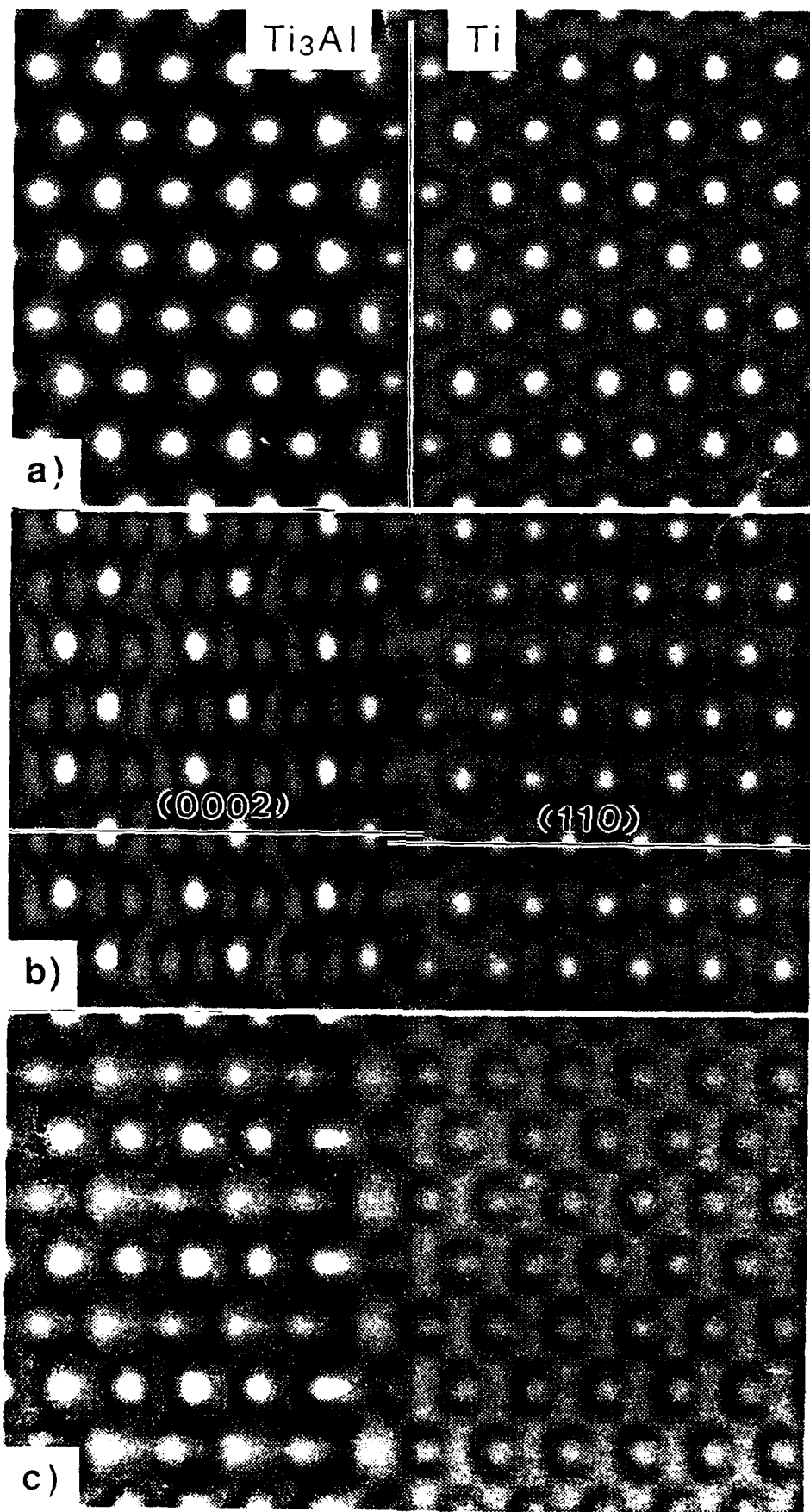


Fig 5



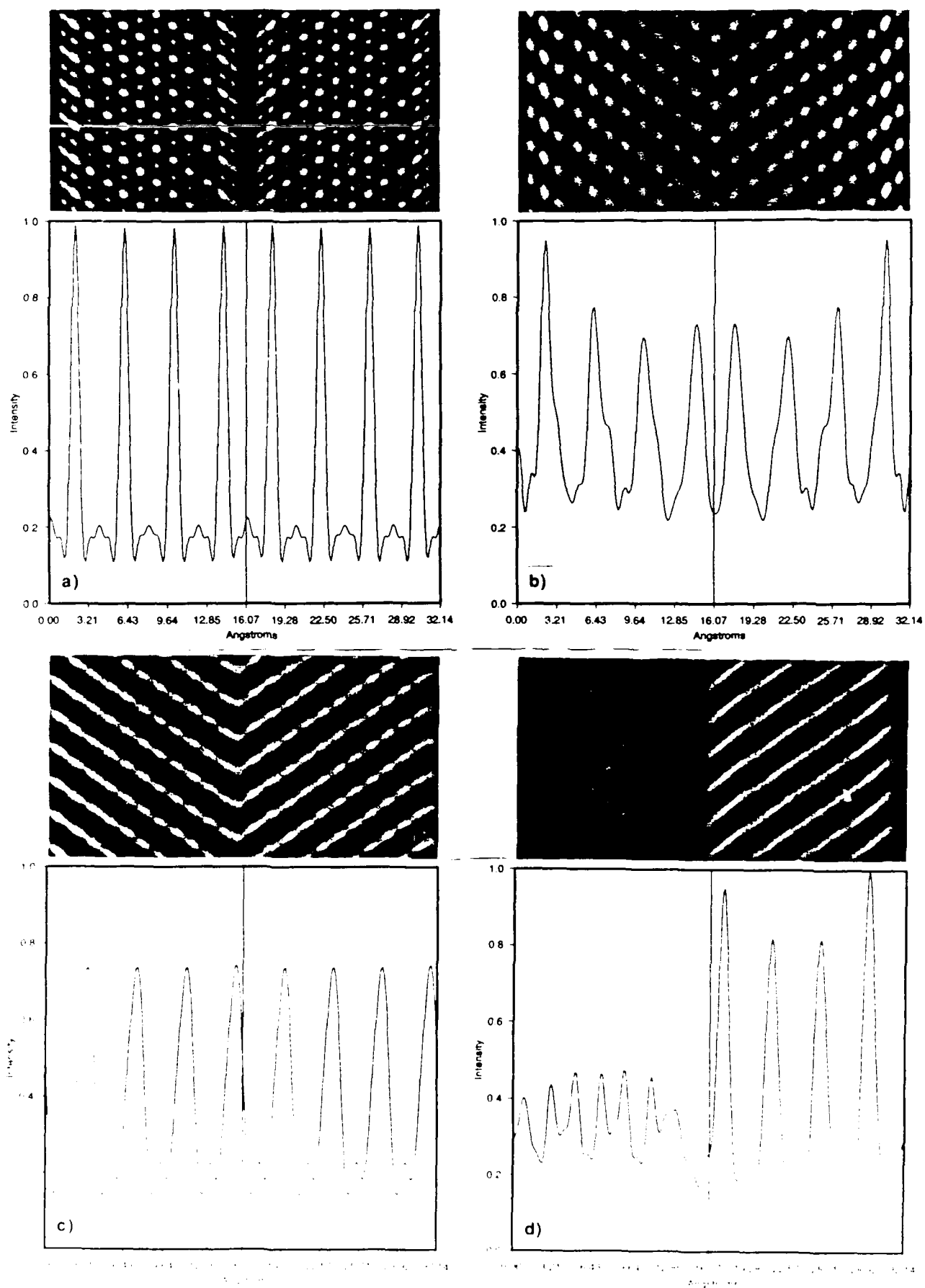


Fig. 6

**PART 3**

**PROPERTIES and PERFORMANCE**

BLANK

## PROPERTIES AND PERFORMANCE

This third section of the Annual Report includes three tasks in the topic area of Properties and Performance. The first of these tasks, entitled "Toughness and Fatigue of Metal Matrix Composites", was conducted at the University of California at Berkeley under the direction of R.O. Ritchie. The experimental work in this task focused on aluminum-matrix materials with particulate reinforcement, regarded as model materials for high-temperature particulate composites. The second task in this section was carried out at Carnegie Mellon University. Entitled "Micromechanisms of High Temperature Composite Behavior", it was directed by A.W. Thompson and (until his departure from Carnegie Mellon in August, 1988) by J.C. Williams. The task concentrated on high temperature properties of titanium aluminide alloys which are expected to be matrix materials for advanced composites. The third task here, also at Carnegie Mellon, had the topic "Thermal and Mechanical History Effects on Composite Properties", and its investigator was W.M. Garrison. A series of Ti-Al-Nb alloys was evaluated for thermal and mechanical stability of both microstructure and mechanical properties, with particular emphasis on the mechanical properties resulting from a variety of histories. Fracture studies on SiC-reinforced aluminum alloys were also conducted. The individual report sections are as follows.

	<u>Page</u>
<b>Task 4</b>	
"Toughness and Fatigue of Metal Matrix Composites", R.O. Ritchie and J.-K. Shang	223
<b>Task 5</b>	
"Creep of High Temperature Composite Matrices", A.W. Thompson	281
<b>Task 6</b>	
"Fracture and History Effects in Composites", D. Symons and W.M. Garrison	325

BLANK

## TASK 4

### FATIGUE OF METAL-MATRIX COMPOSITES

R. O. Ritchie and J.-K. Shang

Department of Materials Science and Mineral Engineering  
University of California, Berkeley, CA 94720

The objective of this task was to identify micromechanisms associated with subcritical crack advance in metal-matrix composites, at ambient temperatures, with particular emphasis on mechanisms affecting fatigue-crack propagation.

Work was focused on characterizing the fatigue resistance (in the presence of long through-thickness cracks) of model particulate-reinforced metallic materials, specifically P/M aluminum alloys reinforced with silicon-carbide particles, with the aim of defining and modelling the role of the reinforcement phase in promoting or impeding cyclic crack extension. Based on a comparison of an unreinforced 9Zn-2+Cu-3Mg aluminum alloy with the same alloy reinforced with 15 or 25 vol.% of either fine (5  $\mu\text{m}$ ) or coarse (16  $\mu\text{m}$ ) SiC particulate (Al/SiC<sub>p</sub>), three separate regimes were identified where behavior in the monolithic and composite alloys are distinctly different and are controlled by specific crack-tip shielding mechanisms.

At high growth rates typically exceeding  $10^{-6}$  m/cycle, fatigue-crack growth rates in the composites were found to be far in excess of those at comparable stress-intensity levels in the unreinforced alloys; this, however, resulted from the much lower fracture-toughness  $K_{Ic}$  values of the composite materials which caused accelerated growth rates as  $K_{max}$  approaches  $K_{Ic}$ .

At intermediate growth rates typically between  $10^{-9}$  and  $10^{-7}$  m/cycle, the composite alloys were observed to show improved fatigue resistance compared to the unreinforced matrix. In this regime, the crack alternatively seeks out "eligible" particles within the plastic zone, leading to limited SiC fracture *ahead* of the crack tip. Although this process tends to accelerate crack advance, the coalescence of these microcracks with the main crack tip additionally leads to the creation of uncracked ligaments *behind* the crack tip, which act to bridge the crack. By modelling the effect of the bridges in terms of a critical crack-opening displacement of critical strain in the ligaments, the degree of crack-tip shielding induced by such crack bridging was computed and shown to be consistent with experiment.

Similarly at near-threshold levels below typically  $10^{-9}$  m/cycle, the composite materials generally were found to show improved fatigue resistance, particularly with the coarser particle distributions, only now due primarily to crack trapping (hindrance of the crack front) and roughness-induced crack closure (crack wedging by fracture-surface asperities) which result from the tendency of the crack path to avoid the SiC particles. By computing the reduction in crack-tip stresses due to the presence of a SiC particle at the tip, a limiting condition for the fatigue threshold in the composite alloys was derived based on the criterion that the *local* tensile stress in the matrix *beyond the particle* must exceed the yield strength  $\sigma_y$  of the material; this implies that the fatigue threshold should be given by  $K_{\max, TH} \propto \sigma_y \sqrt{D_p}$ , where  $D_p$  is the mean particle size, in agreement with experimental measurement.

### Refereed Journals

1. Jianku Shang, W. Yu and R. O. Ritchie: "Role of Silicon-Carbide Particles in Fatigue Crack Growth in SiC-Particulate-Reinforced Aluminum Alloy Composites," Materials Science and Engineering, vol. 102A, 1988, pp. 181-192.
2. Jianku Shang and R. O. Ritchie: "Crack Bridging by Uncracked Ligaments during Fatigue-Crack Growth in SiC-Reinforced Aluminum-Alloy Composites," Metallurgical Transactions A, vol. 20A, May 1989, pp. 897-908.
3. Jianku Shang and R. O. Ritchie: "On the Particle-Size Dependence of Fatigue-Crack Propagation Thresholds in SiC-Particulate-Reinforced Aluminum-Alloy Composites: Role of Crack Closure and Crack Trapping," Acta Metallurgica, vol. 37, Aug. 1989, pp. 2267-2278.

### Refereed Conference Proceedings

4. Jianku Shang and R. O. Ritchie: "Crack-Tip Shielding in Metal-Matrix Composites: Modelling of Crack Bridging by Uncracked Ligaments," in High Temperature/High Performance Composites, MRS Symposium Proceedings, vol. 120, Materials Research Society, Pittsburgh, PA, 1988, pp. 81-87.
5. J.-K. Shang and R. O. Ritchie: "Mechanisms Associated with Near-Threshold Fatigue-Crack Propagation in SiC-Particulate Reinforced Aluminum Composites," in Proceedings of the Seventh Intl. Conf. on Composite Materials (ICCM-7), Canton, China, 1989.

### Book Chapters (Refereed)

6. Jian Ku Shang and R. O. Ritchie, "Fatigue of Discontinuously-Reinforced Metal-Matrix Composites," in Metal Matrix Composites, R. J. Arsenault and R. K. Everett, eds., Academic Press, Boston, MA, 1989.

### Invited Presentations

7. R. O. Ritchie: "Ductile Matrix Composites: Fracture and Fatigue," invited presentation at the 1988 Annual Winter Workshop on Composite Materials, University of California, Santa Barbara, CA, Jan. 1988.
8. R. O. Ritchie: "Toughening Mechanisms in Composite Materials," invited keynote lecture, Topical Symp. on Micromechanisms of Fracture in Metal Matrix Composites, 117th TMS Annual Meeting, Phoenix, AZ, Jan. 1988.
9. R. O. Ritchie: "Fracture and Fatigue-Crack Propagation in Advanced Materials," Seminar to the Department of Materials Science and Metallurgy, Cambridge University, Cambridge, U.K., May 1988.



10. R. O. Ritchie: "Fracture and Fatigue Crack Propagation in Ceramics and Metal-Matrix Composites," invited seminar to the Research Institute of Industrial Science and Technology, Pohang, Korea, May 1988.
11. R. O. Ritchie: "Fatigue and Fracture Studies on Advanced Materials," invited seminar to the Metallurgical Engineering and Mechanical Engineering Departments, Tokyo Institute of Technology, Midoriku, Tokyo, Japan, June 1988.
12. R. O. Ritchie: "Kinetics of Crack Growth in Advanced High-Temperature Materials," invited presentation to the Gordon Conference on *High Temperature Chemistry*, Plymouth, NY, July 1988.
13. J.-K. Shang, W. Yu and R. O. Ritchie: "Fatigue Crack Growth in Particulate and Laminate Reinforced Aluminum-Alloy Composites," invited presentation to Topical Symposium on *Mechanical Behavior of Advanced Composites*, TMS Fall Meeting, Chicago, IL, Sept. 1988.
14. R. O. Ritchie, "Studies of Fracture and Fatigue in Advanced Materials," Department of Materials Science and Mineral Engineering Seminar, University of California, Berkeley, CA, Nov. 1988.
15. Jian Ku Shang and R. O. Ritchie, "Micromechanisms of Fatigue-Crack Propagation in Particulate-Reinforced Metal-Matrix Composites," invited keynote lecture at the Seventh International Conference on Fracture, Houston, TX, March 1989.
16. R. O. Ritchie, "Mechanics of Fatigue and Fracture in Metallic Alloys: Role of Metallic, Ceramic and Polymeric Reinforcements," invited presentation at *Fracture '89*, the Third National Conference on Fracture, Johannesburg, South Africa, June 1989.
17. R. O. Ritchie, "Behavior of Real Materials: Composites," invited presentation at the Physical Metallurgy Gordon Conference, Tilton, NH, August 1989.
18. R. O. Ritchie, "Mechanical Behavior of Metal-Matrix Composites," invited seminar to Korea Institute of Technology, Seoul, Korea, Sept. 1989.
19. R. O. Ritchie, "Fatigue and Fracture of Advanced Composite Materials," invited seminar sponsored by the Chinese Silicate Society, Beijing, PR China, Sept. 1989.
20. Jianku Shang and R. O. Ritchie, "Micromechanisms of Fatigue-Crack Growth in Model Particulate-Reinforced Metal-Matrix Composites," ASM Symposium on *Metal-Matrix Composites*, ASM Fall Meeting, Indianapolis, IN, Oct. 1989.
21. Jianku Shang and R. O. Ritchie, "Crack Bridging during Fatigue-Crack Growth in Metal-Matrix Composites," TMS Symposium on *Structure/Property Relationships in Metal-Matrix Composites*, TMS-AIME Fall Meeting, Indianapolis, IN, Oct. 1989.
22. R. O. Ritchie, "Mechanisms of Fracture and Fatigue in Advanced Aerospace Materials," invited presentation to the Australian Aeronautical Conference - 1989 on *Research and Technology - The Next Decade*, Melbourne, Australia, Oct. 1989.

23. R. O. Ritchie and J.-K. Shang, "Fatigue Resistance and Toughening Mechanisms in Particulate-Reinforced Metal-Matrix Composites," invited presentation to SAMPE Australian Chapter Conf. on *Advanced Composites and Materials*, Melbourne University, Australia, Oct. 1989.

Other Presentations

24. J.-K. Shang and R. O. Ritchie: "Fatigue Crack Propagation Behavior in SiC-Particulate Reinforced Aluminum Alloy Composites," presented at the 117th TMS Annual Meeting, Phoenix, AZ, Jan. 1988.
25. J.-K. Shang and R. O. Ritchie: "On the Role of Crack Tip Shielding during Fatigue Crack Growth in SiC<sub>p</sub>/Al Composites," presented at the Symposium on *High-Temperature/High-Performance Composites*, 1988 Spring Meeting of Materials Research Society, Reno, NV, April 1988.

## I. INTRODUCTION

In recent years, the development of metallic alloys reinforced with high-strength ceramic phases, such as graphite, silicon carbide, and alumina, led to a series of metal-matrix composites which have provided important material alternatives to traditional engineering alloys, such as precipitation-hardened aluminum alloys. The inclusion of such phases in general confers improved stiffness, higher strength and superior wear and elevated-temperature properties compared to the constituent matrix material, although the use of aligned continuous fibers or laminated sheets as the reinforcement results in highly directional properties [1-4]. Discontinuous reinforcements, in the form of chopped fibers, whiskers, platelets or particles, conversely, show essentially isotropic properties and have the added advantages that they are more economical and can be fabricated using conventional metallurgical techniques, such as casting, powder metallurgy, extrusion and hot-forming [3].

Although improved processing techniques are still required to overcome the poor ductility and fracture-toughness properties displayed by many of these composites [5-9], studies on the initiation and *subcritical* growth of incipient cracks in particulate- and whisker-reinforced aluminum alloys have shown improved endurance strengths and high-cycle fatigue resistance, and a potential for superior fatigue-crack growth properties, compared to the unreinforced alloys [10-23].

It is the objective of this chapter to review what is currently known about the cyclic fatigue properties of such discontinuously-reinforced metal-matrix composites, with particular emphasis on aluminum composites. It must be remembered, however, that a mechanistic understanding of fatigue in these materials is far from complete at this time; the intent here is simply to summarize current knowledge such that directions for future research and material development can be identified to best serve the ultimate applications of these materials.

## II. CYCLIC DEFORMATION

Limited data on the cyclic deformation properties of metal-matrix composites are available in the literature, although cyclic stress-strain relations have been reported for powder-metallurgy (P/M) and cast SiC-whisker-reinforced aluminum alloys (SiC<sub>w</sub>/Al) [10,11]. Williams and Fine's [10] data on SiC<sub>w</sub>/2124 are typical; results indicate that the cyclic yield strength ( $\sigma_{yc}$ ) of the composite is significantly higher than that of the unreinforced alloy at the same aging condition (Fig. 1). However, compared

to properties measured under monotonic loading, the composite behaves similarly to unreinforced 2124; both materials show comparable degrees of cyclic hardening (~16% increase in yield strength under cyclic loading), little change in elastic modulus (E), and 6 to 7% higher cyclic yield strengths in compression compared to tension. Typical data, taken from reference 10 for 2124 with 20% SiC whiskers, are shown in Table I.

**Table I. Cyclic Properties of 20% SiC<sub>w</sub>/2124 Composite [10]**

Alloy	Monotonic Properties		Cyclic Properties		
	E (GPa)	$\sigma_y$ (MPa)	E <sub>c</sub> (GPa)	$\sigma_{yc}^1$ (MPa)	$\sigma_{yc}^2$ (MPa)
20% SiC <sub>w</sub> /2124	123	484	128	560	600
2124-T6	74	268	76	310	330

<sup>1</sup>tension, <sup>2</sup>compression

### III. LOW-CYCLE AND HIGH-CYCLE FATIGUE

Hassen *et al.* [12] studied stress-life (S-N) fatigue behavior in several P/M particulate- and whisker-reinforced 6061 aluminum alloys in various environments. Their results, plotted in Fig. 2a in terms of stress amplitude  $\sigma_a$  as a function of number of cycles to failure  $N$  in room-temperature air, show that the two forms of reinforcement have a similar effect; the composites are superior in high-cycle fatigue (HCF) but offer no particular advantage over the unreinforced alloy in low-cycle fatigue (LCF). The superior HCF properties appear to result from the higher stiffness of the composites, as differences between the composite and unreinforced alloys are diminished by replotting the data in Fig. 2a in terms of strain amplitude ( $\sigma_a/E$ ).

Not all reinforced alloys, however, show superior fatigue properties to their constituent matrices. For example, in cast Al-Cu-Mg composites reinforced with "saffil" (short alumina fibers), Harris [13] showed that where the yield strength of the composites exceeded that of the unreinforced alloy, their fatigue strength for both HCF and LCF was also superior. However, where the saffil fibers were too weakly bonded to the matrix to provide strengthening under monotonic loading, the weakened interfaces provided preferential sites for crack initiation; this results in the unreinforced

alloy having the superior low-cycle fatigue strength, although high-cycle fatigue strength was unaffected.

Such dependence of the fatigue strength on monotonic behavior is not uncommon. Hurt [11], in his study of cast saffil-reinforced Al-Mg-Si and Al-Si composites under cyclic strain control, found that in the Al-Si alloys, which are weakened by the addition of the saffil fibers, the LCF properties of the composite were inferior to the unreinforced alloy; conversely, in the Al-Mg-Si alloys, which are strengthened by fiber additions, the LCF properties were comparable (Fig. 3).

Microscopically, the initiation of cracks during low-cycle fatigue has been found to occur much later in the fatigue life of many composites compared to their constituent matrices. Williams [14], for example, found that visible ( $>2.5 \mu\text{m}$ ) fatigue cracks appeared in  $\text{SiC}_w/2124$  composites only after 70 to 80% of the life (at  $\sigma_a = 300 \text{ MPa}$ ), whereas in the unreinforced materials, larger cracks appeared after only 5% of the life at the same stress amplitude. He noted that although the  $\text{SiC}_w/\text{matrix}$  interface was a preferential site for crack initiation in the composites, subsequent small-crack growth was generally inhibited. Such beneficial fatigue properties are apparently not shared by cast saffil-reinforced Al-Si alloys, where the very weakly bonded saffil fibers readily promote interfacial crack initiation, such that a large fraction of cracks is invariably present throughout the life [11].

#### IV. FATIGUE-CRACK PROPAGATION

Fatigue-crack propagation behavior is generally characterized in terms of fracture mechanics; crack-growth rate ( $da/dN$ ) data are displayed as a function of the (applied) stress-intensity range ( $\Delta K = K_{\text{max}} - K_{\text{min}}$ , where  $K_{\text{max}}$  and  $K_{\text{min}}$  are the extremes of stress intensity in the fatigue cycle). Such results are often described by equations of the form [25]:

$$da/dN = C\Delta K^m, \quad (1)$$

where  $C$  and  $m$  are experimentally determined scaling constants. The growth-rate curve, however, is generally sigmoidal in shape as growth rates are accelerated at high  $\Delta K$  levels as  $K_{\text{max}}$  approaches instability or the material's fracture toughness,  $K_{\text{IC}}$ , and tend toward a threshold value,  $\Delta K_{\text{TH}}$ , at low  $\Delta K$  levels, below which long-crack growth is presumed dormant [26].

Since the  $K_{IC}$  values for many metal-matrix composites are of the order of 15 MPa $\sqrt{m}$  the  $\Delta K_{TH}$  values of the order of 3-5 MPa $\sqrt{m}$ , unlike most monolithic metallic alloys, the crack-growth rate curves in composites generally exist over a narrow range of  $\Delta K$ . An example of such data is shown for overaged SiC-particulate-reinforced Al-Zn-Mg-Cu composites in Fig. 4; results are plotted at a load ratio ( $R = K_{min}/K_{max}$ ) of 0.1 and are compared with behavior in the unreinforced matrix alloy after identical aging treatments [21].

Crack-growth rate data in particulate-reinforced composites, as shown in Fig. 4, often display several distinct regimes of behavior, each characterized by a dominant crack-extension mechanism, as illustrated schematically in Fig. 5. At near-threshold levels, below typically  $10^{-9}$  m/cycle, the crack often follows a path that tends in general to avoid the reinforcement particles; this can result in superior crack-growth resistance in many composites, compared to their constituent matrices, due primarily to crack-closure [18] and crack-trapping [21] mechanisms. In fact, the magnitude of the fatigue threshold is often found to be dependent upon mean particle size, an observation which has been shown to be consistent with a crack-trapping mechanism [21]. At higher growth rates, generally between  $10^{-9}$  and  $10^{-6}$  m/cycle, crack-growth resistance can again be somewhat improved in the composite alloys; in this regime, limited fracture of reinforcement particles *ahead* of the main crack tip can lead to the development of uncracked ligaments which act as crack bridges [20]. Finally, at very high crack-growth rates above  $\sim 10^{-6}$  m/cycle, where  $K_{max}$  approaches  $K_{IC}$ , fatigue-crack propagation properties are invariably superior in the unreinforced alloys, as the much lower toughness of the composites leads to characteristically accelerated growth rates [18].

Such conclusions are largely reflected in reported results for whisker-reinforced composites, specifically SiC<sub>w</sub>-reinforced 6061 and 2124 [15,16] and cast saffil-reinforced Al-Mg alloys [23]. For example, data [15] for the SiC<sub>w</sub>/6061 composite, shown in Fig. 6a, indicate slower fatigue-crack growth rates in the composite at near-threshold and intermediate growth rates; however, the advantage offered by reinforcement is lost as  $\Delta K$  levels approach instability. Similarly, fatigue thresholds for many whisker-reinforced composites exceed those for the corresponding unreinforced alloys [15,19], although in other cases  $\Delta K_{TH}$  values are similar [16,18]. One major difference in the properties of the different reinforcements is that, unlike particulate additions, the majority of the whiskers in whisker-reinforced alloys are oriented close to the extrusion direction; these composites thus generally display some orientation

dependence [15,24], as shown by the superior crack-growth properties of the  $\text{SiC}_w/6061$  alloy in the L-T, rather than T-L, orientation (Fig. 6b [15]).

## V. NEAR-THRESHOLD FATIGUE BEHAVIOR

### A. Crack-Closure Mechanisms

Similar to many monolithic alloys, near-threshold fatigue-crack growth in metal-matrix composites shows a strong dependence on the load ratio, principally due to the development of significant levels of crack closure, i.e., premature contact of the crack surfaces during the loading cycle [e.g., 27,28]. Examples of this load-ratio effect are presented in Fig. 7 for several aluminum-alloy composites, reinforced with SiC or saffil whiskers or SiC particulate [7,14,20]. The role of crack closure can be appreciated from compliance measurements during the fatigue cycle on cracked specimens at near-threshold  $\Delta K$  levels (Fig. 8). At high load ratios ( $R = 0.75$ ), a linear relationship exists between applied load,  $P$ , and (back-face) displacement,  $\delta$ , whereas at  $R = 0.1$ , a marked change in compliance can be detected on unloading once the crack surfaces first come into contact.

The degree of crack closure is generally quantified by measuring the closure stress intensity,  $K_{cl}$ , which is determined at first contact of the fracture surfaces during unloading [29]. Typical data [18], for a P/M Al-Zn-Mg-Cu composite (similar to 7091) with either fine ( $\sim 5 \mu\text{m}$ ) or coarse ( $\sim 16 \mu\text{m}$ ) SiC-particle sizes, are shown in Fig. 9. Plotted are measured values of  $K_{cl}$ , normalized with respect to  $K_{max}$ , as a function of the applied  $\Delta K$ ; increasing values of  $K_{cl}$  tend to inhibit crack advance by reducing the local, or effective, stress-intensity range ( $\Delta K_{eff} = K_{max} - K_{cl}$ ) actually experienced at the crack tip (crack-tip shielding). Closure  $K_{cl}/K_{max}$  levels are typically increased with decreasing  $\Delta K$  due to the smaller crack-tip opening displacements (CTODs). Moreover, by subtracting out the influence of closure through a characterization of growth rates in terms of  $\Delta K_{eff}$ , differences in near-threshold behavior at low and high load ratios become minimal (Fig. 10); differences between behavior in the coarse and fine particle composites (e.g., Fig. 4), however, remain, but are reduced [20].

In the SiC-particulate-reinforced Al-Zn-Mg-Cu alloy, it is clear that the magnitude of the closure is enhanced with coarser particle sizes (Fig. 9), and only marginally affected by aging condition (Table II) [21]. Such observations are consistent with the primary source of crack closure in  $\text{SiC}_p/\text{Al}$  composites originating from the

wedging action of fracture-surface asperities (roughness-induced closure [30-32]), as is common in many monolithic alloys [28], although studies by Davidson [22] on SiC<sub>p</sub>/2014 purport to dispute this. On the one hand, metallographic studies [18] in SiC<sub>p</sub>/Al-Zn-Mg-Cu composites show that in general the crack tends to avoid the SiC particles at near-threshold levels (Fig. 11), and since the computed CTOD levels at  $K_{cl}$ ,  $\delta_{cl}$ , are several orders of magnitude larger than the SiC-particle size,  $\bar{D}_p$ , the presence of such reinforcement particles on the fracture surface must provide a potent source of wedging [21]. With increasing particle sizes, the larger particles would be expected to induce more crack meandering and hence would be more effective in generating high closure levels at low load ratios. On the other hand, the lineal roughness of the fracture surfaces of the composites with fine and coarse particle distributions are often similar (~1.07 to 1.10), suggesting that our understanding of this mechanism is far from complete.

**Table II. Fatigue-Threshold Data for SiC<sub>p</sub>/Al-Zn-Mg-Cu<sup>1</sup> Composite Alloys [21]**

Alloy	Aging <sup>2</sup> Condition	$\bar{D}_p$ ( $\mu\text{m}$ )	$\Delta K_{TH}$ ( $\text{MPa}\sqrt{\text{m}}$ )	$\Delta K_{eff,TH}$ ( $\text{MPa}\sqrt{\text{m}}$ )	$K_{cl}/K_{max}$	$K_{cl}$ ( $\text{MPa}\sqrt{\text{m}}$ )	$\delta_{cl}$ <sup>3</sup> (nm)
20% coarse SiC <sub>p</sub> /Al	PA	10.5	4.2	1.3	0.73	3.4	112
	OA		3.5	1.4	0.65	2.5	68
	VO		3.7	1.3	0.69	2.8	85
20% fine SiC <sub>p</sub> /Al	PA	6.1	3.0	1.9	0.42	1.4	26
	OA		2.7	1.9	0.35	1.0	15
	VO		3.0	1.1	0.67	2.2	68
15% coarse SiC <sub>p</sub> /Al	PA	11.4	4.3	1.3	0.73	3.5	127
	OA		3.9	1.5	0.65	2.8	88
	VO		3.5	1.2	0.69	2.7	98
15% fine SiC <sub>p</sub> /Al	PA	4.5	2.6	1.9	0.34	1.0	11
	OA		2.3	1.9	0.28	0.7	6
	VO		2.4	1.3	0.53	1.5	26

<sup>1</sup>the Al-Zn-Mg-Cu matrix of this composite is similar to 7091

<sup>2</sup>PA  $\equiv$  aged at 121°C (24h), OA  $\equiv$  PA + 171°C (15h), VO  $\equiv$  171°C (50h)

<sup>3</sup>computed from  $\delta_{cl} = \frac{1}{2}K_{cl}^2/E\sigma_y$  [33]



The extent of such roughness-induced closure, however, can be assessed theoretically from simple geometric modelling [32] of the wedging of asperities (height  $h$ , width  $w$ ) inside a crack deflecting through angle  $\theta$  (where  $\theta = \tan^{-1}(2h/w)$ ); this gives the closure stress intensity  $K_{cl}$  in terms of  $\theta$ ,  $K_{max}$  and mismatch  $X$ , as:

$$K_{cl} = K_{max}[X \tan\theta/(1 + X \tan\theta)]^{\frac{1}{2}}, \quad (2)$$

where  $X$  is the ratio of Mode II to Mode I unloading displacements ( $u_{II}/u_I$ ). Using this relationship for  $R = 0.1$ , predicted values of  $K_{cl}/K_{max}$  for angles of  $\theta$  between 20 and 75 deg range from 0.29 to 0.70 for a mismatch of 0.25, consistent with the measured maximum closure ratios of 0.28 to 0.73, listed in Table II.

## B. Crack-Trapping Mechanism

Measured fatigue-crack growth threshold stress-intensity  $\Delta K_{TH}$  values, below which (long) cracks are presumed dormant, are generally found to be relatively insensitive to the matrix aging condition in both SiC whisker- and particulate-reinforced aluminum alloys; moreover, they are similar for several different matrices (2014, 2024, 7475) and SiC volume fractions (15-25%) [22]. In particulate alloys, however, the size of the reinforcement particles appears to be important; in general threshold values are increased, and near-threshold growth rates decreased, with increasing particle size (Fig. 12), where the average size,  $\bar{D}_p$ , of particles "sampled" by the crack front is the appropriate measure [21]. At such near-threshold levels, crack-path morphology studies show a strong tendency for the crack to avoid the particles; in coarse SiC<sub>p</sub>/Al-Zn-Mg-Cu composites, a fraction of only ~13% SiC particles are intersected by the crack path (~9% are cracked, ~4% decohere), far less than the ~22 volume % of SiC in the microstructure [18].

As the crack tends to avoid SiC particles at low  $\Delta K$  levels, the particles can be considered to impede crack advance; their presence at the crack tip acts to lower *local* stress intensities and hence their function can be envisioned as crack traps. Based on this notion, the fatigue threshold in particulate-reinforced composites has been modelled in terms of the role of a non-deforming particle at the crack tip (Fig. 13) in affecting the *local* "driving force" required for crack extension [21]. It is significant in these alloy systems at *at*  $\Delta K_{TH}$ , maximum plastic zone sizes ( $r_{y,max}$ ) are comparable with the average particle size  $\bar{D}_p$  (Fig. 14), implying that crack hindrance at particles occurs because of limited local plasticity, which impedes fracture or bypassing of the particle.

Accordingly, a limiting condition for fatigue-crack advance in particulate-reinforced composites can be defined in terms of the matrix stress beyond the particle at the crack tip exceeding the yield strength  $\sigma_y$  of the material, i.e.,  $r_{y,max}$  must exceed  $\bar{D}'_p$  [21].

The presence of a non-deforming inclusion at the crack tip significantly reduces the matrix stresses. Analyses, by Atkinson [34,35] for a finite crack and by Rubinstein [36] for a semi-infinite crack, show that the crack-tip stress intensity decreases i) with decreasing distance between the inclusion and the tip, and ii) with an increasing ratio of the modulus of the inclusion and the matrix; the stress intensity approaches zero as the inclusion approaches the tip. Recent studies [21] for a SiC carbide particle in an aluminum alloy (with a ratio of crack size to particle size of  $\sim 1250$ ) gives the matrix tensile stress distribution just beyond the inclusion as (Fig. 15):

$$\sigma_{yy} = C K / \sqrt{\bar{D}'_p} , \quad (3)$$

where the constant  $C$  equals  $2.4^{-1}$ , and only depends on material constants for a crack large compared to particle size [21].

For a fatigue crack trapped at a SiC particle to propagate, this matrix stress must exceed the matrix yield strength to induce plastic flow; this sets a limiting condition for the threshold as [21]:

$$\sigma_{yy} = \sigma_y , \quad \text{over } r = r_{y,max} \approx \bar{D}'_p , \quad (4)$$

such that:

$$K_{max,TH} \approx 2.4 \sigma_y \sqrt{\bar{D}'_p} . \quad (5)$$

Eq. (5) implies that for particulate-reinforced composites where near-threshold crack advance is influenced primarily by crack trapping, the fatigue threshold is proportional to the yield strength and the square root of the particle size, consistent with experimental observations (Fig. 12).

An alternative model for the threshold in particulate-reinforced composites has been proposed by Davidson [37], based on observations that near-threshold crack growth involves significant Mode II displacements. Here the threshold condition is associated with the generation of a single slip band ahead of the crack tip; crack growth is stopped once the stress at the tip of the band is reduced to  $\sigma_y$ . For SiC-particulate composites,

the limiting slip distance is assumed to be equal to the dislocation mean free path; this gives an expression for  $\Delta K_{TH}$  in terms of the particle size,  $\bar{D}_p$ , and volume fraction,  $f_p$ , as [37]:

$$\Delta K_{TH} \approx \sigma_f \left[ \frac{4\pi}{3} \cdot \bar{D}_p \cdot \left( \frac{1 - f_p}{f_p} \right) \right]^{\frac{1}{2}}, \quad (6)$$

where  $\sigma_f$  is the flow stress at the end of the slip band. Although the dependency on volume fraction has not been reported, the model does predict threshold values in a limited number of particulate-reinforced composite to within ~18%.

## VI. HIGHER GROWTH-RATE BEHAVIOR

### A. General Considerations

At very high stress-intensities where  $K_{max}$  approaches the fracture toughness,  $K_{IC}$ , fatigue-crack growth rates in the composites are invariably faster than in their unreinforced constituent matrix alloys (e.g., Fig. 4). This is primarily of consequence of the much lower toughness of the composites, which leads to accelerated growth rates, typically above  $\sim 10^{-6}$  m/cycle, as conditions approach instability [18].

Conversely, at intermediate growth rates, typically between  $\sim 10^{-9}$  and  $10^{-6}$  m/cycle, the fatigue-crack growth resistance of particulate-reinforced composites is generally somewhat superior to the unreinforced matrix alloys (Fig. 4), although the degree of superiority appears to be dependent on interparticle spacing,  $d_p$ . In alloys with coarse reinforcement particle distributions, e.g., the 15% coarse  $\text{SiC}_p/\text{Al-Zn-Mg-Cu}$  alloy where  $d_p \approx 56 \mu\text{m}$ , growth rates are up to an order of magnitude slower in the composite; in the 20% fine  $\text{SiC}_p/\text{Al-Zn-Mg-Cu}$  alloy, conversely, where  $d_p \approx 23 \mu\text{m}$ , the effect is much smaller (Fig. 16) [18,20].

It appears that in this intermediate regime, compared to near-threshold behavior there is an increasing tendency in many particulate-reinforced composites for the crack path to interact with the particles. For example, in the coarse  $\text{SiC}_p/\text{Al-Zn-Mg-Cu}$  alloy at a  $\Delta K$  of 7 to 10  $\text{MPa}\sqrt{\text{m}}$ , a fraction of ~21% SiC particles is intersected by the crack path (~18% are cracked, ~3% decohere), a figure which is comparable to the ~22 volume % of SiC in the microstructure, but large compared to the ~13% "sampled" at near-threshold levels [18]. Moreover, rather than trapping the crack or promoting crack deflection as at near-threshold levels, the role of the reinforcement phase is now

principally to cause *limited fracture ahead* of the main crack tip. In fact, there is increasing evidence of cracked particles on fatigue fracture surfaces with increasing  $\Delta K$  [18]. The process occurs by the cracking of specific particles (Fig. 17a), or in fewer instances by the formation of voids in the matrix at the sharp corners (poles) of elongated particles (or whiskers) or in constrained material between closely spaced particles (Fig. 17b). Extension of these microcracks and their coalescence with the main crack results in the non-uniform advance of the main crack front and the consequent formation of small uncracked regions (in any two-dimensional section) along the crack length (Fig. 18). Such uncracked ligaments act to restrain crack opening, and thus shield the crack tip by a mechanism of crack bridging [20].

Evidence for such uncracked ligaments can be seen from metallographic sections perpendicular to the crack plane; in composites with smaller interparticle spacing, the ligaments are essentially coplanar (Fig. 18b), whereas with coarser particle distributions they have an overlapping morphology (Fig. 18c), as illustrated schematically in Fig. 19. The latter type of uncracked ligaments, which exist typically over a bridging zone of some 500  $\mu\text{m}$  behind the crack tip, represents the more potent source of crack-tip shielding, as shown by the experimental data in Fig. 16a (c.f., Fig. 16b) and confirmed by the models described below.

It should be noted that the cracking of specific SiC particles ahead of the crack tip is both mechanically and statistically analogous to the cracking of carbides during the cleavage fracture of low carbon steels [38,39]. Since the process is stress-controlled, it is triggered at sites of weak ("eligible") particles (generally the largest ones) *ahead* of the crack tip where the stresses are highest (due to crack-tip blunting). The location of these eligible particles is a function of the crack-tip stress distribution and the statistical distribution of particle strengths (inversely related to particle size) within the plastic zone ("sampling" volume), as described in ref. 38,39. At low  $\Delta K$  levels where the plastic zone, and hence region of high stresses ahead of the tip, are small, the probability of finding a crackable particle is very low (it is essentially zero close to  $\Delta K_{TH}$  where the plastic zone size is no larger than the particle size); with increasing  $\Delta K$  levels, conversely, the plastic zone volume and hence sampling region increases rapidly, such that the probability of finding an eligible particle is substantially enhanced [18].

## B. Models for Crack-Bridging Mechanisms

In general terms, the dominant contribution from bridging reinforcements can be expressed solely as the product of the volume fraction  $f_b$  of the bridging phase with the area under the stress/strain curve, i.e., in terms of the yield strength  $\sigma_y$ , radius  $r_b$ , and  $f_b$  [40]:

$$G_c \approx C \sigma_y r_b f_b , \quad (7)$$

where  $C$  depends on the ductility of the reinforcement phase and the extent of interface debonding. To quantify  $G_c$ , however, it is necessary to derive the appropriate constitutive relationship for the strained bridges which incorporates effects of stress state, inelastic response and so forth. For the present case of bridging by uncracked tensile ligaments along a bridging zone  $\ell$  (which is small compared to crack length) behind the crack tip (Fig. 20), the effect of the bridges can be modelled as a distributed force per unit thickness  $dp(x)$  acting over  $x = \ell$  along the crack faces (Fig. 21), analogous to analyses developed for fiber bridging in ceramic composites and rubber toughening in polymers [e.g., 41-45]. For a semi-infinite crack, this force induces a shielding stress intensity [46]:

$$K_s = (\sqrt{2/\pi}) \int_0^\ell dp(x)/\sqrt{x} , \quad (8)$$

which, when superimposed upon the applied (far-field) stress intensity,  $K_a$ , yields an expression for the effective (near-tip) stress intensity:

$$K_{tip} = K_a + K_s . \quad (9)$$

Solutions to Eqs. 8,9 involve the determination of the distributed force; in particle-reinforced metal-matrix composites, this has been solved by two approaches, based either on a limiting crack-opening displacement or limiting tensile strain in the uncracked ligaments [20].

**Limiting Crack-Opening Displacement Approach:** The basis of this approach, which is more applicable to the case of coplanar bridges, lies with the assertion that the straining of the uncracked ligaments between two crack faces is limited by the critical

crack-opening displacement  $\delta_c$  that ligament material can withstand. By idealizing the fatigue crack as trapezoidal (Fig. 20c), the crack-opening displacement at any distance  $x$  along the crack,  $\delta_x$ , can be related to the crack-tip opening displacement,  $\delta_{tip}$ , by [47]:

$$\delta_x = \delta_{tip} \left( \frac{x + rb}{rb} \right), \quad (10)$$

where  $b$  is the specimen ligament,  $r$  is the rotational factor, which takes values of 0.195 (elastic deformation) to 0.470 (plastic deformation) [48], and  $\delta_{tip}$  is given in terms of the near-tip stress intensity  $K_{tip}$  and yield stress  $\sigma_y$  by [33]:

$$\delta_{tip} = \beta \cdot \frac{K_{tip}^2}{E' \sigma_y}, \quad (11)$$

where  $E' = E$  in plane stress and  $E/(1 - \nu^2)$  in plane strain,  $\nu$  is Poisson's ratio, and  $\beta$  is a constant varying between 0.3 and 1.0 depending upon the yield strain, work-hardening exponent and whether plane-strain or plane-stress conditions apply. Since at  $x = \ell$ ,  $\delta_x = \delta_c$ , the stress  $\sigma(x)$  in the uncracked ligament becomes:

$$\sigma(x) = - \frac{\pi}{2\sqrt{2}} \cdot \sqrt{\frac{\delta_c rb E' \sigma_y}{\beta}} \cdot \left[ \frac{x^{\frac{1}{2}}}{(x + rb)^{3/2}} \right], \quad (12)$$

such that the degree of crack-tip shielding can be expressed in terms of the area fraction of ligaments,  $f_b$ , the applied stress intensity and  $\ell/rb$  [20]:

$$K_s = - f_b K_a [(1 + \ell/rb)^{\frac{1}{2}} - 1] / [1 - f_b + f_b(1 + \ell/rb)^{\frac{1}{2}}]. \quad (13)$$

**Limiting Strain Approach:** An alternative first-order approach, which is more applicable to the case of overlapping ligaments, represents the bridges as tensile ligaments and defines the extent of the bridging zone by the limiting strain in the ligament furthest away from the crack tip being equal to the fracture strain [20].

With reference to Fig. 20c, the strain,  $\epsilon(x)$ , in any ligament within the bridging zone can be estimated by assuming it to be equivalent to the strain in a bent beam, with rotational center at point C and neutral plane at the crack tip:

$$\epsilon(x) = x/rb. \quad (14)$$

Converting to a true strain and substituting into a constitutive law, for the uncracked-ligament material, of the form:

$$\sigma(x) = \sigma_y + k \epsilon(x) , \quad (15)$$

where  $\sigma_y$  is the (initial) yield stress and  $k$  is a constant, provides a second expression for the degree of crack-tip shielding due to uncracked-ligament bridging, in terms of the area fraction of ligaments, the ratio  $\ell/rb$ , and the (constrained) flow properties of the ligament [20]:

$$K_s = f_b \sigma_y \cdot \frac{2\sqrt{2}\ell}{\pi} \left\{ 1 + \frac{k}{\sigma_y} \left[ \ln\left(1 + \frac{\ell}{rb}\right) + 2\left(\sqrt{\frac{rb}{\ell}} \tan^{-1} \sqrt{\frac{\ell}{rb}} - 1\right) \right] \right\} . \quad (16)$$

Application of Eqs. 13 and 16 to predict uncracked-ligament bridging in a given system requires values for  $f_b$ ,  $\ell$ ,  $rb$ ,  $K_a$ ,  $\sigma_y$  and  $k$ . This has been attempted for overaged  $\text{SiC}_p/7091$  composites by serial sectioning through fatigue cracks loaded to a  $\Delta K$  level corresponding to the intermediate range of growth rates [20]; at a  $\Delta K$  of 8  $\text{MPa}\sqrt{\text{m}}$  ( $K_a = 9 \text{ MPa}\sqrt{\text{m}}$ ),  $f_b \approx 27$  to 31%,  $\ell \approx 300$  to 400  $\mu\text{m}$ ,  $rb$  is typically 1 mm for the tested DB(Mz) geometry, and  $\sigma_y$  and  $k$  are 405 and 2200 MPa, respectively, for reinforced bridges. For the fine  $\text{SiC}_p/\text{Al}$  composite where the uncracked ligaments were largely coplanar, the predicted shielding is minimal ( $\sim 6\%$ ) -  $K_s$  is less than 0.5  $\text{MPa}\sqrt{\text{m}}$  - consistent with the insignificant difference in growth rates between the reinforced and unreinforced alloys in this range (Fig. 16b). Conversely, in the coarser  $\text{SiC}_p/\text{Al}$  composites where overlapping ligaments are more prevalent,  $K_s$  is predicted to be  $\sim 2.4 \text{ MPa}\sqrt{\text{m}}$ , consistent with the much larger shift in growth-rate curves between the reinforced and unreinforced alloys at  $\Delta K = 8 \text{ MPa}\sqrt{\text{m}}$  in Fig. 16a.

## V. SUMMARY

The use of discontinuous reinforcements to improve the mechanical properties of metallic alloys has provided a relatively less expensive means to produce materials with improved stiffness, strength, wear, and high-temperature resistance for applications where the very highly directional properties of continuous fiber-reinforced composites are not required. In essence, for structural use, such metal-matrix composites provide an opportunity to reduce both initial costs and life-cycle operating costs in many weight-critical applications [49]. For example, Lockheed has recently fabricated aircraft

vertical tail structures entirely from a SiC-whisker-reinforced 2124 aluminum alloy [50]. However, although initial developments have been motivated by the aerospace industry, the greatest volume potential probably now lies in reciprocating or accelerating mass applications in the commercial/automotive industries or in the area of tribology and thermal management [51]. A notable example of this is the use of an aluminum-matrix composite containing low-density chopped-alumina fibers for the aluminum-matrix composite containing low-density chopped-alumina fibers for the Toyota diesel piston introduced in 1983; this in fact was the first celebrated commercial application of discontinuously-reinforced metal-matrix composites [52].

Whether their primary use is with aerospace or automotive applications, the resistance of metal-matrix composites to failure under cyclic or otherwise varying loads remains paramount. However, while the addition of such particulate or whisker reinforcements can lead to unacceptably low ductility and fracture-toughness properties, the fatigue properties of metal-matrix composites are comparable and in many cases exceed that of their respective unreinforced matrices.

The present brief review has shown that improved fatigue-crack growth properties can be achieved in general with coarser particulate reinforcement-phase distributions, although details on the optimum size, shape, spacing, volume fraction, interface strength, and so forth are uncertain at this time and must await more specific models of their subcritical crack-growth behavior. At ultralow growth rates, however, where mechanistic interpretation suggests that the dominant mechanisms which impede crack advance involve crack deflection around the particles (to induce higher crack-closure levels from asperity wedging) and crack trapping by the particles, the coarser distributions appear to be the most effective. This is illustrated in Fig. 21 where all the fatigue-threshold data [15-22,24] in the literature for SiC/Al alloys are plotted and compared with the predictions of the crack-trapping model (Eq. 5) for mean particle sizes of 5 and 20  $\mu\text{m}$ . Similarly, at higher growth rates where particle fracture ahead of the crack tip leads to crack-bridging phenomena via uncracked ligaments, the alloys with coarser particle distributions again display the superior resistance to fatigue-crack growth.



## ACKNOWLEDGEMENTS

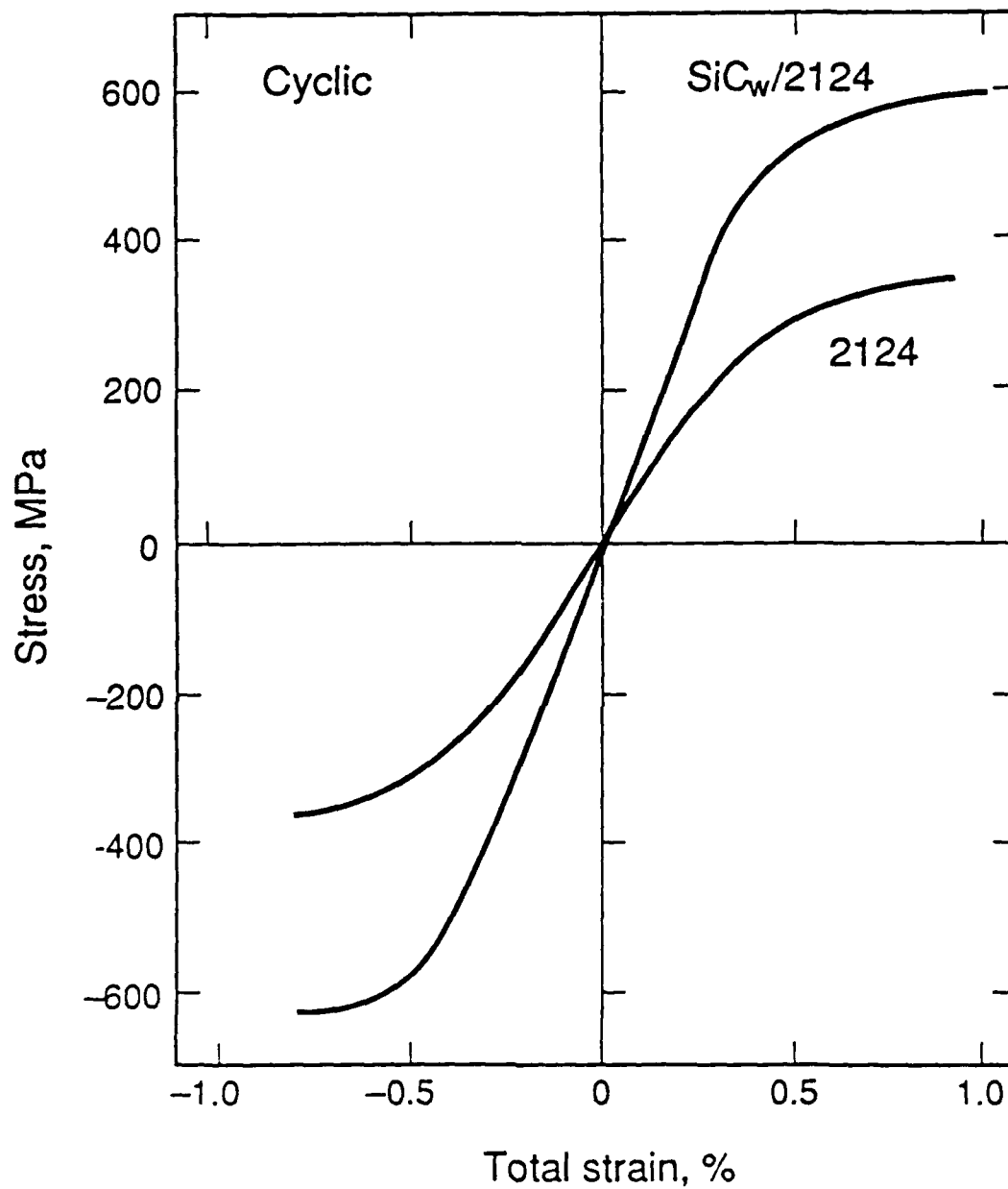
This work was supported by the Air Force Office of Scientific Research, Contract No. F49620-87-- 0017 as part of the University Research initiative program on High Temperature Metal Matrix Composites at Carnegie Mellon University. Thanks are due to Dr. Alan Rosenstein for his continued support, to L. Edelson, J. J. Mason and Drs. R. J. Bucci, W. H. Hunt, J. J. Lewandowski, T. G. Nieh, H. Rack and A. W. Thompson for helpful discussions, and to Madeleine Penton for her assistance in preparing the manuscript.

## REFERENCES

1. A. K. Dhingra, J. Met. **38**, 17 (1986).
2. R. C. Forney, J. Met. **38**, 18 (1986).
3. A. P. DiVecha, S. G. Fishman, and S. D. Karmarkar, J. Met. **33**, 12 (1981).
4. R. J. Arsenault, Mater. Sci. Eng. **64**, 171 (1984).
5. S. V. Nair, J. K. Tien, and R. C. Bates, Int. Metall. Rev. **30**, 275 (1985).
6. D. L. McDaniels, Metall. Trans. A **16A**, 1105 (1985).
7. J. J. Lewandowski, C. Liu, and W. H. Hunt, in "Processing and Properties of Powder Metallurgy Composites" (P. Kumar, K. Vedula, and A. M. Ritter, eds.), p. 513, TMS-AIME, Warrendale, PA, 1987.
8. C. P. You, A. W. Thompson, and I. M. Bernstein, Scr. Metall. **21**, 181 (1987).
9. W. R. Mohn, Res. & Devel. **54** (1987).
10. D. R. Williams and M. E. Fine, in "Proc. 5th Intl. Conf. on Composite Materials" (W. C. Harrigan, Jr., J. Strife, and A. K. Chingra, eds.), p. 639 (1985).
11. N. J. Hurd, Mater. Sci. Tech. **4**, 513 (1988).
12. D. F. Hassen, C. R. Crowe, J. S. Ahearn, and D. C. Cooke, in "Failure Mechanisms in High Performance Materials" (J. G. Early, T. Robert Shives, and J. H. Smith, eds.), p. 147, 1984.
13. S. J. Harris, Mater. Sci. Tech. **4**, 231 (1988).
14. D. R. Williams, Ph.D. Thesis, Northwestern University, 1985.
15. S. S. Yau and G. Mayer, Mater. Sci. Eng. **82**, 45 (1986).

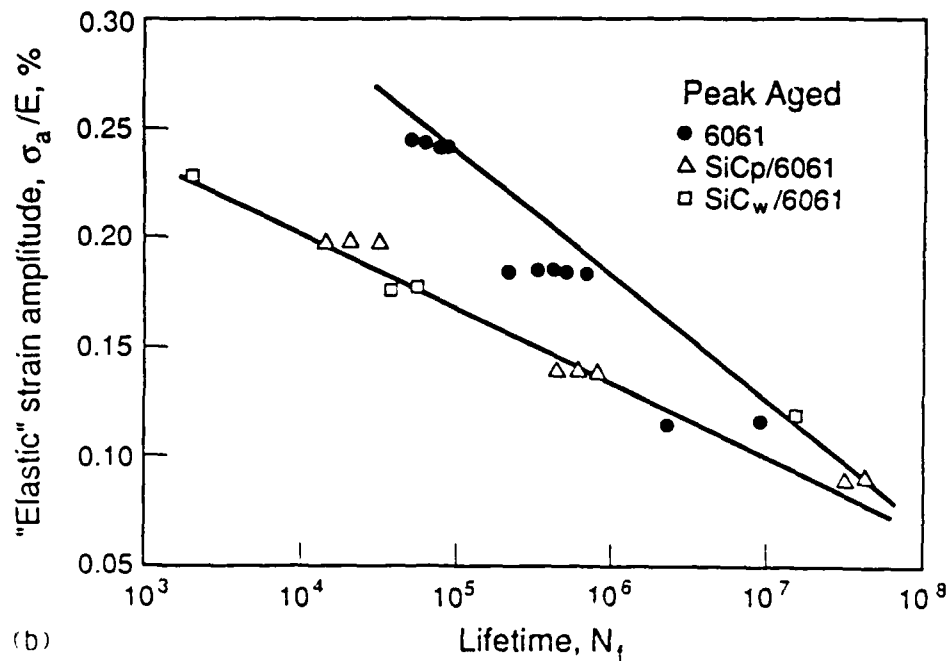
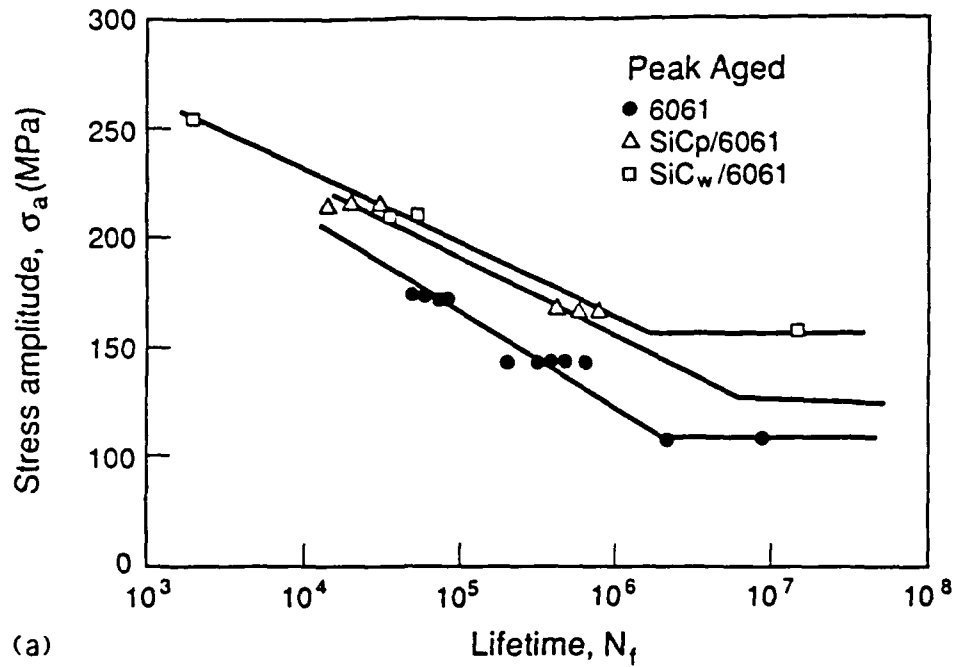
16. W. A. Logsdon and P. K. Liaw, Eng. Fract. Mech. **24**, 737 (1986).
17. D. L. Davidson, Metall. Trans. A **18A**, 2115 (1987).
18. J.-K. Shang, W. Yu, and R. O. Ritchie, Mater. Sci. Eng. **102**, 181 (1988).
19. T. Christman and S. Suresh, Mater. Sci. Eng. **102**, 211 (1988).
20. J.-K. Shang and R. O. Ritchie, Metall. Trans. A **20A**, 897 (1989).
21. J.-K. Shang and R. O. Ritchie, Acta Metall. **37**, 2267 (1989).
22. D. L. Davidson, "Micromechanisms of Fatigue Crack Growth and Fracture Toughness in Metal Matrix Composites," SWRI Report No. 06-8602/5, Southwest Research Institute, San Antonio, TX, 1988.
23. S. Preston, A. Melander, H. L. Groth, and A. F. Blom, in "Thermal and Mechanical Behavior of Ceramic and Metal Matrix Composites," ASTM STP, in press, American Society for Testing and Materials, 1989.
24. J. J. Mason, M.S. Thesis, University of California, Berkeley, 1988.
25. P. C. Paris and F. Erdogan, J. Basic Eng. **85D**, 528 (1963).
26. R. O. Ritchie, Int. Metall. Rev. **20**, 205 (1979).
27. W. Elber, Eng. Fract. Mech. **2**, 37 (1970).
28. S. Suresh and R. O. Ritchie, in "Fatigue Crack Growth Threshold Concepts" (D. L. Davidson and S. Suresh, eds.), p. 227, TMS-AIME, Warrendale, PA, 1984.
29. R. O. Ritchie and W. Yu, in "Small Fatigue Cracks" (R. O. Ritchie and J. Lankford, eds.), p. 167, TMS-AIME, Warrendale, PA, 1986.
30. N. Walker and C. J. Beevers, Fat. Eng. Mat. Struct. **1**, 135 (1979).
31. K. Minakawa and A. J. McEvily, Scripta Metall. **15**, 633 (1981).
32. S. Suresh and R. O. Ritchie, Metall. Trans. A **13A**, 1627 (1982).
33. C. F. Shih, J. Mech. Phys. Solids **29**, 305 (1981).
34. C. Atkinson, Int. J. Engng. Sci. **10**, 45 (1972).
35. C. Atkinson, Int. J. Engng. Sci. **10**, 127 (1972).
36. A. A. Rubinstein, J. Appl. Mech. **53**, 505 (1986).
37. D. L. Davidson, Acta Metall. **36**, 2275 (1988).
38. T. Lin, A. G. Evans, and R. O. Ritchie, J. Mech. Phys. Solids **34**, 447 (1986).

39. T. Lin, A. G. Evans, and R. O. Ritchie, Metall. Trans. A **18A**, 641 (1987).
40. A. G. Evans, in "Fracture Mechanics (20th Symp.)" (R. P. Wei and R. P. Gangloff, eds.), ASTM STP, in press, American Society for Testing and Materials, 1989.
41. S. Kunz-Douglass, P. W. R. Beaumont, and M. F. Ashby, J. Mater. Sci. **15**, 1109 (1980).
42. D. B. Marshall, B. N. Cox, and A. G. Evans, Acta Metall. **33**, 2013 (1985).
43. B. Budiansky, J. W. Hutchinson, and A. G. Evans, J. Mech. Phys. Solids **34**, 167 (1986).
44. L. R. F. Rose, Mech. Mater. **6**, 11 (1987).
45. Y. Mai and B. R. Lawn, J. Am. Ceram. Soc. **70**, 289 (1987).
46. G. C. Sih, "Handbook on Stress Intensity Factors," Lehigh University Press, Bethlehem, PA, 1972.
47. J.-L. Tzou, C. H. Hsueh, A. G. Evans, and R. O. Ritchie, Acta Metall. **33**, 117 (1985).
48. C. C. Veerman and T. Muller, Eng. Fract. Mech. **4**, 25 (1972).
49. P. Niskanen and W. R. Mohn, Adv. Mater. Proc. **133**, 39 (1988).
50. Anon, Research and Development, 83 (Oct. 1988).
51. A. Mortensen, J. A. Cornie, and M. C. Flemings, J. Met. **40**, 12 (1988).
52. T. Donomoto, N. Miura, K. Funatani, and N. Miyaka, "Ceramic Fiber Reinforced Piston for High Performance in Diesel Engines," SAE Technical Paper No. 83052, Detroit, MI, 1983.



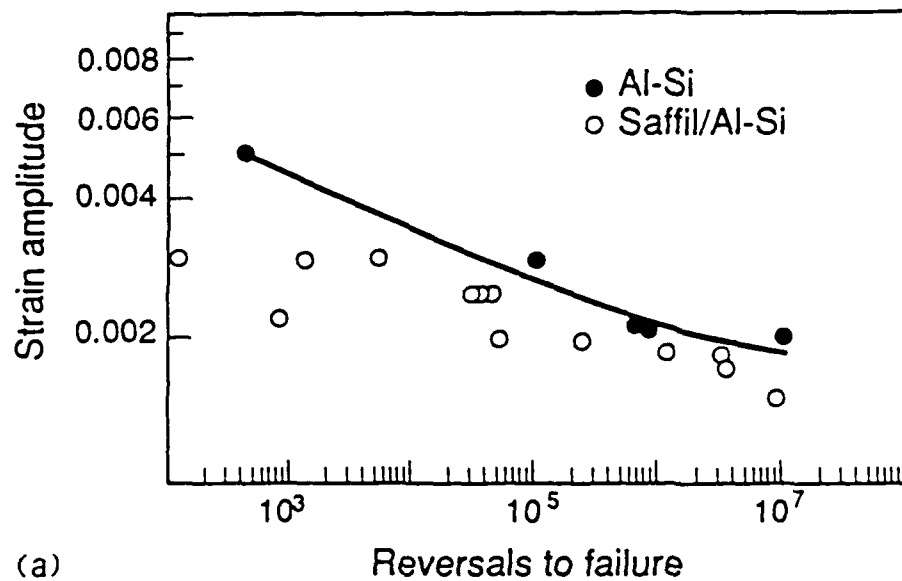
XBL 893-6551

Fig. 1. Cyclic stress/strain behavior for unreinforced and SiC-whisker-reinforced Al-Cu 2124 alloys (after Williams and Fine [10]). Reprinted with permission from the *Proceedings of the 5th International Conference on Composite Materials (ICCM-V)*, edited by W. C. Harrigan, James Strife, and A. K. Dhingra, 1985, The Metallurgical Society, 420 Commonwealth Drive, Warrendale, Pennsylvania 15086.

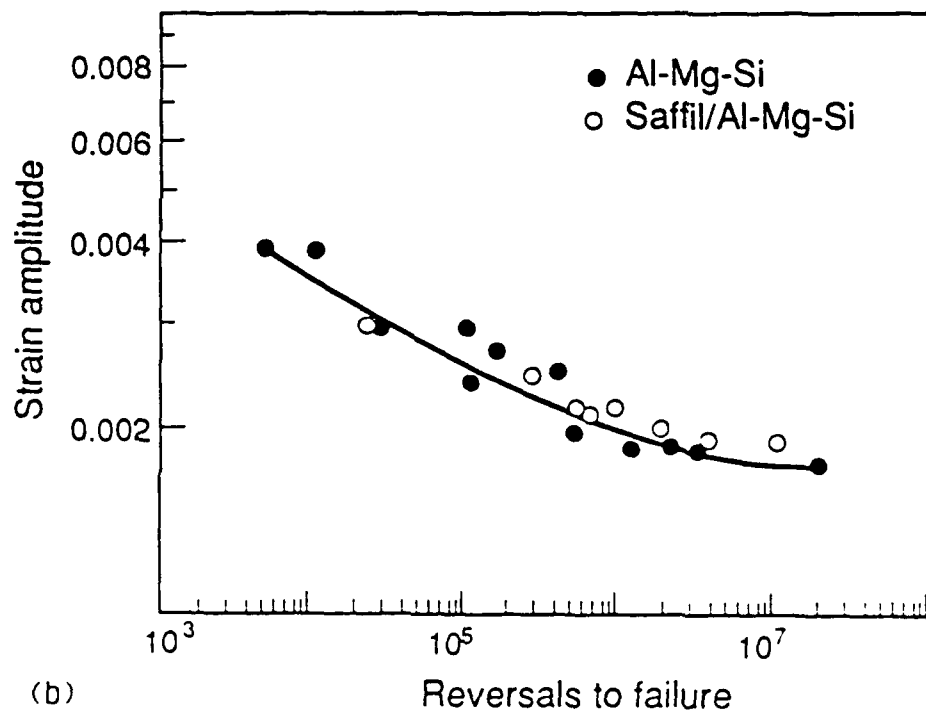


XBL 893-6550

Fig. 2. Stress amplitude vs life (S-N) curves for unreinforced, SiC-particulate-reinforced and SiC-whisker-reinforced Al-Mg-Si 6061 alloy in the peak-aged condition. Fatigue lifetime data are presented as a function of both a) stress amplitude  $\sigma_a$  and b) elastic strain amplitude  $\sigma_a/E$  (after Hassen *et al.* [12]).



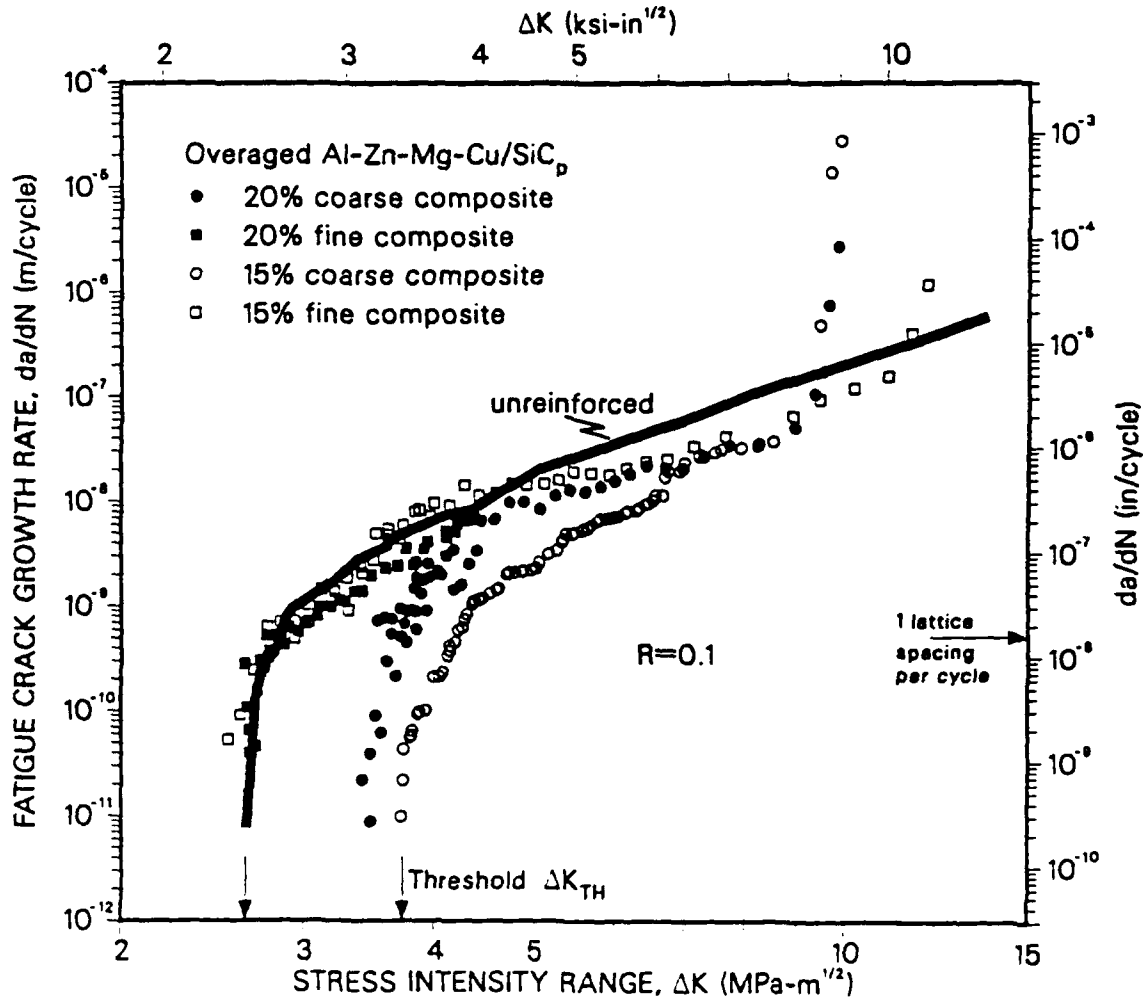
(a)



(b)

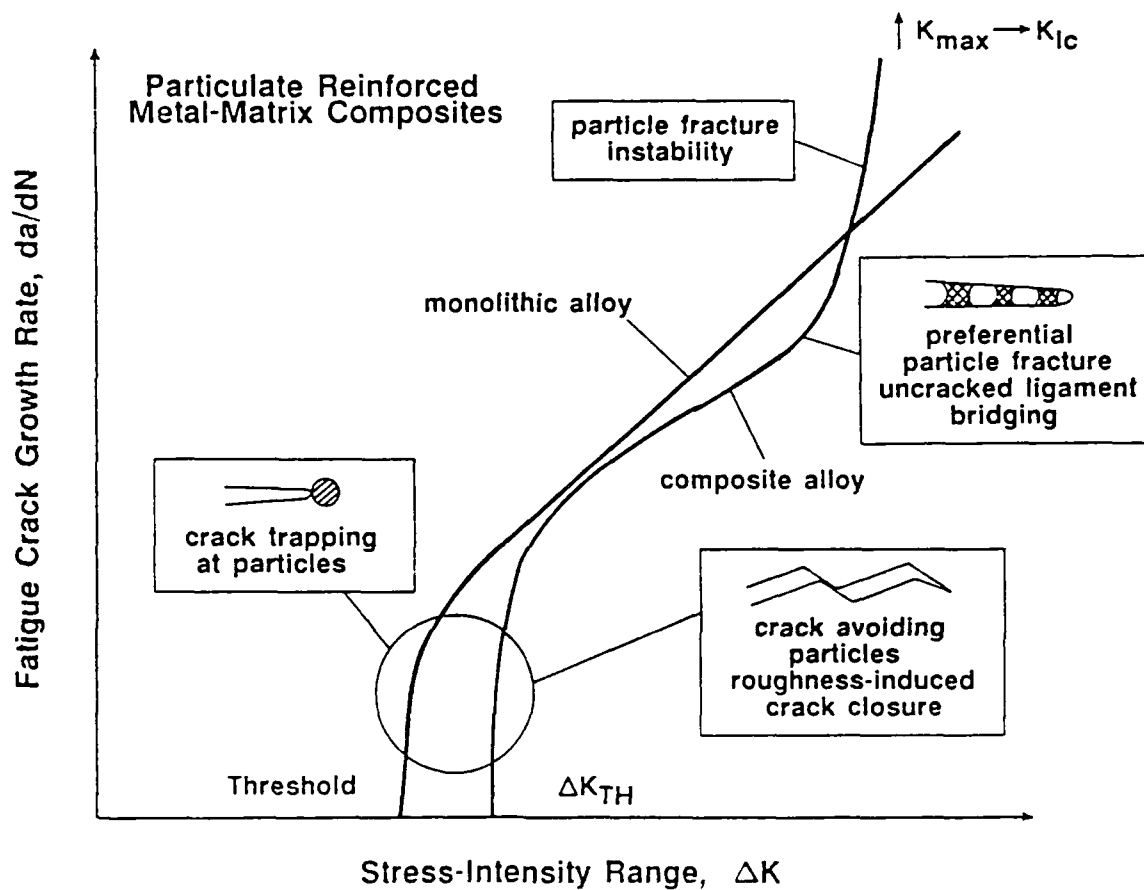
XBL93-6549

Fig. 3. Strain amplitude vs. life curves for cast unreinforced and saffil-fiber reinforced-aluminum alloy composites. Plotted are results for a) Al-Mg-Si alloys, where the composite has the lower tensile strength, and b) Al-Si alloys, where the matrix material has the lower strength (after Hurd [11]).



XBL 895-1829

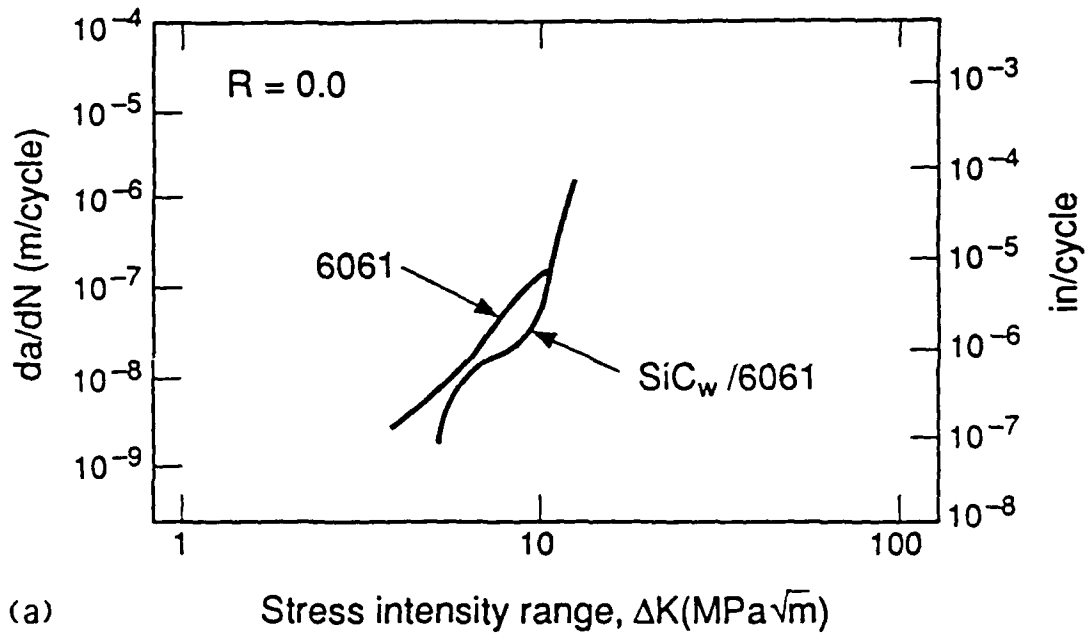
Fig. 4. Variation in fatigue-crack propagation rates,  $da/dN$ , with the stress-intensity range,  $\Delta K$ , for overaged (15h at 171°C) SiC-reinforced Al-Zn-Mg-Cu alloys at room temperature, showing behavior at a load ratio of 0.1. Plotted are data for 15 and 20% reinforcement with either fine or coarse SiC particulate (nominal size 5 and 16  $\mu\text{m}$ , respectively). Results for the unreinforced alloy (solid line) are shown for comparison [21]. The matrix of this alloy is similar to 7091.



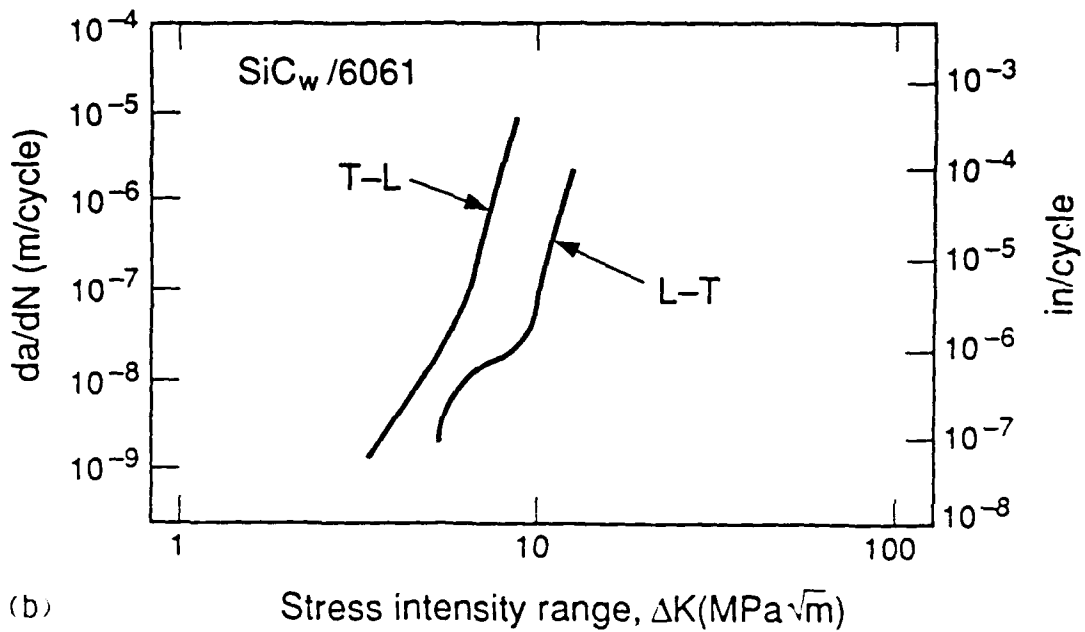
XBL 894-1300

Fig. 5. Schematic illustration showing a comparison between the variation in fatigue-crack propagation rates with  $\Delta K$  for unreinforced and particulate-reinforced metal-matrix composites; shown are the salient micromechanisms associated with crack growth in each regime.





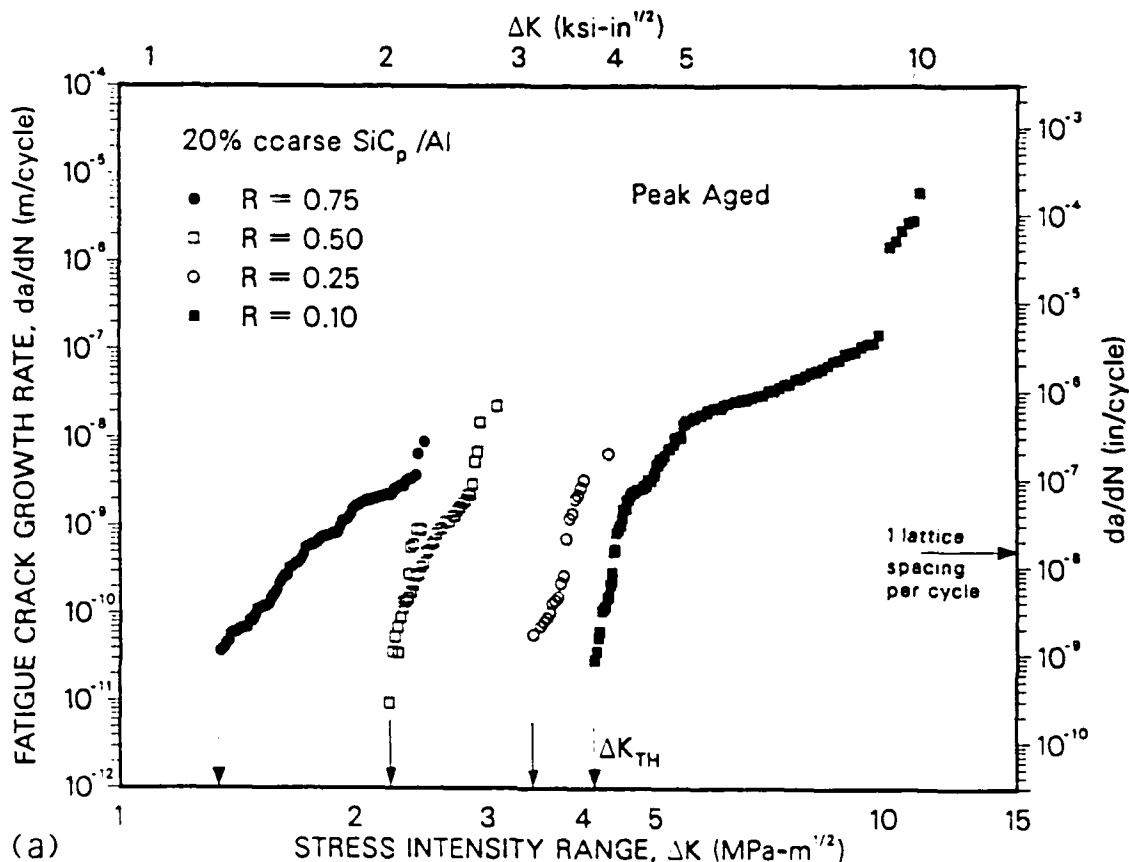
(a) Stress intensity range,  $\Delta K(\text{MPa}\sqrt{\text{m}})$



(b) Stress intensity range,  $\Delta K(\text{MPa}\sqrt{\text{m}})$

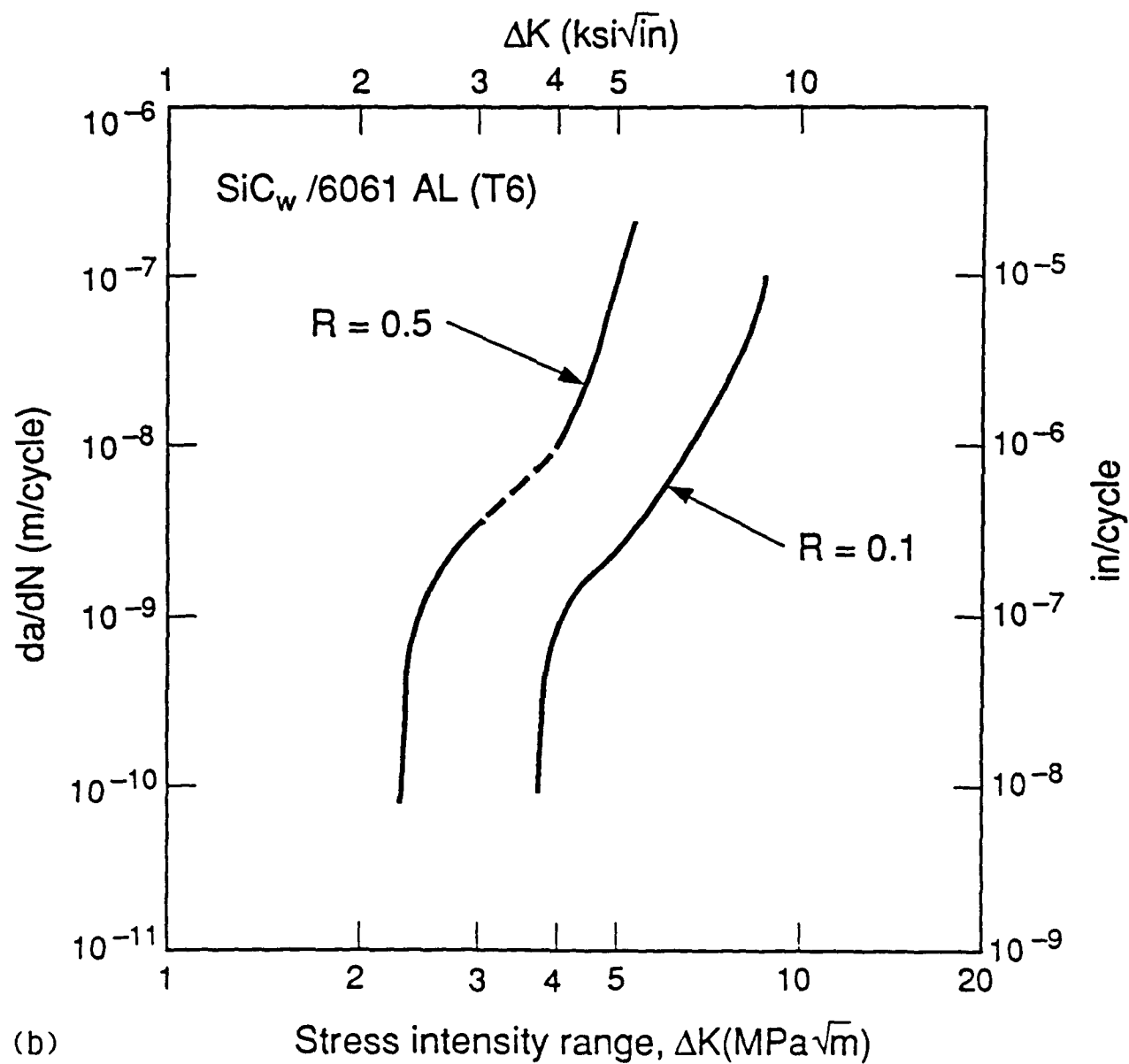
XBL 893-6548

Fig. 6. Fatigue-crack growth behavior, as a function of  $\Delta K$ , for unreinforced and SiC-whisker-reinforced 6061 aluminum alloys at a load ratio of 0. Plotted are a comparison a) between the composite and constituent matrix alloys, and b) between the T-L and L-T orientations in the composite material (after Yau and Mayer [15]).



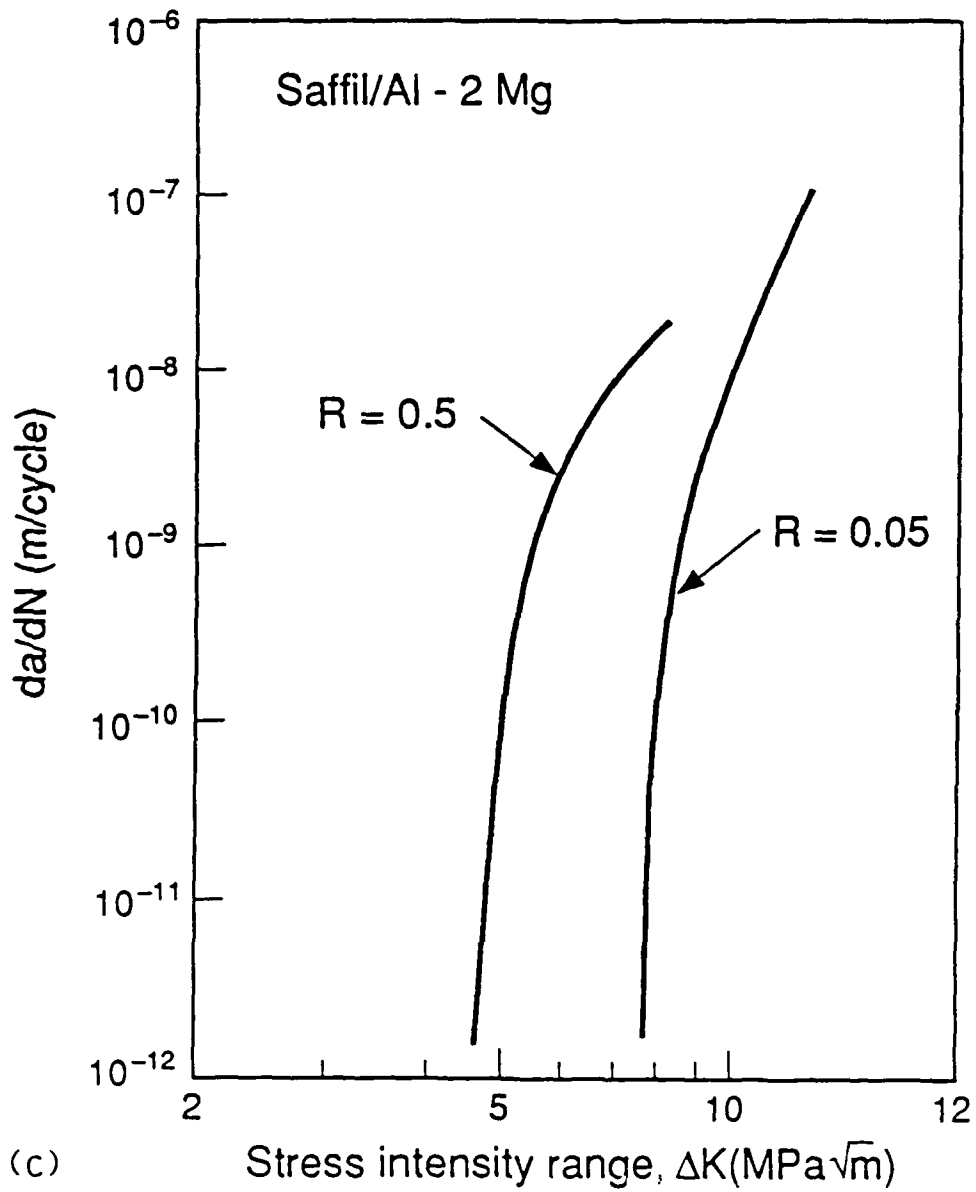
XBL 894-1301

Fig. 7. Variation in fatigue-crack propagation rates in metal-matrix composites with load ratio ( $R = K_{min}/K_{max}$ ). Data are shown for a) peak-aged (24 h at  $121^\circ\text{C}$ ) Al-Zn-Mg-Cu alloy reinforced with 20 vol% SiC particulate, b) peak-aged 6061 aluminum alloy reinforced with SiC whiskers (after Logsdon and Liaw [16]), and c) 10 vol% saffil-fiber reinforced Al-2Mg alloy (after Preston *et al.* [23]).



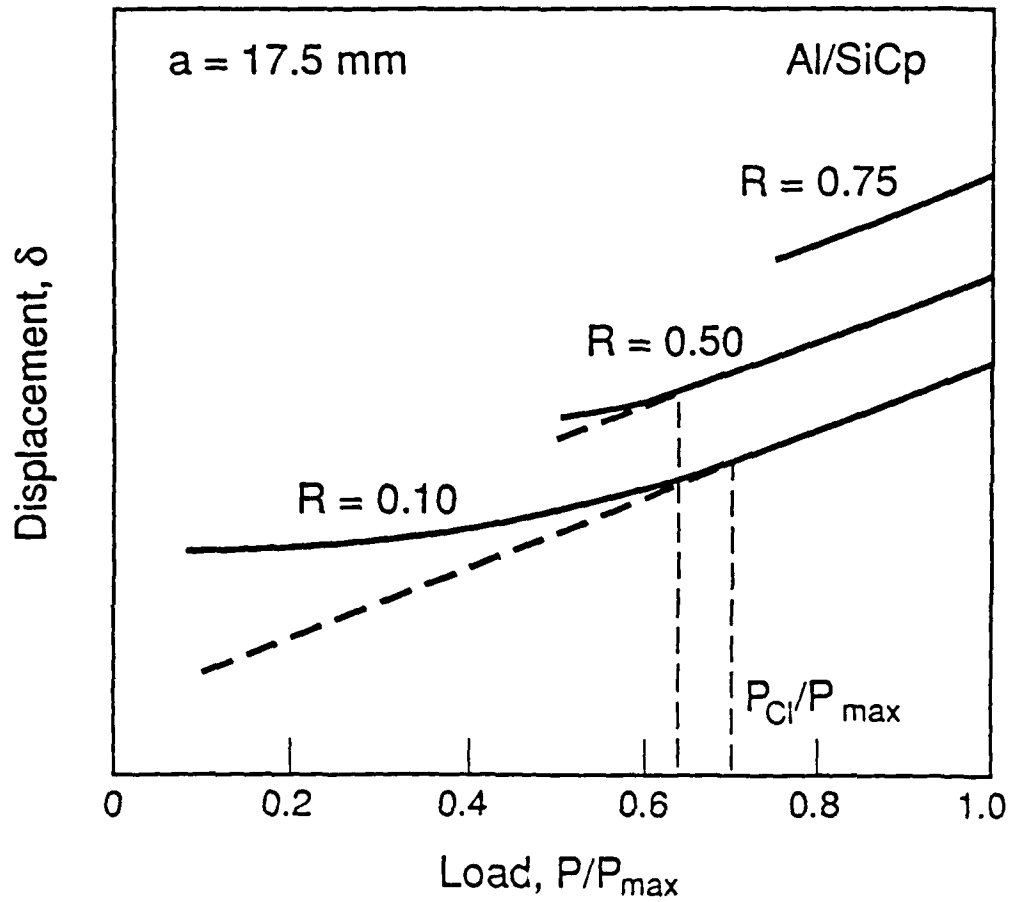
XBL 893-6547  
TID/lg

Fig. 7(b)



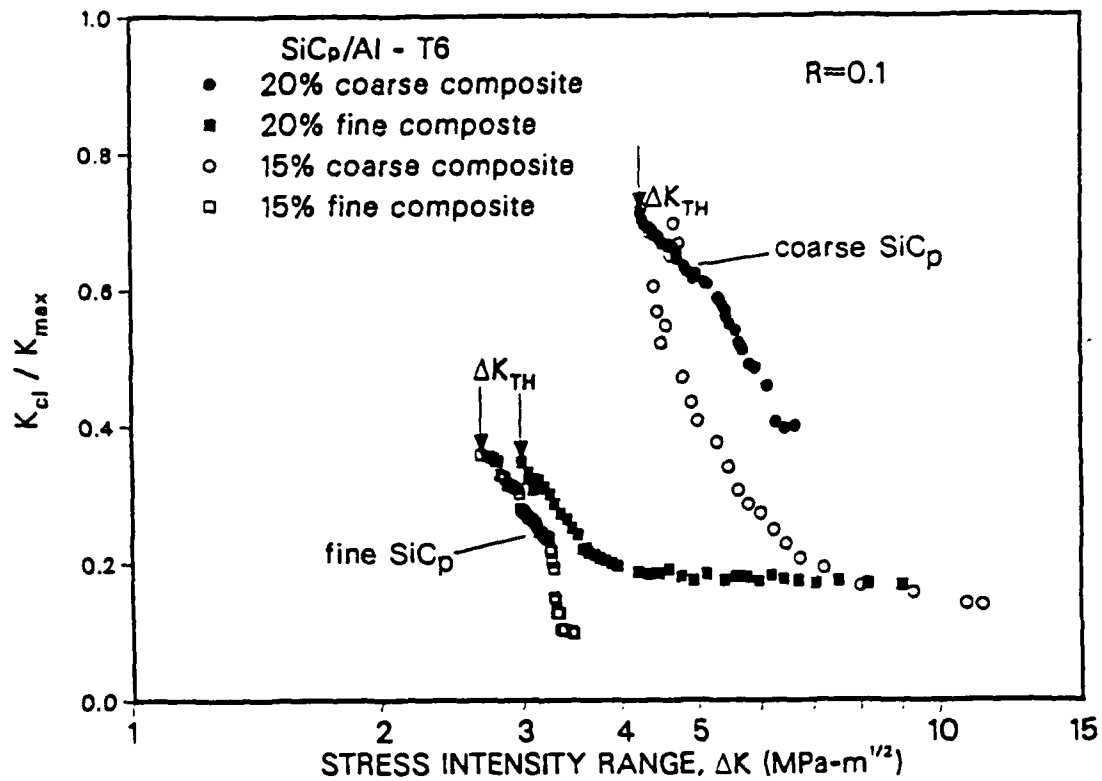
XBL 893-6545  
TID/g

Fig. 7(c)



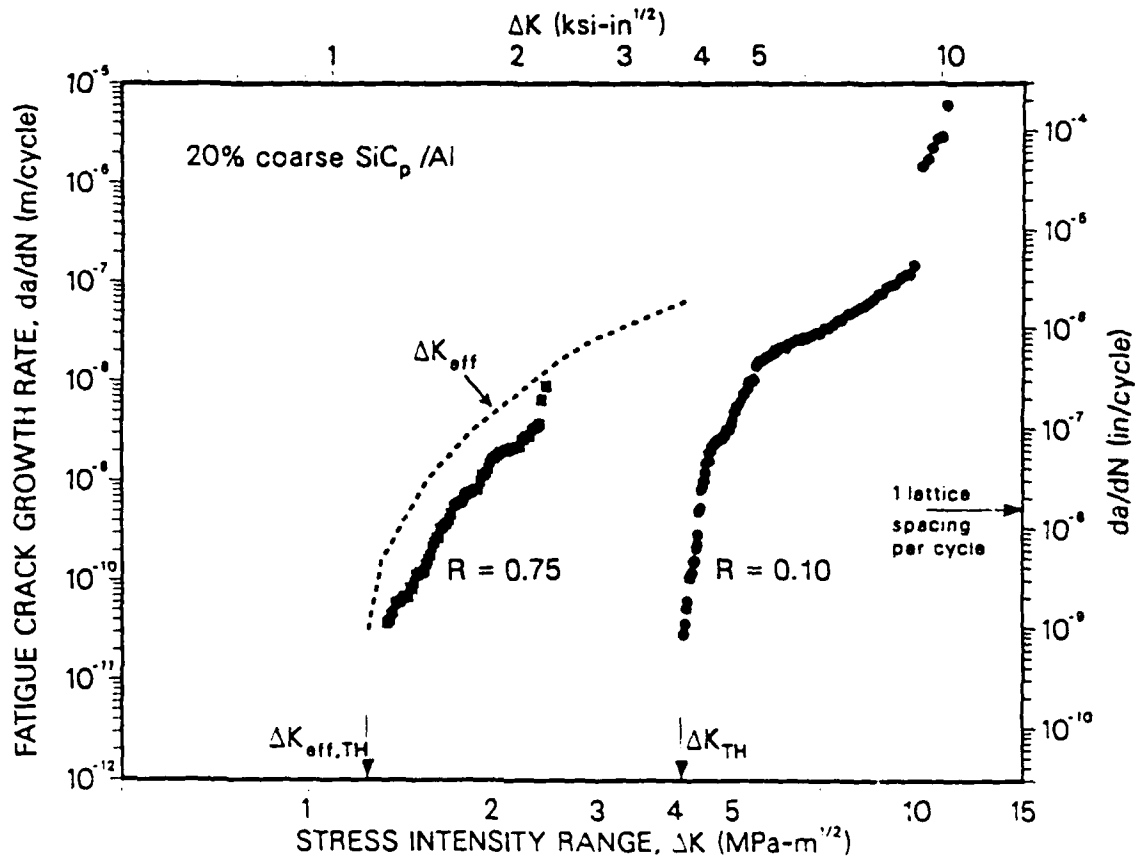
XBL 893-6546

Fig. 8. Compliance curves of crack-mouth opening displacement,  $\delta$ , as a function of applied load,  $P$ , for double-cantilever bend specimens, of SiC<sub>p</sub>-reinforced Al-Zn-Mg-Cu alloy, containing a fatigue crack. Note how the compliance for crack growth at low load ratio ( $R = 0.1$ ) shows an inflection at  $P_{CI}$ , indicative of crack-surface contact, or crack closure; no closure in the fatigue cycle is apparent at  $R = 0.75$ .



XBL 887-2670

Fig. 9. Variation in crack closure, plotted as the ratio of closure stress intensity to maximum stress intensity,  $K_{cl}/K_{max}$ , as a function of  $\Delta K$  for peak-aged Al-Zn-Mg-Cu alloy reinforced with fine (5  $\mu\text{m}$ ) or coarse (16  $\mu\text{m}$ ) SiC particulate. Note how the coarse particle distributions promote crack closure, particularly at the smaller crack-tip opening displacements associated with crack advance at low  $\Delta K$  levels [21].



XBL 894-1302

Fig. 10. Influence of load ratio  $R$  on fatigue-crack propagation rates in peak-aged Al-Zn-Mg-Cu alloy reinforced with 20 vol% SiC particulate, showing increased growth rates and lower threshold  $\Delta K_{\text{TH}}$  values at high  $R$ . Note, however, that the effect of load ratio can be normalized by accounting for the role of crack closure, i.e., by characterizing crack-growth rates in terms of the effective stress-intensity range ( $\Delta K_{\text{eff}} = K_{\text{max}} - K_{\text{cl}}$ ), rather than  $\Delta K$  ( $= K_{\text{max}} - K_{\text{min}}$ ).

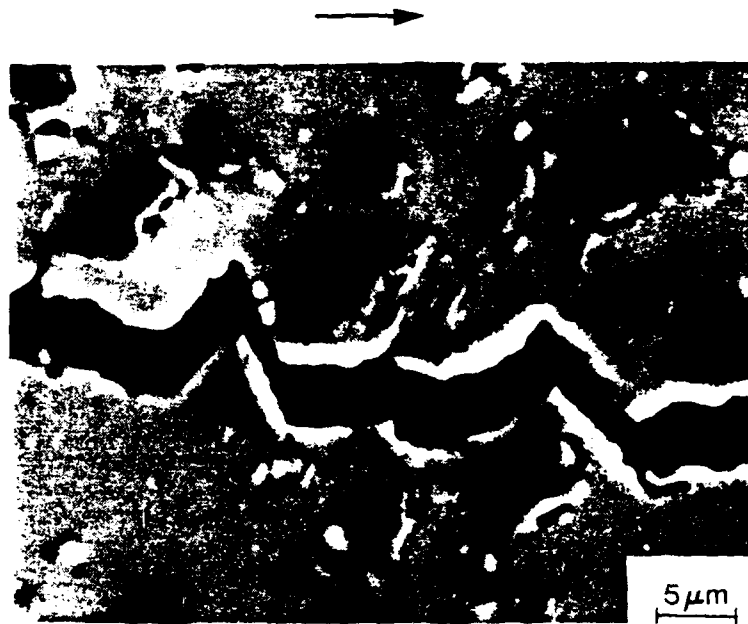
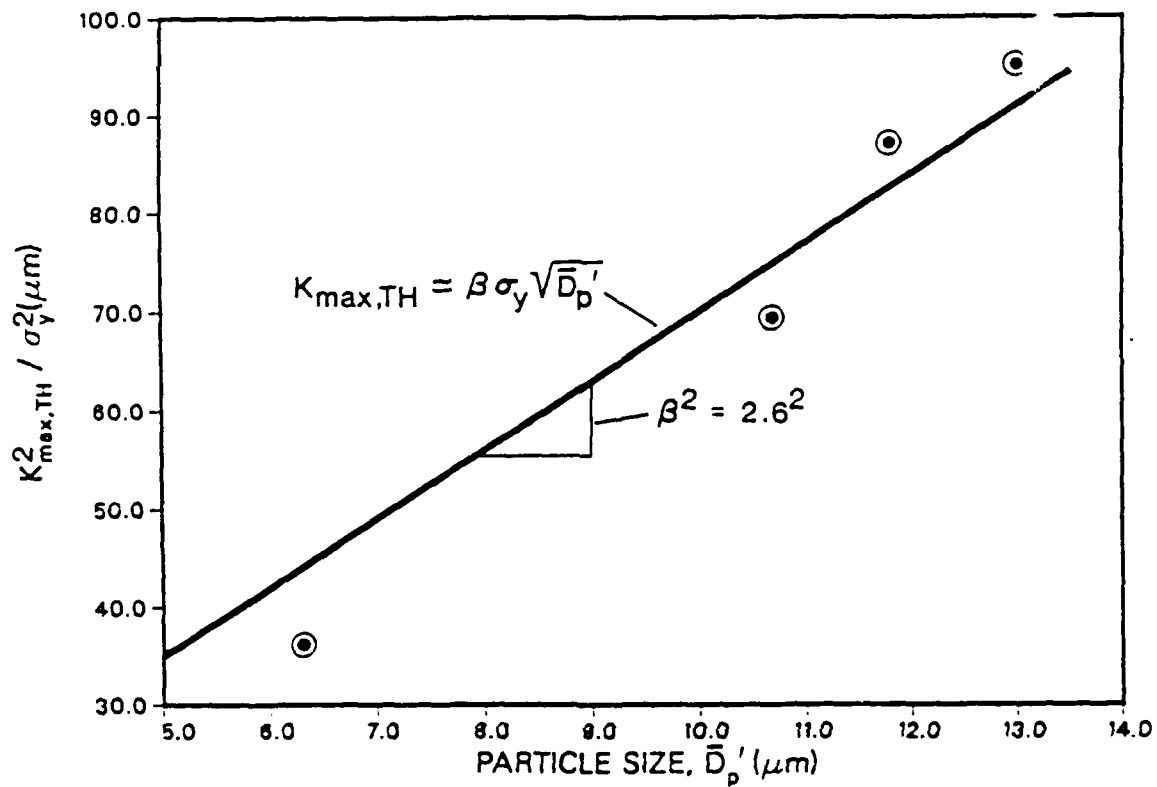


Fig. 11. Mechanisms associated with the interaction of the fatigue crack with reinforcement particles at near-threshold levels in SiC-reinforced Al-Zn-Mg-Cu alloy, showing crack deflection and consequently rougher fracture surfaces as the crack in general seeks to avoid the SiC particles. Arrow indicates direction of crack growth [21].





XBL 887-2672

Fig. 12. Experimental results (data points) and predicted variation (Eq. 5) for the relationship between the fatigue threshold maximum stress intensity,  $K_{\max,TH}$ , plotted as  $K_{\max,TH}^2 / \sigma_y^2$ , and the effective mean particle size,  $\bar{D}_p'$ , for Al-Zn-Mg-Cu alloys reinforced with SiC particulate, tested at  $R = 0.1$  [2].

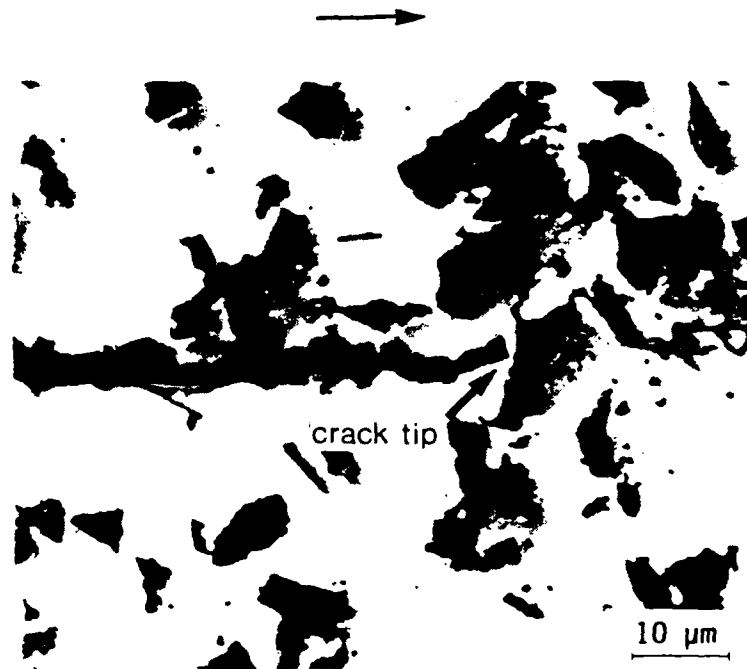
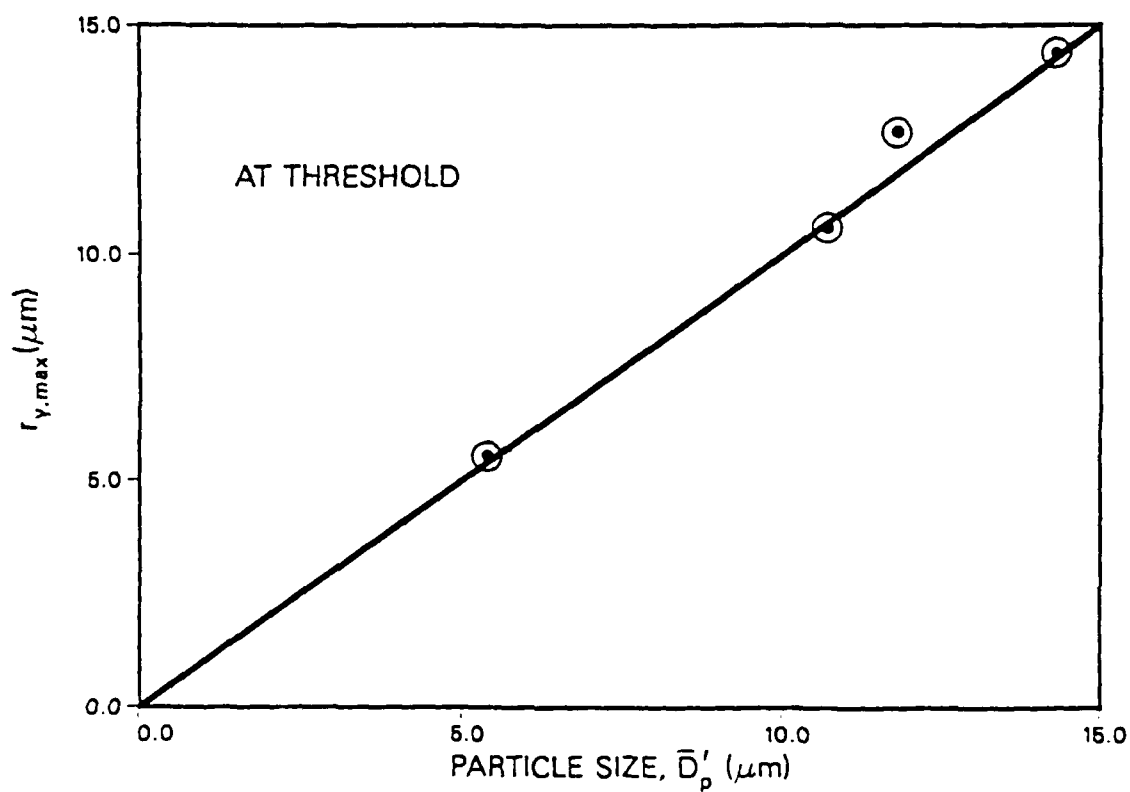
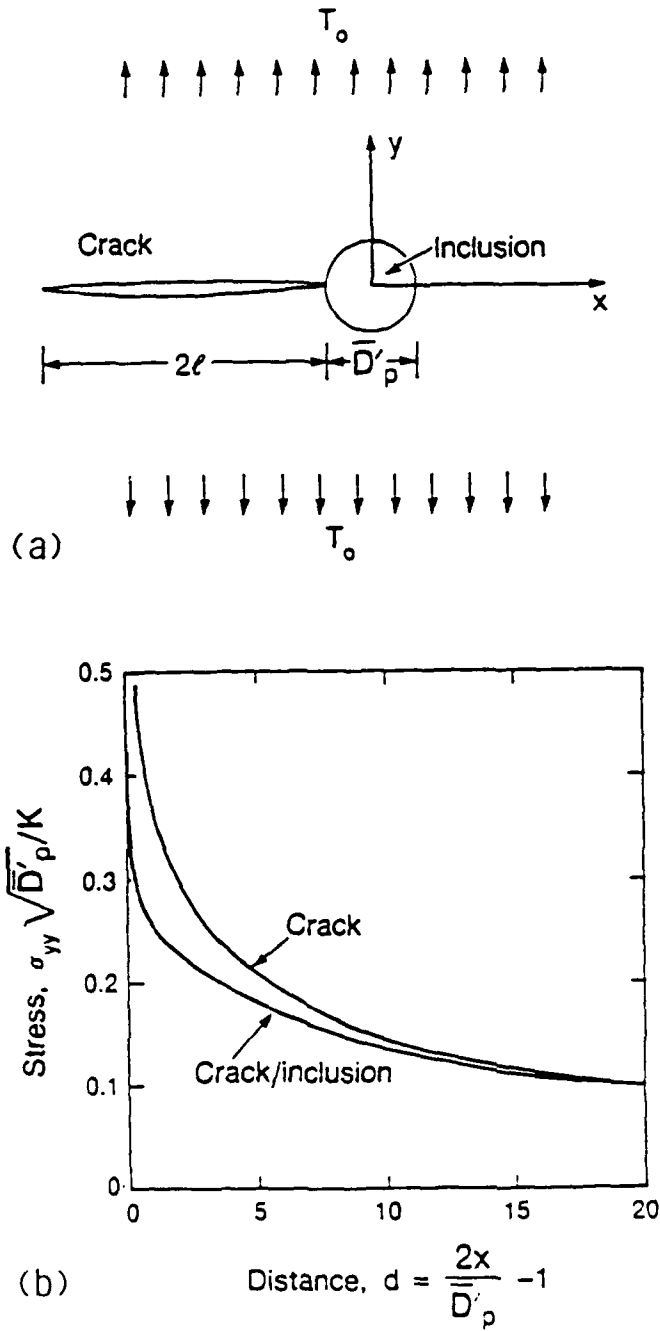


Fig. 13. Mechanisms associated with the interaction of the fatigue crack with reinforcement particles at the threshold stress intensity in SiC-reinforced Al-Zn-Mg-Cu alloy, showing crack trapping at SiC particles. Arrow indicates direction of crack growth [21].



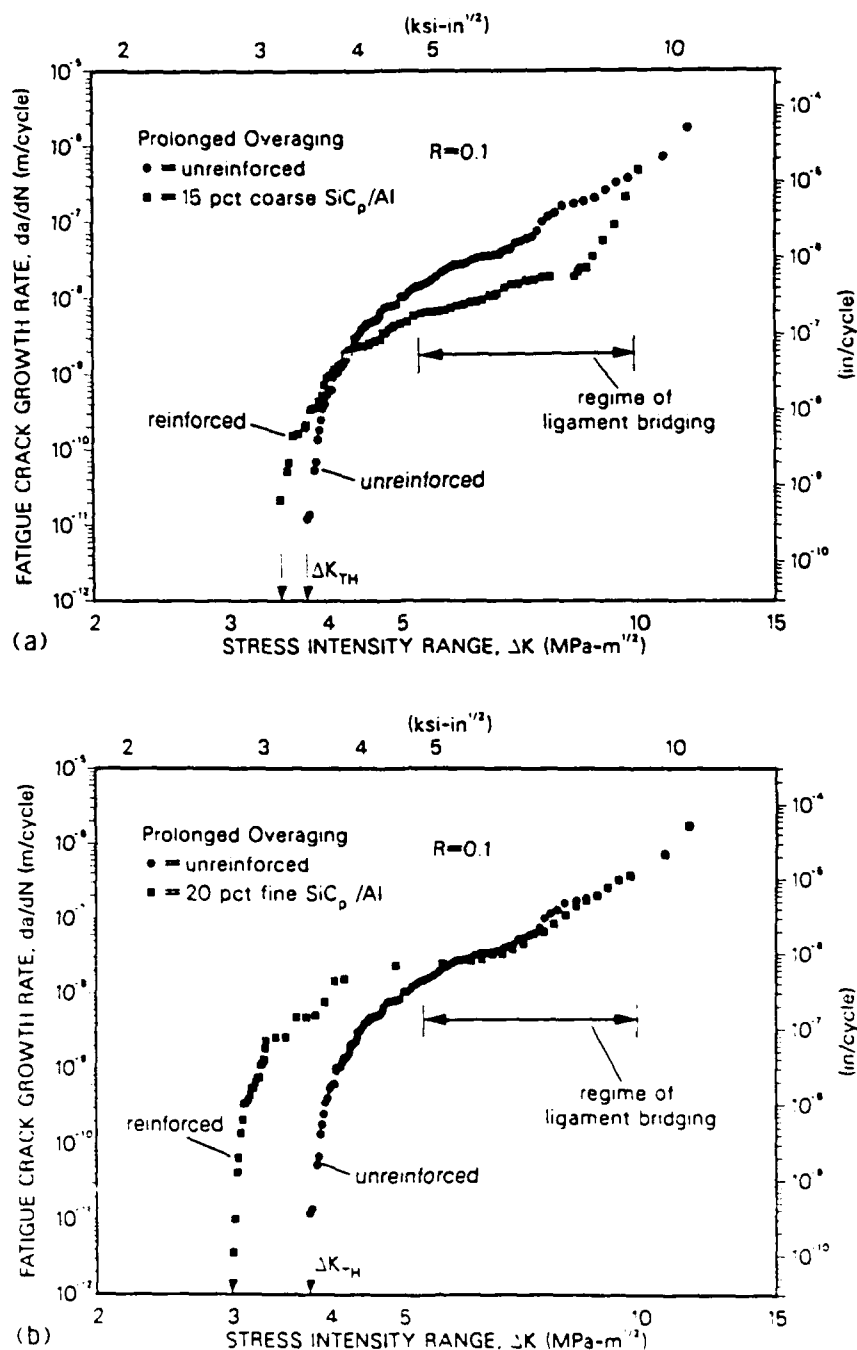
XBL 392-611

Fig. 14. Plot showing the equivalence in SiC-particulate-reinforced aluminum-alloy composites of the maximum plastic-zone size,  $r_{y,max}$ , and the effective particle size,  $\bar{D}'_p$ , at the fatigue threshold stress intensity.



XBL 386-3694

Fig. 15. a) Schematic illustration of the crack/inclusion interaction, showing b) predicted distribution of normalized tensile stress in the matrix,  $\sigma_{yy}$ , as a function of normalized distance ahead of the crack/inclusion, compared to the crack-tip stress distribution in a homogeneous solid. Calculations [21] are for a ratio of crack size to inclusion size of over  $10^3$ , and a ratio of shear modulus of inclusion and matrix of 3.



XBL 883-997 3

Fig. 16. Fatigue-crack growth rates at  $R = 0.1$  in SiC-particulate-reinforced Al-Zn-Mg-Cu alloys in a prolonged overaged (50 h at 171°C) condition, compared to behavior in the unreinforced matrix alloy. Crack bridging via uncracked ligaments predominates over the range  $\sim 10^{-9}$  to  $10^{-6}$  m/cycle. Such bridging is effective in a) the alloy containing coarse (16  $\mu m$ ) SiC particles, where bridges are overlapping; it is less effective in b) the alloy with fine (5  $\mu m$ ) particles, where bridges are coplanar [20].

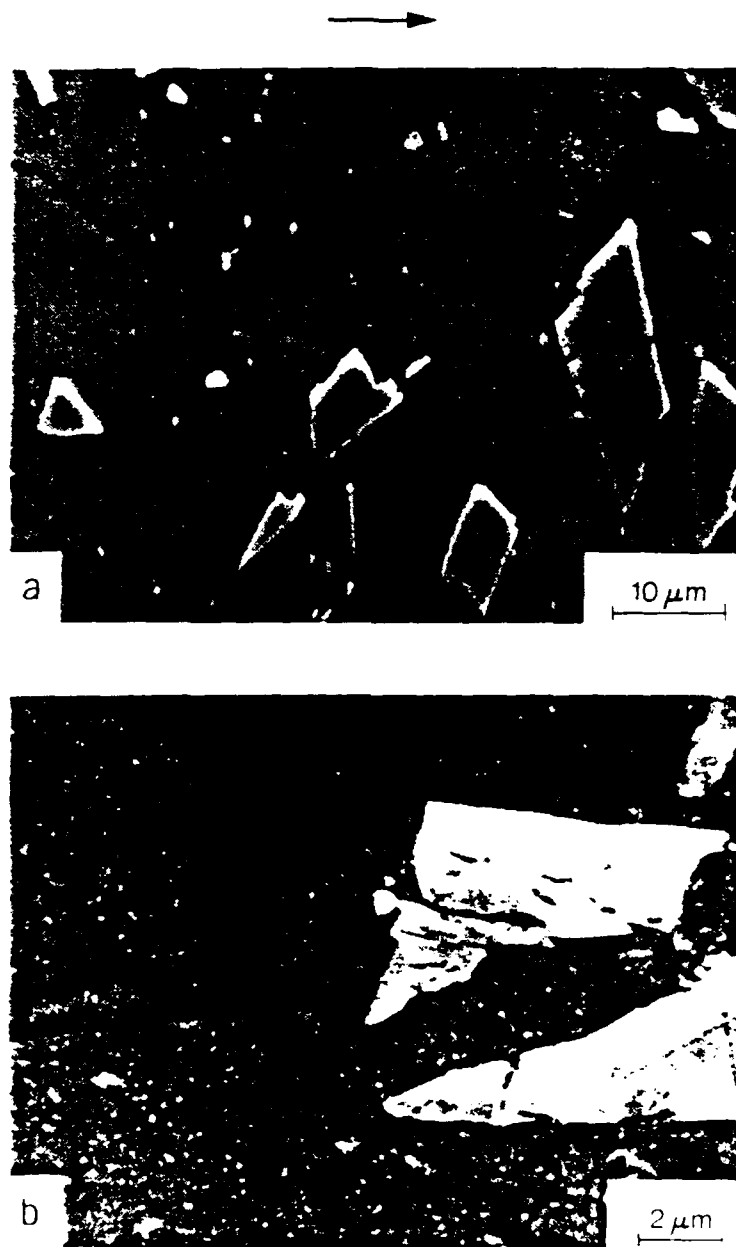


Fig. 17. Micrographs illustrating the generation of microcracks, voids at, or near, SiC-reinforcement particles *ahead* of the main crack tip at intermediate stress-intensity ranges in SiC<sub>p</sub>/Al composites, showing a) limited cracking of specific SiC particles, and b) formation of microvoids in constrained matrix material between closely spaced particles. Arrow indicates the general direction of crack growth.

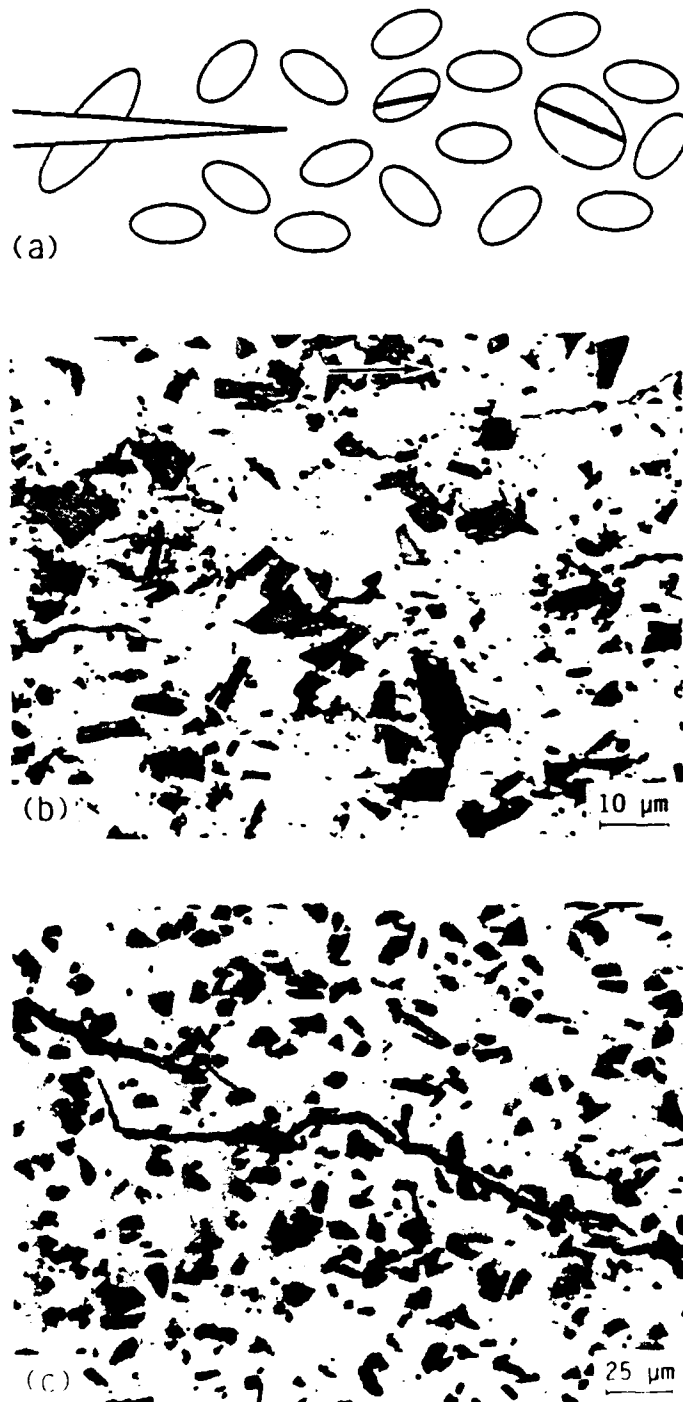
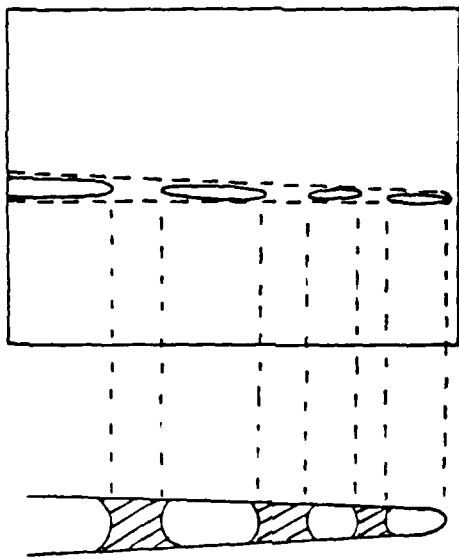


Fig. 18. Evidence for the creation of uncracked ligaments in particulate-reinforced metal-matrix composites, resulting from limited particle fracture, both ahead and in the wake of the crack tip. Shown are a) schematic illustration of the cracking process, and bridging from b) coplanar uncracked ligaments in a fine SiC<sub>p</sub>/Al-alloy composite, and c) "overlapping" ligaments in a coarse SiC<sub>p</sub>/Al-alloy composite. Horizontal arrow indicates general direction of crack growth [20].

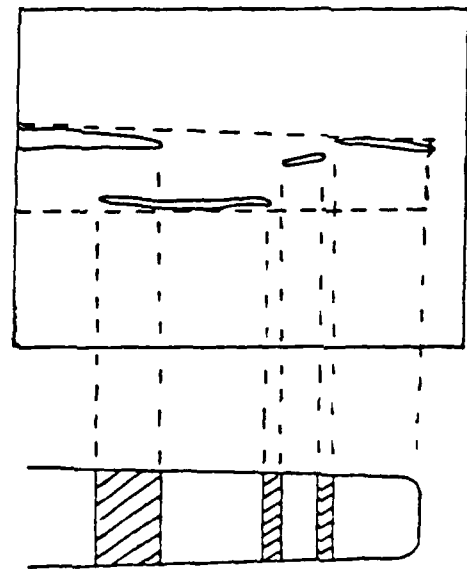
## UNCRACKED LIGAMENT BRIDGING

coplanar ligaments



(a)

overlapping ligaments

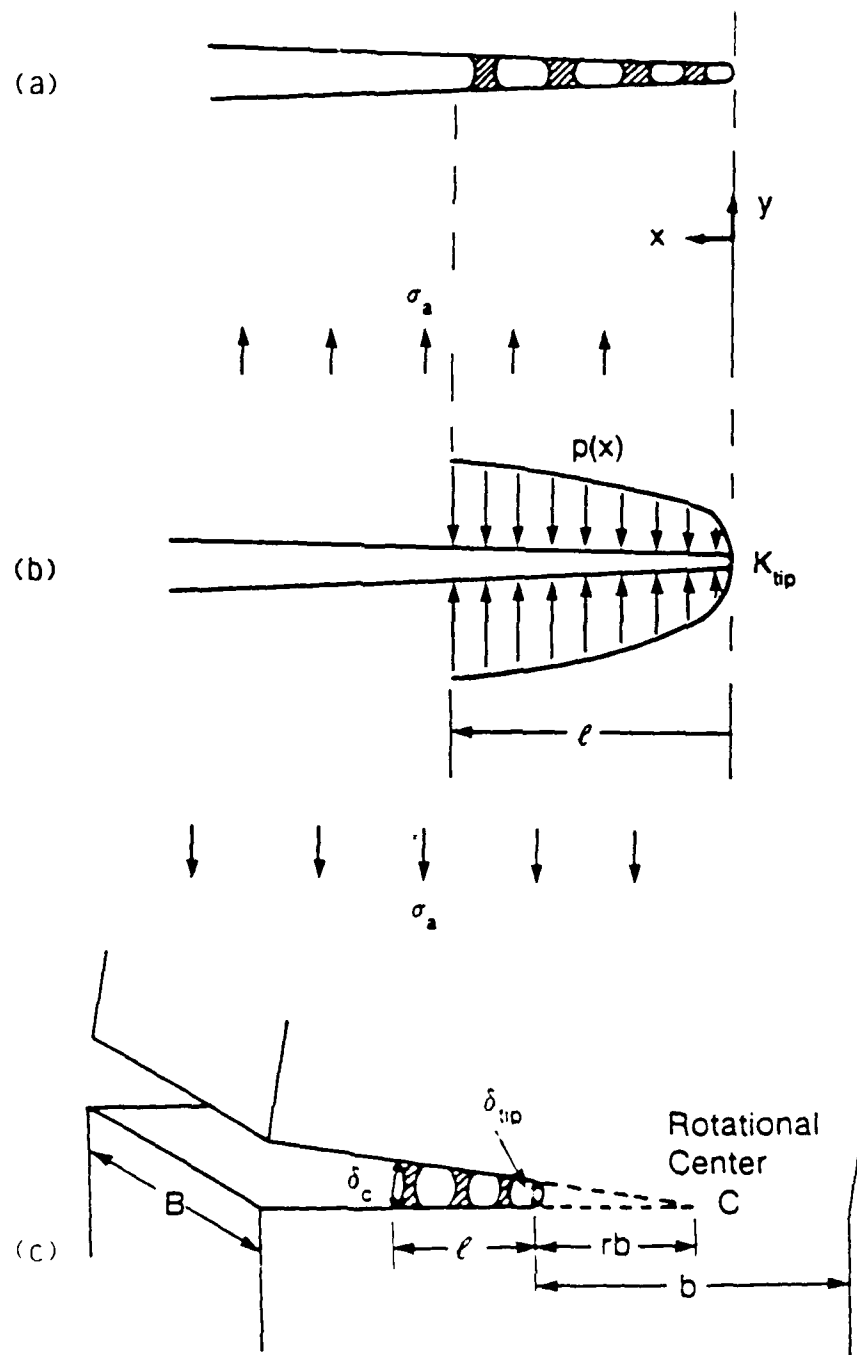


(b)

XBL 894-1303

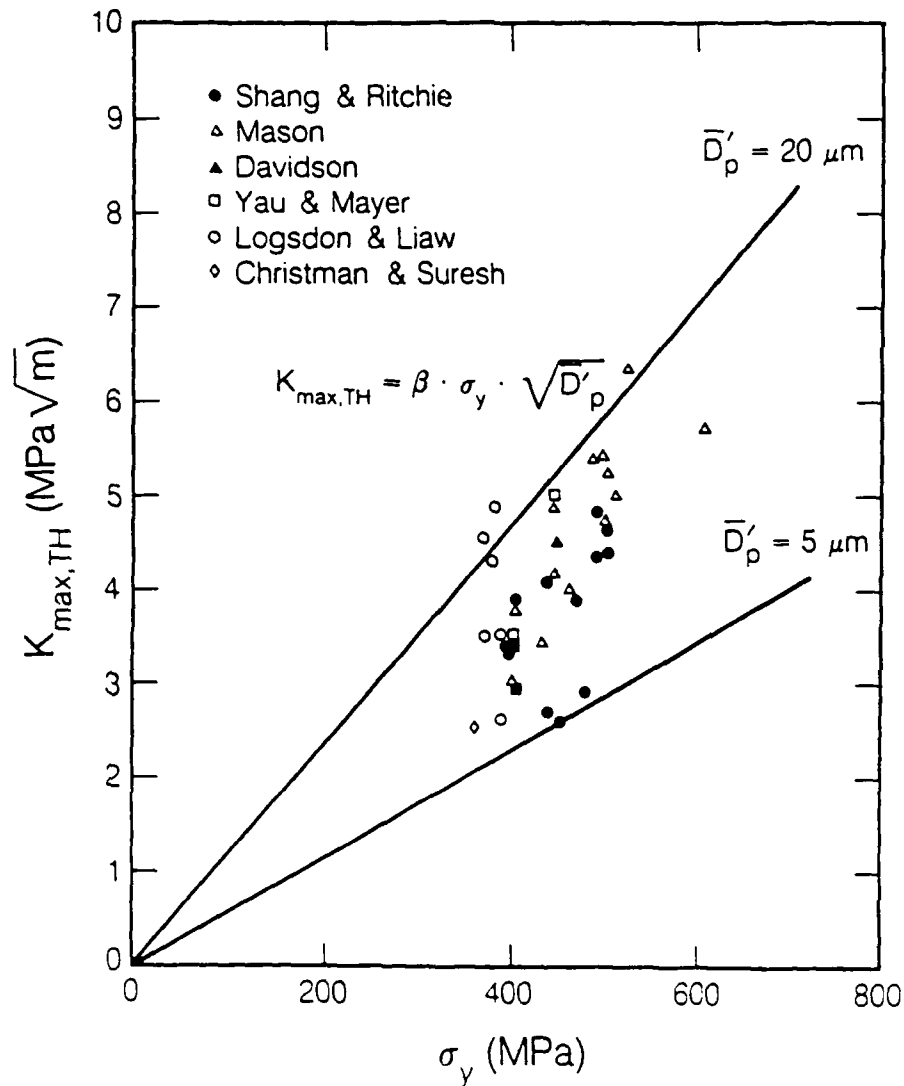
Fig. 19. Schematic illustration of uncracked ligament bridging from a) coplanar and b) overlapping ligaments.





XBL 883-9587 A

Fig. 20. Schematic illustrations of the basis for models of a) uncracked ligament bridging, with b) a bridging zone stretching over distance  $\ell$  behind the tip of a crack subjected to an externally applied stress,  $\sigma_y$ . c) The crack is assumed to open around a rotational center C located at distance  $rb$  ahead of the tip, where  $b$  is the uncracked specimen ligament and  $r$  is the rotational constant [20].



XBL 892-6508

Fig. 21. Summary plot of the variation in fatigue threshold  $K_{\max,TH}$  values for SiC-reinforced aluminum alloys with yield strength  $\sigma_y$ , showing a comparison of experimentally measured threshold data [15-24] with the predicted trends from the crack-trapping model (Eq. 5) for particle sizes  $\bar{D}'_p$  of 5 and 20  $\mu\text{m}$ .

### CRACK-TIP SHIELDING IN METAL-MATRIX COMPOSITES: MODELLING OF CRACK BRIDGING BY UNCRACKED LIGAMENTS

JIAN KU SHANG AND R. O. RITCHIE

Department of Materials Science and Mineral Engineering, University of California, Berkeley, CA 94720

#### ABSTRACT

As part of an investigation into the micro-mechanisms of crack-tip shielding associated with the growth of fatigue cracks in metal-matrix composites, simple models are developed for the role of crack bridging in high-strength aluminum alloys reinforced with SiC particulate (Al/SiC<sub>p</sub>). Based on experimental observations of crack growth, crack-tip shielding and crack-path morphology in these alloys, the bridges are found to be associated with uncracked ligaments in the wake of the crack tip, and are modelled in terms of approaches based on a critical crack-opening displacement or critical tensile strain in the ligament.

#### INTRODUCTION

Over the past ten years, much work in metals, ceramics, rocks and composites has focused on the role of crack-tip shielding in enhancing toughness, or more generally in impeding crack advance, by locally reducing the "crack driving force" actually experienced at the crack tip; notable examples are transformation toughening in ceramics and fatigue-crack closure in metals, as reviewed in [1,2]. In certain composite and monolithic materials, however, a prominent shielding mechanism occurs from bridging between the crack faces by strong fibers or unbroken ligaments in the wake of the crack tip [3-13]. In brittle fiber-reinforced ceramic-matrix composites where the fibers are sufficiently strong and the fiber/matrix interface sufficiently weak, preferential failure in the matrix can leave intact fibers spanning the crack for some distance behind the crack tip [1,3-8]. The fibers act as a series of springs which restrain crack opening and thereby shield the crack tip from the applied far-field loading, resulting in lower, yet crack-size dependent, growth-rate behavior [3-8].

In metallic materials, similar effects have been reported for aluminum laminates reinforced with epoxy-resin sheets impregnated with aramid fibers (ARALL Laminates<sup>®</sup>), where the fiber/epoxy interfaces now are weak enough to permit controlled delamination and thus bridging of unbroken fibers across the crack [13,14]. However, in most metal-matrix composites, such as aluminum alloys discontinuously reinforced with SiC fibers (or whiskers or particles), the reinforcement phase invariably fractures due to its strong interface with the matrix, with the result that fiber-bridging is essentially insignificant [15-17].

Recently, however, studies on fatigue-crack growth in aluminum alloy/SiC-particulate composites (Al/SiC<sub>p</sub>) have revealed a different mechanism of bridging, induced by the presence of uncracked ligaments behind the crack tip [15,16]. Such ligaments, although not continuous in three dimensions, act in any one two-dimensional section to inhibit crack opening. This mechanism, which has also been observed in monolithic materials [10-12], appears to result from fracture events triggered ahead of the crack tip or from general non-uniform or discontinuous advance of the crack front: in Al/SiC<sub>p</sub> composites it predominates at intermediate fatigue-crack growth rates ( $10^{-9}$  to  $10^{-6}$  m/cycle) where cleavage of SiC particles ahead of the crack tip becomes significant [15].

It is the objective of the present note briefly to characterize such uncracked-ligament bridging in Al/SiC<sub>p</sub> composites, and to develop simple models to quantify the magnitude of the induced shielding.

### FATIGUE CRACK BRIDGING IN Al/SiC<sub>p</sub> COMPOSITES

Two types of ligament bridging have been observed during fatigue-crack propagation at intermediate stress intensities in Al/SiC<sub>p</sub> composites, as described in [15,16] for SiC-particulate reinforced P/M Al-Zn-Mg-Cu alloys. In alloys with higher SiC volume fractions and small interparticle spacings, the uncracked ligaments are predominantly co-planar with the crack, and directly associated with fracture of carbides ahead of the crack tip (Fig. 1a); however, by comparison to behavior in the unreinforced alloy, the resulting effect on crack-growth rates is small (Fig. 1b). In alloys with lower volume fractions of more dispersed SiC particles, conversely, the ligaments are principally formed by overlapping cracks on different planes (Fig. 1c); the effect on growth rates is now considerably larger (Fig. 1d).

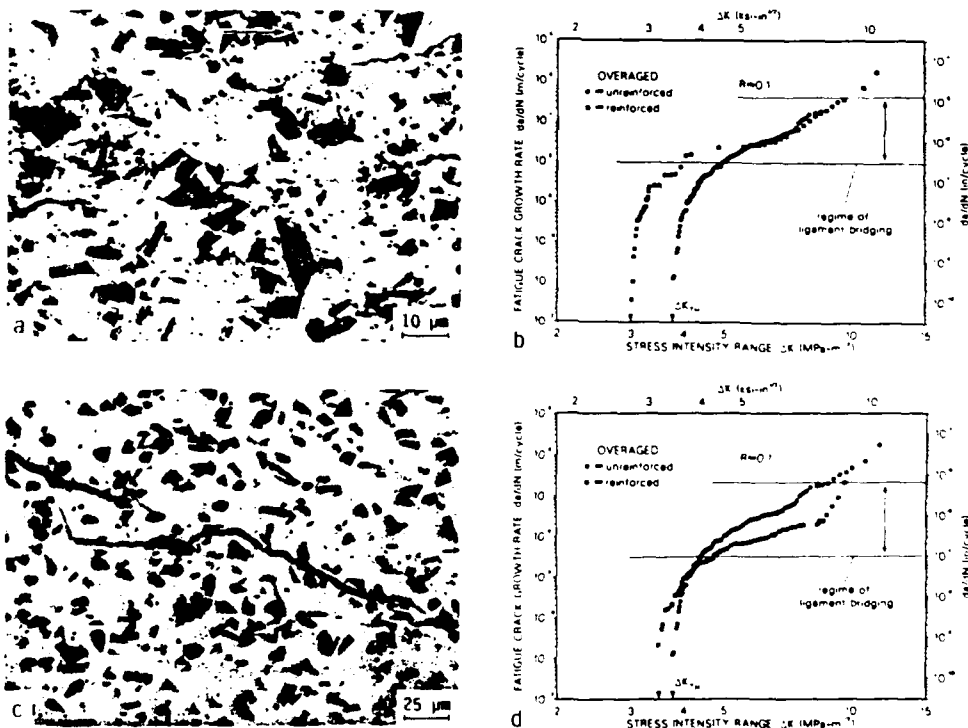


Fig. 1: Uncracked-ligament bridging in Al/SiC<sub>p</sub> composites, showing a) co-planar ligaments in 20 vol% (6-μm-sized) SiC alloy, and b) corresponding effect on fatigue-crack growth rates (by comparison of behavior in the reinforced and unreinforced alloy over the range  $10^{-8}$  -  $10^{-6}$  m/cycle); c) "overlapping" ligaments in 15 vol% (11-μm-sized) SiC alloy, and d) corresponding effect on growth rates. Note: Growth-rate differences at low  $\Delta K$  levels are associated with primarily crack closure; no bridging is observed in this regime. Arrow indicates general direction of crack growth.

## CRACK-BRIDGING MODELS

There have been several previous models to evaluate the role of bridging in metals, ceramics and composites [3-13], although only one (for ARALL Laminates) is specific to cyclic loading [13]. In essence, the key problem lies in defining the force in the bridges as a function of the crack-opening displacement or distance from the crack tip. A listing of the force-separation functions utilized in five prominent models [5,9-12] is given in Table I. The fiber-bridging model of Marshall et al. [5] and the rubber-particle toughening model of Kunz-Douglass et al. [9] compute the strain in the bridges from the strain compatibility between the fiber and matrix during fiber pull-out or from the shape change of rubber particles, and are thus mechanism-specific. Mai and Lawn [10] in their ligament-bridging model, conversely, simply adopt a trial exponential force-separation function, with parameters set by the particular mechanism. The equilibrium-crack models of Gerberich [11] and Rosenfield and Majumdar [12], on the other hand, are more general, but assume simply that the stress in the bridges is equal to the yield or fracture stress, respectively.

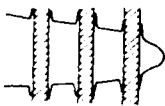
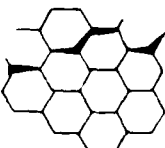


In the current work, two approaches are taken to model the forms of ligament bridging observed during fatigue-crack growth in Al/SiC<sub>p</sub>, i.e., based on a limiting crack-opening displacement or a limiting strain in the uncracked ligaments; analyses are described below.

### General Principles

The effect of an area fraction,  $f$ , of uncracked ligaments on the crack plane, existing over a distance  $x = l$  (the bridging zone) behind the crack tip (Fig. 2), is represented by a distributed force,  $p(x)$ , given in terms of the stress  $\sigma(x)$  in the ligaments by:

$$dp(x) = f \sigma(x) dx \quad (1)$$

Table I. Force-Separation Functions for Various Models

	Marshall Cox Evan.	Mai Lawn	Kunz-Douglass Beaumont Ashby	Gerberich	Rosenfield Majumdar
Separation- Function	$p(x) = 2\sigma_i [u + (E_f/E_m)(1-\nu)/R]^3$ $\sigma_i$ - interfacial stress $E_f$ - fiber modulus $R$ - fiber radius $\nu$ - $E_f \nu_f / E_m (1 - \nu_f)$	$p(u) = p^* (1 - \frac{u}{u^*})^m$ $u^*, p^*$ - limiting values $m$ - mechanism-dependent $p = f \cdot \sigma(x)$	$\sigma = G \cdot (\epsilon - \frac{1}{\epsilon^*})$ $G$ - modulus $\epsilon$ - true strain	$\sigma = \sigma_0$	$\sigma = \sigma_0$
Method	pull-out mechanics (strain compatibility)	trial function	constitutive eqn. for rubber	yield strength	fracture stress
Applications	fiber bridging in ceramic matrix composites	interfacial bridging	rubber-toughened plastics	general	
					

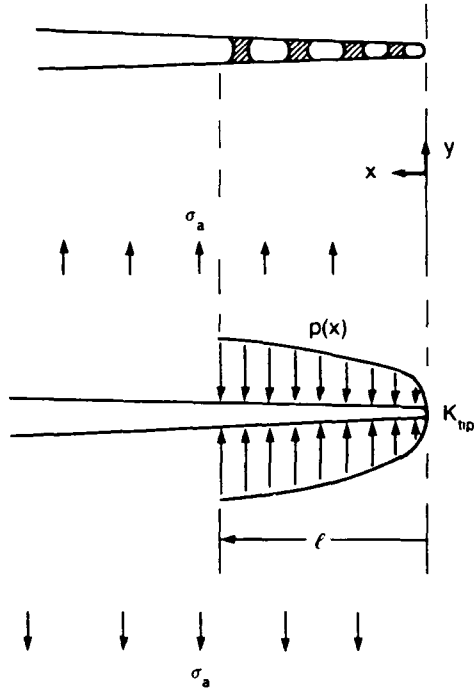


Fig. 2: Idealization of the bridging zone over distance  $l$  behind the tip of a crack subjected to an externally applied stress  $\sigma_a$ .

For a semi-infinite crack, this distributed force induces a stress intensity given by [18]:

$$K_s = \frac{\sqrt{2}}{\pi} \int_0^l \frac{dp(x)}{\sqrt{x}} \quad (2)$$

If the crack is subjected to an applied stress field, superposition of the shielding stress intensity,  $K_s$ , due to bridging with the globally applied (far-field) stress intensity,  $K_a$ , yields an expression for the effective (near-tip) stress intensity,  $K_{tip}$ , experienced locally at the crack tip (Fig. 2):

$$K_{tip} = K_a + K_s \quad (3)$$

This is related to a crack-opening displacement,  $\delta_{tip}$ , in terms of Young's modulus,  $E$ , and yield strength,  $\sigma_y$ , of the ligament, by:

$$K_{tip} = \sqrt{\frac{E' \sigma_y \delta_{tip}}{d}} \quad (4)$$

where  $E' = E$  in plane stress and  $E/(1 - \nu^2)$  in plane strain.  $\nu$  is Poisson's ratio, and  $d$  is a constant varying between 0.3 and 1.0 depending upon the yield strain and work-hardening exponent and whether plane-strain or plane-stress conditions apply [19]. Solutions to Eqs. 2-4 are given below.

### Limiting Crack-Opening Displacement Approach

The basis of this approach is that the stress in any ligament behind the crack tip is related to the crack opening at that point; specifically the displacement in the last intact ligament at the end of the bridging zone must approach the limiting crack-opening displacement,  $\delta_c$ , for fracture of that ligament. By assuming for simplicity that an idealized fatigue crack can be taken as trapezoidal (Fig. 3), the crack-opening displacement,  $\delta_x$ , at any distance  $x$  along the crack length can be determined in terms of the crack-tip opening displacement,  $\delta_{tip}$ , and specimen ligament,  $b$ :

$$\delta_x = \delta_{tip} \cdot \left( \frac{x + rb}{rb} \right) \quad (5)$$

assuming that the crack opens about some rotational axis at a distance,  $rb$ , ahead of the crack tip;  $r$  is the rotational factor and takes values between 0.195 for elastic deformation and 0.470 for plastic deformation [20].

To maintain equilibrium such that the crack may extend without breaking ligaments along the bridging zone, the crack-opening displacement at any point within the zone,  $\delta_x$ , must satisfy:

$$\delta_x \leq \delta_c, \quad 0 \leq x \leq 1 \quad (6a)$$

whereas at the end of the bridging zone:

$$\delta_x = \delta_c, \quad \text{at } x = 1 \quad (6b)$$

where  $\delta_c$ , the maximum displacement in the ligament corresponding to its failure, is independent of the size of bridging zone but varies with the area fraction  $f$  of ligaments. Thus, assuming that a partially-bridged crack, with  $f < 1$ , is analogous to a fully-bridged crack with an effective thickness  $f$  times the full specimen thickness, Eq. 2 becomes:

$$\sqrt{\frac{\delta_c rb E' \sigma_y}{d(2 + rb)}} = K_d + \frac{\sqrt{2}}{\pi} \int_0^1 \frac{\sigma(x) dx}{\sqrt{x}} \quad (7)$$

yielding an expression for the stress,  $\sigma(x)$  in the ligaments:

$$\sigma(x) = -\frac{\pi}{2\sqrt{2}} \sqrt{\frac{\delta_c rb E' \sigma_y}{d}} \left[ \frac{\sqrt{x}}{(x + rb)^{3/2}} \right] \quad (8)$$

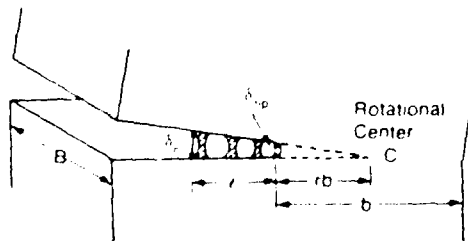


Fig. 3: Schematic illustration of idealized fatigue crack with bridging zone, showing definitions of the rotational axis and crack-opening displacements.

With substitution, Eq. 8 provides an expression for the degree of crack-tip shielding due to uncracked-ligament bridging, in terms of the area fraction of ligaments, the applied stress intensity and the ratio  $\ell/rb$ :

$$K_S = -f K_A [(1 + \ell/rb)^{\frac{1}{2}} - 1] / [1 - f + f(1 + \ell/rb)^{\frac{1}{2}}] \quad (9)$$

#### Limiting Strain Approach

An alternative, first-order solution to Eqs. 2-4 can be obtained by representing the bridges as tensile ligaments, where the stress in a ligament is proportional to the strain. With reference to Fig. 3, the strain,  $\epsilon(x)$ , in any ligament within the bridging zone can be estimated by assuming it to be equivalent to the strain in a bent beam, with rotational center at point C and neutral plane at the crack tip, such that:

$$\epsilon(x) = x/rb \quad (10)$$

Converting to a true strain and substituting into a constitutive law for the uncracked-ligament material, of the form:

$$\sigma(x) = \sigma_y + k \cdot \epsilon(x) \quad (11)$$

where  $\sigma_y$  is the (initial) yield stress and  $k$  is a constant, provides a second expression for the degree of crack-tip shielding due to uncracked-ligament bridging, in terms of the area fraction of ligaments, the ratio  $\ell/rb$  and the (constrained) flow properties of the ligament:

$$K_S = -f \sigma_y \cdot \frac{2\sqrt{\ell}}{\pi} \left[ 1 + \frac{k}{\sigma_y} (1 + \frac{\ell}{rb}) - 2 \left( \sqrt{\frac{rb}{\ell}} \cdot \tan^{-1} \sqrt{\frac{\ell}{rb}} \right) \right] \quad (12)$$

#### **RESULTS AND DISCUSSION**

As ligament bridging in the Al/SiC<sub>p</sub> alloys predominates between  $\sim 10^{-9}$  and  $10^{-6}$  m/cycle, estimates of the degree of shielding were made for a stress-intensity range  $\Delta K$  of 8 MPa $\sqrt{m}$  ( $K_A = 9$  MPa $\sqrt{m}$ ). Metallographic studies of the crack-path morphology using serial sectioning indicated an area fraction of bridges of  $\sim 27$  to 31% along a bridging zone of approximately 400  $\mu m$  behind the crack tip;  $rb$  is typically 1 mm for the C(T) geometry and the values of  $\sigma_y$  and  $k$  are 380 and 1600 MPa for the overaged alloy.

To apply the proposed models to the cyclic crack-growth behavior in Fig. 1, we note that the stretching of co-planar uncracked ligaments is controlled by the crack opening; the degree of crack-tip shielding is thus more appropriately described by the limiting crack-opening displacement model (Eq. 9). Using the measured values of  $f$ ,  $\ell$  and  $rb$  defined above, the stress intensity  $K_S$  due to bridging is predicted to be approximately 0.5 MPa $\sqrt{m}$  at an applied  $K_A$  of 9 MPa $\sqrt{m}$ . This form of bridging thus induces minimal shielding ( $\sim 6\%$  in this case), consistent with the minimal difference in growth rates between the reinforced and unreinforced 20 vol% SiC alloys at  $\Delta K = 8$  MPa $\sqrt{m}$  (Fig. 1L). Conversely, the deformation of uncracked ligaments resulting from overlapping cracks is less a function of the crack opening but rather is limited by the strength of the ligament; the limiting-strain model (Eq. 12) is therefore more appropriate. Here using measured values of  $f$ ,  $\ell$ ,  $rb$ ,  $\sigma_y$  and  $k$  at  $K_A = 9$  MPa $\sqrt{m}$ , the stress intensity  $K_S$  due to bridging is predicted to be 3.2 MPa $\sqrt{m}$ . This clearly represents a more



substantial degree of shielding ( $\sim 30\%$ ) and is consistent with the larger shift in growth-rate curves between the reinforced and unreinforced 15 vol% SiC alloys at  $\Delta K = 8 \text{ MPa}\sqrt{\text{m}}$  (Fig. 1d).

Finally, it might be noted that co-planar uncracked ligaments can be considered either as a bridging zone behind the crack tip or a damage zone ahead of it, the only difference being the definition of the crack tip. Recent work by Thouless, however, has shown that the two approaches are equivalent and that identical crack-extension rates are predicted [21].

## CONCLUSIONS

Based on a study of crack bridging via uncracked ligaments in Al/SiC<sub>p</sub> composites, simple models are developed to predict the magnitude of crack-tip shielding during fatigue-crack growth. It is found that bridging models based upon a limiting crack-opening displacement in the bridge predict only minimal shielding but are most appropriate to co-planar ligaments. Conversely, models based on a limiting strain are appropriate to ligaments formed by overlapping cracks, and predict larger levels of shielding.

## Acknowledgments

This work was supported by the Air Force Office of Scientific Research under University Research Initiative No. F49620-87-C-0017 to Carnegie Mellon University. Thanks are due to Dr. Alan Rosenstein for his continued support and to Warren Hunt and Dr. Bob Bucci of Alcoa for supplying the alloys.

## References

1. A. G. Evans, in Fracture Mechanics, 20th Symp., ASTM STP, edited by R.P. Wei and R.P. Gangloff (ASTM, Philadelphia, PA, 1988).
2. R. O. Ritchie, in Mechanical Behaviour of Materials - V, edited by M.G. Yan, S.H. Zhang and Z.M. Zheng (Pergamon, Oxford, U.K., 1988), vol. III.
3. J. Aveston, G. Cooper and A. Kelly, in Properties of Fiber Composites, NPL Conf. Proc. (IPC Sci. & Tech. Press, Surrey, U.K., 1971), pp. 15-26.
4. B. Budiansky, J. W. Hutchinson and A. G. Evans, J. Mech. Phys. Solids, **34**, 167 (1986).
5. D. B. Marshall, B. N. Cox and A. G. Evans, Acta Met., **33**, 2013 (1985).
6. L. N. McCartney, Proc. Roy. Soc., **A409**, 329 (1987).
7. L. R. F. Rose, J. Mech. Phys. Solids, **35**, 383 (1987).
8. B. Budiansky, in Proc. 10th U.S. Cong. Appl. Mech., (Austin, TX, 1986).
9. S. Kunz-Douglass, P. W. R. Beaumont and M. F. Ashby, J. Mater. Sci., **15**, 1109 (1980).
10. Y. Mai and B. R. Lawn, J. Am. Ceram. Soc., **70**, 289 (1987).
11. W. W. Gerberich, in Fracture: Interactions of Microstructure, Mechanisms and Mechanics, edited by J.M. Wells and J.D. Landes (TMS-AIME, Warrendale, PA, 1984), pp. 49-74.
12. A. R. Rosenfield and B. S. Majumdar, Metall. Trans. A, **18A**, 1053 (1987).
13. P. Marissen, in Fatigue 87, Proc. Third Intl Conf. on Fatigue, edited by R.O. Ritchie and E.A. Starke (EMAS Ltd., 1988), vol. 3, pp. 1271-79.
14. R. O. Ritchie, W. Yu and R. J. Bucci, Eng. Fract. Mech., (1988) in press.
15. J.-K. Shang, W. Yu and R. O. Ritchie, Mater. Sci. Eng., (1988) in press.
16. J.-K. Shang and R. O. Ritchie, Metall. Trans. A, **19A** (1988) in review.
17. T. Christman and S. Suresh, Mater. Sci. Eng., (1988) in press.
18. G. C. Sih, Handbook of Stress Intensity Factors (Lehigh University Press, Bethlehem, PA, 1972).
19. C. F. Shih, J. Mech. Phys. Solids, **29**, 305 (1981).
20. C. C. Veerman and T. Muller, Eng. Fract. Mech., **4**, 25 (1972).
21. M. D. Thouless, J. Am. Ceram. Soc., **71** (1988) in press.

**MECHANISMS ASSOCIATED WITH NEAR-THRESHOLD FATIGUE-CRACK PROPAGATION  
IN SiC-PARTICULATE-REINFORCED ALUMINUM COMPOSITES**

J.-K. Shang and R. O. Ritchie

Department of Materials Science and Mineral Engineering  
University of California, Berkeley, CA 94720

February 1989

to be presented at  
the Seventh International Conference on Composite Materials (ICCM-7)  
Beijing, China, August 1989

Work supported by the Air Force of Scientific Research under the University Research Initiative No. F49620-87-C-0017 to Carnegie Mellon University.

# MECHANISMS ASSOCIATED WITH NEAR-THRESHOLD FATIGUE-CRACK PROPAGATION IN SiC-PARTICULATE-REINFORCED ALUMINUM COMPOSITES

J.-K. Shang and R. O. Ritchie

(Department of Materials Science and Mineral Engineering  
University of California, Berkeley, CA 94720)

## ABSTRACT

Micro-mechanisms associated with fatigue-crack propagation in metal-matrix composites have been studied in several powder-metallurgy aluminum alloys reinforced with different volume fractions and sizes of SiC particulate, with emphasis on behavior at near-threshold stress intensities. Specifically, the fatigue threshold,  $\Delta K_{TH}$ , below which (long) cracks are presumed dormant, is found to increase with the SiC-particle size; such behavior is associated with mechanisms of crack trapping and crack closure from enhanced fracture-surface roughness. Based on this notion, a limiting condition for fatigue-crack advance in particulate-reinforced composites is derived, which requires the maximum crack-tip plastic zone size to exceed the particle size. This condition is represented by a critical stress criterion that the matrix stress beyond the particle is greater than the yield strength of the material, and provides a good description of the magnitude of the measured threshold values.

## INTRODUCTION

Metal-matrix composites consisting of an aluminum-alloy matrix reinforced with ceramic particles (SiC, alumina, graphite, etc.) have attracted some degree of attention in recent years because superior stiffness, strength, wear and elevated-temperature properties can be achieved at relatively low cost compared to monolithic alloys [1-4]. Although improved processing techniques are still required to overcome the poor ductility and fracture toughness of these alloys [1,3,4], studies on fatigue performance have indicated that their crack initiation and growth properties are generally superior to the constituent matrix alloys [5-14].

The superior crack-growth resistance of SiC-reinforced aluminum alloys has been related to several salient mechanisms of crack-tip shielding [15], which act to lower the local "crack driving force" actually experienced at the crack tip. At intermediate growth rates, typically between  $10^{-9}$  and  $10^{-6}$  m/cycle, propagation rates tend to be marginally lower in the composites due to crack bridging from uncracked ligaments along the crack length, resulting from SiC-particle fracture ahead of the tip [11]. At near-threshold levels below  $10^{-9}$  m/cycle, propagation rates also are generally found to be lower than in the unreinforced alloys; threshold  $\Delta K_{TH}$  values are corresponding higher although specific alloys do show contrary results [7-14]. It has been suggested that the higher  $\Delta K_{TH}$  values are associated with a critical crack opening displacement - higher thresholds are predicted because of the higher modulus of the composites [10] - although alternative explanations have been proposed based on enhanced crack-closure levels due to the tendency at near-threshold levels for the crack to avoid the particles [9].

In this paper, a new limiting condition for the fatigue-crack propagation threshold in particulate-reinforced metal-matrix composites is proposed, based on the notion

of crack trapping by the reinforcement particles. The mechanism, which is based on the observed avoidance of the particles by the crack path at near-threshold levels [9], is shown to be consistent with the measured particle-size dependence of  $\Delta K_{TH}$  values in these materials.

### EXPERIMENTAL PROCEDURES

The metal-matrix composites studied consisted of a powder-metallurgy Al-9Zn-3Mg-2Cu matrix, reinforced with either 15 or 20 volume % of coarse F-600 grade SiC (nominal size 16  $\mu\text{m}$ ) or fine F-1000 grade (nominal size 5  $\mu\text{m}$ ) SiC particulate. Average particle sizes and room-temperature mechanical properties are listed in Table I for the four SiC<sub>p</sub>/Al composites, heat-treated to a peak aged condition (T6 - solution treated 4 h at 530°C, cold water quenched, aged 24 h at 121°C). Further details of the alloys are given in refs. 4,9,11,12.

Fatigue-crack propagation rates,  $da/dN$ , were measured in general accordance with ASTM Standard E 647-86A on 6.4-mm-thick double-cantilever-beam DB(M<sub>2</sub>) specimens machined in S-T orientation. Tests were performed in controlled room air (22°C, 45% relative humidity) at a load ratio ( $R = K_{min}/K_{max}$ ) of 0.1 and a sinusoidal frequency of 50 Hz. Fatigue thresholds ( $\Delta K_{TH}$ ) were approached under automated stress-intensity control (normalized K-gradient of  $-0.15 \text{ mm}^{-1}$ ) to a growth rate less than  $10^{-11} \text{ m/cycle}$ . Crack lengths and crack closure were monitored using d.c. electrical potential and back-face strain compliance techniques [16], respectively; stress-intensity factors,  $K$ , were computed from standard solutions [17]. Subsequent fractography involved microscopy of fracture surfaces and of crack-path profiles (from sections cut at specimen mid-thickness); the distribution of SiC particles on the fracture surfaces was estimated with X-ray mapping techniques [9].

Table I. Mechanical properties and particle sizes in peak-aged (T6) matrix and SiC<sub>p</sub>/Al composite alloys

Volume fraction	Particle size $\bar{D}_p$ ( $\mu\text{m}$ )	Young's modulus (GPa)	Yield strength (MPa)	Redn. Area (%)	Toughness $K_{IC}$ (MPa $\sqrt{\text{m}}$ )	Fatigue threshold <sup>a</sup> $\Delta K_{TH}$ (MPa $\sqrt{\text{m}}$ )	Size of cracked SiC <sub>p</sub> $\bar{D}_p$ ( $\mu\text{m}$ )
20%	10.5	101	500	4.9	16	4.2	11.8
20%	6.1	94	400	13.5	14	3.0	10.7
15%	11.4	99	490	4.5	-	4.3	13.0
15%	4.5	91	480	4.9	-	2.6	6.3
0%	-	69	520	35.2	33	4.1	-

a) at  $R = 0.1$

### RESULTS AND DISCUSSION

Fatigue-crack growth rates for the the coarse and fine SiC<sub>p</sub>/Al composites are shown as a function of the nominal stress-intensity range,  $\Delta K$ , in Fig. 1. Although behavior at intermediate to high growth rates (above  $10^{-9} \text{ m/cycle}$ ) is essentially independent of the size and volume fraction of SiC, near-threshold crack-growth rates are decreased, and values of  $\Delta K_{TH}$  increased (Table I), with the coarser reinforcement-particle distributions.

Crack-path morphology studies in these alloys show a strong tendency for the near-threshold fatigue crack to avoid the SiC particles; in the coarse SiC<sub>p</sub>/Al composite, a fraction of only ~13% SiC particles are intersected by the crack path (~9% are cracked, ~4% decohere), far less than the ~23% volume fraction in the microstructure [9]. Moreover, the average size,  $\bar{D}_p$ , of the particles involved in the cracking

process generally exceeds the overall average particle size (Table I) [12], presumably because the larger particles are more susceptible to cracking.

As the crack tends to avoid SiC particles at low  $\Delta K$  levels, the particles can be considered to impede crack advance; their presence at the tip of the crack acts to lower local stress intensities and hence their function can be envisioned as crack traps. Based on this notion, the fatigue threshold stress intensity is modelled here in terms of the role of a non-deforming particle at the crack tip (Fig. 2a) in affecting the local "driving force" required for crack extension. It is significant that at  $\Delta K_{TH}$ , maximum plastic zone sizes ( $r_{y,max}$ ) in these composites are comparable with the average size,  $\bar{D}_p$ , of particles sampled by the near-threshold crack (Fig. 2b). This implies that crack hindrance occurs because of limited local plasticity, which impedes the fracture or bypassing of the SiC particle. Accordingly, a limiting condition for fatigue-crack advance in particulate-reinforced composites can be defined in terms of the matrix stress beyond the particle at the crack tip exceeding the yield strength  $\sigma_y$  of the material, i.e.,  $r_{y,max}$  must exceed  $\bar{D}_p$ .

The proposed threshold condition of crack trapping is akin to dislocation pinning by second phase particles. Recent crack-trapping solutions by Rice [18] show that the exact solution to the three-dimensional problem depends on the shape of the crack-front perturbation, which is a function of matrix and particle properties; additional complications arise from matrix plasticity, which makes the crack front less predictable. A micro-mechanical analysis, however, is performed below on the simplified plane problem (Fig. 3), based on the elastic interaction between a crack and an inclusion.

The presence of a non-deforming inclusion at the crack tip significantly reduces the matrix stresses; this has been computed [12] for a SiC particle in aluminum (for a ratio of crack size to particle size of  $\sim 1250$ ) and gives the tensile stress  $\sigma_{yy}$  distribution just beyond the inclusion as (Fig. 3):

$$\sigma_{yy} = C K / \sqrt{\bar{D}_p}, \quad (1)$$

where the constant  $C$  equals  $2.4^{-1}$ , and only depends on material constants for a crack large compared to particle size [12,19,20].

Evoking the proposed limiting threshold condition that for crack advance in SiCp/Al composites that:

$$\sigma_{yy} = \sigma_y, \text{ over } r = r_{y,max} \approx \bar{D}_p, \quad (2)$$

the fatigue-crack growth fatigue threshold is given by:

$$\begin{aligned} &\text{or} \\ &K_{max,TH} \approx 2.4 \sigma_y \sqrt{\bar{D}_p}, \\ &\Delta K_{TH} \approx 2.4 (1 - R) \sigma_y \sqrt{\bar{D}_p}. \end{aligned} \quad (3)$$

Eq. (3) implies that for particulate-reinforced composites where near-threshold crack advance is influenced by crack trapping, the fatigue threshold is proportional to the square root of the particle size, consistent with experimental observations (Fig. 4 - see also ref. 13).

It should be noted that this approach is valid if the particles lie on the crack front and act to retard crack extension; exceptions to this are in cases of extensive premature fracture of the SiC due to poor particle quality, particle clustering, interfacial decohesion and deflection around particles (where the closure component becomes more important). In addition, in materials containing very small fractions of large particles, i.e., metallic alloys with inclusions, the particles may not be "sampled" by the crack-tip process zone and therefore would

contribute little to the crack-growth kinetics [21]. Finally, where interparticle spacings are comparable to particle sizes, the analysis based on the crack/isolated-inclusion interaction becomes inadequate; hence, direct application of Eq. (3) to materials with high particle volume fractions (greater than ~0.5) is inappropriate.

#### CONCLUDING REMARKS

It is apparent that non-deforming reinforcement particles such as SiC in SiC<sub>p</sub>/Al composites can impede near-threshold fatigue-crack propagation in two primary ways: i) by deflecting the crack and thus promoting roughness-induced crack closure, and ii) by crack trapping. Analysis of the latter mechanism in terms of the crack/particle interaction yields a limiting requirement for the intrinsic fatigue threshold condition that the maximum plastic zone size exceeds the average particle size; by considering crack-tip stress distributions, this implies that for fatigue-crack advance, the tensile stresses in the matrix beyond the particle must be larger than the yield stress. The model suggests that enhanced fatigue-crack propagation resistance is achieved in composites with coarser particle distributions, consistent with experimental evidence.

#### ACKNOWLEDGMENTS

The work was supported by the Air Force Office of Scientific Research under University Research Initiative No. F49620-87-C-0017. The authors thank Dr. A. H. Rosenstein for his support, Drs. R. J. Bucci and W. H. Hunt of Alcoa for supplying the alloys, and Madeleine Penton for preparing the manuscript.

#### REFERENCES

1. Nair, S.V., Tien, J.K. and Bates, R.C., *Int. Met. Rev.*, 30 (1985), 275.
2. Mohn, W.R., *Research & Development* (1987), 54.
3. McDaniels, D.L., *Metall. Trans. A*, 16 (1985), 1105.
4. Lewandowski, J.J., Liu, C. and Hunt, W.H., In: *Processing and Properties of Powder Metallurgy Composites*, P. Kumar et al., eds., TMS-AIME, Warrendale, PA (1988), 117.
5. Hasson, D.F., Crowe, C.R., Ahearn, J.S. and Cooke, D.C., In: *Failure Mechanisms in High Performance Materials*, J.G. Early et al., eds. (1984), 147.
6. Yau, S.S. and Mayer, G., *Mater. Sci. Eng.*, 82 (1986), 45.
7. Logsdon, W.A. and Liaw, P.K., *Eng. Fract. Mech.*, 24 (1986), 737.
8. Davidson, D.L., *Metall. Trans. A*, 18A (1987), 2115.
9. Shang, J.-K. and Ritchie, R.O., *Mater. Sci. Eng.*, 102 (1988), 181.
10. Christman, T. and Suresh, S., *Mater. Sci. Eng.*, 102 (1988), 211.
11. Shang, J.-K. and Ritchie, R.O., *Metall. Trans. A*, 20A (1989), in press.
12. Shang, J.-K. and Ritchie, R.O., *Acta Metall.*, 37 (1989), in review.
13. Davidson, D.L., "Micromechanisms of Fatigue Crack Growth and Fracture Toughness in Metal Matrix Composites," Report No. 06-8602/5, Southwest Research Institute, San Antonio, TX (1989).
14. Preston, S., Melander, A., Groth, H.L. and Blom, A.F., In: *Thermal and Mechanical Behavior of Ceramic and Metal Matrix Composites*, ASTM STP, ASTM, Philadelphia, PA (1989), in review.
15. Ritchie, R.O., *Mater. Sci. Eng. A*, 103A (1988), 15.
16. Ritchie, R.O. and Yu, W., In: *Small Fatigue Cracks*, R.O. Ritchie and J. Lankford, eds., TMS-AIME, Warrendale, PA (1986), 167.
17. Srawley, J.E. and Gross, B., *Mater. Res. Stand.*, 7 (1967), 155.
18. Rice, J.R., In: *Fracture Mechanics - 20th Symp.*, R.P. Wei and R.P. Gangloff, eds., ASTM STP, ASTM, Philadelphia, PA (1989), in press.
19. Atkinson, C., *Int. J. Engng. Sci.*, 10 (1972), 127.
20. Rubinstein, A.A., *J. Appl. Mech.*, 53 (1986), 505.
21. Heiser, F.A. and Hertzburg, R.W., *J. Basic Eng.*, 93 (1971), 211.
22. Mason, J.J., M.S. thesis, University of California, Berkeley (1989).

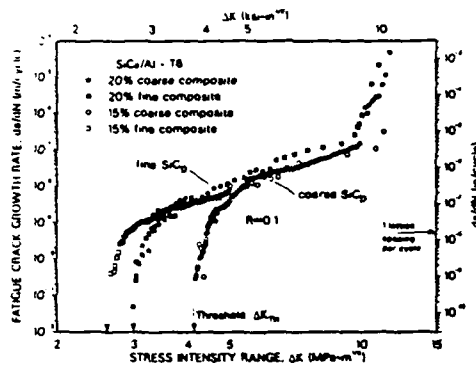


Fig. 1: Variation in fatigue-crack propagation rates ( $da/dN$ ) with stress-intensity range ( $\Delta K$ ) at  $R = 0.10$  for the 15 and 20% fine and coarse  $SiC_p/Al$  composites (T6 peak aged) at room temperature.

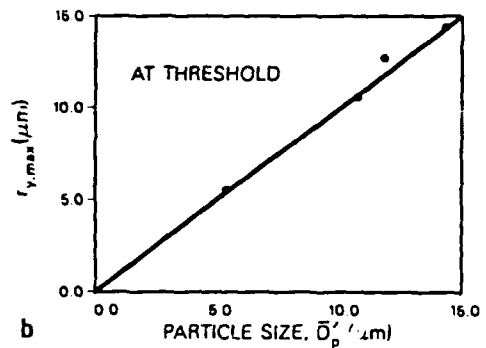
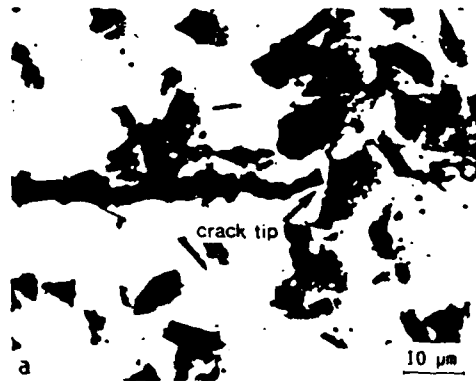


Fig. 2: a) Crack trapping by  $SiC$  particles at the fatigue threshold  $\Delta K_{TH}$ , and b) associated 1:1 correlation of the maximum plastic zone size ( $r_{y,max}$ ) at  $\Delta K_{TH}$  with the effective mean particle size ( $\bar{D}_p$ ).

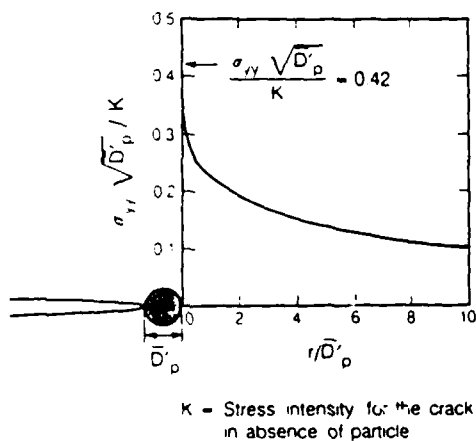


Fig. 3: Computed distribution of normalized matrix tensile stress ( $\sigma_{yy}$ ) as a function of normalized distance ahead of the crack/inclusion [12].

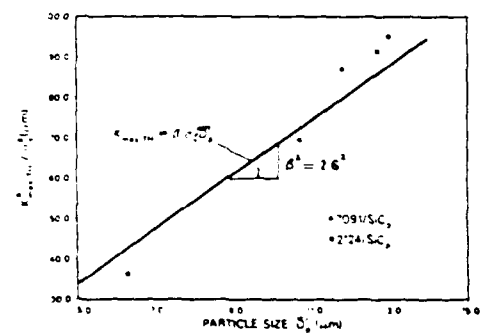


Fig. 4: Model predictions (Eq. 3) and experimental data showing relationship between the threshold  $K_{TH,max}$ , normalized by the yield stress ( $\sigma_y$ ), and the effective mean particle size ( $\bar{D}_p$ ) for  $SiC_p/Al$  composites. Also plotted are data on  $SiC_p/2124$  alloy [22].

## TASK 5

### Creep of High Temperature Composite Matrices

A.W. Thompson, Investigator

Task 5 of the URI on High-Temperature Metal Matrix Composites had the task title of "Micromechanisms of High Temperature Composite Behavior". Work has concentrated on matrix materials for such composites, in particular the titanium aluminide alloys Ti-24 Al-11 Nb and Ti-25 Al-10 Nb-3 V-1 Mo (atomic percentages), both of which are based on the compound  $Ti_3Al$  and are near-commercial alloys. A variety of both ambient and elevated temperature mechanical properties were explored, with particular interest in creep behavior and high-temperature fracture of the alloys. The first work completed was done on Ti-25-10-3-1, and the published report on that research, carried out by Dr. W. Cho, a Postdoctoral Associate, is attached. The second part, on the Ti-24-11 alloy, was conducted by a Ph.D. student, D. Albert. A preliminary manuscript on her work is also attached. Additional research on medium and high temperature deformation, fracture, fatigue and toughness of Ti-25-10-3-1, was initiated by a second Ph.D. Student, F. Dary, and that work has been continued after the completion of the URI program under sponsorship from Alcoa. The third attached manuscript is the Aeromat '90 presentation shown below under presentations.

Listed below are papers published or in press, as well as the following oral presentations, based on work done in the task, which were presented in the course of the third program year. Presentations in prior years were listed in the Annual Reports for years 1 and 2. The former co-investigator on this task, Dr. J.C. Williams, left Carnegie Mellon University in August, 1988, to join the Aircraft Engines Business Group of General Electric.

#### Publications

W. Cho, A.W. Thompson and J.C. Williams, "Effect of Microstructure on Deformation Behavior of Ti-25 Al-10 Nb-3 V-1 Mo", in *1988 Titanium Aluminides Meeting*, Vol. 1, Textron Lycoming, Stratford, CT (1988), paper 9.

C.H. Ward, J.C. Williams, A.W. Thompson, D.G. Rosenthal, and F.H. Froes, "Fracture Mechanisms in Titanium Aluminide Intermetallics", in *Titanium Science, Technology and Applications* (Proc. 6th World Conf. on Ti), P. Lacombe, R. Tricot and G. Beranger, eds., Les Editions de Physique, Paris (1989) 1103-1108. (Reprinted in *Mem. Etudes Sci. Rev. de Metall.*, Oct. 1989, pp. 647-653).

W. Cho, A.W. Thompson and J.C. Williams, "Creep Behavior of Ti-25 Al-10 Nb-3 V-1 Mo," *Metall. Trans. A*, 1990, vol. 21A, pp. 641-651

A.W. Thompson, "Creep of Alpha-2 Titanium Aluminides," in *Titanium Aluminides* (papers from Aeromat '90), C.G. Rhodes and H.A. Lipsitt, eds., Rockwell Science Center, Thousand Oaks, CA, 1990.

D.E. Albert and A.W. Thompson, "Creep Behavior of Ti-24 Al-11 Nb," in *Microstructure/Property Relationships in Titanium Alloys and Titanium Aluminides*, R.R. Boyer and J.A. Hall, eds., TMS-AIME, Warrendale, PA, in press.



### Presentations

W. Cho, J.C. Williams and A.W. Thompson, "Effect of Microstructure on Deformation Behavior of Ti-25-10-3-1", in *Mechanical Performance of Advanced Composites*, TMS Mechanical Metallurgy Committee Symposium, Fall Meeting, TMS-AIME, Chicago, IL, 28 Sept. 1988.

A.W. Thompson, "The University Research Initiative Program on Metal Matrix Composites at Carnegie Mellon," URI Winter Study Group, Univ. of California, Santa Barbara, CA, 12 Jan. 1989.

W. Cho, J.C. Williams and A.W. Thompson, "Creep Behavior of an Advanced Titanium Aluminide Alloy Based on  $Ti_3Al$ ," in *Symposium on Creep of Composite Materials*, Annual Meeting, AIME, Las Vegas, NV, 27 Feb. 1989.

A.W. Thompson, "Current Research Results on Titanium Aluminides," Departmental Seminar, Materials Science and Engineering Program, Dept. of Mechanical Engineering, Univ. of Texas, Austin, TX, 20 April 1989.

A.W. Thompson, "Relations between Microstructure and Mechanical Properties at Ambient Temperature" (invited), Gordon Research Conference on Physical Metallurgy, Tilton, NH, 9 August 1989.

D. Albert and A.W. Thompson, "Creep Behavior of Ti-24-11," in *Symposium on Creep, Fatigue and Fracture of Titanium Aluminides*, Fall Meeting, TMS-AIME, Indianapolis, IN, 3 Oct. 1989.

A.W. Thompson, "Metallurgy and Mechanical Behavior of Titanium Aluminides," Departmental Seminar, Metals Science and Engineering, Pennsylvania State University, State College, PA, 16 April 1990.

A.W. Thompson, "Creep of Alpha-2 Titanium Aluminide Alloys," in *Symposium on Titanium Aluminides*, Aeromat '90, Long Beach, CA, 23 May 1990.

D. Albert and A.W. Thompson, "The Effect of Microstructure on Creep of Ti-24-11," in *Microstructure/Property Relationships in Titanium Alloys and Titanium Aluminides*, sponsored by TMS Titanium Committee, TMS Fall Meeting, Detroit, MI, 9 Oct. 1990.

## CREEP BEHAVIOR OF Ti-24Al-11Nb

Diane E. Albert and Anthony W. Thompson  
Department of Metallurgical Engineering and Materials Science  
Carnegie Mellon University, Pittsburgh, Pa. 15213

### Introduction

The steady state creep behavior of Ti-24Al-11Nb has been investigated. The effect of microstructure on creep was determined at temperatures between 650°C and 870°C utilizing steady state creep rate vs. stress tests. The apparent activation energy for creep,  $Q_c$ , was determined for some structures in the low stress regime.

### Experimental Procedures

The Ti-24-11 material was received from the RMI Company, Niles, Ohio in the form of 12.5 cm thick cross-rolled plate. Thermomechanical processing of the material at RMI involved hot rolling, annealing at 1038°C for one hour and subsequent air cooling. The chemical composition is shown in Table I and the as-received (AR) microstructure is shown in Figure 1a. This microstructure is a relatively equiaxed  $\alpha_2$  morphology with very little of the ordered BCC or  $\beta_0$  phase present between the  $\alpha_2$  regions, as has been seen in other work.(1) Blanks approximately 12.5 cm square and 10 cm long were cut by bandsaw from this as-received material; heat treatment and machining into cylindrical creep specimens followed.

TABLE I  
Chemical Composition of Cross-Rolled Ti-24Al-11Nb Plate.

Al	Nb	Fe	O	C	H	Ti
24.6	10.5	0.068	0.161	0.039	0.02	bal (at%)
14.0	20.6	0.08	0.054	0.01	$4.8 \times 10^{-5}$	bal (wt%)

Three heat treatments were selected to produce three microstructures. Solutionizing in the  $\beta$  phase field at 1200°C for one hour then air cooling produced fine acicular  $\alpha_2$  plates arranged in a Widmanstätten basketweave morphology, as shown in Figure 1b. Solutionizing at 1200°C for one hour with a subsequent  $\alpha_2 + \beta$  phase field (1000°C) solutionizing for 15 minutes and air cool resulted in a fine Widmanstätten basketweave morphology with primary and secondary acicular  $\alpha_2$  plates as seen in Figure 1c. Holding for 30 minutes at 1000°C resulted in  $\alpha_2$  plate coarsening, as seen in Figure 1d.

An analysis of the effect which microstructural features have on steady state creep rate is possible by comparing creep behavior of selected specimens. Comparing creep rate

differences between the materials held at 1000°C for 15 minutes and 30 minutes allows a determination of the effect of  $\alpha_2$  plate size on creep, as the degree of  $\alpha_2$  plate coarseness is the only microstructural variable. The  $\alpha_2$  plate size of the 1200AC and 1000AC-15 is very similar; however the 1000AC-15 material will have a decreased amount of  $\beta_0$  phase and a corresponding increase in amount of  $\alpha_2$  phase present. The morphology of the as-received microstructure is roughly equiaxed  $\alpha_2$ , not acicular, basketweave  $\alpha_2$ . Evidence of texture is supported by the presence of elongated, aligned  $\alpha_2$ .

The specimen used in the high-temperature constant-load creep tests was of a typical cylindrical configuration. A groove between the threads and the gage length on each end of the specimen allows for extensometer placement. Sufficient material was removed from the blank after exposure to high temperatures to ensure no oxygen-enriched material remained. Constant temperature creep tests were conducted at 650°C, 760°C, and 870°C in air, under decreasing tensile stresses.(2) Single lever creep frames with a load ratio of 20:1 were used in all tests. Steady state creep rate vs. temperature tests were conducted at 100 MPa and 31.38 MPa to determine the apparent activation energy of creep. Creep strain was measured using an extensometer and a SLVC transducer which allowed a strain resolution of  $5 \times 10^{-6}$ . During creep tests, specimen temperatures were monitored continuously with type-K thermocouples attached to the gage length. Temperature variation during the tests was not greater than 2° C.

### Results and Discussion

The results of steady state creep rate vs. stress tests for each microstructure at the three temperatures are shown in Figures 2, 3, and 4. For materials which undergo power-law creep, plotting  $\log \dot{\epsilon}_s$  vs.  $\log \sigma$  will result in a straight line with a slope equal to  $n$ , the power law exponent.(3-5) It is seen that the as-received microstructure has the poorest resistance to creep at all temperatures. At both 650°C and 760°C, note that the 1200AC and 1000AC-15 structures have almost identical creep rates with 1000AC-30 displaying a superior creep rate. At 870°C, however, the creep resistance of 1000AC-15 is seen to be superior to both 1200AC and 1000AC-30, except at high stresses where 1000AC-30 has slightly better creep resistance.

In Figure 5, each microstructure's creep behavior at each of the three test temperatures are plotted together on one graph. The slope,  $n$ , of each curve is indicated. In all cases, an increase in test temperature leads to a decrease in the value of  $n$  in the high stress region. At lower temperatures and lower stresses, 1000AC-30, AR, and 1200AC structures display a change in slope and ostensibly a change in creep mechanism. At high stresses, the value of  $n$  is large; at low stresses the slope is much less steep. Higher values of  $n$  (3 to 10) indicate dislocation glide and climb processes [6]; low values indicate boundary sliding mechanisms.[7] The low stress slopes of these materials approximate the slope of the curves at high temperatures, where diffusion processes are dominant.

In Figure 6, 650°C creep of the 1200AC structure is compared with other titanium aluminides. The 1200AC steady state creep vs. stress behavior is comparable to that of a  $\beta$ -solutionized Ti-24Al-11Nb material with a fully transformed microstructure.[8] A continuous slope change is noted in the latter material. The Ti-25Al-10Nb-3V-1Mo material [9] has a  $\beta$ -solutionized colony microstructure and possesses superior creep resistance, as does the stoichiometric Ti<sub>3</sub>Al.[7] The steady state creep rate of 1000°C solutionized, air cooled Ti-24-11 has also been determined. [10]

In Figure 7, the results of steady state creep rate vs. temperature tests are shown. Again, assuming power law creep, when  $\log \dot{\epsilon}_s$  vs.  $1/T$  is plotted, a straight line with a slope equal to  $Q_c$ , the apparent activation energy of creep, results. A creep activation energy of 206 kJ/mol for stoichiometric Ti<sub>3</sub>Al at all stresses and temperatures has been measured. Widmanstätten basketweave Ti-25-10-3-1 in the climb-controlled creep regime was found to have a  $Q_c$  of 305 kJ/mol. The activation energy in the low stress regime for Ti-24-11 with a 100% transformed  $\beta$  microstructure was determined to be 120 kJ. It is thought that the

apparent activation energies for high temperature creep in metals are independent of creep stress and strain[11], but different mechanisms seem to be dominant in different stress regimes. In this work, the AR microstructure had an average  $Q_c$  of 110 kJ/mol; the 1000AC-15, 142 kJ/mol; and the 1200AC structure, a value of 134 kJ/mol. All values were measured in the low stress regime, and are in fairly good agreement with the value of 121 kJ/mol for fine-grained titanium at low stresses.[12]

### Discussion

Recrystallization and grain growth during creep,  $\alpha$  plate width,  $\beta$  volume fraction, and  $\alpha/\alpha$  vs.  $\beta/\beta$  boundaries are all factors that are thought to influence steady-state creep rate in conventional titanium alloys.(13) If only plate size is considered to control steady state creep rate in titanium aluminides, then we would expect the microstructure with the smallest plates, that is, the 1200AC and 1000AC-15 structures, to have the best creep resistance, due to their short slip length. It is seen, however, that 1000AC-30 has superior creep resistance up to 870°C. Therefore, slip distance and corresponding dislocation motion within plates is not the sole controlling factor in creep in the temperature and stress range studied. Rather, since the 1000AC-30 plates are coarser than the plates present in 1000AC-15 and 1200AC, then it is true that there is less interphase boundary per unit area in this structure. The ratio  $\epsilon_{gb}/\epsilon_t$ , the strain due to grain boundary sliding to the total creep strain, was found to increase with increasing temperatures(14) or decreasing stresses(15). Also, the 1000AC structures should contain smaller amounts of  $\beta_0$  phase. This phase has a higher diffusion rate and thus, inferior creep resistance. This would explain the fact that 1000AC structures creep more slowly than the 1200AC structure. Examination of microstructures in crept specimens demonstrated that recrystallization and grain growth did not occur appreciably during creep. The presence of crystallographic texture, i.e. perhaps an alignment in basal planes, in the as-received material could help explain its high steady state creep rate.

### Conclusions

Steady state creep rates as functions of stress and temperature of selected microstructural variants of Ti-24Al-11Nb were determined. The as-received (AR) microstructure was found to possess the poorest creep resistance at all temperatures, possibly due to texture. The 1000AC-30 microstructure possessed superior creep resistance at all stresses when tested at low temperatures. The 1000AC-15 microstructure had superior creep resistance only in the low stress regime at 870°C. For each structure, increasing temperature caused a decrease in the value of  $n$  in the high stress region. If a slope change occurred, the value of  $n$  in the low stress region was found to be close to unity, indicative of boundary sliding mechanisms. The apparent activation energy of creep for all microstructures was found to be 142 kJ/mol, 140 kJ/mol, and 115 kJ/mol for 1000AC-15, 1200AC and AR respectively. These values are very similar to the activation energy obtained for grain boundary diffusion in pure titanium. This evidence leads to the conclusion that a diffusion controlled process, such as boundary sliding, is dominant in the stress and temperature regimes considered in this work. Dislocation dynamics within  $\alpha_2$  plates would not be rate-controlling.

### References

1. D. Banerjee, T. Nandi, and A.K. Gogia, *Scripta metall.* 21, p. 597 (1987).
2. N.E. Paton and M.W. Mahoney, *Metall. Trans. A* 7, p. 1685 (1976).
3. E.N.d.c. Andrade: "The Concept of Creep," in *Creep and Recovery*, Proceedings of the Thirty-Eighth Nat'l Metal Congress and Exhibition, Cleveland, Ohio, (1957), pp. 176-198.

4. S. Takeuchi and A.S. Argon: "Review: Steady-State Creep of Single-Phase Crystalline Material at High Temperature," *J. Mat. Sci.*, Vol. 11, (1976), pp. 1542-1566.
5. A.M. Brown and M.F. Ashby: "On the Power-Law Creep Equation," *Scripta metall.*, Vol. 14, (1980), pp. 1297-1302.
6. H.J. Frost and M.F. Ashby: *Deformation Mechanism Maps: The Plasticity and Creep of Metals and Ceramics*, Pergamon Press, Oxford, England, 1982, pp.11-14.
7. M. Mendiratta and H.A. Lipsitt: "Steady-State Creep Behavior of Ti<sub>3</sub>Al-Base Intermetallics," *J. Mat. Sci.*, Vol. 15, (1980), pp. 2985-2990.
8. R. Mishra and D. Banerjee: "Microstructure and Steady State Creep in Ti-24Al-11Nb," to be published.
9. W. Cho, A.W. Thompson and J.C. Williams: "Creep Behavior of Ti-25Al-10Nb-3V-1Mo," *Metall. Trans. A*, Vol. 21, (1990), pp. 64-651.
10. R.W. Hayes: "The Creep Behavior of the Ti<sub>3</sub>Al Alloy Ti-24Al-11Nb," *Scripta metall.*, Vol. 23, (1989), pp.1931-1936.
11. A.K. Mukherjee, J.E. Bird and J.E. Dorn: "Experimental Correlatiuons for High-Temperature Creep," *Trans. ASM*, Vol. 62, (1969), pp.155-179.
12. G. Malakondaiah and P. Rama Rao: "Creep of Alpha-Titanium at Low Stresses," *Acta Metall.*, Vol. 29, pp. 1263-1275.
13. W. Cho, J.W. Jones, J.E. Allison and W.T. Donlon: "Creep Behavior of Ti-6242: The Effect of Microstructure and Silicon Content," in *Proceedings of the Sixth World Conference on Titanium*, Vol. 1, Cannes, France, (1988), P. Lacombe, R. Tricot, and G. Béranger, eds., Les Editions de Physique, Les Ulis, France, pp. 187-192.
14. D. McLean and M.H. Farmer: "The Relation During Creep Between Grain-Boundary Sliding, Sub-Crystal Size, and Extension," *J.Inst. Met.*, Vol. 85, (1956-57), pp.41-50.
15. D. McLean: "Grain-Boundary Slip During Creep of Aluminum," *J.Inst. Met.*, Vol. 81, (1952-53), pp. 293-300.

(a)

(b)

(c)

(d)

FIG. 1

(a) AR (b) 1200AC (c) 1000AC-15 (d) 1000AC-30.

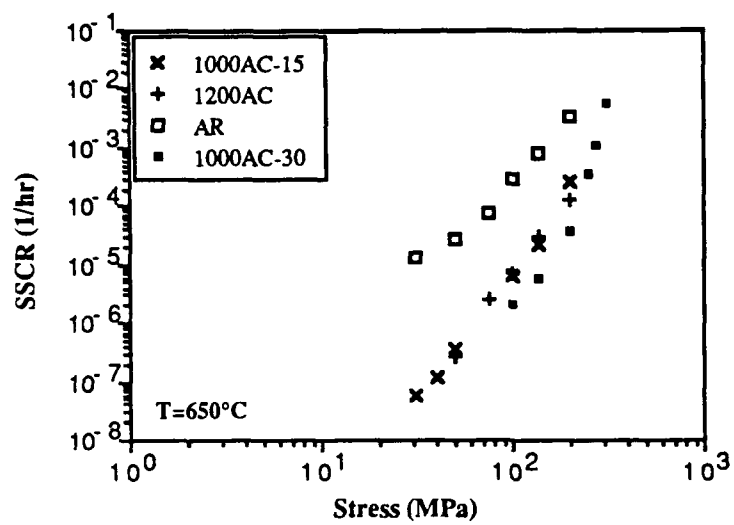


FIG. 2  
SSCR vs  $\sigma$  for all microstructures at  $650^\circ\text{C}$ .

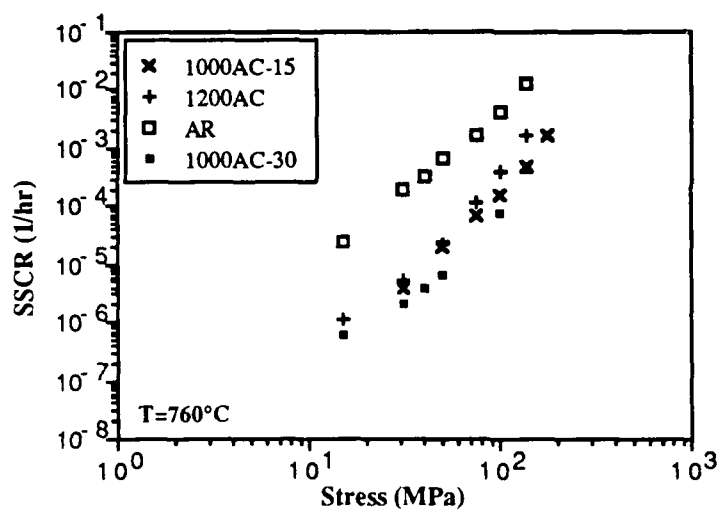
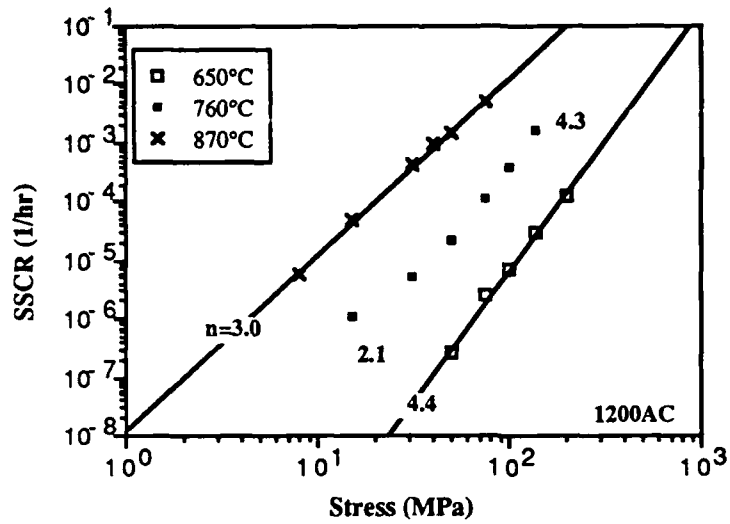
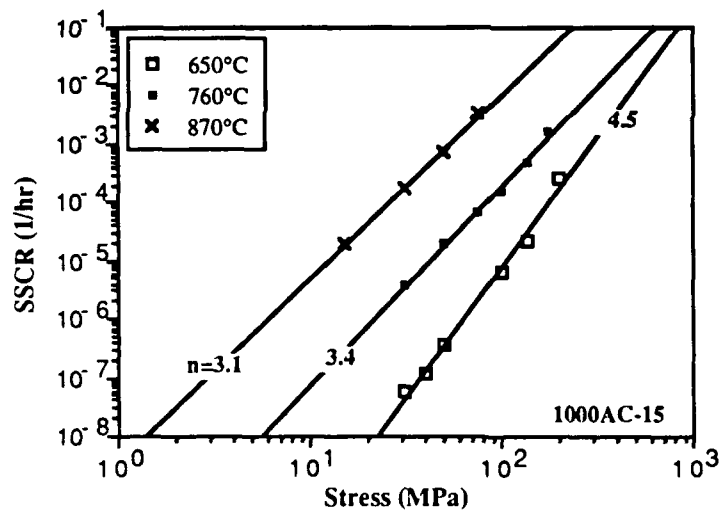


FIG. 3  
SSCR vs  $\sigma$  for all microstructures at  $760^\circ\text{C}$ .

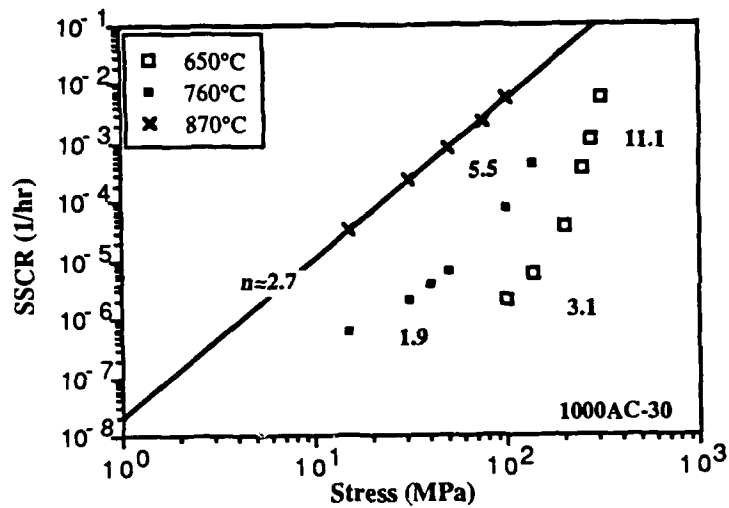


(b)

FIG. 5  
Effect of temperature on SSCR and  $n$  of (a) AR (b) 1200AC.



(c)



(d)

Figure 5 (continued). Effect of temperature on SSCR and  $n$  of (a) AR (b) 1200AC (c) 1000AC-15 (d) 1000AC-30

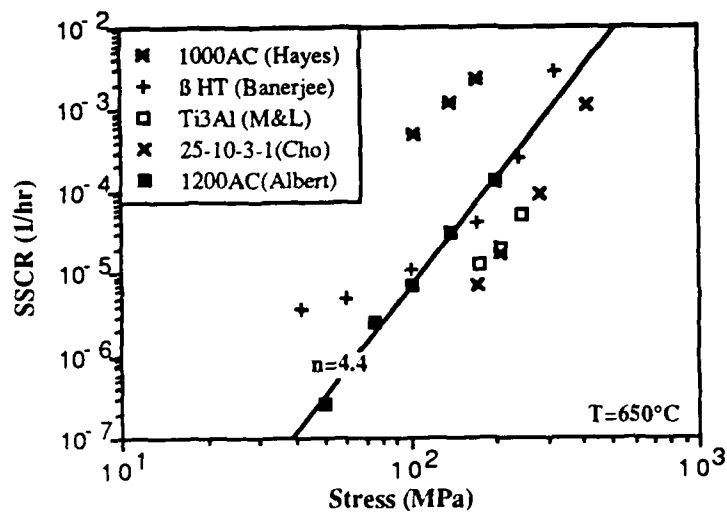
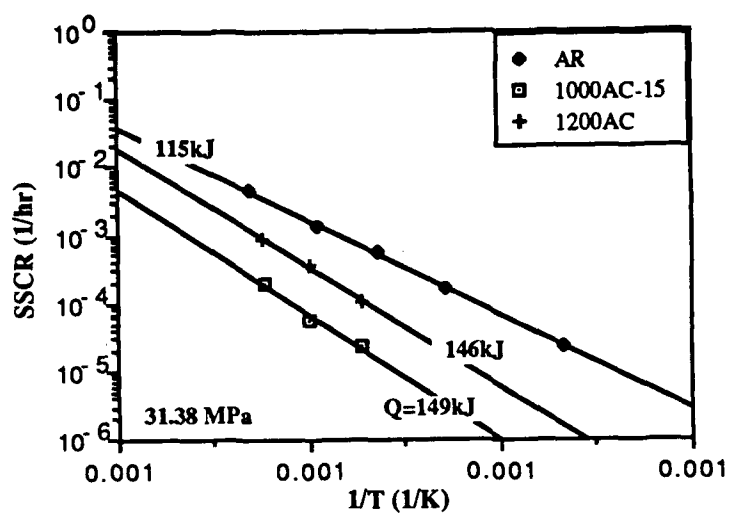
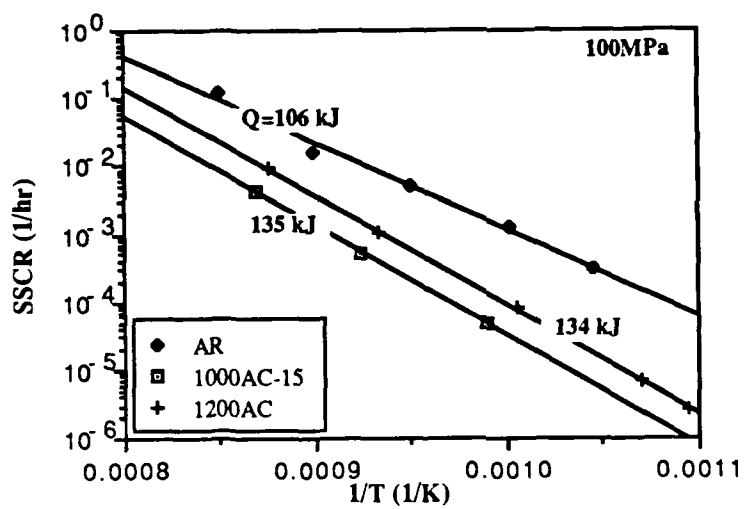


Figure 6. Comparison of Ti-based alloys at  $650^\circ\text{C}$ .





(a)



(b)

Figure 7. SSCR vs.  $1/T$  at (a) 31.38 MPa (b) 100 MPa



# Creep Behavior of Ti-25Al-10Nb-3V-1Mo

WONSUK CHO, ANTHONY W. THOMPSON, and JAMES C. WILLIAMS

A study has been made of the role of microstructure in room-temperature tensile properties as well as elevated-temperature creep behavior of an advanced Ti<sub>3</sub>Al-base alloy, Ti-25Al-10Nb-3V-1Mo (atomic percent). Creep studies have been performed on this alloy as a function of stress and temperature between 650 °C and 870 °C, since the use of conventional titanium alloys has generally been restricted to temperatures below 600 °C. A pronounced influence of microstructure on creep resistance was found. Generally, the  $\beta$  solution-treated colony-type (slow-cooled or SC) microstructure showed superior creep resistance. This improved creep resistance in  $\beta$ /SC is accompanied by lower room-temperature tensile strength and ductility. Study of the stress dependence of steady-state creep rate indicates that increasing temperature caused a gradual decrease in the stress exponent  $n$  and a transition in creep mechanism at 870 °C, depending on applied stress level. Transmission electron microscopy (TEM) observations of deformed dislocation structures developed during steady-state creep and room-temperature tensile tests, as well as the corresponding fracture modes, were used to interpret properties as a function of temperature. Finally, creep behavior of the present Ti<sub>3</sub>Al alloy was found to be superior to that of conventional near- $\alpha$  titanium alloys.

## I INTRODUCTION

IN recent years, considerable effort has been made to develop advanced titanium aluminide alloys based on Ti<sub>3</sub>Al for aircraft turbine engine components and other high-temperature applications. These aluminides retain adequate creep strength to much higher temperatures than do conventional titanium alloys, but they show low ductility at room temperature.<sup>[1,2]</sup> Therefore, the alloy development goals have been focused on an optimum combination of room-temperature ductility and elevated-temperature creep strength. Additions of niobium have proven successful in providing some of these benefits in alloys such as Ti-24Al-11Nb (values are atomic percent), and more recently, the alloy Ti-25Al-10Nb-3V-1Mo (referred to below as Ti-25-10-3-1) was developed with further additions of  $\beta$ -phase stabilizers. Additionally, it was recognized that substitution of some vanadium for niobium would be desirable, to reduce both density and cost.<sup>[3]</sup>

To date, most studies on creep behavior of alloys based on titanium have been performed on near- $\alpha$  titanium alloys, such as Ti-6242S<sup>[4]</sup> and IMI 685.<sup>[5]</sup> The past creep studies have shown that the creep resistance of conventional near- $\alpha$  titanium alloys is strongly dependent on microstructure. In general, Widmanstätten microstructures, produced by solution treating above the  $\beta$  transus, offer creep resistance at high temperatures superior to that provided by equiaxed microstructures produced by processing in the  $\alpha + \beta$  phase field. The same

studies also revealed that creep resistance is maximized at intermediate cooling rates from the  $\beta$  solution-treatment temperatures.

In contrast, very few data on creep behavior of Ti<sub>3</sub>Al-base alloys have been published. In particular, there has apparently been little systematic investigation of the creep behavior in terms of microstructural influences for the optimization of mechanical behavior in this important class of alloys. The only significant study<sup>[6,7]</sup> was performed to investigate the steady-state creep behavior of Ti<sub>3</sub>Al and Ti<sub>3</sub>Al + 10 wt pct Nb (about 5 at. pct Nb) in the temperature range of 550 °C to 825 °C. In that study, it was shown that at temperatures above 700 °C, the stress exponent  $n$  of the power law creep equation indicated a transition in mechanism, and in the high-stress and -temperature regime, addition of Nb increased the apparent activation energy for creep deformation.

In the present investigation, room-temperature tensile and elevated-temperature creep studies have been performed on various microstructures of Ti-25-10-3-1. We were particularly interested in the creep behavior of this alloy at the temperatures between 650 °C and 870 °C, since the use of conventional titanium alloys has generally been restricted to temperatures below 600 °C. The intent was to explore the influence of microstructure, stress, and temperature on creep behavior, taking due account of fracture modes and thin foil observations of dislocation structures responsible for each deformation process.

## II. EXPERIMENTAL PROCEDURE

The experimental material was taken from a pancake forging of Ti-25-10-3-1 with 4.4-cm thickness and 35-cm diameter, which had been forged in the  $\alpha_2 + \beta$  phase field and solution treated in the  $\beta$  phase region followed by air cooling. Some tests were performed on this as-received material. Additional microstructures were produced by re-solution treating in either the  $\alpha_2 + \beta$  or

WONSUK CHO, formerly with Carnegie Mellon University, is Senior Research Staff Member, Kia Technical Center, Yeosu, P.O. Box 560, Seoul, Korea. ANTHONY W. THOMPSON, Professor and Department Head, is with the Department of Metallurgical Engineering and Materials Science, Carnegie Mellon University, Pittsburgh, PA 15213. JAMES C. WILLIAMS, formerly Dean of Engineering, Carnegie Mellon University, is Manager, Engineering Materials Technology Laboratories, General Electric Aircraft Engines, Cincinnati, OH 45215.

Manuscript submitted March 16, 1989.

the  $\beta$  phase field and controlling the cooling rate from the solution-treatment temperature. Transformed  $\beta$  microstructures were produced by a 1-hour  $\beta$  solution treatment at 1150 °C followed by one of the following cooling schemes: slow or furnace cooling, SC; controlled cooling, CC; air cooling, AC. The SC, CC, and AC treatments produced average cooling rates of 0.1 °C, 0.5 °C, and 10 °C/s, respectively, when measured between the solution-treatment temperature and 760 °C. The  $\alpha_2/\beta$  microstructures were produced by solution treating at 1045 °C for 1 hour followed by the same cooling schemes as above. The  $\beta$  transus temperature for the alloy Ti-25-10-3-1 has been reported to be in the range of 1065 °C to 1093 °C.<sup>[3]</sup>

Tensile testing was performed at room temperature with various crosshead speeds from 0.05 to 500 mm/min (initial strain rates of  $1.62 \times 10^{-5}$  to  $1.62 \times 10^{-1} \text{ s}^{-1}$ ). Creep tests were conducted in air under constant tensile load, using specimens having a 6.4-mm diameter and a 37-mm effective gage length, with sufficient metal removal during machining to ensure that contaminated surfaces were removed. Test procedures followed ASTM E139-79. Creep strain was measured using an SLVC transducer which allowed a strain resolution of  $5 \times 10^{-6}$ .

The fracture surfaces were examined in a CamScan 4 scanning electron microscope and the dislocation structures were studied by transmission electron microscopy (TEM) in a PHILIPS\* EM420 operated at 120 kV.

\*PHILIPS is a trademark of Philips Instruments Corporation, Mahwah, NJ.

### III. RESULTS AND DISCUSSION

#### A. As-Received Microstructure and Thermal Stability

The as-received microstructure, shown in Figure 1, consisted of very fine Widmanstätten  $\alpha_2$  platelets and retained ordered  $\beta$  phase, consistent with the processing history of the as-received material. The microstructure

had relatively large prior  $\beta$  grains with 0.74-mm average intercept length and showed little effect of forging direction.

The thermal stability of Ti-25-10-3-1 was investigated by long-term aging of the as-received microstructure at 650 °C and 760 °C for times up to 1000 hours and by monitoring microstructural changes and determining changes in microhardness as a function of aging time. Exposure at both temperatures led to  $\beta$ -phase decomposition resulting in "breakup" in the ordered  $\beta$ -phase film (discussed below), as shown in Figure 1(c). In addition, the decomposition process left behind dislocation structures which are believed to occur for accommodation of this transformation. Detailed analysis of the decomposition product remains for future work. Room-temperature microhardness data (Figure 2) obtained as a function of aging time can be related to microstructural changes. Microhardness decreased rapidly just after short-term aging at both temperatures. The ordered  $\beta$ -phase decomposition, or recovery of defects in rapid-cooled substructures of as-received material, is thought to be responsible for the loss in hardness. The point to be made here is that at both temperatures, "microstructural changes" in a Widmanstätten-type microstructure can be finished in a reasonably short period to reach a quasi-equilibrium microstructure. This can be also true for microstructural evolution during creep exposures, as we point out below.

#### B. Microstructural Development

Light microscopy was used to characterize the various microstructures after heat treating, as an aid to understanding the relationship between the structure and the creep properties.

Figure 3 shows the microstructures resulting from three different cooling schemes from the  $\beta$  solution-treatment temperature. The significant variables in these microstructures are the size and morphology of  $\alpha_2$  phase and the amount of ordered retained  $\beta$  phase. Air cooling

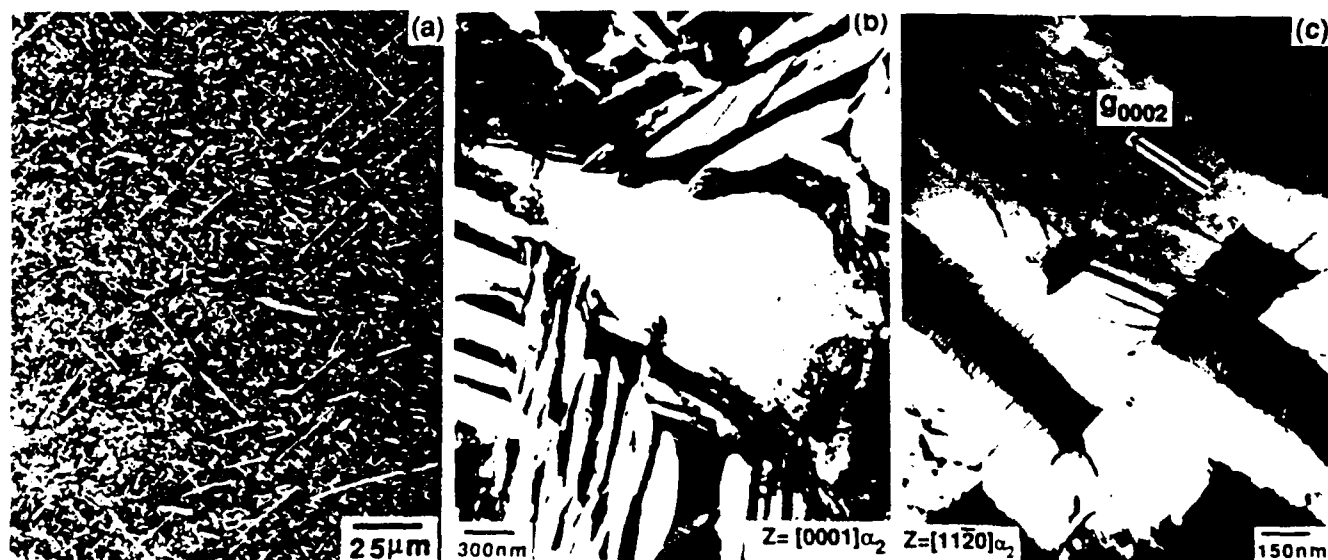


Fig. 1—As-received microstructure and thermal stability: (a) and (b) light and TEM micrographs of as-received microstructure and (c) after aging 100 h at 760 °C.

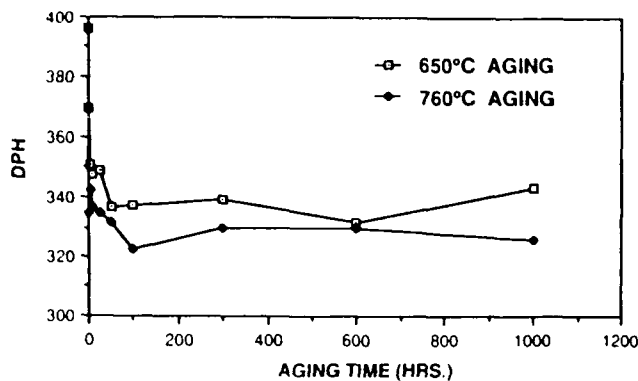


Fig. 2—Influence of thermal exposure on room-temperature microhardness for the as-received microstructure (very fine Widmanstätten).

( $\beta$ /AC), the fastest cooling rate, produced fine  $\alpha_2$  precipitates with a large amount of retained  $\beta$  phase. Additionally, in the  $\beta$ /AC microstructure, relatively small subgrain boundaries were etched out by much longer etching exposure (5 minutes) than the normal etching condition, using Kroll's reagent which revealed  $\beta$ /CC and  $\beta$ /SC microstructures. With the normal etching condition (10-second exposure), only prior  $\beta$  grain boundaries were visible. Furnace cooling ( $\beta$ /SC), the slowest cooling rate, produced moderately sized colonies of similarly aligned, coarse Widmanstätten  $\alpha_2$  plates. These Widmanstätten  $\alpha_2$  plates are separated by thin films of retained  $\beta$  phase. At the intermediate cooling rate,  $\beta$ /CC, the microstructure consists of thin, basketweave  $\alpha_2$  with a substantial amount of retained  $\beta$  phase. The resulting morphologies are quite similar to those found in conventional high-temperature near- $\alpha$  alloys, particularly in basketweave and colony microstructures. However, the kinetics of  $\beta$ -phase transformation seem to be different in different alloy systems.

It is possible for the retained  $\beta$  phase in  $\text{Ti}_3\text{Al}$  alloys to be ordered or disordered. Even though the details of retained  $\beta$  phase were not investigated in detail via TEM in the present study, it is believed from the earlier reports<sup>[8,9,10]</sup> that retained  $\beta$  phase has a fully transformed ordered structure (B2, CsCl type). In those papers, it has been shown that addition of  $\beta$  stabilizers such as Mo, Nb, or V results in the ordering of the  $\beta$  phase to a B2 structure. Recently, in the study of Strychor *et al.*,<sup>[10]</sup> the nature of  $\beta$ -phase ordering even in water-quenched specimens of Ti-27.8Al-11.7Nb (atomic percent) was confirmed through the examination of  $\beta$  zones which show superlattice reflections characteristic of a CsCl B2 structure. This type of behavior has been observed in  $\text{Ti}_3\text{Al} + \text{Nb}$  alloys whose Nb contents lie between about 15 and 35 wt pct, even though the extent of this field at the high Nb end is still largely undetermined.<sup>[12,10]</sup>

The microstructures resulting from  $\alpha_2/\beta$  solution treatment followed by three cooling schemes are shown in Figure 4. The  $\alpha_2/\beta$  process produced elongated primary  $\alpha_2$  in a transformed  $\beta$  matrix similar to that of  $\beta$  solution-treated microstructures. The microstructure with slow cooling ( $\alpha_2 + \beta$ /SC) was selected as representative of  $\alpha_2/\beta$  processed microstructures in order to compare room-temperature tensile properties as well as elevated-temperature creep behavior with  $\beta$  processed microstructures.

### C. Room-Temperature Tensile Properties

Room-temperature tensile properties were characterized as a function of strain rate for the microstructures discussed above. Four crosshead speeds were used: 0.05, 5, 50, and 500 mm/min (initial strain rates  $1.62 \times 10^{-5}$ ,  $1.62 \times 10^{-3}$ ,  $1.62 \times 10^{-2}$ , and  $1.62 \times 10^{-1} \text{ s}^{-1}$ ). The tensile properties, ultimate tensile strength or fracture strength, 0.2 pct yield strength, and percent elongation

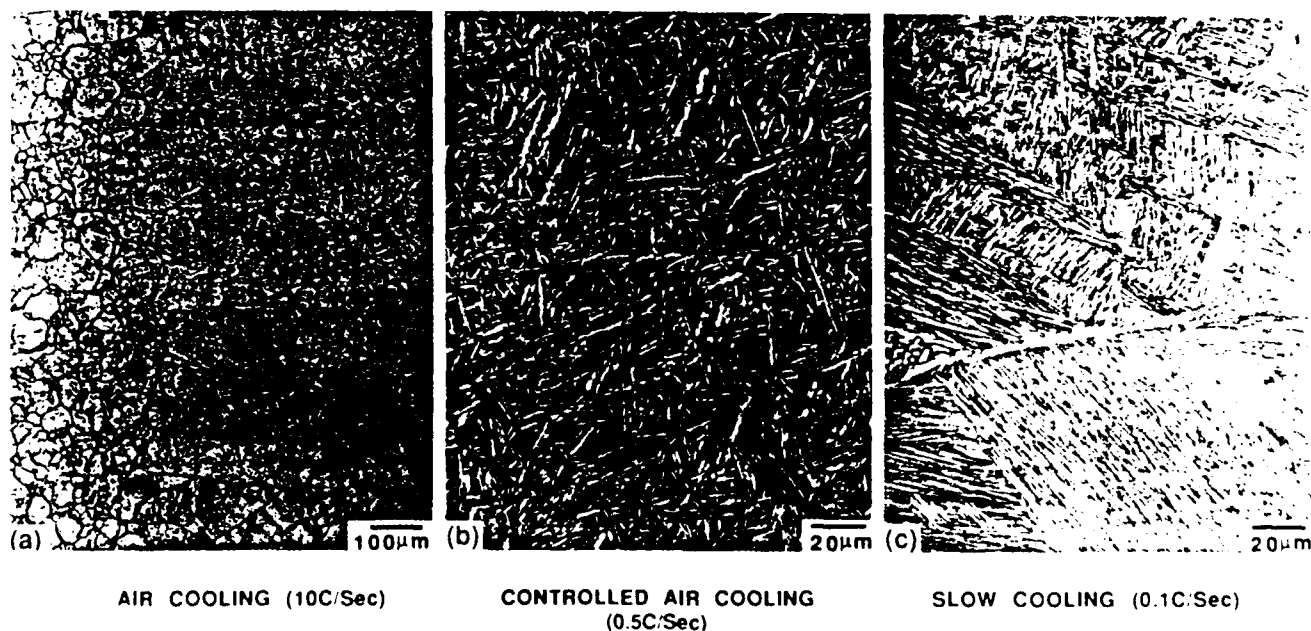


Fig. 3—Effect of cooling rate from  $\beta$  region on microstructure. (a)  $\beta$ /AC, (b)  $\beta$ /CC, and (c)  $\beta$ /SC.

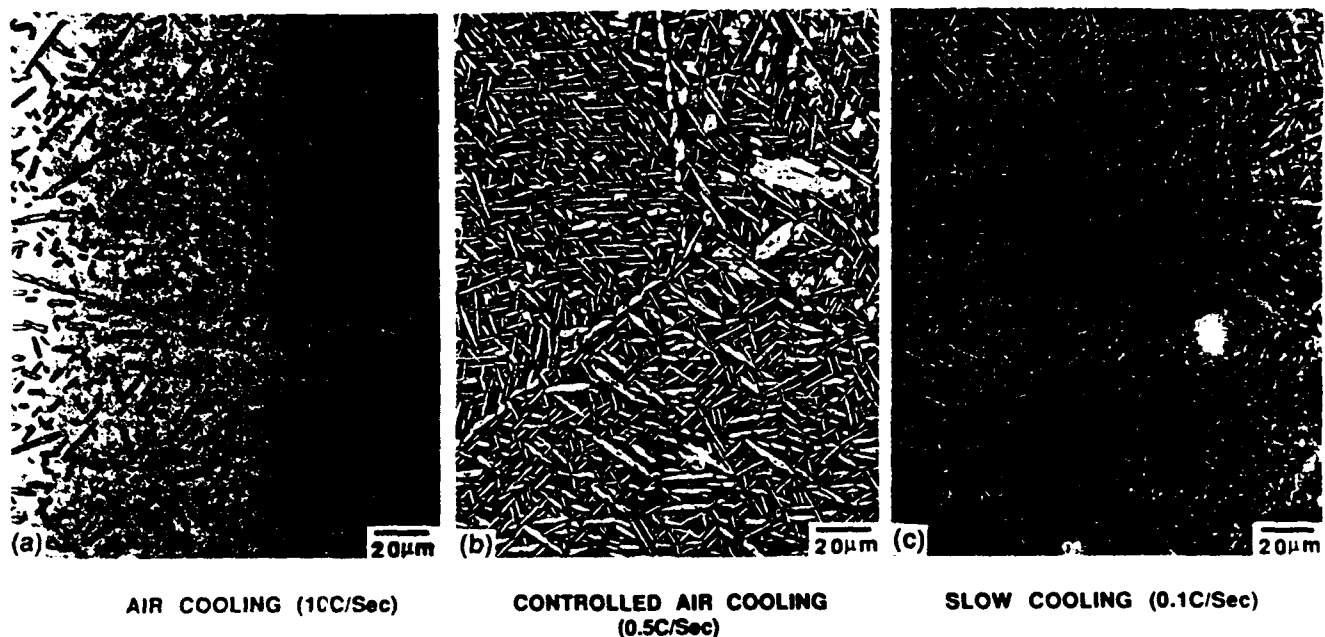


Fig. 4—Effect of cooling rate from  $\alpha_2 + \beta$  region on microstructure: (a)  $\alpha_2 + \beta/AC$ , (b)  $\alpha_2 + \beta/CC$ , and (c)  $\alpha_2 + \beta/SC$ .

are all shown in Figure 5. Particularly, the influence of cooling rate after  $\beta$  solution treatment on 0.2 pct yield stress and ductility is highlighted in Figure 6, using the slowest strain rate and 6.4-mm-diameter  $\times$  137-mm gage length specimens. These properties supplement those in Figure 5, which were obtained from pin-loaded small sheet specimens with 12.7-mm gage length.

The  $\alpha_2 + \beta$  processed microstructures exhibited higher strength values (yield and ultimate) than the  $\beta$  processed microstructure ( $\alpha_2 + \beta/SC$  vs  $\beta/SC$ ). It is thought that this behavior resulted from microstructural unit size difference controlling deformation, which is pronounced if one takes into account the dimensions of the colonies for  $\beta$  processed microstructures and of the elongated primary  $\alpha_2$  grains for  $\alpha_2 + \beta$  processed microstructures, as similarly explained in  $\alpha/\beta$  titanium alloys.<sup>[11,12,13]</sup> The  $\alpha_2 + \beta/SC$  microstructure was observed to be more ductile as compared to the  $\beta/SC$  microstructure. This increase in ductility might be attributed to the reduced dislocation pileup length<sup>[11]</sup> with decreasing microstructural unit size, as well as slightly enhanced retention of  $\beta$  phase due to enrichment of  $\beta$ -stabilizing elements in the  $\beta$  phase during  $\alpha_2 + \beta$  solution treatment.

In  $\beta$  processed microstructures, generally, both the strength and ductility increase as cooling rate is increased, except at very high strain rates. At very high strain rates, only  $\sigma_F$  was determined, because the X-Y chart recorder speed lagged the strain rate. Very little information is available on the influence of cooling rate on the mechanical properties of titanium aluminide alloys. Blackburn *et al.*<sup>[14]</sup> found similar behavior in Ti-24Al-11Nb to that of the present investigation, using three cooling rates from  $\beta$  solution treatment. Slow cooling resulting in a colony microstructure produced low strength and ductility, while intermediate cooling rate, resulting in a fine Widmanstätten (basketweave) microstructure, caused good ductility and strength level. A rapid cooling

rate (15 °C/s), producing a partially transformed structure, also brought the highest yield strength, but a very low ductility, even lower than that of the colony microstructure. In near- $\alpha$  alloys, such as IMI 829,<sup>[15]</sup> no significant change in the strength and ductility was found in the  $\beta$  heat-treated condition due to changes in the cooling rate, which resulted in similar morphologies, as in the case of the present  $\alpha_2$  alloy.

When the room-temperature tensile properties are considered from the viewpoint of the strain-rate variable, it can be seen that the influence of strain rate on the flow stress depends on microstructure. For as-received  $\beta/CC$  and  $\alpha_2 + \beta/SC$  microstructures, the flow stress is independent of strain rate, whereas for  $\beta/AC$  and  $\beta/SC$  microstructures, the flow stress decreases rapidly at the very high strain rate ( $1.62 \times 10^{-1} \text{ s}^{-1}$ ) but attains a constant value for strain rates slower than  $1.62 \times 10^{-2} \text{ s}^{-1}$ . The degree of decrease is much higher in the  $\beta/SC$  microstructure than that in the  $\beta/AC$  microstructure. As can be seen in Figure 5(a), the tensile strength or the fracture strength of  $\beta/SC$  microstructure dropped to approximately half of that found at lower strain rates. Even though some data scatter is found, ductility, as measured by the total elongation of all the microstructures, seems to be independent of strain rate.

The observed strain-rate independence of room-temperature strength would be expected to be consistent with the temperature dependence of strength. In the case of monolithic  $\alpha_2$ , the static strength and stiffness did not degrade very rapidly with increasing temperature.<sup>[16]</sup> Similar behavior has been observed both in monolithic  $\gamma'$  ( $\text{Ni}_3\text{Al}$ ,  $L1_2$  structure)<sup>[17]</sup> and  $\gamma/\gamma'$  alloys.<sup>[18]</sup> It was shown that samples deformed before the peak temperature, where a positive temperature dependence in monolithic  $\gamma'$  and a temperature independence in  $\gamma/\gamma'$  alloys of the flow stress were characterized, exhibited a very small positive strain-rate dependence of the flow stress.

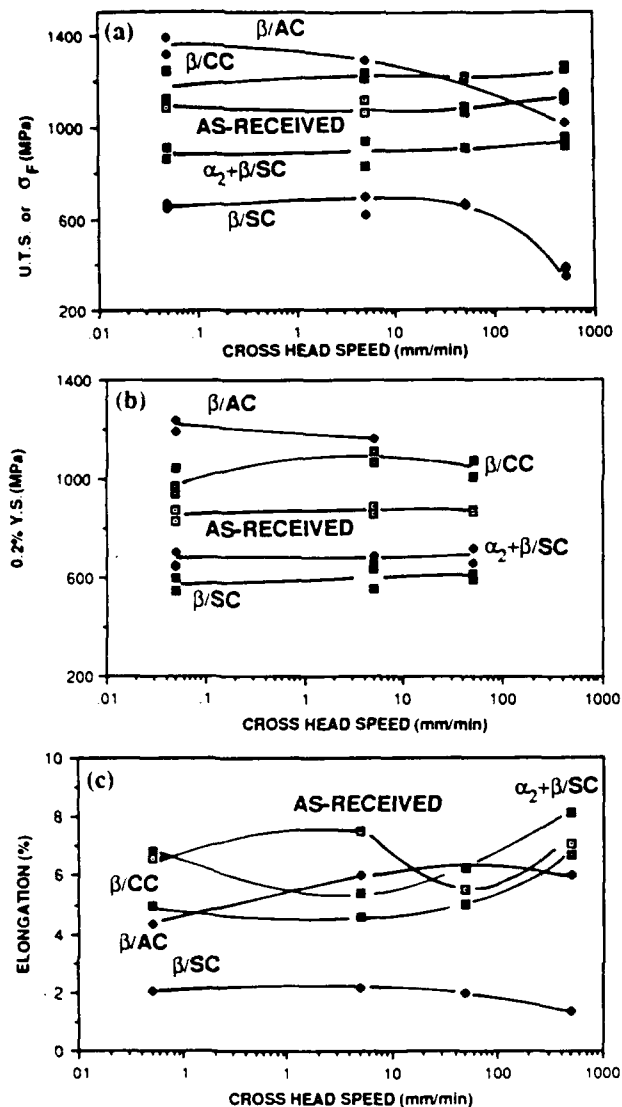


Fig. 5—Effect of microstructure on room-temperature tensile properties: (a) ultimate tensile strength or  $\sigma_F$ , (b) 0.2 pct yield strength, and (c) elongation.

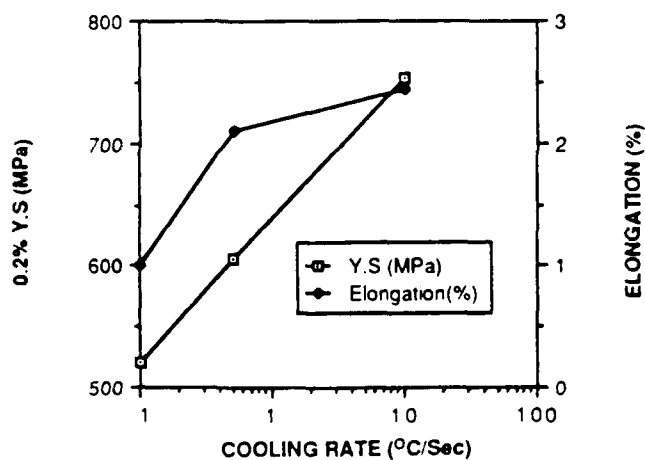


Fig. 6—Effect of cooling rate from  $\beta$  solution treatment on room-temperature tensile properties.

However, samples deformed at higher temperatures after the peak, where the flow stress decreased very rapidly with increasing temperature, demonstrated a very strong positive effect of strain rate on the flow stress.

#### D. Creep Behavior

##### 1. Role of microstructure

The effect of microstructure on creep behavior was studied as a function of stress and temperature between 650  $^{\circ}C$  and 870  $^{\circ}C$ . Apparent stress exponent  $n$  measurements were made by decreasing load from the load pan during testing in order to provide a step change in stress and thus strain rate.<sup>[19]</sup> At each new stress level, the test continued until a new steady-state creep rate could be determined, thus minimizing structural changes for each successive decrease in load. Most tests were terminated during steady-state creep, and the specimens were cooled down under load to preserve and investigate dislocation structures responsible for creep deformation.

As shown in Figures 7 and 8, the creep curves obtained at 650  $^{\circ}C/414$  MPa and 760  $^{\circ}C/207$  MPa demonstrate the pronounced influence of microstructure. Generally, most of the creep curves have a classical behavior with a primary or transient period followed by a steady-state regime. It is useful, here, to characterize creep behavior with two processing parameters: (1) solution-treatment temperature ( $\beta/SC$  vs  $\alpha_2 + \beta/SC$ ) and (2) cooling rate from the  $\beta$  region ( $\beta/AC$ ,  $\beta/CC$ ,  $\beta/SC$ ).

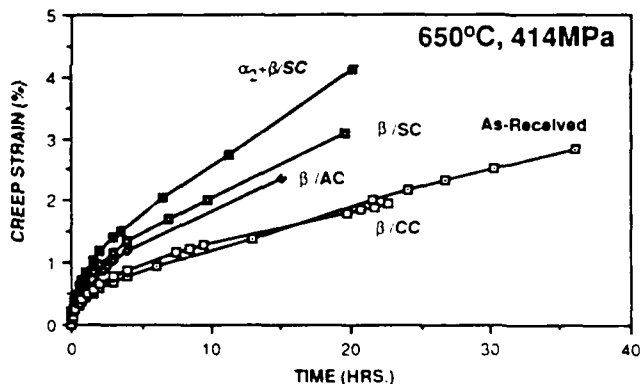


Fig. 7—Effect of microstructure on creep behavior at 650  $^{\circ}C$  / 414 MPa.

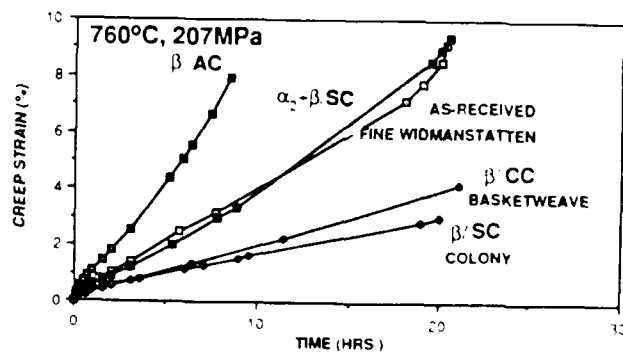


Fig. 8—Effect of microstructure on creep behavior at 760  $^{\circ}C$  / 207 MPa.

At both temperatures, the  $\alpha_2 + \beta$  processed microstructure ( $\alpha_2 + \beta$ /SC) which has elongated primary  $\alpha_2$  grains shows lower creep resistance when compared to the  $\beta$  solution-treated microstructure ( $\beta$ /SC), although the magnitude of the effect of the solution treating process was much greater at 760 °C/207 MPa.

The  $\beta$  solution treatment alone is not sufficient to characterize creep resistance. The effect of cooling rate from the  $\beta$  phase region on microstructure and its role in creep performance needs to be taken into account. Figure 9 shows the effect of cooling rate on creep strain after a certain amount of time, obtained from Figures 7 and 8. Creep resistance increased with decreasing cooling rate at 760 °C/207 MPa; thus, creep resistance of the slow-cooled colony microstructure (0.1 °C/s) was significantly improved. However, at 650 °C/414 MPa, creep resistance increased with increasing cooling rate through a maximum at an intermediate cooling rate of 0.5 °C/s, which produced a basketweave microstructure. At higher cooling rates, creep resistance at 650 °C again decreased.

To investigate further the role of microstructure in creep resistance, steady-state creep rates were measured as a function of stress at constant temperatures of 650 °C and 760 °C, as shown in Figure 10. The apparent exponents  $n$  were obtained to show the stress dependence of steady-state creep rate, following the usual power law creep equation:

$$\dot{\epsilon}_s = A\sigma^n \exp(-Q_c/RT)$$

where  $\dot{\epsilon}_s$  is the steady-state creep rate at a tensile stress  $\sigma$ ,  $n$  and  $A$  are constants,  $Q_c$  is the apparent activation energy,  $R$  the gas constant, and  $T$  the absolute temperature. At 760 °C (Figure 10(b)), microstructural variation has little effect on  $n$  values in the range of stress studied; thus, at all stresses, the colony microstructure ( $\beta$ /SC) shows lower creep rate than that of the fine Widmanstätten microstructure (as-received). In contrast, at 650 °C (Figure 10(a)), it can be seen that the influence of microstructure on steady-state creep depends on stress level. The  $\beta$ /SC material had a larger  $n$  value (5.8) than that of  $\beta$ /CC (4.2); thus, a crossover point was found on the stress vs steady-state creep-rate plot. At high

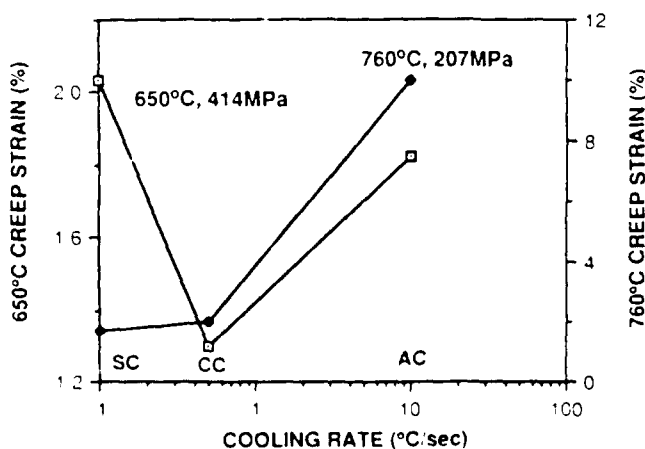


Fig. 9—Effect of cooling rate from  $\beta$  solution treatment on creep strain

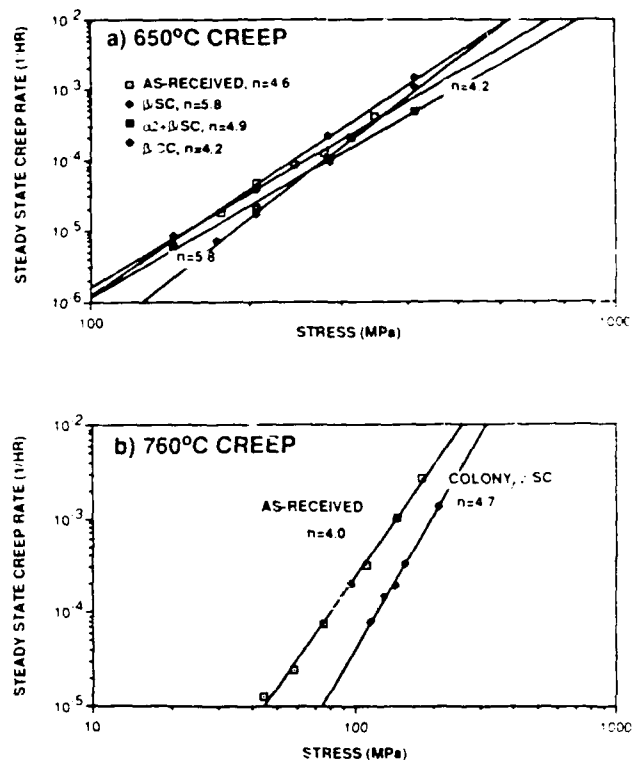


Fig. 10—Stress dependence of steady-state creep rate for various microstructures: (a) at 650 °C and (b) at 760 °C.

stresses,  $\beta$ /CC exhibits the lowest steady-state creep rate, while at low stresses,  $\beta$ /SC does again.

For different microstructures, the difference in creep response under identical testing conditions can be attributed to differences in microstructural variables. Moreover, the role of microstructure is thought to differ for the different creep regimes. Based on determined  $n$  values, it can be concluded that in the present regimes studied, creep strain accumulation is controlled by dislocation motion. Most recently, a phenomenological model<sup>[14,20]</sup> was proposed to correlate creep behavior of near- $\alpha$  titanium alloys with structural factors. In this model, the existence of an optimum cooling rate for maximum creep resistance was explained in terms of the trade-off between an increasing amount of retained  $\beta$  phase (detrimental in creep resistance) and decreasing  $\alpha$  plate size (beneficial in creep resistance). The present observations on the interaction between microstructure and creep deformation can be rationalized in a similar manner as in the case of near- $\alpha$  titanium alloys.

First, it is suggested that the effective slip length in elevated-temperature creep deformation is controlled by primary  $\alpha_2$  size in  $\alpha_2 + \beta$  processed microstructures and by Widmanstätten  $\alpha_2$  in  $\beta$  processed microstructures. Even though the Burgers relationship is expected to exist between  $\alpha_2$  and ordered  $\beta$  phase, as it does between  $\alpha$  and  $\beta$  phase,<sup>[21]</sup> it is not surprising that  $\alpha_2$ /B2 boundaries are effective barriers to slip and act to confine active dislocations to individual  $\alpha_2$  platelets because of the relatively low applied stresses, necessitated by the high creep temperatures. Therefore, inferior creep resistance of the  $\alpha_2 + \beta$ /SC microstructure is attributed to a larger slip length than that of the  $\beta$ /SC microstructure.



If only  $\alpha_2$  platelet size controlled creep deformation, it would be expected that the microstructure with fine Widmanstätten  $\alpha_2$  platelets would exhibit superior creep resistance. The maximum in creep resistances that occurs in the slow-cooled microstructure ( $\beta$ /SC) at 760 °C and 650 °C and low stresses suggests that other microstructural factors must be considered. The other microstructural factor competing with  $\alpha_2$  plate dimension is the amount of retained ordered  $\beta$  phase (B2). Fast cooling increases the amount of B2 phase, resulting in poor creep resistance, because of its ductility and intrinsic high diffusion coefficient. It is, therefore, required to have optimum  $\alpha_2$  plate size and optimum amount of retained B2 phase for superior creep resistance at elevated temperatures. However, at 650 °C and high stresses, a somewhat complicated role of microstructure was observed because of differences in stress dependence. Minimum creep resistance in  $\beta$ /SC microstructure in this regime suggests that a different structural unit beyond  $\alpha_2$  plate size would be active, similar to that of room-temperature tensile behavior, or that the thermally activated deformation process in retained B2 phase would not be significantly important to control creep deformation at this temperature. Generally, 650 °C creep seems to behave like a transition between patterns of room-temperature deformation and those of high-temperature creep deformation.

## 2. Evaluation of creep parameters

One of the most powerful means of establishing the controlling mechanism in creep deformation<sup>[22]</sup> is based on a knowledge of the activation energy ( $Q_c$ ) and the stress exponent  $n$ . The apparent temperature dependence of steady-state creep rate was determined for the as-received microstructure between 650 °C and 760 °C at a constant stress of 207 MPa, using the power law creep equation described previously, as shown in Figure 11. A creep activation energy of 305 kJ/mol was obtained from a least-squares calculation. Mendiratta and Lipsitt<sup>[7]</sup> measured the activation energy in  $\text{Ti}_3\text{Al}$  and  $\text{Ti}_3\text{Al} + 10$  wt pct Nb in the temperature range of 550 °C to 825 °C, even though they failed to relate these data to the controlling mechanism because of the nonavailability of diffusion data for  $\alpha_2$  alloys. They found that addition of Nb increased the activation energy from 206 kJ/mol in monolithic  $\alpha_2$  to 285 kJ/mol in  $\alpha_2 + 10$  wt pct Nb in the temperature range of 650 °C to 825 °C. These values

are broadly consistent with the present investigation's value of 305 kJ/mol, although Ti-25-10-3-1 contains significantly more  $\beta$ -stabilizing additions than in the earlier work. It is therefore possible that additions of  $\beta$ -phase stabilizers have a nonlinear effect on creep activation energy. In addition, from their work, it was found that the activation energy of the  $\alpha_2 + \text{Nb}$  alloy decreased to a value of 195 kJ/mol below 650 °C to 550 °C, which would support a transition in mechanism. This observation is consistent with the suggestion that 650 °C creep in the present investigation represents a transition behavior between deformation at room temperature and creep at temperatures above 760 °C.

The obtained stress exponents  $n$  indicate<sup>[23]</sup> that the creep process is dominated by the generation and movement of dislocations in the test regimes studied. These exponents are generally within the range of values ( $n = 3$  to 5) predicted by theoretical models<sup>[23]</sup> of dislocation-controlled creep which depend on detailed dislocation hardening and recovery processes. In Figure 12, the stress dependence of steady-state creep rate was obtained as a function of temperature with the use of as-received microstructure (fine Widmanstätten). It may be noted that there is a tendency for  $n$  to decrease as temperature is increased, and at a very high temperature (870 °C), a transition in mechanism might occur, even though a clear change in  $n$  value is not shown ( $n = 2.8$  to 3.5). One possibility is that with increasing temperature, emergence of grain boundary sliding would occur, and thus, the exponent  $n$  would decrease, since grain boundary sliding tends to decrease  $n$ , relative to a material without grain boundary sliding.<sup>[24,25]</sup> It has been pointed out that grain boundary sliding is not an independent mechanism producing a steady-state creep strain and must be integrally connected with intracrystalline creep deformation.<sup>[24,26]</sup> Accordingly, it is possible that two mechanisms are operative at the test temperature of 870 °C. It is thought that creep rate may be controlled either by the intrinsic viscosity of the grain boundary or by the accommodation process, depending on stress level.<sup>[25]</sup> Thus, at high stresses, grain boundaries behave effectively rigidly, while at low stresses, the boundaries slide relatively freely.

Mendiratta and Lipsitt<sup>[7]</sup> also obtained the stress exponents for temperatures varying from 650 °C to 800 °C in  $\text{Ti}_3\text{Al}$  and  $\text{Ti}_3\text{Al} + 10$  wt pct Nb. As is consistent with the present results, a transition in mechanism was found

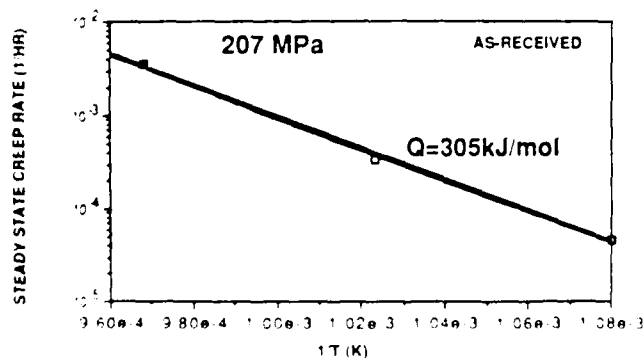


Fig. 11—Temperature dependence of steady state creep rate of as-received microstructure in the range of 650 °C to 760 °C.

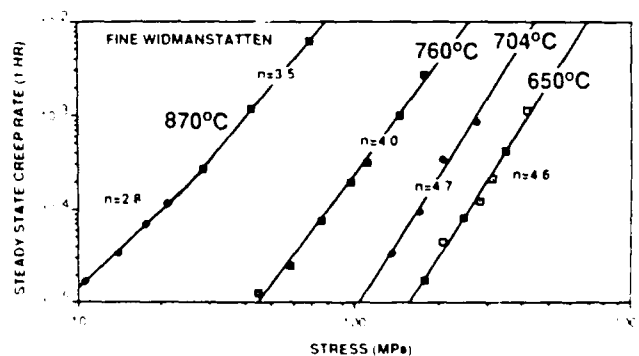


Fig. 12—Stress dependence of steady-state creep rate of as-received microstructure as a function of temperature.

for both intermetallic alloys above around 700 °C; for  $\text{Ti}_3\text{Al}$ , 4.5 to 2.5, and for  $\text{Ti}_3\text{Al} + 10 \text{ wt pct Nb}$ , 6.5 to 2.5. However, in contrast to the present investigation, their data for all temperatures could be represented by nearly parallel straight lines at high stresses, indicating temperature independence of the stress exponent. Whether that difference resulted from differences in alloy composition, microstructure, or other variables is not known.

In Figure 13, creep behavior of Ti-25-10-3-1 is compared at 650 °C and 760 °C with those of two near- $\alpha$  titanium alloys, Ti-6242S<sup>(4)</sup> and Ti-1100,<sup>(27)</sup> the latter of which is a newly developed alloy which achieves improved creep resistance with a larger amount of Si (0.45 pct) and smaller amounts of  $\beta$ -phase stabilizers. For comparison, the optimum microstructure (colony) was used for all alloys. Generally, creep resistance of Ti-25-10-3-1 is improved by one order of magnitude over Ti-1100 and by two orders of magnitude over Ti-6242S. Unlike near- $\alpha$  alloys, a transition in mechanism in Ti-25-10-3-1 was not found at 760 °C in the similar stress range studied.

### E. Fracture Modes and Dislocation Structures

#### 1. Fractography

Figure 14 shows the influence of cooling rate on tensile fracture mode ( $\beta/\text{AC}$ ,  $\beta/\text{CC}$ ,  $\beta/\text{SC}$ ). Much of the fracture surface is brittle-looking and resembles cleavage. As the cooling rate is increased (the amount of retained  $\beta$  phase is increased), regions of the fracture

showing a ductile fracture mode become increasingly evident. In basketweave and colony microstructures, fracture modes were found to be consistent with the behavior of microstructural units. The ridges of the ductile tearing are seen to lie along the length of the ordered  $\beta$ -phase film, parallel to the  $\alpha_2/\beta$  interfaces, while the fracture is totally cleavage-like in the  $\alpha_2$  plate.

Creep fracture modes were investigated at 650 °C and 760 °C for the as-received microstructure, as shown in Figures 15 and 16. At 650 °C (Figure 15), a similar transgranular mode of failure was found as that of room temperature, although it should not necessarily be inferred that the local fracture processes are the same at room and elevated temperature. However, at the edge of the specimen, fine dimples resulting from overload fracture were found. At 760 °C (Figure 16), it was observed that creep ductility increased very rapidly, and an increased tendency for intergranular cracking was recognized. This observation is quite consistent with previous findings in  $\text{Ti}_3\text{Al}$ .<sup>(16)</sup> In addition, at 760 °C, larger dimples than those in 650 °C crept specimens were found around the edge of specimens.

#### 2. Dislocation structures

Thin foils prepared from the gage sections of the room-temperature tensile and elevated-temperature crept samples ( $\beta/\text{SC}$ ) were examined to establish the associated slip character. Figure 17 shows the room-temperature tensile deformation mode in which  $a_0/3$   $\langle 11\bar{2}0 \rangle$ ,  $\bar{a}$ -type dislocations are predominant. A slip trace analysis indicates a high degree of slip planarity on prism planes and some evidence of basal slipbands. In addition, some extended faults were found. At high temperatures, cross slip of  $\bar{a}$  dislocations between the basal, prismatic, and pyramidal planes, which is difficult at low temperatures, is evidently easier to accomplish, as shown in Figure 18. At all temperatures, most of the dislocations are homogeneously distributed.

In addition to  $\bar{a}$ -type dislocations, a moderate number of fairly straight dislocations with nonbasal Burgers vectors which are in contrast with  $\mathbf{g}_{0002}$  were found at all temperatures. Increasing temperature did not significantly change the mode and occurrence of these dislocations. The foregoing observations are all consistent with previous work.<sup>(11,16,28)</sup>

### IV. SUMMARY

1. The influence of microstructure on creep behavior of Ti-25Al-10Nb-3V-1Mo atomic percent has been determined as a function of stress and temperature (650 °C to 870 °C). In addition, room-temperature tensile properties were characterized as a function of strain rate.
2. Generally, increasing cooling rate from  $\beta$  solution-treatment temperature increased room-temperature tensile strength and ductility, evidently because of refinement of microstructural unit size and retention of ductile  $\beta$  phase. The strain-rate dependence of room-temperature tensile strength was dependent on microstructure.
3. At high temperatures,  $\beta$  solution-treated microstructure exhibited superior creep resistance

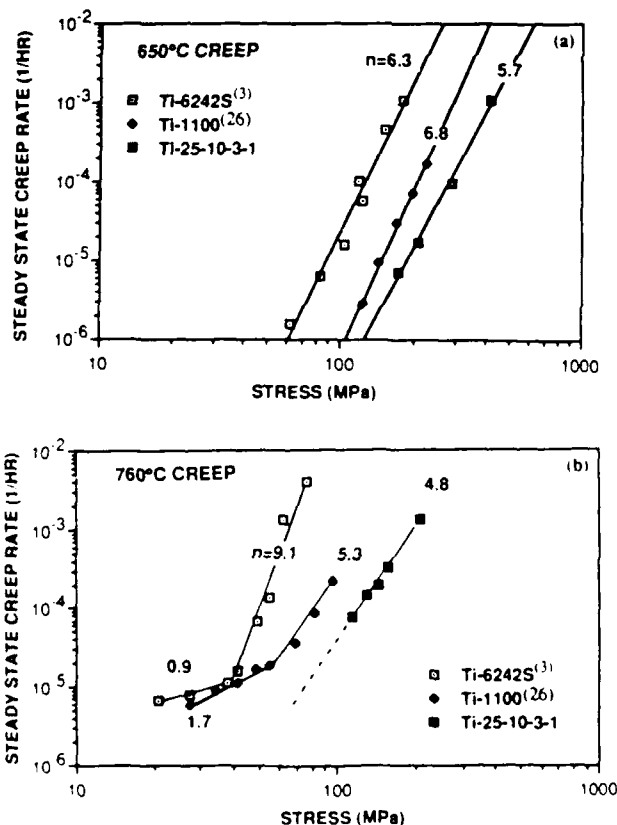


Fig. 13—A comparison of creep behavior of Ti-25-10-3-1 with two conventional near- $\alpha$  titanium alloys (Ti-6242S and Ti-1100), using colony microstructure: (a) 650 °C creep and (b) 760 °C creep.

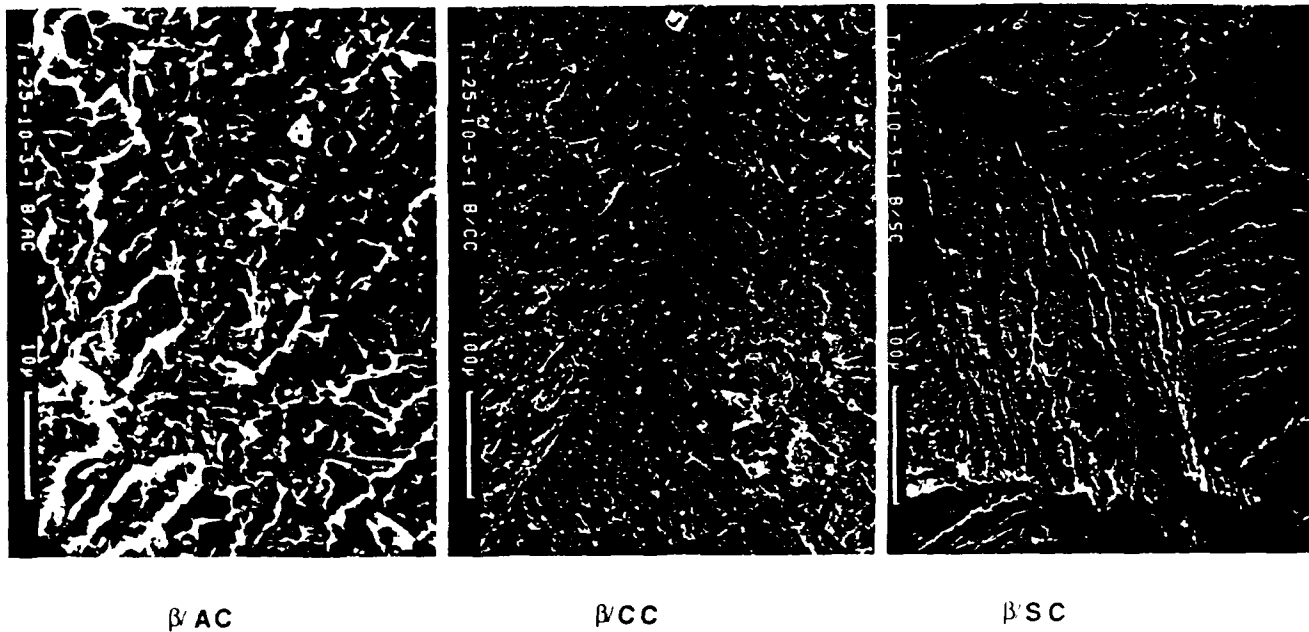


Fig. 14—Effect of cooling rate on room-temperature tensile fracture mode.

compared to  $\alpha_2 + \beta$  processed microstructure ( $\alpha_2 + \beta/SC$  vs  $\beta/SC$ ).

4. A pronounced influence of cooling rate from the  $\beta$  solution-treatment temperature on creep was observed. At 760 °C,  $\beta/SC$  (colony) was proven to be an optimum microstructure for creep resistance at all stresses studied. However, at 650 °C, a somewhat

complicated effect that depends on stress level was found. At this temperature,  $\beta/SC$  shows superior creep performance only at relatively low stresses. It is believed that 650 °C creep shows a transition deformation behavior between room-temperature and elevated-temperature behavior.

5. Increasing temperature decreased the stress exponent

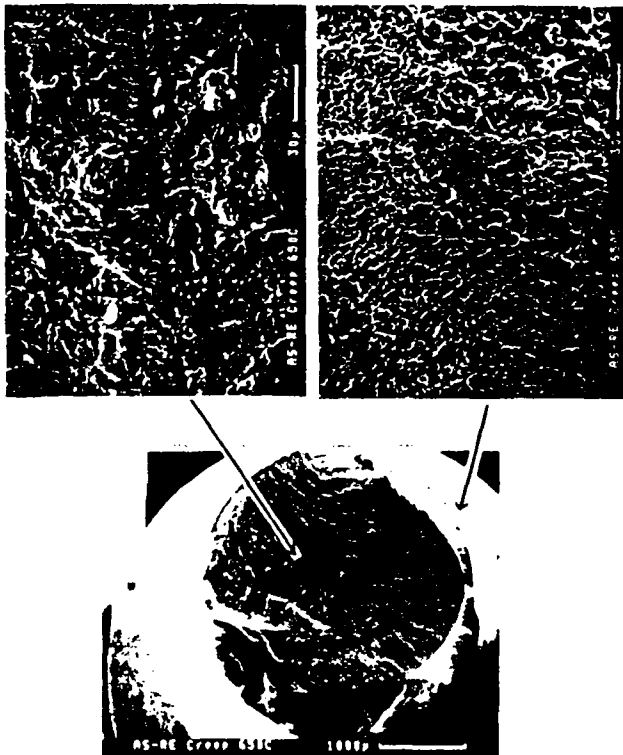


Fig. 15—High-temperature creep fracture mode at 650 °C (as-received microstructure)



Fig. 16—High-temperature creep fracture mode at 760 °C (as-received microstructure)

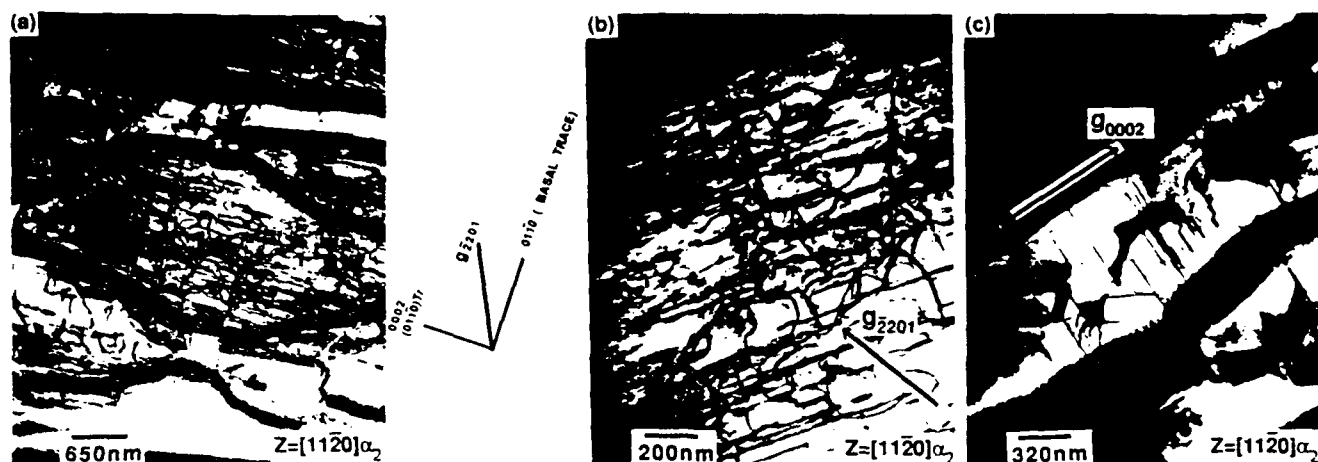


Fig. 17—TEM micrographs showing room-temperature tensile deformed dislocation structures: (a) overall slip mode, (b) higher magnification of (a), and (c) dislocations with nonbasal Burgers vector.

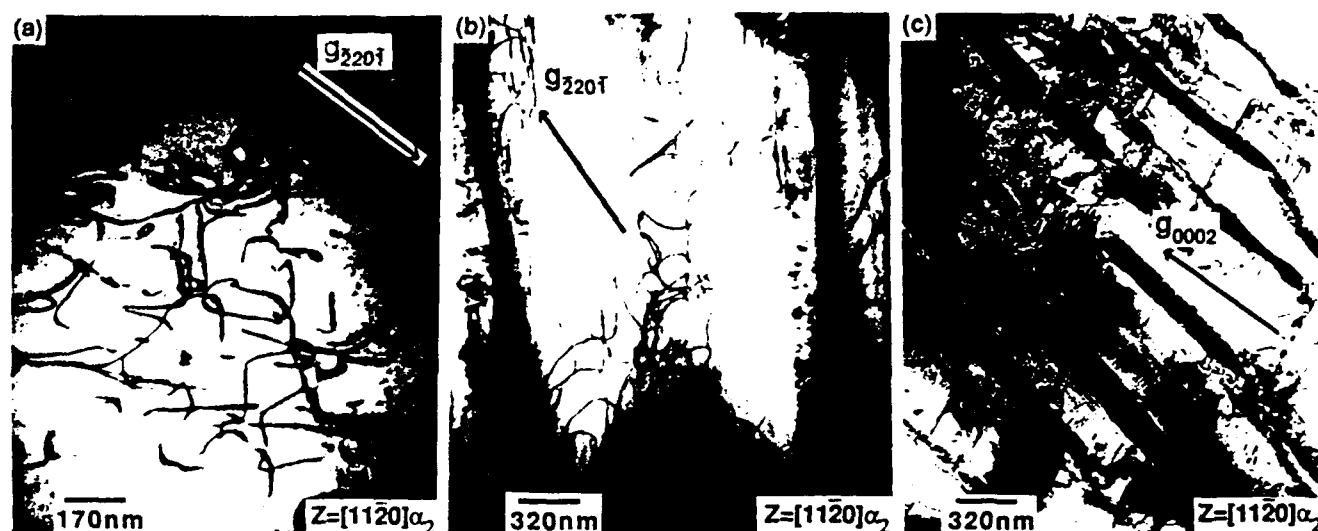


Fig. 18—TEM micrographs showing elevated-temperature creep deformation: (a) and (b) wavy  $\alpha$  dislocations in 650 °C and 760 °C crept specimens, respectively. (c) Dislocations with nonbasal Burgers vector in 760 °C crept specimen.

$n$  and caused an apparent transition in creep mechanism at 870 °C, depending on stress level. The obtained exponents are generally within the range of values predicted by theoretical models of dislocation-controlled creep. A creep activation energy of 305 kJ/mol was measured in the temperature range of 650 °C to 760 °C.

- Creep resistance of Ti-25-10-3-1 was compared to two creep-resistant near- $\alpha$  titanium alloys and was found to be improved by one order of magnitude in steady-state creep rate over Ti-1100, and by two orders of magnitude over Ti-6242S, in the test regimes studied, when the optimum microstructure (colony) is used for all alloys.

#### ACKNOWLEDGMENTS

We appreciate support of this work by the United States Air Force Office of Scientific Research, Contract No.

F49620-87-C-0017, as part of the University Research Initiative program on High Temperature Metal Matrix Composites at Carnegie Mellon University.

#### REFERENCES

- H.A. Lipsitt: *High-Temperature Ordered Intermetallic Alloys*, MRS Symp. Proc., MRS, Pittsburgh, PA, 1985, vol. 39, pp. 351-64.
- R.L. Fleischer, D.M. Dimiduk, and H.A. Lipsitt: *Intermetallic Compounds for Strong High-Temperature Materials: Status and Potential*, Materials Research Laboratory Report 88CRD326, General Electric Corporate Research and Development, Schenectady, NY, Dec. 1988.
- M.J. Blackburn and M.P. Smith: Technical Report, AFWAL-TR-4086, AFWAL, Wright-Patterson Air Force Base, Dayton, OH, 1982.
- W. Cho, J.W. Jones, J.E. Allison, and W.T. Donlon: *Proc. 6th Int. Conf. on Titanium*, Cannes, France, 1988, in press.
- P.A. Blenkinsop, D.F. Neal, and R.E. Goosey: *Titanium and Titanium Alloys*, J.C. Williams and A.F. Belov, eds., Plenum Press, New York, NY, 1976, vol. 3, pp. 2003-14.

6. M.G. Mendiratta and N.S. Choudhury: Technical Report, AFML-TR-78-112, AFML, Wright-Patterson Air Force Base, Dayton, OH, 1978.
7. M.G. Mendiratta and H.A. Lipsitt: *J. Mater. Sci.*, 1980, vol. 15, pp. 2985-90.
8. T. Hamajima, G. Lütjering, and S. Weissmann: *Metall. Trans.*, 1973, vol. 4, pp. 847-56.
9. D. Banerjee, T. Nandi, and A.K. Gogia: *Scripta Metall.*, 1987, vol. 21, pp. 597-601.
10. R. Strychor, J.C. Williams, and W.A. Soffa: *Metall. Trans. A*, 1988, vol. 19A, pp. 225-34.
11. J.C. Williams and G. Lütjering: *Titanium '80, Science and Technology*, H. Kimura and O. Izumi, eds., TMS-AIME, Warrendale, PA, 1980, vol. 1, p. 671.
12. A. Gysler and G. Lütjering: *Metall. Trans. A*, 1982, vol. 13A, pp. 1435-43.
13. F.S. Lin, E.A. Starke, S.B. Chakraborty, and A. Gysler: *Metall. Trans. A*, 1984, vol. 15A, pp. 1229-46.
14. M.J. Blackburn, D.L. Ruckle, and C.F. Bevan: Technical Report, AFML-TR-78-18, AFML, Wright-Patterson Air Force Base, Dayton, OH, 1978.
15. G. Sridhar, V.V. Kutumbarao, and D.S. Sarma: *Metall. Trans. A*, 1987, vol. 18A, pp. 877-91.
16. H.A. Lipsitt, D. Shechtman, and R.E. Schafrik: *Metall. Trans. A*, 1980, vol. 11A, pp. 1369-75.
17. J.K. Tien, S. Eng, and J.M. Sanchez: *High Temperature Ordered Intermetallic Alloys II*, MRS Symp. Proc., MRS, Pittsburgh, PA, 1987, vol. 81, p. 183.
18. G.R. Leverant, M. Gell, and S.W. Hopkins: *Mater. Sci. Eng.*, 1971, vol. 8, pp. 125-33.
19. N.E. Paton and M.W. Mahoney: *Metall. Trans. A*, 1976, vol. 7A, pp. 1685-94.
20. W. Cho: Ph.D. Thesis, The University of Michigan, Ann Arbor, MI, 1987.
21. J.C. Williams: *Titanium Science and Technology*, R.I. Jaffe and H.M. Burte, eds., Plenum Press, New York, NY, 1973, vol. 3, pp. 1433-94.
22. R. Lagneborg: *Int. Metall. Rev.*, 1972, vol. 17, pp. 130-46.
23. W.D. Nix and B. Ilshner: *Strength of Metals and Alloys* (Proc. ICSMA 5), P. Haasen, V. Gerold, and G. Kostorz, eds., Pergamon Press, New York, NY, 1980, pp. 1507-30.
24. F.W. Crossman and M.F. Ashby: *Acta Metall.*, 1975, vol. 23, pp. 425-40.
25. H. Riedel: *Fracture at High Temperature*, Springer-Verlag, New York, NY, 1987.
26. S. Takeuchi and A.S. Argon: *J. Mater. Sci.*, 1976, vol. 11, pp. 1542-66.
27. W. Cho, J.W. Jones, and J.E. Allison: The University of Michigan, Ann Arbor, MI, unpublished research, 1987.
28. W.J.S. Yang: *Metall. Trans. A*, 1982, vol. 13A, pp. 324-28.



# **TITANIUM ALUMINIDES**

**PAPERS PRESENTED AT**

**AEROMAT '90**

**LONG BEACH, CALIFORNIA**

**21-24 MAY 1990**

**SESSION ORGANIZERS:**

**C.G. RHODES  
H.A. LIPSITT**



**Rockwell International**

**Science Center  
1049 Camino Dos Rios  
Thousand Oaks, CA 91360**

# **CREEP OF ALPHA-2 TITANIUM ALUMINIDES**

Anthony W. Thompson

**Carnegie Mellon University  
Pittsburgh, PA 15213**



## Creep of Alpha-2 Titanium Aluminide Alloys

Anthony W. Thompson  
Dept. of Metallurgical Engineering and Materials Science  
Carnegie Mellon University  
Pittsburgh, PA 15206

The interest in titanium aluminide alloys includes elevated temperature applications, for which creep resistance is a primary property. Tests have been made between 650°C and 870°C on a variety of microstructures of Ti-24 Al-11 Nb and Ti-25 Al-10 Nb-3 Mo-1 V (atomic percent) alloys. It has been found that microstructure plays an important role in creep of these materials, so that thermal and mechanical history is important. Creep activation energies are similar to or somewhat less than for stoichiometric  $\text{Ti}_3\text{Al}$ . As is usually found in structural alloys, microstructural characteristics which increase ductility and toughness at low temperature tend to accelerate creep considerably, particularly the presence of beta phase, and most notably when arranged as locally-continuous  $\beta$  films between plates of the alpha-two phase. Comparison to alpha-beta titanium alloys which have been developed for creep resistance shows better performance, especially above 700°C.

In the following presentation, creep data for Ti-24-11 and Ti-25-10-3-1 are presented in some detail, together with comparisons to other alloys. Fuller discussion is available in the published version of the Ti-25-10-3-1 paper, *Metall. Trans. A*, 1990, Vol. 21A, pp. 641-651.

Ti-24 Al-11 Nb (at. %)

Diane Albert

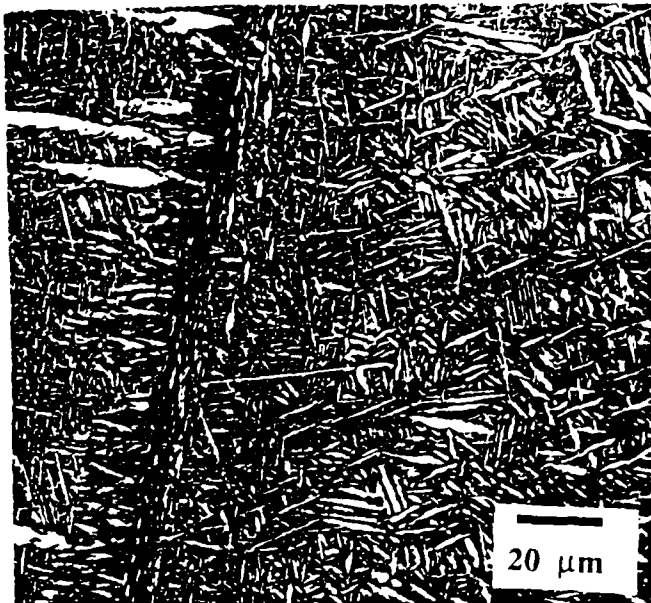
**Sponsored by URI through AFOSR,  
completed by AFOSR**

Chemical Composition of Ti-24-11 ( $\alpha_2$  +  $\beta$  forged pancake)

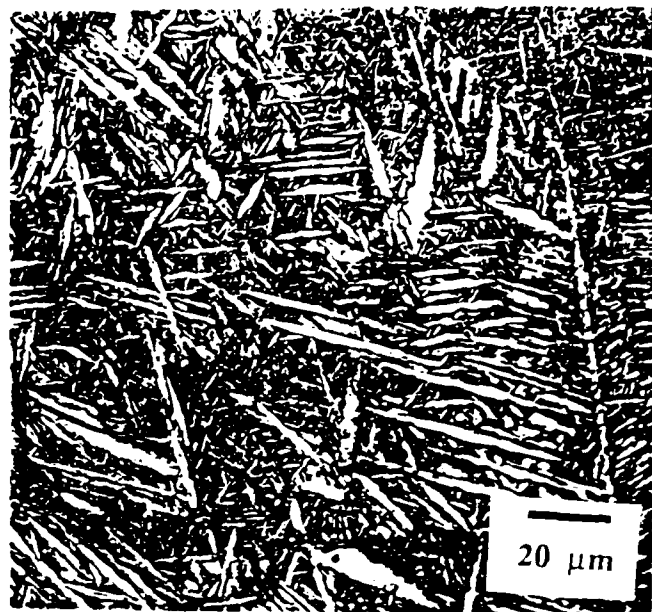
Al	Nb	Fe	O	N	Ti
13.5	21.0	0.037	0.058	0.003	bal (wt%)
23.85	10.8				(at%)

## Chemical Composition of of Ti-24-11 (cross-rolled plate)

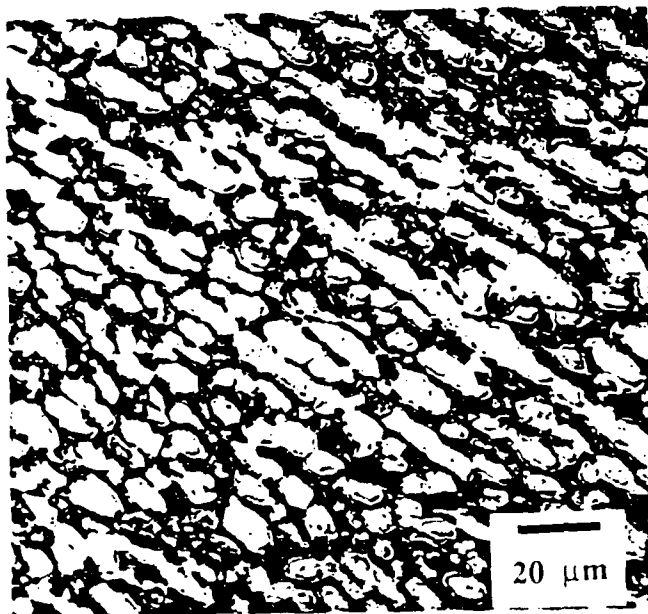
Al	Nb	Fe	O	N	C	H	Ti
14.0	20.6	0.08	0.054	-	0.01	$4.8 \times 10^{-5}$	bal (wt%)



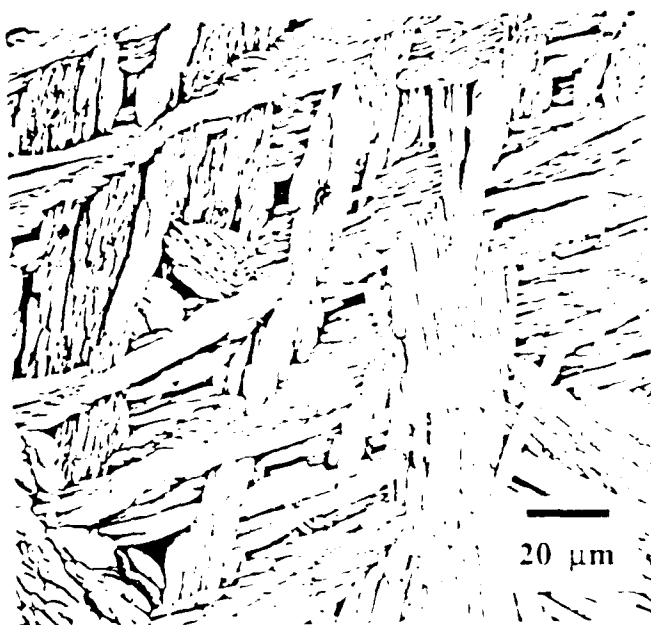
1200AC



1000AC-15



As Received



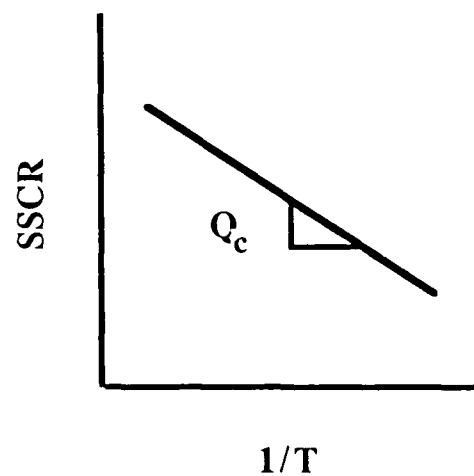
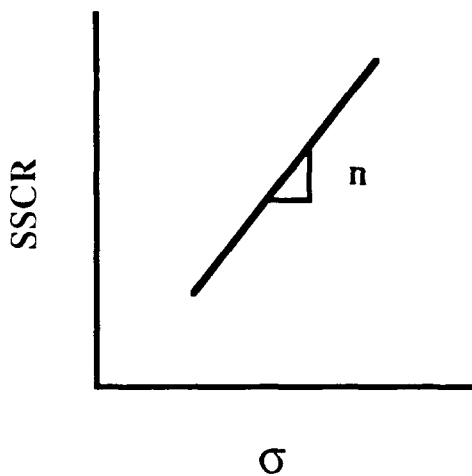
1000AC-30

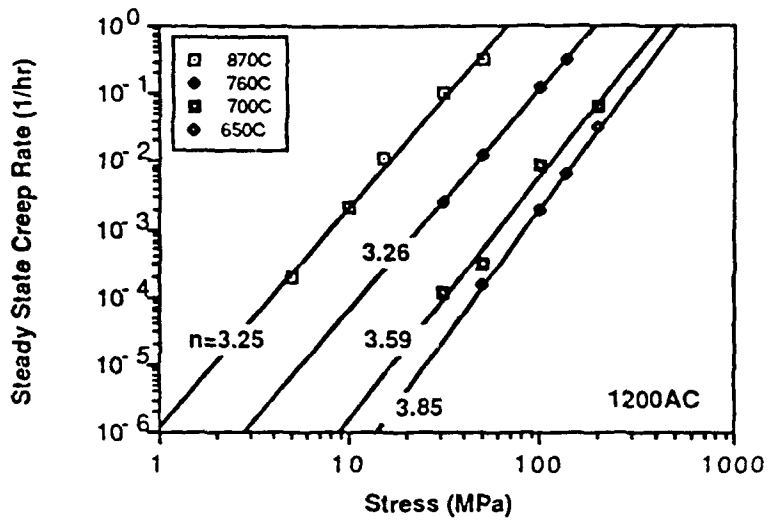
## POWER LAW CREEP

Steady state creep is described by an empirical power law relation

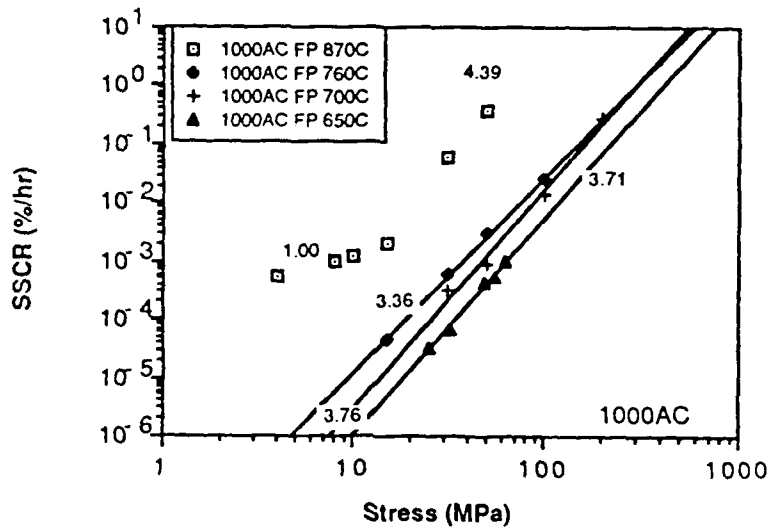
$$\dot{\epsilon}_s = A \left( \sigma / E \right)^n \exp \left( -Q_c / kT \right) \quad T > 0.5 T_m$$

$\dot{\epsilon}_s$ :	Steady-state creep rate	$n$ :	Power law exponent
$A$ :	Constant	$Q_c$ :	Creep activation energy
$\sigma$ :	Tensile stress	$k$ :	Boltzmann's constant
$E$ :	Elastic modulus	$T$ :	Temperature, K

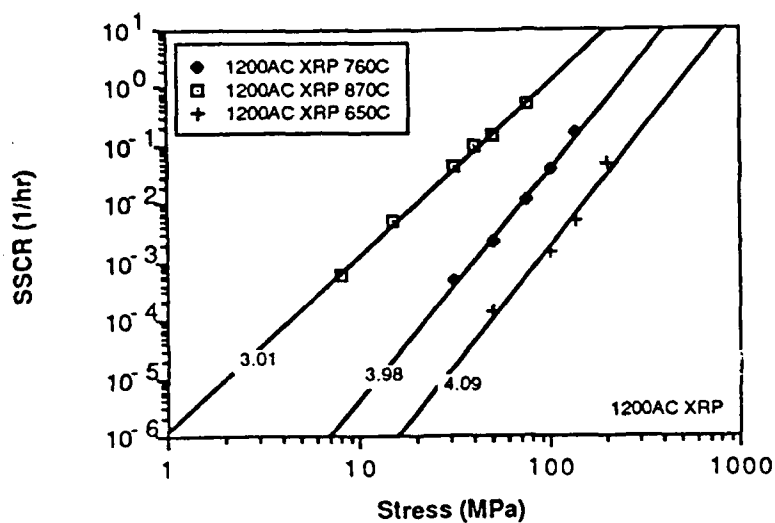




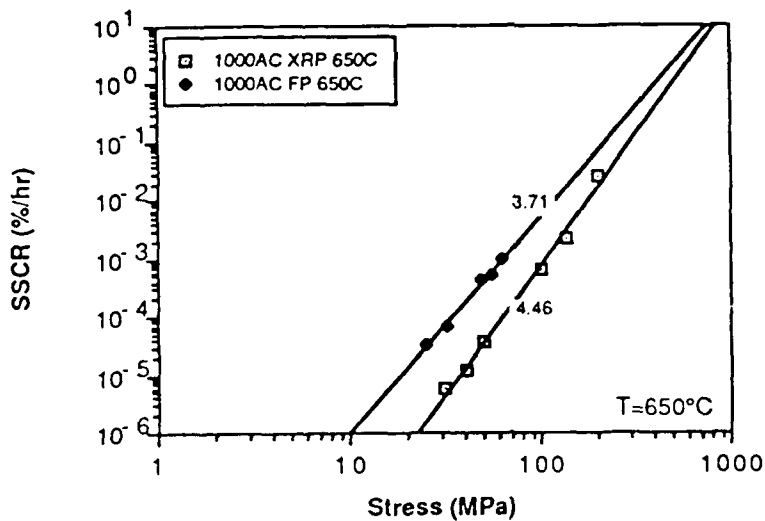
Steady state creep rate vs. stress of 1200AC specimens originating from forged pancake, tested at different temperatures.



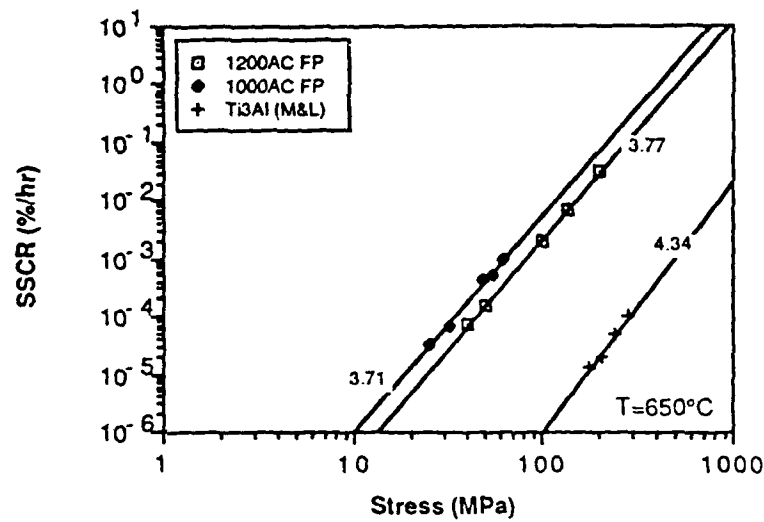
Steady state creep rate vs. stress of 1000AC specimens originating from forged pancake, tested at different temperatures.



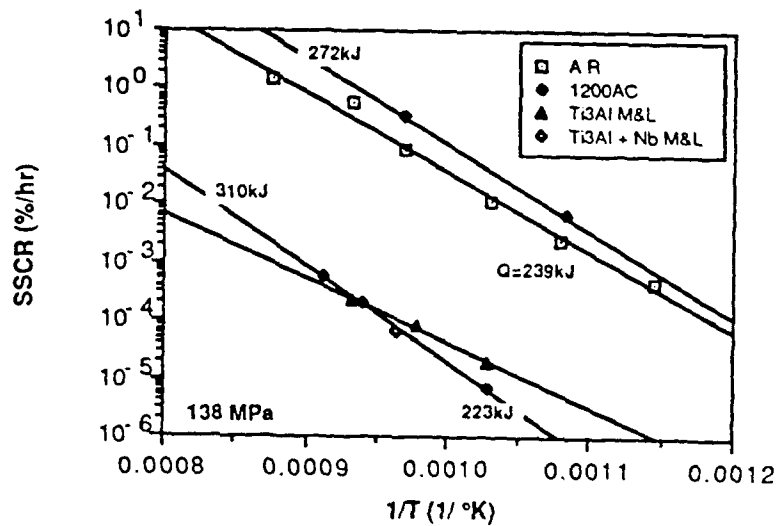
SSCR vs. stress for Ti-24-11, cross-rolled plate, 1200AC, 650°C, 760°C, and 870°C.



SSCR vs. stress for Ti-24-11, cross-rolled plate and forged pancake, 1000AC, 650°C.

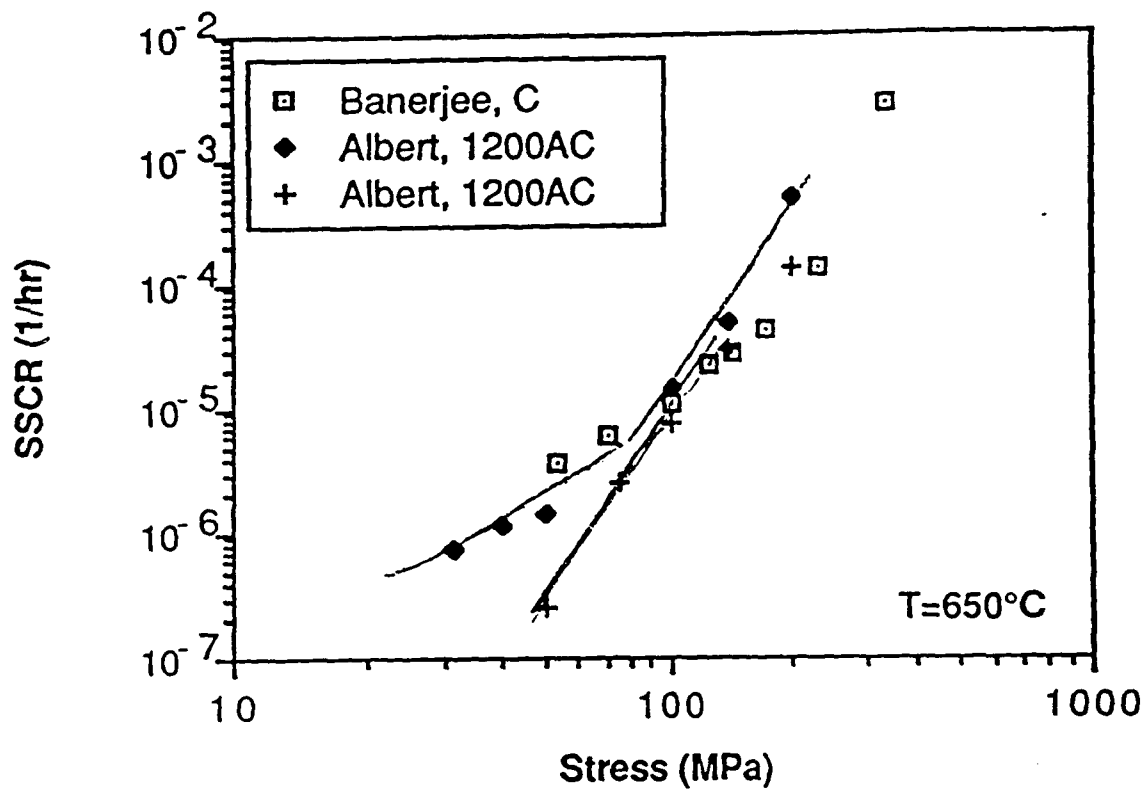


Steady-state creep rate vs. stress of specimens originating from forged pancake, tested at  $650^\circ\text{C}$ . Also shown for comparison is Mendiratta and Lipsitts' work on stoichiometric  $\text{Ti}_3\text{Al}$ ;



Activation energies for various titanium aluminides, 138 MPa.

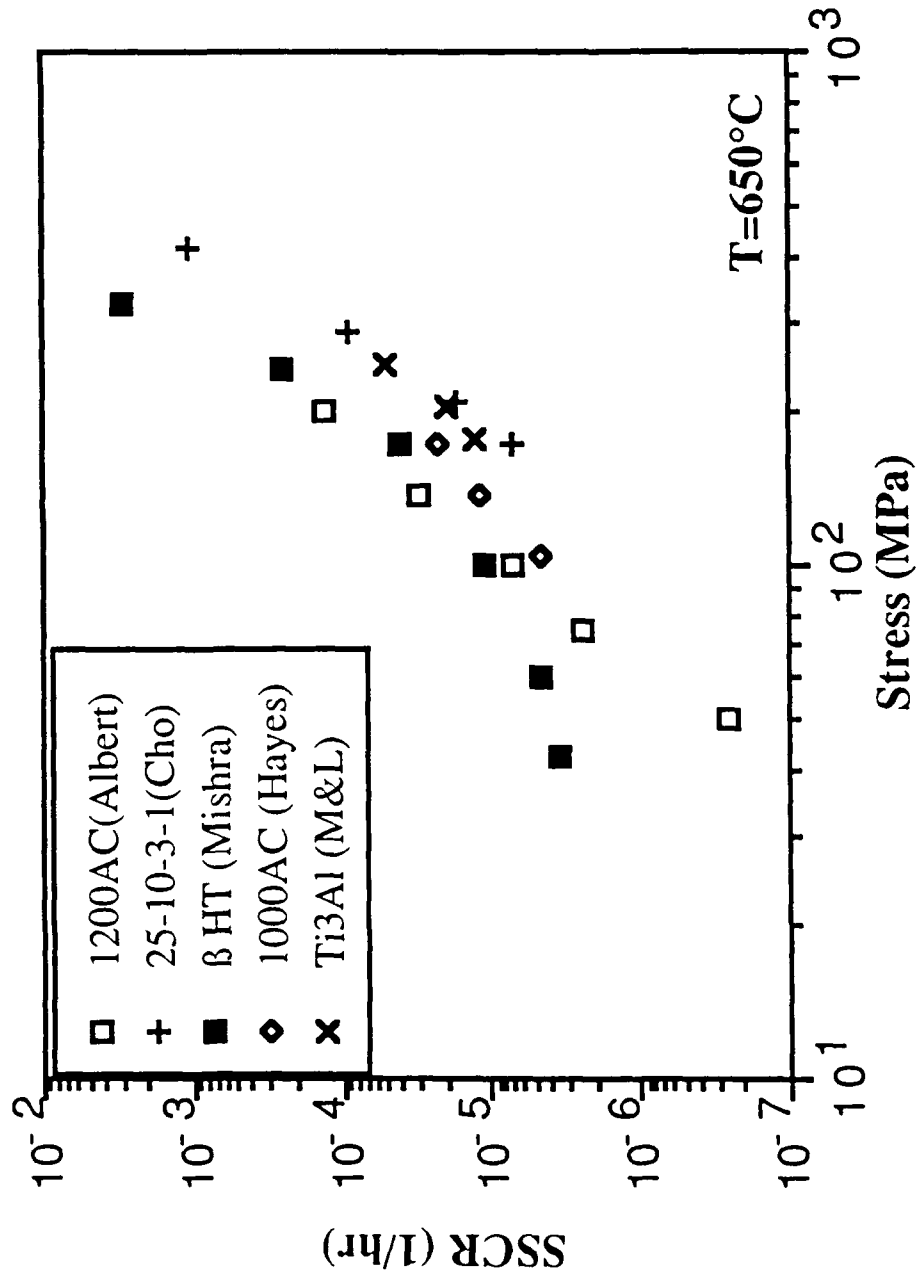




**Banerjee:** Condition C, 1150°C/ 4 hr/ argon quench + 850°C /24 hr/ air cool

**Microstructure:** 100% transformed  $\beta$

**Albert:** 1200AC XRP:  $\beta$  solutionized at 1200 °C for 1 hr then air cooled



## CONCLUSIONS

- Plate size (and thus slip length) does not control creep rate in all stress and temperature regimes investigated.
- Boundary sliding is the rate-controlling mechanism at low stresses and high temperatures.
- At high stresses, dislocation glide and climb processes dominate.
- Apparent creep activation energies at low stresses are approximately equal to diffusion activation energy in pure titanium.

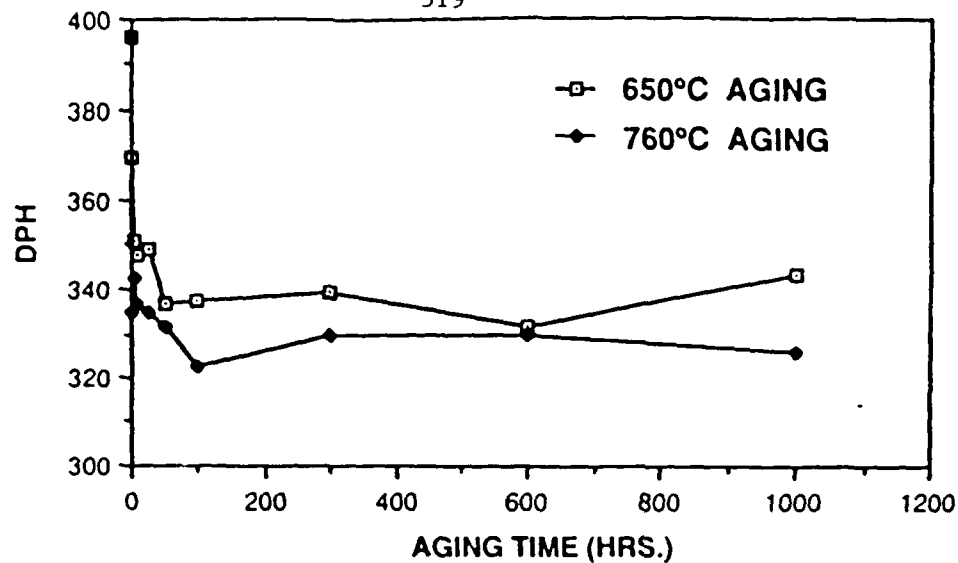
Ti-25 Al-10 Nb-3 V-1 Mo

Won-suk Cho

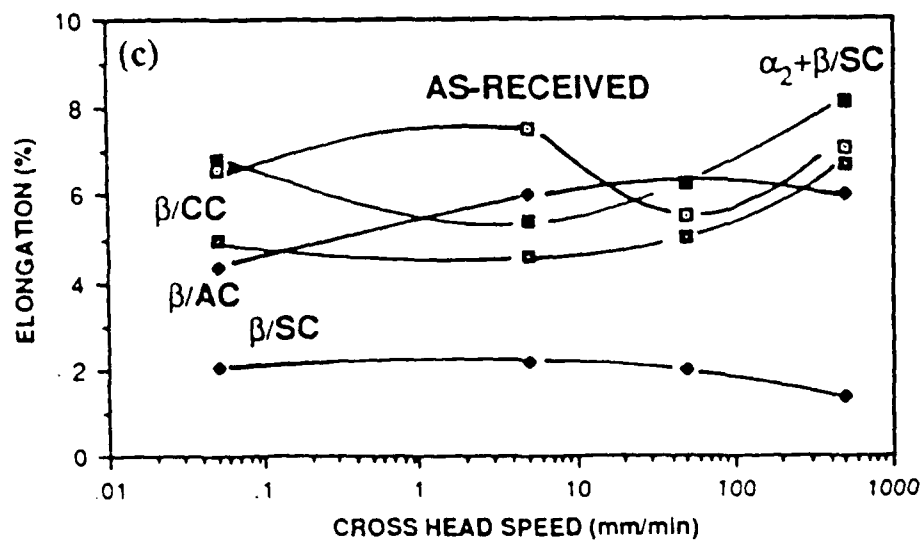
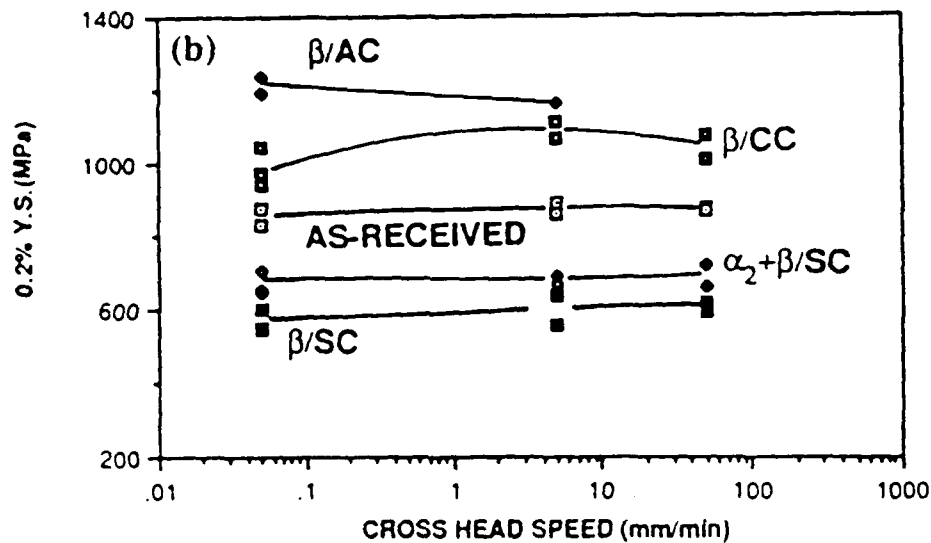
**Sponsored by URI through AFOSR**

METALLURGICAL TRANSACTIONS A

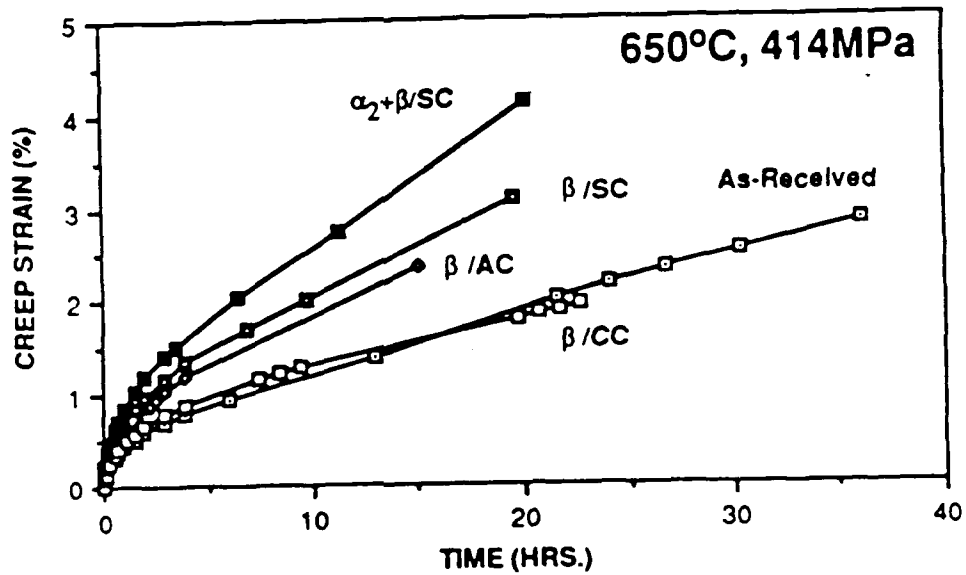
VOLUME 21A, MARCH 1990



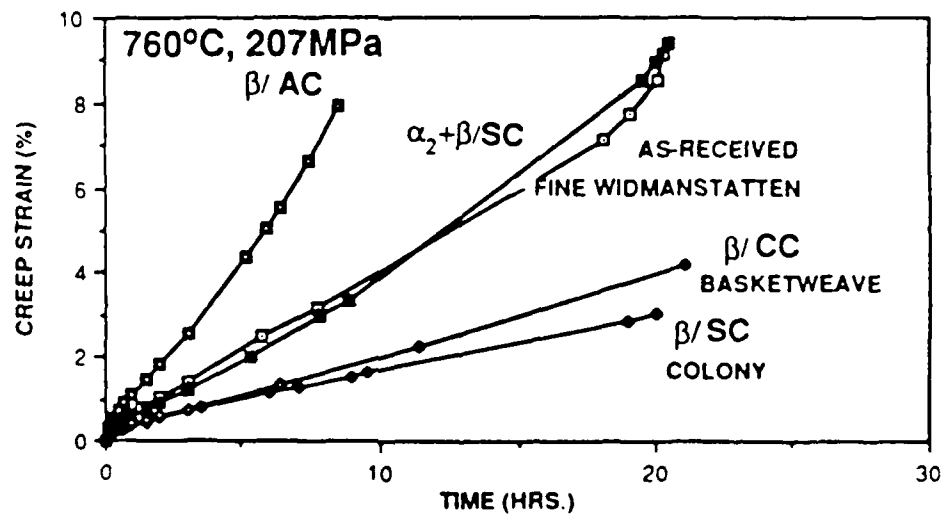
Influence of thermal exposure on room-temperature micro-hardness for the as-received microstructure (very fine Widmanstätten).



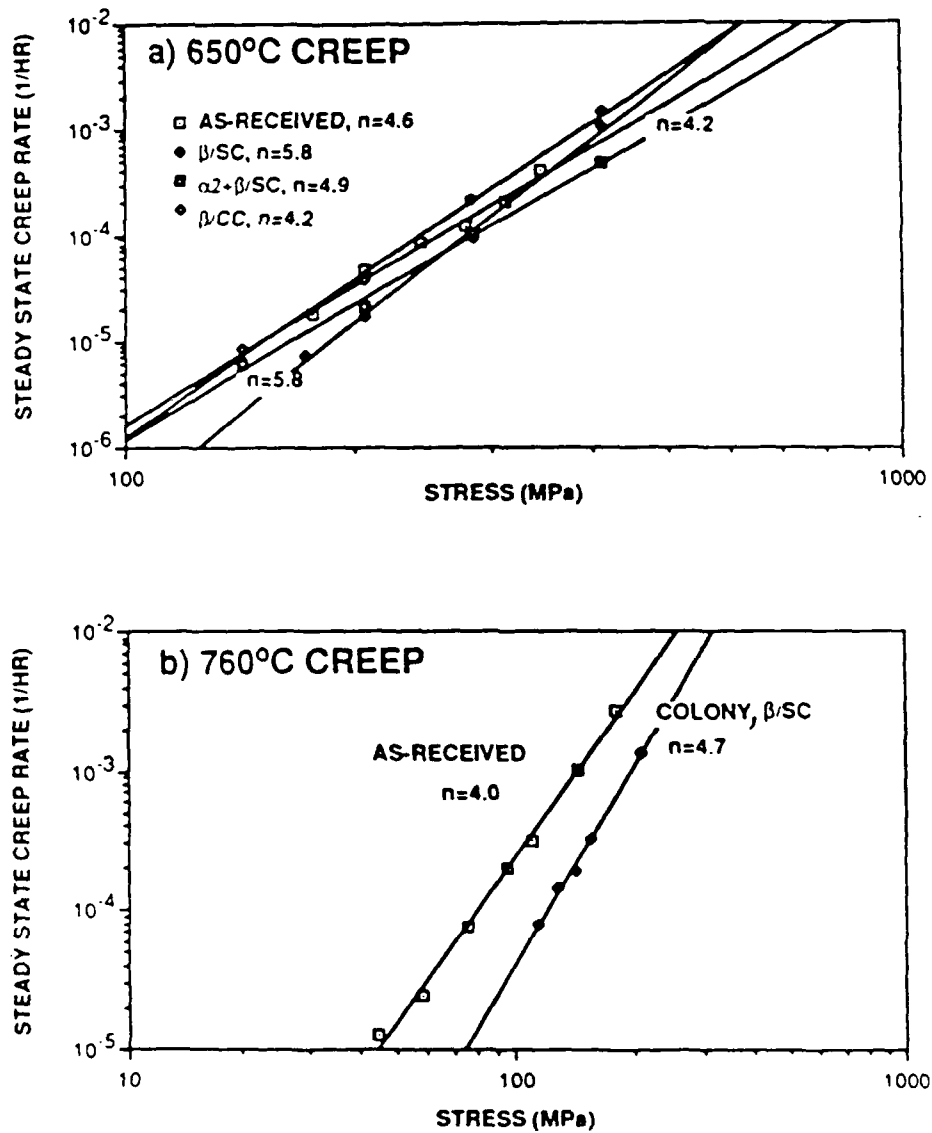
Effect of microstructure on room-temperature tensile properties:  
(b) 0.2 pct yield strength, and (c) elongation.



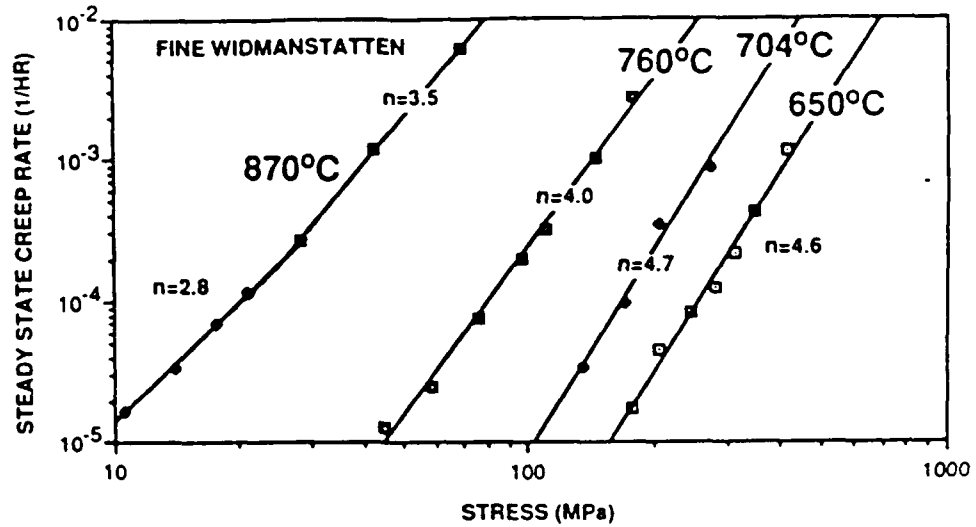
Effect of microstructure on creep behavior at 650 °C/ 414 MPa.



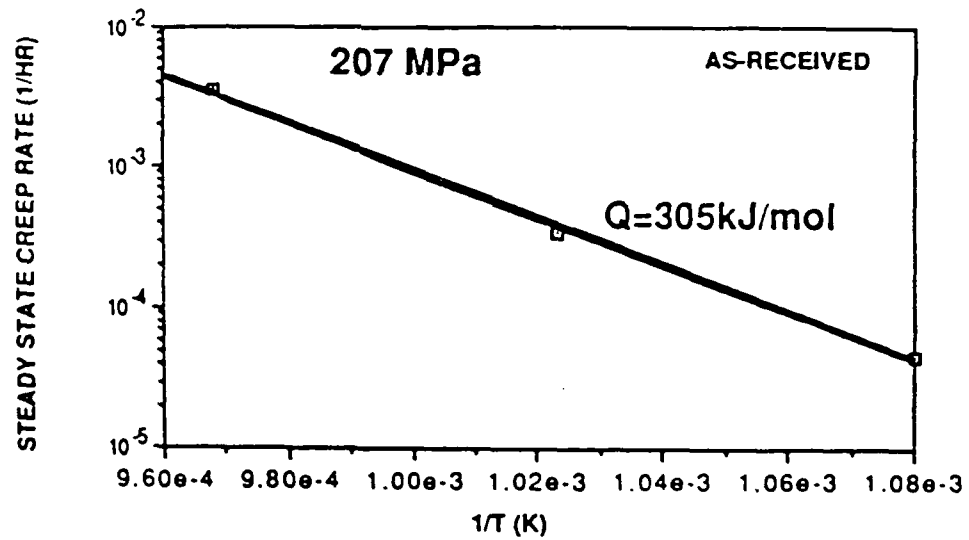
Effect of microstructure on creep behavior at 760 °C/ 207 MPa.



Stress dependence of steady-state creep rate for various microstructures: (a) at 650 °C and (b) at 760 °C.

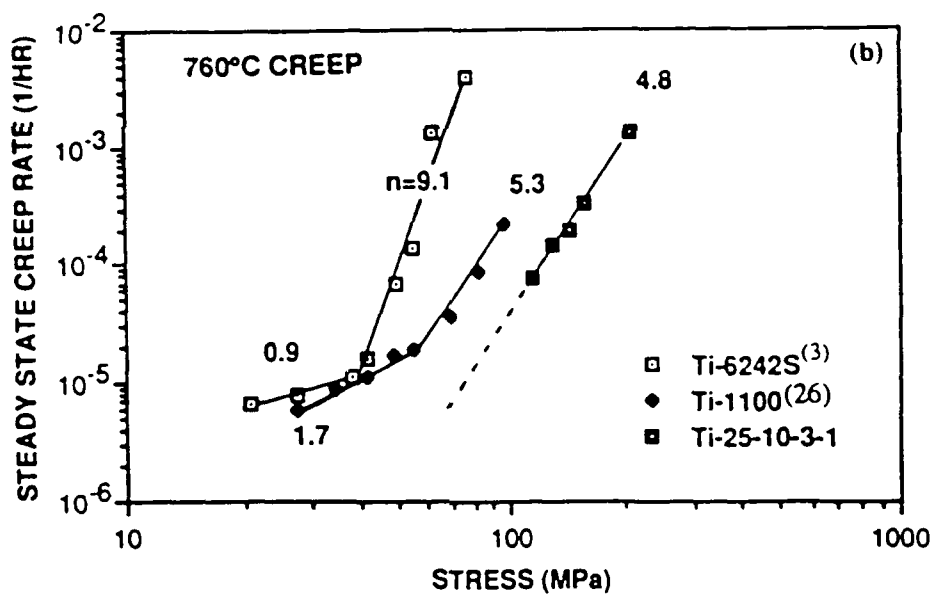
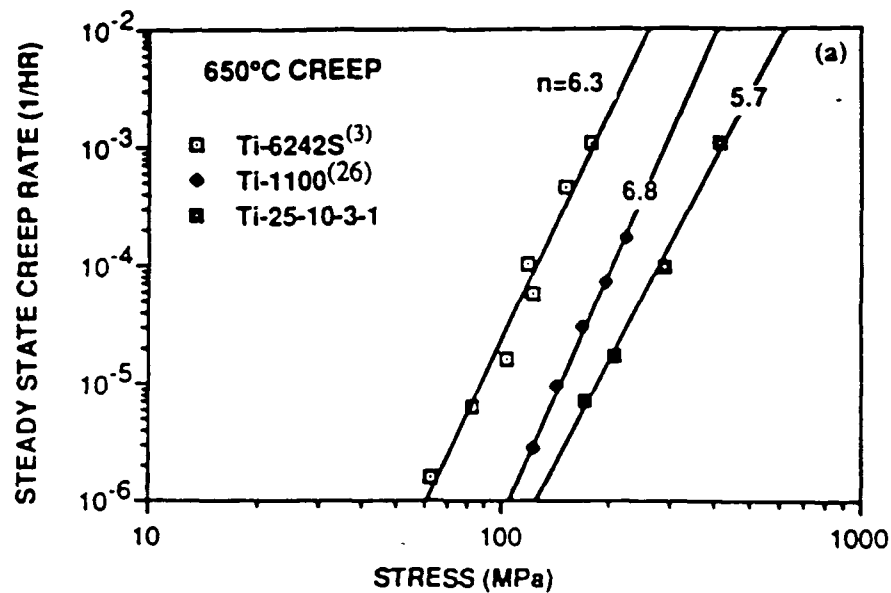


Stress dependence of steady-state creep rate of as-received microstructure as a function of temperature.



Temperature dependence of steady-state creep rate of as-received microstructure in the range of 650 °C to 760 °C.





A comparison of creep behavior of Ti-25-10-3-1 with two conventional near- $\alpha$  titanium alloys (Ti-6242S and Ti-1100), using colony microstructure: (a) 650 °C creep and (b) 760 °C creep.

BLANK

## TASK 6

### Fracture and History Effects in Composites

W.M. Garrison, Investigator

Task 6 of the URI on High-Temperature Metal Matrix Composites was entitled "Fracture and History Effects in Composites." Work on thermal and mechanical history effects was conducted on matrix materials for composites, in particular ternary titanium aluminide alloys of the Ti-Al-Nb system, including Ti-24 Al-11 Nb (atomic percentages), which are based on the compound  $Ti_3Al$ . A second study on a model metal-matrix composite, SiC-reinforced aluminum with two particle sizes and two volume fractions of SiC particles, was focused on fracture effects. Both projects were initiated by a Ph.D. student, D. Symons, and reports on each are appended.

	<u>Page</u>
"Thermal and Mechanical History Effects", W.M. Garrison and D. Symons	327
"Fracture Mechanisms of a SiC Particle Reinforced Aluminum Matrix Composite", D. Symons and W.M. Garrison	347

BLANK

## THERMAL AND MECHANICAL HISTORY EFFECTS

W. M. Garrison and D. Symons  
Dept. of Metallurgical Engineering and Materials Science  
Carnegie Mellon University  
Pittsburgh, PA 15213

### I. Introduction

An important factor in the design of materials for high temperature service is that their microstructures will not be altered during service in a manner which would impair their mechanical properties. It is possible that prolonged exposure at elevated temperatures during service could alter the microstructure in such a way as to degrade mechanical properties. Further, especially in the case of high temperature composite materials, there is the possibility that service stresses could enhance high temperature microstructural changes as well as introducing damage or defects during creep deformation of the material. The broad objectives of this program are to investigate how and to what extent service temperature and stresses degrade the microstructure, strength and fracture behavior of high temperature materials, particularly composites, and to model the observed fracture behavior in terms of the microstructures and the micromechanisms of the fracture process. In this summary the following topics will be considered. First, the materials selected and the rationale for their selection will be discussed. Second, we will discuss the fracture behavior of these materials and how various microstructural parameters may influence the fracture process. Next the importance of microstructural control in this work will be emphasized and studies designed to permit this microstructural control and perhaps to allow independent variation of the key microstructural variables will be discussed. Finally initial results concerning the effect of microstructure and test temperature on tensile properties and fracture mode will be presented as will be the effects of long time aging on strength and ductility.

## II. Materials Selection

The focus of this work will be monolithic titanium aluminides. The selection of compositions for study has been guided by a large body of information which suggests that both strength and tensile ductility of the  $Ti_3Al$  materials can be substantially improved by substituting niobium for the titanium. The data of Blackburn (1) shown in Table I shows that at 425°C the yield strength and tensile ductility of titanium aluminide air cooled from the solutionizing temperature increased from 69 ksi to 97 ksi and 1.4% to 8%, respectively, as the niobium content was increased from 11 to 15 atomic percent. According to our reading of the literature the beneficial effects of niobium on both strength and ductility are not understood. Accordingly we have prepared three heats of aluminide material: Ti-24Al-11Nb, Ti-24Al-15Nb and Ti-24Al-19Nb.

## III. Program Objectives

The specific objectives of this program are the following. They are first to understand how niobium additions influence the strength, tensile ductility and fracture toughness as a function of test temperature. Second they are to investigate the degree to which the initial microstructures and their associated mechanical properties are degraded by prolonged exposure to high temperatures and high temperatures in combination with high stresses.

## IV. Microstructure and Mechanical Properties

Niobium additions apparently can influence both the strength and the fracture behavior of  $Ti_3Al$  material (1-3). Niobium additions can unfortunately introduce a variety of microstructural changes which may influence the mechanical properties. Assuming for the present that the structure with or without the niobium is a Widmanstätten structure of  $\alpha_2$  plates formed by the transformation of the  $\beta$  during either isothermal or continuous transformation, the available phase diagrams (4,5) suggest niobium will lead to an increased amount of  $\beta$  in the structure, with the caveat that the  $\beta$  may become ordered (6). Further the niobium may also increase the amount of c+a slip in the  $\alpha_2$  (2). Finally the

niobium additions could possibly result in a finer  $\alpha_2$  plate size if a constant transformation path is used. (We suggest this possibility based on our results which suggest the  $\alpha_2$  plate size can significantly influence the yield strength at constant niobium level and the known influence of Nb on strength.)

While the effect of niobium on strength may be related to its effect on  $\alpha_2$  plate size it is possible that the improvement in tensile ductilities with increasing niobium content may be due to any (or possibly to some extent all) of the above possible microstructural changes. The titanium aluminides appear to fracture by a cleavage related process. Therefore niobium could possibly improve the ductility by increasing the amount of the second phase (presumed and likely to be ductile). It has also been suggested that increasing the niobium will increase the amount of c+a slip and this will result in greater uniformity of strain and an improvement in ductility. Finally the possible refinement of  $\alpha_2$  plate size by niobium additions could improve resistance to cleavage type fracture by increasing the cleavage fracture stress. Thus to understand how niobium additions alter fracture behavior it would be desirable to vary these microstructural variables, amount of second phase, degree of c+a slip and  $\alpha_2$  plate size independently. If this is to be done it is important to understand how niobium influences the transformation characteristics of the titanium aluminide.

## V. Microstructural Evolution

It is possible to vary the microstructures of the  $Ti_3Al$  type aluminides extensively by varying the solution treatment temperature and the temperature-time path used to cool from the solutionizing temperature. Our first instinct is to solutionize in the single phase  $\beta$  field and select the solutionizing temperature for each alloy so that the  $\beta$  grain size is a constant. Thus the microstructure will be varied by changing the cooling path from the solutionizing temperature. In selecting heat treatments for the alloys with the goal of varying microstructural parameters independently it is necessary to determine how various cooling

paths will influence the microstructure. Preliminary work of this type has been carried out for Ti-24Al-11Nb using a heat of the composition given in Table 2.

In this work the alloy was solution treated for 45 minutes at 1200°C and then transformed isothermally or by continuous cooling. The isothermal transformation temperatures investigated were 700°C and 400°C, both as a function of time. The continuous cooling was done by an air cool and a control cool which was ten times slower than the air cool. As shown in Fig. 1, for the 700°C isothermal the isothermal transformations were extremely rapid and are almost 50% complete after one minute. As shown in Figure 2, lowering the isothermal transformation from 700°C to 400°C led to marked refinement of the microstructure. For both transformation temperatures the microstructure was a Widmanstatten structure of  $\alpha_2$  plates. Air cooling produced a Widmanstatten microstructure almost identical to the microstructure after isothermally transforming at 700°C. The slower control cool resulted in a colony microstructure as shown in Fig. 2.

## VI. Mechanical Properties

The room temperature tensile properties of the microstructures associated with the two continuous cooling paths and the 700°C (20 min.) and 400°C (20 min.) isothermal transformations are listed in Table 3. The 400°C isothermally transformed material has the highest yield strength, 138 ksi, which is 52 ksi greater than the yield strength of the 700°C isothermally transformed material. This higher strength of the 400°C isothermally transformed material is coincident with a dramatic reduction in  $\alpha_2$  plate size. The material transformed during air cooling has almost the same microstructure as the 700°C isothermal and almost the same yield strength. The control cool and the as-received material, both of which have colony type microstructures, have the lowest yield strengths. In addition to the tensile properties the cleavage fracture stress has been measured for the above microstructures except for the as-received material. The fracture stress was taken as the maximum tensile stress at fracture of a single edge notch bend specimen containing a notch



of the geometry used in Charpy impact specimens. These stresses are listed in Table 3. The fracture stress is lowest for the 700°C isothermal (141 ksi) and highest for the 400°C isothermal (338 ksi). Although the 700°C isothermal and the air cool microstructures appear very similar and have similar yield strengths, the fracture stress of the air cool microstructure is higher (217 ksi).

A fracture surface of the as-received microstructure is shown in Fig. 3. The fracture is cleavage or quasi-cleavage through the  $\alpha_2$  grains. Plateau etching suggests a second phase between the  $\alpha_2$  grains. The fracture surfaces of the control cool are very similar; as shown in Fig. 4. The cleavage facets are often relatively smooth and through steps join together to form relatively large regions where the fracture appears to follow the same crystallographic planes. The fracture surface of the air cool structure is much rougher as shown in Fig. 5 and as shown in Fig. 6, the fracture surfaces of the air cool and 700°C isothermal are very similar. The fracture surface of the 400°C isothermal is shown in Fig. 7 and exhibits only rarely large facets which can be unambiguously identified with cleavage or quasi-cleavage.

The tensile properties have been measured as a function of room temperature for the fine Widmanstätten microstructure shown in Fig. 2d. These tests differed from the previous tensile tests in that the specimen diameters were smaller by a factor of two (0.25 inches vs. 0.125 inches). The room temperature yield strength was 141 ksi, agreeing with the previously measured 138 ksi. Testing at 300°C and 500°C decreased the yield strength from 141 ksi to 128 and 115 ksi respectively. The fracture stress coincided with the yield strength at room temperature, but decreased only slightly with increasing test temperature. The ductility as measured by percent elongation increased from 0.18% at room temperature to 0.5% and 1.9% at 300°C and 500°C respectively. The percent elongation at room temperature was less than obtained with the larger specimens (1.6%). In addition, regions of ductile fracture were observed at all three test temperatures (Figs. 8-10) with the average

void sizes increasing with test temperature (Table IV) and the area associated with ductile fracture also increasing with test temperature.

## VII. Microstructural coarsening

Specimens of the fine Widmanstatten material were aged at 700°C for 316 hours. The microstructure was substantially coarsened by this aging treatment and room temperature yield strength was only 62 ksi compared to 138 ksi prior to the long time age at 700°C. These results suggest that the Widmanstatten microstructures can coarsen readily with a resulting impairment of mechanical properties.

## VIII. Summary

Isothermal transformations of a 24Al-11Nb alloy have been studied as a function of time at transformation temperatures of 700°C and 400°C and the resulting microstructures and properties compared to those after continuous cooling. Isothermal transformation of the  $\beta$  begin at very short times and transformation kinetics are very sensitive to the rate of cooling from the solution temperature. Isothermal transformation at 700°C results in a Widmanstatten microstructure similar to that obtained after an air cool; however, the ductility of the isothermally transformed microstructure is less than that of the air cooled microstructure. Isothermal transformation at 400°C results in a very fine Widmanstatten microstructure which, at room temperature, has a yield strength of 138 ksi, considerably higher than obtained after air cooling or an isothermal transformation at 700°C. This fine Widmanstatten structure maintains a yield strength of 115 ksi at a test temperature of 500°C, but this structure coarsens after a hold at 700°C for 316 hours and the room temperature yield strength after this coarsening treatment is 62 ksi.

### References

1. M.J. Blackburn and M.P. Smith, "Research to Conduct an Exploratory, Experimental and Analytical Investigation of Alloys", AFML-TR-80-4175, Aug. 1980.
2. S.M.L. Sastry and H.A. Lipsitt, *Met. Trans. A*, 1977, Vol. 8A, 1543.
3. C.F. Yolton, T. Lizzi, V.K. Chandok and J.H. Moll, *Titanium-Rapid Solidification Technology*, ed. by F.H. Froes and D. Eylon, TMS-AIME, Warrendale, PA, 1986, pg. 263.
4. O.N. Andreyev, *Russian Metallurgy*, 1970, Vol. 2, 127.
5. T.T. Nartova and G.G. Sopochnik, *Russian Metallurgy*, 1970, Vol. 2, 138.
6. D. Banerjee, A.K. Gogia, T.K. Nandi and V.A. Joshi, *Acta Met.*,

**Table I**

Influence of Nb Additions on the Tensile Properties  
for  $\beta$  Solutionized and Air Cooled Material Tested at 425°C<sup>(1)</sup>

Nb (At%)	Yield Strength (ksi)	Elongation (%)
0	68.8	1.4
11	76	6.5
15	97	8

**Table II**

Chemistry of Ti-24Al-11Nb Alloy Used In Preliminary Studies (at%)

<u>Ti</u>	<u>Al</u>	<u>Nb</u>	<u>C</u>	<u>O</u>	<u>H</u>
Bal.	25	11.1	0.17	0.18	0.34

**Table III**  
 Influence of Microstructure on the Room Temperature Tensile and  
 Single Edge Notch Bend Properties of Ti-24Al-11Nb

Heat Treatment	Microstructure	Yield Strength (ksi)	Elongation (%)	SENB $\sigma_f$ (ksi)
400°C Iso.	Fine Widmanstätten	138	1.6	338
700°C Iso.	Coarse Widmanstätten	87	1.4	141
Air Cool	Coarse Widmanstätten	92	3.0	217
Control Cool	Colony	67	0.8	156
As Received	Colony	78	1.4	-

**Table IV**  
Influence of Test Temperature on the Tensile Properties of the  
Fine Widmanstätten Microstructure

Test Temperature	Yield Strength (ksi)	Fracture Stress (ksi)	Elongation (%)	Dimple Diameter ( $\mu\text{m}$ )
R.T.	141	141	0.18	0.71
300°C	128	140	0.5	1.16
500°C	115	137	1.9	1.4



**a**



**b**



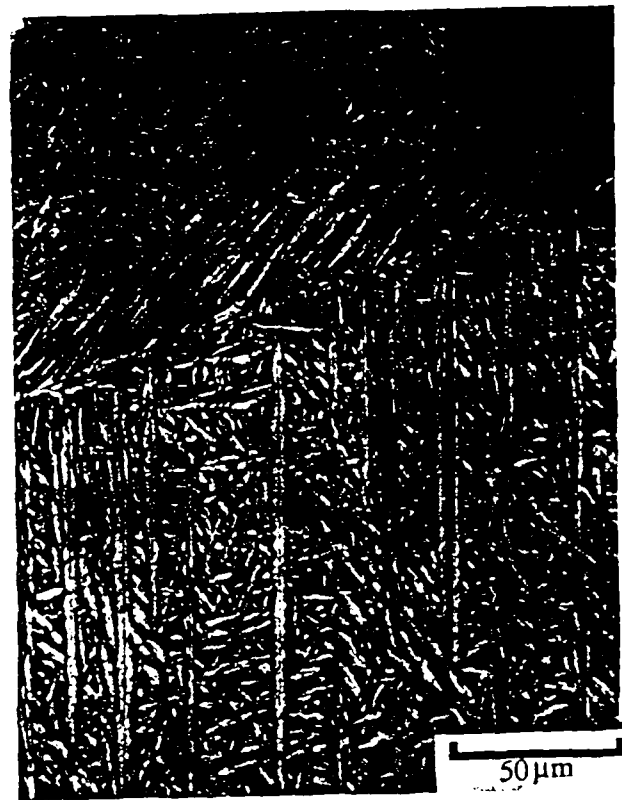
**c**



**d**



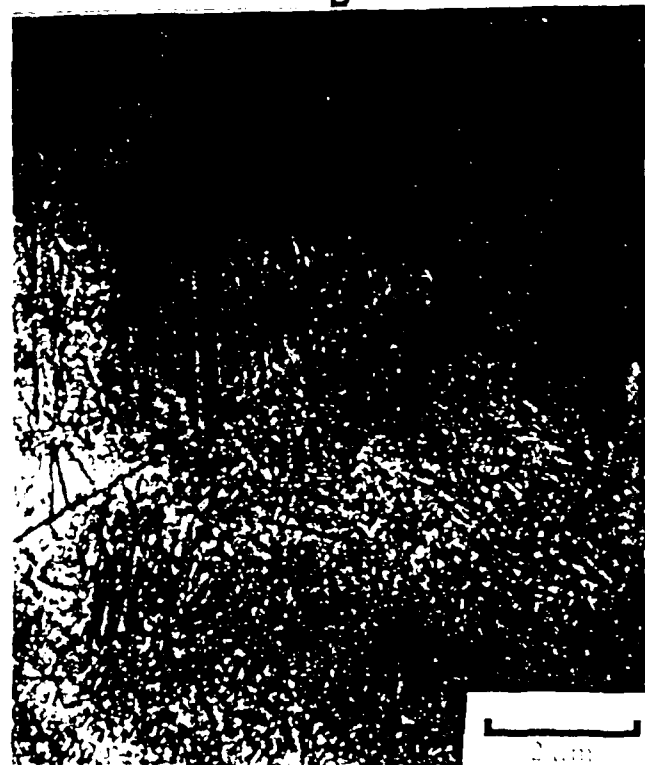
A



B



C



D

Fig. 2. Microstructures obtained by (a) control cool, (b) air cool, (c) isothermally transformation for 20 min. at 700°C and (d) isothermally transformation for 20 min. at 400°C.



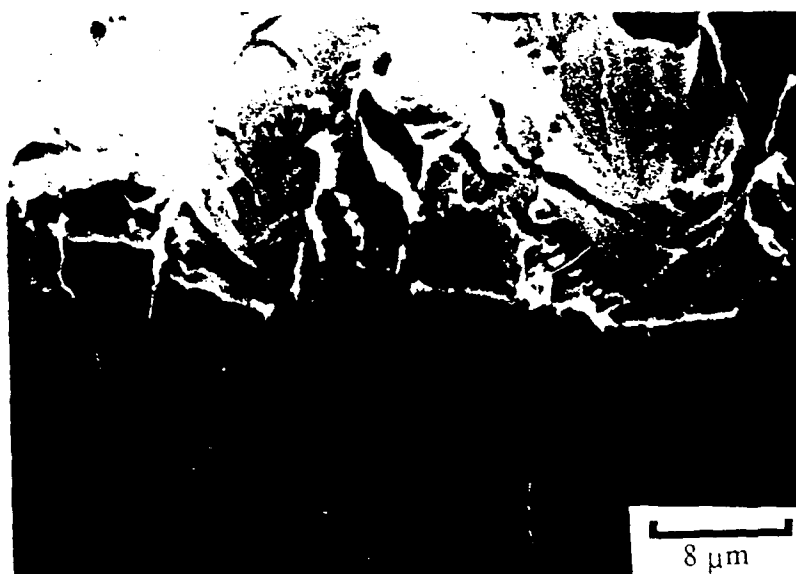
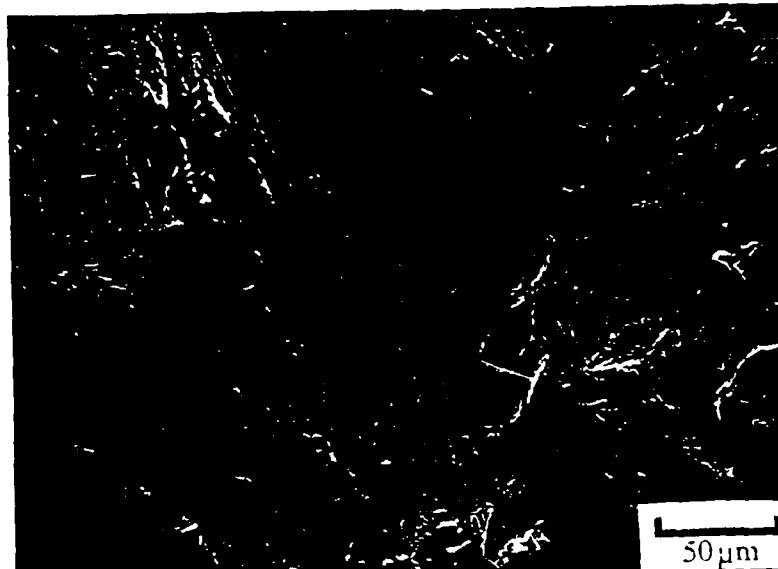


Fig. 3      *Fracture surface as as-received material which has been plateau etched.*

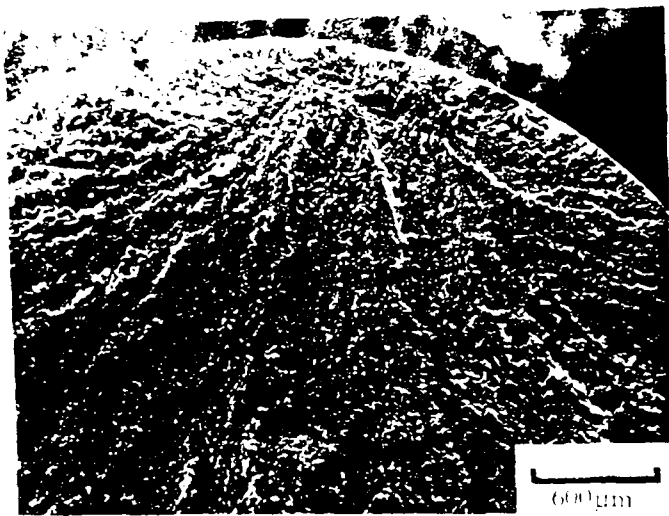


A



B

Fig. 4 Fractographs of the control-cool microstructure showing (a) the fracture surface and (b) a plateau etch.



A



B



C

Fig. 5 Fractographs of the air cooled material are shown in (a) and (b). A plateau *etch* is shown in (c).

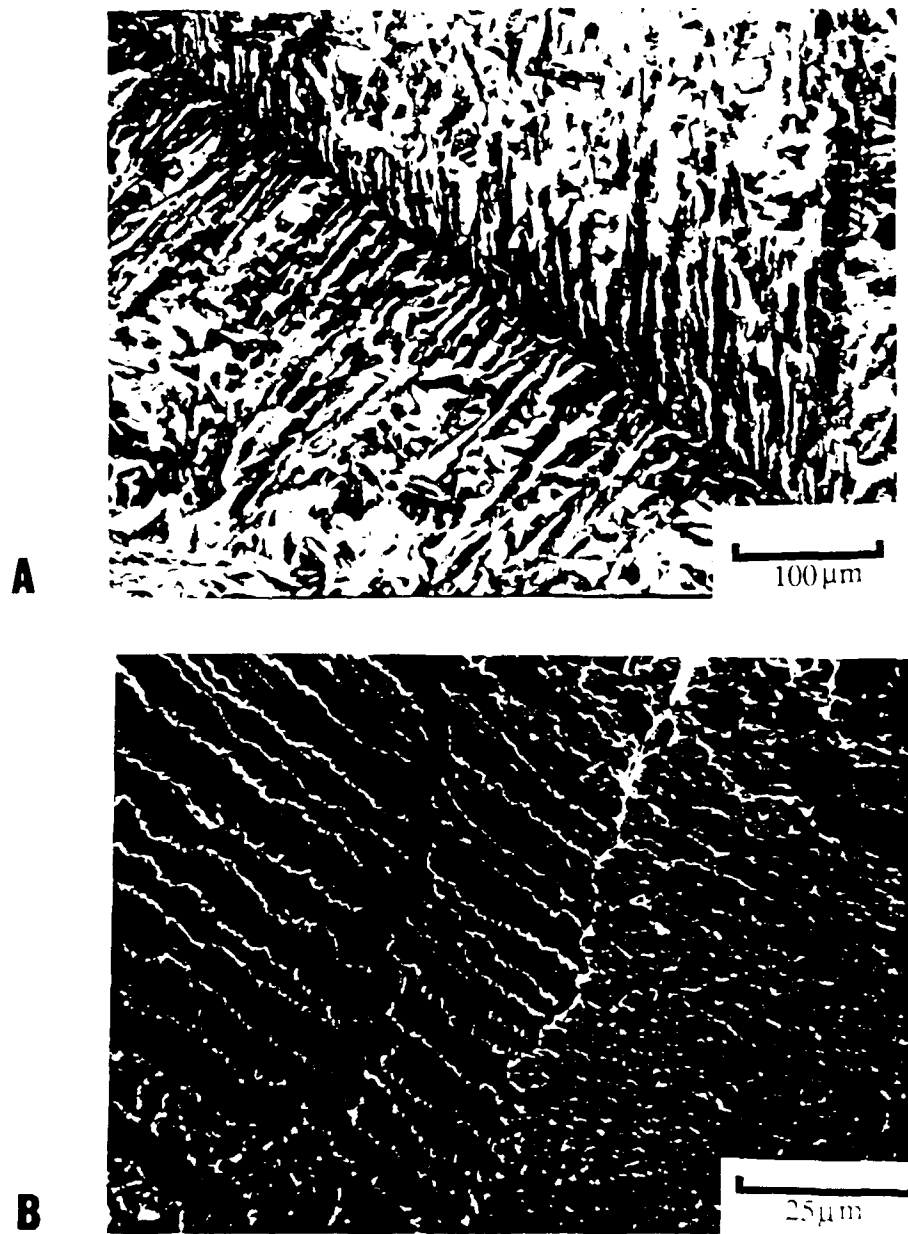


Fig. 6 Comparison of fracture surfaces of (a) the 700°C isothermal microstructure and of (b) the air cooled microstructure.



Fig. 7 Fractographs of the 400°C isothermal microstructure showing (a) a fracture surface and (b) a plateau etch.

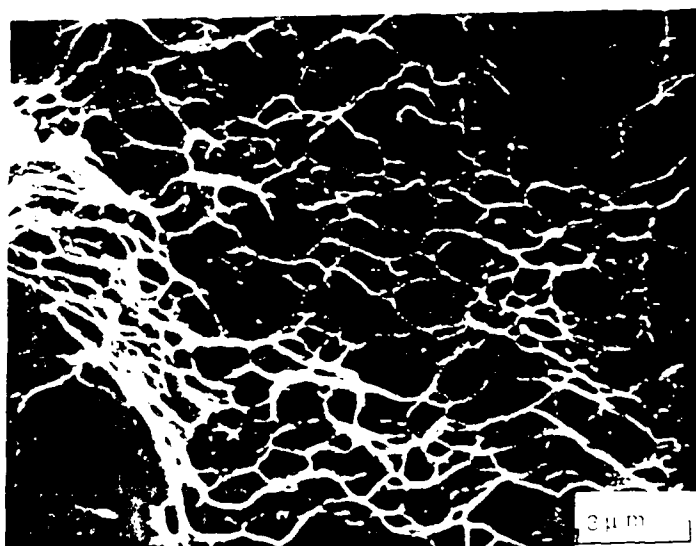
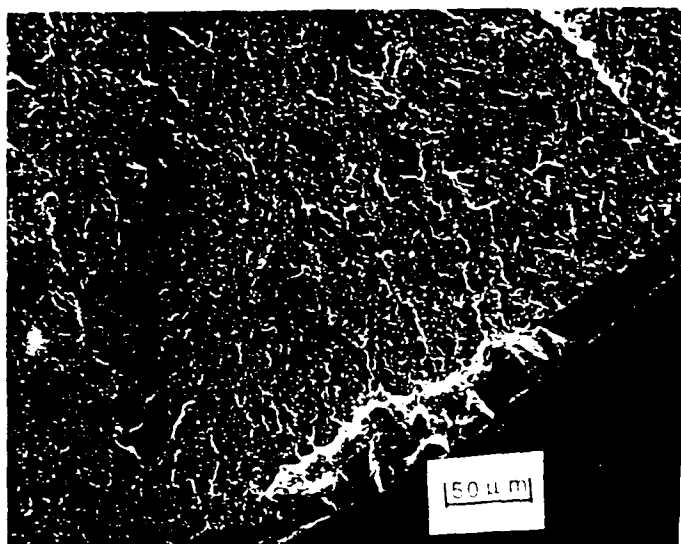
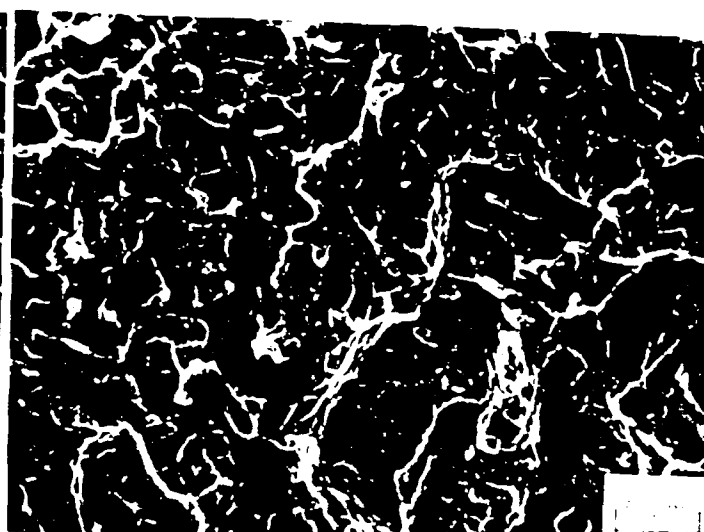
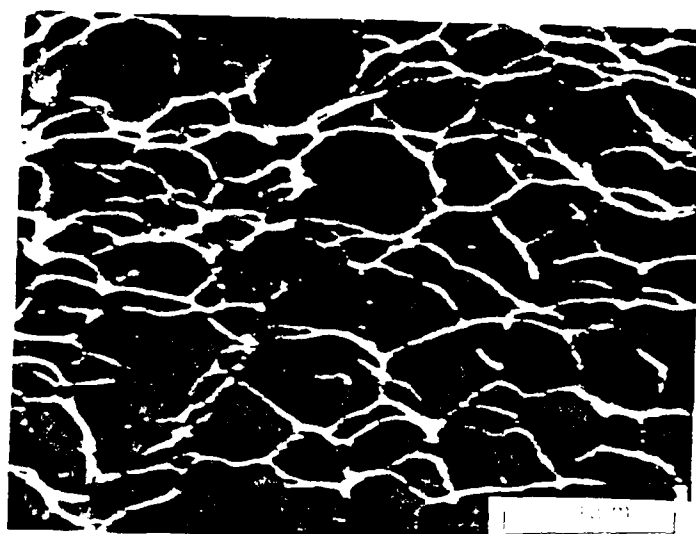
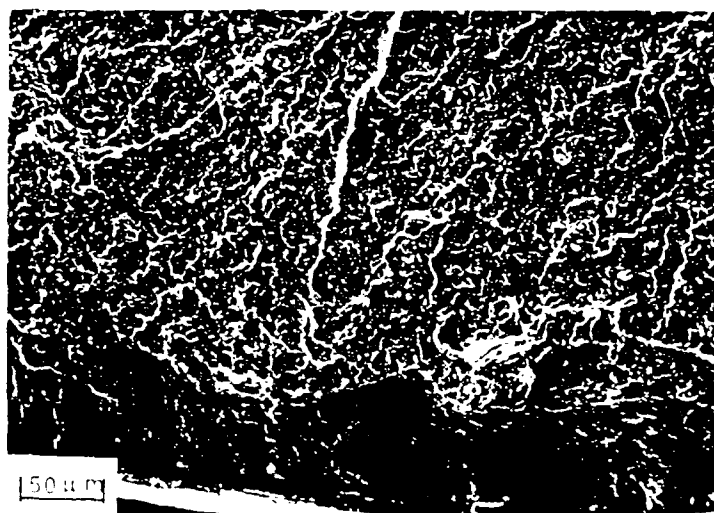
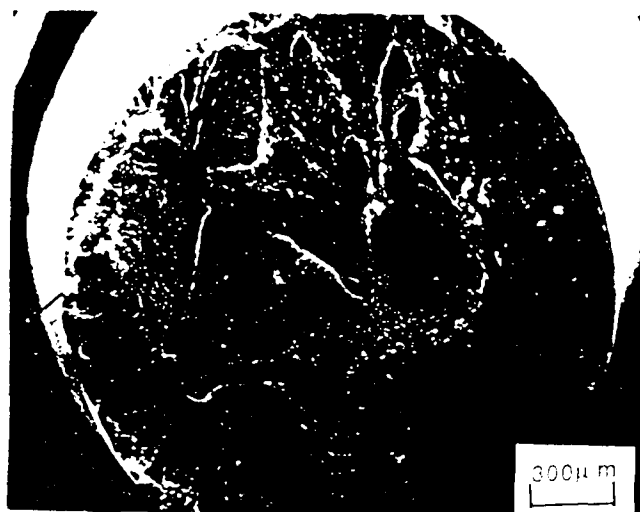


Fig. 8. Fractographs of the fine Widmanstätten structure material tested at room temperature.



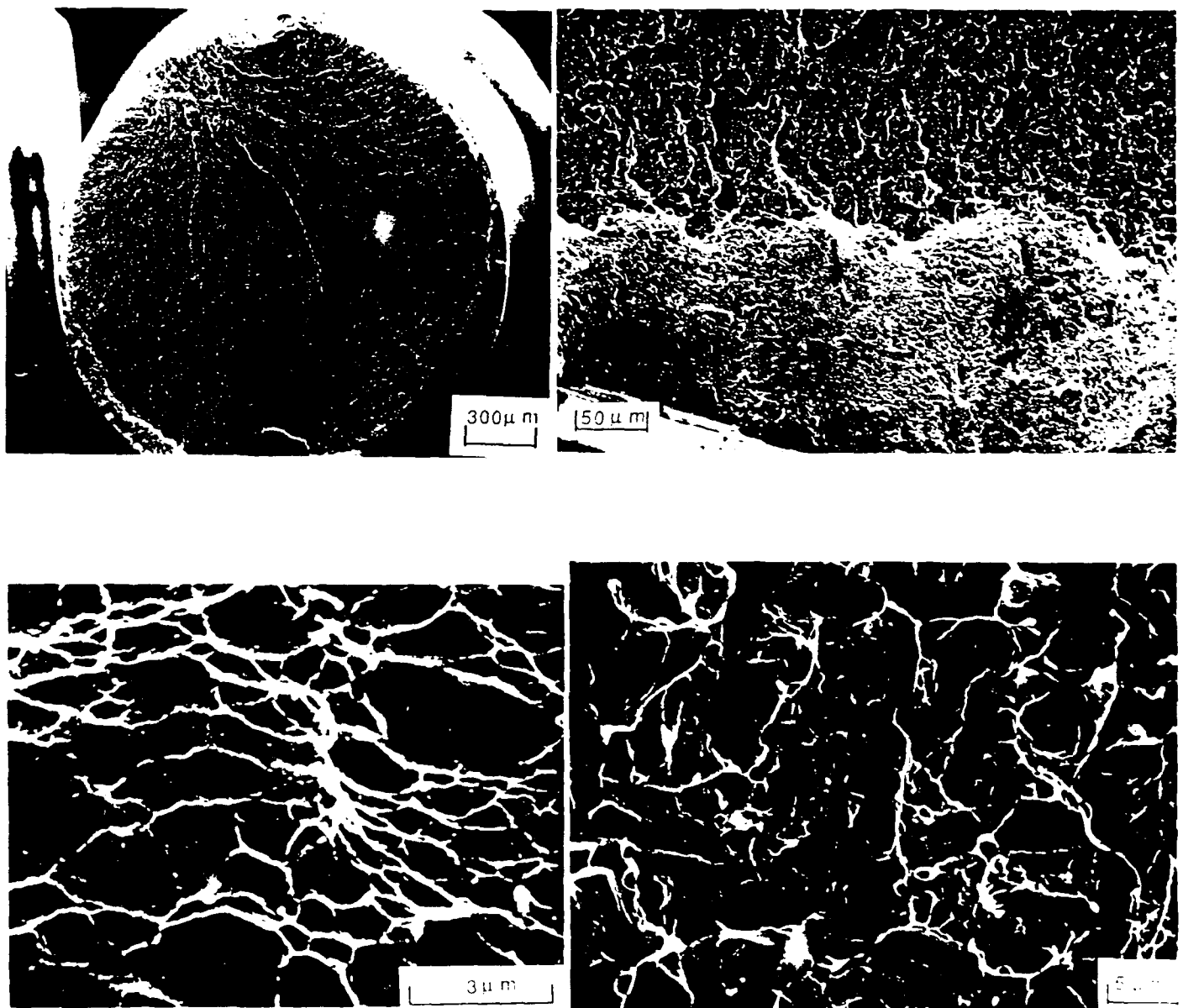


Fig. 10. Polyethylene-Wulman-tartrate structure material,  $\times 1500$ .



## **FRACTURE MECHANISMS OF A SiC PARTICLE REINFORCED ALUMINIUM MATRIX COMPOSITE**

**D. Symons  
W. M. Garrison, Jr.**

Department of Metallurgical Engineering and Materials Science  
Carnegie Mellon University  
Pittsburgh, PA 15213

### **I. INTRODUCTION**

High volume fractions of second phase particles or fibers are increasingly being used to alter the properties of metallic materials, such as increasing the modulus [1-3]. However, the use of particles or fibers to reinforce a metal matrix normally results in a material whose toughness and ductility are markedly inferior to those of the monolithic matrix alloy. For example, introducing 20 vol.% SiC particles into an aluminum alloy matrix can reduce the tensile reduction in area from 50% for the monolithic matrix to less than 10% for the composite. These severe losses in ductility are not unexpected based on the work of Baldwin [4] and others [5] which have shown that measures of ductility decrease rapidly with the volume fraction of equiaxed pores and second phase particles weakly bonded to the matrix.

However, it may be inappropriate to regard the fracture of particle reinforced composites as a simple extension of the processes normally envisioned in ductile fracture. According to this conventional picture the fracture of aluminum SiC particle composites would begin with either fracture of the SiC particles or decohesion of the SiC particle-matrix interface. Thus by one of these two mechanisms voids are initiated at the SiC particles and fracture occurs by a coalescence mechanism in which the voids initiated at the particles either grow to impingement or there is fracture of the matrix material between these voids. Indeed, most fractographs of SiC particle reinforced aluminum composites appear consistent with this image. However, if void nucleation at SiC particles does occur,

it is not clear if the decohesion is precisely at the SiC particle-matrix interface. EDS of unfractured SiC particles on fracture surfaces have shown the surface can be essentially aluminum [6]. This suggests decohesion occurs in the matrix, close to, but not at the particle matrix interface. Further, You *et al.* [7] observed primarily fractured SiC particles on the fracture surface; but they suggested that for their material, fracture of the matrix actually preceded fracture of the SiC particles.

The purpose of this work has been to investigate the micromechanisms of fracture of SiC particle reinforced aluminum alloy matrix composites. The primary emphasis has been on where fracture initiates, whether in the system investigated matrix fracture precedes void nucleation at the SiC particles and, if particle-matrix decohesion is observed, does it occur in a manner consistent with our conventional picture of void initiation by particle-matrix decohesion.

## II. MATERIALS PROCESSING AND CHARACTERIZATION

The materials investigated were produced by a powder process. The matrix alloy composition was 7 wt% Zn, 2 wt% Mg, 2 wt% Cu and 0.14 wt% Zr with balance aluminium. The reinforced materials contained SiC particles of two average sizes (average diameters of 7  $\mu\text{m}$  and 16  $\mu\text{m}$ ) at volume fractions of 15% and 20%. The average size of the powder of the matrix alloy was about 23  $\mu\text{m}$ . Thus there were five materials, a control containing no SiC and four reinforced materials.

After blending, the powders were cold compacted to approximately 75%-80% of theoretical density and subsequently degassed and vacuum hot pressed to near (*i.e.*, 99%) theoretical density. All of the compaction processes were carried out at temperatures below the solidus temperature of the matrix. The billets were subsequently fabricated by direct extrusion to a rectangular bar of cross section 25.5 mm x 76.2 mm at an extrusion ratio of 21:1. Samples from as-extruded materials were subsequently solution heat treated at 526 C for 1.5 hrs and then water quenched. Samples were held in liquid nitrogen until they were

aged. All material discussed here was aged at 160 C for 8 hours. This corresponds to the peak hardness at this aging temperature.

Electron and light microscopy were used to characterize the microstructure. The grain structures of the control material and of the reinforced materials are very similar as seen in Figures 1 and 2. The control and reinforced alloys showed the grains to be equiaxed in the transverse direction. In metallographic sections of the longitudinal (extrusion) direction the grains were slightly elongated in the longitudinal direction, and aligned so that many grains share a common interface parallel to the extrusion direction. In the reinforced materials there are regions that are free of particles and other areas that are banded with a higher than average volume fraction of particles: these may be seen in Fig. 1b, a micrograph of the longitudinal section of a reinforced alloy. Inclusions are also present in these materials, ranging in size from 10 to 30  $\mu\text{m}$ ; a typical inclusion is seen in Fig. 3. Transmission electron microscopy revealed fine precipitates in the matrix with larger precipitates on the grain boundary and a precipitate free zone surrounding the grain boundary (Fig. 4). Also in this figure dispersoids are seen to be present along the grain boundary.

### III. MECHANICAL TEST SPECIMENS

Four different test methods were employed in studying the mechanisms of fracture of these materials. They were smooth axisymmetric tensile specimens, double notched axisymmetric tensile specimens, notched flat tensile specimens used to examine the fracture process directly in the scanning microscope and double notch bend specimens.

The axisymmetric tensile specimens had a gage length of 1 inch and a gage diameter of 0.25 inches. The initial strain rate was 0.008 in/min. Specimens oriented both parallel and transverse to the extrusion direction were employed.

The double notched tensile specimens were of the same geometry as the axisymmetric tensile samples prior to the machining notches. These specimens were oriented with the gage length perpendicular to the extrusion direction. The notch centers

were equally spaced  $3/16$  of an inch from the center of the gage section with a notch radius of 0.08 inches. Thus diameter of the specimen at the center of the notch was  $3/16$  of an inch. This is shown schematically in Fig. 5.

The specimens that were strained in the SEM were flat tensile specimens shown schematically in Fig. 5. These samples had a 1 inch gage length, were 0.015 inches thick and 0.125 inches wide. A notch was introduced in order to decrease the area that needed to be viewed. The notch reduced the width to 0.0938 inches and had a root radius of 0.012 inches.

The final sample type was the double notch bend specimen. This had two Charpy notches introduced symmetrically from the center (Fig. 5). The goal of using a double notched specimen is of course that fracture will occur at one notch and will be very close to initiation at the second notch. However, for the double notched bend specimens metallographic cross sections did not reveal damage ahead of the notch at which fracture did not occur. It is felt that the inability to get exact alignment of the bend samples produced differences in the stresses at the notches. The fracture of these composites seems to be quite sensitive to stress level, so that when one notch would fail, the second would not be near failure.

#### IV. RESULTS AND DISCUSSION

The tensile properties of the axisymmetric tensile specimens are shown in Table 1. This data shows that the reinforced material has a lower yield and ultimate strength than the control. At a constant volume fraction the ductility of the reinforced materials was influenced by the average particle size. The ductility of the materials characterized by the smaller average particle size was less than the ductility of the materials characterized by the larger average particle size. It is believed this is due to the increased clustering of the smaller particles [8]. At a constant average particle size the ductility decreases with particle volume fraction. Fracture of the reinforced materials occurred just after necking.

Fractographs of the control material are shown in Fig. 6. These fractures are characterized by long parallel striations in the plane of fracture. The tensile specimen used to obtain these fractographs was of the transverse orientation. Therefore these striations are parallel to the extrusion direction and to the long, continuous interfaces observed in Fig. 1. The spacing of the striations is about the same as the spacing of these long continuous interfaces. Thus it would appear that these interfaces are preferential sites for fracture. In Fig. 7a is shown a polished and etched cross section of a tensile specimen of the control material just below the fracture surface. The tensile direction is vertical and the extrusion direction is into the plane of the figure; thus the long continuous grain boundaries are perpendicular to the plane of the picture. As shown in this figure there are large voids or cracks in the material just below the fracture surface which correspond to fracture of the interfaces parallel to the extrusion direction.

Examination of polished and etched cross-sections of material at the center of the unfractured notch in the double-notched tensile specimens also suggest these interfaces are prone to fracture; such cross-sections as shown in Fig. 7b show grain boundary fractures occur prior to fracture of the matrix. Such fractures were observed only in the center of the specimen and no voids or damage was observed close to the surface of the specimen. The grain boundaries which fail do so by microvoid coalescence; the voids on the interfaces (Fig. 7c) are extremely fine and the sizes are consistent with the particles observed on grain boundaries (Fig. 4).

Fracture of smooth axisymmetric tensile specimens of the reinforced material did not initiate in the interior of the specimen as did tensile fractures of the control material. As shown in Fig. 8 the fracture initiation site for the composites appeared to be large SiC carbides at the surface of the specimen. The composite materials were very sensitive to small surface defects; hardness indentations on the surface of tensile specimens reduced the ductility and fracture invariably was initiated at the hardness indentation. While fracture initiation in smooth axisymmetric tensile specimens appears to initiate close to the surface at

large SiC particles the fracture process appears to involve grain boundary fracture, fracture of SiC particles and cracks following SiC/matrix interfaces.

The fracture surfaces of the transverse tensile specimens of the composites (Fig. 9b,c) differ from that of the control in that SiC particles are visible and the parallel striations seen in the control are not clearly as visible. That the striations are not as visible does not necessarily imply the grain boundaries in the composite are less prone to fracture than those of the control; it is more likely the SiC particles alter the fracture path sufficiently to make the fracture of grain boundaries less apparent. The importance of the grain boundaries in the composite materials is reinforced by fracture surfaces in Fig. 9d,e. Here the tensile axis is to the right and the extrusion direction and the direction of the long continuous grain boundaries is also to the right. Fracture of these continuous interfaces is clearly suggested. Cross-sections of the remaining notch in double notched tensile specimens also indicate that these grain boundaries are prone to fracture. As shown in Fig. 10, a micrograph of a region at the base of the unbroken notch, grain boundary fractures appear to run between unfractured SiC particles. This micrograph indicates that, at least in some regions, grain boundary fracture of the matrix can precede fracture of SiC particles or decohesion of SiC/matrix interfaces. Another micrograph (Fig. 11), again close to the base of the unfractured notch, shows SiC particles which have fractured and voids or SiC/matrix decohesion. Fracture through the matrix connects the fractured particles and the voids at the SiC/matrix interfaces.

Examination of notched tensile specimens deformed in the SEM reinforce this picture. A specimen prior to deformation is shown in Fig. 12a. As shown in Fig. 12b, fracture initiated at an inclusion and then propagated by going around the SiC particle next to the inclusion, then going through the matrix and then by fracture of a SiC particle; the fracture of the second SiC particle appeared to be assisted by a pre-existing defect. Also shown in Fig. 13 are SiC particles below the fracture surface which were initially unbroken and have fractured. Finally, a secondary crack associated with the fracture of an *in situ*

specimen is seen in Fig. 14. The matrix fracture seems to follow grain boundaries. Crack advance is also associated with the fracture of particles and by decohesion of the SiC particle matrix interface.

## V. CONCLUSIONS

1. The reduction in area in uniaxial tensile specimens is about 0.33 for the unreinforced matrix alloy but the reductions in area for the matrix alloy reinforced by SiC particles are less than 0.05. The yield strengths of the composite materials are slightly less than that of the matrix alloy.
2. The grain boundaries of the matrix alloy are highly prone to fracture. In uniaxial tension grain boundary fracture precedes any intra-grain fracture. The matrix grain boundaries are also susceptible to fracture in the reinforced alloys; in some regions grain boundary fracture precedes either SiC fracture or decohesion of SiC/matrix interfaces.
3. The tensile fractures of the control and of the composites are fundamentally different in that the fracture of the control initiates in the center of the tensile neck while that of the composites initiates at the surface of the specimen. In smooth axisymmetric tensile specimens, fracture appears to be associated with large SiC particles close to the specimen surface.
4. Metallographic examination of cross-sections of the remaining notch in double-notch tensile specimens and observations of tensile specimens in the SEM suggest that in some regions grain-boundary fracture of matrix material can precede fracture of SiC particles or decohesion of SiC/matrix interfaces. In addition, cracks, once initiated, are often observed to grow along the SiC/matrix interface; this means that many of the SiC particles seen on the fracture surface have not been fractured.

## REFERENCES

1. Divecha, Fishman and Karmarker, *Journal of Metals* 33, 12 (1981).
2. Nair, Tien and Bates, *International Met. Rev.* 30, 275 (1985).
3. Arsenault, and Fisher, *Scripta Met.* 17, 67 (1983).
4. Edelson and Baldwin, *Transactions of ASM* 55, 230 (1962).
5. A. Gangulec and J. Gurland, *Trans. AIME* 239, 269 (1967).
6. C.R. Crowe, R.A. Gray and D.F. Hasson, in Proceedings of the Fifth International Conference on Composite Materials (ICCMV), eds. H.C. Harrigan, Jr., J. Strife, A.K. Dhringra, The Metallurgical Society, Warrendale, PA, 843-866 (1986).
7. You, Thompson and Bernstein, *Scripta Met.* 21, 181 (1987).
8. J.J. Lewandowski, C. Liu and W. Hunt, *Mat. Sci. and Engrg.* A107, 241 (1989).



TABLE 1

## TENSILE DATA

SiC f(R <sub>0</sub> )	Y.S. (ksi)	UTS (ksi)	% RA	n
0.0	83.5	86.5	33.3	0.040
.15 (5 μm)	71.8	78.8	4.3	0.052
.15 (16 μm)	74.9	80.3	5.3	0.046
.20 (5 μm)	69.5	77.7	3.6	0.055
.20 (16 μm)	72.8	78.4	4.7	0.048

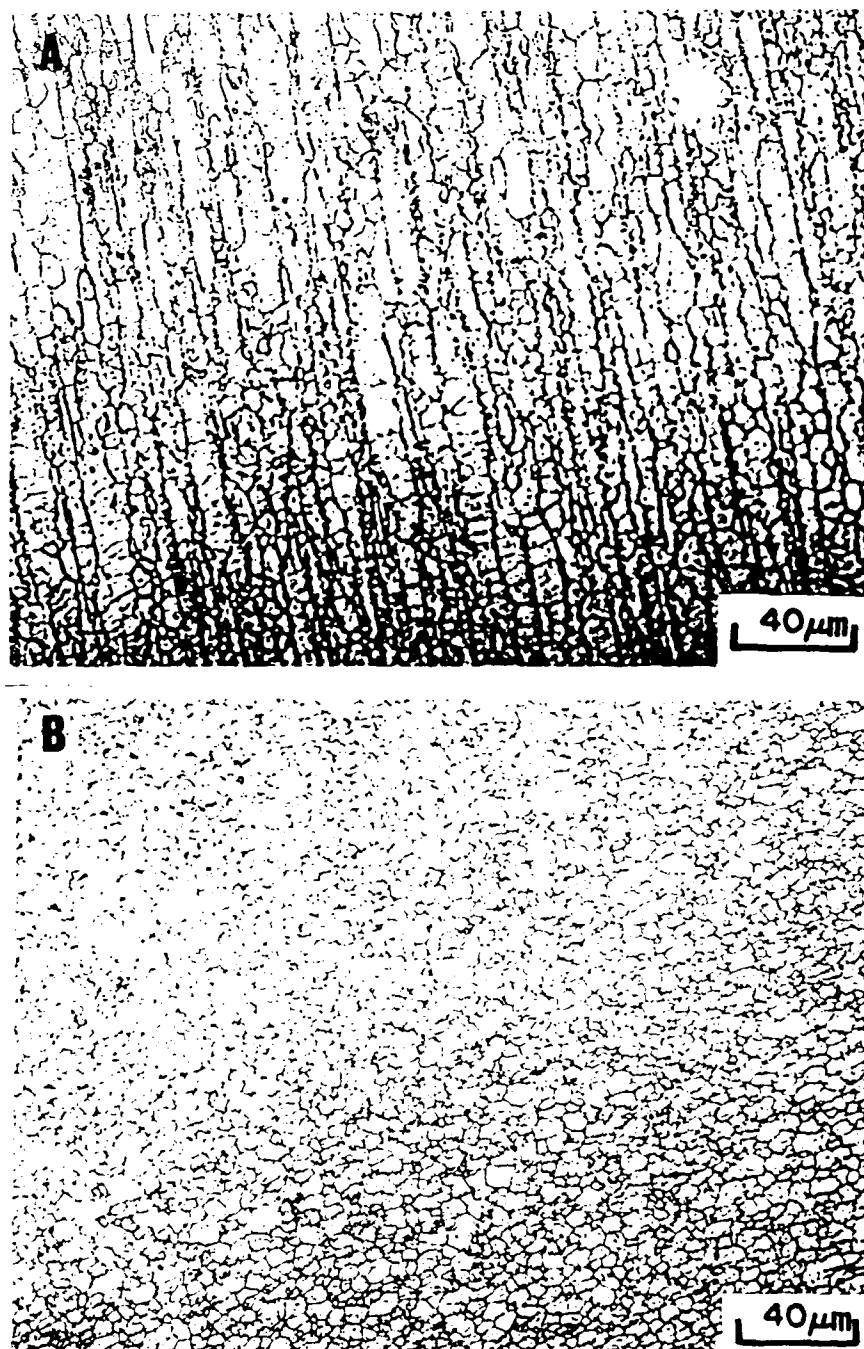


Fig. 1 Optical micrographs of (a) longitudinal and (b) transverse sections of the matrix material containing no SiC particles (control).

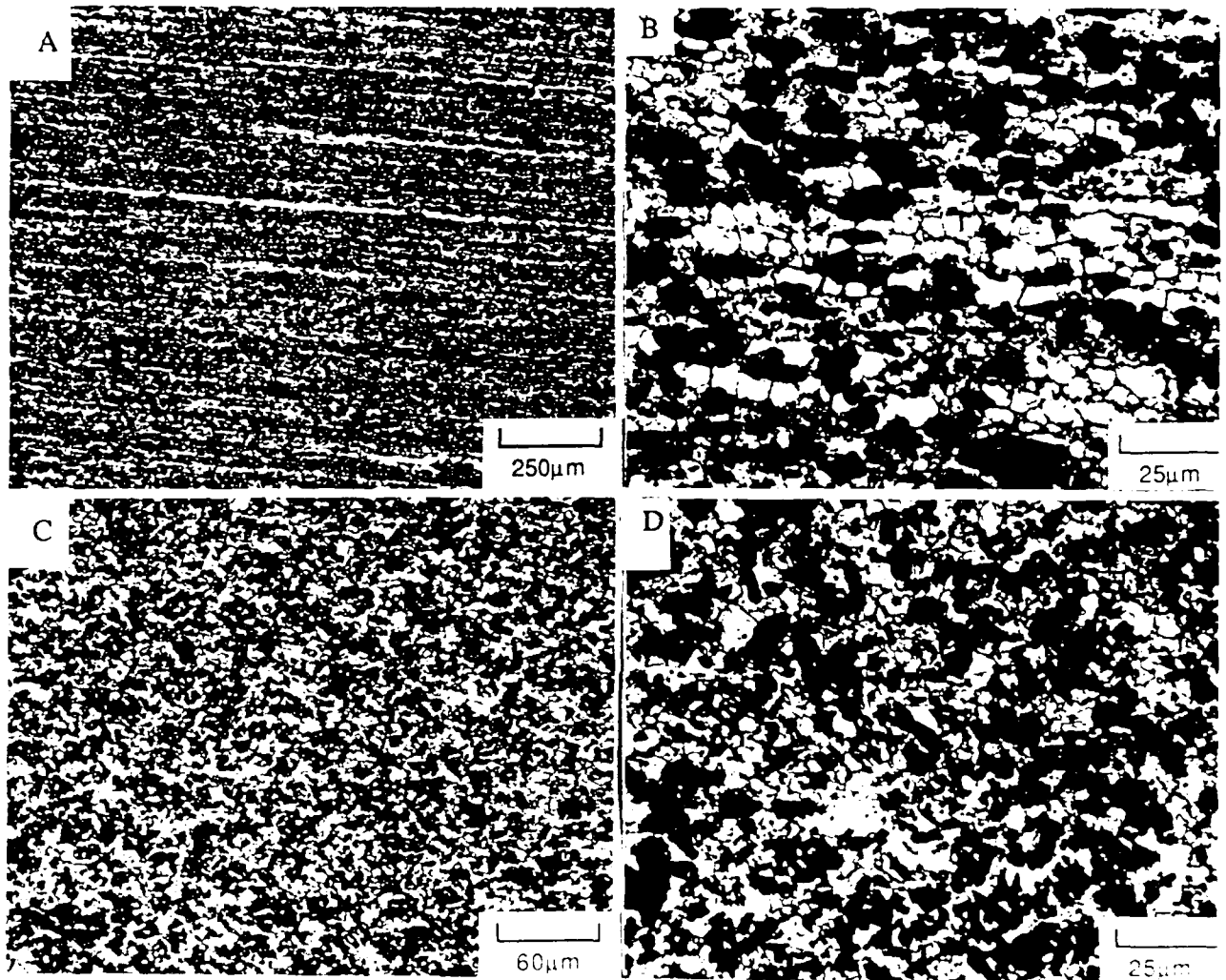


Fig. 2 Optical micrographs of the reinforced material containing 20 vol.% of 7μm SiC particles. The micrographs in (a) and (b) are of planes parallel to the extrusion direction (longitudinal section) and the micrographs in (c) and (d) are of planes perpendicular to the extrusion direction (transverse section).

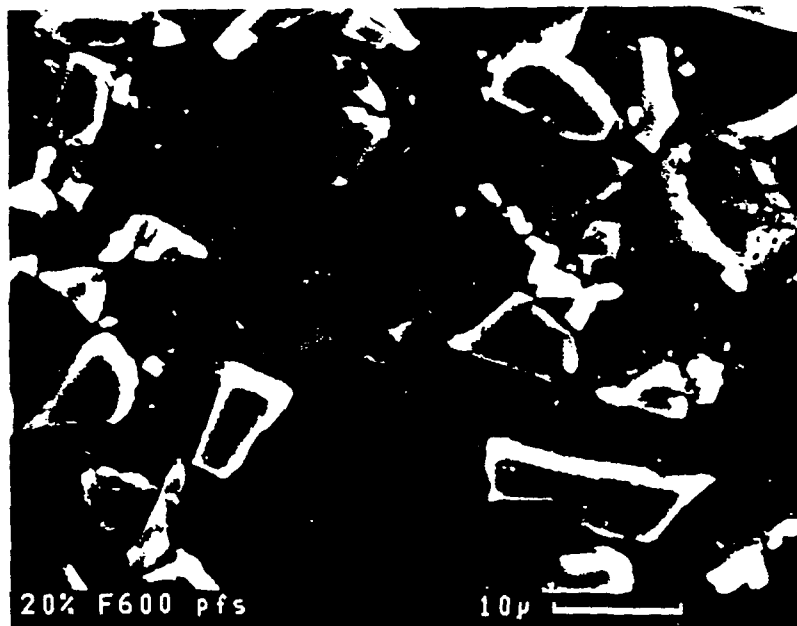


Fig. 3. A large inclusion typical of those in both the matrix and reinforced materials. The inclusion contained aluminium, copper and iron.

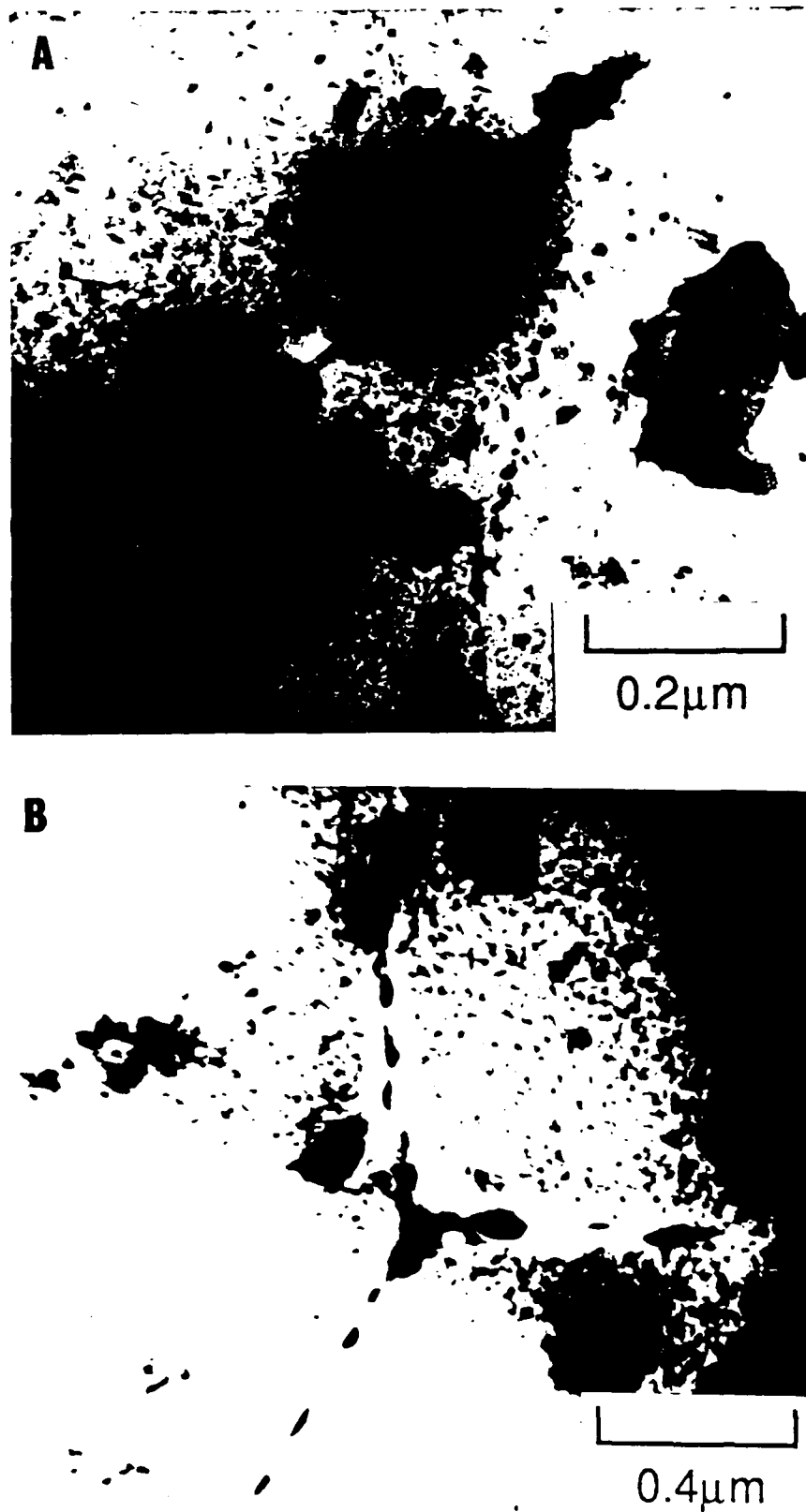
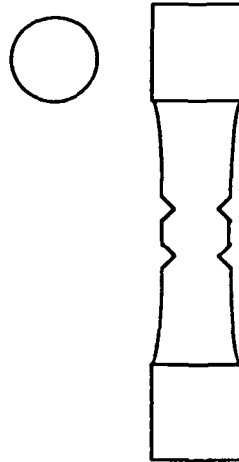


Fig. 4 TEM bright field micrographs showing precipitates within the matrix and at the grain boundaries, a precipitate free zone and dispersoids at the grain boundaries.

## 1. DOUBLE NOTCH BEND SPECIMENS



## 2. DOUBLE NOTCH TENSILE SPECIMENS



## 3. IN-SITU TENSILE SAMPLES

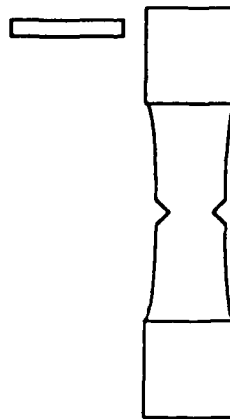


Fig. 5 Schematic diagrams of specimens used to investigate the fracture process.

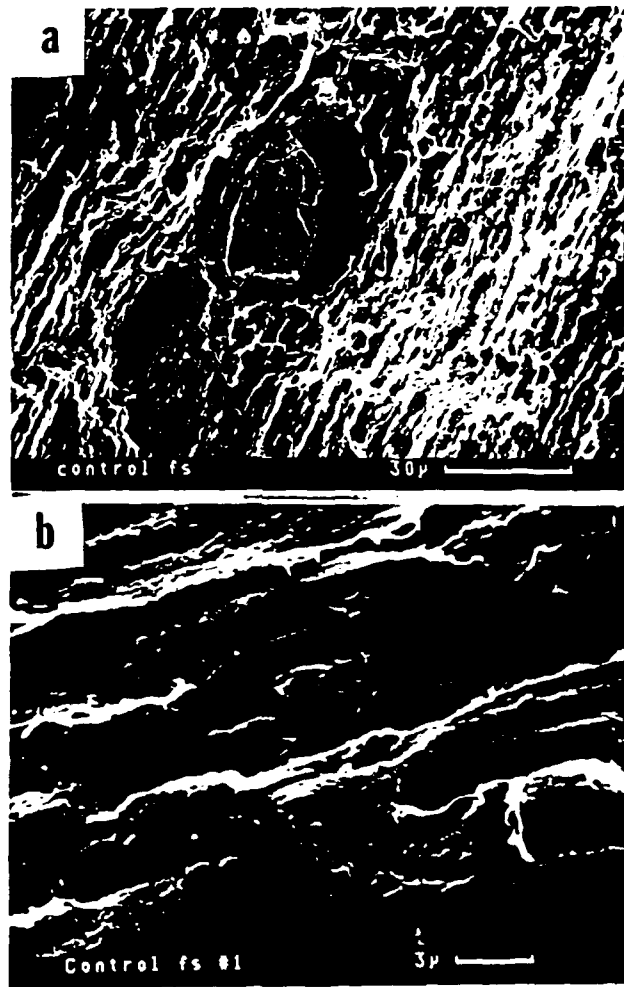


Fig. 6 Fractographs of tensile specimens of the control material. The tensile axis of this specimen was normal to the extrusion direction. Note the striations on the fracture surface which run parallel to the extrusion direction.

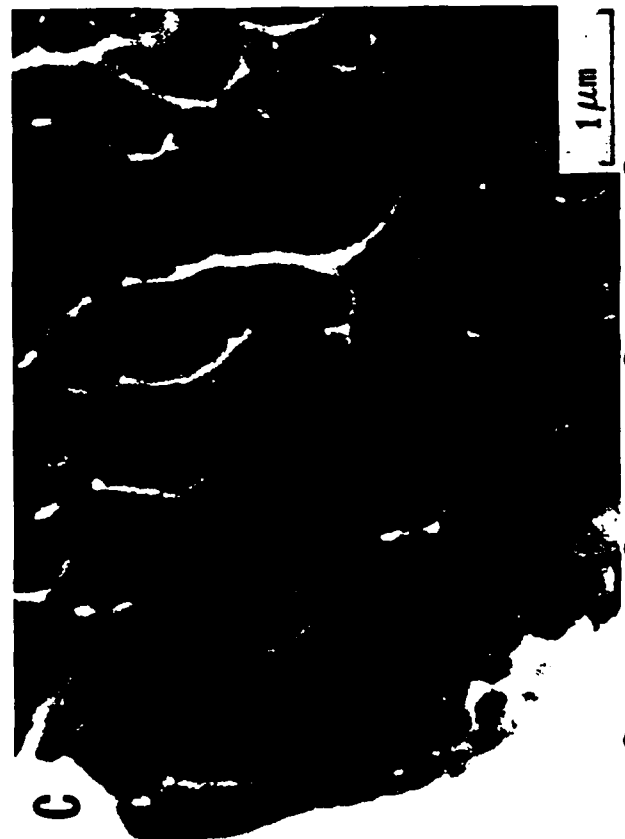
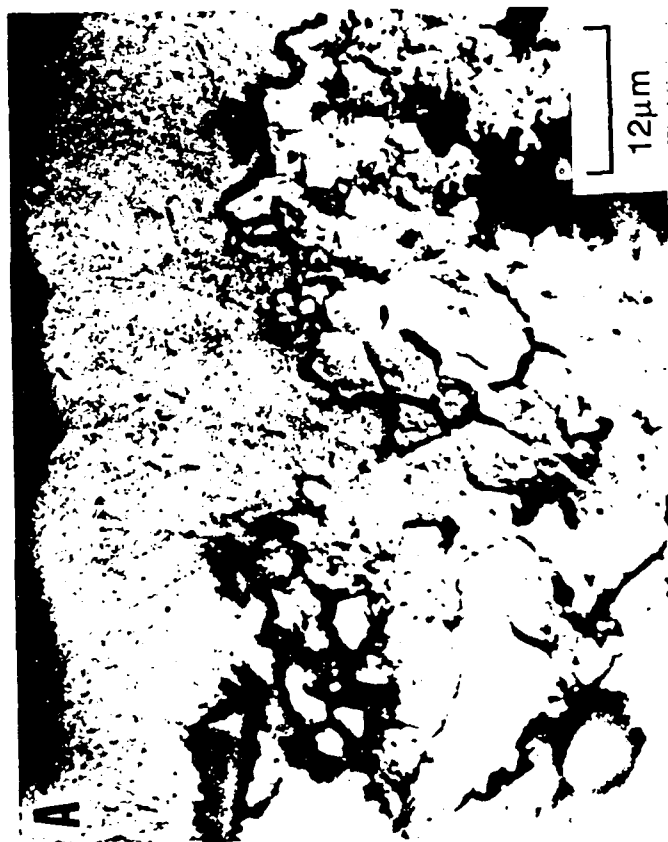


Fig. 7 (a) The cross section of a fractured tensile specimen of the control showing grain boundary fracture below the fracture surface. (b) A cross section of the center portion of the unfractured notch in a double notched tensile specimen of the control. Voids are observed at grain boundaries. (c) A higher magnification micrograph of the flat parallel regions associated with fracture of the control as seen in Fig. 6b.



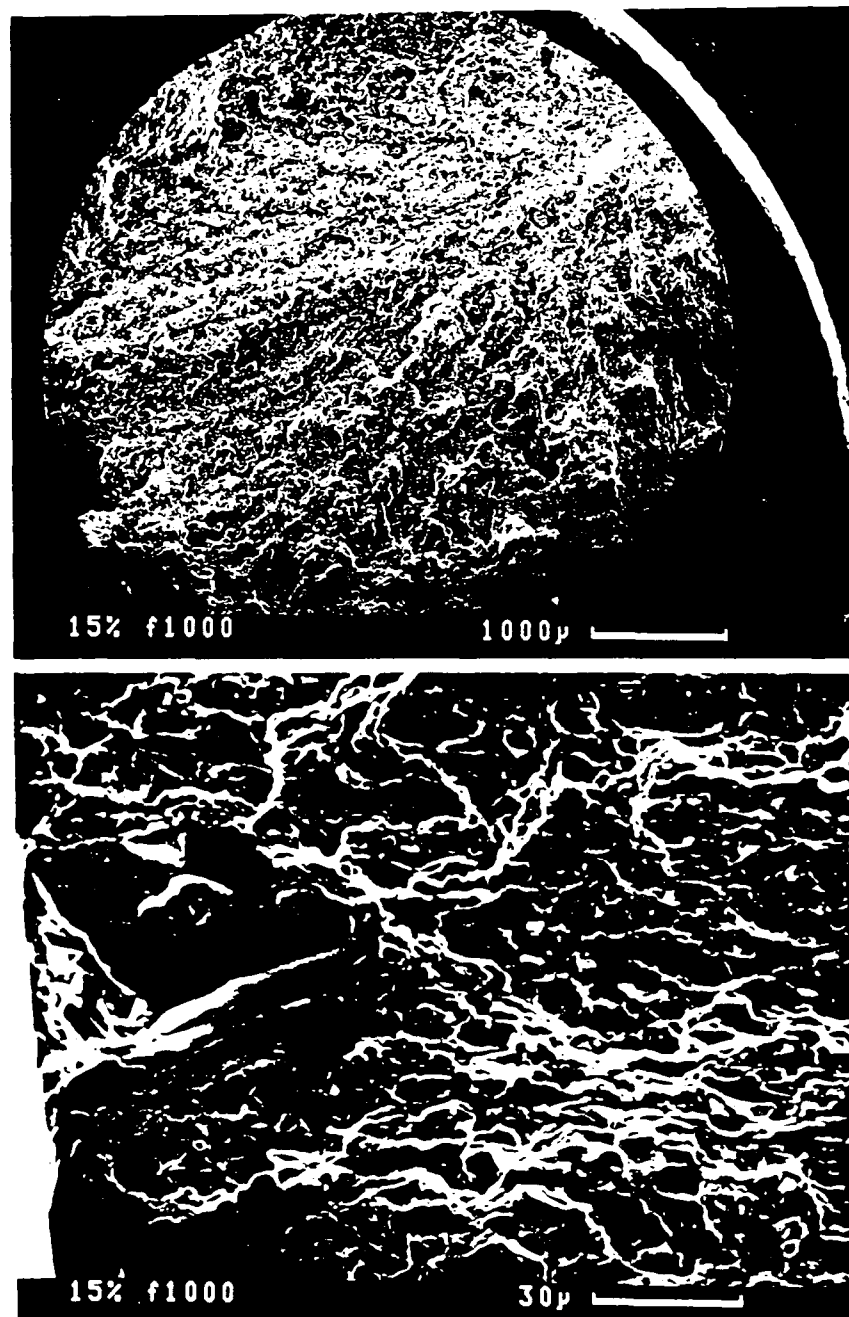


Fig. 8 Fractographs of tensile specimens of the composite containing  $f=0.15$  of  $7\mu\text{m}$  SiC particles. Fracture has initiated close to the surface at a large SiC particle. This was typical of all tensile specimens of the composites.

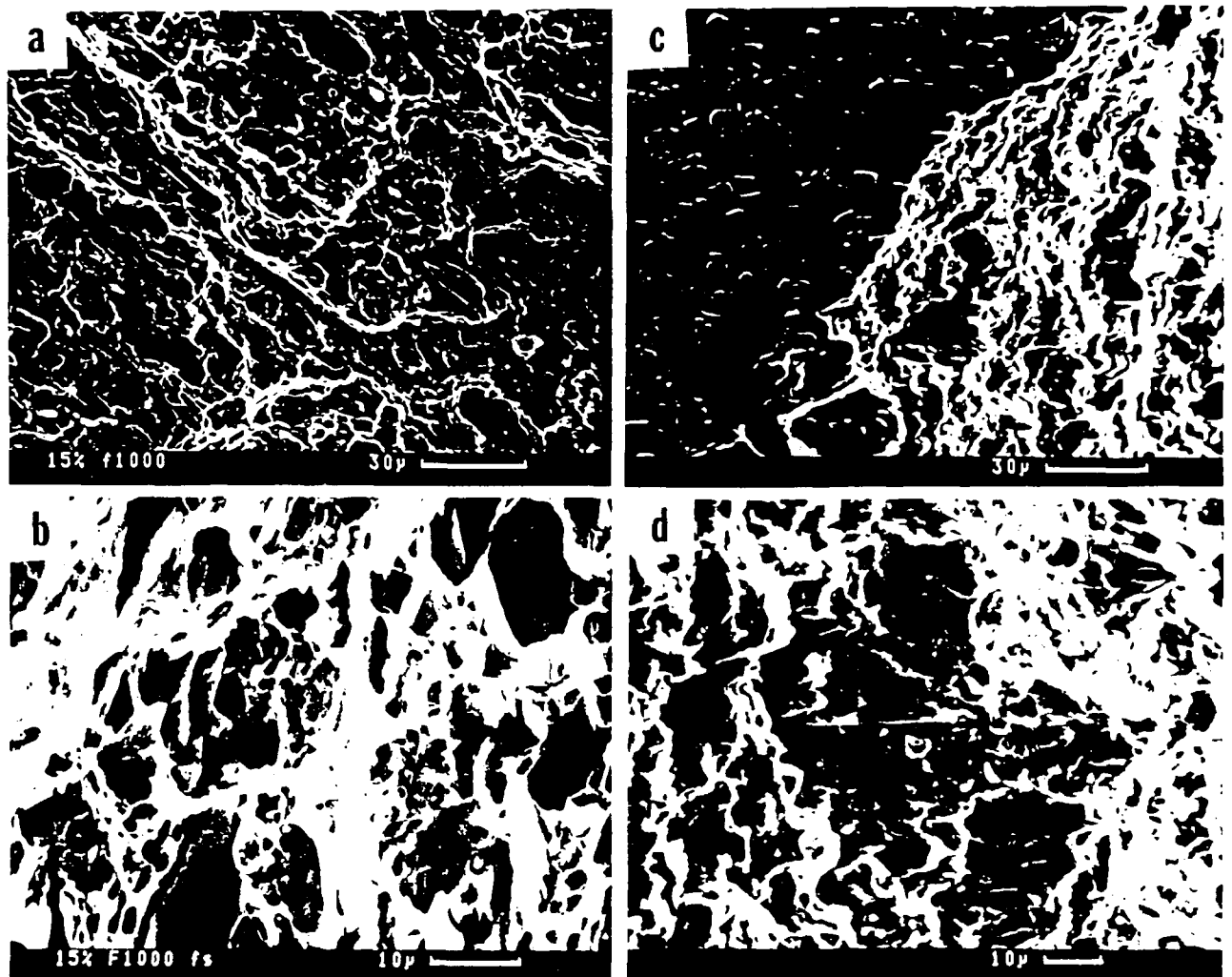


Fig. 9 Shown in (a) and (b) are fractographs of tensile specimens  $f=0.15$  composite containing  $7\mu\text{m}$  SiC particles. The tensile axis was normal to the extrusion direction. The striations parallel to the extrusion direction are not as obvious as for the control. Shown in (c) and (d) are micrographs of the fracture surface of a tensile specimen of the  $f=0.15$  composite containing  $7\mu\text{m}$  SiC particles. The tensile axis is parallel to the extrusion direction. Grain boundary fracture is evident.

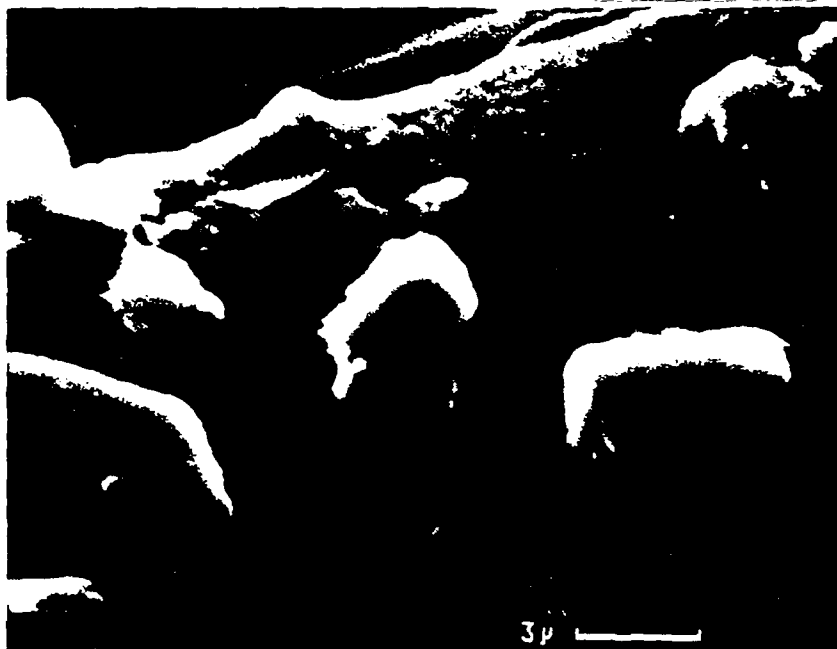


Fig. 10 A cross-section of the unfactured notch in a double notch specimen of the  $f=0.15$  composite containing  $7\mu\text{m}$  SiC particles. The region is close to the base of the notch.

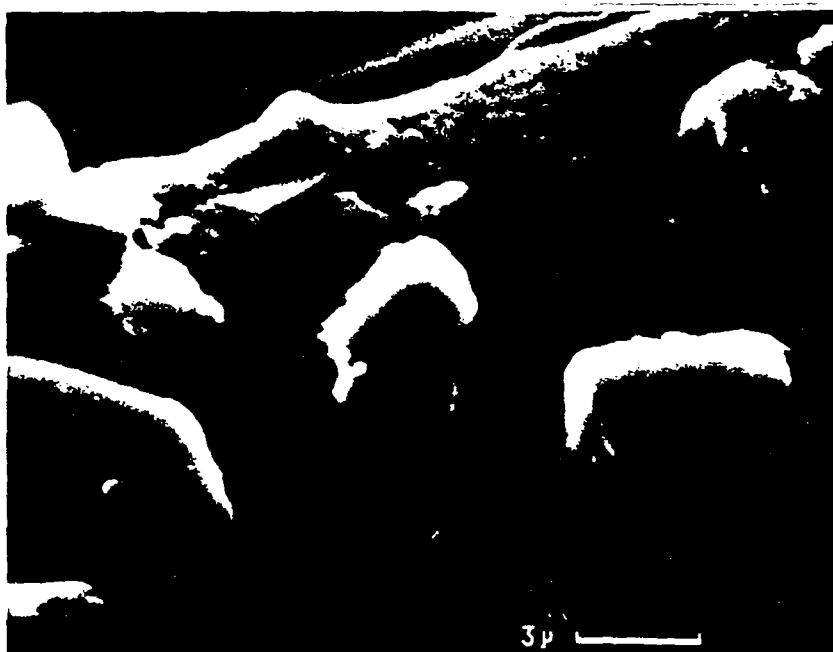


Fig. 10 A cross-section of the unfractured notch in a double notch specimen of the  $f=0.15$  composite containing  $7\mu\text{m}$  SiC particles. The region is close to the base of the notch.

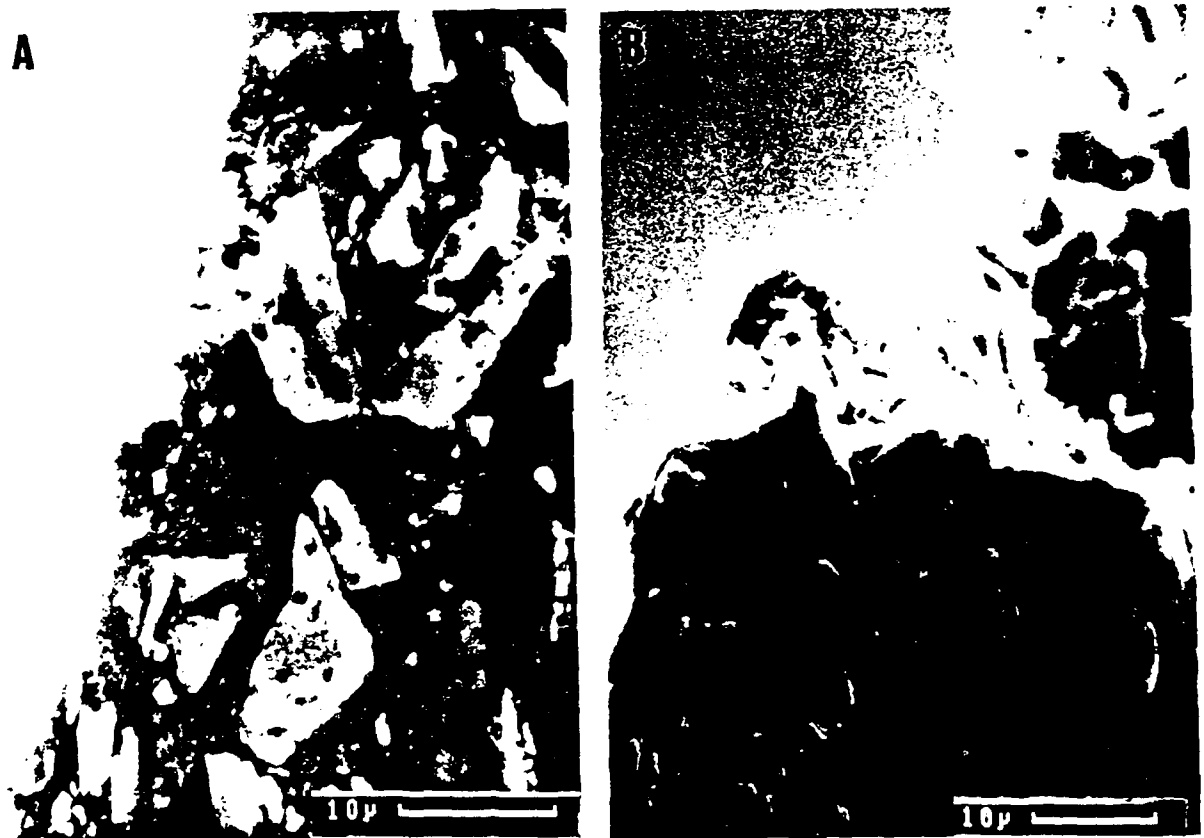


Fig. 12 Micrographs of an *in-situ* specimen prior to fracture (left) and after fracture (right). Fracture began at an inclusion at the surface, ran around a SiC particle, through the matrix and then through a SiC particle. Note the open cracks in some of the SiC particles below the fracture surface.



Fig. 13 Micrographs showing fractured SiC particles below the fracture surface of an *in-situ* tensile specimen.

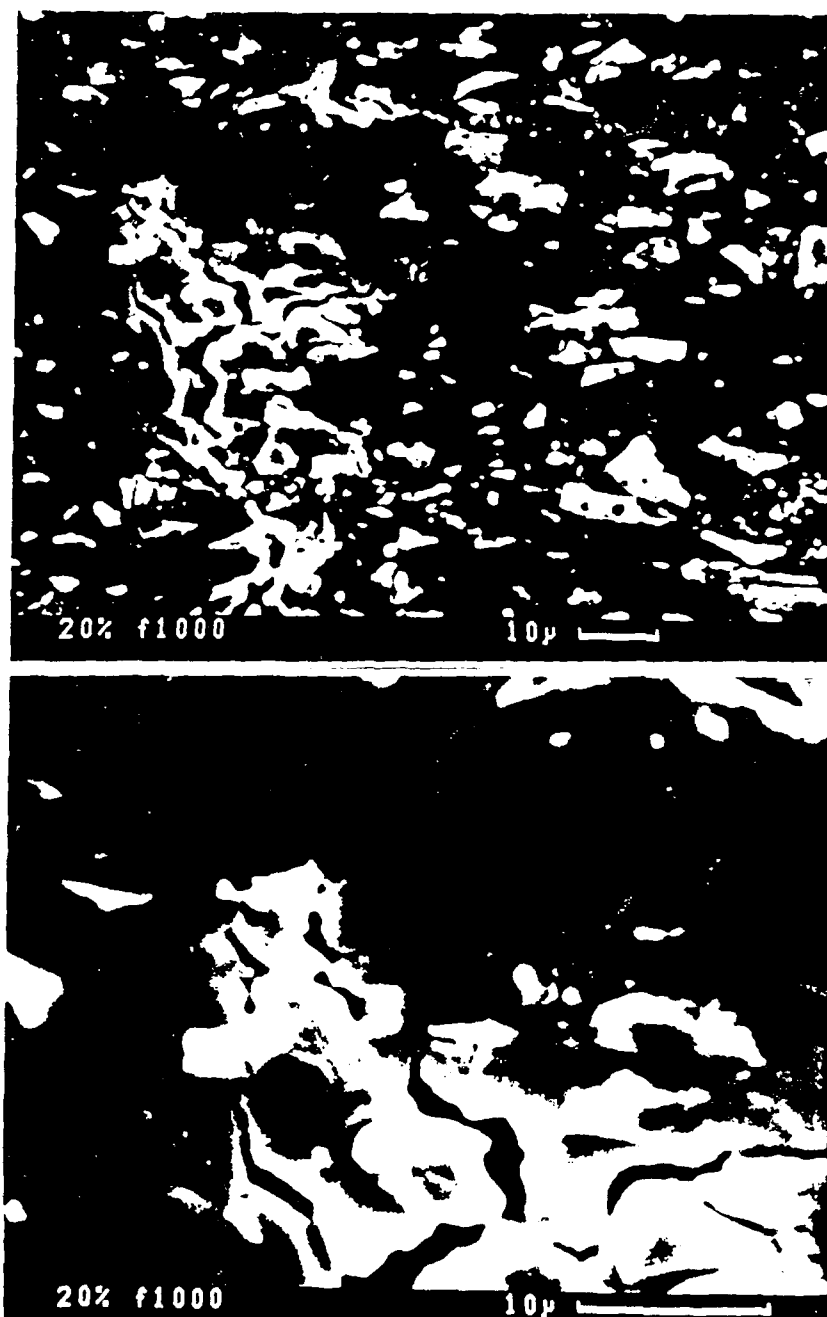


Fig. 14 Micrographs of a branching secondary crack. Note the path appears to be intergranular as it runs through the matrix. Fractured SiC particles are evident as are cracks running along matrix-SiC interfaces.

